Structural acoustics of perforated panels

Anoop A. M.

Department of Mechanical Engineering
Indian Institute of Science
Bangalore, India

This thesis is submitted for the degree of
Doctor of Philosophy

June 2019

I would like to dedicate this thesis to my school teachers *Naṁbēśaṅ māṣ, Padmaja teacher* and *Vāsudēvaṅ māṣ*.

Declaration

I hereby declare that except where specific reference is made to the work of others, the contents of this dissertation are original and have not been submitted in whole or in part for consideration for any other degree or qualification in this, or any other university. This dissertation is my own work and contains nothing which is the outcome of work done in collaboration with others, except as specified in the text and Acknowledgements.

Anoop A. M.
June 2019

Acknowledgements

I am deeply indebted to my advisor Prof. Venkata R. Sonti for his fundamental role in my doctoral work. He has been my constant source of guidance, assistance and wisdom during my research work. In addition to the academic relationship, I greatly value the personal rapport that Prof. Sonti and I have forged over years. My Ph.D. work would never have been possible without the help of Prof. Gourav Tomar, who provided me the much needed computation infrastructure. Thank you Sir. I owe a great debt of gratitutde to my M.Tech. advisors Dr. Manjuprasad and Dr. Somenath Mukherjee at the National Aerospace Laboratory, Bangalore. They were the reason why I decided to pursue a career in research.

I would like to thank all my teachers at the Indian Institute of Science, especially Prof. C. S. Jog, Prof. C. S. Manohar, Prof. Rudra Pratap, Prof. Ananthasuresh for the significant help their courses have had on my research. I am very thankful to Prof. Namrata Gundiah and Prof. J. H. Arakeri for providing me the financial assistance during a critical period in my research work. I gratefully acknowledge the members of DCC, in particular Prof. Bobji and Prof. Govardhan for their valuable advices on the progress of my Ph.D. work.

The members of the two labs, the Vibro-Acoustics Lab and the Multiphase Flow Simulation Lab have contributed immensely to my personal and professional time at IISc. The two groups have been constant source of friendship and collaboration. I would particularly like to thank Ananthan, Kiran, Prapanch, Maneesh, Biswajith, Vachan, Reginald and Sreekumar. I am fortunate to have Aswin, Maddy, Anirudh, Jayee, Nidhil and Sayuj by my side who are more than just friends to me. Thank you mates! My time at IISc. was also enriched by the Malayali cultural group 'SIMA'. I thank my friends Deekshith, Sreeraman, Ravi, Manu, Umesh, Koshy, Mithun Menon, Nipin, Sandeep and Greegar in the SIMA group. I would also like to extend my thanks to Somavathi, Chinnamma, Devaki, Banu, Sampath and Mangala at the ME Office.

My life as a Ph.D. student was extremely tempestuous. I thank the almighty for seeing me through those stormy situations. I am deeply thankful to my family for their love, support, and sacrifices. Without them, this thesis would never have been written.

This last word of acknowledgement I have saved for my dear wife Rakhee who has been patient, supportive, encouraging and stood by my side all these years. Thank you!

Abstract

In this work, radiation and transmission of sound through flexible perforated panels set in infinite rigid baffles are investigated. The treatment is largely analytical using Fourier transforms and contour integrations. Numerical calculations are only used occasionally. The work is largely divided into three parts: the first part involves radiation and transmission studies using the one-way coupled formulation, the second part investigates the same problems using the two-way coupled (or the fully-coupled) formulation and the third part involves derivations of closed form expressions for the modal coupling coefficient using contour integration.

In the first part, the panel with perforations is placed in a baffle that is perforated or unperforated. Having an unperforated or a differently perforated baffle presents challenges. It causes a certain coupling of wavenumbers leading to an integral equation. In the literature so far, the baffle has been taken to be similarly perforated, thus, simplifying the situation. The perforations are arrays of circular holes and are mathematically modeled using a perforation ratio. An existing model for a circular hole that transmits sound is used and the collective array is modeled using a perforate impedance. Since, there is an escape of fluid through the perforations as the panel vibrates (radiating or transmitting sound) an averaged fluid particle velocity over the panel surface is derived using fluid continuity and momentum equations. This averaged fluid velocity is then used along with impedances to compute the pressures and sound powers. In addition, the presence of the holes shifts the resonance frequencies and modifies the modeshapes. This shift is accounted for using the Receptance method. The entire derivation is done in the wavenumber domain (spatial Fourier transform). And at the end, numerical calculations are done. For the radiation and transmission problems, the results are presented in terms of the radiation efficiency and the transmission loss, respectively.

It is observed that the perforations reduce the *in vacuo* natural frequencies of the panel. For the radiation problem, analytical expressions for the radiated power and radiation efficiency are derived in an integral form and numerical results are obtained for different perforation parameters such as perforation ratio, hole diameter and number of holes. It is observed that a reduction in the perforate impedance leads

to a decrease in the radiated power and also in the radiation efficiency. The effects of resistive and reactive hole impedances on the sound radiation are also discussed. For the transmission problem, it is found that the perforate impedance acts in parallel to the panel impedance and for a real-world scenario, where the perforate impedance is less than the panel impedance, a reduction in the transmission loss (TL) can be achieved with perforations on the panel. For small holes at lower frequencies the resistive impedance dominates over the reactive impedance. This results in a higher TL at lower frequencies for a micro-perforated panel as compared to that for a panel of same perforation ratio but with larger holes.

In the second part, the same two problems of radiation and transmission of sound through perforated panels set in rigid baffles are studied using the two-way coupled or fully coupled formulation. In addition to the details presented for the one-way cases above, here two equations are derived where the average fluid particle velocity and the panel velocity depend on each other. Thus, a coupled problem needs to be solved. Due to the inclusion of the fluid loading, a modal coupling coefficient arises in the formulation. This coupling coefficient is indicative of the degree of coupling between the *in vacuo* panel modes caused by the acoustic fluid. In several of the earlier studies on unperforated panels, in the literature, largely the self modal coupling has been investigated. Only a few studies have presented studies on the cross modal coupling. These studies were restricted to the low frequencies. The formulation is reduced to a single coupled equation and the system of equations (including the modal coupling coefficient) are solved numerically. Again, the results are presented in terms of the radiation efficiency and the transmission loss. The natural frequencies are identified from the peaks in the mean panel quadratic velocity spectrum and compared with results from the literature.

It is observed that the radiation efficiency decreases with the increase in the perforation ratio, irrespective of the surrounding acoustic medium. For a given perforation ratio, the water-loaded panel radiation efficiency is found to be less than that for a panel immersed in air. It is also observed that for a light fluid like air, a one-way coupled formulation is adequate. Further, a fully coupled model for the transmission problem is also developed. It is observed that the TL of a perforated panel acquires negative values at low frequencies. This apparent anomaly is resolved by taking into account the additional power component that flows from the baffle region onto the panel at low frequencies.

In the last part of the thesis, approximate expressions in closed form are obtained for the modal coupling coefficient using the contour integration. Analytical expressions valid for any given fluid loading conditions are derived for the modal interactions between the corner modes, single and double edge modes and the acoustically fast modes. This is further used to evaluate the natural frequencies and the radiation efficiency of the perforated panel. The results agree very well with those obtained earlier in the thesis using the numerical integration. Also, plots of the resistive and reactive parts of the modal coupling coefficient are presented and discussed.

Table of contents

List of figures

List of tables

Nomenclature

$< |v_p|^2 >$ Spatially averaged squared panel velocity

B_r Modal coefficient of the r^{th} mode

D Bending stiffness of an unperforated panel

D^* Effective bending stiffness of a perforated panel

E Young's modulus of the panel material

F Magnitude of the point harmonic force

M_r Modal mass of the r^{th} mode

N_0 Number of holes in a panel

S_h Total area of the hole region

S_p Area of the panel

W Radiated power

W_i Power of the incident plane wave

W_t Transmitted power

W_{flow} Power flow through the perforated panel

$W_{\text{inc-rad}}$ Additional power incident due to diffraction

W_{refl} Reflected power

Z_0 Hole impedance

Z_a Acoustic impedance

Z_w Wave impedance of an acoustically loaded panel

Z_{0b} Hole impedance over the baffle region

Z_{0p} Hole impedance over the panel region

Z_{react} Reactive impedance of a hole

Z_{resist} Resistive impedance of a hole

Z_{wp} Wave impedance of an *in vacuo* panel

η Damping loss factor

η_0 Viscosity of the acoustic medium

λ, μ Wavenumber transforms of the x and y coordinates, respectively

$\lambda_{1,2}$ Branch points

ν Poisson's ratio

ω Frequency in rad/s

ω_r Natural frequency of the r^{th} mode of a perforated panel

ω_{co} Coincidence frequency of an infinite panel

ω_{mn} Natural frequency of the $(m, n)^{\mathrm{th}}$ mode of an unperforated panel

$\overline{<|v_p|^2>}$ Spatially averaged squared panel velocity averaged over all forcing locations

$\overline{W}$ Radiated power averaged over all the forcing locations

$\overline{\Theta}_{mnpq}$ Modal coupling coefficient

$\overline{\sigma}$ Average sound radiation efficiency

ϕ_{mn} $(m, n)^{\mathrm{th}}$ mode shape of an unperforated panel

ψ_r r^{th} mode shape of a perforated panel

ρ_0 Density of the acoustic medium

ρ_p Density of the panel material

σ Sound radiation efficiency

σ_b Perforation ratio of a baffle

σ_p Perforation ratio of a panel

τ Sound transmission coefficient

AF Acoustically fast

EP Effect of perforation

LAFP Locally averaged fluid particle

TL Sound transmission loss

θ, ϕ Polar and azimuthal angles, respectively

$\tilde{W}$ Total incident power

a, b, h Panel dimensions

c Velocity of sound in the acoustic medium

k Acoustic wavenumber

k_b Free bending wavenumber in the panel

k_m, k_n, k_p, k_q Modal wavenumbers

k_x, k_y, k_z Components of the acoustic wavenumber in the x, y and z directions, respectively

m, n, p, q, r, s Mode indices

p^+ Radiated pressure field in the $z > 0$ region

p^- Radiated pressure field in the $z < 0$ region

p_1, p_2 Total pressure field surrounding the panel-baffle system

p_i Incident pressure field

p_r Reflected pressure field

p_t Transmitted pressure field

r_p Radius of hole in the panel

v_a Locally averaged fluid particle velocity

v_f Velocity of flow through hole

v_i Normal velocity of the incident plane wave

v_p Panel velocity

w Displacement of the panel in the z direction

x, y, z Coordinates of a Cartesian coordinate system

Part I

Introduction

Chapter 1

Introduction

1.1 Motivation for research

Thin panels are commonly used in industrial applications such as machine casings, walls and roofs of machine shops, hulls of ships and fuselages of airplanes. However, it is commonly known that these panels are efficient sound radiators. More recently, panels with perforations are being used in order to reduce sound radiation and also to facilitate sound absorption. Their applications can be found in machine enclosures, safety guard coverings of fly wheels and belt drives, diesel generator housings, jet engine exhaust liners, etc. In applications like underwater sonar acoustic domes and exhaust mufflers, perforated panels are subjected to heavy fluid loading conditions. The structural acoustics of these perforated panels will constitute the central theme of this thesis for which a motivation is provided in this section.

Looking at the geometry of these perforated panels, the size of perforations can vary from sub-millimeters (as in micro-perforated panels (MPP)) to several millimeters as in the wall panels. The holes in the panels are uniformly arranged in a specific lattice pattern. In most of the applications, the perforated panels are thin in construction so that their vibration cannot be ignored in determining the sound radiation and transmission characteristics. The main advantages of perforated panels over the acoustic liners and fillers are their wide-band sound attenuation, robust construction, durability and aesthetic appeal.

In the literature, there are a few mathematical models of perforated panels available with slight differences among themselves, specially with regard to how the subsystems are modeled. The list is as follows:

- There are models for perforations (holes) in infinite rigid baffles [1].

- There are models for perforations in infinite flexible panels [2].
- There are models for perforations in finite membranes fixed on a rim [3].
- There are models of a finite panel set in an infinite rigid baffle with the same perforation ratio [4] (having a similar perforation in the baffle causes a significant simplification in the problem formulation).
- Further, there exist perforated panel models with perforations having a purely imaginary impedance or a complex impedance depending on the hole size [4, 5].

All the above studies use only one-way coupling (except for the membrane study). Thus, these models can be improved by incorporating more realistic situations such as unperforated baffles, resonance shifts in the panel due to perforations and full coupling (or two-way coupling) between the panel vibrations and the surrounding acoustic field. Further, if this study with the above augmented assumptions could be conducted using analytical or semi-analytical methods such that closed form solutions could be had, then understanding the physics will be further facilitated. Thus, the total intent of this thesis is to incorporate the above assumptions/improvements into the current existing literature on the structural acoustics of perforated panels.

1.2 Objective

In this thesis, a simply supported finite flexible perforated panel set in an infinite rigid baffle which is either unperforated or has a perforation ratio different from the panel (see Fig. 1.1) is considered. This assumption being realistic complicates the problem formulation significantly. It is the intend of this thesis to study the sound radiation and transmission through such a panel. Moreover, in the model, the resonance shifts in the panel caused by the introduction of perforations are accounted for. Lastly, the model developed is based on a fully coupled formulation, i.e., the panel vibration and the developed pressure influence each other simultaneously. The investigation is largely analytical or semi-analytical in nature with numerics brought in at the very last step. The main results involve the radiation efficiency or the transmission loss as a function of the various system parameters. The specific objectives are:

- First, using a one-way coupled formulation in the wavenumber (spatial Fourier Transform) domain, the radiation and the transmission problems are separately studied. The radiation efficiency and the transmission loss are obtained as functions of the system parameters.

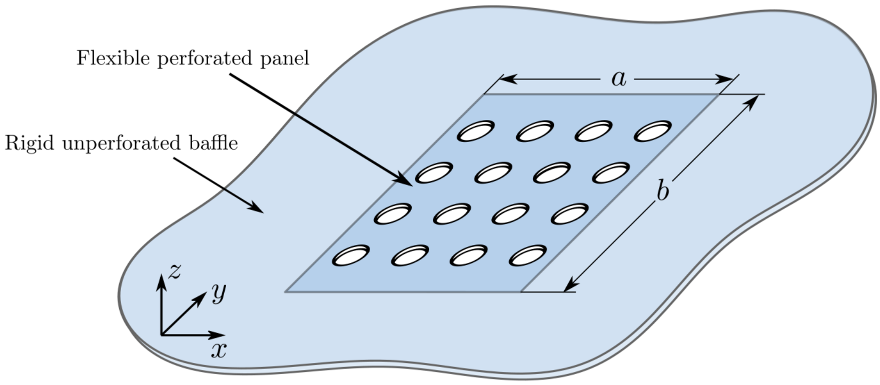

Fig. 1.1 Schematic of a perforated panel set in an unperforated baffle.

- Next, the same two problems (of radiation and transmission) are studied using a fully coupled formulation.
- Lastly, the modal coupling coefficients are classified according to their respective modal wavenumbers and approximations are obtained in closed form for each of the cases using contour integrations.

1.3 Organization of Thesis

In chapter 2, the relevant literature on the structural acoustics of unperforated and perforated panels is reviewed. It also contains additional background material that will facilitate the reading of this thesis. The intent of this is that the reader should not need to refer too much outside material in order to follow the work.

The original work reported in this thesis is organized into three parts.

- The first part is devoted to the one-way coupled analysis and is presented in chapters 3 and 4.
  - In chapter 3, a one-way coupled formulation in the wavenumber domain for the sound radiation from a finite flexible perforated panel set in a rigid baffle is developed. The formulation is general so that both the panel and the baffle can have different perforation ratios. A harmonic point force excitation of the panel is considered. The model is based on the *in vacuo* modeshapes and natural frequencies of a simply supported perforated panel. The dependence of the radiation efficiency on the various system parameters is discussed.

  - In chapter 4, the sound transmission loss of the perforated panel subjected to an incident acoustic plane wave is studied. The development in this chapter is similar to that of chapter 3.

- The second part is devoted to the two-way coupled analysis presented in chapters 5 and 6. The fluid loading is captured by the modal coupling coefficient in the panel equation of motion. And the modal coupling coefficient is expressed as a double integral over the wavenumber domain. In this part of the thesis, the double integral is evaluated numerically.

  - Chapter 5 discusses the panel vibration response to a harmonic point force excitation and the associated radiation efficiency. The shift in the resonance frequencies of the fluid-loaded perforated panel from its *in vacuo* values is also computed.
  - Chapter 6 develops the fully-coupled formulation for the transmission of a plane acoustic wave through a perforated panel.

- Chapter 7 is devoted to finding closed form expressions for the modal coupling coefficients. Individual approximate expressions are obtained depending on the panel modal wavenumbers. The expressions are general in the sense that they can be used for panels of any given perforation ratio and fluid loading conditions.

- In chapter 8, conclusions are drawn from all the important results obtained in the thesis. The avenues for future work are also briefly mentioned in this chapter.

  Appendices are provided at the end of the thesis which detail the step by step derivation of the expressions given in the main text.

Chapter 2

Background and literature survey

2.1 Introduction

This chapter presents material that will facilitate the reading of the thesis. The idea being that the reader should not need to refer too much outside material in order to follow the current work. In addition, in this chapter a survey of the relevant literature is presented.

Initially, a brief introduction to the structural acoustic analysis is presented in section 2.2. The mathematical modeling of a typical structural acoustic problem is also discussed in this section. In section 2.3, some key results for the infinitely long flexible panel are discussed. A detailed review of the studies on the sound radiation and transmission characteristics of finite unperforated panels is presented in section 2.4. The one-way and the two-way coupled models for the finite unperforated panel are also discussed here. Next, in section 2.5, an overview of the pertinent literature on the sound radiation and transmission characteristics of perforated panels is presented. In sections 2.6, 2.7 and 2.8, some of the important concepts and methods which will be used later in this thesis are discussed.

2.2 Structural acoustics

In structural acoustics, two standard methods are adopted in solving for the unknown variables in the fluid and the structural domains. The first method assumes the structure to be present in vacuum and the velocity response is computed. The structure is then placed in the acoustic medium and the velocity obtained earlier is used to compute the acoustic pressure. This is called the uncoupled or the one-way coupled formulation.

In the second method, the fluid domain and the structural domain PDEs are solved simultaneously, i.e., the fluid pressure and the structural velocity are simultaneously unknowns. This is known as the coupled or the two-way coupled formulation and is used when the fluid loading cannot be ignored [6, 7].

2.2.1 Mathematical modeling

The governing differential equation for the structure can be represented as [8]

$$\mathcal{L}\mathbf{u_s} = \mathbf{f}, \tag{2.1}$$

where $\mathcal{L}$ represents a differential operator specific to the structure model, $\mathbf{u_s}$ the generalized displacement vector and $\mathbf{f}$ the generalized force vector. The generalized force is composed of the direct excitation by any mechanical loading on the structure, denoted as $\mathbf{f_s}$, and the force exerted by the surrounding acoustic medium at the fluid-structure interface, denoted as $\mathbf{f}_{\text{int}}$ [9]. Thus we have

$$\mathbf{f} = \mathbf{f_s} + \mathbf{f}_{\text{int}}. \tag{2.2}$$

The pressure field p in the acoustic medium satisfies the Helmholtz equation

$$(\nabla^{\mathbf{2}} + \mathbf{k^2})p = 0. \tag{2.3}$$

The kinematic boundary condition at the fluid-structure interface insists that the fluid and the structural velocity at the interface in the normal direction be the same, i.e.,

$$\dot{u}_s|_{\text{int}} = \dot{u}_a|_{\text{int}} \qquad \text{(normal to the interface).} \tag{2.4}$$

The sound radiation problem

For a sound radiation problem, a direct mechanical force excites the structure and the pressure field in the acoustic medium is generated by the structural vibrations alone (radiated pressure field). The associated pressure loading on the structure can be represented as $\mathbf{f}_{\text{int}} = \mathbf{f}_{\text{rad}}$. Thus,

$$\mathbf{f} = \mathbf{f_s} + \mathbf{f}_{\text{rad}}. \tag{2.5}$$

In the one-way coupled formulation, the structure domain equation (Eq. (2.1)) is solved neglecting the radiated pressure loading from the acoustic domain, i.e., $\mathbf{f} = \mathbf{f_s}$. Now, the acoustic pressure field can be obtained using Eqs. (2.3) and (2.4).

In the two-way coupled formulation, we do not neglect the radiated pressure field. We solve Eqs. (2.1), (2.3) and (2.5) with the boundary condition Eq. (2.4), simultaneously.

The sound transmission problem

For a sound transmission problem, the structure is excited by an acoustic wave alone. No direct mechanical loading on the structure is considered for the transmission problem, i.e., $\mathbf{f_s} = \mathbf{0}$. The total pressure in the acoustic medium consists of the contributions from the incident and the radiated pressure fields. Hence, we can write $\mathbf{f}_{\text{int}} = \mathbf{f}_{\text{inc}} + \mathbf{f}_{\text{rad}}$. Thus,

$$\mathbf{f} = \mathbf{f}_{\text{inc}} + \mathbf{f}_{\text{rad}}. \tag{2.6}$$

In the one-way coupled formulation, we have $\mathbf{f} = \mathbf{f}_{\text{inc}}$ (by neglecting the radiated pressure field). We can compute the structural velocity by solving Eq. (2.1). And the acoustic pressure field is obtained by solving Eqs. (2.3) and (2.4).

In the two-way coupled formulation, we solve Eqs. (2.1), (2.3) and (2.6) with the boundary condition Eq. (2.4), simultaneously.

2.3 Structural acoustics of planar structures of infinite extent

2.3.1 Sound radiation from an infinite panel in an unbounded acoustic fluid

A 2-D problem is considered where an infinite 1-D panel is in contact with an infinite acoustic half-space on one side ($y > 0$) and has vacuum on the other side [7]. The equation of motion of the panel is

$$D\frac{\partial^4 v}{\partial x^4} + m_p\frac{\partial^2 v}{\partial t^2} = \tilde{f}\,\mathrm{e}^{\mathrm{i}k_x x - \mathrm{i}\omega t} - p(x,0,t),$$

where D is the bending stiffness of the panel, m_p is the mass per unit area of the panel, v is the displacement of the panel in the y direction. Next, $\tilde{f}$ is the complex amplitude of the external force of wavenumber k_x and frequency ω and $p(x,0,t)$ represents the acoustic pressure acting on the panel surface. The wave impedance of the acoustically loaded panel is given by

$$Z_w = Z_{wp} + Z_{wf},$$

where

$$Z_{wp} = \frac{\mathrm{i}}{\omega}\left(Dk_x^4 - m_p\omega^2\right)$$

is the *in vacuo* panel wave impedance and

$$Z_{wf} = \frac{\rho_0\omega}{k_y}, \qquad \text{where } k_y = \begin{cases} \sqrt{k^2 - k_x^2} & \text{if } k_x < k \\ \mathrm{i}\sqrt{k_x^2 - k^2} & \text{if } k_x > k \end{cases}$$

represents the acoustic impedance.

When $k_x < k$ or when the phase speed of the forcing field is greater than the speed of the acoustic wave, Z_{wf} is purely real and indicates that the acoustic fluid acts as a damper to the panel vibrations. The vibrational energy from the panel is radiated away in the form of acoustic plane waves at an angle $\cos^{-1}(k_x/k)$ to the panel surface. When $k_x > k$, the acoustic impedance is negative imaginary and the surrounding fluid acts as an inertia loading on the panel. The added inertia is equivalent to the mass of a fluid layer of thickness $1/|k_y|$. In this case, only evanescent waves are generated in the acoustic medium, which decay exponentially. To summarize, for a fluid-loaded infinite panel, the sound radiation occurs only when the phase speed of the forcing field is greater than the speed of sound in the acoustic medium. When it is less, only the surface waves exist in the acoustic medium and the fluid loading is inertial in nature.

2.3.2 Sound transmission through an infinite panel in an unbounded acoustic fluid

This is again a 2-D problem consisting of an infinite 1-D panel having an acoustic half-space on either side. An acoustic plane wave of wavenumber k and frequency ω is incident on the panel at an angle ϕ to the normal as shown in Fig. 2.1. The trace wavenumber (along the panel surface) of the incident acoustic plane wave is $k_z = k\sin\phi$ and the wavenumber normal to the panel surface is $k_x = k\cos\phi$. Following the incidence of the plane wave, the panel vibrates and pressure waves are transmitted to the other half-space. The sound power transmission coefficient, a ratio of the power transmitted per unit area of the panel to the total incident power per unit area of the panel is given by

$$\tau = \left| \frac{2Z_{wf}}{2Z_{wf} + Z_{wp}} \right|^2,$$

where

$$Z_{wp} = \frac{\mathrm{i}}{\omega}\left(Dk_z^4 - m_p\omega^2\right) + \frac{D\eta k_z^4}{\omega}$$

is the *in vacuo* panel wave impedance and

$$Z_{wf} = \frac{\rho_0\omega}{k_x}$$

represents the acoustic impedance.

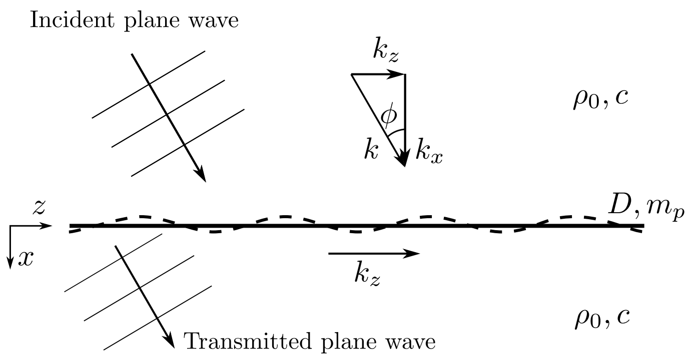

Fig. 2.1 Transmission of an acoustic plane wave through an infinite flexible panel.

The transmission coefficient is found to be the maximum when the reactive part of $2Z_{wf} + Z_{wp}$ vanishes and is referred to as the coincidence condition. At coincidence, the free bending wavenumber in the panel ($k_b = \left(m\omega^2/D\right)^{1/4}$) is equal to the trace wavenumber in the acoustic medium (k_z). Thus, for a given angle of incidence of the plane wave, the coincidence frequency is given by

$$\omega_{co} = \left(\frac{m_p}{D}\right)^{1/2}\left(\frac{c}{\sin\phi}\right)^2,$$

where c is the speed of sound in the acoustic medium of density ρ_0.

When $k_z < k_b$, i.e., the trace wave speed of the incident acoustic field is greater than the phase speed of the free bending waves in the fluid, the power transmission coefficient is dominated by the inertia term and we can approximate

$$\tau \approx \frac{1}{1 + \left(\frac{\omega m_p \cos\phi}{2\rho_0 c}\right)^2}.$$

Now, when $k_z > k_b$, the stiffness term dominates in the power transmission coefficient and we can approximate

$$\tau \approx \frac{1}{1 + \left(\frac{Dk^4 \sin^4 \phi \cos \phi}{2\rho_0 c\omega} \right)^2}.$$

At coincidence, i.e., $k_z = k_b$, the transmission coefficient is controlled by the structural damping η.

In [10], Junger summarizes the evolution of analytical solutions of the fluid-loaded panel response. For a flexible panel of infinite extent, the flexural vibration field can be expressed using a single wavenumber component [7]. However, for a finite panel, there exist flexural waves of many wavenumbers due to the reflections from the boundary. The next section presents the structural acoustics of finite unperforated panels.

2.4 Structural acoustics of finite unperforated panels

The radiation and transmission of sound related to rectangular panels has been discussed extensively in the literature. For the radiation problem, the panel set in an infinite rigid baffle is excited by an external force and the acoustic pressure field generated by the panel vibration is obtained by solving the Helmholtz equation with the boundary condition imposed at the panel-fluid boundary [7]. The resulting sound power can be evaluated by integrating the sound intensity either over a hemisphere enclosing the panel or over the surface of the vibrating panel [11]. The results are presented in terms of the radiation efficiency which is defined as the ratio of the sound power radiated by the panel to that of a uniformly vibrating baffled piston having the same surface area as that of the panel [7], i.e.,

$$\sigma = \frac{W}{\frac{1}{2}\rho_0 cab < |v_p|^2 >},$$

where W is the radiated power from the panel of dimensions $a \times b$, $< |v_p|^2 >$ is the spatially averaged squared velocity of the panel and ρ_0 is the density of the acoustic medium in which the sound propagates at a speed c. Another quantity which is discussed in the literature is the radiation resistance and it can be obtained by multiplying the radiation efficiency by the acoustic impedance of the medium and the surface area of the panel.

On the other hand, for a sound transmission problem, the panel is excited by an incident acoustic plane wave. The quantities of interest are the transmitted sound power, the sound transmission coefficient and the sound transmission loss. The sound transmission coefficient (τ) is the ratio of the power transmitted by the panel (W_t) to that incident on it (W_i). The sound transmission loss is defined as

$$\mathrm{TL} = 10\log_{10}\left(\frac{W_i}{W_t}\right) = 10\log_{10}\left(\frac{1}{\tau}\right).$$

2.4.1 The one-way coupled analysis

The sound radiation problem

As discussed before, in the one-way coupled analysis, the effect of the radiated pressure field is neglected while computing the panel response. For a finite panel, the flexural vibration can be expressed as a superposition of the *in vacuo* natural modes. Each mode is associated with a certain wavenumber in the panel. Maidanik classified the panel modes with respect to their modal wavenumbers in the wavenumber space [12]. The modal radiation in each of these wavenumber regions was analyzed with the help of a two-dimensional array of rectangular piston radiators (monopoles). Maidanik then obtained approximate expressions for the modal radiation resistance for all types of modes below the coincidence frequency.

Following the work of Maidanik, a similar classification of the panel wavenumbers is used in this thesis. This classification is illustrated in Fig. 2.2 [7]. In the figure, k_m and k_n are the panel modal wavenumbers in the x and y directions, respectively, when it is vibrating in the $(m,n)^{\mathrm{th}}$ mode. The corner modes are characterized by the panel wavenumbers such that $k_m, k_n > k$ and in this case, only the corner quarter cells in the panel contribute significantly to the sound radiation. The X edge ($k_m < k$ and $k_n > k$) and the Y edge ($k_m > k$ and $k_n < k$) modes are more efficient radiators than the corner modes. In these cases, a strip of half-cell width along the X or the Y edges of the panel radiates efficiently. For the XY edge modes ($k_m < k$, $k_n < k$ and $k_m^2 + k_n^2 > k^2$), significant radiation is due to the edge strips extending over the entire perimeter. The above modes are responsible for the sound radiation below the critical frequency. The critical frequency is the frequency at which the speed of the sound in the acoustic medium is equal to the speed of the flexural waves in an infinite panel of the same material and thickness. Above the critical frequency, the whole panel surface radiates efficiently and the sound radiation is due to the modes which satisfy the condition $k_m, k_n < k$ and $k_m^2 + k_n^2 < k^2$ (the acoustically fast modes).

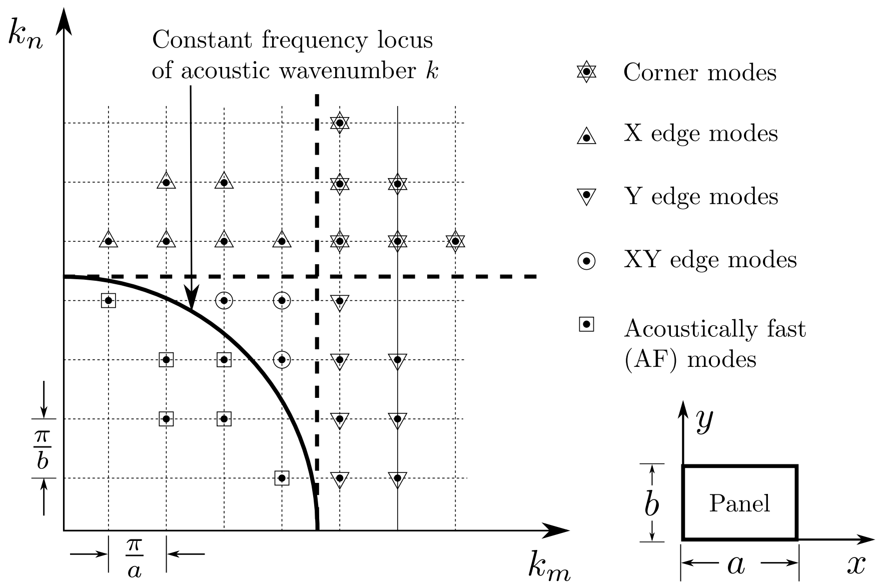

Fig. 2.2 Classification of the panel modes in the wavenumber space with respect to the acoustic wavenumber.

Wallace studied the sound radiation from a simply supported rectangular panel in an infinite baffle [13]. He used the Rayleigh integral to obtain the radiated power in the farfield. The integral for the radiation resistance was obtained and computed numerically for various modes spanning the entire frequency range. Wallace also obtained approximate closed form expressions for the radiation resistance at frequencies well below the critical frequency. The paper also investigated the effects of inter-nodal areas and their aspect ratios on the radiation resistance.

Gomperts used the Rayleigh integral to investigate the effects of various panel boundary conditions on the radiation efficiency of a finite rectangular baffled panel [14]. He observed that a panel with two opposite edges guided and the other two free (guided-free) showed a larger radiation efficiency than a guided-guided case. Gomperts concluded that a more edge-constrained panel did not always result in a larger radiation efficiency than a less edge-constrained one. Gomperts also noted that a two-dimensional vibration analysis resulted in a lower radiation efficiency as compared to the one-dimensional analysis [15]. Maidanik reported that the radiation efficiency of an all edge clamped panel was more than that of a simply supported panel by ~3 dB for frequencies up to half the critical frequency [16]. Leppington obtained asymptotic expressions for the radiation efficiency of a clamped panel as a correction to that of the simply supported panel [17]. He found that below the coincidence frequency, the correction factor was approximately two and above the coincidence it was one. Williams obtained a power series expansion for the radiated power from a single mode of a baffled rectangular panel for the simply supported, clamped and the free boundary conditions [18]. He used the Maclaurin expansion for the panel velocity in the wavenumber space.

The sound radiation from a rectangular panel set in a baffle with a general boundary condition was studied by authors [19, 20]. Berry et al. obtained the panel response for a point force excitation by extremizing the Hamiltonian of the panel constrained against both deflection and rotation at the edges [19]. It was observed that a low deflection stiffness at the panel boundary resulted in a significant reduction in the sound radiation. Zhang and Li developed power series expressions for evaluating the radiation resistance matrix [20]. These expressions were independent of the panel boundary conditions and were only dependent upon the aspect ratio of the panel.

Keltie and Peng studied the interaction between the panel modes at different frequencies in terms of the coupled modal radiation resistances [21]. The analysis was however performed using a one-dimensional vibration fieldl. It was observed that the effect of the modal coupling was negligible for the resonant or high frequency excitations. However, they were significant for the off-resonant or low frequency excitations of the panel. Li and Gibeling investigated the effects of the coupled radiation resistances using a two-dimensional model of the sound radiation from a simply supported rectangular panel in a baffle [22]. The cross radiation resistance values were obtained from the associated self radiation resistances.

Li used a Maclaurin series expansion of the Green's function to find the approximate expressions for the coupled radiation resistance of a simply supported rectangular panel in a baffle [23]. Both, the self and the cross modal radiation resistances were expressed in the form of a power series of the non-dimensional acoustic wavenumber. The approximations were valid for the entire wavenumber domain, although a large number of terms were required for convergence at higher frequencies. The results showed that the values of the self and the cross modal radiation resistances were of comparable magnitudes in a fairly wide frequency range.

Leppington et al. derived asymptotic expressions for the average power radiated from a panel of finite width and infinite extent at frequencies below, above or near the critical frequency [24]. The averaging was performed with respect to all possible force locations and over an appropriate frequency band. The cross modal radiation resistance terms were however neglected in the formulation. The average radiation efficiency for a rectangular panel was derived by Xie and Thompson based on the farfield sound intensity [11]. It was shown that by averaging the radiated power over all the possible forcing locations, the cross modal contributions averaged out to zero.

They also derived approximate expressions for the average radiation efficiency of panels with large aspect ratios.

It can be understood that for a one-way coupled analysis, the most difficult part in evaluating the radiated sound power from the finite panel is finding the modal radiation resistance matrix. The modal radiation resistance is expressed either as a double integral over the wavenumber domain or as a quadruple integral over the spatial domain. Several approximations for the self modal radiation resistance are found in the literature. However, the cross modal radiation resistance has attracted very little attention. It could perhaps be ignored for light fluid loading conditions, however, where the fluid loading is significant, the cross modal radiation impedance cannot be ignored.

The sound transmission problem

Utley observed that at frequencies below the coincidence, the sound transmission loss measured for a finite panel differed considerably from the 'mass law' behavior of the infinite panel [25]. However, above the coincidence frequency, the infinite panel theory predictions were found to agree with the experimental measurements on finite panels. Brekke studied the significance of the panel resonances below the critical frequency and observed that the resonant transmission by a finite panel cannot be neglected if the panel is highly stiffened or has a very low total loss factor [26]. A simple wave based approach, which is based on the infinite panel and the diffuse field incidence assumptions can be used for finding the transmission characteristics of the finite panels. A detailed review of the wave approach applied to the sound transmission problems can be found in [27]. The wave approach, however, does not take into account the effects of the boundary conditions and the resonances of the finite panel and hence the low frequency predictions are not reliable. Although the infinite panel formula includes the effect of fluid loading, the wave approach is not strictly two-way coupled in the sense that the modal interactions due to the fluid loading are completely ignored in the formulation.

Roussos developed a model for the sound transmission through a rectangular panel in an infinite baffle under plane wave incidence [28]. The model used the Rayleigh integral to obtain the acoustic pressure field generated by the panel vibration that is expressed as a superposition of the modal contributions. The model was then used to study a) the coupling between the incident sound and the panel vibrations, b) the resonance behavior of the panel and c) the coupling between the panel vibrations and the transmitted sound at various frequencies, above and below the coincidence.

Ljunggren derived a prediction formulae for the transmission loss of finite panels separating two rooms [29]. The influence of the panel resonances (resonant contribution) and the forced response due to the exciting acoustic field (non-resonant contribution) were accounted for below and above the coincidence frequency.

Villot et al. used a spatial windowing function for the finite panel vibration field to find the radiated sound power [30]. This technique was then extended to find the transmission coefficients for multi-layered finite panels. Davy proposed an approximation for the average sound transmission coefficient of a finite panel below the critical frequency without using the earlier limiting angle approximation used with the infinite panel formula [31]. A diffuse field limp panel mass law for a finite sized wall was derived using the average diffuse field single-sided radiation efficiency approach.

The influence of the radiation impedance over the finite panel area on the sound transmission was considered by Brunskog [32]. Both the inertia and the radiation loading on the panel were taken into account. Brunskog's study was only for the forced sound transmission and did not consider the resonant sound transmission contribution. He used the wave approach to define the vibration field of the panel and obtained approximate expressions for the sound transmission coefficient at various frequencies. Except near the coincidence, the results agreed well with the experimental measurements.

It can be observed that there exist several approximations related to the sound transmission through finite panels. Most of the literature is devoted to finding the forced transmission using the infinite panel theory (wave approach) to predict the transmission loss of finite panels. The reflections at the boundary of panel and the boundary conditions are ignored. If one has to include the effects of the resonances of the finite panel, a modal approach as demonstrated by Roussos [28] is preferred.

2.4.2 The two-way coupled analysis

The sound radiation problem

In the two-way coupled analysis, the effect of the radiated pressure field is taken into account while finding the panel response. The radiated pressure field can be obtained by solving the Helmholtz equation with the boundary condition in terms of the panel velocity. Thus, both the structure and the acoustic domains are now coupled and one needs to solve both the domains simultaneously. The panel response can still be expressed as the superposition of the *in vacuo* modes [33]. The radiated pressure field induces coupling between these *in vacuo* modes. The coupling is expressed in the form of a modal coupling coefficient in the resulting equation of motion for the panel.

Davies developed an analytical expression for the modal coupling coefficient of a simply supported panel set in an infinite rigid baffle and fluid loaded only on one side [33]. The analytical expressions were valid only at low frequencies where the panel modal wavenumbers were greater than the acoustic wavenumber, or when all the panel modes were subsonic. Such modes are referred to as the corner modes [12]. The real parts of the coupling coefficients were related to the radiation damping on the panel response and the imaginary parts led to a virtual mass addition to the panel mass. An approximate solution of the infinite set of modal equations for the panel-fluid system was derived. Further, an approximate expression for the radiated power spectral density was also obtained. The effect of structural damping on the modal coupling coefficients and thus on the spectral density of the sound field generated by a panel excited by a turbulent boundary layer was also discussed.

Davies observed that the effect of the cross modal inertia coupling terms in determining the modified natural frequencies of the water-loaded panel was negligible [33]. It was largely influenced by the self inertia terms. The amplitudes of the panel velocity response were altered by both the radiation and the inertia coupling terms. The structural damping also determined the amount of modal interaction among the panel modes. For a lightly damped structure, the vibrational energy was mostly contained within a single resonant mode. Thus, the radiation damping was only due to the associated acoustic field generated by the resonant mode. However, when the structural damping was large, several modes were excited over a wide frequency band. Hence, the input energy was dissipated by many modes. As a result the total damping to the structure was increased. Consequently, the vibration velocity response and the radiated power were decreased. Pope and Leibowitz presented more complete calculations for the modal coupling coefficients [34] than that given by Davies [33]. They derived approximate expressions for the coupling coefficients involving the corner, edge and the acoustically fast modes.

The vibration and the resulting sound radiation from a water-loaded finite panel with a concentrated mass and set in an infinite rigid baffle was studied by Sandman [35]. The formulation was general and the panel response was assumed to be a linear combination of the *in vacuo* modes. Both the fluid loading and the concentrated mass induced the coupling between the *in vacuo* panel modes. The associated modal coupling coefficients were evaluated numerically at low frequencies, considering only 10 modes in the truncated equation of motion. Sandman demonstrated that the water-loading essentially reduces the radiated power from a point excited panel with or without the concentrated mass. The effect of the concentrated mass is significant only at relatively high frequencies. In addition to the reduction in the response of the panel and also in the radiated power, the concentrated mass also causes changes in the directivity of sound radiation.

The low frequency acoustic radiation from a fluid-loaded panel elastically restrained against rotation at the edges was studied by Lomas and Hayek [36]. The vibration response was expressed as a modal sum of the *in vacuo* mode shapes of a simply supported panel, in spite of the inhomogeneity at the boundary. The solution to the panel vibration was obtained as a sum of the response of a simply supported fluid loaded panel to a point excitation and that of a panel to line moments at the boundary. The first case dealt with an inhomogeneous differential equation of motion and a homogeneous boundary condition. Whereas the second one had a homogeneous differential equation of motion and an inhomogeneous boundary condition. Lomas and Hayek compared both the self and cross modal coupling coefficients for the lower order modes (obtained numerically) with those values obtained using Davies' approximations for the corner-corner interactions [33] and found a good match between them. The natural frequencies of a few lower order modes were also obtained for both the simply supported and the clamped boundary conditions.

Berry studied the sound radiation from a fluid-loaded panel set in a baffle for a general boundary condition [37]. The edges of the panel were restrained against both deflection and rotation and the formulation allowed arbitrary variations of both the linear and rotary stiffness along the edges. A variational method was used to model the fluid-structure interaction, where the flexural vibration of the panel was expressed as a series of trial functions based on the Taylor series expansion of the Green's function. The modal coupling coefficients were thus expressed as an integral involving simple Taylor functions. The Rayleigh-Ritz method was employed to solve the equation of motion for the unknown coefficients of the displacement function. The modal coupling coefficients were evaluated numerically. It was verified that at low frequencies, for both the simply supported and the clamped boundary conditions, the odd-odd modes resulted in a monopole like radiation behavior, the even-odd or odd-even modes caused a dipole kind of behavior and for the even-even modes the behavior was mostly quadrupole like. The paper also discussed the mean quadratic velocity of a water-loaded panel and the resulting radiated power for various boundary conditions.

Graham obtained asymptotic expressions for the modal coupling coefficients, both the radiation and inertia coupling terms, of a simply supported rectangular panel [38, 39]. In [39], the analysis considered a case where the panel dimensions were large with respect to the modal wavelength but not the acoustic wavelength. The parameter regime studied was the same as that was considered by Davies [33]. Graham solved the doubly infinite integral of the coupling coefficients using the contour integration. The results were validated against the numerical solutions. The expressions derived for the radiation coupling coefficients were found to be asymptotically equivalent to that derived earlier for the corner - corner modal interactions by Davies [33], except for the cross modal inertia coefficient.

Crighton and Innes studied the effect of the fluid loading on the response of a thin infinite panel at low frequencies (when the ratio of the excitation frequency to the coincidence frequency was $\mathcal{O}(\epsilon^2)$) using the asymptotic method [40]. They also examined the effect of ribs on the infinite planar structure and found that at low frequencies, there was substantial transmission of structural energy across a rib. The authors also considered the response of a panel of finite width but of infinite length to a line excitation. It was found that the modes of the fluid-loaded finite panel were of the same shape as that of the *in vacuo* case, however of a different scale due to the fluid loading. The vibration field of the finite panel, beyond a wavelength from the edge, consisted of the incident wave and the reflected wave with a phase lag. This phase lag was decided by the edge conditions of the panel.

The effect of fluid loading on the response of periodically stiffened panels was discussed in [41, 42]. Eatwell and Butler obtained asymptotic expressions for the response of a beam stiffened fluid-loaded panel to point and line excitations [41]. They studied the farfield responses of a periodically stiffened panel and of a finitely stiffened panel of infinite extent. Due to the inhomogeneities (beams) in the farfield, the response of a periodically stiffened panel was characterized by the acoustically fast waves. In contrast, the farfield displacement waves in the finitely stiffened panel were always acoustically slow. Mead analyzed the free wave motion in an infinite panel with periodic stiffening along one or both the orthogonal directions [42]. The fluid loading effects on the panel response were included in the analysis by the use of the space harmonics.

The sound transmission problem

We have seen for the one-way coupled case that the total sound transmission through the finite panels comprises of the resonant and the non-resonant contributions. When we include the fluid loading effects, necessary modifications to these contributions occur.

Sewell derived a low frequency approximation for the sound transmission coefficient of a rectangular baffled panel for a plane wave incidence [43]. The formulation was general and considered the effect of fluid loading on the *in vacuo* panel modes (included both the resonant and the non-resonant terms). However, while finding the approximate expression for the transmission coefficient, he did not account for any resonance contribution from the panel modes and it was applicable below the coincidence frequency. The modal coupling term considered only the reactive loading from the surrounding acoustic medium. Also, the cross modal coupling terms were neglected while deriving the transmission coefficient. However, the model agreed well with the experimental results for panels with mass per unit area larger than 10 $\mathrm{kg/m^2}$. A study of finite panel transmission at low frequencies was done by Mulholland and Lyon [44]. They investigated the characteristics of the resonant and the non-resonant sound transmission when the finite panel was coupled to two rooms.

Leppington et al. derived asymptotic expressions for the sound transmission coefficient valid for frequencies below, near and above the coincidence frequency using a one-dimensional panel model [45]. Using the insights from the one-dimensional model, he proposed approximate expressions for the transmission coefficient of a two-dimensional panel. These expressions were able to predict both the resonant and the non-resonant contributions below the coincidence frequency and were in good agreement with the experimental measurements.

Takahashi considered a two-dimensional problem in which the panel had a finite width in one direction but had an infinite extent in the other [46]. The cross modal coupling was ignored in the analysis. Approximate expressions for the self modal coupling coefficients were obtained and the sound transmission loss at different frequencies was discussed. The band-averaged transmission loss was found to be sensitive to the panel area below the critical frequency. Above the critical frequency, the transmission loss was almost the same as that of the infinite panel. It was also observed that below the critical frequency, the panel resonances affect the band-averaged sound transmission. The significance of the panel resonances (resonant contribution) below the critical frequency was studied in detail by Lee and Ih [47] for a rectangular panel set in an infinite baffle. They investigated the band-averaged difference between the total and the non-resonant transmission losses with respect to a non-dimensional participation factor which was a function of the size, thickness and the loss factor of the panel. A frequency range for neglecting the resonant contribution was also proposed.

Recently, Wang derived an expression for the equivalent self modal coupling coefficient which includes the effects of the cross modal coupling between the *in vacuo* modes of a finite panel [48]. The overall sound transmission coefficient was then expressed as a superposition of all the modal transmission coefficients. The effect of the cross modal coupling on the overall transmission coefficient was found to be significant only when the participating modes were subsonic. In a following study [49], Wang derived asymptotic expressions for both the modal and the overall transmission coefficients. The derivation assumed a low bending stiffness for the panel. The asymptotic expressions, although valid for the whole frequency range, were applicable only for the non-resonant contribution in the sound transmission.

Several studies are reported on the sound transmission of finite panels using numerical methods like the boundary element method (BEM) [50] and the finite element method (FEM) [51]. In [50], the acoustic loading was modeled as an added mass on the panel and a comparison of the transmission loss was made with the experimental values. Chazot and Guyader presented a new method called the patch-mobility method to study the sound transmission through finite panels [52]. The patch-mobilities of the component sub-systems were defined separately before coupling. The mesh size required for this method was only half of the panel wavelength which was very large compared to the standard finite element mesh criterion [51]. Both the finite element and the patch-mobility methods gave the same results for the sound transmission loss of double panels at low frequencies. At high frequencies, the proposed method results were superior to the finite element results.

It can be seen that there have been many attempts to find the non-resonant or the forced excitation contribution to the sound transmission from fluid loaded finite panels. Inclusion of the resonant contribution requires a complete solution to the modal coupling coefficient and it has been largely ignored due to its mathematical complexity. Hence, a total solution to the finite panel sound transmission is not available, although some *ad hoc* methods exist [48]. In the next section, a summary of the important contributions in the literature on structural acoustics of perforated panels is presented.

2.5 Structural acoustics of perforated panels

One means of reducing the sound radiation from panel like structures is to make them perforated [5]. Perforated panels are found in applications like the protective cover over flywheels and belt drives, product collection hoppers, etc. [53]. When the perforated panel is backed by cavity filled with air or some porous materials, it acts as a good sound absorber [54, 55].

Maa proposed an analytical expression for the acoustic impedance offered by each hole in a perforated panel by solving the acoustic plane wave propagation in a short cylindrical tube [1]. End corrections to the hole impedance were also made to include (1) the resistance due to air flow friction on the surface of the panel as the flow was squeezed into the small inlet end of the hole and (2) the mass reactance due to the piston like sound radiator at both the ends of the hole. Using the hole impedance model, Maa studied the sound absorption by a micro-perforated panel-cavity (MPP) system. The perforations consisted of holes with sub-millimeter diameters and were separated by a distance greater than the hole diameter. The micro-perforated panel was assumed to be rigid and of infinite extent. The sound absorption coefficient calculated using the proposed hole impedance model was found to agree well with the experimental results. It was shown in the paper that the MPP could provide wide-band sound absorption up to 3 octaves. Bolton and Kim used computational fluid dynamics (CFD) based studies to find the hole impedance of square shaped holes [56]. Herdtle et al. conducted similar studies on tapered holes using CFD models and proposed modifications to Maa's hole impedance formula [57].

The effect of flexibility of the perforated panels on the associated acoustic field was investigated by Takahashi and Tanaka [2]. The panels were assumed to be of infinite extent with air on both the sides. A spatially averaged velocity was defined at the panel-fluid interface which accounted for the continuity of flow through the perforation and the force due to the relative motion between the panel and the fluid within the perforation. The model assumed that the hole size and the hole separation were relatively small compared to the acoustic wavelength. The model was then used to find the radiated power from an infinitely long perforated panel excited by a point harmonic force. The effect of perforation on the radiated power was significant below the coincidence frequency. The sound absorption coefficient of the perforated panel excited by an acoustic plane wave was also evaluated. It was found that when the perforation ratio was increased, the effect of the panel vibration on the absorption coefficient decreased. The developed model of the infinitely long perforated panel was used in a later work [58] to study the absorption characteristics of a perforated panel backed by a rigid cavity; the perforated panel considered was of infinite extent. Toyoda et al. proposed the sound absorption model for a perforated panel system with subdivided air cavities instead of the undivided backing cavity [59]. Recently, Li et al. proposed a modified expression for the impedance of a micro-perforated membrane, taking into account the no-slip boundary condition at the hole walls [3]. The formula was valid for a circular membrane.

The effect of the perforation on the sound radiation from a finite panel was studied by Fahy and Thompson [5]. The panel was assumed to be simply supported on a similarly perforated baffle. Later, a dissimilar perforation case was studied for the sound radiation from a perforated strip piston in an unperforated baffle. The effect of the flexibility of the panel was ignored in this case. While modeling the hole impedance, only the reactance due to the mass of the air within the perforation was considered. A one-dimensional formulation in the wavenumber domain was used. It was noted that a dissimilar perforate impedance on the edges along the panel-baffle boundary created a 'window' effect which coupled different wavenumber spectral components in the resulting acoustic velocity field.

Putra and Thompson included the aspect of flexibility of the finite perforated panel in their sound radiation model [4]. Two configurations of the panel were considered. In one, the panel was set in an infinite baffle and both the panel and the baffle had the same perforation ratio. In the second configuration, the perforated panel was assumed to be unbaffled. The perforation on the panel was modeled as a continuously distributed surface impedance. The model considered holes having several millimeters as diameter and hence the perforate impedance included only the inertia term and neglected the viscous term. An average velocity on the perforated panel surface was defined following the method developed by Takahashi and Tanaka [2]. The formulation of the baffled case was an extension of the work done by Fahy and Thompson [5] and the problem was modeled using the 2-D wavenumber transforms of the pressure and velocity fields (one-way coupled). For the baffled case, Putra and Thompson observed a reduction in the radiation efficiency of the panel with the increase in the perforation ratio. For a given perforation ratio, decreasing the hole size also resulted in the reduction of radiation efficiency. The reduction in the radiation efficiency was largely due to the perforation in the infinite baffle. An approximate expression for the effect of perforation at low frequencies was also proposed. The effect of perforation is a measure of the reduction in the radiated sound power due to the perforations in the panel. Although this paper extended the knowledge gained from the work of Fahy and Thompson [5] on the similarly perforated panel and baffle, the treatment of dissimilar perforate impedance along the panel-baffle edge was completely ignored. In [60], Putra and Thompson studied the sound radiation from unbaffled perforated panels.

For a rigid MPP absorber, as discussed by Maa [1], the sound absorption is due to the Helmholtz type resonance formed by the hole and the backing cavity. However, for a flexible perforated panel, the panel vibration alters the absorption spectrum. Sakagami et al. studied in detail the absorption mechanism of a flexible micro-perforated panel of infinite extent and backed by a cavity [61]. They observed that both the Helmholtz type and the panel/membrane type absorption coexist in the absorption spectra. Dupont et al. investigated the transmission and absorption characteristics of a rigid micro-perforated panel coupled to a flexible panel through an air gap [62]. The configuration studied was limited to infinite panels. The normal and the oblique incidence of the plane wave were considered and the formulation was done using the wave approach. Dupont et al. observed that the presence of a flexible backing panel in the MPP system increased the transmission loss and reduced the reflection coefficient.

The sound absorption by a perforated panel with a finite backing cavity was studied by Lee et al. [63]. They investigated the effect of the panel resonances on the absorption spectrum. However, a more comprehensive study (one-way coupled) can be found in [54]. The flexibility of a micro-perforated panel was so important that it essentially resulted in several peaks and dips in the absorption spectrum of the micro-perforated panel absorber (MPPA) system [54]. Bravo et al. observed that the panel-air relative velocity altered the input acoustic impedance of thin MPPAs [55]. A coupled mode analysis revealed that the resonances were due to either the panel-cavity, hole-cavity or the panel-controlled modes.

For a perforated panel set in an unperforated baffle, the discontinuity in the perforate impedance at the panel-baffle boundary denied any simple solution to both the sound radiation and the sound transmission problems. Although a one-dimensional piston model was developed by Fahy and Thompson [5], they did not account for the flexibility of the panel, let alone the fluid loading effects.

2.6 The locally averaged fluid particle velocity

As mentioned in the previous section, the flexibility of the perforated panel was modeled by Takahashi and Tanaka [2]. They obtained an expression for the average fluid particle velocity over the perforated panel surface, taking into account the continuity of flow through the perforation and the linear momentum balance within each hole. In this section, the Reynold's Transport Theorem is used to introduce the reader to the concept of locally averaged fluid particle (LAFP) velocity at the perforated panel surface. Note, that the following derivation assumes a plane wave propagation through the perforation, i.e., the hole diameter is much less than the acoustic wavelength.

2.6.1 Conservation of mass

The Reynold's transport theorem (RTT) is given by [64]

$$\frac{\mathrm{d}}{\mathrm{d}t}\mathbf{B_{system}} = \frac{\mathrm{d}}{\mathrm{d}t}\left[\int_{CV} \beta\rho_0 \,\mathrm{d}V\right] + \int_{CS} \beta\rho_0 \left(\mathbf{v_r}.\mathbf{n}\right)\, \mathrm{d}S,$$

where ρ_0 is the density of the fluid and

$$\beta = \frac{\mathrm{d}\mathbf{B_{system}}}{\mathrm{d}m}.$$

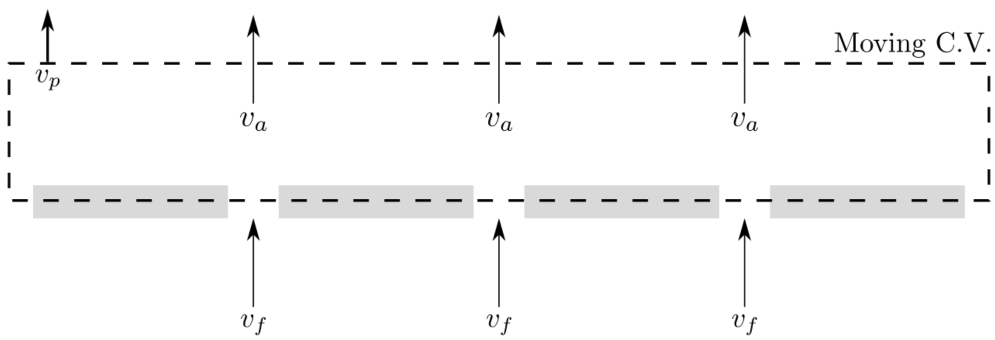

Fig. 2.3 Schematic of the control volume (conservation of mass).

Consider a control volume (CV) as shown in Fig. 2.3. The CV encompasses the fluid just above the flexible perforated panel vibrating with a velocity $\mathbf{v_p}$. The CV moves with the same velocity as that of the panel. The influx through the perforation into the CV is at a velocity $\mathbf{v_f}$. The fluid exits the CV at the top surface with a velocity $\mathbf{v_a}$, the locally averaged fluid particle (LAFP) velocity. The velocities are defined with respect to an inertial frame of reference. The conservation of mass states that the total mass of the system remains unchanged. Let us assume $\mathbf{B_{system}} = m$, the mass of the fluid within the control volume. Therefore,

$$\beta = \frac{\mathrm{d}\mathbf{B_{system}}}{\mathrm{d}m} = 1.$$

The conservation of mass of the system can be written as

$$\frac{\mathrm{d}m}{\mathrm{d}t} = 0.$$

Thus, the RTT for the conservation of mass gives

$$0 = \frac{\mathrm{d}}{\mathrm{d}t}\left[\int_{CV} \rho_0 \, \mathrm{d}V\right] - \rho_0 \left(\mathbf{v_f} - \mathbf{v_p}\right) S_h + \rho_0 \left(\mathbf{v_a} - \mathbf{v_p}\right) S_p,$$

where S_p is the panel area (including the hole area) and S_h is the hole area alone. Assume that the density ρ_0 is constant over time and space and the control volume translates but does not deform. Therefore, the time derivative of the volume integral (first term on the right hand side of the above equation) vanishes. Thus,

$$\begin{aligned} 0 &= -\left(\mathbf{v_f} - \mathbf{v_p}\right) S_h + \left(\mathbf{v_a} - \mathbf{v_p}\right) S_p \\ \mathbf{v_a} S_p &= \left(\mathbf{v_f} - \mathbf{v_p}\right) S_h + \mathbf{v_p} S_p \\ \mathbf{v_a} &= \left(\mathbf{v_f} - \mathbf{v_p}\right) \frac{S_h}{S_p} + \mathbf{v_p}. \end{aligned}$$

Defining $\frac{S_h}{S_p} = \sigma_p$ as the perforation ratio, the LAFP velocity at the panel surface is given by

$$\mathbf{v_a} = \mathbf{v_p}\left(1 - \sigma_p\right) + \mathbf{v_f}\sigma_p.$$

2.6.2 Conservation of linear momentum

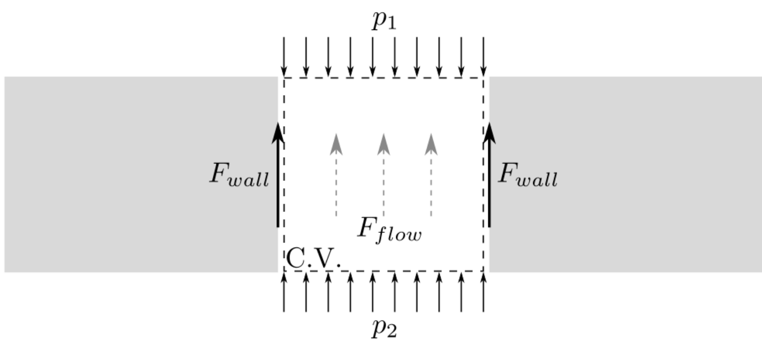

Fig. 2.4 Schematic of the control volume (conservation of linear momentum).

Consider a control volume inside one circular hole of the perforated panel, as shown in Fig. 2.4. The CV moves with a velocity $\mathbf{v_p}$, same as the panel velocity. The fluid within the hole moves with a velocity $\mathbf{v_f}$. Let the pressure on the top and the bottom control surfaces (CS) be p_1 and p_2, respectively. An external wall shear force $\mathbf{F_{wall}}$

acts on the lateral surface of the CV. Here, the body force of the fluid within the CV is neglected.

Let,

$$\frac{\mathrm{d}\mathbf{B_{system}}}{\mathrm{d}t} = \mathbf{F_{system}},$$

where

$$\mathbf{B_{system}} = (m\mathbf{v_f})_{\text{system}}\,.$$

Therefore,

$$\beta = \frac{\mathrm{d}\mathbf{B_{system}}}{\mathrm{d}m} = \mathbf{v_f}.$$

Now, the RTT for the conservation of linear momentum can be written as

$$\frac{\mathrm{d}}{\mathrm{d}t}\mathbf{B_{system}} = \frac{\mathrm{d}}{\mathrm{d}t}\left[\int_{CV} \beta\rho_0\,\mathrm{d}V\right] + \int_{CS} \beta\rho_0\,(\mathbf{v_r}.\mathbf{n})\,\mathrm{d}S.$$

Or,

$$\mathbf{F_{system}} = \frac{\mathrm{d}}{\mathrm{d}t}\left[\int_{CV} \mathbf{v_f}\rho_0\,\mathrm{d}V\right] - \mathbf{v_f}\rho_0\,(\mathbf{v_f} - \mathbf{v_p})\,A_h + \mathbf{v_f}\rho_0\,(\mathbf{v_f} - \mathbf{v_p})\,A_h,$$

where A_h is the (top/bottom) area of the hole. Since the inflow and the outflow of the fluid is the same, the sum corresponding to the integral over the CS vanishes. Therefore,

$$\mathbf{F_{system}} = \frac{\mathrm{d}}{\mathrm{d}t}\left[\int_{CV} \mathbf{v_f}\rho_0\,\mathrm{d}V\right]. \tag{2.7}$$

$\mathbf{F_{system}}$ represents the sum of all the external forces (surface and body forces) acting on the system. In the absence of any body forces we have

$$\mathbf{F_{system}} = \mathbf{F_{wall}} + (p_2 - p_1)A_h\hat{\mathbf{n}},$$

where the wall shear force $\mathbf{F_{wall}}$ is due to the viscous boundary layer on the panel wall inside the hole and depends on the relative velocity of the flow past the hole surface. $\hat{\mathbf{n}}$ is a unit vector normal to the top surface of the CV. Now, for a harmonic excitation, the fluid velocity $\mathbf{v_f}$ can be written as

$$\mathbf{v_f} = \mathbf{V_f}\,\mathrm{e}^{-\mathrm{i}\omega t}.$$

Assume that the fluid velocity $\mathbf{v_f}$ and the fluid density ρ_0 are uniform within the CV (for an acoustic plane wave propagation) and the CV only translates but does not deform. Then, the time derivative of the volume integral on the right hand side of

Eq. (2.7) can be written as

$$\frac{\mathrm{d}}{\mathrm{d}t}\left[\int_{CV} \mathbf{v_f}\rho_0 \,\mathrm{d}V\right] = -\mathrm{i}\omega\mathbf{v_f}\rho_0 A_h h,$$

where h is the panel thickness. Therefore,

$$\mathbf{F_{wall}} + (p_2 - p_1)A_h\hat{\mathbf{n}} = -\mathrm{i}\omega\mathbf{v_f}\rho_0 A_h h.$$

Or,

$$-\mathrm{i}\omega\rho_0 h\mathbf{v_f} - \frac{\mathbf{F_{wall}}}{A_h} = (p_2 - p_1)\hat{\mathbf{n}}. \tag{2.8}$$

The first term on the left hand side of the above equation represents the inertial characteristics of the fluid within the CV and it is purely imaginary. Thus, the first term can be written as

$$-\mathrm{i}\omega\rho_0 h\mathbf{v_f} = Z_{\mathrm{react}}\mathbf{v_f}, \tag{2.9}$$

where Z_{react} represents the reactive impedance of the hole. As mentioned before, the wall shear force $\mathbf{F_{wall}}$ is a function of the relative velocity of the fluid past the hole wall surface $(\mathbf{v_f} - \mathbf{v_p})$ and it acts in a direction opposite to the relative velocity of the fluid. In addition, the wall shear term signifies the dissipation at the viscous boundary layer and hence it is purely a real term. Thus,

$$\frac{\mathbf{F_{wall}}}{A_h} = -Z_{\mathrm{resist}}\left(\mathbf{v_f} - \mathbf{v_p}\right), \tag{2.10}$$

where Z_{resist} represents the resistive impedance of the hole. Thus, substituting Eqs. (2.9) and (2.10) into Eq. (2.8) we get

$$Z_{\mathrm{react}}\mathbf{v_f} + Z_{\mathrm{resist}}\left(\mathbf{v_f} - \mathbf{v_p}\right) = \mathbf{\Delta p}.$$

In the above equation, the resistive and the reactive parts of the hole impedance $(Z_0 = Z_{\mathrm{resist}} + Z_{\mathrm{react}})$ can be obtained by solving the equation for the propagation of sound wave in a short tube, as derived by Maa [1].

2.7 The Receptance method

The Receptance method can be used to determine the modal characteristics of a complex vibrating system using the vibration behavior of its sub-structural elements. A perforated panel can be thought of as a panel with small mass voids. The Receptance method is used to mathematically subtract the inertia of the void from that of a panel with sufficient accuracy [65]. A detailed analysis on the Receptance method can be found in [65]. In this thesis, the Receptance method is used to find the resonances and the modeshapes of a perforated panel from the receptances of an unperforated panel and a point mass. A brief description on the Receptance method is given below.

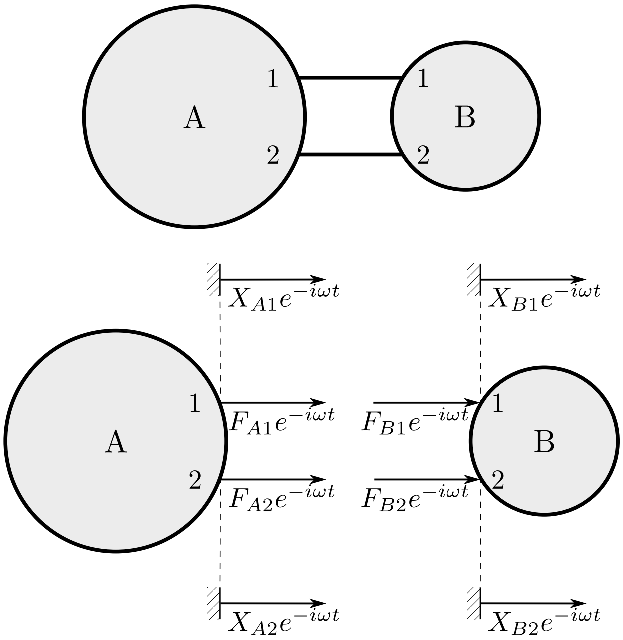

Fig. 2.5 Two systems connected at two different points

Consider two systems A and B which are connected at two points as shown in Fig. 2.5. Let, F_{A1} and F_{A2} be the amplitudes of forces acting on system A at points 1 and 2, respectively and let X_{A1} and X_{A2} be the resulting displacements. The force-displacement relation for system A is given by

$$\begin{Bmatrix} X_{A1} \\ X_{A2} \end{Bmatrix} = \begin{bmatrix} \alpha_{11} & \alpha_{12} \\ \alpha_{21} & \alpha_{22} \end{bmatrix} \begin{Bmatrix} F_{A1} \\ F_{A2} \end{Bmatrix}. \tag{2.11}$$

Similarly, for system B, we can obtain

$$\begin{Bmatrix} X_{B1} \\ X_{B2} \end{Bmatrix} = \begin{bmatrix} \beta_{11} & \beta_{12} \\ \beta_{21} & \beta_{22} \end{bmatrix} \begin{Bmatrix} F_{B1} \\ F_{B2} \end{Bmatrix}. \tag{2.12}$$

where α_{ij} and β_{ij} represent the receptances of system A and B, respectively. The receptance has a unit of displacement per unit force. Thus, α_{ij} $(i, j = 1, 2)$ denotes the displacement at point i due to a unit force at point j on system A. When $i = j$, they are known as the drive point receptances and when $i \neq j$, they are referred to as the cross point receptances. When two such systems are joined together, the forces F_A and F_B become internal forces and they must be equal and opposite. Thus,

$$\{F_A\} = -\{F_B\}. \tag{2.13}$$

And the displacement at the joining points on both the systems must be equal. Hence,

$$\{X_A\} = \{X_B\}. \tag{2.14}$$

Thus, for the combined system we get

$$[[\alpha] + [\beta]]\{F_A\} = \{0\}. \tag{2.15}$$

A non-trivial solution to the above equation is obtained by setting the determinant of the receptance matrix $[[\alpha] + [\beta]]$ to zero. Thus, the characteristic equation is obtained as

$$|[\alpha] + [\beta]| = 0. \tag{2.16}$$

The roots of the above characteristic equation provide the new natural frequencies of the combined system.

For a panel with several mass voids (holes), one has to mathematically subtract the vibrational effects of the missing masses from that of the panel. Such problems can be solved approximately using the Receptance method for subtracting structural subsystems. It is possible to think of system B being subtracted from system A as the addition of a negative system B to A [65]. Let α represent the receptance of the panel (system A) and β represent the receptance of the missing panel mass (system B). Hence, using Eq. (2.15), the equation for the panel with mass voids can be written as

$$[[\alpha] - [\beta]]\{F_A\} = \{0\}. \tag{2.17}$$

The characteristic equation is given by

$$|[\alpha] - [\beta]| = 0. \tag{2.18}$$

The roots of the above characteristic equation provide the new natural frequencies of the panel with holes. The receptances of a panel and a point mass are derived below.

2.7.1 Receptance matrix of a simply supported panel

For a simply supported panel ($-a/2 \leq x \leq a/2$, $-b/2 \leq y \leq b/2$) acted on by a harmonic force of magnitude F and frequency ω at (x_i, y_i), the displacement at point (x, y) is given by [65, 66]

$$w(x, y, t) = \sum_{m=1}^{\infty} \sum_{n=1}^{\infty} \frac{1}{M_{mn}} \frac{\phi_{mn}(x_i, y_i) F e^{-i\omega t}}{\omega_{mn}^2 - \omega^2} \phi_{mn}(x, y), \tag{2.19}$$

where $\phi_{mn}(x, y)$ is the modeshape of the panel and is given by

$$\phi_{mn}(x, y) = \sin \frac{m\pi(x + a/2)}{a} \sin \frac{n\pi(y + b/2)}{b}. \tag{2.20}$$

The term M_{mn} is

$$M_{mn} = \int_{-b/2}^{b/2} \int_{-a/2}^{a/2} \rho_p h \phi_{mn}^2(x, y) \, \mathrm{d}x \, \mathrm{d}y = \frac{\rho_p h a b}{4}, \tag{2.21}$$

where ρ_p is the density of the panel and h is the panel thickness. Now, using Eq. (2.19), the receptance α_{ij} of the panel is given by

$$\begin{aligned} \alpha_{ij} &= \frac{w(x_i, y_i, t)}{F e^{-i\omega t}} \\ &= \frac{4}{\rho_p h a b} \sum_{m=1}^{\infty} \sum_{n=1}^{\infty} \frac{\phi_{mn}(x_j, y_j)}{\omega_{mn}^2 - \omega^2} \phi_{mn}(x_i, y_i). \end{aligned} \tag{2.22}$$

2.7.2 Receptance of a point mass

The receptance of a point mass (system B) of mass m is obtained from its equation of motion

$$\begin{aligned} -m\omega^2 X_B e^{-i\omega t} &= F e^{-i\omega t} \\ X_B e^{-i\omega t} &= -\frac{F e^{-i\omega t}}{m\omega^2}. \end{aligned}$$

For a hole of radius r_p, the mass is $m_h = \rho_p h \pi r_p^2$. Now, the receptance is given by

$$\beta = \frac{X_B e^{-i\omega t}}{F e^{-i\omega t}} = -\frac{1}{m_h \omega^2}. \tag{2.23}$$

As the point masses are discrete, force on one point mass does not cause the other to respond. Therefore, for system B, the cross receptances are zero and hence, the receptance matrix is diagonal.

2.7.3 Receptance matrix of a simply supported perforated panel

For a simply supported panel with two holes, the receptance matrix is given by Eq. (2.17). The characteristic equation is

$$\begin{vmatrix} \alpha_{11} + \dfrac{1}{m_h\omega^2} & \alpha_{12} \\ \alpha_{21} & \alpha_{22} + \dfrac{1}{m_h\omega^2} \end{vmatrix} = 0. \tag{2.24}$$

Now, for the case of N_0 holes in the panel, the receptance matrix is of size $N_0 \times N_0$ and the roots of the characteristic equation give the natural frequencies of the perforated panel. The modeshapes of the perforated panel can be determined from the point response expression of the original panel [65]. For the case of a panel with single hole, when the excitation frequency ω is set to the natural frequency of the perforated panel ω_r, Eq. (2.19) gives the r^{th} modeshape of the perforated panel, where (x_i, y_i) is the location of the hole in the panel. Extending to the case of N_0 holes, the panel experiences forces at each of the hole locations and the magnitudes of these point forces are given by the elements of the eigenvector corresponding to the zero eigenvalue of the receptance matrix evaluated at the new natural frequency ω_r [66]. Thus, the r^{th} modeshape of the perforated panel is given by

$$\psi_r(x,y) = \frac{4}{\rho_p hab} \sum_{m=1}^{\infty}\sum_{n=1}^{\infty} \frac{\sum_{i=1}^{N_0} \phi_{mn}(x_i,y_i)F_{ir}}{\omega_{mn}^2 - \omega_r^2} \phi_{mn}(x,y). \tag{2.25}$$

Or

$$\psi_r\,(x,y) = \sum_{m=1}^{\infty}\sum_{n=1}^{\infty} U_{mnr} \sin\frac{m\pi(x+a/2)}{a} \sin\frac{n\pi(y+b/2)}{b}, \tag{2.26}$$

where

$$U_{mnr} = \frac{4}{\rho_p hab} \frac{\sum_{i=1}^{N_0} \sin\frac{m\pi(x_i+a/2)}{a} \sin\frac{n\pi(y_i+b/2)}{b} F_{ir}}{\omega_{mn}^2 - \omega_r^2}. \tag{2.27}$$

The summation over index i denotes the sum of point forces at each hole location and F_{ir} represents the i^{th} element of the eigenvector corresponding to the zero eigenvalue of the perforated panel receptance matrix at the r^{th} natural frequency ω_r. From Eq. (2.26), it can be seen that the modeshape $\psi_r(x,y)$ of a perforated panel is a linear combination of natural modes of a simply supported unperforated panel.

2.8 Contour integration

In chapter 7, the contour integration technique is used to find approximate expressions for the modal coupling coefficient of a perforated panel. Various theorems pertaining to the contour integration in the complex domain are used to obtain the closed form expressions. In this section, some of the theorems which will be used in chapter 7 are presented and one example problem involving contour integration is solved.

Theorem 1 (Cauchy residue theorem)**:** Let $f(z)$ be analytic inside and on a simple closed contour C, except for a finite number of isolated singular points $z_1, z_2, ..., z_N$ located inside C. Then

$$\oint f(z)\,\mathrm{d}z = 2\pi\mathrm{i}\sum_{j=1}^{N} a_j,$$

where a_j is the residue of $f(z)$ at $z = z_j$, denoted by a_j=Res(z_j).

Let $f(z)$ be defined by

$$f(z) = \frac{\phi(z)}{(z-z_0)^m},$$

where $\phi(z)$ is analytic in the neighborhood of $z = z_0$ and m is a positive integer. If $\phi(z_0) \neq 0$, then $f(z)$ has a pole of order m at $z = z_0$. Then the residue of $f(z)$ at $z = z_0$ is given by

$$\mathrm{Res}\,(z_0) = \frac{1}{(m-1)!}\,\frac{\mathrm{d}^{m-1}\phi(z)}{\mathrm{d}z^{m-1}}\bigg|_{z=z_0}.$$

Theorem 2: (a) Suppose that on the contour C_ϵ, depicted in Fig. 2.6, we have $(z-z_0)f(z) \to 0$ uniformly as $\epsilon \to 0$. Then

$$\lim_{\epsilon\to 0}\int_{C_\epsilon} f(z)\,\mathrm{d}z = 0.$$

(b) Suppose $f(z)$ has a simple pole at $z = z_0$ with residue $\mathrm{Res}\,(z_0) = C_{-1}$. Then for the contour C_ϵ

$$\lim_{\epsilon \to 0} \int\limits_{C_\epsilon} f(z)\,\mathrm{d}z = \mathrm{i}\,\phi\, C_{-1},$$

where the integration is carried out in the positive (counterclockwise) sense.

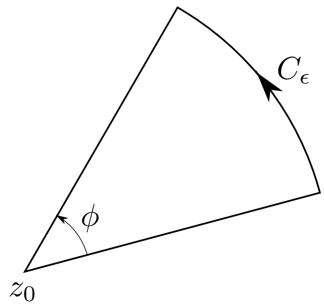

Fig. 2.6 The small circular contour C_ϵ of Theorem 2.

Theorem 3: If on a circular arc C_R of radius R and center $z = 0$, $zf(z) \to 0$ uniformly as $R \to \infty$, then

$$\lim_{R \to \infty} \int\limits_{C_R} f(z)\,\mathrm{d}z = 0.$$

The reader may refer to [67] for the detailed discussions and the proofs of the above theorems. Next, an example problem is solved using the contour integration technique.

Example: Use contour integration to evaluate

$$I = \int\limits_0^\infty \frac{\mathrm{d}x}{\sqrt{x}\,(1 + x^2)}.$$

Consider the contour integral

$$J = \oint\limits_C \frac{\mathrm{d}z}{\sqrt{z}\,(1 + z^2)}. \tag{2.28}$$

Consider the square root function $\sqrt{z} = r^{1/2}\,\mathrm{e}^{\mathrm{i}\theta/2}$, with $0 \le \theta < 2\pi$, in the neighborhood of $z = 0$. As we vary θ from 0 to 2π around $z = 0$, a jump in the function value is encountered. This is a typical example of a *branch point* of a multi-valued complex function. Branch point of a multi-valued complex function is defined as a point in the complex plane around which when a continuous function is evaluated on a closed contour enclosing the point, the starting value of the function differs from the end value. A *branch cut* is a line joining the branch points such that the function value takes a jump for points across the branch cut. For the selected range of θ, the branch cut for the function $\sqrt{z}$ is along the positive real axis, as shown in Fig. 2.7. Thus, along the real axis, we have

$$\sqrt{z} = \begin{cases} r^{1/2} & \text{if } \theta = 0 \\ -r^{1/2} & \text{if } \theta = 2\pi. \end{cases} \tag{2.29}$$

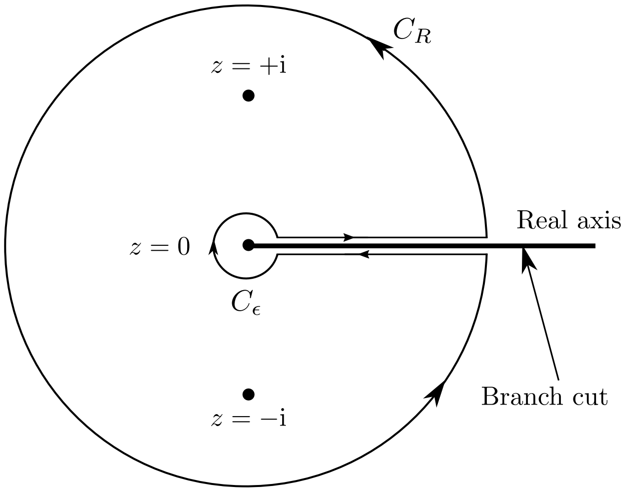

Fig. 2.7 The ‘key-hole’ contour of the example problem.

Consider the ‘key-hole’ contour as shown in Fig. 2.7. Substituting $z = r\,\mathrm{e}^{\mathrm{i}\theta}$ into Eq. (2.28) and using the appropriate definition of $\sqrt{z}$ across the branch cut from Eq. (2.29), we can rewrite the contour integral as

$$J = \lim_{\substack{\epsilon\to 0\\ R\to\infty}} \int_{\epsilon}^{R} \frac{\mathrm{d}r}{r^{1/2}\,(1+r^2)} + \lim_{R\to\infty} \int_{C_R} \frac{\mathrm{d}z}{\sqrt{z}\,(1+z^2)} + \lim_{\substack{\epsilon\to 0\\ R\to\infty}} \int_{R}^{\epsilon} \frac{\mathrm{d}r}{-r^{1/2}\,(1+r^2)} + \lim_{\epsilon\to 0} \int_{C_\epsilon} \frac{\mathrm{d}z}{\sqrt{z}\,(1+z^2)}.$$

The first and the third integrals on the right hand side are the same. Therefore,

$$J = 2 \lim_{\substack{\epsilon\to 0\\ R\to\infty}} \int_{\epsilon}^{R} \frac{\mathrm{d}r}{r^{1/2}\,(1+r^2)} + \lim_{R\to\infty} \int_{C_R} \frac{\mathrm{d}z}{\sqrt{z}\,(1+z^2)} + \lim_{\epsilon\to 0} \int_{C_\epsilon} \frac{\mathrm{d}z}{\sqrt{z}\,(1+z^2)}. \tag{2.30}$$

Consider the integral over the contour C_R. We have the integrand

$$f(z) = \frac{1}{\sqrt{z}\,(1+z^2)}$$

with $z = R\,\mathrm{e}^{\mathrm{i}\theta}$ over C_R. Now,

$$\lim_{R\to\infty} |z f(z)| = \lim_{R\to\infty} \left| \frac{R\,\mathrm{e}^{\mathrm{i}\theta}}{R^{1/2}\,\mathrm{e}^{\mathrm{i}\,\theta/2}\,(1+R^2\,\mathrm{e}^{\mathrm{i}2\theta})} \right| = \lim_{R\to\infty} \left| \frac{R^{1/2}\,\mathrm{e}^{\mathrm{i}\,\theta/2}}{(1+R^2\,\mathrm{e}^{\mathrm{i}2\theta})} \right|.$$

Using the inequality $|z_1 + z_2| \geq ||z_1| - |z_2||$ we get

$$\lim_{R\to\infty} |z f(z)| \leq \lim_{R\to\infty} \frac{R^{1/2}}{|R^2 - 1|} \to 0.$$

Therefore, by Theorem 3 we get

$$\lim_{R\to\infty} \int_{C_R} \frac{\mathrm{d}z}{\sqrt{z}\,(1+z^2)} = 0.$$

Now consider the integral over the contour C_ϵ. We have the integrand

$$f(z) = \frac{1}{\sqrt{z}\,(1+z^2)}$$

with $z = \epsilon\,\mathrm{e}^{\mathrm{i}\theta}$ over C_ϵ. Now,

$$\lim_{\epsilon\to 0} |z f(z)| = \lim_{\epsilon\to 0} \left| \frac{\epsilon\,\mathrm{e}^{\mathrm{i}\theta}}{\epsilon^{1/2}\,\mathrm{e}^{\mathrm{i}\,\theta/2}\,(1+\epsilon^2\,\mathrm{e}^{\mathrm{i}2\theta})} \right| = \lim_{\epsilon\to 0} \left| \frac{\epsilon^{1/2}\,\mathrm{e}^{\mathrm{i}\,\theta/2}}{(1+\epsilon^2\,\mathrm{e}^{\mathrm{i}2\theta})} \right| \leq \lim_{\epsilon\to 0} \frac{\epsilon^{1/2}}{|1-\epsilon^2|} \to 0$$

Above, we have used the inequality $|z_1 + z_2| \geq ||z_1| - |z_2||$. Thus, by Theorem 2 (a) we get

$$\lim_{\epsilon\to 0} \int_{C_\epsilon} \frac{\mathrm{d}z}{\sqrt{z}\,(1+z^2)} = 0.$$

Thus, the integrals over C_R and C_ϵ vanish. Therefore, Eq. (2.30) can be written as

$$J = 2 \lim_{\substack{\epsilon\to 0\\ R\to\infty}} \int_{\epsilon}^{R} \frac{\mathrm{d}r}{r^{1/2}\,(1+r^2)}. \tag{2.31}$$

The integrand of Eq. (2.28) has poles at $z = \pm\mathrm{i}$. The residue at $z = \mathrm{i}$ is given by

$$\mathrm{Res}\,(\mathrm{i}) = \left.\frac{(z-\mathrm{i})}{\sqrt{z}(1+z^2)}\right|_{z=\mathrm{i}} = \left.\frac{1}{|z|^{1/2}\,\mathrm{e}^{\mathrm{i}\theta/2}(z+\mathrm{i})}\right|_{z=\mathrm{i}} = \frac{1}{2\mathrm{i}\,\mathrm{e}^{\mathrm{i}\pi/4}}. \tag{2.32}$$

The residue at $z = -\mathrm{i}$ is given by

$$\mathrm{Res}\,(-\mathrm{i}) = \left.\frac{(z+\mathrm{i})}{\sqrt{z}(1+z^2)}\right|_{z=-\mathrm{i}} = \left.\frac{1}{|z|^{1/2}\,\mathrm{e}^{\mathrm{i}\theta/2}(z-\mathrm{i})}\right|_{z=-\mathrm{i}} = \frac{1}{2\mathrm{i}\,\mathrm{e}^{-\mathrm{i}\,\pi/4}}. \tag{2.33}$$

Now by Cauchy residue theorem (Theorem 1) we get

$$J = \oint_C \frac{\mathrm{d}z}{\sqrt{z}\,(1+z^2)} = 2\pi\mathrm{i}\left[\mathrm{Res}\,(\mathrm{i}) + \mathrm{Res}\,(-\mathrm{i})\right]. \tag{2.34}$$

Therefore, by Eqs. (2.31)-(2.34) we have

$$\lim_{\substack{\epsilon\to 0\\ R\to\infty}} \int_\epsilon^R \frac{\mathrm{d}r}{r^{1/2}\,(1+r^2)} = \pi\cos\frac{\pi}{4} = \frac{\pi}{\sqrt{2}}.$$

Or,

$$\int_0^\infty \frac{\mathrm{d}x}{\sqrt{x}\,(1+x^2)} = \frac{\pi}{\sqrt{2}}. \tag{2.35}$$

2.9 Conclusions

In this chapter, the relevant literature that precedes the present work is discussed. Also, some of the important concepts and methods which will be used in the following chapters are discussed. The original work carried out in this thesis is presented from the next chapter onwards.

Part II

The one-way coupled analysis

Chapter 3

Sound radiation from a perforated panel: One-way coupling

3.1 Introduction

This thesis begins with a one-way coupled model for the sound radiation from a finite 2-D perforated flexible panel with simply supported boundary conditions set in a rigid baffle. By considering an unperforated baffle, this thesis extends the studies by Fahy and Thompson [5] and Putra and Thompson [4] (where a perforated baffle was considered). Also, here, the effect of the perforations on the panel natural frequencies is accounted for using the Receptance method. As the hole impedance takes into account the resistive and the reactive components, it can directly be applied to micro-perforated panels as well. The model assumes arbitrary perforation ratios and/or the hole sizes for the panel and the baffle regions.

In the following section (3.2), an expression for the radiated pressure field is derived in terms of a locally averaged fluid particle velocity which satisfies the continuity equation.

3.2 Radiated pressure on a perforated panel surface set in a baffle

Consider a finite thin elastic rectangular perforated panel ($-a/2 \leq x \leq a/2$, $-b/2 \leq y \leq b/2$) lying in the plane $z = 0$ with simply-supported boundary conditions, set in an infinite rigid baffle (see Fig. 3.1). Here, the baffle could be perforated or unperforated. The partition separates the fluid (air) into two regions of characteristic acoustic

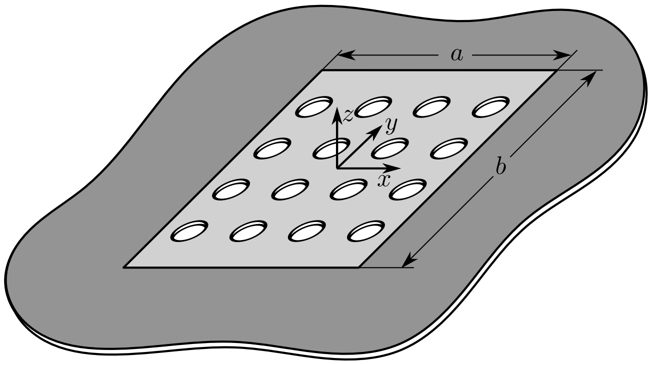

Fig. 3.1 Schematic of a perforated panel set in an unperforated baffle.

impedance $\rho_0 c$. Perforations are of a circular profile and have a diameter much less than the wave length of the incident acoustic field. The panel is excited by a point harmonic force of magnitude F at an angular frequency ω. The panel vibration creates a pressure difference across its plane. On the side $z < 0$, the total pressure p_1 is given by [7]

$$p_1(x, y, z, t) = p^-(x, y, z, t). \tag{3.1}$$

The total pressure field in the half space $z > 0$ comprises of the associated radiated pressure field given by

$$p_2(x, y, z, t) = p^+(x, y, z, t). \tag{3.2}$$

However,

$$p^-(x, y, z, t) = -p^+(x, y, -z, t). \tag{3.3}$$

Thus,

$$p_1(x, y, z, t) = -p^+(x, y, -z, t) \tag{3.4}$$

and the pressure difference across the $z = 0$ plane is given by

$$\Delta p(x, y, z = 0, t) = p_1(x, y, z = 0, t) - p_2(x, y, z = 0, t) = -2p^+(x, y, z = 0, t). \tag{3.5}$$

The temporal term $\exp(-i\omega t)$ in the acoustic wave propagation present in all the associated equations is omitted in further derivations. The radiated pressure $p^+(x, y, z)$ satisfies the 3-D Helmholtz equation

$$\left(\nabla^2 + k^2\right) p^+(x, y, z) = 0. \tag{3.6}$$

Taking a *double Fourier transform* of the above equation in the x and y directions we obtain

$$\left(\frac{\mathrm{d}^2}{\mathrm{d}z^2} + \left(k^2 - \lambda^2 - \mu^2\right)\right) P^+(\lambda, \mu, z) = 0, \tag{3.7}$$

where $P^+(\lambda, \mu, z)$ is defined as

$$P^+(\lambda, \mu, z) = \frac{1}{2\pi} \int_{-\infty}^{\infty} \int_{-\infty}^{\infty} p^+(x, y, z)\, e^{i\lambda x + i\mu y}\, \mathrm{d}x\, \mathrm{d}y. \tag{3.8}$$

Eq. (3.7) can be solved for $P^+(\lambda, \mu, z)$ as

$$P^+(\lambda, \mu, z) = A(\lambda, \mu) e^{-i\sqrt{k^2-\lambda^2-\mu^2}z} + B(\lambda, \mu) e^{i\sqrt{k^2-\lambda^2-\mu^2}z}. \tag{3.9}$$

From causality, $A(\lambda, \mu) = 0$. Hence, for a forward traveling wave (in the region $z > 0$) the solution takes the form

$$P^+(\lambda, \mu, z) = B(\lambda, \mu) e^{i\sqrt{k^2-\lambda^2-\mu^2}z}. \tag{3.10}$$

And for an evanescent wave, $P^+(\lambda, \mu, z) = B(\lambda, \mu) \exp\left(-\sqrt{\lambda^2 + \mu^2 - k^2}z\right)$. In order to find $B(\lambda, \mu)$, we invoke the boundary condition at the solid-fluid interface (at $z = 0$) in the Fourier transform domain as

$$\frac{\partial}{\partial z} P^+(\lambda, \mu, z = 0) = i\rho_0 ck V_a(\lambda, \mu, z)\big|_{z=0}, \tag{3.11}$$

where ρ_0 is the fluid density and $V_a(\lambda, \mu, z)$ is the double Fourier transform of the fluid particle velocity $v_a(x, y, z)$ given by

$$V_a(\lambda, \mu, z) = \frac{1}{2\pi} \int_{-\infty}^{\infty} \int_{-\infty}^{\infty} v_a(x, y, z)\, e^{i\lambda x + i\mu y}\, \mathrm{d}x\, \mathrm{d}y. \tag{3.12}$$

Using Eq. (3.10), the boundary condition can be rewritten as

$$\sqrt{k^2 - \lambda^2 - \mu^2} P^+(\lambda, \mu, z = 0) = \rho_0 ck V_a(\lambda, \mu, z = 0).$$

Or

$$B(\lambda, \mu) = P^+(\lambda, \mu, z = 0) = Z_a(\lambda, \mu) V_a(\lambda, \mu, z = 0), \tag{3.13}$$

where $Z_a(\lambda, \mu)$ is the acoustic impedance given by

$$Z_a(\lambda, \mu) = \frac{\rho_0 ck}{\sqrt{k^2 - \lambda^2 - \mu^2}}. \tag{3.14}$$

Therefore,

$$P^+(\lambda, \mu, z) = Z_a(\lambda, \mu) V_a(\lambda, \mu, z = 0) e^{i\sqrt{k^2-\lambda^2-\mu^2}z}. \tag{3.15}$$

Thus, if $V_a(\lambda, \mu, z = 0)$ is known, the radiated pressure can be found. However, $V_a(\lambda, \mu, z = 0)$ is not the transform of the panel velocity v_p. It is related to the mean fluid particle velocity on $z > 0$ after accounting for the leakage through the perforations. Hence, a locally averaged fluid particle velocity (LAFP) $v_a(x, y, t)$ needs to be defined, which is done in the following section.

3.3 Locally averaged fluid particle velocity (LAFP) over a perforated panel

Takahashi and Tanaka [2] developed a model for the average acoustic particle velocity at the fluid-panel interface that conserves the volume flow through the perforations. The same model is adopted here.

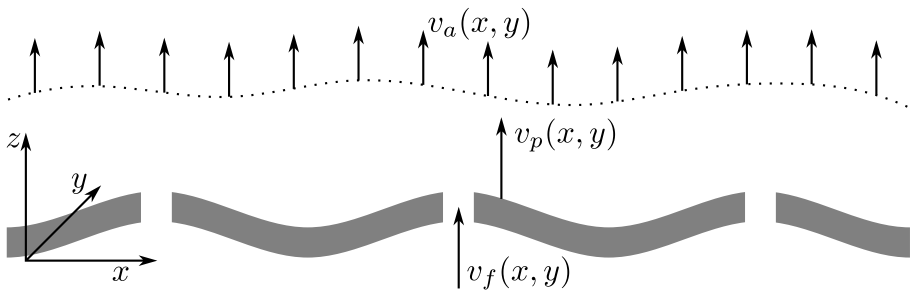

Fig. 3.2 Schematic of the panel and the fluid velocities in the perforated panel model

Referring to Fig. 3.2, let v_p be the velocity of the panel, v_a be the mean particle velocity just above the panel surface and v_f be the average fluid velocity within a single hole. The impedance of a single hole is $Z_0 = Z_{resist} + Z_{react}$ where, Z_{resist} depends on the viscous force at the fluid-structure interface within the hole and is related to the relative fluid particle velocity inside the hole. Whereas, Z_{react} depends on the inertia of the fluid contained within the hole and the effect of radiation at the hole entrance. From the continuity equation using a control volume, the mean particle velocity of the air for $z > 0$ is given by [2]

$$S_p v_a = S_h v_f + (S_p - S_h)\, v_p \quad \Rightarrow \quad v_a = v_p + (v_f - v_p)\, \sigma_p, \tag{3.16}$$

where S_p is the panel area, S_h is the hole area and $(S_p - S_h)$ represents the effective panel area. $\sigma_p = \frac{N_0 \pi r^2}{ab}$ is the perforation ratio defined as the fraction of the area of the apertures to the total area of the plate. N_0 is the total number of apertures and r is the radius of each aperture.

And from the momentum equation on a control volume we get [2]

$$Z_{resist}\,(v_f - v_p) + Z_{react} v_f = \Delta p. \tag{3.17}$$

Please note that the viscous force at the air-solid interface in the hole depends on relative velocity $v_f - v_p$ and the forces due to air inertia and acoustic radiation at hole entrance are related to v_f alone.

For wave propagation in a circular tube that is short compared to the acoustic wavelength, an approximate expression for the specific acoustic impedance Z_0 is given by Maa [1] as

$$\begin{aligned} Z_0 &= Z_{resist} + Z_{react} \\ &= \frac{8\eta_0 h}{(d/2)^2}\left(\sqrt{1+\frac{X^2}{32}} + \frac{\sqrt{2}dX}{8h}\right) - i\rho_0\omega h\left(1 + \frac{1}{\sqrt{9+X^2/2}} + \frac{0.85d}{h}\right), \end{aligned} \tag{3.18}$$

where $X = \frac{d}{2}\sqrt{\frac{\rho_0\omega}{\eta_0}}$, d and h are the diameter of the hole and thickness of the panel respectively, ρ_0 is the air density and η_0 is the air viscosity ($= 1.8 \times 10^{-5}\mathrm{Ns/m^2}$). The term X is called the perforate constant which is proportional to the ratio of the radius to the viscous boundary layer thickness inside the tube. The above approximation is valid for the entire range of the perforate constant values. It also includes the end corrections due to airflow friction at the panel surface as the flow is squeezed into the hole area and the mass reactance at the ends of the hole.

Hence, using Eqs. (3.16) and (3.17), LAFP velocity over the panel surface can be obtained as

$$v_a = \zeta_I v_p + \frac{\Delta p}{Z_0}\sigma_p = \zeta_I v_p + \frac{\Delta p}{Z}, \tag{3.19}$$

where $\zeta_I = 1 - (Z_{react}/Z_0)\,\sigma_p$. This equation can be considered as a balance over a small panel area. Hence, for the entire panel one can write

$$v_a(x, y) = \zeta_I v_p(x, y) + \frac{\Delta p(x, y)}{Z_0}\sigma_p = \zeta_I v_p(x, y) + \frac{\Delta p(x, y)}{Z}, \tag{3.20}$$

This LAFP velocity information can be used as a homogeneous continuity boundary condition at the fluid-structure interface of a perforated panel, under any acoustic loading. In the above treatment, it is assumed that the hole size is smaller than the acoustic wavelength, so that the fluid motion inside the hole can be considered to be uniform across the cross sectional area. Eq. (3.20) evaluates the LAFP velocity in the spatial domain. The radiated pressure Eq. (3.15) requires the LAFP velocity in the wavenumber domain. The LAFP velocity is obtained in the wavenumber domain in the following section.

3.4 Fourier transform of the LAFP velocity over the panel-baffle plane

Let the panel and the baffle have the perforation ratios σ_p and σ_b, respectively. Using Eqs. (3.5) and (3.19), the LAFP velocity over the panel-baffle plane ($z = 0$) is defined as

$$\begin{aligned} v_{ap}(x, y, z = 0) &= \zeta_I v_p(x, y) - \frac{2\sigma_p}{Z_{0p}} p^+(x, y, z = 0), \quad \text{within the panel area} \\ v_{ab}(x, y, z = 0) &= -\frac{2\sigma_b}{Z_{0b}} p^+(x, y, z = 0), \quad \text{outside the panel area} \end{aligned} \tag{3.21}$$

where Z_{0p} and Z_{0b} are the hole impedances over the panel and the baffle regions, respectively. Here, an arbitrary case is assumed in which $\sigma_p \neq \sigma_b$ and $Z_{0p} \neq Z_{0b}$.

Taking the Fourier transform of the above equation (Eq. (3.21))

$$\begin{aligned} V_a(\lambda, \mu, z = 0) = \frac{1}{2\pi} \int\limits_{-b/2}^{b/2} \int\limits_{-a/2}^{a/2} v_{ap}(x, y)\, e^{i\lambda x + i\mu y}\, \mathrm{d}x\, \mathrm{d}y \\ + \text{ integral over the region beyond panel surface.} \end{aligned}$$

Thus,

$$V_a(\lambda, \mu, z=0) = \frac{1}{2\pi} \int_{-b/2}^{b/2} \int_{-a/2}^{a/2} v_{ap}(x,y)\, e^{i\lambda x + i\mu y}\, \mathrm{d}x\, \mathrm{d}y + \frac{1}{2\pi} \left(\int_{-\infty}^{\infty} \int_{-\infty}^{\infty} - \int_{-b/2}^{b/2} \int_{-a/2}^{a/2} \right) v_{ab}(x,y)\, e^{i\lambda x + i\mu y}\, \mathrm{d}x\, \mathrm{d}y.$$

Substituting for v_{ap} and v_{ab} from Eq. (3.21) we obtain

$$\begin{aligned} V_a(\lambda, \mu, z=0) = & \frac{1}{2\pi} \int_{-b/2}^{b/2} \int_{-a/2}^{a/2} \left[\zeta_I v_p(x,y) - \frac{2\sigma_p}{Z_{0p}} p^+(x,y,z=0) \right] e^{i\lambda x + i\mu y}\, \mathrm{d}x\, \mathrm{d}y \\ & - \frac{1}{2\pi} \int_{-\infty}^{\infty} \int_{-\infty}^{\infty} \frac{2\sigma_b}{Z_{0b}} p^+(x,y,z=0)\, e^{i\lambda x + i\mu y}\, \mathrm{d}x\, \mathrm{d}y \\ & + \frac{1}{2\pi} \int_{-b/2}^{b/2} \int_{-a/2}^{a/2} \frac{2\sigma_b}{Z_{0b}} p^+(x,y,z=0)\, e^{i\lambda x + i\mu y}\, \mathrm{d}x\, \mathrm{d}y. \end{aligned}$$

Or

$$\begin{aligned} V_a(\lambda, \mu, z=0) = & \zeta_I V_p(\lambda, \mu) - \frac{2\sigma_b}{Z_{0b}} P^+(\lambda, \mu, z=0) \\ & + \frac{1}{2\pi} \int_{-b/2}^{b/2} \int_{-a/2}^{a/2} \left[\frac{2\sigma_b}{Z_{0b}} - \frac{2\sigma_p}{Z_{0p}} \right] p^+(x,y,z=0)\, e^{i\lambda x + i\mu y}\, \mathrm{d}x\, \mathrm{d}y, \end{aligned} \tag{3.22}$$

where

$$V_p(\lambda, \mu) = \frac{1}{2\pi} \int_{-b/2}^{b/2} \int_{-a/2}^{a/2} v_p(x,y)\, e^{i\lambda x + i\mu y}\, \mathrm{d}x\, \mathrm{d}y. \tag{3.23}$$

Using the inverse Fourier transform

$$p^+(x,y,z) = \frac{1}{2\pi} \int_{-\infty}^{\infty} \int_{-\infty}^{\infty} P^+(\lambda', \mu', z)\, e^{-i\lambda' x - i\mu' y}\, \mathrm{d}\lambda'\, \mathrm{d}\mu'. \tag{3.24}$$

Therefore,

$$\frac{1}{2\pi}\int_{-b/2}^{b/2}\int_{-a/2}^{a/2} p^+(x,y,z)\, e^{i\lambda x+i\mu y}\,\mathrm{d}x\,\mathrm{d}y$$
$$= \frac{1}{4\pi^2}\int_{-b/2}^{b/2}\int_{-a/2}^{a/2}\left[\int_{-\infty}^{\infty}\int_{-\infty}^{\infty} P^+(\lambda',\mu',z)\, e^{-i\lambda' x-i\mu' y}\,\mathrm{d}\lambda'\,\mathrm{d}\mu'\right] e^{i\lambda x+i\mu y}\,\mathrm{d}x\,\mathrm{d}y.$$

Rearranging,

$$\frac{1}{2\pi}\int_{-b/2}^{b/2}\int_{-a/2}^{a/2} p^+(x,y,z)\, e^{i\lambda x+i\mu y}\,\mathrm{d}x\,\mathrm{d}y$$
$$= \frac{1}{4\pi^2}\int_{-\infty}^{\infty}\int_{-\infty}^{\infty} P^+(\lambda',\mu',z)\left[\int_{-b/2}^{b/2}\int_{-a/2}^{a/2} e^{i(\lambda-\lambda')x+i(\mu-\mu')y}\,\mathrm{d}x\,\mathrm{d}y\right]\mathrm{d}\lambda'\,\mathrm{d}\mu'.$$

However, we know that

$$\int_{-b/2}^{b/2}\int_{-a/2}^{a/2} e^{i(\lambda-\lambda')x+i(\mu-\mu')y}\,\mathrm{d}x\,\mathrm{d}y = ab\,\mathrm{sinc}\left[\frac{(\lambda-\lambda')a}{2}\right]\,\mathrm{sinc}\left[\frac{(\mu-\mu')b}{2}\right]. \tag{3.25}$$

Hence,

$$\frac{1}{2\pi}\int_{-b/2}^{b/2}\int_{-a/2}^{a/2} p^+(x,y,z)\, e^{i\lambda x+i\mu y}\,\mathrm{d}x\,\mathrm{d}y$$
$$= \frac{ab}{4\pi^2}\int_{-\infty}^{\infty}\int_{-\infty}^{\infty} P^+(\lambda',\mu',z)\,\mathrm{sinc}\left[\frac{(\lambda-\lambda')a}{2}\right]\,\mathrm{sinc}\left[\frac{(\mu-\mu')b}{2}\right]\,\mathrm{d}\lambda'\,\mathrm{d}\mu'.$$

At $z = 0$

$$\frac{1}{2\pi}\int_{-b/2}^{b/2}\int_{-a/2}^{a/2} p^{+}(x, y, z = 0)\, e^{i\lambda x + i\mu y}\,\mathrm{d}x\,\mathrm{d}y$$
$$= \frac{ab}{4\pi^2}\int_{-\infty}^{\infty}\int_{-\infty}^{\infty} P^{+}(\lambda', \mu', z = 0)\,\mathrm{sinc}\left[\frac{(\lambda-\lambda')a}{2}\right]\,\mathrm{sinc}\left[\frac{(\mu-\mu')b}{2}\right]\,\mathrm{d}\lambda'\,\mathrm{d}\mu'.$$

However, from Eq. (3.13)

$$P^{+}(\lambda', \mu', z = 0) = Z_a(\lambda', \mu')V_a(\lambda', \mu', z = 0),$$

where $Z_a(\lambda, \mu)$ is the acoustic impedance given by Eq. (3.14). Therefore, the previous integral can be written as

$$\frac{1}{2\pi}\int_{-b/2}^{b/2}\int_{-a/2}^{a/2} p^{+}(x, y, z = 0)\, e^{i\lambda x + i\mu y}\,\mathrm{d}x\,\mathrm{d}y$$
$$= \frac{ab}{4\pi^2}\int_{-\infty}^{\infty}\int_{-\infty}^{\infty} Z_a(\lambda', \mu')V_a(\lambda', \mu', z = 0)\,\mathrm{sinc}\left[\frac{(\lambda-\lambda')a}{2}\right]\,\mathrm{sinc}\left[\frac{(\mu-\mu')b}{2}\right]\,\mathrm{d}\lambda'\,\mathrm{d}\mu'. \tag{3.26}$$

Using Eqs. (3.13) and (3.26), the spatial Fourier transform of the mean fluid particle velocity (at panel-baffle plane, $z = 0$) in Eq. (3.22) can be written as

$$V_a(\lambda, \mu, z = 0) = \zeta_I V_p(\lambda, \mu) - \frac{2\sigma_b}{Z_{0b}} Z_a(\lambda, \mu)V_a(\lambda, \mu, z = 0) + \frac{ab}{2\pi^2}\left[\frac{\sigma_b}{Z_{0b}} - \frac{\sigma_p}{Z_{0p}}\right]$$
$$\times\left\{\int_{-\infty}^{\infty}\int_{-\infty}^{\infty} Z_a(\lambda', \mu')V_a(\lambda', \mu', z = 0)\,\mathrm{sinc}\left[\frac{(\lambda-\lambda')a}{2}\right]\,\mathrm{sinc}\left[\frac{(\mu-\mu')b}{2}\right]\,\mathrm{d}\lambda'\,\mathrm{d}\mu'\right\},$$

or

$$\left[1 + \frac{2\sigma_b}{Z_{0b}} Z_a(\lambda,\mu)\right] V_a(\lambda,\mu,z=0) = \zeta_I V_p(\lambda,\mu) + \frac{ab}{2\pi^2}\left[\frac{\sigma_b}{Z_{0b}} - \frac{\sigma_p}{Z_{0p}}\right]$$
$$\times \left\{ \int_{-\infty}^{\infty}\int_{-\infty}^{\infty} Z_a(\lambda',\mu') V_a(\lambda',\mu',z=0)\,\mathrm{sinc}\left[\frac{(\lambda-\lambda')a}{2}\right] \mathrm{sinc}\left[\frac{(\mu-\mu')b}{2}\right] \mathrm{d}\lambda'\,\mathrm{d}\mu' \right\}, \tag{3.27}$$

where $Z_a(\lambda',\mu')$ is the acoustic impedance of the medium given by

$$Z_a(\lambda',\mu') = \frac{\rho_0 c k}{\sqrt{k^2 - \lambda'^2 - \mu'^2}}.$$

The presence of sinc() function in the above equation shows that for a perforated panel set in a baffle with a different perforation ratio, there exists a ‘coupling’ effect between the different wavenumbers in the spectrum of the LAFP velocity [5].

Let us consider a case where the panel and the baffle are identically perforated, i.e., $\sigma_p = \sigma_b$ and $Z_{0p} = Z_{0b}$. In such a scenario, there exists no ‘coupling’ in the LAFP velocity spectrum as given below.

$$\left[1 + \frac{2\sigma_p}{Z_{0p}} Z_a(\lambda,\mu)\right] V_a(\lambda,\mu,z=0) = \zeta_I V_p(\lambda,\mu). \tag{3.28}$$

This case is taken up in the following section.

The case of a perforated panel set in an unperforated baffle can be represented by choosing $\sigma_b = 0$. Thus, the spectrum of the LAFP velocity is given by

$$V_a(\lambda,\mu,z=0) = \zeta_I V_p(\lambda,\mu) - \frac{ab}{2\pi^2}\frac{\sigma_p}{Z_{0p}}$$
$$\times \left\{ \int_{-\infty}^{\infty}\int_{-\infty}^{\infty} Z_a(\lambda',\mu') V_a(\lambda',\mu',z=0)\,\mathrm{sinc}\left[\frac{(\lambda-\lambda')a}{2}\right] \mathrm{sinc}\left[\frac{(\mu-\mu')b}{2}\right] \mathrm{d}\lambda'\,\mathrm{d}\mu' \right\}. \tag{3.29}$$

Given the panel velocity spectrum $V_p(\lambda,\mu)$, Eqs. (3.27) and (3.29) can be solved numerically for $V_a(\lambda,\mu)$ by formulating the equations in a matrix form using discretized values of λ and μ. The integral is approximated by a sum over the range of discrete values of λ and μ (Appendix A).

3.5 Sound radiation from a perforated panel set in a similarly perforated baffle

The sound radiation from a perforated panel fixed in a baffle is discussed in this section. The baffle is assumed to be perforated in a similar fashion as that of the panel, i.e., $\sigma_b = \sigma_p$ and $Z_{0b} = Z_{0p}$. The derivation presented is very brief as it is almost the same as that of Putra and Thompson [4]. The only difference is that the hole impedance used here has a non-zero resistive component. Thus, the curves highlight the validity of including/ignoring this resistive component. The equality of the perforate impedances in the baffle and the panel eliminates the 'coupling' of wavenumbers in the LAFP velocity over the panel (See Eq. (3.28)). This coupling issue was discussed by Fahy and Thompson [5] and Putra and Thompson [4].

The Fourier transform of the LAFP velocity over the perforated panel, for a similarly perforated baffle case is given by Eq. (3.28).

$$V_a(\lambda, \mu, z = 0) = \frac{\zeta_I}{\left[1 + \frac{2\sigma_p}{Z_{0p}} Z_a(\lambda, \mu)\right]} V_p(\lambda, \mu). \tag{3.30}$$

Here, it must be noted that Z_{0p} has the resistive component unlike [4]. And it is known that the time averaged power from a vibrating panel set in a rigid baffle (both unperforated) is [11]

$$W = \frac{1}{2}\mathrm{Re}\left\{ \int_{-\infty}^{\infty}\int_{-\infty}^{\infty} P^+(\lambda, \mu, z = 0) V_p^*(\lambda, \mu)\, \mathrm{d}\lambda\, \mathrm{d}\mu \right\}, \tag{3.31}$$

in which $P^+(\lambda, \mu, z = 0)$ is given by Eq. (3.13)

$$P^+(\lambda, \mu, z = 0) = Z_a(\lambda, \mu) V_p(\lambda, \mu, z = 0),$$

where $P^+(\lambda, \mu, z = 0)$ and $V_p(\lambda, \mu, z = 0)$ are the Fourier transforms of the panel surface pressure and panel velocity. For the case of a perforated panel in a perforated baffle, $V_p(\lambda, \mu, z = 0)$ needs to be replaced by the LAFP velocity $V_a(\lambda, \mu, z = 0)$. The rest of the derivation is the same as in [4] and is given in Appendix B.

3.5.1 Results

Comparison with existing modal summation theory

Putra's average radiation efficiency expression is given by

$$\sigma = \frac{\sum_{m=1}^{\infty}\sum_{n=1}^{\infty}\overline{W_{mn}}}{\frac{1}{2}\rho_0 cab(1-\sigma_p)\sum_{m=1}^{\infty}\sum_{n=1}^{\infty}\overline{<|v_{mn}|^2>}}, \tag{3.32}$$

where

$$\overline{<|v_{mn}|^2>} = \frac{\overline{|U_{mn}|^2}}{4}.$$

Note that in the denominator of the expression for the radiation efficiency (Eq. (3.32)), only the solid part of the perforated plate area is considered. However, the term $(1-\sigma_p)$ has a significant effect at high perforation ratios.

Fig. 3.3 shows the comparison of Eq. (B.25) with those derived by Putra (Eq. (3.32)) for a unit force excitation. These results are for a plate with dimensions $0.455 \times 0.546 \times 0.003$ m and $\eta = 0.1$. The panel density $\rho_p = 2700$ kg/m^3, the Young's modulus $E = 70$ GPa and Poisson's ratio $\nu = 0.33$. All the modes below 10^4 Hz are considered while performing the modal summation. While evaluating the radiation efficiency using Eq. (B.25) the denominator is multiplied by $(1-\sigma_p)$ so that only the solid part of the perforate area is considered. The reader may note that the hole impedance adopted by the current method considers both the viscous dissipation at the walls (resistive) and the mass like behavior of the fluid inside the perforations (reactive part) and is given by Eq. (3.18) [1]. Whereas, Putra considers only the mass like behavior of the fluid inside the hole to define the perforate impedance as given by [4]

$$Z_0 = i\rho_0 c\Theta\sigma_p, \tag{3.33}$$

where $\Theta = \frac{k}{\sigma_p}\left[h + \frac{8d}{3\pi}\right]$ denotes the non-dimensional specific acoustic reactance. The variation in the hole impedance as a function of the frequency for both the cases (Eqs. (3.18) and (3.33)) is plotted in Fig. 3.4. For the size of the hole and the frequencies of interest, the reactive impedance dominates over the resistive component and at high frequencies, the resistive part is relatively negligible. This is the reason why Putra's purely reactive model compares so well.

So far we have discussed the sound radiation from a perforated panel fixed in a perforated baffle with the same value of the perforation ratio. In the following section, the baffle has a different perforation from that of the panel.

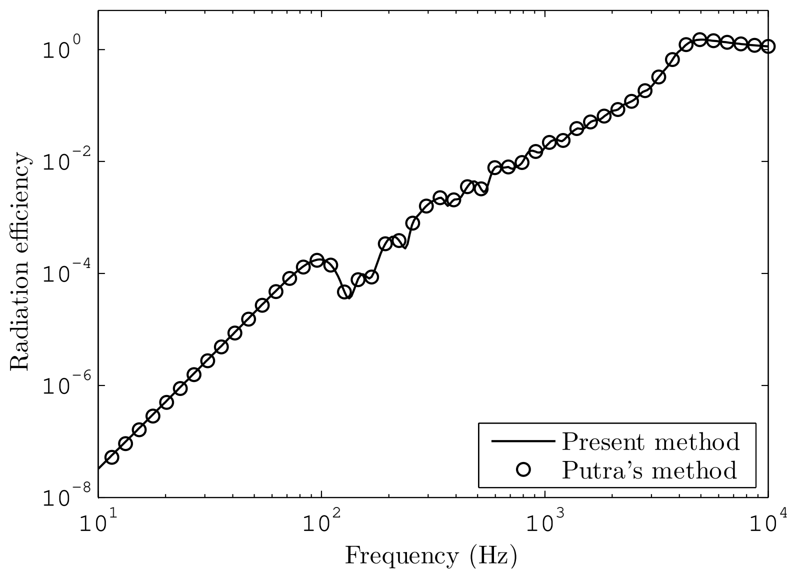

Fig. 3.3 Radiation efficiency of a perforated panel in a baffle (present method and Putra's method). The baffle is similarly perforated. The perforation ratio is $\sigma_p = 9.61\%$ and the holes are of radius $r_p = 5$ mm.

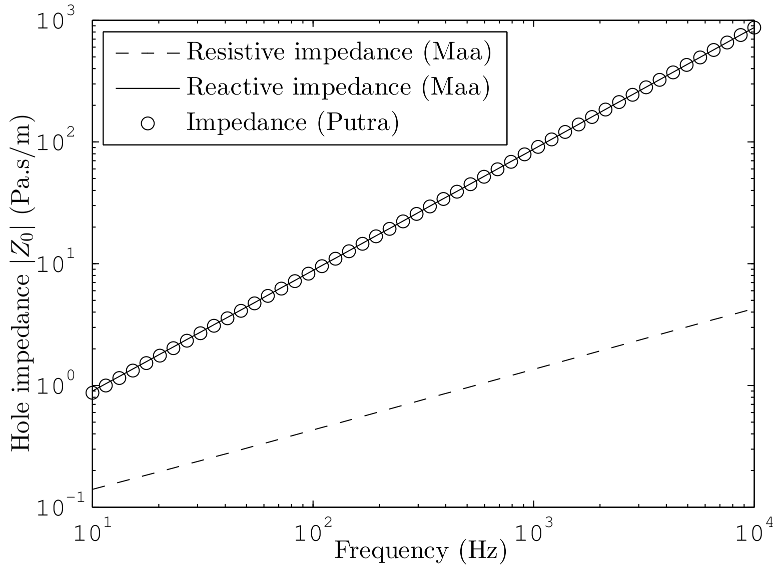

Fig. 3.4 Comparison of hole impedances. The impedance used in this article (Maa [1]) is given by Eq. (3.18) and the impedance used by Putra is given by Eq. (3.33). The hole radius is $r_p = 5$ mm and the length of the hole (panel thickness) is $h = 3$ mm.

3.6 Sound radiation from a perforated panel set in a differently perforated baffle

In this section, the sound radiation from a perforated flexible simply-supported rectangular panel set in a differently perforated baffle excited by a point harmonic force is considered. Here, the panel resonance frequency shifts due to the presence of the holes are accounted for, i.e., the modifications to modal inertia and modal stiffness are included in the calculation.

3.6.1 Response of a perforated panel to point harmonic excitation

The response of the perforated panel can be expressed in terms of a modal sum. However, the perforations change the stiffness and the inertial properties of the panel. Thus, the new resonant frequencies and modeshapes of the perforated panel have to be found out. Soler and Hill [68] proposed a formulation for the effective static bending stiffness of a rectangular perforated strip for different hole array configurations. The formulation is deduced based on various experimental data and a series of curve fits. The effective static bending stiffness is a function of the solidity factor f, the thickness of the panel h and the hole array configuration parameters (hole diameter $d = 2r_p$, distance between two adjacent holes in the array (pitch) p and ligament width $t = p - d$).

The solidity factor f is defined as the ratio of the solid area of the perforated panel to the total panel area, i.e.,

$$f = \frac{\text{panel area after drilling}}{\text{unperforated panel area}}.$$

In other words, $f = 1 - \alpha$, where α is the perforation ratio ($0 < f \leq 1$). Of the various array configurations studied in their work, the rectangular array configuration with a square pitch is of particular interest to the problem under consideration. Fig. 3.5 shows the schematic of a typical rectangular array of perforations, where b is the width of the repeating pattern of holes in the perforated panel. When the width is the same as that of the pitch ($b = p$), it is referred to as the square pitch. For a rectangular array with a square pitch, the solidity factor is found to be of the form

$$f = \frac{p^2 - \frac{\pi}{4}d^2}{p^2} = 1 - \frac{\pi}{4}\left(\frac{d}{p}\right)^2 = 1 - \frac{\pi}{4}\left(1 - \frac{t}{p}\right)^2. \tag{3.34}$$

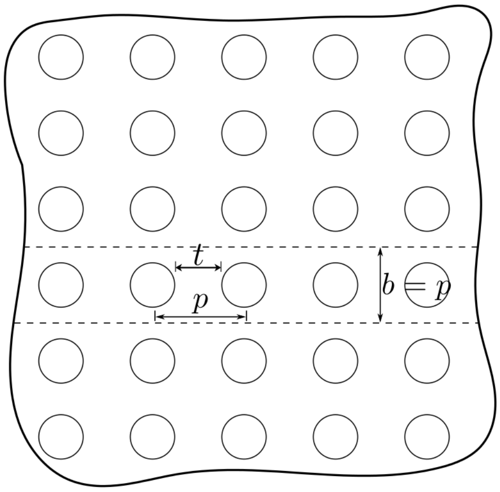

Fig. 3.5 Schematic of a rectangular array of holes with a square pitch.

Let D be the bending stiffness of an unperforated panel ($D = Eh^3/12(1-\nu^2)$) and D^* be the effective bending stiffness of the perforated panel. According to Soler and Hill [68]

$$\frac{D^*}{D} = f^\gamma, \quad \gamma = \gamma\left(\frac{t}{p}, \frac{h}{2p}\right). \tag{3.35}$$

Let χ be a thickness coefficient given by

$$\chi = \frac{h/2p - 1}{h/2p + 1}.$$

Using curve fits on the experimental data, Soler and Hill have deduced that

$$\gamma = \frac{13+3\chi}{8}\left[1 + \frac{(3-\chi)}{4}\frac{t}{p} + \frac{(1+\chi)}{2}\frac{h}{p}\left(1-\frac{t}{p}\right)^2\right]. \tag{3.36}$$

Using Eqs. (3.34), (3.35) and (3.36), we may now find the effective bending stiffness as

$$D^* = f^\gamma D. \tag{3.37}$$

A perforated panel can be thought of as a panel with small mass voids and with reduced bending stiffness. The bending stiffness of the perforated panel is modified first as explained above. Then the Receptance method is used to mathematically subtract the inertia of the void from that of a panel with sufficient accuracy [65]. This results in the modified resonances and modeshapes. The new resonance frequencies and modeshapes are derived in 2.7 using the Receptance method.

Having found the modeshapes of the perforated panel from 2.7, the displacement of a perforated panel at the point (x, y) to a point harmonic force excitation of magnitude F and frequency ω can be obtained as

$$w(x, y, t) = \sum_{r=1}^{\infty} \frac{1}{M_r} \frac{\psi_r(x_i, y_i) F e^{-i\omega t}}{[\omega_r^2(1 - i\eta) - \omega^2]} \psi_r(x, y), \tag{3.38}$$

where (x_i, y_i) is the point of excitation, η is the damping loss factor and the term M_r represents modal mass given by

$$M_r = \int_{-b/2}^{b/2} \int_{-a/2}^{a/2} \rho_p h \psi_r^2(x, y) \,\mathrm{d}x \,\mathrm{d}y = \frac{\rho_p hab}{4} \sum_{m=1}^{\infty} \sum_{n=1}^{\infty} |U_{mnr}|^2. \tag{3.39}$$

A detailed derivation of M_r is presented in Appendix C. The transverse velocity of the perforated panel can be expressed in the modal summation form as

$$v_p\left(x, y\right) = \sum_{r=1}^{\infty} B_r \psi_r\left(x, y\right). \tag{3.40}$$

Using Eq. (3.38), the modal coefficient for the r^{th} mode of the perforated panel B_r can be obtained as

$$B_r = \frac{-i\omega\psi_r(x_i, y_i) F}{M_r\left[\omega_r^2(1 - i\eta) - \omega^2\right]}, \tag{3.41}$$

where ω_r is the natural frequency of the r^{th} mode of the perforated panel. From 2.7, substituting for $\psi_r\left(x, y\right)$ (Eq. (2.26)) in Eq. (3.40) and using the double Fourier transform we obtain

$$V_p\left(\lambda, \mu\right) = \sum_{r=1}^{\infty} B_r \sum_{m=1}^{\infty} \sum_{n=1}^{\infty} U_{mnr} \Phi_{mn}\left(\lambda, \mu\right), \tag{3.42}$$

where

$$\Phi_{mn}\left(\lambda, \mu\right) = \frac{1}{2\pi} \int_{-b/2}^{b/2} \int_{-a/2}^{a/2} \sin\frac{m\pi(x + a/2)}{a} \sin\frac{n\pi(y + b/2)}{b} e^{i\lambda x + i\mu y} \,\mathrm{d}x \,\mathrm{d}y.$$

Note that as the panel velocity $v_p(x, y)$ is zero over the baffle region, while finding the Fourier transform, the integration is limited to the panel area alone. Thus,

$$\Phi_{mn}(\lambda, \mu) = \frac{a_m b_n}{2\pi} \frac{\left[(-1)^m e^{i\lambda a/2} - e^{-i\lambda a/2}\right]}{[\lambda^2 - a_m^2]} \frac{\left[(-1)^n e^{i\mu b/2} - e^{-i\mu b/2}\right]}{[\mu^2 - b_n^2]}, \tag{3.43}$$

with $a_m = \frac{m\pi}{a}$ and $b_n = \frac{n\pi}{b}$.

Now, the spatial Fourier transform of the LAFP velocity at the panel-baffle plane ($z = 0$) is given by Eq. (3.27), i.e.,

$$\left[1 + \frac{2\sigma_b}{Z_{0b}} Z_a(\lambda, \mu)\right] V_a(\lambda, \mu, z = 0) = \zeta_I V_p(\lambda, \mu) + \frac{ab}{2\pi^2}\left[\frac{\sigma_b}{Z_{0b}} - \frac{\sigma_p}{Z_{0p}}\right]$$
$$\times \left\{ \int_{-\infty}^{\infty}\int_{-\infty}^{\infty} Z_a(\lambda', \mu') V_a(\lambda', \mu', z = 0) \,\mathrm{sinc}\left[\frac{(\lambda - \lambda')a}{2}\right] \mathrm{sinc}\left[\frac{(\mu - \mu')b}{2}\right] \mathrm{d}\lambda' \,\mathrm{d}\mu' \right\},$$

where $Z_a(\lambda', \mu')$ is the acoustic impedance of air given by

$$Z_a(\lambda', \mu') = \frac{\rho_0 c k}{\sqrt{k^2 - \lambda'^2 - \mu'^2}}.$$

Given the spectrum of the plate velocity $V_p(\lambda, \mu)$, Eq. (3.27) (given above) is solved numerically for $V_a(\lambda, \mu)$ by formulating the equations in a matrix form using discretized values of λ and μ. The integral is approximated by a sum over the range of discrete values of λ and μ. Next, the double Fourier transform of the radiated pressure can be obtained from Eq. (3.13) as

$$P^+(\lambda, \mu, z = 0) = Z_a(\lambda, \mu) V_a(\lambda, \mu, z = 0).$$

3.6.2 Radiated power from a perforated panel in a baffle

We may now find the radiated power from the perforated panel due to a point harmonic excitation. The expression for the radiated power is

$$W = \frac{1}{2}\mathrm{Re}\left\{ \int_{-\infty}^{\infty}\int_{-\infty}^{\infty} P^+(\lambda, \mu, z = 0) V_a^*(\lambda, \mu) \,\mathrm{d}\lambda \,\mathrm{d}\mu \right\},$$

where we use the LAFP velocity due to the panel motion and the fluid flow through the perforations to evaluate the radiated power. In the above equation, only the wavenumber components satisfying the inequality $k^2 > \lambda^2 + \mu^2$ will radiate into the far field. Hence, for the power radiated into the far field, the limits of integration are as shown below:

$$W = \frac{1}{2}\mathrm{Re}\left\{ \int_{-k}^{k} \int_{-\sqrt{k^2-\mu^2}}^{\sqrt{k^2-\mu^2}} P^{+}(\lambda, \mu, z=0) V_a^{*}(\lambda, \mu)\, \mathrm{d}\lambda\, \mathrm{d}\mu \right\} \tag{3.44}$$

In the above equation, the Fourier transforms of the radiated pressure and the plate velocity are obtained as explained earlier. Here again, the integral is approximated by a sum over the range of discrete values of λ and μ.

3.6.3 Radiation efficiency of a perforated panel in a baffle

The radiation efficiency of a perforated panel subjected to a point harmonic excitation is given by

$$\sigma = \frac{W}{\frac{1}{2}\rho_0 c a b < |v_p|^2 >}, \tag{3.45}$$

where W is the radiated power (Eq. (3.44)) and $< |v_p|^2 >$ is the spatially averaged squared velocity of the perforated panel. The spatially averaged squared velocity is defined as

$$< |v_p|^2 > = \frac{1}{ab} \int_{-b/2}^{b/2} \int_{-a/2}^{a/2} |v_p(x, y)|^2 \, \mathrm{d}x\, \mathrm{d}y,$$

where the panel flexural velocity is given by Eq. (3.40).

$$v_p(x, y) = \sum_{r=1}^{\infty} B_r \sum_{m=1}^{\infty} \sum_{n=1}^{\infty} U_{mnr} \sin \frac{m\pi(x + a/2)}{a} \sin \frac{n\pi(y + b/2)}{b}. \tag{3.46}$$

Substituting for $v_p(x,y)$ from above we get

$$
\begin{aligned}
< |v_p|^2 > &= \frac{1}{ab} \int_{-b/2}^{b/2} \int_{-a/2}^{a/2} \left[\sum_{r=1}^{\infty} B_r \sum_{m=1}^{\infty} \sum_{n=1}^{\infty} U_{mnr} \sin \frac{m\pi(x+a/2)}{a} \sin \frac{n\pi(y+b/2)}{b} \right] \\
&\qquad \times \left[\sum_{s=1}^{\infty} B_s^* \sum_{p=1}^{\infty} \sum_{q=1}^{\infty} U_{pqs}^* \sin \frac{p\pi(x+a/2)}{a} \sin \frac{q\pi(y+b/2)}{b} \right] \mathrm{d}x\,\mathrm{d}y \\
&= \frac{1}{ab} \sum_{r=1}^{\infty} \sum_{s=1}^{\infty} \sum_{m=1}^{\infty} \sum_{n=1}^{\infty} \sum_{p=1}^{\infty} \sum_{q=1}^{\infty} B_r B_s^* U_{mnr} U_{pqs}^* \\
&\times \int_{-b/2}^{b/2} \int_{-a/2}^{a/2} \sin \frac{m\pi(x+a/2)}{a} \sin \frac{n\pi(y+b/2)}{b} \sin \frac{p\pi(x+a/2)}{a} \sin \frac{q\pi(y+b/2)}{b} \,\mathrm{d}x\,\mathrm{d}y.
\end{aligned}
$$

However, we know that

$$
\int_{-b/2}^{b/2} \int_{-a/2}^{a/2} \sin \frac{m\pi(x+a/2)}{a} \sin \frac{n\pi(y+b/2)}{b} \sin \frac{p\pi(x+a/2)}{a} \sin \frac{q\pi(y+b/2)}{b} \,\mathrm{d}x\,\mathrm{d}y
= \begin{cases} \dfrac{ab}{4} & \text{when } m=p \text{ and } n=q \\ 0 & \text{otherwise} \end{cases}
$$

Therefore,

$$
< |v_p|^2 >= \frac{1}{4} \sum_{r=1}^{\infty} \sum_{s=1}^{\infty} \sum_{m=1}^{\infty} \sum_{n=1}^{\infty} B_r B_s^* U_{mnr} U_{mns}^*. \tag{3.47}
$$

Hence, by Eqs. (3.44) and (3.47), the radiation efficiency of a perforated panel subjected to a point harmonic excitation (Eq. (3.45)) is

$$
\sigma = \frac{4}{\rho_0 cab \sum\limits_{r=1}^{\infty} \sum\limits_{s=1}^{\infty} \sum\limits_{\substack{m=1 \\ n=1}}^{\infty} B_r B_s^* U_{mnr} U_{mns}^*} \mathrm{Re} \left\{ \int_{-k}^{k} \int_{-\sqrt{k^2-\mu^2}}^{\sqrt{k^2-\mu^2}} P^+(\lambda,\mu,z=0) V_a^*(\lambda,\mu) \,\mathrm{d}\lambda\,\mathrm{d}\mu \right\} \tag{3.48}
$$

The above integral is approximated by a sum over the range of discrete values of λ and μ.

In the following section, a particular case is taken up and numerical results are presented.

3.6.4 Results

Natural frequencies of a perforated panel

The specific panel considered has dimensions $0.455 \times 0.546 \times 0.003$ m^3 in which the hole radius is taken as $r_p = 5$ mm. There are 16 holes in the panel and the perforation ratio is $\sigma_p = 0.51\%$. The material properties are: density $\rho_p = 2700$ kg/m^3, Young's modulus $E = 70$ GPa, Poisson's ratio $\nu = 0.33$. The perforated panel natural frequencies and modeshapes are obtained using the Receptance method as given in 2.7. All the modes below the frequency 10000 Hz are obtained. In Table 3.1 are listed a few resonance frequencies using the Receptance method and a comparison with those obtained from the modal analysis using a finite element solver (ANSYS) is presented. It is found that the Receptance method predictions agree very closely with the finite element solutions (maximum deviation obtained is $\approx 1.5\%$ at the modes near 4000 Hz). The validation till 10000 Hz using ANSYS was not possible because of the system limitations.

Mode	Receptance method	ANSYS	Difference (%)
1	59.80	59.66	0.23
2	133.33	133.05	0.21
3	165.68	165.42	0.16
4	239.22	238.56	0.28
5	255.91	255.40	0.20
6	342.14	341.65	0.14
7	361.81	360.67	0.32
8	415.69	414.60	0.26
9	427.68	426.45	0.29
10	533.61	531.59	0.38
-	-	-	-
91	3750.25	3717.3	0.89
92	3815.61	3791.4	0.64
93	3844.40	3812.1	0.85
94	3844.65	3814.4	0.79
95	3923.33	3883.6	1.02
96	4057.97	4017.7	1.00
97	4102.02	4048.2	1.33
98	4129.76	4109.2	0.50
99	4169.16	4135.5	0.81
100	4178.27	4140.9	0.90

Table 3.1 Comparison of perforated panel natural frequencies in Hz.

Sound radiation from a perforated panel fixed in a differently perforated baffle

A harmonic force of unit magnitude is exerted at point $(0, 0)$ on the above panel. Although, the formulation can handle any degree of perforations in the baffle, only the following two cases are considered: 1) the baffle is similarly perforated as that of the panel and 2) the baffle is unperforated.

The unperforated panel has 250 modes below 10^4 Hz and the perforations cause a slight increase in this number. The presence of perforations reduces both the stiffness and the mass of the panel. The resultant effect on the natural frequencies of the perforated panel is shown in Table 3.2. There are two cases one with $\sigma_p = 5.93\%$ ($r_p = 0.0025$ m, $N_0 = 750$) and the other with $\sigma_p = 23.71\%$ ($r_p = 0.005$ m, $N_0 = 750$). It can be seen that for low perforation ratios the shift in natural frequencies is small. However, as the perforation ratio increases, the reduction in the stiffness of the panel exceeds that of the mass of the panel and results in much lower natural frequencies. This shift brings changes in the radiation efficiency curves as seen in Fig. 3.6.

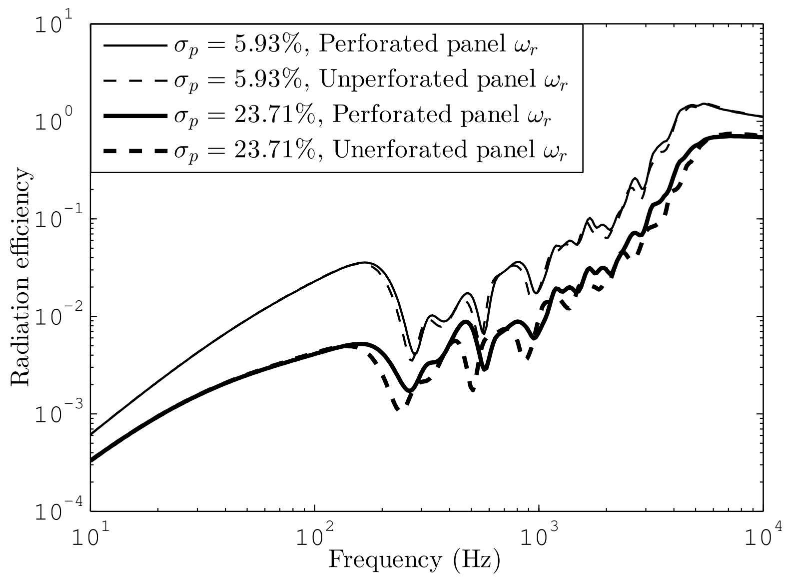

Fig. 3.6 Comparison of radiation efficiency for perforated panels (with perforation ratios $\sigma_p = 5.93\%$ and $\sigma_p = 23.71\%$) set in an unperforated baffle using 1) the perforated panel natural frequencies and 2) the unperforated panel natural frequencies.

The radiation efficiency of a perforated panel set in an unperforated baffle is shown in Fig. 3.7. For comparison, similar curves for an equally perforated baffle case and for an unperforated case are also shown. Note, that in all the curves, as the point of excitation is at the node of the second mode (128.98 Hz), the effect of first mode

Mode index	Unperforated case natural frequency (Hz)	Perforated case $\sigma_p = 5.93\%$ Natural frequency (Hz)	Perforated case $\sigma_p = 5.93\%$ Difference (%)	Perforated case $\sigma_p = 23.71\%$ Natural frequency (Hz)	Perforated case $\sigma_p = 23.71\%$ Difference (%)
1	60.06	59.80	-0.42	53.26	-11.31
2	133.90	133.33	-0.42	118.75	-11.31
3	166.39	165.68	-0.43	147.56	-11.31
4	240.23	239.22	-0.42	213.05	-11.31
5	256.96	255.91	-0.41	227.89	-11.31
6	343.60	342.14	-0.43	304.73	-11.31
7	363.29	361.81	-0.41	322.20	-11.31
8	417.44	415.69	-0.42	370.22	-11.31
9	429.26	427.68	-0.37	380.70	-11.31
10	535.59	533.61	-0.37	458.25	-14.44
-	-	-	-	-	-
121	5045.72	5023.92	-0.43	4474.94	-11.31
122	5119.56	5099.55	-0.39	4529.00	-11.54
123	5128.42	5122.62	-0.11	4548.28	-11.31
124	5143.19	5120.30	-0.45	4561.38	-11.31
125	5174.69	5158.89	-0.31	4589.32	-11.31
-	-	-	-	-	-
241	9771.46	9750.75	-0.21	8640.05	-11.58
242	9826.60	9770.52	-0.57	8715.00	-11.31
243	9845.30	9793.31	-0.53	8731.59	-11.31
244	9880.75	9825.98	-0.55	8763.02	-11.31
245	9925.05	9872.67	-0.53	8802.31	-11.31

Table 3.2 Comparison of unperforated and perforated panel natural frequencies in Hz.

(57.85 Hz) at the lower frequencies is a bit more prolonged [53]. It can be seen that while the panel perforations themselves reduce the radiation efficiency, the addition of perforations in the baffle cause a further severe reduction as the fluid has enough time to escape. It can also be seen that in the monopole region, the unperforated panel and baffle curve has a slope of 20 dB/decade and that of the similarly perforated baffle has a slope of 40 dB/decade. The perforated panel but unperforated baffle case has a slope < 20 dB/decade and this is mainly due to the sinc term in V_a that represents the flow of the fluid from the baffle onto the panel and finally through the holes.

In Fig. 3.8, only the panel is perforated. The hole radius is kept constant ($r_p = 2.5$ mm) and the number of holes is increased. It is expected that the sound radiation reduces with an increased perforation ratio. Since the radius is held constant,

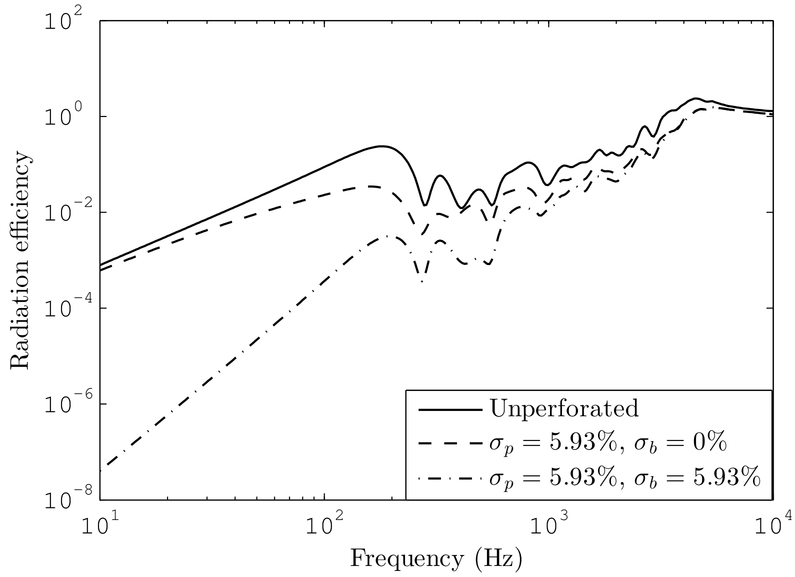

Fig. 3.7 Radiation efficiency of a perforated panel set in an unperforated baffle. The figure also shows the curves for an unperforated panel and for a panel set in a similarly perforated baffle. For the perforated cases, the perforation ratio is set to be $\sigma_p = 5.93\%$ and the hole radius is assumed to be $r_p = 2.5$ mm.

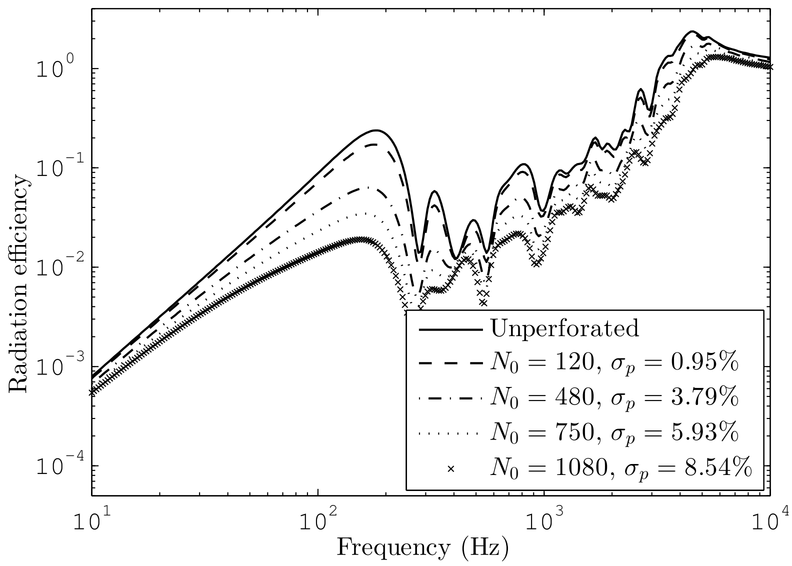

Fig. 3.8 Radiation efficiencies of a perforated panel set in an unperforated baffle for various perforation ratios. The hole radius is kept constant $r_p = 2.5$ mm.

$|Z_0|$ remains a constant but the perforate impedance $|Z_0|/\sigma_p$ reduces with increased perforation ratio (σ_p). The fluid escapes more easily to the back side. Further insight

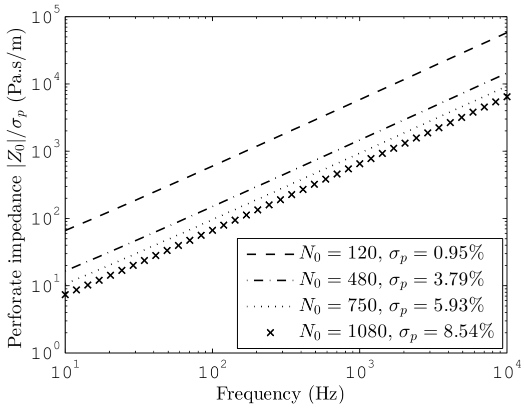

(a)

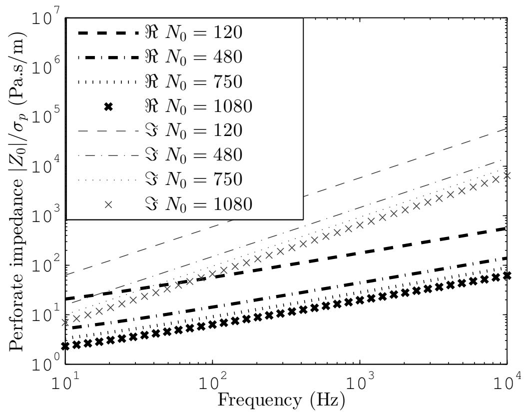

(b)

Fig. 3.9 Perforate impedances for different perforation ratios. (constant hole radius, $r_p = 2.5$ mm). (a) Absolute perforate impedance. (b) Resistive ($\Re$) and reactive ($\Im$) components of the perforate impedance.

can be gained from Fig. 3.9 where the perforate impedance and the corresponding real and imaginary parts are plotted. The absolute perforate impedance decreases with decreasing frequency and hence, the radiation is low at low frequencies. At high frequencies, both the resistance and reactance increase making it difficult for the fluid to escape and thus the radiation efficiency goes up. It can also be seen that the reactance dominates over the resistance at the higher frequencies. At further higher frequencies, the inertia of the fluid inside the hole is so high that it stops moving.

In Fig. 3.10, the total number of holes in the panel is kept constant ($N_0 = 750$) and different perforation ratios are achieved by varying the hole radius. The corresponding perforate impedance curves are plotted in Fig. 3.11. The radiation efficiency decreases with an increase in perforation ratio, as an expected outcome of the reduction in the perforate impedance. But, in comparison to panels with large hole radii, the impedance

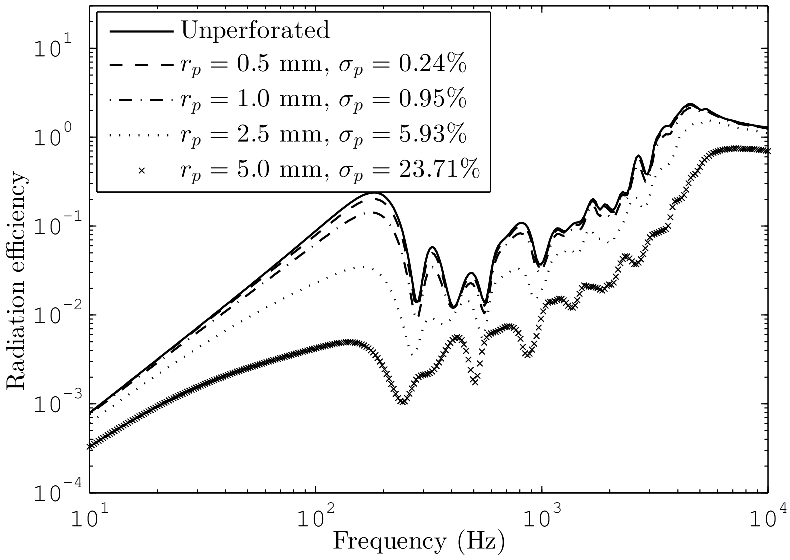

Fig. 3.10 Radiation efficiencies of a perforated panel set in an unperforated baffle for various perforation ratios. The total number of holes in the panel is kept constant $N_0 = 750$.

curve for a small radius ($r_p = 0.5$ mm) behaves differently at the lower frequencies (Fig. 3.11a). It can be noticed from Fig. 3.11b that at the lower frequencies, for a small hole radius, the resistive impedance dominates slightly over the reactance. This causes a small increase in the radiation efficiency at the lower frequencies. However, this slight increase is not clearly visible in the radiation efficiency curve in Fig. 3.10, as the curve for $r_p = 0.5$ mm lies very close to the unperforated one.

To understand this further, we need a case where the perforation ratio is held constant as the radii and number of holes are varied. Fig. 3.12 shows the radiation efficiencies for panels with the same perforation ratios ($\sigma_p = 0.95\%$). The hole radii chosen for the different cases vary from 0.5 mm to 5 mm. The corresponding perforate impedance curves are given in Fig. 3.13. Fig. 3.13a shows that at high frequencies, the absolute perforate impedance is lower for panels with small holes. As the frequency comes down, the curves for the smaller holes begin to dominate and cross over the other curves. This can be understood from Fig. 3.13b where for a given hole radius, the high frequency region is dominated by the reactive impedance and the lower frequencies by the resistive impedance. Thus, the resistive impedance crosses over as one comes down in frequency. This crossing happens at a higher frequency for a smaller hole radius. The crossing of impedance curves affects the radiation efficiency curves of Fig. 3.12. The crossing of radiation efficiency curve for $r_p = 0.5$ mm with that for $r_p = 1$ mm is

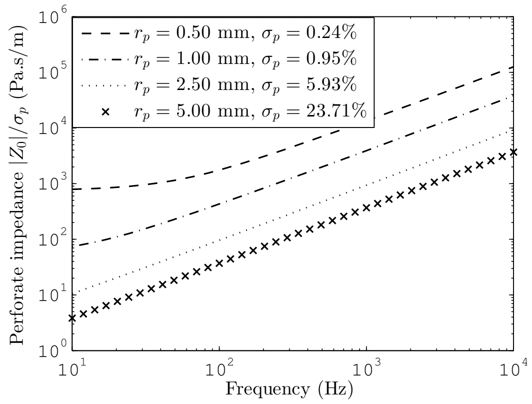

(a)

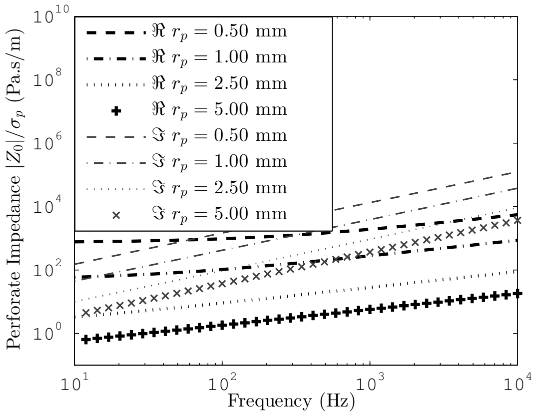

(b)

Fig. 3.11 Perforate impedances for different perforation ratios with a constant number of holes ($N_0 = 750$). (a) Absolute perforate impedance. (b) Resistive ($\Re$) and reactive ($\Im$) components of the perforate impedance.

depicted in the top inset of Fig. 3.12 and the bottom inset shows the crossing with $r_p = 2.5$ mm curve.

3.6.5 Average radiation efficiency

The power radiated from the panel varies with the excitation location. In order to obtain a mean value, let us average the radiated power over all the possible forcing points on the panel. The radiated power from the perforated panel is given by Eq. (3.44).

$$W = \frac{1}{2}\mathrm{Re}\left\{ \int_{-k}^{k} \int_{-\sqrt{k^2-\mu^2}}^{\sqrt{k^2-\mu^2}} P^{+}(\lambda,\mu,z=0)V_a^{*}(\lambda,\mu)\,\mathrm{d}\lambda\,\mathrm{d}\mu \right\},$$

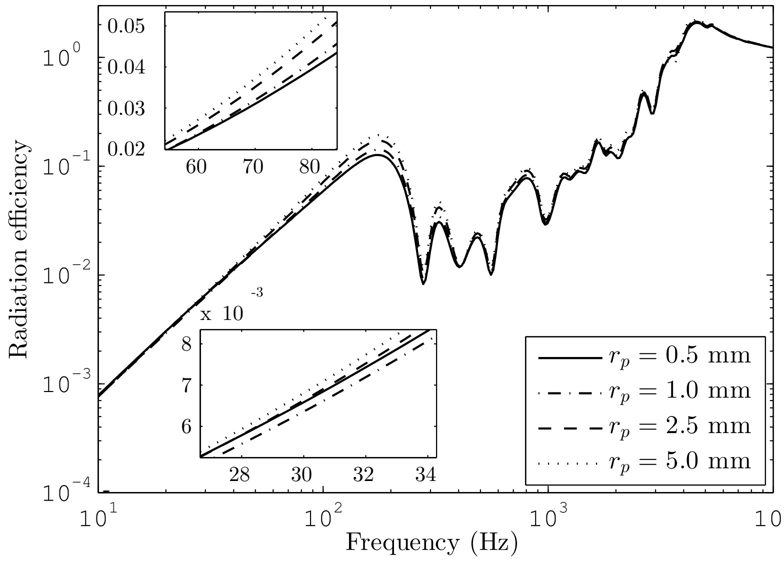

Fig. 3.12 Radiation efficiencies of a perforated panel set in an unperforated baffle for a constant perforation ratio ($\sigma_p = 0.95\%$). The total number of holes and the hole radius are varied to achieve same perforation ratio.

where we use the LAFP velocity due to the panel motion and the fluid flow through the perforate to evaluate the radiated power. Substituting for $P^{+}(\lambda, \mu, z=0)$ from Eq. (3.13) we get

$$W = \frac{1}{2}\mathrm{Re}\left\{ \int\limits_{-k}^{k} \int\limits_{-\sqrt{k^2-\mu^2}}^{\sqrt{k^2-\mu^2}} Z_a(\lambda,\mu)|V_a(\lambda,\mu,z=0)|^2 \,\mathrm{d}\lambda\,\mathrm{d}\mu \right\}.$$

Averaging the radiated power over all the forcing locations we get

$$\overline{W} = \frac{1}{ab} \int\limits_{-b/2}^{b/2} \int\limits_{-a/2}^{a/2} W(x_i, y_i)\,\mathrm{d}x_i\,\mathrm{d}y_i. \tag{3.49}$$

Substituting for W into the equation above and rearranging the order of integration we obtain

$$\overline{W} = \frac{1}{2}\mathrm{Re}\left\{ \int\limits_{-k}^{k} \int\limits_{-\sqrt{k^2-\mu^2}}^{\sqrt{k^2-\mu^2}} Z_a(\lambda,\mu)\overline{|V_a(\lambda,\mu,z=0)|^2} \,\mathrm{d}\lambda\,\mathrm{d}\mu \right\}, \tag{3.50}$$

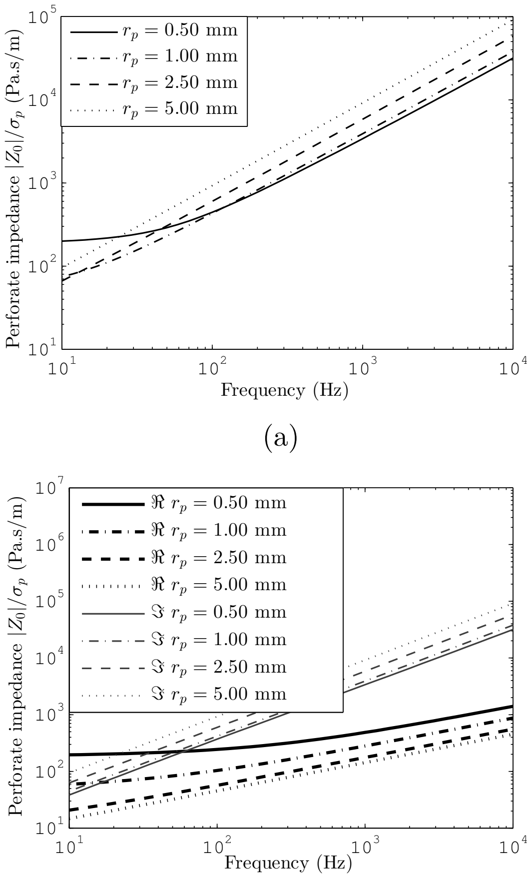

(a)

(b)

Fig. 3.13 Perforate impedances for different of hole sizes and number of holes but with a constant perforation ratio ($\sigma_p = 0.95\%$). (a) Absolute perforate impedance. (b) Resistive ($\Re$) and reactive ($\Im$) components of the perforate impedance.

where

$$\overline{|V_a(\lambda, \mu, z = 0)|^2} = \frac{1}{ab} \int_{-b/2}^{b/2} \int_{-a/2}^{a/2} |V_a(\lambda, \mu, z = 0)|^2 \, \mathrm{d}x_i \, \mathrm{d}y_i. \tag{3.51}$$

Using the equation for $V_a(\lambda, \mu, z = 0)$ (Eq. (3.27)), the integral on the right hand side of the above equation is evaluated numerically over the panel area. Substituting for the average of the LAFP squared velocity in Eq. (3.50), the average radiated power is evaluated.

The average radiation efficiency is defined as

$$\overline{\sigma} = \frac{\overline{W}}{\frac{1}{2}\rho_0 cab \overline{< |v_p|^2 >}}, \tag{3.52}$$

where $\overline{W}$ is the average radiated power given by Eq. (3.50). $\overline{<|v_p|^2>}$ is the spatially averaged squared panel velocity averaged over all forcing locations. The spatially averaged squared panel velocity is given by Eq. (3.47) (and repeated here)

$$<|v_p|^2>=\frac{1}{4}\sum_{r=1}^{\infty}\sum_{s=1}^{\infty}\sum_{m=1}^{\infty}\sum_{n=1}^{\infty}B_r B_s^* U_{mnr}U_{mns}^*.$$

Averaging over all the forcing locations

$$\begin{aligned}\overline{<|v_p|^2>} &= \frac{1}{ab}\int_{-b/2}^{b/2}\int_{-a/2}^{a/2}<|v_p(x_i,y_i)|^2>\,\mathrm{d}x_i\,\mathrm{d}y_i \\ &= \frac{1}{4}\sum_{r=1}^{\infty}\sum_{s=1}^{\infty}\sum_{m=1}^{\infty}\sum_{n=1}^{\infty}U_{mnr}U_{mns}^*\frac{1}{ab}\int_{-b/2}^{b/2}\int_{-a/2}^{a/2}B_r(x_i,y_i)B_s^*(x_i,y_i)\,\mathrm{d}x_i\,\mathrm{d}y_i.\end{aligned}$$

Substituting for $B_r(x_i,y_i)$ and $B_s^*(x_i,y_i)$ and using the orthogonality property (of the *in vacuo* panel modes) we obtain

$$\overline{<|v_p|^2>}=\frac{1}{16}\sum_{r=1}^{\infty}\sum_{s=1}^{\infty}\sum_{m=1}^{\infty}\sum_{n=1}^{\infty}\sum_{p=1}^{\infty}\sum_{q=1}^{\infty}\frac{\omega^2|F|^2U_{mnr}U_{mns}^*U_{pqr}U_{pqs}^*}{M_rM_s^*\left[\omega_r^2(1-i\eta)-\omega^2\right]\left[\omega_s^2(1-i\eta)-\omega^2\right]^*}. \tag{3.53}$$

Substituting for $\overline{<|v_p|^2>}$ (Eq. (3.53)) and $\overline{W}$ (Eq. (3.50)) into Eq. (3.52), we obtain the average radiation efficiency of a perforated panel fixed in a baffle.

3.6.6 Results

Average radiation efficiency of a perforated panel

The panel dimensions and properties are the same as before. There are 120 holes in the panel and the radius of each hole is 2.5 mm. We know that the behavior of a radiation efficiency curve varies with the point of excitation. Fig. 3.14 depicts the radiation efficiency curves for unit amplitude point harmonic excitations. Six sample forcing locations are chosen and each thin line represents a different excitation location. It also shows the radiation efficiency averaged over 100 point force locations (thick line). A convergence test was done and an average over 100 uniformly distributed locations was found to be adequate.

Variation in the radiation efficiency for different perforation ratios are plotted in Fig. 3.15. Different perforation ratios are achieved by varying the hole size. The

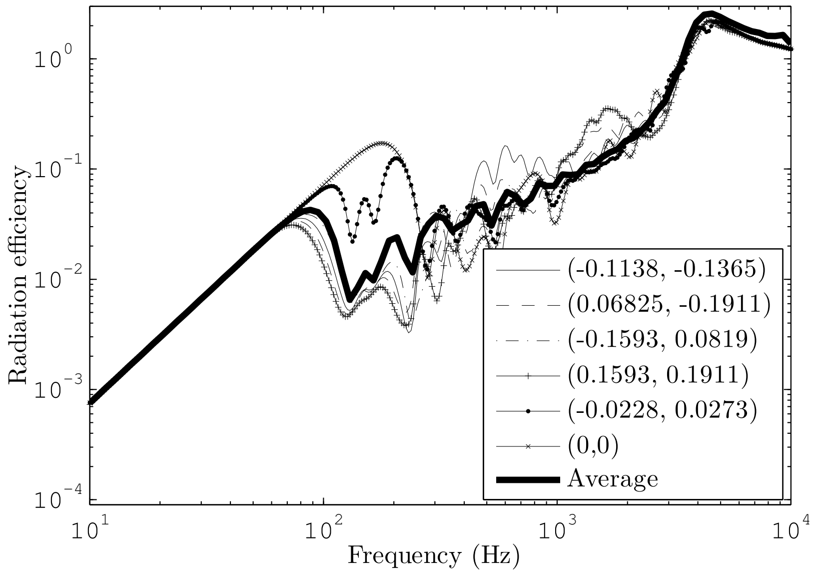

Fig. 3.14 Radiation efficiencies for different excitation points (Eq. (3.48)) and the radiation efficiency averaged over 100 excitation points (Eq. (3.52)). The hole radius is $r_p = 2.5$ mm and the number of holes is $N_0 = 120$. The perforated panel is lying in the region $-0.2275 \leq x \leq 0.2275$, $-0.2730 \leq y \leq 0.2730$.

radiation efficiency decreases with increase in the perforation ratio, as expected. It is worth stating that the computational overhead while evaluating the average radiation efficiency increases enormously with the increase in the number of holes in the panel. For all the perforated panel cases shown in Fig. 3.15, the number holes is $N_0 = 120$. But, in most of the micro-perforated panel applications, the number of holes is of the order of a few thousands requiring substantial computational machinery.

3.7 Conclusions

The radiation efficiency of a perforated panel set in a rigid baffle with simply supported boundary conditions is investigated using the 2-D wavenumber domain approach. Initially, the radiation efficiency of a perforated panel set in a similarly perforated baffle is compared with that from the literature. The proposed model includes the resistive and the reactive impedances of the holes. Whereas, in the literature only the reactive component is included. For the given geometry, the match is found to be good. This is expected since at high frequencies the reactive component dominates. It may be noted that the formulation can accommodate other boundary conditions as long as the modes are expressible in an analytical form.

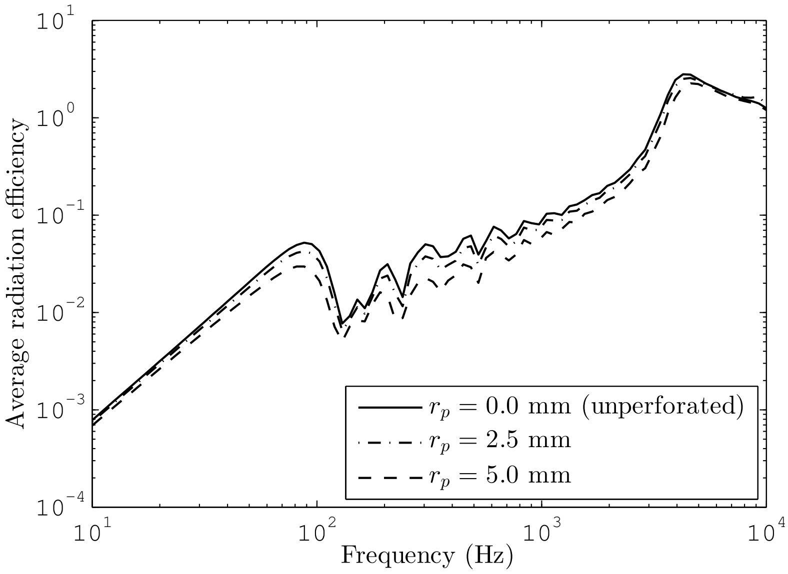

Fig. 3.15 Radiation efficiencies for different hole sizes/perforation ratios averaged over all force locations. The number of holes for the perforated cases is $N_0 = 120$.

Next, a perforated panel set in an unperforated baffle is considered using the same approach. The dissimilarity of the perforate impedance over the panel-baffle plane is treated appropriately and it is found that due to the discontinuity in the impedance, there exists a coupling of wavenumbers in the resulting locally mean fluid velocity relation. The perforations alter the resonant frequencies and the modeshapes of the panel. With the aid of the Receptance method, the new natural frequencies and modeshapes are obtained and used to find the radiation efficiency from a point harmonic excitation.

In general, the absolute perforate impedance increases with increase in frequency. Within this, the lower frequencies are dominated by the resistive component and the high frequencies by the reactive component. Thus, for a given hole size and perforation ratio, there is a cross over between the resistive and reactive impedances. For a smaller hole radius, the dominance of the reactive component over the resistive component happens at a higher frequency. Since, the model includes both the resistive and the reactive components of the hole impedance, it is directly applicable to micro-perforated panels. Curves for the radiation efficiency are presented and the effect of the resistive and the reactive hole impedances on the sound radiation is discussed. The radiation efficiency curve that is averaged over all the forcing locations is also presented. The computational cost is found to be large for such averaging.

So far, we have been discussing the sound radiation problem in which the external excitation is by a point harmonic force. The one-way coupled method developed here can be carried forward to study the sound transmission through the perforated panel where the panel vibration is due to an incident plane wave. This problem is discussed in the next chapter.

Chapter 4

Sound transmission through a perforated panel: One-way coupling

4.1 Introduction

In this chapter, the sound transmission through a flexible simply supported perforated panel set in a rigid unperforated baffle is investigated using the one-way coupled formulation presented in the previous chapter. The sound power transmitted by the panel is analyzed (in terms of the transmission loss) for an acoustic plane wave incidence. This being a one-way coupled analysis, the influence of the radiated pressure field on the panel response is neglected and the forcing acoustic field consists only of the incident and the reflected pressure waves. However, the effect of the radiated pressure field is included while finding the average fluid velocity at the panel-fluid interface.

In the following section, the total pressure on the incident and the transmitted sides of the perforated panel in terms of the incident, radiated and the transmitted pressure fields is obtained.

4.2 The pressure fields on the incident and the transmitted sides

Consider a flexible perforated panel of finite extent in the region $-a/2 \leq x \leq a/2$ and $-b/2 \leq y \leq b/2$. The panel is set in a rigid unperforated baffle of infinite extent in the $z = 0$ plane, as shown in Fig. 4.1. In the $z > 0$ region, a harmonic plane wave of frequency ω, wavenumeber k and amplitude $\tilde{P}_i$ is incident upon the panel at an angle θ (polar angle) and ϕ (azimuthal angle). This creates flexural vibrations in the

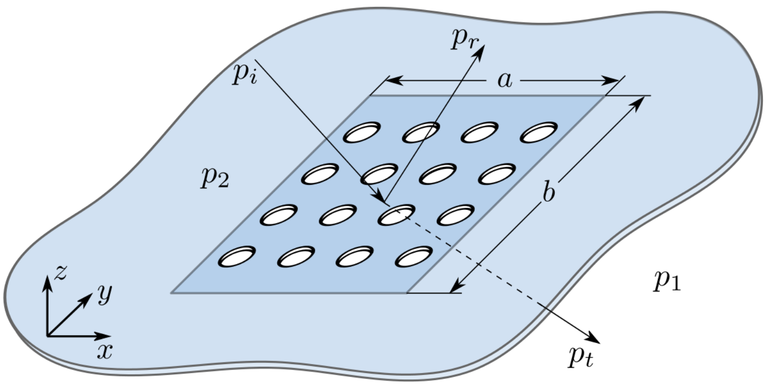

Fig. 4.1 Transmission of sound (plane wave) through a perforated panel set in a baffle.

perforated panel and results in the transmission of sound through the panel into the $z < 0$ region. Let, $p_1(x, y, z, t)$ and $p_2(x, y, z, t)$ be the resulting pressure fields in the transmitted ($z < 0$) and in the incident ($z > 0$) regions, respectively (see Fig. 4.1). The transmitted pressure field $p_1(x, y, z, t)$ is due to (1) the radiation of sound by the vibrating perforated panel and (2) the direct transmission of sound through the holes in the panel. Whereas on the incident side, the total pressure field $p_2(x, y, z, t)$ comprises of the incident and the reflected pressure terms. Let the incident pressure field $p_i(x, y, z, t)$ be

$$p_i(x, y, z, t) = \tilde{P}_i\, e^{ik_x x + ik_y y - ik_z z}\, e^{-i\omega t}, \tag{4.1}$$

where $k_x = k\, \sin\theta\, \cos\phi$, $k_y = k\, \sin\theta\, \sin\phi$ and $k_z = k\, \cos\theta$. The total pressure field on the incident side is

$$p_2(x, y, z, t) = \tilde{P}_i\, e^{ik_x x + ik_y - ik_z z}\, e^{-i\omega t} + p_r(x, y, z)\, e^{-i\omega t}, \tag{4.2}$$

where $p_r(x, y, z)$ is the reflected pressure field. In the following derivations the dependence on time $e^{-i\omega t}$ is suppressed.

The transmitted pressure field $p_1(x, y, z)$ comprises the radiated pressure field $p^-(x, y, z)$ in the $z < 0$ region. The radiated pressure field, by defining an average fluid particle velocity profile on the panel-baffle surface, takes care of both the radiation of sound by the panel vibration and the direct transmission of sound through the perforations. The radiated pressure field satisfies the 3-D Helmholtz equation

$$\left(\nabla^2 + k^2\right) p^-(x, y, z) = 0. \tag{4.3}$$

On taking a *double Fourier transform* in the $x - y$ domain

$$\left[\frac{\mathrm{d}^2}{\mathrm{d}z^2} + \left(k^2 - \lambda^2 - \mu^2\right)\right] P^-(\lambda, \mu, z) = 0, \tag{4.4}$$

where $P^-(\lambda, \mu, z)$ represents the double Fourier transform of the transmitted pressure field and is defined as

$$P^-(\lambda, \mu, z) = \frac{1}{2\pi} \int_{-\infty}^{\infty} \int_{-\infty}^{\infty} p^-(x, y, z)\, e^{i\lambda x + i\mu y}\, \mathrm{d}x\, \mathrm{d}y. \tag{4.5}$$

The general solution to Eq. (4.4) is

$$P^-(\lambda, \mu, z) = A(\lambda, \mu)\, e^{i\sqrt{k^2-\lambda^2-\mu^2}z} + B(\lambda, \mu)\, e^{-i\sqrt{k^2-\lambda^2-\mu^2}z}. \tag{4.6}$$

For a traveling wave in the $-z$ direction, by causality, we must have $A(\lambda, \mu) = 0$. Therefore, the solution takes the form

$$P^-(\lambda, \mu, z) = B(\lambda, \mu)\, e^{-i\sqrt{k^2-\lambda^2-\mu^2}z}. \tag{4.7}$$

And the evanescent wave in the $-z$ direction is

$$P^-(\lambda, \mu, z) = B(\lambda, \mu)\, e^{\sqrt{\lambda^2+\mu^2-k^2}z}.$$

$B(\lambda, \mu)$ can be found by invoking the double Fourier transform of the Euler boundary condition at the solid-fluid interface ($z = 0$) as

$$\frac{\partial}{\partial z} P^-(\lambda, \mu, z = 0) = i\rho_0 ck V_a(\lambda, \mu, z = 0), \tag{4.8}$$

where ρ_0 is the fluid density and $V_a(\lambda, \mu, z = 0)$ is the double Fourier transform of the fluid particle velocity at the boundary $v_a(x, y, z = 0)$ as given by

$$V_a(\lambda, \mu, z = 0) = \frac{1}{2\pi} \int_{-\infty}^{\infty} \int_{-\infty}^{\infty} v_a(x, y, z = 0)\, e^{i\lambda x + i\mu y}\, \mathrm{d}x\, \mathrm{d}y. \tag{4.9}$$

Using Eqs. (4.7) and (4.8) we get

$$B(\lambda, \mu) = P^-(\lambda, \mu, z = 0) = -Z_a(\lambda, \mu) V_a(\lambda, \mu, z = 0), \tag{4.10}$$

where $Z_a(\lambda,\mu)$ is the complex acoustic impedance given by

$$Z_a(\lambda,\mu) = \frac{\rho_0 ck}{\sqrt{k^2-\lambda^2-\mu^2}}. \tag{4.11}$$

Therefore

$$P^-(\lambda,\mu,z) = -Z_a(\lambda,\mu)V_a(\lambda,\mu,z=0)e^{-i\sqrt{k^2-\lambda^2-\mu^2}z}. \tag{4.12}$$

Thus, if $V_a(\lambda,\mu,z=0)$ is known, the radiated pressure can be found. For a perforated panel, $V_a(\lambda,\mu,z=0)$ takes into account both the panel vibrations and the leakage through holes. In the limiting case of an unperforated panel it represents the panel velocity alone. The next section derives the double Fourier transform of the locally averaged fluid particle (LAFP) velocity, $V_a(\lambda,\mu,z=0)$, for the transmission of sound through a perforated panel set in a baffle of any perforation ratio.

Next, taking the double Fourier transform of Eq. (4.2)

$$P_2(\lambda,\mu,z) = \frac{1}{2\pi}\int\limits_{-\infty}^{\infty}\int\limits_{-\infty}^{\infty}\tilde{P}_i\, e^{ik_x x+ik_y y-ik_z z}\, e^{i\lambda x+i\mu y}\,\mathrm{d}x\,\mathrm{d}y + P_r(\lambda,\mu,z), \tag{4.13}$$

where

$$P_r(\lambda,\mu,z) = \frac{1}{2\pi}\int\limits_{-\infty}^{\infty}\int\limits_{-\infty}^{\infty} p_r(x,y,z)\, e^{i\lambda x+i\mu y}\,\mathrm{d}x\,\mathrm{d}y. \tag{4.14}$$

Using the identity

$$\int\limits_{-\infty}^{\infty}\int\limits_{-\infty}^{\infty} e^{i(\lambda+k_x)x+i(\mu+k_y)y}\,\mathrm{d}x\,\mathrm{d}y = 4\pi^2\delta(\lambda+k_x)\,\delta(\mu+k_y) \tag{4.15}$$

we get

$$P_2(\lambda,\mu,z) = 2\pi\tilde{P}_i\,\delta(\lambda+k_x)\,\delta(\mu+k_y)\,e^{-ik_z z} + P_r(\lambda,\mu,z). \tag{4.16}$$

However, the pressure field $p_2(x,y,z)$ should satisfy the 3-D Helmholtz equation

$$\left(\nabla^2+k^2\right)p_2(x,y,z) = 0. \tag{4.17}$$

Taking the double Fourier transform,

$$\left[\frac{\mathrm{d}^2}{\mathrm{d}z^2} + \left(k^2-\lambda^2-\mu^2\right)\right]P_2(\lambda,\mu,z) = 0. \tag{4.18}$$

The general solution to Eq. (4.18) is

$$P_2\left(\lambda, \mu, z\right) = C(\lambda, \mu)\, e^{i\sqrt{k^2-\lambda^2-\mu^2}z} + D(\lambda, \mu)\, e^{-i\sqrt{k^2-\lambda^2-\mu^2}z}. \tag{4.19}$$

Comparing Eqs. (4.16) and (4.19) and knowing that $P_r(\lambda, \mu)$ consists only of forward traveling waves in the z direction,

$$P_2\left(\lambda, \mu, z\right) = 2\pi \tilde{P}_i\, \delta(\lambda + k_x)\, \delta(\mu + k_y)\, e^{-ik_z z} + C(\lambda, \mu)\, e^{i\sqrt{k^2-\lambda^2-\mu^2}z}. \tag{4.20}$$

The pressure $p_2(x, y, z)$ is related to the fluid particle velocity at the solid-fluid interface of the incident region ($v_a(x, y, z = 0)$) through the Euler boundary condition. Taking the double Fourier transform of the boundary condition we get

$$\frac{\partial}{\partial z} P_2\left(\lambda, \mu, z = 0\right) = i\rho_0 ck V_a\left(\lambda, \mu, z = 0\right). \tag{4.21}$$

Substituting for $P_2(\lambda, \mu, z)$ from Eq. (4.20)

$$-ik_z 2\pi \tilde{P}_i\, \delta(\lambda + k_x)\, \delta(\mu + k_y) + i\sqrt{k^2 - \lambda^2 - \mu^2}\, C(\lambda, \mu) = i\rho_0 ck V_a\left(\lambda, \mu, z = 0\right).$$

Or

$$C(\lambda, \mu) = \frac{\rho_0 ck}{\sqrt{k^2 - \lambda^2 - \mu^2}} V_a\left(\lambda, \mu, z = 0\right) + \frac{k_z}{\sqrt{k^2 - \lambda^2 - \mu^2}} 2\pi \tilde{P}_i\, \delta(\lambda + k_x)\, \delta(\mu + k_y).$$

$C(\lambda, \mu)$ is related to the forward traveling wave in the incident region. For a forward traveling wave (related to the reflected pressure field component in $P_2(\lambda, \mu, z)$), when $\lambda = -k_x$ and $\mu = -k_y$, $\sqrt{k^2 - \lambda^2 - \mu^2} = k_z$ and using Eq. (4.11)

$$C(\lambda, \mu) = Z_a(\lambda, \mu) V_a\left(\lambda, \mu, z = 0\right) + 2\pi \tilde{P}_i\, \delta(\lambda + k_x)\, \delta(\mu + k_y). \tag{4.22}$$

Therefore, using Eq. (4.22), the double Fourier transform of the total pressure at the incident region (Eq. (4.20)) is

$$P_2\left(\lambda, \mu, z\right) = Z_a(\lambda, \mu) V_a\left(\lambda, \mu, z = 0\right)\, e^{i\sqrt{k^2-\lambda^2-\mu^2}z} + 4\pi \tilde{P}_i\, \delta(\lambda + k_x)\, \delta(\mu + k_y)\, \cos k_z z. \tag{4.23}$$

And at $z = 0$

$$P_2\left(\lambda, \mu, z = 0\right) = \underbrace{Z_a(\lambda, \mu) V_a\left(\lambda, \mu, z = 0\right)}_{\text{radiated pressure field}} + \underbrace{4\pi \tilde{P}_i\, \delta(\lambda + k_x)\, \delta(\mu + k_y)}_{\text{blocked pressure field}}. \tag{4.24}$$

Thus, the total pressure field on the incident side is the sum of the radiated and the blocked pressure fields. Similar observation can be found for incidence of a plane wave on an infinite flexible panel [7]. In the infinite panel model, the radiated wave carries the same wavenumbers as that of the incident one (k_x, k_y and k_z). Whereas, here, we have contributions from an infinite spectrum of wavenumbers owing to the finiteness of the panel (see the first term on the right hand side of Eq. (4.23)). Now, the total pressure can be found if $V_a(\lambda, \mu, z = 0)$ is known.

Next, using Eqs. (4.12) and (4.24), the double Fourier transform of the pressure difference across the perforated panel is given by

$$\begin{aligned}\Delta P(\lambda, \mu) &= P^-(\lambda, \mu, z = 0) - P_2(\lambda, \mu, z = 0) \\ &= 2P^-(\lambda, \mu, z = 0) - 4\pi \tilde{P}_i \, \delta(\lambda + k_x) \, \delta(\mu + k_y). \quad (4.25)\end{aligned}$$

It can be seen that $\Delta P(\lambda, \mu)$ depends on $V_a\,(\lambda, \mu, z = 0)$, which we derive in the next section.

4.3 Locally averaged fluid particle (LAFP) velocity and its Fourier transform

The fluid particle on the surface of an unperforated panel (at $z = 0^{\pm}$) moves with the same velocity as that of the panel. If there are perforations on the panel we need to find a locally averaged fluid particle (LAFP) velocity, which is function of the panel velocity and the velocity with which the fluid passes through perforations. This LAFP velocity has been derived in section 2.6. It is found that the LAFP velocity $v_a(x, y)$ is a function of the panel velocity $v_p(x, y)$, the pressure difference across the perforated panel $\Delta p(x, y)$, the panel perforation ratio σ_p and the hole impedance Z_0. Thus,

$$v_a(x, y) = \zeta_I v_p(x, y) + \frac{\Delta p(x, y)}{Z_0} \sigma_p, \quad (4.26)$$

where $\zeta_I = 1 - \dfrac{Z_{react}}{Z_0} \sigma_p$; Z_{react} being the reactive impedance of each hole. An expression for the hole impedance Z_0 was derived by Maa [1] and is given in Eq. (3.18) of the previous chapter.

Now, let the panel and the baffle have perforation ratios σ_p and σ_b, respectively. Also, let the corresponding specific acoustic impedance of holes be Z_{0p} and Z_{0b}, respectively. Assume that the perforate impedance over the panel and the baffle regions differ, i.e.,

$\frac{Z_{0p}}{\sigma_p} \neq \frac{Z_{0b}}{\sigma_b}$. Owing to the discontinuity in the perforate impedance over the panel-baffle plane and the flexibility of the panel, we have a discontinuous LAFP velocity field at $z = 0$. Thus, using Eq. (4.26) we get

$$\begin{aligned} v_{ap}(x, y, z = 0) &= \zeta_I v_p(x, y) + \frac{\Delta p(x, y)}{Z_{0p}} \sigma_p, \quad \text{over the panel region} \\ v_{ab}(x, y, z = 0) &= \frac{\Delta p(x, y)}{Z_{0b}} \sigma_b, \qquad\qquad\quad\;\; \text{over the baffle region} \end{aligned} \tag{4.27}$$

where $\Delta p(x, y)$ is the inverse Fourier transform of $\Delta P(\lambda, \mu)$.

Now, the double Fourier transform of the LAFP velocity is

$$V_a(\lambda, \mu, z = 0) = \frac{1}{2\pi} \int_{-\infty}^{\infty} \int_{-\infty}^{\infty} v_a(x, y, z = 0)\, e^{i\lambda x + i\mu y}\, \mathrm{d}x\, \mathrm{d}y.$$

Or

$$\begin{aligned} V_a(\lambda, \mu, z = 0) = {} & \frac{1}{2\pi} \int_{-b/2}^{b/2} \int_{-a/2}^{a/2} v_{ap}(x, y, z = 0)\, e^{i\lambda x + i\mu y}\, \mathrm{d}x\, \mathrm{d}y \\ & + \frac{1}{2\pi} \left(\int_{-\infty}^{\infty} \int_{-\infty}^{\infty} - \int_{-b/2}^{b/2} \int_{-a/2}^{a/2} \right) v_{ab}(x, y, z = 0)\, e^{i\lambda x + i\mu y}\, \mathrm{d}x\, \mathrm{d}y. \end{aligned}$$

Substituting for v_{ap} and v_{ab} we get

$$\begin{aligned} V_a(\lambda, \mu, z = 0) = {} & \frac{1}{2\pi} \int_{-b/2}^{b/2} \int_{-a/2}^{a/2} \Bigg[\zeta_I v_p(x, y) \\ & + \frac{\sigma_p}{Z_{0p}} \frac{1}{2\pi} \int_{-\infty}^{\infty} \int_{-\infty}^{\infty} \Delta P\left(\lambda', \mu'\right) e^{-i\lambda' x - i\mu' y}\, \mathrm{d}\lambda'\, \mathrm{d}\mu' \Bigg] e^{i\lambda x + i\mu y}\, \mathrm{d}x\, \mathrm{d}y \\ & + \frac{1}{2\pi} \int_{-\infty}^{\infty} \int_{-\infty}^{\infty} \left[\frac{\sigma_b}{Z_{0b}} \frac{1}{2\pi} \int_{-\infty}^{\infty} \int_{-\infty}^{\infty} \Delta P\left(\lambda', \mu'\right) e^{-i\lambda' x - i\mu' y}\, \mathrm{d}\lambda'\, \mathrm{d}\mu' \right] e^{i\lambda x + i\mu y}\, \mathrm{d}x\, \mathrm{d}y \\ & - \frac{1}{2\pi} \int_{-b/2}^{b/2} \int_{-a/2}^{a/2} \left[\frac{\sigma_b}{Z_{0b}} \frac{1}{2\pi} \int_{-\infty}^{\infty} \int_{-\infty}^{\infty} \Delta P\left(\lambda', \mu'\right) e^{-i\lambda' x - i\mu' y}\, \mathrm{d}\lambda'\, \mathrm{d}\mu' \right] e^{i\lambda x + i\mu y}\, \mathrm{d}x\, \mathrm{d}y. \end{aligned}$$

Or

$$V_a(\lambda,\mu,z=0) = \zeta_I V_p(\lambda,\mu) + \frac{\sigma_b}{Z_{0b}} \Delta P(\lambda,\mu) + \frac{1}{2\pi}\left[\frac{\sigma_p}{Z_{0p}} - \frac{\sigma_b}{Z_{0b}}\right] \times \int\limits_{-b/2}^{b/2}\int\limits_{-a/2}^{a/2}\left[\frac{1}{2\pi}\int\limits_{-\infty}^{\infty}\int\limits_{-\infty}^{\infty}\Delta P\left(\lambda',\mu'\right) e^{-i\lambda' x - i\mu' y}\,\mathrm{d}\lambda'\,\mathrm{d}\mu'\right] e^{i\lambda x + i\mu y}\,\mathrm{d}x\,\mathrm{d}y,$$

where $V_p(\lambda,\mu)$ is the double Fourier transforms of the panel velocity given by

$$V_p(\lambda,\mu) = \frac{1}{2\pi}\int\limits_{-b/2}^{b/2}\int\limits_{-a/2}^{a/2} v_p(x,y)\, e^{i\lambda x + i\mu y}\,\mathrm{d}x\,\mathrm{d}y. \tag{4.28}$$

Substituting ΔP from Eq. (4.25) we get

$$\begin{aligned} V_a(\lambda,\mu,z=0) &= \zeta_I V_p(\lambda,\mu) + \frac{2\sigma_b}{Z_{0b}}\, P^-(\lambda,\mu,z=0) - 2\pi \tilde{P}_i\, \frac{2\sigma_b}{Z_{0b}}\, \delta(\lambda+k_x)\,\delta(\mu+k_y) \\ &+ \left[\frac{2\sigma_p}{Z_{0p}} - \frac{2\sigma_b}{Z_{0b}}\right]\frac{1}{4\pi^2}\int\limits_{-b/2}^{b/2}\int\limits_{-a/2}^{a/2}\left[\int\limits_{-\infty}^{\infty}\int\limits_{-\infty}^{\infty} P^-\left(\lambda',\mu',z=0\right) e^{-i\lambda' x - i\mu' y}\,\mathrm{d}\lambda'\,\mathrm{d}\mu'\right] e^{i\lambda x + i\mu y}\,\mathrm{d}x\,\mathrm{d}y \\ &- \left[\frac{2\sigma_p}{Z_{0p}} - \frac{2\sigma_b}{Z_{0b}}\right]\frac{1}{4\pi^2}\int\limits_{-b/2}^{b/2}\int\limits_{-a/2}^{a/2}\left[\int\limits_{-\infty}^{\infty}\int\limits_{-\infty}^{\infty} 2\pi\tilde{P}_i\,\delta(\lambda'+k_x)\,\delta(\mu'+k_y) e^{-i\lambda' x - i\mu' y}\,\mathrm{d}\lambda'\,\mathrm{d}\mu'\right] \\ &\times e^{i\lambda x + i\mu y}\,\mathrm{d}x\,\mathrm{d}y. \end{aligned}$$

Rearranging the above equation

$$\begin{aligned} V_a(\lambda,\mu,z=0) &= \zeta_I V_p(\lambda,\mu) + \frac{2\sigma_b}{Z_{0b}}\, P^-(\lambda,\mu,z=0) - 2\pi \tilde{P}_i\, \frac{2\sigma_b}{Z_{0b}}\, \delta(\lambda+k_x)\,\delta(\mu+k_y) \\ &+ \left[\frac{2\sigma_p}{Z_{0p}} - \frac{2\sigma_b}{Z_{0b}}\right]\frac{1}{4\pi^2}\int\limits_{-\infty}^{\infty}\int\limits_{-\infty}^{\infty} P^-\left(\lambda',\mu',z=0\right)\left[\int\limits_{-b/2}^{b/2}\int\limits_{-a/2}^{a/2} e^{i(\lambda-\lambda')x + i(\mu-\mu')y}\,\mathrm{d}x\,\mathrm{d}y\right]\mathrm{d}\lambda'\,\mathrm{d}\mu' \\ &- \left[\frac{2\sigma_p}{Z_{0p}} - \frac{2\sigma_b}{Z_{0b}}\right]\frac{1}{2\pi}\int\limits_{-b/2}^{b/2}\int\limits_{-a/2}^{a/2} \tilde{P}_i\, e^{i(\lambda+k_x)x + i(\mu+k_y)y}\,\mathrm{d}x\,\mathrm{d}y. \end{aligned}$$

But, we know that

$$\int_{-b/2}^{b/2}\int_{-a/2}^{a/2} e^{i(\lambda-\lambda')x+i(\mu-\mu')y}\,\mathrm{d}x\,\mathrm{d}y = ab\,\mathrm{sinc}\left[\frac{(\lambda-\lambda')a}{2}\right]\,\mathrm{sinc}\left[\frac{(\mu-\mu')b}{2}\right] \tag{4.29}$$

and

$$\int_{-b/2}^{b/2}\int_{-a/2}^{a/2} e^{i(\lambda+k_x)x+i(\mu+k_y)y}\,\mathrm{d}x\,\mathrm{d}y = ab\,\mathrm{sinc}\left[\frac{(\lambda+k_x)a}{2}\right]\,\mathrm{sinc}\left[\frac{(\mu+k_y)b}{2}\right]. \tag{4.30}$$

Therefore

$$\begin{aligned}V_a(\lambda,\mu,z=0) &= \zeta_I V_p(\lambda,\mu) + \frac{2\sigma_b}{Z_{0b}}\,P^-(\lambda,\mu,z=0) - 2\pi\tilde{P}_i\,\frac{2\sigma_b}{Z_{0b}}\,\delta(\lambda+k_x)\,\delta(\mu+k_y)\\ &+ \left[\frac{2\sigma_p}{Z_{0p}}-\frac{2\sigma_b}{Z_{0b}}\right]\frac{ab}{4\pi^2}\int_{-\infty}^{\infty}\int_{-\infty}^{\infty} P^-\left(\lambda',\mu',z=0\right)\,\mathrm{sinc}\left[\frac{(\lambda-\lambda')a}{2}\right]\,\mathrm{sinc}\left[\frac{(\mu-\mu')b}{2}\right]\mathrm{d}\lambda'\,\mathrm{d}\mu'\\ &- \left[\frac{2\sigma_p}{Z_{0p}}-\frac{2\sigma_b}{Z_{0b}}\right]\frac{\tilde{P}_i ab}{2\pi}\,\mathrm{sinc}\left[\frac{(\lambda+k_x)a}{2}\right]\,\mathrm{sinc}\left[\frac{(\mu+k_y)b}{2}\right],\end{aligned} \tag{4.31}$$

where, from Eq. (4.12), $P^-(\lambda,\mu,z=0) = -Z_a(\lambda,\mu)\,V_a(\lambda,\mu,z=0)$. If we know the LAFP velocity $V_a(\lambda,\mu,z=0)$, then all the pressures can be computed. However, from the equation above we see that the LAFP velocity depends on $V_p(\lambda,\mu)$. Thus, in the next section, we derive the expression for the panel velocity.

4.4 The response of a perforated panel

4.4.1 Modified natural frequencies and modeshapes

The perforations in the panel alter its elastic and inertial properties. The effective bending stiffness D^* of the perforated panel [68] is given in section 3.6 (Eq. (3.37)). Next, the change in the inertia property is accounted for using the Receptance method and the new resonance frequencies and mode shapes are obtained as detailed in section 2.7.

The perforated panel velocity as a modal sum is given by

$$v_p(x, y) = \sum_{r=1}^{\infty} B_r \psi_r(x, y) = \sum_{r=1}^{\infty} B_r \sum_{m=1}^{\infty} \sum_{n=1}^{\infty} U_{mnr} \phi_{mn}(x, y), \tag{4.32}$$

where B_r is the modal coefficient and $\psi_r(x, y)$ are the new modeshapes. Taking the double Fourier transform

$$V_p(\lambda, \mu) = \sum_{r=1}^{\infty} B_r \sum_{m=1}^{\infty} \sum_{n=1}^{\infty} U_{mnr} \Phi_{mn}(\lambda, \mu), \tag{4.33}$$

where

$$\Phi_{mn}(\lambda, \mu) = \frac{1}{2\pi} \int_{-b/2}^{b/2} \int_{-a/2}^{a/2} \phi_{mn}(x, y)\, e^{i\lambda x + i\mu y}\, \mathrm{d}x\, \mathrm{d}y.$$

Substituting for $\phi_{mn}(x, y)$ from Eq. (2.20)

$$\begin{aligned} \Phi_{mn}\left(\lambda, \mu\right) = -\frac{ab}{8\pi} &\left\{ e^{im\pi/2} \operatorname{sinc}\left[\frac{(\lambda + m\pi/a)\, a}{2}\right] - e^{-im\pi/2} \operatorname{sinc}\left[\frac{(\lambda - m\pi/a)\, a}{2}\right] \right\} \\ &\times \left\{ e^{in\pi/2} \operatorname{sinc}\left[\frac{(\mu + n\pi/b)\, b}{2}\right] - e^{-in\pi/2} \operatorname{sinc}\left[\frac{(\mu - n\pi/b)\, b}{2}\right] \right\}. \end{aligned} \tag{4.34}$$

Detailed derivation of $\Phi_{mn}\left(\lambda, \mu\right)$ is given in Appendix D. The above derived new modeshapes will be used in the panel equation of motion for computing the modal amplitudes. In the following section, we examine the modified equation of motion for the perforated panel.

4.4.2 The perforated panel equation of motion

The equation of motion for the perforated panel is

$$D^*(1 - i\eta)\nabla^4 v_p(x, y, t) + m_p \frac{\partial^2 v_p(x, y, t)}{\partial t^2} = -i\omega\, \Delta p(x, y, z = 0, t), \tag{4.35}$$

where D^* is the effective bending stiffness, m_p is the mass per unit area and η is the damping loss factor of the perforated panel. The transverse velocity of the perforated panel $v_p(x, y)$ can be expressed as a modal sum as shown in Eq. (4.32). Substituting for $v_p(x, y)$ and expanding Eq. (4.35) we get

$$\sum_{r,m,n} \left[D^*(1 - i\eta) \left\{ \left(\frac{m\pi}{a} \right)^2 + \left(\frac{n\pi}{b} \right)^2 \right\}^2 - m_p\omega^2 \right] B_r U_{mnr} \phi_{mn}(x, y)$$
$$= -i\omega \, \Delta p(x, y, z = 0).$$

Now, taking the double Fourier transform of the above equation

$$\sum_{r,m,n} \left[D^*(1 - i\eta) \left\{ \left(\frac{m\pi}{a} \right)^2 + \left(\frac{n\pi}{b} \right)^2 \right\}^2 - m_p\omega^2 \right] B_r U_{mnr} \Phi_{mn}(\lambda, \mu) = -i\omega \, \Delta P \left(\lambda, \mu \right), \tag{4.36}$$

where $\Phi_{mn} \left(\lambda, \mu \right)$ and $\Delta P \left(\lambda, \mu \right)$ are given by Eqs. (4.34) and (4.25), respectively. While taking the Fourier transform of the left hand side, note that $v_p(x, y) = 0$ in the region beyond the panel surface.

Now, substituting $\Delta P \left(\lambda, \mu \right)$ from Eq. (4.25) in Eq. (4.36)

$$\sum_{r,m,n} \left[D^*(1 - i\eta) \left\{ \left(\frac{m\pi}{a} \right)^2 + \left(\frac{n\pi}{b} \right)^2 \right\}^2 - m_p\omega^2 \right] B_r U_{mnr} \Phi_{mn}(\lambda, \mu)$$
$$= -2i\omega \, P^-(\lambda, \mu, z = 0) + 4\pi i\omega \, \tilde{P}_i \, \delta(\lambda + k_x) \, \delta(\mu + k_y). \tag{4.37}$$

Note that the forcing on the panel (right hand side of the above equation) consist of contributions from the radiated pressure fields on either side of the perforated panel and the blocked pressure field due to the incident plane wave. Thus, the perforated panel response depends upon both the incident pressure and the radiated pressure fields. In cases where the acoustic medium is air, we may neglect the effect of fluid loading on the panel vibrations by neglecting the radiated pressure term $P^-(\lambda, \mu, z = 0)$. Thus,

$$\sum_{r,m,n} \left[D^*(1 - i\eta) \left\{ \left(\frac{m\pi}{a} \right)^2 + \left(\frac{n\pi}{b} \right)^2 \right\}^2 - m_p\omega^2 \right] B_r U_{mnr} \Phi_{mn}(\lambda, \mu)$$
$$= 4\pi i\omega \, \tilde{P}_i \, \delta(\lambda + k_x) \, \delta(\mu + k_y). \tag{4.38}$$

The above equation is uncoupled and it is easier to find B_r and $V_p \left(\lambda, \mu \right)$. If the radiated pressure term was included, we have to solve a set of coupled equations (Eqs. (4.31) and (4.37)) simultaneously to obtain the panel response.

Now, multiplying the above equation (Eq. (4.38)) by $\sum_{p,q} U_{pqs}\Phi_{pq}(-\lambda,-\mu)$ and integrating over the wavenumber domain

$$\int_{-\infty}^{\infty}\int_{-\infty}^{\infty}\sum_{r,m,n} B_r \bar{U}_{mnr}\Phi_{mn}(\lambda,\mu)\sum_{p,q} U_{pqs}\Phi_{pq}(-\lambda,-\mu)\,\mathrm{d}\lambda\,\mathrm{d}\mu$$
$$= 4\pi i\omega\,\tilde{P}_i\int_{-\infty}^{\infty}\int_{-\infty}^{\infty}\delta(\lambda+k_x)\,\delta(\mu+k_y)\,\sum_{p,q} U_{pqs}\Phi_{pq}(-\lambda,-\mu)\,\mathrm{d}\lambda\,\mathrm{d}\mu,$$

where

$$\bar{U}_{mnr} = \left[D^*(1-i\eta)\left\{\left(\frac{m\pi}{a}\right)^2+\left(\frac{n\pi}{b}\right)^2\right\}^2 - m_p\omega^2\right] U_{mnr}. \tag{4.39}$$

Rearranging the above equation

$$\sum_{r,m,n}\sum_{p,q} B_r\bar{U}_{mnr}U_{pqs}\int_{-\infty}^{\infty}\int_{-\infty}^{\infty}\Phi_{mn}(\lambda,\mu)\,\Phi_{pq}(-\lambda,-\mu)\,\mathrm{d}\lambda\,\mathrm{d}\mu$$
$$= 4\pi i\omega\,\tilde{P}_i\sum_{p,q} U_{pqs}\Phi_{pq}(k_x,k_y). \tag{4.40}$$

The integral on the left hand side of the above equation can be evaluated analytically (see Appendix E) and is given by

$$\int_{-\infty}^{\infty}\int_{-\infty}^{\infty}\Phi_{mn}(\lambda,\mu)\Phi_{pq}(-\lambda,-\mu)\,\mathrm{d}\lambda\,\mathrm{d}\mu = \frac{ab}{4}\,\delta_{mp}\,\delta_{nq}. \tag{4.41}$$

Therefore, Eq. (4.40) turns out to be

$$\frac{ab}{4}\sum_{r,m,n} B_r\bar{U}_{mnr}U_{mns} = 4\pi i\omega\,\tilde{P}_i\sum_{m,n} U_{mns}\Phi_{mn}(k_x,k_y). \tag{4.42}$$

Or in a matrix form

$$\frac{ab}{4}\,[U_{mn,s}]^T\left[\bar{U}_{mn,r}\right]\{B_r\} = 4\pi i\omega\,\tilde{P}_i\,[U_{mn,s}]^T\{\Phi_{mn}(k_x,k_y)\}. \tag{4.43}$$

Now, the modal amplitude B_r of the perforated panel velocity can be obtained as

$$\{B_r\} = \frac{16\pi i\omega\,\tilde{P}_i}{ab}\left[\bar{U}_{mn,r}\right]^{-1}[U_{mn,s}]^{-T}[U_{mn,s}]^T\{\Phi_{mn}(k_x,k_y)\}.$$

Or

$$\{B_r\} = \frac{16\pi i\omega\,\tilde{P}_i}{ab}\,\left[\bar{U}_{mn,r}\right]^{-1}\{\Phi_{mn}(k_x, k_y)\}\,.$$

Thus, the perforated panel modal amplitude can be evaluated if the incident pressure amplitude and the modal behavior of the perforated panel are known. Now, $V_p(\lambda, \mu)$ (Eq. (4.33)) can be obtained in a matrix form as

$$V_p(\lambda, \mu) = \{B_r\}^T\,[U_{mn,r}]^T\,\{\Phi_{mn}(\lambda, \mu)\}\,. \tag{4.44}$$

And $V_a(\lambda, \mu, z = 0)$ is obtained from Eq. (4.31) as

$$\begin{aligned} V_a(\lambda, \mu, z = 0) \;&=\; \zeta_I V_p(\lambda, \mu) + \frac{2\sigma_b}{Z_{0b}}\,P^-(\lambda, \mu, z = 0) - 2\pi\tilde{P}_i\,\frac{2\sigma_b}{Z_{0b}}\,\delta(\lambda + k_x)\,\delta(\mu + k_y) \\ &+ \left[\frac{2\sigma_p}{Z_{0p}} - \frac{2\sigma_b}{Z_{0b}}\right]\frac{ab}{4\pi^2}\int_{-\infty}^{\infty}\int_{-\infty}^{\infty} P^-\left(\lambda', \mu', z = 0\right)\,\mathrm{sinc}\left[\frac{(\lambda - \lambda')a}{2}\right]\,\mathrm{sinc}\left[\frac{(\mu - \mu')b}{2}\right]\,\mathrm{d}\lambda'\,\mathrm{d}\mu' \\ &- \left[\frac{2\sigma_p}{Z_{0p}} - \frac{2\sigma_b}{Z_{0b}}\right]\frac{\tilde{P}_i ab}{2\pi}\,\mathrm{sinc}\left[\frac{(\lambda + k_x)a}{2}\right]\,\mathrm{sinc}\left[\frac{(\mu + k_y)b}{2}\right]. \end{aligned}$$

The above equation is an integral equation having the LAFP velocity on both the sides of the equation. The solution methodology is given in Appendix F. Thus, from Eq. (4.12), the transmitted pressure on the perforated panel surface is given by

$$P^-\left(\lambda, \mu, z = 0\right) = -Z_a\left(\lambda, \mu\right)V_a(\lambda, \mu, z = 0). \tag{4.45}$$

Since the LAFP velocity and the pressures on either side of the panel are known, we can obtain the transmitted sound power and hence the transmission loss.

4.5 Sound transmission loss of a perforated panel in a baffle

The expression for the transmitted power is

$$W_t = \frac{1}{2}\mathrm{Re}\left\{\int_{-\infty}^{\infty}\int_{-\infty}^{\infty} P^-(\lambda, \mu, z = 0)V_a^*(\lambda, \mu, z = 0)\,\mathrm{d}\lambda\,\mathrm{d}\mu\right\}, \tag{4.46}$$

where $P^{-}(\lambda, \mu, z = 0)$ and $V_a(\lambda, \mu, z = 0)$ are given by Eq. (4.45) and Eq. (4.31), respectively. In the above equation, only the wavenumber components satisfying the inequality $k^2 > \lambda^2 + \mu^2$ travel to the farfield. Hence, the farfield transmitted power is obtained by truncating the limits of integration as

$$W_t = \frac{1}{2}\mathrm{Re}\left\{\int_{-k}^{k}\int_{-\sqrt{k^2-\mu^2}}^{\sqrt{k^2-\mu^2}} P^{-}(\lambda, \mu, z = 0)V_a^*(\lambda, \mu, z = 0)\,\mathrm{d}\lambda\,\mathrm{d}\mu\right\}. \tag{4.47}$$

Note that while deriving the above equation, only the panel is assumed to be perforated. If the baffle is also perforated, a modified expression or rather a general expression has to be used, as shown below.

$$W_t = \frac{ab}{8\pi^2}\mathrm{Re}\left\{\int_{-k}^{k}\int_{-\sqrt{k^2-\mu'^2}}^{\sqrt{k^2-\mu'^2}}\int_{-k}^{k}\int_{-\sqrt{k^2-\mu^2}}^{\sqrt{k^2-\mu^2}} P^{-}(\lambda, \mu, z = 0)\,V_a^*(\lambda', \mu', z = 0)\right.$$
$$\left.\times\mathrm{sinc}\left[\frac{(\lambda' - \lambda)a}{2}\right]\,\mathrm{sinc}\left[\frac{(\mu' - \mu)b}{2}\right]\,\mathrm{d}\lambda\,\mathrm{d}\mu\,\mathrm{d}\lambda'\,\mathrm{d}\mu'\right\}. \tag{4.48}$$

The derivations of both the power expressions, one for an unperforated baffle case and the other for a perforated baffle case are given Appendix G. The integrals in the above equations are approximated by a sum over the range of discrete values of λ and μ.

Now, the total power incident on the perforated panel is

$$W_i = \frac{|\tilde{P}_i|^2 \cos\theta\; ab}{2\rho_0 c}, \tag{4.49}$$

where θ is the polar angle.

The sound transmission coefficient τ is the ratio of the transmitted to the incident sound powers

$$\tau = \frac{W_t}{W_i}. \tag{4.50}$$

And the sound transmission loss TL is

$$\mathrm{TL} = 10\log_{10}\left(\frac{1}{\tau}\right). \tag{4.51}$$

4.6 Results

In this section, the transmission loss characteristics of a perforated panel set in an unperforated baffle is discussed. To begin, we compare the results for an unperforated panel set in a baffle with that reported by Roussos [28].

4.6.1 Validation case: The unperforated panel TL

Here, the same parameter values are used as those in [28]. The rectangular panel is of size $0.38 \times 0.15 \times 0.00081$ m^3 and is set in a baffle of infinite extend with simply supported boundary condition. A plane harmonic wave of amplitude $\tilde{P}_i = 1$ and frequency ω is incident upon it. The material properties of the panel are: density $\rho_p = 2700$ kg/m^3, Young's modulus $E = 70$ GPa, Poisson's ratio $\nu = 0.33$ and the damping loss factor $\eta = 0.1$. The plane wave is assumed to be incident at a polar angle $\theta = 60^0$ and an azimuthal angle $\phi = 0^0$. In the proposed model, the panel velocity can be obtained from Eq. (4.33). Since the panel is assumed to be unperforated the LAFP velocity at the panel surface is the same as the panel velocity (Eq. (4.31)). The transmitted power (Eq. (4.47)), the incident power (Eq. (4.49)) and the transmission coefficient (Eq. (4.50)) are evaluated. The TL can now be obtained using Eq. (4.51). All the flexural modes of the simply supported panel below 25,000 Hz are considered for the analysis. The TL curve using the proposed method and that by Roussos' are shown in Fig. 4.2. The match is good. For an infinite flexible panel the sound transmission coefficient is given by [7]

$$\tau_\infty = \frac{\left(\frac{2\rho_0 c}{\omega m_p}\right)^2 \sec^2\theta}{\left[\frac{2\rho_0 c}{\omega m_p}\sec\theta + \left(\frac{k}{k_b}\right)^4 \eta \sin^4\theta\right]^2 + \left[1 - \left(\frac{k}{k_b}\right)^4 \sin^4\theta\right]^2}, \tag{4.52}$$

where k_b is the free flexural wavenumber in the plate and is given by

$$k_b = \left(\frac{\omega^2 m_p}{D}\right)^{1/4}. \tag{4.53}$$

Now, TL can be obtained by replacing τ with τ_∞ in Eq. (4.51). This result is also plotted in Fig. 4.2.

For a finite panel, below the first resonance, the transmitted power increases with frequency. Therefore, we see a reduction in the TL till the first resonance. At resonance, the TL is controlled by the structural damping factor. Above the first

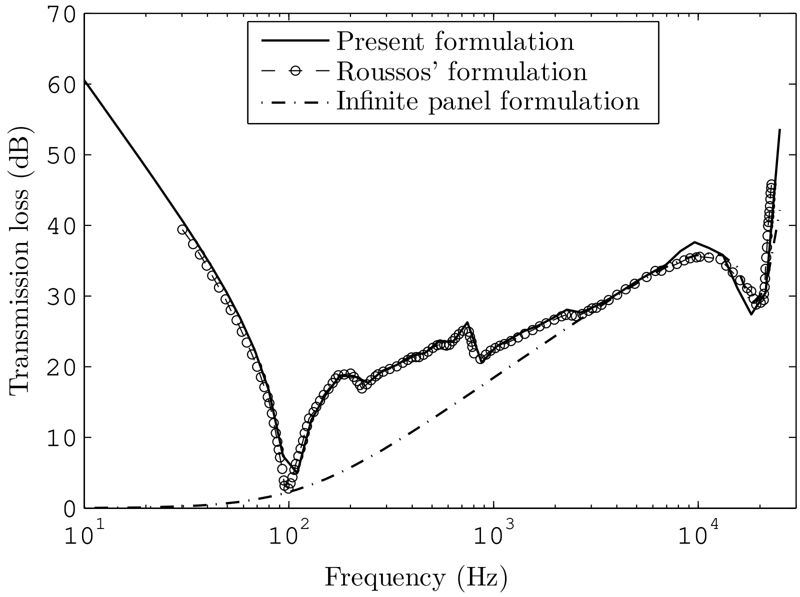

Fig. 4.2 Comparison of the transmission loss of an unperforated panel set in an (unperforated) infinite baffle. Results using the proposed formulation and that reported by Roussos [28] along with the infinite panel theory are shown. The plane wave is incident upon the panel at an angle $\theta = 60^0$ and $\phi = 0^0$.

resonance and below the coincidence frequency, the finite panel TL is similar to that of the infinite panel (mass law) - the small difference is due to the panel resonances. At the coincidence frequency, the structural damping controls the sound transmission. Beyond the coincidence, the sound transmission is controlled by the stiffness of the panel and both the finite and the infinite panel theories predict identical TL values. Thus, the finite panel formulation is found to be relevant at lower frequencies (when the panel dimensions are comparable with the acoustic wavelength). At higher frequencies, however, one can use the infinite panel formulation to obtain the TL with good accuracy.

4.6.2 Perforated panel sound transmission loss

This section discusses the TL of a perforated panel set in an unperforated baffle with simply supported boundary condition. The panel dimension is $0.455 \times 0.546 \times 0.003$ m^3 and the material properties are the same as before. A plane harmonic wave of unit amplitude ($\tilde{P}_i = 1$) hits the panel at a polar angle $\theta = 60^0$ and azimuthal angle $\phi = 0^0$. All the flexural modes of the perforated panel below 10,000 Hz are considered for the analysis.

Fig. 4.3 depicts the variation in TL for different hole radius. The total number of holes in the panel is fixed constant ($N_0 = 750$). The TL curve for the unperforated panel is also shown for comparison. It can be seen from Fig. 4.3 that by introducing perforations, the TL reduces considerably. We know that the equivalent impedance of a perforated panel consists of the perforate and the panel impedances arranged in parallel [7, 61]. The perforate impedance is given by $\frac{Z_{0p}}{\sigma_p}$. Even for a small hole radius ($r_p = 0.5$ mm) and the perforation ratio ($\sigma_p = 0.24\%$), the perforate impedance is less than the panel impedance. This results in an easier direct transmission of acoustic waves through the perforations than by the panel vibrations. It is observed that for large perforation ratios, the dips corresponding to the panel resonances do not exist in the TL spectrum.

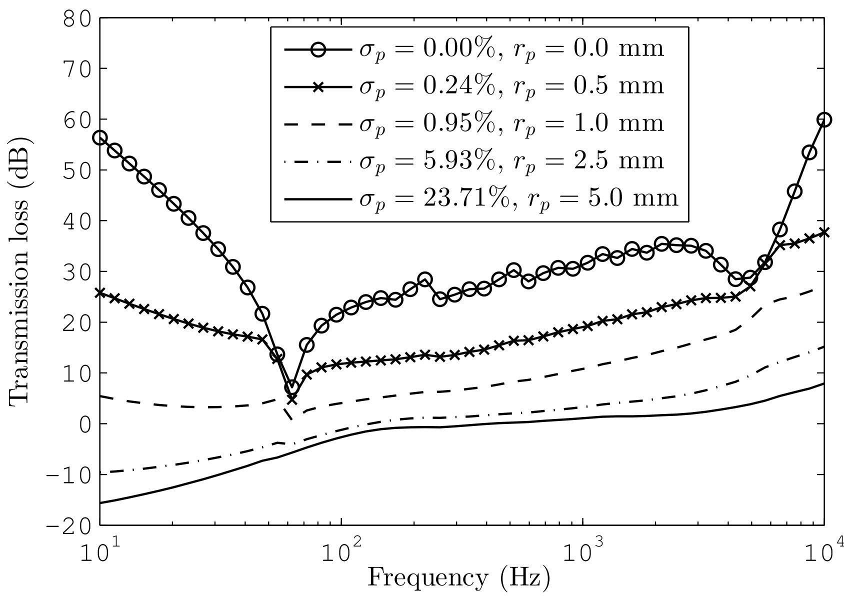

Fig. 4.3 Variation in the transmission loss of perforated panels for different hole radii/perforation ratios. Total number of holes in the panel is kept constant at $N_0 = 750$. The baffle is assumed to unperforated. The plane wave is incident upon the panel at an angle $\theta = 60^0$ and $\phi = 0^0$.

An increase in the hole radius results in a larger perforation ratio and hole impedance. However, the resultant perforate impedance $\frac{Z_{0p}}{\sigma_p}$ decreases with the increase in the hole size. The perforate impedance for different hole radii are shown in Fig. 4.4. A reduction in the perforate impedance increases the transmitted power and hence results in a lower TL. For a given hole radius, the perforate impedance increases with the frequency, so does the TL.

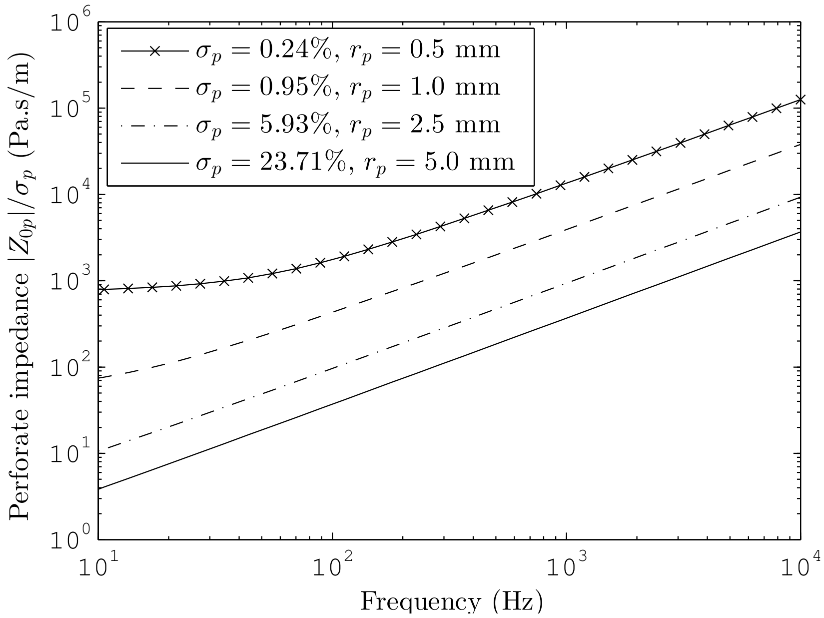

Fig. 4.4 Absolute perforate impedance of perforated panels for different hole radii/perforation ratios. Total number of holes in the panel is kept constant at $N_0 = 750$.

At low frequencies, for larger perforation ratios, the TL is negative (see Fig. 4.3). Negative TL cases were reported in the sound diffraction through circular apertures [69, 70]. More about this phenomenon will be discussed later in chapter 6.

If we keep the hole radius constant and vary the total number of holes in the panel, the perforate impedance variation is only due to the changes in the perforation ratio. Fig. 4.5 depicts the variation in the TL for different number of holes in the panel, but for a constant hole radius ($r_p = 2.5$ mm). The corresponding perforate impedances are plotted in Fig. 4.6. The perforate impedance decreases as the perforation ratio/the number of holes is increased. Thus, the TL decreases with the increase in the perforation ratio.

In Fig. 4.4, at low frequencies, the slope of the perforate impedance for small hole radii is different from that of the larger ones. To analyze this further, we choose a set of r_p and N_0 parameters so that the perforation ratio is constant. In this problem, the perforate impedance $\frac{Z_{0p}}{\sigma_p}$ differs across the cases due to the variation in the hole impedance alone. Fig. 4.7 shows the variation in TL for different hole sizes (or total number of holes) with $\sigma_p = 0.95\%$. The corresponding perforate impedance curves are shown in Fig. 4.8.

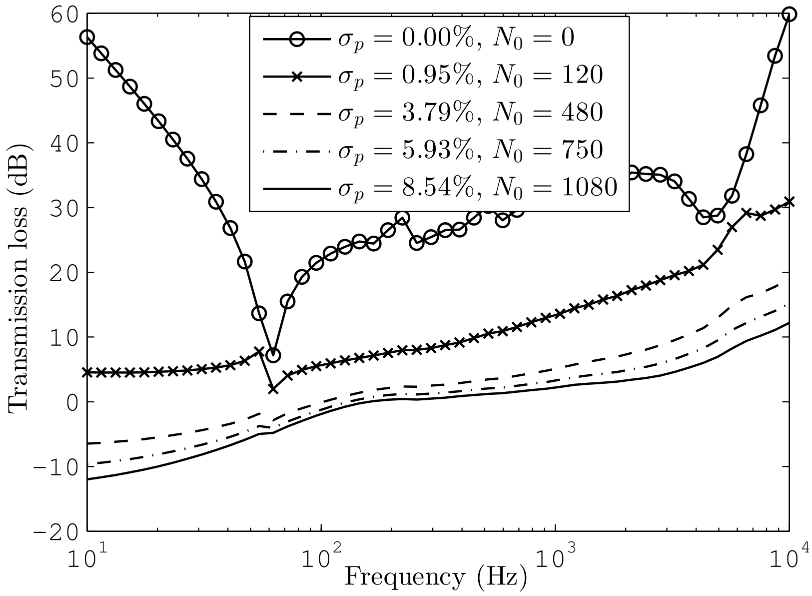

Fig. 4.5 The transmission loss variation with respect to the perforation ratio. The perforation ratio is varied by changing the total number of holes in the panel. Hole radius in all the cases is $r_p = 2.5$ mm. The baffle is assumed to be unperforated. The plane wave is incident upon the panel at an angle $\theta = 60^0$ and $\phi = 0^0$.

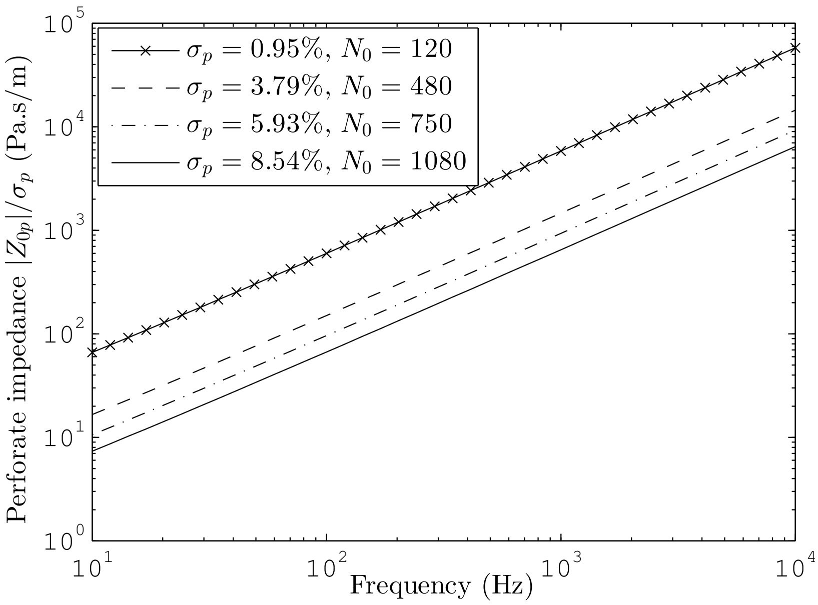

Fig. 4.6 Absolute perforate impedance of perforated panels for different perforation ratios. Different perforation ratios are achieved by varying the total number of holes in the panel. Hole radius in all the cases is $r_p = 2.5$ mm.

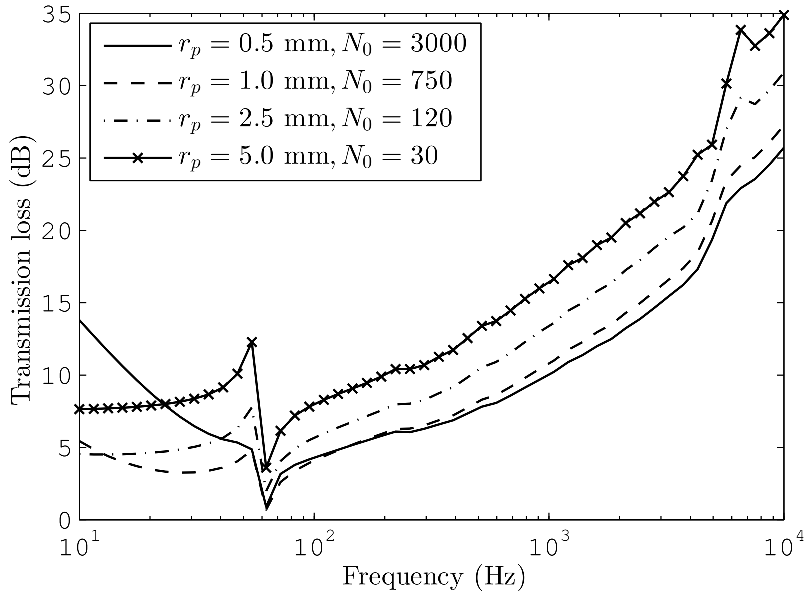

Fig. 4.7 The transmission loss variation with respect to the hole radii/total number of holes. The perforation ratio of the panel is the same ($\sigma_p = 0.95\%$) for all the cases. The baffle is assumed to be unperforated. The plane wave is incident upon the panel at an angle $\theta = 60^0$ and $\phi = 0^0$.

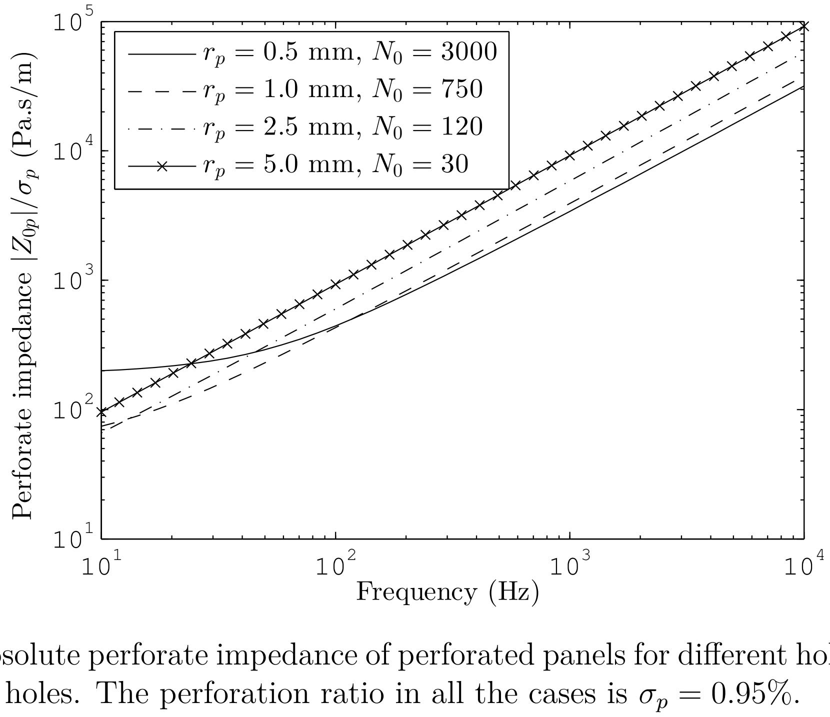

Fig. 4.8 Absolute perforate impedance of perforated panels for different hole radius/total number of holes. The perforation ratio in all the cases is $\sigma_p = 0.95\%$.

In Fig. 4.8, the $r_p = 0.5$ mm curve crosses all the other perforate impedance curves. This is caused by an increase in the hole resistance at lower frequencies for the $r_p = 0.5$ mm case, as shown in Fig. 4.9. A larger perforate resistance implies that more energy is being dissipated at the perforation walls and hence causes a higher transmission loss. Fig. 4.7 depicts this higher TL at lower frequencies for the $r_p = 0.5$ mm case. In fact, the larger hole radii cases also show an increase in the TL values, but at much lower frequencies.

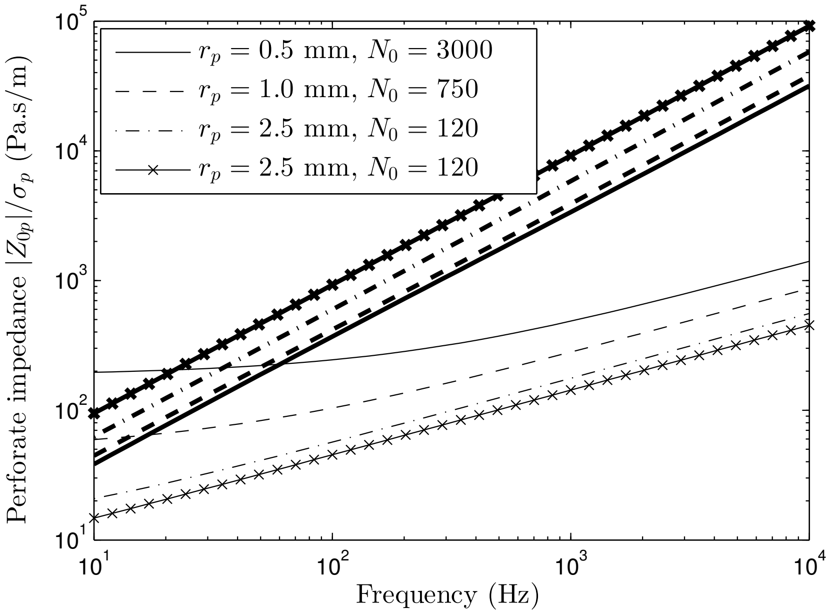

Fig. 4.9 Resistive (thin line) and reactive (thick line) components of perforate impedance for panels with the same perforation ratio ($\sigma_p = 0.95\%$). The total number of holes and the radius of holes in the panel are varied in each case to obtain a constant perforation ratio.

In all the above analysis, it is assumed that $\theta = 60^0$ and $\phi = 0^0$. Fig. 4.10 shows the variation in TL with respect to the polar angle of incidence (θ), keeping $\phi = 0^0$. For all the cases $N_0 = 750$ and $r_p = 1.0$ mm with a perforation ratio $\sigma_p = 0.95\%$. It is observed that the transmission loss decreases with the increase in θ. It can be seen from Fig. 4.11 that the transmitted power does not vary significantly with θ (as the perforate impedance is independent of θ and the effect of the panel impedance is negligible in determining the transmitted power). However, the normal incident power varies significantly with the angle of incidence (due to the $\cos\theta$ term in the Eq. (4.49)). Thus, it is the variation in the normal incident power that causes the reduction in the transmission loss for the gracing incidence of the plane wave.

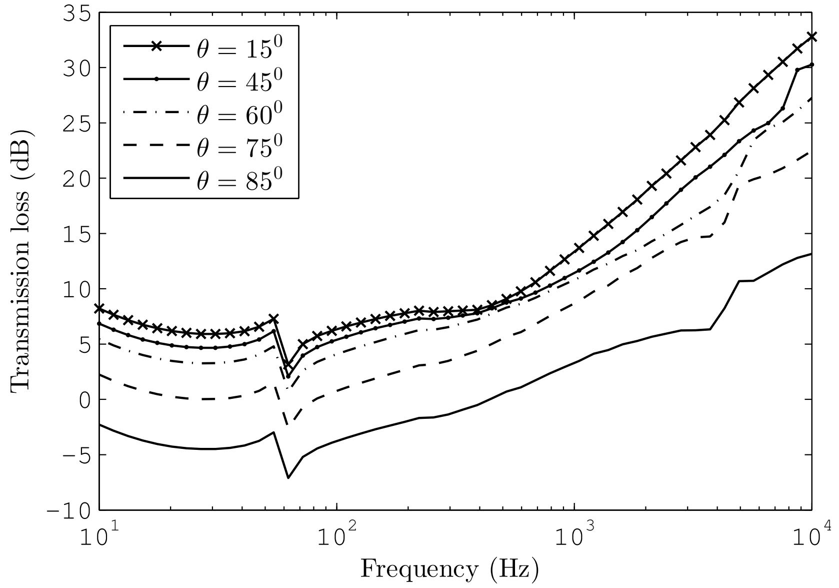

Fig. 4.10 Comparison of the perforated panel transmission loss for different polar angle of incidence θ of the plane wave. The azimuthal angle is the same for all the cases $\phi = 0^0$. The panel has $N_0 = 50$ and $r_p = 1.0$ mm. The baffle is assumed to be unperforated.

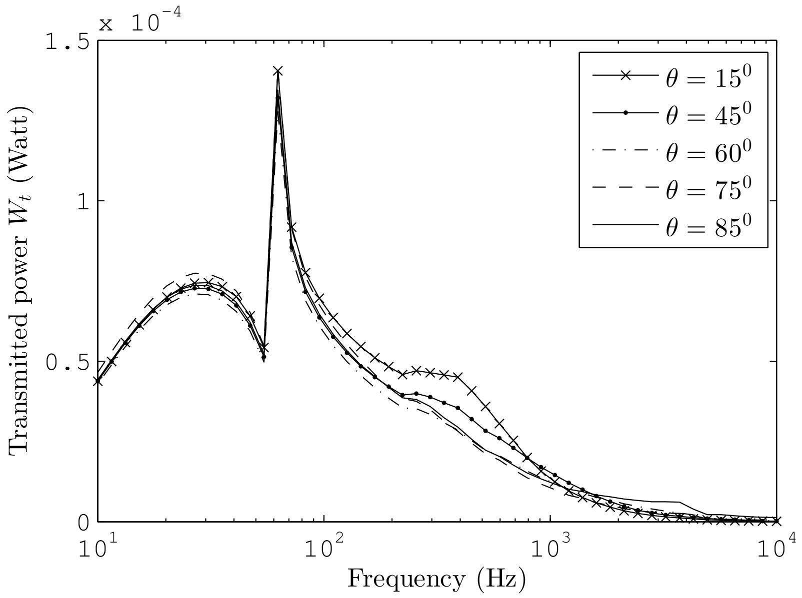

Fig. 4.11 Comparison of the perforated panel transmitted power for different polar angle of incidence θ of the plane wave. The azimuthal angle is the same for all the cases $\phi = 0^0$. The panel has $N_0 = 750$ and $r_p = 1.0$ mm. The baffle is assumed to be unperforated.

4.7 Conclusions

The sound transmission through a flexible, simply supported perforated panel set in a differently perforated baffle is modeled in the 2-D wavenumber domain. The discontinuity in the perforate impedance along the panel edges results in a coupling of wavenumbers in the average velocity field at the fluid-structure interface. In the one-way coupled model developed here, the effect of radiated pressure field on the panel response is neglected. However, the effect of radiated pressure in driving the fluid through the perforations is accounted for while finding the average velocity at the fluid-structure interface. The natural frequencies and the modeshapes of the perforated panel are obtained using the Receptance method. The developed one-way coupled model is numerically verified for the specific case of sound transmission through an unperforated panel set in a baffle.

The perforations in the panel reduce the transmission loss. Various cases of perforations are simulated and it is found that the transmission loss reduces with decreasing perforate impedance. For a panel having sub-millimeter size perforations (as for a micro-perforated panel), the resistive hole impedance dominates over the reactive impedance at low frequencies. This restricts the sound transmission through a micro-perforated panel at low frequencies in comparison to a panel with a larger hole radius. As the perforate impedance is independent of the angle of incidence of the plane wave (θ), the transmitted power does not vary significantly with θ. However, the normal incident power varies significantly with the angle of incidence and thus, the TL reduces with the increase in θ.

In the one-way coupled analysis, the effect of the radiated pressure field on the panel response is neglected. It is a major simplification and can only be used when the panel is attached to light fluids. For heavy fluid loading, one has to include the radiated pressure term in the equation of motion for the structure. This will require solving the structural and the acoustical equations simultaneously (two-way coupled formulation). In the following chapters, the two-way coupled models for the sound radiation and transmission through perforated panels are presented.

Part III

The two-way coupled analysis

Chapter 5

Sound radiation from a perforated panel: Two-way coupling

5.1 Introduction

In the previous chapters, the uncoupled or the one-way formulation was presented for the radiation and transmission of sound related to perforated panels. In many applications this is adequate, as with metallic panels and air as the medium. However, for different panel material and acoustic media combinations, or even for a light acoustic medium but enclosed environments or at specific frequencies, or for a heavy acoustic medium like water, the one-way coupled formulation may be inadequate. In such cases, as a result of the fluid loading, the structure and the acoustic domains interact and a two-way coupled fluid-structure analysis is required to compute the field variables of both the domains. The following chapters present the coupled structural acoustic radiation and transmission models for the finite flexible perforated panel set in an unperforated baffle. In this chapter, the radiation problem is considered. In the next section, a relation between the radiated pressure and the LAFP velocity is derived.

5.2 The pressure fields at the surface of a vibrating perforated panel

A finite flexible panel of size $a \times b$ and thickness h is simply supported on a rigid baffle of infinite extent (lying in the $z = 0$ plane). The panel has uniform circular perforations, whereas the baffle is unperforated. There is an acoustic medium of density ρ_0 on both sides of the panel-baffle system as shown in Fig. 5.1. The panel is excited by a

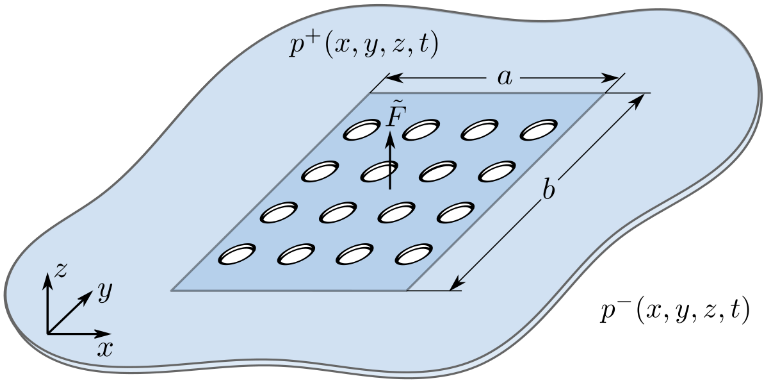

Fig. 5.1 Schematic of sound radiation from a perforated panel set in an unperforated baffle.

harmonic point force of amplitude $\tilde{F}$ and frequency ω at (x_0, y_0). The resulting flexural vibrations of the perforated panel radiate sound in the surrounding fluid medium. Let $p^+(x,y,z,t)$ and $p^-(x,y,z,t)$ be the resulting pressure fields above $(z > 0)$ and below $(z < 0)$ the panel (see Fig. 5.1), respectively. In this section, a formula relating the two pressures to the fluid particle velocity at the panel fluid interface is derived in the wavenumber domain.

The radiated pressure fields satisfy the 3-D Helmholtz equation. Applying the Helmholtz equation in the $z > 0$ region we get

$$\left(\nabla^2 + k^2\right) p^+(x,y,z) = 0. \tag{5.1}$$

Taking the *double Fourier transform* in the x and y directions results in

$$\left[\frac{\mathrm{d}^2}{\mathrm{d}z^2} + \left(k^2 - \lambda^2 - \mu^2\right)\right] P^+(\lambda,\mu,z) = 0, \tag{5.2}$$

where

$$P^+(\lambda,\mu,z) = \frac{1}{2\pi}\int_{-\infty}^{\infty}\int_{-\infty}^{\infty} p^+(x,y,z)\, e^{i\lambda x + i\mu y}\,\mathrm{d}x\,\mathrm{d}y. \tag{5.3}$$

The general solution to Eq. (5.2) is

$$P^+(\lambda,\mu,z) = A(\lambda,\mu)\, e^{i\sqrt{k^2-\lambda^2-\mu^2}z} + B(\lambda,\mu)\, e^{-i\sqrt{k^2-\lambda^2-\mu^2}z}. \tag{5.4}$$

By causality, since sound on the $+z$ side should travel only away from the panel, $B(\lambda, \mu) = 0$. Therefore

$$P^{+}(\lambda, \mu, z) = A(\lambda, \mu)\, e^{i\sqrt{k^2-\lambda^2-\mu^2}z}. \tag{5.5}$$

And the evanescent wave in the $+z$ direction is

$$P^{+}(\lambda, \mu, z) = A(\lambda, \mu)\, e^{-\sqrt{\lambda^2+\mu^2-k^2}z}.$$

The time dependence $e^{-i\omega t}$ is suppressed in the entire the formulation.

In the wavenumber domain, the Euler boundary condition at the solid-fluid interface (at $z = 0$) is

$$\frac{\partial}{\partial z} P^{+}(\lambda, \mu, z = 0) = i\rho_0 ck V_a(\lambda, \mu, z = 0), \tag{5.6}$$

where c is the velocity of sound in the acoustic medium and $V_a(\lambda, \mu, z = 0)$ is the double Fourier transform of the fluid particle velocity at the boundary and is given by

$$V_a(\lambda, \mu, z = 0) = \frac{1}{2\pi} \int_{-\infty}^{\infty}\int_{-\infty}^{\infty} v_a(x, y, z = 0)\, e^{i\lambda x + i\mu y}\, \mathrm{d}x\, \mathrm{d}y. \tag{5.7}$$

Using Eqs. (5.5) and (5.6) we get

$$A(\lambda, \mu) = P^{+}(\lambda, \mu, z = 0) = Z_a(\lambda, \mu) V_a(\lambda, \mu, z = 0), \tag{5.8}$$

where

$$Z_a(\lambda, \mu) = \frac{\rho_0 ck}{\sqrt{k^2 - \lambda^2 - \mu^2}} \tag{5.9}$$

is the complex acoustic impedance. Therefore

$$P^{+}(\lambda, \mu, z) = Z_a(\lambda, \mu)\, V_a(\lambda, \mu, z = 0)\, e^{i\sqrt{k^2-\lambda^2-\mu^2}z}. \tag{5.10}$$

For an unperforated panel, $V_a(\lambda, \mu, z = 0)$ is the same as the double Fourier transform of the panel velocity. However, for a perforated panel, $V_a(\lambda, \mu, z = 0)$ is the resultant of both the panel velocity and the fluid velocity through the perforations. Thus, $V_a(\lambda, \mu, z = 0)$ becomes the Locally Averaged Fluid Particle (LAFP) velocity (see section 3.3).

Similarly, the pressure field on the negative side is

$$P^{-}(\lambda, \mu, z) = -Z_a(\lambda, \mu)\, V_a(\lambda, \mu, z = 0)\, e^{-i\sqrt{k^2-\lambda^2-\mu^2}z}. \tag{5.11}$$

Note, the -ve sign in the exponential term represents the waves traveling in the $-z$ direction. It can also be seen that the pressure fields on the two sides of the panel have opposite signs. And the radiated pressure fields (Eqs. (5.10) and (5.11)) have infinite wavenumber components due to the finiteness of the perforated panel [5].

Using Eqs. (5.10) and (5.11), the pressure difference (in the wavenumber domain) across the panel-baffle surface is

$$\begin{aligned}\Delta P(\lambda,\mu) &= P^{-}(\lambda,\mu,z=0) - P^{+}(\lambda,\mu,z=0) = -2\,P^{+}(\lambda,\mu,z=0)\\ &= -2\,Z_a(\lambda,\mu)\,V_a(\lambda,\mu,z=0).\end{aligned} \tag{5.12}$$

The radiated pressures depend on the LAFP velocity. Hence, an expression for the double Fourier transform of the LAFP velocity over the panel-baffle surface is derived in the following section. The formulation is general and can treat any degree of perforations over the panel-baffle plane.

5.3 Locally averaged fluid particle (LAFP) velocity and its Fourier transform

The LAFP velocity was derived in chapter 3 section 3.4. Only the final result is presented here in order to avoid repetition. The LAFP velocity is related to the panel velocity, the acoustic pressures and the perforate impedance as follows:

$$\begin{aligned}&\left[1+\frac{2\sigma_b}{Z_{0b}}Z_a(\lambda,\mu)\right]V_a(\lambda,\mu,z=0) = \zeta_I V_p(\lambda,\mu) + \frac{ab}{2\pi^2}\left[\frac{\sigma_b}{Z_{0b}} - \frac{\sigma_p}{Z_{0p}}\right]\\ &\times\left\{\int_{-\infty}^{\infty}\int_{-\infty}^{\infty} Z_a(\lambda',\mu')V_a(\lambda',\mu',z=0)\,\mathrm{sinc}\left[\frac{(\lambda-\lambda')a}{2}\right]\,\mathrm{sinc}\left[\frac{(\mu-\mu')b}{2}\right]\,\mathrm{d}\lambda'\,\mathrm{d}\mu'\right\}.\end{aligned} \tag{5.13}$$

Here, $V_p(\lambda,\mu)$ and $V_a(\lambda,\mu,z=0)$ are the only unknowns. If we know the panel velocity $V_p\,(\lambda,\mu)$, the above equation can be solved for $V_a\,(\lambda,\mu,z=0)$. The next section presents the derivation for $V_p\,(\lambda,\mu)$, the velocity of a perforated panel. It turns out that the perforated panel velocity is a function of the LAFP velocity. Thus, one has to solve two coupled equations simultaneously to obtain the two velocities.

5.4 The velocity response of the perforated panel

5.4.1 Modified natural frequencies and modeshapes

As mentioned at the end of the last section, the panel velocity is required for obtaining the LAFP velocity. The panel now is perforated and hence, the new modeshapes and resonances need to be computed before the forced response can be derived. A detailed derivation of the new resonance frequencies and modeshapes of a perforated panel was presented in sections 2.7 and 3.6. Hence, the derivation is not repeated here. It is assumed here that the new resonances and modeshapes are available.

The modified (r^{th}) modeshape of a perforated panel is obtained as

$$\psi_r\left(x,y\right) = \sum_{m=1}^{\infty}\sum_{n=1}^{\infty} U_{mnr}\phi_{mn}(x,y), \tag{5.14}$$

where $\phi_{mn}(x,y)$ is the $(m,n)^{\text{th}}$ modeshape of an unperforated simply-supported panel given by

$$\phi_{mn}(x,y) = \sin\frac{m\pi(x+a/2)}{a}\sin\frac{n\pi(y+b/2)}{b} \tag{5.15}$$

and

$$U_{mnr} = \frac{4}{\rho_p hab}\frac{\sum_{i=1}^{N_0}\phi_{mn}(x_i,y_i)F_{ir}}{\omega_{mn}^2-\omega_r^2}. \tag{5.16}$$

In the above expression, ω_{mn} represents the $(m,n)^{\text{th}}$ resonance frequency of the unperforated panel. The index i denotes the hole locations. F_{ir} represents the i^{th} element of the eigenvector corresponding to the zero eigenvalue of the perforated plate receptance matrix at the r^{th} natural frequency ω_r (see section 2.7). From Eq. (5.14), it can be seen that the modeshape $\psi_r\left(x,y\right)$ of a perforated panel is a linear combination of natural modes of a simply-supported unperforated panel.

We may now express the perforated panel velocity as a modal sum given by

$$v_p(x,y) = \sum_{r=1}^{\infty} B_r\psi_r(x,y) = \sum_{r=1}^{\infty} B_r\sum_{m=1}^{\infty}\sum_{n=1}^{\infty} U_{mnr}\phi_{mn}(x,y), \tag{5.17}$$

where B_r is the modal coefficient. Taking the double Fourier transform of $v_p(x,y)$

$$V_p(\lambda,\mu) = \sum_{r=1}^{\infty} B_r\sum_{m=1}^{\infty}\sum_{n=1}^{\infty} U_{mnr}\Phi_{mn}(\lambda,\mu), \tag{5.18}$$

where

$$\Phi_{mn}(\lambda,\mu) = \frac{1}{2\pi}\int_{-b/2}^{b/2}\int_{-a/2}^{a/2}\phi_{mn}(x,y)\,e^{i\lambda x+i\mu y}\,\mathrm{d}x\,\mathrm{d}y.$$

Substituting for $\phi_{mn}(x,y)$ from Eq. (5.15) into the above equation

$$\begin{aligned}\Phi_{mn}\left(\lambda,\mu\right) = -\frac{ab}{8\pi}&\left\{e^{im\pi/2}\,\mathrm{sinc}\left[\frac{\left(\lambda+m\pi/a\right)a}{2}\right] - e^{-im\pi/2}\,\mathrm{sinc}\left[\frac{\left(\lambda-m\pi/a\right)a}{2}\right]\right\}\\ &\times\left\{e^{in\pi/2}\,\mathrm{sinc}\left[\frac{\left(\mu+n\pi/b\right)b}{2}\right] - e^{-in\pi/2}\,\mathrm{sinc}\left[\frac{\left(\mu-n\pi/b\right)b}{2}\right]\right\}.\end{aligned} \tag{5.19}$$

The detailed derivation of $\Phi_{mn}\left(\lambda,\mu\right)$ is given in Appendix D. Now, since the new modeshapes and resonances are available, we proceed to find the panel response to a point force.

5.4.2 The perforated panel equation of motion

Assume that the perforated panel is excited by a point harmonic force of amplitude $\tilde{F}$ and frequency ω at (x_0,y_0). Then, the equation of motion for a thin perforated panel is given by

$$\begin{aligned}D^*(1-i\eta)\nabla^4 v_p(x,y,t) + m_p\,\frac{\partial^2 v_p(x,y,t)}{\partial t^2}\\ = -i\omega\left[\Delta p(x,y,z=0,t) + \tilde{F}\,\delta\left(x-x_0\right)\,\delta\left(y-y_0\right)\,e^{-i\omega t}\right],\end{aligned} \tag{5.20}$$

where D^* is the effective bending stiffness, m_p is the modified mass per unit area ($=\rho_p h(1-\sigma_p)$) and η is the damping loss factor of the perforated panel. $\Delta p(x,y,z=0)$ is the inverse Fourier transform of $\Delta P(\lambda,\mu)$ (Eq. (5.12)). Substituting for $v_p(x,y)$ from Eq. (5.17) into Eq. (5.20) we get

$$\begin{aligned}\sum_{r,m,n}\left[D^*(1-i\eta)\left\{\left(\frac{m\pi}{a}\right)^2+\left(\frac{n\pi}{b}\right)^2\right\}^2 - m_p\omega^2\right]B_r U_{mnr}\phi_{mn}(x,y)\\ = -i\omega\left[\Delta p(x,y,z=0,t) + \tilde{F}\,\delta\left(x-x_0\right)\,\delta\left(y-y_0\right)\,e^{-i\omega t}\right].\end{aligned}$$

And in the wavenumber domain

$$\sum_{r,m,n}\left[D^*(1-i\eta)\left\{\left(\frac{m\pi}{a}\right)^2+\left(\frac{n\pi}{b}\right)^2\right\}^2-m_p\omega^2\right]B_rU_{mnr}\Phi_{mn}(\lambda,\mu)$$
$$=-i\omega\,\Delta P\,(\lambda,\mu)-\frac{i\omega\tilde{F}}{2\pi}\,e^{i\lambda x_0+i\mu y_0},$$

where $\Phi_{mn}\,(\lambda,\mu)$ and $\Delta P\,(\lambda,\mu)$ are given by Eqs. (5.19) and (5.12), respectively. Substituting for $\Delta P\,(\lambda,\mu)$ from Eq. (5.12) we get

$$\sum_{r,m,n}\left[D^*(1-i\eta)\left\{\left(\frac{m\pi}{a}\right)^2+\left(\frac{n\pi}{b}\right)^2\right\}^2-m_p\omega^2\right]B_rU_{mnr}\Phi_{mn}(\lambda,\mu)$$
$$=2i\omega\,Z_a(\lambda,\mu)\,V_a(\lambda,\mu,z=0)-\frac{i\omega\tilde{F}}{2\pi}\,e^{i\lambda x_0+i\mu y_0}. \quad (5.21)$$

Now we can see that the perforated panel displacement depends upon both the external harmonic excitation and the LAFP velocity and hence we need to solve the two coupled equations (Eqs. (5.13) and (5.21)), simultaneously, to obtain the panel response $V_p\,(\lambda,\mu)$. In the next section, a single equation is derived by combining Eqs. (5.13) and (5.21) and is solved for the perforated panel velocity response.

5.5 The coupled formulation and its solution

5.5.1 The coupled equation

Rearranging Eq. (5.21) we get

$$V_a(\lambda,\mu,z=0)=\frac{1}{2i\omega Z_a\,(\lambda,\mu)}\left\{\frac{i\omega\tilde{F}}{2\pi}\,e^{i\lambda x_0+i\mu y_0}\right.$$
$$\left.+\sum_{r,m,n}\left[D^*(1-i\eta)\left\{\left(\frac{m\pi}{a}\right)^2+\left(\frac{n\pi}{b}\right)^2\right\}^2-m_p\omega^2\right]B_rU_{mnr}\Phi_{mn}(\lambda,\mu)\right\}. \quad (5.22)$$

Substituting $V_p(\lambda,\mu)$ (Eq. (5.18)) and $V_a(\lambda,\mu,z=0)$ (Eq. (5.22)) into Eq. (5.13)

$$\begin{aligned}
&\left[1+\frac{2\sigma_b}{Z_{0b}}Z_a(\lambda,\mu)\right]\left[\frac{1}{2i\omega Z_a\left(\lambda,\mu\right)}\sum_{r,m,n}B_r\bar{U}_{mnr}\Phi_{mn}(\lambda,\mu)+\frac{\tilde{F}}{4\pi Z_a\left(\lambda,\mu\right)}\,e^{i\lambda x_0+i\mu y_0}\right]\\
&\qquad=\ \zeta_I\sum_{r,m,n}B_rU_{mnr}\Phi_{mn}(\lambda,\mu)\\
&\qquad-\frac{ab}{2\pi^2}\,\left[\frac{\sigma_p}{Z_{0p}}-\frac{\sigma_b}{Z_{0b}}\right]\int_{-\infty}^{\infty}\int_{-\infty}^{\infty}\left[\frac{1}{2i\omega}\sum_{r,m,n}B_r\bar{U}_{mnr}\Phi_{mn}(\lambda',\mu')+\frac{\tilde{F}}{4\pi}\,e^{i\lambda' x_0+i\mu' y_0}\right]\\
&\qquad\times\operatorname{sinc}\left[\frac{(\lambda-\lambda')a}{2}\right]\,\operatorname{sinc}\left[\frac{(\mu-\mu')b}{2}\right]\,\mathrm{d}\lambda'\,\mathrm{d}\mu',
\end{aligned}\tag{5.23}$$

where

$$\bar{U}_{mnr}=\left[D^*(1-i\eta)\left\{\left(\frac{m\pi}{a}\right)^2+\left(\frac{n\pi}{b}\right)^2\right\}^2-m_p\omega^2\right]U_{mnr}.\tag{5.24}$$

After a few simplifications (see Appendix H)

$$\begin{aligned}
&\frac{1}{2i\omega}\left[1+\frac{2\sigma_b}{Z_{0b}}Z_a(\lambda,\mu)\right]\sum_{r,m,n}B_r\bar{U}_{mnr}\Theta_{mn}(\lambda,\mu)-\zeta_I\sum_{r,m,n}B_rU_{mnr}\Phi_{mn}(\lambda,\mu)\\
&+\frac{ab}{8\pi^2 i\omega}\,\left[\frac{2\sigma_p}{Z_{0p}}-\frac{2\sigma_b}{Z_{0b}}\right]\sum_{r,m,n}B_r\bar{U}_{mnr}X_{mn}(\lambda,\mu)\ =-\frac{\tilde{F}}{4\pi}\,\frac{2\sigma_p}{Z_{0p}}\,e^{i\lambda x_0+i\mu y_0}-\frac{\tilde{F}}{4\pi}\,\frac{e^{i\lambda x_0+i\mu y_0}}{Z_a\left(\lambda,\mu\right)},
\end{aligned}\tag{5.25}$$

where

$$\Theta_{mn}(\lambda,\mu)=\frac{\Phi_{mn}(\lambda,\mu)}{Z_a(\lambda,\mu)}\tag{5.26}$$

and

$$X_{mn}(\lambda,\mu)=\int_{-\infty}^{\infty}\int_{-\infty}^{\infty}\Phi_{mn}(\lambda',\mu')\operatorname{sinc}\left[\frac{(\lambda-\lambda')a}{2}\right]\,\operatorname{sinc}\left[\frac{(\mu-\mu')b}{2}\right]\,\mathrm{d}\lambda'\,\mathrm{d}\mu'.\tag{5.27}$$

The above equation (Eq. (5.25)) can be solved for B_r, the modal coefficients of the perforated panel velocity.

5.5.2 Solution to the coupled equation

Multiplying Eq. (5.25) by $\sum_{p,q} U_{pqs}\Phi_{pq}(-\lambda,-\mu)$ and integrating over λ and μ we obtain

$$
\begin{aligned}
&\frac{1}{2i\omega}\sum_{r,m,n}\sum_{p,q} B_r\bar{U}_{mnr}U_{pqs}\int_{-\infty}^{\infty}\int_{-\infty}^{\infty}\Theta_{mn}(\lambda,\mu)\Phi_{pq}(-\lambda,-\mu)\,\mathrm{d}\lambda\,\mathrm{d}\mu \\
&\quad+\frac{1}{2i\omega}\frac{2\sigma_b}{Z_{0b}}\sum_{r,m,n}\sum_{p,q} B_r\bar{U}_{mnr}U_{pqs}\int_{-\infty}^{\infty}\int_{-\infty}^{\infty}\Phi_{mn}(\lambda,\mu)\Phi_{pq}(-\lambda,-\mu)\,\mathrm{d}\lambda\,\mathrm{d}\mu \\
&\quad-\zeta_I\sum_{r,m,n}\sum_{p,q} B_r U_{mnr}U_{pqs}\int_{-\infty}^{\infty}\int_{-\infty}^{\infty}\Phi_{mn}(\lambda,\mu)\Phi_{pq}(-\lambda,-\mu)\,\mathrm{d}\lambda\,\mathrm{d}\mu \\
&\quad+\frac{ab}{8\pi^2 i\omega}\left[\frac{2\sigma_p}{Z_{0p}}-\frac{2\sigma_b}{Z_{0b}}\right]\sum_{r,m,n}\sum_{p,q} B_r\bar{U}_{mnr}U_{pqs}\int_{-\infty}^{\infty}\int_{-\infty}^{\infty}X_{mn}(\lambda,\mu)\Phi_{pq}(-\lambda,-\mu)\,\mathrm{d}\lambda\,\mathrm{d}\mu \\
&\quad= -\frac{\tilde{F}}{4\pi}\sum_{p,q}U_{pqs}\int_{-\infty}^{\infty}\int_{-\infty}^{\infty}\frac{\Phi_{pq}(-\lambda,-\mu)}{Z_a(\lambda,\mu)}\,e^{i\lambda x_0+i\mu y_0}\,\mathrm{d}\lambda\,\mathrm{d}\mu \\
&\quad-\frac{\tilde{F}}{4\pi}\frac{2\sigma_p}{Z_{0p}}\sum_{p,q}U_{pqs}\int_{-\infty}^{\infty}\int_{-\infty}^{\infty}\Phi_{pq}(-\lambda,-\mu)\,e^{i\lambda x_0+i\mu y_0}\,\mathrm{d}\lambda\,\mathrm{d}\mu. \qquad (5.28)
\end{aligned}
$$

The first integral on the left and on the right hand sides of the above equation are evaluated numerically and the rest are integrated analytically. Note, that the acoustic impedance term $Z_a(\lambda,\mu)$ appears in the denominator of the integrands. This helps in avoiding the square root singularity while numerically evaluating the respective integrals. The integrals on the left hand side represent the modal coupling coefficients. The analytical derivation of the integrals is given in Appendix I and the results are given below:

$$\int_{-\infty}^{\infty}\int_{-\infty}^{\infty}\Phi_{mn}(\lambda,\mu)\Phi_{pq}(-\lambda,-\mu)\,\mathrm{d}\lambda\,\mathrm{d}\mu=\frac{ab}{4}\,\delta_{mp}\,\delta_{nq}, \qquad (5.29)$$

$$\int_{-\infty}^{\infty}\int_{-\infty}^{\infty}X_{mn}(\lambda,\mu)\Phi_{pq}(-\lambda,-\mu)\,\mathrm{d}\lambda\,\mathrm{d}\mu=\pi^2\,\delta_{mp}\,\delta_{nq} \qquad (5.30)$$

and

$$\int_{-\infty}^{\infty}\int_{-\infty}^{\infty} \Phi_{pq}(-\lambda,-\mu)\, e^{i\lambda x_0 + i\mu y_0}\, \mathrm{d}\lambda\, \mathrm{d}\mu = 2\pi\, \phi_{pq}\left(x_0, y_0\right). \tag{5.31}$$

Now substituting the above integrals into Eq. (5.28)

$$\begin{aligned}
&\frac{1}{2i\omega}\sum_{r,m,n}\sum_{p,q} B_r \bar{U}_{mnr} U_{pqs} \bar{\Theta}_{mnpq} \;+\; \frac{ab}{8i\omega}\frac{2\sigma_b}{Z_{0b}}\sum_{r,m,n}\sum_{p,q} B_r \bar{U}_{mnr} U_{pqs}\, \delta_{mp}\, \delta_{nq} \\
&-\; \frac{ab}{4}\zeta_I \sum_{r,m,n}\sum_{p,q} B_r U_{mnr} U_{pqs}\, \delta_{mp}\, \delta_{nq} \;+\; \frac{ab}{8i\omega}\left[\frac{2\sigma_p}{Z_{0p}} - \frac{2\sigma_b}{Z_{0b}}\right]\sum_{r,m,n}\sum_{p,q} B_r \bar{U}_{mnr} U_{pqs}\, \delta_{mp}\, \delta_{nq} \\
&\qquad = -\frac{\tilde{F}}{4\pi}\sum_{p,q} U_{pqs}\, \gamma_{pq}\left(x_0, y_0\right) \;-\; \frac{\tilde{F}}{2}\frac{2\sigma_p}{Z_{0p}}\sum_{p,q} U_{pqs}\, \phi_{pq}\left(x_0, y_0\right),
\end{aligned}$$

where

$$\bar{\Theta}_{mnpq} = \int_{-\infty}^{\infty}\int_{-\infty}^{\infty} \Theta_{mn}(\lambda,\mu)\Phi_{pq}(-\lambda,-\mu)\, \mathrm{d}\lambda\, \mathrm{d}\mu \tag{5.32}$$

and

$$\gamma_{pq}\left(x_0, y_0\right) = \int_{-\infty}^{\infty}\int_{-\infty}^{\infty} \frac{\Phi_{pq}(-\lambda,-\mu)}{Z_a\left(\lambda,\mu\right)}\, e^{i\lambda x_0 + i\mu y_0}\, \mathrm{d}\lambda\, \mathrm{d}\mu. \tag{5.33}$$

Simplifying,

$$\begin{aligned}
&\frac{1}{2i\omega}\sum_{r,m,n}\sum_{p,q} B_r \bar{U}_{mnr} U_{pqs} \bar{\Theta}_{mnpq} + \frac{ab}{8i\omega}\frac{2\sigma_p}{Z_{0p}}\sum_{r,m,n} B_r \bar{U}_{mnr} U_{mns} - \frac{ab}{4}\zeta_I \sum_{r,m,n} B_r U_{mnr} U_{mns} \\
&\qquad = -\frac{\tilde{F}}{4\pi}\sum_{p,q} U_{pqs}\, \gamma_{pq}\left(x_0, y_0\right) \;-\; \frac{\tilde{F}}{2}\frac{2\sigma_p}{Z_{0p}}\sum_{p,q} U_{pqs}\, \phi_{pq}\left(x_0, y_0\right).
\end{aligned} \tag{5.34}$$

In a matrix form, the above equation becomes

$$\begin{aligned}
&\frac{1}{2i\omega}\left[U_{pq,s}\right]^T \left[\bar{\Theta}_{mn,pq}\right]^T \left[\bar{U}_{mn,r}\right]\left\{B_r\right\} \;+\; \frac{ab}{8i\omega}\frac{2\sigma_p}{Z_{0p}}\left[U_{mn,s}\right]^T \left[\bar{U}_{mn,r}\right]\left\{B_r\right\} \\
&\qquad -\; \frac{ab}{4}\zeta_I \left[U_{mn,s}\right]^T \left[U_{mn,r}\right]\left\{B_r\right\} \\
&\qquad = -\frac{\tilde{F}}{4\pi}\left[U_{pq,s}\right]^T \left\{\gamma_{pq}\left(x_0, y_0\right)\right\} \;-\; \frac{\tilde{F}}{2}\frac{2\sigma_p}{Z_{0p}}\left[U_{pq,s}\right]^T \left\{\phi_{pq}\left(x_0, y_0\right)\right\}.
\end{aligned}$$

Thus, the modal coefficients are given by

$$\{B_r\} = [Z_{s,r}]^{-1} \{F_s\}, \tag{5.35}$$

where

$$[Z_{s,r}] = \frac{1}{2i\omega} [U_{pq,s}]^T \left[\bar{\Theta}_{mn,pq}\right]^T \left[\bar{U}_{mn,r}\right] + \frac{ab}{8i\omega} \frac{2\sigma_p}{Z_{0p}} [U_{mn,s}]^T \left[\bar{U}_{mn,r}\right] - \frac{ab}{4} \zeta_I [U_{mn,s}]^T [U_{mn,r}] \tag{5.36}$$

and

$$\{F_s\} = -\frac{\tilde{F}}{4\pi} [U_{pq,s}]^T \{\gamma_{pq}(x_0, y_0)\} - \frac{\tilde{F}}{2} \frac{2\sigma_p}{Z_{0p}} [U_{pq,s}]^T \{\phi_{pq}(x_0, y_0)\}. \tag{5.37}$$

Using Eqs. (5.18) and (5.35), the perforated panel velocity is obtained as

$$V_p(\lambda, \mu) = \{B_r\}^T [U_{mn,r}]^T \{\Phi_{mn}(\lambda, \mu)\}. \tag{5.38}$$

And the LAFP velocity $V_a(\lambda, \mu, z = 0)$ can now be evaluated from Eq. (5.13) (see Appendix A). From $V_a(\lambda, \mu, z = 0)$, the radiated pressure is obtained as

$$P^+(\lambda, \mu, z = 0) = Z_a(\lambda, \mu) V_a(\lambda, \mu, z = 0). \tag{5.39}$$

Since, the velocities and radiated pressures are now known, we proceed to compute the radiated power and the radiation efficiency.

5.6 The radiation efficiency

The far-field radiated power from the perforated panel set in an unperforated baffle is

$$W = \frac{1}{2} \mathrm{Re} \left\{ \int_{-k}^{k} \int_{-\sqrt{k^2-\mu^2}}^{\sqrt{k^2-\mu^2}} P^+(\lambda, \mu, z = 0) V_a^*(\lambda, \mu) \,\mathrm{d}\lambda \,\mathrm{d}\mu \right\}. \tag{5.40}$$

The limits of integration account only for the far-field radiating components in the wavenumber spectrum which satisfy the inequality $k^2 > \lambda^2 + \mu^2$. The integral is approximated by a sum over the range of discrete values of λ and μ.

The radiation efficiency of a perforated panel to a point harmonic excitation is [7]

$$\sigma = \frac{W}{\frac{1}{2}\rho_0 cab < |v_p|^2 >}, \tag{5.41}$$

where W is the radiated power (Eq. (5.40)) and $< |v_p|^2 >$ is the spatially averaged squared velocity of the perforated panel defined as [7]

$$< |v_p|^2 >= \frac{1}{ab} \int_{-b/2}^{b/2} \int_{-a/2}^{a/2} |v_p(x,y)|^2 \, \mathrm{d}x \, \mathrm{d}y.$$

Substituting the perforated panel velocity $v_p(x,y)$ (Eq. (5.17)) and simplifying we get

$$< |v_p|^2 >= \frac{1}{4} \sum_{r,s} \sum_{m,n} B_r B_s^* U_{mnr} U_{mns}^*, \tag{5.42}$$

where * represents the complex conjugate. In a matrix form

$$< |v_p|^2 >= \frac{1}{4} \left\{B_r\right\}^T \left[U_{mn,r}\right]^T \left[U_{mn,s}^*\right] \left\{B_s^*\right\}. \tag{5.43}$$

Using Eqs. (5.40) and (5.42), the radiation efficiency of a perforated panel to a point harmonic excitation (Eq. (5.41)) is

$$\sigma = \frac{4}{\rho_0 cab \sum\limits_{r,s} \sum\limits_{m,n} B_r B_s^* U_{mnr} U_{mns}^*} \mathrm{Re} \left\{ \int_{-k}^{k} \int_{-\sqrt{k^2-\mu^2}}^{\sqrt{k^2-\mu^2}} P^+(\lambda,\mu,z=0) V_a^*(\lambda,\mu) \, \mathrm{d}\lambda \, \mathrm{d}\mu \right\}. \tag{5.44}$$

In the literature, the work by Berry [37] is relevant here. Berry presents radiation efficiencies of an unperforated panel having water on one side and vacuum on the other. In the following section, the same problem is solved using the method proposed here and thus serves as validation of the new model. Subsequently, the perforated panel case is solved using the proposed model.

5.7 Sound radiation from a fluid-loaded unperforated panel with one side vacuum

In this section, the sound radiation from an unperforated panel set in an unperforated baffle under harmonic point force excitation is discussed when the panel is coupled to a dense fluid in the half-space $z > 0$. The other half-space ($z < 0$) is vacuum. The panel is simply supported on the baffle. This case was studied by Berry [37]. The expressions for the panel velocity and the radiated pressure are first derived from the previous perforated panel case by neglecting the fluid loading on one side of the panel. The unperforated panel and baffle case is then realized by equating $\sigma_p = \sigma_b = 0$ and $\zeta_I = 1$.

If the half-space $z < 0$ is vacuum, then $P^-(\lambda, \mu, z) = 0$. Therefore the pressure difference (Eq. (5.12)) is modified to

$$\Delta P(\lambda, \mu) = -Z_a(\lambda, \mu)\, V_a(\lambda, \mu, z = 0). \tag{5.45}$$

The LAFP velocity expression (Eq. (5.13)) modifies to

$$\left[1 + \frac{\sigma_b}{Z_{0b}}\, Z_a(\lambda, \mu)\right] V_a(\lambda, \mu, z = 0) = \zeta_I V_p(\lambda, \mu) - \frac{ab}{4\pi^2}\left[\frac{\sigma_p}{Z_{0p}} - \frac{\sigma_b}{Z_{0b}}\right]$$
$$\times \int_{-\infty}^{\infty}\int_{-\infty}^{\infty} Z_a(\lambda', \mu')\, V_a(\lambda', \mu', z = 0)\, \mathrm{sinc}\left[\frac{(\lambda - \lambda')a}{2}\right] \mathrm{sinc}\left[\frac{(\mu - \mu')b}{2}\right] \mathrm{d}\lambda'\, \mathrm{d}\mu'. \tag{5.46}$$

And Eq. (5.22) takes the form

$$V_a(\lambda, \mu, z = 0) = \frac{1}{i\omega Z_a(\lambda, \mu)} \left\{ \frac{i\omega \tilde{F}}{2\pi}\, e^{i\lambda x_0 + i\mu y_0} + \sum_{r,m,n} \left[D^*(1 - i\eta) \right.\right.$$
$$\left.\left. \times \left\{ \left(\frac{m\pi}{a}\right)^2 + \left(\frac{n\pi}{b}\right)^2 \right\}^2 - m_p\omega^2 \right] B_r U_{mnr} \Phi_{mn}(\lambda, \mu) \right\}. \tag{5.47}$$

Following a similar procedure as in section 5.5, the panel velocity amplitude can be obtained. Then the modal coefficients in a matrix form are

$$\{B_r\} = [Z_{s,r}]^{-1} \{F_s\},$$

where

$$[Z_{s,r}] = \frac{1}{i\omega}[U_{pq,s}]^T\left[\bar{\Theta}_{mn,pq}\right]^T\left[\bar{U}_{mn,r}\right] + \frac{ab}{4i\omega}\frac{\sigma_p}{Z_{0p}}[U_{mn,s}]^T\left[\bar{U}_{mn,r}\right] - \frac{ab}{4}\zeta_I[U_{mn,s}]^T[U_{mn,r}] \tag{5.48}$$

and

$$\{F_s\} = -\frac{\tilde{F}}{2\pi}[U_{pq,s}]^T\{\gamma_{pq}(x_0,y_0)\} - \tilde{F}\frac{\sigma_p}{Z_{0p}}[U_{pq,s}]^T\{\phi_{pq}(x_0,y_0)\}. \tag{5.49}$$

For an unperforated panel set in an unperforated baffle, the panel modal amplitude is obtained from the above relation by equating $\sigma_p = \sigma_b = 0$, $\zeta_I = 1$ and $U_{mnr} = \delta_{mnr}$, where δ is the kronecker delta. The radiated power, the spatially averaged squared velocity and the radiation efficiency are then evaluated using Eqs. (5.40), (5.43) and (5.44), respectively.

5.7.1 Numerical validation

Panel dimensions	$a = 0.455$ m, $b = 0.375$ m and $h = 0.001$ m
Panel material properties (steel)	$E = 210$ GPa, $\rho_p = 7850$ kg/m^3, $\nu = 0.3$ and $\eta = 0.01$
Properties of the acoustic medium (water)	$\rho_0 = 998.2$ kg/m^3, $c = 1481$ m/s and $\eta_0 = 8.9 \times 10^{-4}$ Ns/m^2

Table 5.1 The panel dimensions and material properties considered for the validation case.

Consider an unperforated panel immersed in water. The panel dimensions and the material properties are given in Table 5.1 along with the properties of water. In the numerical implementation, the summations over m and n indices are truncated at $m = 20$ and $n = 20$, which essentially includes all the *in vacuo* modes below 5000 Hz. Fig. 5.2 shows the spectra of radiated power and mean quadratic panel velocity for a unit amplitude force when the excitation is at (0,0), the center of the panel. The mean quadratic panel velocity as defined in [37] is equal to one half of the spatially averaged squared panel velocity (Eq. (5.43)), i.e., $\frac{<|v_p|^2>}{2}$. Fig. 5.3 depicts the radiation efficiency of the water-loaded panel when the forcing is at the center. Due to symmetry of the forcing, only the odd-odd modes are excited. This is manifested in the prolonged piston like radiation characteristics of mode (1,1) at lower frequencies (the adjoining (2,1), (1,2), (2,2) modes are absent in the response spectra).

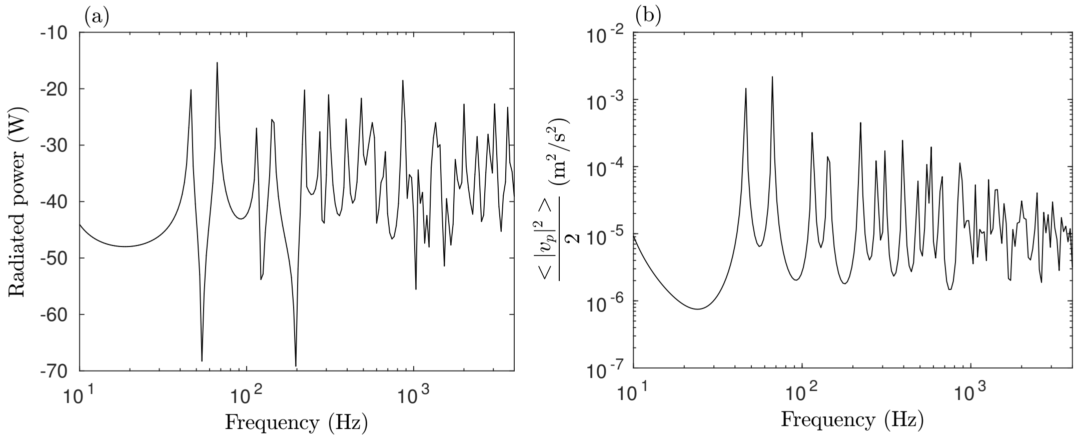

Fig. 5.2 (a) Radiated power and (b) mean quadratic panel velocity ($\frac{<|v_p|^2>}{2}$) spectrum of a water-loaded panel (one half-space vacuum) with excitation at the center.

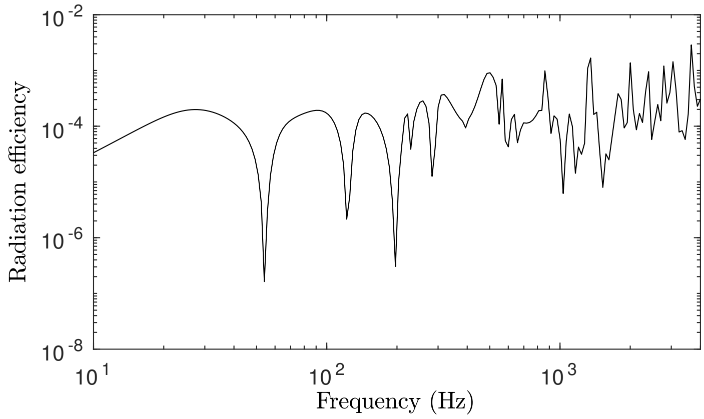

Fig. 5.3 Radiation efficiency of a water-loaded panel (one half-space vacuum) with excitation at the center.

Fig. 5.4 depicts the radiated power and the mean quadratic velocity of the same panel when it is being forced at (0.1,0.1), an off-center location. The corresponding radiation efficiency plot is given in Fig. 5.5. The additional peaks in the mean quadratic panel velocity plot denote the resonances of modes which are naturally absent in Fig. 5.2. The results are in good agreement with those of Berry [37] (see Figs. 6 and 8 in [37]).

The natural frequencies of the water-loaded panel can now be determined from the peaks of the mean quadratic panel velocity plots. The first six natural frequencies are listed in Table 5.2 along with the respective *in vacuo* values. The resonance points are taken from Fig. 5.4b, corresponding to the off-center excitation case, as it includes all mode types of the rectangular panel. An approximate expression for the natural

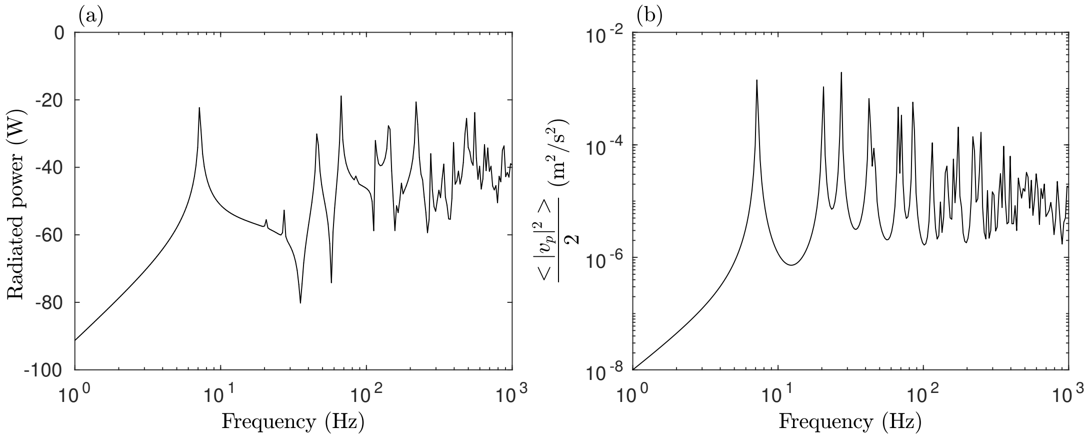

Fig. 5.4 (a) Radiated power and (b) mean quadratic panel velocity ($\frac{<|v_p|^2>}{2}$) spectrum of a water-loaded panel (one half-space vacuum) with excitation at (0.1,0.1).

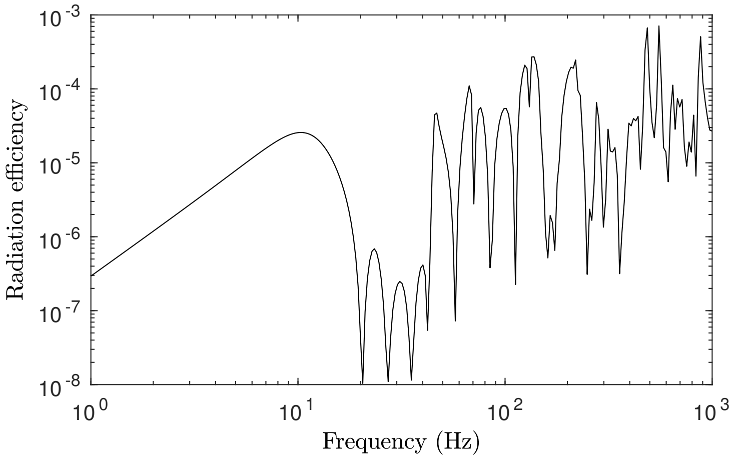

Fig. 5.5 Radiation efficiency of a water-loaded panel (one half-space vacuum) with excitation at (0.1,0.1).

frequency of a fluid-loaded panel, ω'_{mn}, is given by Fahy [7]

$$\omega'_{mn} = \omega_{mn} \left(1 + \frac{\rho_0}{m_p k_{mn}}\right)^{-1/2}, \tag{5.50}$$

where ω_{mn} is the *in vacuo* natural frequency and $k_{mn} = \sqrt{\left(\frac{m\pi}{a}\right)^2 + \left(\frac{n\pi}{b}\right)^2}$ is the primary modal wavenumber component. This expression, however, is applicable only when the plate bending wavenumber is much greater than the acoustic wavenumber, or rather when the fluid loading on the panel is reactive. Table 5.2 also lists the natural frequencies using the above expression. It is verified that the modeshapes remain unchanged for the *in vacuo* and the water-loaded cases, as pointed out by Fahy [7].

Mode order	In vacuo (Hz)	Water-loaded (Hz)	
		Fig. 5.4b	Eq. (5.50)
(1,1)	29.36	7.14	8.23
(2,1)	64.99	20.55	21.82
(1,2)	81.81	27.27	28.89
(2,2)	117.44	42.24	44.85
(3,1)	124.37	45.63	48.09
(1,3)	169.23	67.11	69.80

Table 5.2 Natural frequencies of the unperforated panel under *in vacuo* and water-loaded (with one half-space vacuum) conditions.

Having validated the proposed method against the results of Berry, it can now be used to solve the problem of sound radiation from a perforated panel.

5.8 Sound radiation from a fluid-loaded perforated panel

Here, there is water on both sides of the panel-baffle system. The perforated panel response is given by Eq. (5.35). The resulting LAFP velocity and radiated pressure fields are then obtained from Eqs. (5.13) and (5.39), respectively. We may now find the radiated power (Eq. (5.40)), the spatially averaged squared panel velocity (Eq. (5.43)) and the radiation efficiency (Eq. (5.44)) using the expressions derived in section 5.6.

Panel dimensions	$a = 0.455$ m, $b = 0.546$ m and $h = 0.003$ m
Panel material properties (aluminum)	$E = 70$ GPa, $\rho_p = 2700$ kg/m^3, $\nu = 0.33$ and $\eta = 0.1$
Properties of water	$\rho_0 = 998.2$ kg/m^3, $c = 1481$ m/s and $\eta_0 = 8.9 \times 10^{-4}$ Ns/m^2
Properties of air	$\rho_0 = 1.204$ kg/m^3, $c = 343$ m/s and $\eta_0 = 1.8 \times 10^{-5}$ Ns/m^2

Table 5.3 The perforated panel dimensions and material properties.

The panel dimensions and material properties used are given in Table 5.3. The panel is excited at its center. Fig. 5.6 depicts the radiation efficiency for different perforation ratios of the panel. Here, the total number of holes $N_0 = 750$ is kept constant for all the curves and the perforation ratio is varied by changing the hole radius. All the *in vacuo* modes below 10,000 Hz are considered for the numerical prediction. An unperforated case is also shown for comparison. Since the excitation is at the center of the panel, the initial monopole behavior (20 dB/decade) in the radiation efficiency plot at lower frequencies is prolonged (the (1,2), (2,1) and (2,2) modes are not excited). As the perforation ratio increases the perforate impedance Z_{0p}/σ_p decreases. Consequently, the radiated power and radiation efficiency reduce with increase in σ_p. More fluid slips away through the perforations.

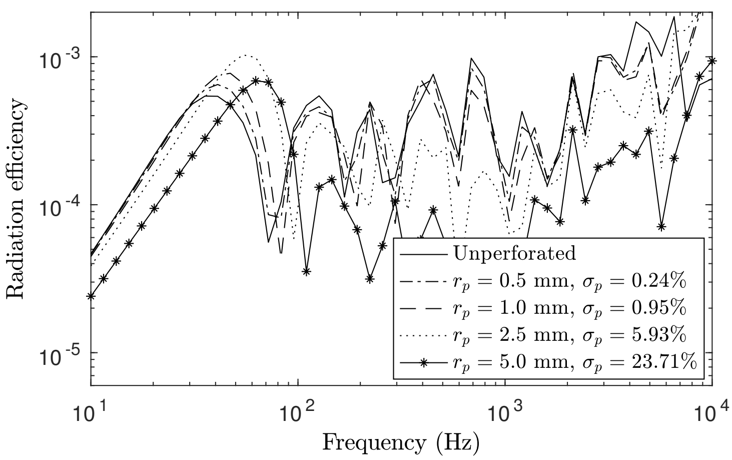

Fig. 5.6 Radiation efficiency of a water-loaded (in both the half-spaces) perforated panel for various perforation ratios. The excitation is at the center of the panel. In all the cases, the total number of holes is assumed to be a constant ($N_0 = 750$).

In order to find the natural frequencies of the perforated panel immersed in water, the panel is excited at an off-center location ($x = 0.1$ m and $y = 0.1$ m) by a unit amplitude harmonic force. The panel material and dimensions are the same as above. However, to locate the resonances more precisely, a small value is chosen for the damping loss factor ($\eta = 0.01$). The mean quadratic velocity ($\frac{<|v_p|^2>}{2}$) is obtained using Eq. (5.43) for all the panels and is plotted in Fig. 5.7. The peaks in the mean quadratic velocity spectrum correspond to the panel natural frequencies. For each of the cases shown in Fig. 5.7, the first four natural frequencies and the respective mode orders are listed in Table 5.4 along with the corresponding *in vacuo* values. Note, that as the excitation is at an off-center location, the even-even, even-odd and odd-even modes are also participating in the response spectrum.

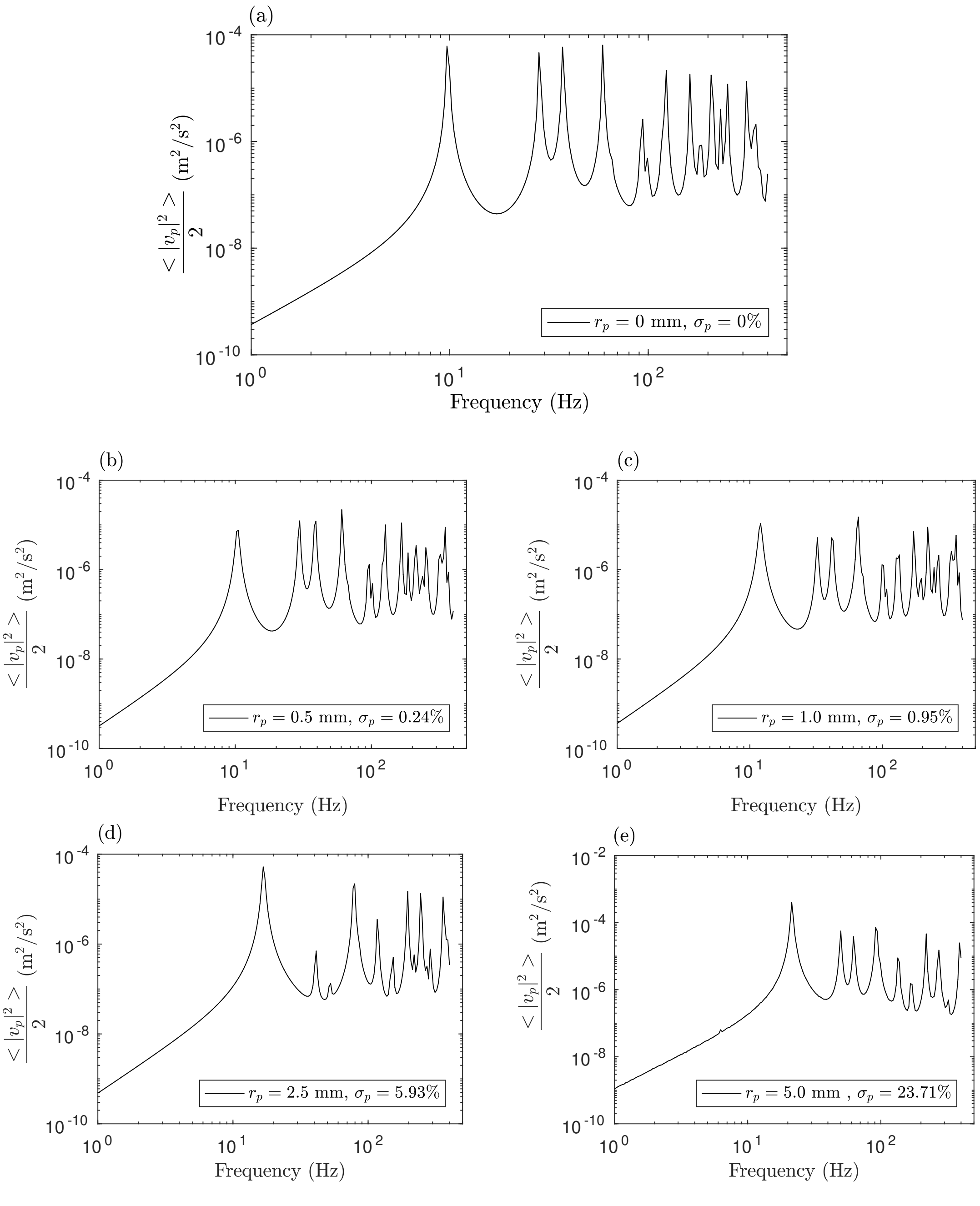

Fig. 5.7 Mean quadratic velocity ($\frac{<|v_p|^2>}{2}$) for various perforated panels under water-loading condition (in both the half-spaces). Total number of holes in each of the panels is $N_0 = 750$. The panels are being excited at (0.1,0.1). The peaks in the mean quadratic velocity plots correspond to the resonances.

For the *in vacuo* condition, we know that as the perforation ratio increases, both the stiffness and mass of the panel reduce. But the reduction in stiffness is larger such

Mode order	$\sigma_p = 0\%$ (Hz)		$\sigma_p = 0.24\%$ (Hz)		$\sigma_p = 0.95\%$ (Hz)		$\sigma_p = 5.93\%$ (Hz)		$\sigma_p = 23.71\%$ (Hz)	
	In vacuo	Water-loaded (Fig. 5.7(a))	In vacuo	Water-loaded (Fig. 5.7(b))	In vacuo	Water-loaded (Fig. 5.7(c))	In vacuo	Water-loaded (Fig. 5.7(d))	In vacuo	Water-loaded (Fig. 5.7(e))
(1,1)	60.06	9.69	59.95	10.52	59.65	12.06	57.85	16.74	53.26	21.42
(1,2)	133.90	28.15	133.66	29.74	132.99	32.28	128.98	41.29	118.75	50.01
(2,1)	166.39	37.01	166.09	39.10	165.26	41.29	160.28	52.82	147.56	62.25
(2,2)	240.23	58.93	239.80	60.57	238.60	65.75	231.40	79.62	213.05	91.30

Table 5.4 Natural frequencies of the panel under *in vacuo* and water-loaded (both the half-spaces) conditions for different perforation ratios.

that a higher perforation ratio results in a lower natural frequency (see section 3.5.1). For the unperforated case, once the fluid loading is included, all the natural frequencies get lowered [36]. For the perforated fluid-loaded case, as the perforation ratio increases, the effective solid area of the panel decreases and hence the total inertial loading of the adjoining acoustic medium over the perforated panel reduces. And for water, the reduction in the total inertial loading plus the panel mass is more than the reduction in panel stiffness. Thus, we see an increase in the natural frequency of a given mode as the perforation ratio increases (see Table 5.4). The perforated panel radiation efficiencies when the excitation is at (0.1,0.1) are shown in Fig. 5.8. In contrast to Fig. 5.6 for the center-excited panel, here, the dips corresponding to even-even, even-odd and odd-even resonances are evident in the radiation efficiency spectrum. From a purely physics point of view, as the panel area is reduced, the radiation efficiency should decrease regardless of the acoustic medium. This is not clearly evident in Fig. 5.8 because of the closely packed resonances.

Fig. 5.9 depicts the radiation efficiencies of the same perforated panels when it is surrounded by air. For all the cases, the forcing is applied at the center of the panel. The corner mode, edge mode and the high frequency regions are clearly seen in this case. At low frequencies (in comparison to the critical frequency), the fluid loading being dominantly inertial [33], the reactance offered by air is small as compared to that offered by water. As a result, the radiation efficiency when the panel is immersed in air is higher than that when it is immersed in water (see Fig. 5.6). This just means that for the same forcing, the panel response is lower for the water case. The results of Fig. 5.9 match well with that predicted using a one-way coupled formulation presented in chapter 3 (see Fig. 3.10). For air, the light-loading conditions shift the natural frequencies very little from their *in vacuo* values. Therefore a one-way coupled formulation is sufficient if the acoustic medium is light.

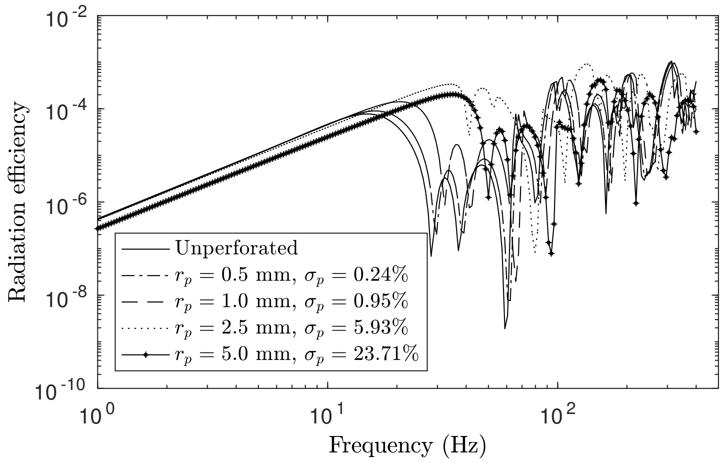

Fig. 5.8 Radiation efficiencies for water-loaded (in both the half-spaces) perforated panels of different perforation ratios when the excitation is at an off-center location (0.1,0.1). Total number of holes in each of the panels is $N_0 = 750$.

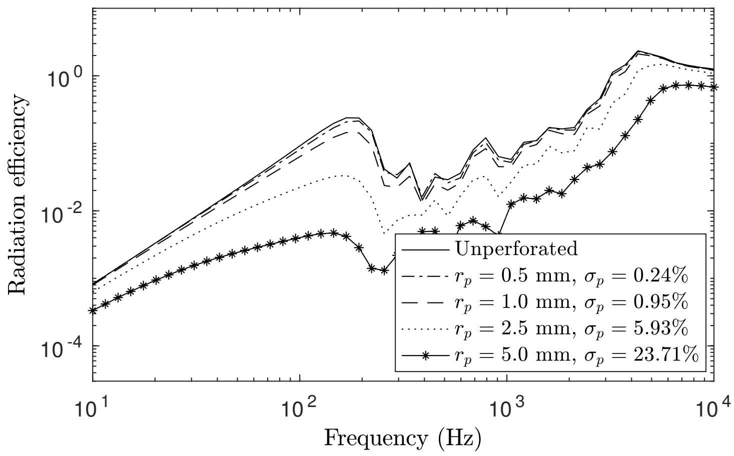

Fig. 5.9 Radiation efficiency of a perforated panel immersed in air (in both the half-spaces) for various perforation ratios. The excitation is at the center of the panel. In all the cases, the total number of holes is assumed to be a constant ($N_0 = 750$).

5.9 Conclusions

A fully coupled formulation in the 2-D wavenumber domain is used to model the sound radiation from a finite flexible perforated panel set in an infinite rigid unperforated baffle. The panel is assumed to be simply supported on the baffle and is coupled to the acoustic medium above and below. A locally averaged fluid particle velocity is derived, which takes into account the panel vibrations and the flow through perforations. The discontinuity in the perforate impedance at the panel-baffle boundary causes a coupling of different wavenumbers in the locally averaged fluid particle velocity spectrum. A single coupled equation is derived to obtain the perforated panel response. This is done in such a way that there are no square root singularities present in the self and cross modal coupling coefficients. This enables us to evaluate the coupling coefficients with ease.

A validation of proposed formulation is done by comparing the results with those of Berry [37] for the case of an unperforated panel set in an unperforated baffle. Here, only one half-space is filled with water and the other half-space is vacuum. The radiated power and panel mean quadratic velocity spectra for the center and off-center excitations show a good match. The mean quadratic velocity for the off-center excitation is then used to find the natural frequencies of the water-loaded unperforated panel. The predicted natural frequencies match very well with those reported in the literature [37].

The radiation efficiencies of the water-loaded (both half-spaces) perforated panels are computed for different perforation ratios for both the center and the off-center excitations. As the perforation ratio increases, the perforate impedance decreases and hence the radiated power and radiation efficiency decrease (more clearly seen in Fig. 5.6). The same observation is made when the acoustic medium is air. However, the response of the panel is lower when it is immersed in water as opposed to air. This causes a lower radiation efficiency for the water case.

With regard to coupled natural frequencies, the water case differs from the *in vacuo* case. For the *in vacuo* case, as the perforation ratio increases, both the stiffness and the panel mass reduce. However, the reduction in stiffness is more significant causing a net reduction in the natural frequencies. In contrast, for the water case, the net reduction in inertia dominates over the stiffness reduction. Thus, the natural frequencies go up.

It is also found that for the case of air, the radiation efficiencies of perforated panels match very well with those using a one-way coupled formulation. Thus, for a light acoustic medium, the one-way coupled formulation is adequate to predict the radiation efficiency.

After the two-way coupled analysis on the sound radiation from fluid-loaded perforated panels, it is natural to extend the model to study the effect of fluid loading on the sound transmission through perforated panels. This is the subject matter of the following chapter.

Chapter 6

Sound transmission through a perforated panel: Two-way coupling

6.1 Introduction

In this chapter, the two-way coupled formulation is extended to analyze the transmission of sound through a finite flexible perforated panel set in an unperforated baffle. A relation between the transmitted pressure and the LAFP velocity is derived in the next section.

6.2 The incident and the transmitted pressure fields at the panel surface

Consider a flexible perforated panel of finite extent lying in the $z = 0$ plane, in the region $-a/2 \leq x \leq a/2$ and $-b/2 \leq y \leq b/2$. The panel is placed in a rigid baffle of infinite extent in the $z = 0$ plane, as shown in Fig. 6.1. A harmonic plane wave of frequency ω, wavenumber k and amplitude $\tilde{P}_i$ is incident upon the panel-baffle surface from the $z > 0$ region, from the direction θ and ϕ (θ, polar angle and ϕ, azimuthal angle). This creates flexural vibrations in the perforated panel which transmits the sound to the $z < 0$ region. Let $p_1(x, y, z, t)$ and $p_2(x, y, z, t)$ be the resulting pressure fields in the transmitted ($z < 0$) and the incident ($z > 0$) regions, respectively (see Fig. 6.1). The transmitted pressure field $p_1(x, y, z, t)$ is due to the vibrating perforated panel and the direct transmission of sound through the holes in the panel. Whereas on

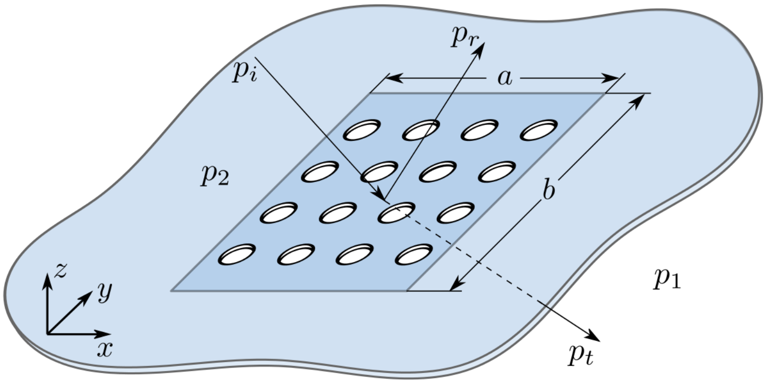

Fig. 6.1 Transmission of sound (plane wave) through a perforated panel set in a baffle.

the incident side, the total pressure field $p_2(x, y, z, t)$ comprises the incident and the reflected pressure terms. Let the incident pressure field $p_i(x, y, z, t)$ be

$$p_i(x, y, z, t) = \tilde{P}_i \, \mathrm{e}^{\mathrm{i}k_x x + \mathrm{i}k_y y - \mathrm{i}k_z z} \, \mathrm{e}^{-\mathrm{i}\omega t}, \tag{6.1}$$

where $k_x = k \, \sin\theta \, \cos\phi$, $k_y = k \, \sin\theta \, \sin\phi$ and $k_z = k \, \cos\theta$. The total pressure field on the incident side is given by

$$p_2(x, y, z, t) = \tilde{P}_i \, \mathrm{e}^{\mathrm{i}k_x x + \mathrm{i}k_y - \mathrm{i}k_z z} \, \mathrm{e}^{-\mathrm{i}\omega t} + p_r(x, y, z) \, \mathrm{e}^{-\mathrm{i}\omega t}, \tag{6.2}$$

where $p_r(x, y, z)$ is the reflected pressure field. In the following derivations the dependence on time $\mathrm{e}^{-\mathrm{i}\omega t}$ is suppressed.

The transmitted pressure $p_1(x, y, z)$, i.e., $p^-(x, y, z)$ in the $z < 0$ region accounts for both the radiation of sound by the panel vibration and the direct transmission of sound through the perforations. The $p^-(x, y, z)$ satisfies the 3-D Helmholtz equation

$$\left(\nabla^2 + k^2\right) p^-(x, y, z) = 0. \tag{6.3}$$

On taking a *double Fourier transform* of the above equation in the x and y directions we get

$$\left[\frac{\mathrm{d}^2}{\mathrm{d}z^2} + \left(k^2 - \lambda^2 - \mu^2\right)\right] P^-(\lambda, \mu, z) = 0, \tag{6.4}$$

where $P^{-}(\lambda, \mu, z)$ represents the double Fourier transform of $p^{-}(x, y, z)$ and is defined as

$$P^{-}(\lambda, \mu, z) = \frac{1}{2\pi} \int_{-\infty}^{\infty} \int_{-\infty}^{\infty} p^{-}(x, y, z)\, \mathrm{e}^{\mathrm{i}\lambda x + \mathrm{i}\mu y}\, \mathrm{d}x\, \mathrm{d}y. \tag{6.5}$$

The general solution to Eq. (6.4) is given by

$$P^{-}(\lambda, \mu, z) = A(\lambda, \mu)\, \mathrm{e}^{\mathrm{i}\sqrt{k^2-\lambda^2-\mu^2}z} + B(\lambda, \mu)\, \mathrm{e}^{-\mathrm{i}\sqrt{k^2-\lambda^2-\mu^2}z}. \tag{6.6}$$

For a traveling wave in the $-z$ direction, by causality, we must have $A(\lambda, \mu) = 0$, leading to

$$P^{-}(\lambda, \mu, z) = B(\lambda, \mu)\, \mathrm{e}^{-\mathrm{i}\sqrt{k^2-\lambda^2-\mu^2}z}. \tag{6.7}$$

And the evanescent wave in the $-z$ direction is

$$P^{-}(\lambda, \mu, z) = B(\lambda, \mu)\, \mathrm{e}^{\sqrt{\lambda^2+\mu^2-k^2}z}.$$

$B(\lambda, \mu)$ can be found by invoking the double Fourier transform of the Euler boundary condition at the solid-fluid interface (at $z = 0$) as

$$\frac{\partial}{\partial z} P^{-}(\lambda, \mu, z = 0) = \mathrm{i}\rho_0 ck V_a(\lambda, \mu, z = 0), \tag{6.8}$$

where ρ_0 is the fluid density and $V_a(\lambda, \mu, z = 0)$ is the double Fourier transform of the fluid particle velocity at the boundary $v_a(x, y, z = 0)$ and is given by

$$V_a(\lambda, \mu, z = 0) = \frac{1}{2\pi} \int_{-\infty}^{\infty} \int_{-\infty}^{\infty} v_a(x, y, z = 0)\, \mathrm{e}^{\mathrm{i}\lambda x + \mathrm{i}\mu y}\, \mathrm{d}x\, \mathrm{d}y. \tag{6.9}$$

Using Eqs. (6.7) and (6.8) we get

$$B(\lambda, \mu) = P^{-}(\lambda, \mu, z = 0) = -Z_a(\lambda, \mu) V_a(\lambda, \mu, z = 0), \tag{6.10}$$

where $Z_a(\lambda, \mu)$ is the complex acoustic impedance given by

$$Z_a(\lambda, \mu) = \frac{\rho_0 ck}{\sqrt{k^2 - \lambda^2 - \mu^2}}. \tag{6.11}$$

Therefore

$$P^{-}(\lambda, \mu, z) = -Z_a(\lambda, \mu) V_a(\lambda, \mu, z = 0) \mathrm{e}^{-\mathrm{i}\sqrt{k^2-\lambda^2-\mu^2}z}. \tag{6.12}$$

Thus, if the LAFP velocity $V_a(\lambda, \mu, z = 0)$ is known, the radiated pressure can be found. The LAFP velocity was derived in section 4.3.

For the incident side, taking the double Fourier transform of Eq. (6.2) we get

$$P_2\,(\lambda, \mu, z) = \frac{1}{2\pi} \int_{-\infty}^{\infty} \int_{-\infty}^{\infty} \tilde{P}_i \, \mathrm{e}^{\mathrm{i}k_x x + \mathrm{i}k_y y - \mathrm{i}k_z z} \, \mathrm{e}^{\mathrm{i}\lambda x + \mathrm{i}\mu y} \, \mathrm{d}x \, \mathrm{d}y + P_r(\lambda, \mu, z), \tag{6.13}$$

where

$$P_r\,(\lambda, \mu, z) = \frac{1}{2\pi} \int_{-\infty}^{\infty} \int_{-\infty}^{\infty} p_r\,(x, y, z) \, \mathrm{e}^{\mathrm{i}\lambda x + \mathrm{i}\mu y} \, \mathrm{d}x \, \mathrm{d}y. \tag{6.14}$$

Using the identity

$$\int_{-\infty}^{\infty} \int_{-\infty}^{\infty} \mathrm{e}^{\mathrm{i}(\lambda + k_x)x + \mathrm{i}(\mu + k_y)y} \, \mathrm{d}x \, \mathrm{d}y = 4\pi^2 \delta(\lambda + k_x) \, \delta(\mu + k_y), \tag{6.15}$$

we get

$$P_2\,(\lambda, \mu, z) = 2\pi \tilde{P}_i \, \delta(\lambda + k_x) \, \delta(\mu + k_y) \, \mathrm{e}^{-\mathrm{i}k_z z} + P_r(\lambda, \mu, z). \tag{6.16}$$

The pressure field $p_2(x, y, z)$ should satisfy the 3-D Helmholtz equation

$$\left(\nabla^2 + k^2\right) p_2\,(x, y, z) = 0. \tag{6.17}$$

Taking the double Fourier transform

$$\left[\frac{\mathrm{d}^2}{\mathrm{d}z^2} + \left(k^2 - \lambda^2 - \mu^2\right)\right] P_2\,(\lambda, \mu, z) = 0. \tag{6.18}$$

The general solution to Eq. (6.18) is

$$P_2\,(\lambda, \mu, z) = C(\lambda, \mu) \, \mathrm{e}^{\mathrm{i}\sqrt{k^2 - \lambda^2 - \mu^2} z} + D(\lambda, \mu) \, \mathrm{e}^{-\mathrm{i}\sqrt{k^2 - \lambda^2 - \mu^2} z}. \tag{6.19}$$

Comparing Eqs. (6.16) and (6.19) and knowing that $P_r(\lambda, \mu)$ consists only of the forward traveling waves in the z direction

$$P_2\,(\lambda, \mu, z) = 2\pi \tilde{P}_i \, \delta(\lambda + k_x) \, \delta(\mu + k_y) \, \mathrm{e}^{-\mathrm{i}k_z z} + C(\lambda, \mu) \, \mathrm{e}^{\mathrm{i}\sqrt{k^2 - \lambda^2 - \mu^2} z}. \tag{6.20}$$

The pressure $p_2(x, y, z)$ is related to the fluid particle velocity at the solid-fluid interface of the incident region $(v_a(x, y, z = 0))$ through the Euler boundary condition. Taking the double Fourier transform of the boundary condition

$$\frac{\partial}{\partial z} P_2\left(\lambda, \mu, z=0\right) = \mathrm{i}\rho_0 ck V_a\left(\lambda, \mu, z=0\right). \tag{6.21}$$

Substituting for $P_2(\lambda, \mu, z)$ from Eq. (6.20)

$$-\mathrm{i}k_z 2\pi \tilde{P}_i\, \delta(\lambda + k_x)\, \delta(\mu + k_y) + \mathrm{i}\sqrt{k^2 - \lambda^2 - \mu^2}\, C(\lambda, \mu) = \mathrm{i}\rho_0 ck V_a\left(\lambda, \mu, z=0\right).$$

Or

$$C(\lambda, \mu) = \frac{\rho_0 ck}{\sqrt{k^2 - \lambda^2 - \mu^2}} V_a\left(\lambda, \mu, z=0\right) + \frac{k_z}{\sqrt{k^2 - \lambda^2 - \mu^2}} 2\pi \tilde{P}_i\, \delta(\lambda + k_x)\, \delta(\mu + k_y).$$

As said before, $C(\lambda, \mu)$ is related to the forward traveling wave in the incident region. For a forward traveling wave (related to the reflected pressure field component in $P_2(\lambda, \mu, z)$), when $\lambda = -k_x$ and $\mu = -k_y$, $\sqrt{k^2 - \lambda^2 - \mu^2} = k_z$. Using Eq. (6.11)

$$C(\lambda, \mu) = Z_a(\lambda, \mu) V_a\left(\lambda, \mu, z=0\right) + 2\pi \tilde{P}_i\, \delta(\lambda + k_x)\, \delta(\mu + k_y). \tag{6.22}$$

Therefore, using Eq. (6.22), the double Fourier transform of the total pressure on the incident region (Eq. (6.20)) is given by

$$P_2\left(\lambda, \mu, z\right) = Z_a(\lambda, \mu) V_a\left(\lambda, \mu, z=0\right)\, \mathrm{e}^{\mathrm{i}\sqrt{k^2-\lambda^2-\mu^2} z} + 4\pi \tilde{P}_i\, \delta(\lambda + k_x)\, \delta(\mu + k_y)\, \cos k_z z. \tag{6.23}$$

And at $z = 0$

$$P_2\left(\lambda, \mu, z=0\right) = \underbrace{Z_a(\lambda, \mu) V_a\left(\lambda, \mu, z=0\right)}_{\text{radiated pressure field}} + \underbrace{4\pi \tilde{P}_i\, \delta(\lambda + k_x)\, \delta(\mu + k_y)}_{\text{blocked pressure field}}. \tag{6.24}$$

Thus, the total pressure field on the incident side is the sum of the radiated and the blocked pressure fields and can be found if $V_a(\lambda, \mu, z=0)$ is known.

Using Eqs. (6.12) and (6.24), the double Fourier transform (over $x - y$ domain) of the pressure difference across the perforated panel is

$$\begin{aligned} \Delta P(\lambda, \mu) &= P^-(\lambda, \mu, z=0) - P_2(\lambda, \mu, z=0) \\ &= 2P^-(\lambda, \mu, z=0) - 4\pi \tilde{P}_i\, \delta(\lambda + k_x)\, \delta(\mu + k_y). \end{aligned} \tag{6.25}$$

In the next section, the double Fourier transform of the LAFP velocity over a discontinuous perforate impedance surface (the panel-baffle surface) is derived.

6.3 Locally averaged fluid particle (LAFP) velocity and its Fourier transform

The LAFP velocity was derived in chapter 4 (section 4.3). The final result is presented here.

$$
\begin{aligned}
V_a(\lambda,\mu,z=0) \;&=\; \zeta_I V_p(\lambda,\mu) + \frac{2\sigma_b}{Z_{0b}}\,P^-(\lambda,\mu,z=0) - 2\pi\tilde{P}_i\,\frac{2\sigma_b}{Z_{0b}}\,\delta(\lambda+k_x)\,\delta(\mu+k_y) \\
&+ \left[\frac{2\sigma_p}{Z_{0p}} - \frac{2\sigma_b}{Z_{0b}}\right]\frac{ab}{4\pi^2}\int_{-\infty}^{\infty}\int_{-\infty}^{\infty} P^-\left(\lambda',\mu',z=0\right)\,\mathrm{sinc}\left[\frac{(\lambda-\lambda')a}{2}\right]\,\mathrm{sinc}\left[\frac{(\mu-\mu')b}{2}\right]\mathrm{d}\lambda'\,\mathrm{d}\mu' \\
&- \left[\frac{2\sigma_p}{Z_{0p}} - \frac{2\sigma_b}{Z_{0b}}\right]\frac{\tilde{P}_i ab}{2\pi}\,\mathrm{sinc}\left[\frac{(\lambda+k_x)a}{2}\right]\,\mathrm{sinc}\left[\frac{(\mu+k_y)b}{2}\right], \qquad (6.26)
\end{aligned}
$$

The LAFP velocity thus depends on the panel velocity. However, the panel responds to pressures that are functions of the LAFP velocity. Thus, it becomes necessary to solve a set of coupled equations to obtain the panel response. The derivation of the panel velocity is presented in the next section.

6.4 The vibration response of the perforated panel

6.4.1 Modified natural frequencies and modeshapes

As in the cases above that account for the modifications in the natural frequencies and modeshapes of the panel due to perforations, here also we express the perforated panel velocity as a modal sum given by

$$
v_p(x,y) = \sum_{r=1}^{\infty} B_r\psi_r(x,y) = \sum_{r=1}^{\infty} B_r \sum_{m=1}^{\infty}\sum_{n=1}^{\infty} U_{mnr}\phi_{mn}(x,y), \qquad (6.27)
$$

where B_r is the modal coefficient. Taking the double Fourier transform of $v_p(x,y)$

$$
V_p(\lambda,\mu) = \sum_{r=1}^{\infty} B_r \sum_{m=1}^{\infty}\sum_{n=1}^{\infty} U_{mnr}\Phi_{mn}(\lambda,\mu), \qquad (6.28)
$$

where

$$\Phi_{mn}(\lambda,\mu) = \frac{1}{2\pi}\int\limits_{-b/2}^{b/2}\int\limits_{-a/2}^{a/2}\phi_{mn}(x,y)\,\mathrm{e}^{\mathrm{i}\lambda x+\mathrm{i}\mu y}\,\mathrm{d}x\,\mathrm{d}y.$$

Substituting for $\phi_{mn}(x,y)$ from Eq. (2.20) into the above equation

$$\begin{aligned}\Phi_{mn}(\lambda,\mu) = -\frac{ab}{8\pi}&\left\{\mathrm{e}^{\mathrm{i}m\pi/2}\operatorname{sinc}\left[\frac{(\lambda+m\pi/a)\,a}{2}\right] - \mathrm{e}^{-\mathrm{i}m\pi/2}\operatorname{sinc}\left[\frac{(\lambda-m\pi/a)\,a}{2}\right]\right\}\\ &\times\left\{\mathrm{e}^{\mathrm{i}n\pi/2}\operatorname{sinc}\left[\frac{(\mu+n\pi/b)\,b}{2}\right] - \mathrm{e}^{-\mathrm{i}n\pi/2}\operatorname{sinc}\left[\frac{(\mu-n\pi/b)\,b}{2}\right]\right\}. \quad (6.29)\end{aligned}$$

The detailed derivation of $\Phi_{mn}(\lambda,\mu)$ is given in Appendix D. The new modeshapes will be substituted in the modified panel equation of motion in order to obtain the modal amplitudes. The modified equation of motion of the panel is examined in the following section.

6.4.2 The perforated panel equation of motion

The equation of motion for the perforated panel is given by

$$D^*(1-\mathrm{i}\eta)\nabla^4 v_p(x,y,t) + m_p\,\frac{\partial^2 v_p(x,y,t)}{\partial t^2} = -\mathrm{i}\omega\,\Delta p(x,y,z=0,t), \quad (6.30)$$

where D^* is the effective bending stiffness, m_p is the modified mass per unit area and η is the damping loss factor of the perforated panel. Substituting for $v_p(x,y)$ from Eq. (6.27) into Eq. (6.30) we get

$$\begin{aligned}\sum_{r,m,n}\left[D^*(1-\mathrm{i}\eta)\left\{\left(\frac{m\pi}{a}\right)^2+\left(\frac{n\pi}{b}\right)^2\right\}^2 - m_p\omega^2\right]B_rU_{mnr}\phi_{mn}(x,y)&\\ = -\mathrm{i}\omega\,\Delta p(x,y,z=0).&\end{aligned}$$

Now, taking the double Fourier transform of the above equation

$$\begin{aligned}\sum_{r,m,n}\left[D^*(1-\mathrm{i}\eta)\left\{\left(\frac{m\pi}{a}\right)^2+\left(\frac{n\pi}{b}\right)^2\right\}^2 - m_p\omega^2\right]B_rU_{mnr}\Phi_{mn}(\lambda,\mu)&\\ = -\mathrm{i}\omega\,\Delta P\left(\lambda,\mu\right), \quad (6.31)&\end{aligned}$$

where $\Phi_{mn}(\lambda,\mu)$ and $\Delta P(\lambda,\mu)$ are given by Eqs. (6.29) and (6.25), respectively. While taking the Fourier transform of the left hand side, note that $v_p(x,y)=0$ in the region beyond the panel surface.

Next, substituting $\Delta P(\lambda,\mu)$ from Eq. (6.25) into Eq. (6.31)

$$\sum_{r,m,n}\left[D^*(1-\mathrm{i}\eta)\left\{\left(\frac{m\pi}{a}\right)^2+\left(\frac{n\pi}{b}\right)^2\right\}^2-m_p\omega^2\right]B_rU_{mnr}\Phi_{mn}(\lambda,\mu)$$
$$=-2\mathrm{i}\omega\,P^-(\lambda,\mu,z=0)+4\pi\mathrm{i}\omega\,\tilde{P}_i\,\delta(\lambda+k_x)\,\delta(\mu+k_y). \tag{6.32}$$

The radiated pressure on the right hand side can be obtained from Eq. (6.12) as

$$P^-(\lambda,\mu,z=0)=-Z_a(\lambda,\mu)V_a(\lambda,\mu,z=0).$$

Thus, the perforated panel displacement depends upon both the incident pressure and the radiated pressure fields. However, the radiated pressure $P^-(\lambda,\mu,z=0)$ through $V_a(\lambda,\mu,z=0)$ depends upon the panel displacement, as shown in the expression for the LAFP velocity in Eq. (6.26). Hence, it becomes necessary to solve the two coupled equations (Eqs. (6.26) and (6.32)) to obtain the panel response $V_p(\lambda,\mu)$. In the next section, a single equation is derived by combining Eqs. (6.26) and (6.32) and is solved to obtain the perforated panel velocity response.

6.5 The coupled formulation and its solution

6.5.1 The coupled equation

Substituting $P^-(\lambda,\mu,z=0)=-Z_a(\lambda,\mu)\,V_a(\lambda,\mu,z=0)$ (Eq. (6.12)) into Eq. (6.32) and rearranging

$$V_a(\lambda,\mu,z=0)=-\frac{2\pi}{Z_a(\lambda,\mu)}\,\tilde{P}_i\,\delta(\lambda+k_x)\,\delta(\mu+k_y)$$
$$+\frac{1}{2\mathrm{i}\omega Z_a(\lambda,\mu)}\sum_{r,m,n}\left[D^*(1-\mathrm{i}\eta)\left\{\left(\frac{m\pi}{a}\right)^2+\left(\frac{n\pi}{b}\right)^2\right\}^2-m_p\omega^2\right]B_rU_{mnr}\Phi_{mn}(\lambda,\mu). \tag{6.33}$$

Similarly, by substituting $P^{-}(\lambda, \mu, z=0) = -Z_a(\lambda, \mu)\, V_a(\lambda, \mu, z=0)$ and $V_p(\lambda, \mu)$ (Eq. (6.28)) into Eq. (6.26)

$$\begin{aligned}
\left[1+\frac{2\sigma_b}{Z_{0b}} Z_a(\lambda,\mu)\right] V_a(\lambda,\mu,z=0) \;=\; & \zeta_I \sum_{r,m,n} B_r U_{mnr} \Phi_{mn}(\lambda,\mu) \\
& - 2\pi \tilde{P}_i \,\frac{2\sigma_b}{Z_{0b}}\, \delta(\lambda+k_x)\, \delta(\mu+k_y) \\
& - \left[\frac{2\sigma_p}{Z_{0p}} - \frac{2\sigma_b}{Z_{0b}}\right] \frac{ab}{4\pi^2} \int\limits_{-\infty}^{\infty}\int\limits_{-\infty}^{\infty} Z_a(\lambda',\mu') V_a(\lambda',\mu',z=0) \\
& \times \operatorname{sinc}\left[\frac{(\lambda-\lambda')a}{2}\right] \operatorname{sinc}\left[\frac{(\mu-\mu')b}{2}\right] \mathrm{d}\lambda'\, \mathrm{d}\mu' \\
& - \left[\frac{2\sigma_p}{Z_{0p}} - \frac{2\sigma_b}{Z_{0b}}\right] \frac{\tilde{P}_i ab}{2\pi} \operatorname{sinc}\left[\frac{(\lambda+k_x)a}{2}\right] \operatorname{sinc}\left[\frac{(\mu+k_y)b}{2}\right]. \qquad (6.34)
\end{aligned}$$

Next, using Eq. (6.33) for $V_a(\lambda, \mu)$ in the above equation

$$\begin{aligned}
& \left[1+\frac{2\sigma_b}{Z_{0b}} Z_a(\lambda,\mu)\right] \left[\frac{1}{2\mathrm{i}\omega Z_a(\lambda,\mu)} \sum_{r,m,n} B_r \bar{U}_{mnr} \Phi_{mn}(\lambda,\mu) - \frac{2\pi \tilde{P}_i}{Z_a(\lambda,\mu)} \delta(\lambda+k_x)\, \delta(\mu+k_y)\right] \\
& = \zeta_I \sum_{r,m,n} B_r U_{mnr} \Phi_{mn}(\lambda,\mu) - \frac{2\sigma_b}{Z_{0b}}\, 2\pi \tilde{P}_i\, \delta(\lambda+k_x)\, \delta(\mu+k_y) \\
& - \left[\frac{2\sigma_p}{Z_{0p}} - \frac{2\sigma_b}{Z_{0b}}\right] \frac{\tilde{P}_i ab}{2\pi} \operatorname{sinc}\left[\frac{(\lambda+k_x)a}{2}\right] \operatorname{sinc}\left[\frac{(\mu+k_y)b}{2}\right] \\
& - \left[\frac{2\sigma_p}{Z_{0p}} - \frac{2\sigma_b}{Z_{0b}}\right] \frac{ab}{4\pi^2} \int\limits_{-\infty}^{\infty}\int\limits_{-\infty}^{\infty} \left[\frac{1}{2\mathrm{i}\omega} \sum_{r,m,n} B_r \bar{U}_{mnr} \Phi_{mn}(\lambda',\mu') - 2\pi \tilde{P}_i\, \delta(\lambda'+k_x)\, \delta(\mu'+k_y)\right] \\
& \qquad \times \operatorname{sinc}\left[\frac{(\lambda-\lambda')a}{2}\right] \operatorname{sinc}\left[\frac{(\mu-\mu')b}{2}\right] \mathrm{d}\lambda'\, \mathrm{d}\mu', \qquad (6.35)
\end{aligned}$$

where

$$\bar{U}_{mnr} = \left[D^*(1-\mathrm{i}\eta)\left\{\left(\frac{m\pi}{a}\right)^2 + \left(\frac{n\pi}{b}\right)^2\right\}^2 - m_p\omega^2\right] U_{mnr}. \qquad (6.36)$$

After a few simplifications (see Appendix J)

$$\frac{1}{2\mathrm{i}\omega}\left[1+\frac{2\sigma_b}{Z_{0b}}Z_a(\lambda,\mu)\right]\sum_{r,m,n}B_r\bar{U}_{mnr}\Theta_{mn}(\lambda,\mu)-\zeta_I\sum_{r,m,n}B_rU_{mnr}\Phi_{mn}(\lambda,\mu)$$
$$+\frac{ab}{8\pi^2\mathrm{i}\omega}\left[\frac{2\sigma_p}{Z_{0p}}-\frac{2\sigma_b}{Z_{0b}}\right]\sum_{r,m,n}B_r\bar{U}_{mnr}X_{mn}(\lambda,\mu) \;=\; \frac{2\pi\tilde{P}_i}{Z_a\left(\lambda,\mu\right)}\,\delta(\lambda+k_x)\,\delta(\mu+k_y), \tag{6.37}$$

where

$$\Theta_{mn}(\lambda,\mu)=\frac{\Phi_{mn}(\lambda,\mu)}{Z_a(\lambda,\mu)} \tag{6.38}$$

and

$$X_{mn}(\lambda,\mu)=\int_{-\infty}^{\infty}\int_{-\infty}^{\infty}\Phi_{mn}(\lambda',\mu')\,\mathrm{sinc}\left[\frac{(\lambda-\lambda')a}{2}\right]\,\mathrm{sinc}\left[\frac{(\mu-\mu')b}{2}\right]\,\mathrm{d}\lambda'\,\mathrm{d}\mu'. \tag{6.39}$$

The above equation (Eq. (6.37)) represents the coupled equation for the perforated panel response. Next, the above equation is solved for B_r, the modal coefficients of the perforated panel velocity.

6.5.2 Solution to the coupled equation

We know that the modal coefficient B_r must be independent of λ and μ. Multiplying Eq. (6.37) by $\sum_{p,q} U_{pqs}\Phi_{pq}(-\lambda,-\mu)$ and integrating over λ and μ domain we get

$$\begin{aligned}
&\frac{1}{2\mathrm{i}\omega}\sum_{r,m,n}\sum_{p,q} B_r \bar{U}_{mnr} U_{pqs} \int_{-\infty}^{\infty}\int_{-\infty}^{\infty} \Theta_{mn}(\lambda,\mu)\Phi_{pq}(-\lambda,-\mu)\,\mathrm{d}\lambda\,\mathrm{d}\mu \\
&\quad + \frac{1}{2\mathrm{i}\omega}\frac{2\sigma_b}{Z_{0b}}\sum_{r,m,n}\sum_{p,q} B_r \bar{U}_{mnr} U_{pqs} \int_{-\infty}^{\infty}\int_{-\infty}^{\infty} \Phi_{mn}(\lambda,\mu)\Phi_{pq}(-\lambda,-\mu)\,\mathrm{d}\lambda\,\mathrm{d}\mu \\
&\quad + \frac{ab}{8\pi^2\mathrm{i}\omega}\left[\frac{2\sigma_p}{Z_{0p}} - \frac{2\sigma_b}{Z_{0b}}\right]\sum_{r,m,n}\sum_{p,q} B_r \bar{U}_{mnr} U_{pqs} \int_{-\infty}^{\infty}\int_{-\infty}^{\infty} X_{mn}(\lambda,\mu)\Phi_{pq}(-\lambda,-\mu)\,\mathrm{d}\lambda\,\mathrm{d}\mu \\
&\quad - \zeta_I \sum_{r,m,n}\sum_{p,q} B_r U_{mnr} U_{pqs} \int_{-\infty}^{\infty}\int_{-\infty}^{\infty} \Phi_{mn}(\lambda,\mu)\Phi_{pq}(-\lambda,-\mu)\,\mathrm{d}\lambda\,\mathrm{d}\mu \\
&\qquad = \frac{2\pi \tilde{P}_i}{Z_a(-k_x,-k_y)}\sum_{p,q} U_{pqs}\Phi_{pq}(k_x,k_y)\,. \qquad (6.40)
\end{aligned}$$

In the equation above, except the first integral (which is evaluated numerically), the rest can be evaluated analytically. The integrals in the above equation arise from the interaction between the *in vacuo* panel modes. The integrals are evaluated in Appendix I and the results are given below.

$$\int_{-\infty}^{\infty}\int_{-\infty}^{\infty} \Phi_{mn}(\lambda,\mu)\Phi_{pq}(-\lambda,-\mu)\,\mathrm{d}\lambda\,\mathrm{d}\mu = \frac{ab}{4}\,\delta_{mp}\,\delta_{nq}. \qquad (6.41)$$

$$\int_{-\infty}^{\infty}\int_{-\infty}^{\infty} X_{mn}(\lambda,\mu)\Phi_{pq}(-\lambda,-\mu)\,\mathrm{d}\lambda\,\mathrm{d}\mu = \pi^2\,\delta_{mp}\,\delta_{nq}. \qquad (6.42)$$

Substituting the above results in Eq. (6.40) we get

$$\frac{1}{2\mathrm{i}\omega}\sum_{r,m,n}\sum_{p,q}B_r\bar{U}_{mnr}U_{pqs}\bar{\Theta}_{mnpq}+\frac{ab}{8\mathrm{i}\omega}\frac{2\sigma_b}{Z_{0b}}\sum_{r,m,n}\sum_{p,q}B_r\bar{U}_{mnr}U_{pqs}\,\delta_{mp}\,\delta_{nq}$$
$$+\frac{ab}{8\mathrm{i}\omega}\left[\frac{2\sigma_p}{Z_{0p}}-\frac{2\sigma_b}{Z_{0b}}\right]\sum_{r,m,n}\sum_{p,q}B_r\bar{U}_{mnr}U_{pqs}\,\delta_{mp}\,\delta_{nq}$$
$$-\frac{ab}{4}\zeta_I\sum_{r,m,n}\sum_{p,q}B_rU_{mnr}U_{pqs}\,\delta_{mp}\,\delta_{nq}\;=\;\frac{2\pi\tilde{P}_i}{Z_a\left(-k_x,-k_y\right)}\sum_{p,q}U_{pqs}\Phi_{pq}\left(k_x,k_y\right),$$

where

$$\bar{\Theta}_{mnpq}=\int_{-\infty}^{\infty}\int_{-\infty}^{\infty}\Theta_{mn}(\lambda,\mu)\Phi_{pq}(-\lambda,-\mu)\,\mathrm{d}\lambda\,\mathrm{d}\mu. \tag{6.43}$$

Canceling the identical terms and simplifying

$$\frac{1}{2\mathrm{i}\omega}\sum_{r,m,n}\sum_{p,q}B_r\bar{U}_{mnr}U_{pqs}\bar{\Theta}_{mnpq}+\frac{ab}{8\mathrm{i}\omega}\frac{2\sigma_p}{Z_{0p}}\sum_{r,m,n}B_r\bar{U}_{mnr}U_{mns}$$
$$-\frac{ab}{4}\zeta_I\sum_{r,m,n}B_rU_{mnr}U_{mns}\;=\;\frac{2\pi\tilde{P}_i}{Z_a\left(-k_x,-k_y\right)}\sum_{p,q}U_{pqs}\Phi_{pq}\left(k_x,k_y\right).$$

In a matrix form

$$\frac{1}{2\mathrm{i}\omega}\left[U_{pq,s}\right]^T\left[\bar{\Theta}_{mn,pq}\right]^T\left[\bar{U}_{mn,r}\right]\left\{B_r\right\}+\frac{ab}{8\mathrm{i}\omega}\frac{2\sigma_p}{Z_{0p}}\left[U_{mn,s}\right]^T\left[\bar{U}_{mn,r}\right]\left\{B_r\right\}$$
$$-\frac{ab}{4}\zeta_I\left[U_{mn,s}\right]^T\left[U_{mn,r}\right]\left\{B_r\right\}\;=\;\frac{2\pi\tilde{P}_i}{Z_a\left(-k_x,-k_y\right)}\left[U_{pq,s}\right]^T\left\{\Phi_{pq}\left(k_x,k_y\right)\right\}.$$

Thus, the modal coefficients are given by

$$\left\{B_r\right\}=\left[Z_{s,r}\right]^{-1}\left\{F_s\right\}, \tag{6.44}$$

where

$$\left[Z_{s,r}\right]=\frac{1}{2\mathrm{i}\omega}\left[U_{pq,s}\right]^T\left[\bar{\Theta}_{mn,pq}\right]^T\left[\bar{U}_{mn,r}\right]+\frac{ab}{8\mathrm{i}\omega}\frac{2\sigma_p}{Z_{0p}}\left[U_{mn,s}\right]^T\left[\bar{U}_{mn,r}\right]-\frac{ab}{4}\zeta_I\left[U_{mn,s}\right]^T\left[U_{mn,r}\right] \tag{6.45}$$

and

$$\{F_s\} = \frac{2\pi \tilde{P}_i}{Z_a\left(-k_x, -k_y\right)} \left[U_{pq,s}\right]^T \left\{\Phi_{pq}\left(k_x, k_y\right)\right\}. \tag{6.46}$$

From the modal coefficients B_r (Eq. 6.44)

$$V_p\left(\lambda, \mu\right) = \left\{B_r\right\}^T \left[U_{mn,r}\right]^T \left\{\Phi_{mn}\left(\lambda, \mu\right)\right\}. \tag{6.47}$$

Having found $V_p(\lambda, \mu)$, the $V_a(\lambda, \mu, z = 0)$ can be obtained from Eq. (6.26) (see Appendix F). From $V_a(\lambda, \mu, z = 0)$, the radiated pressure can be found as

$$P^-\left(\lambda, \mu, z = 0\right) = -Z_a\left(\lambda, \mu\right) V_a(\lambda, \mu, z = 0).$$

Since the pressures and the LAFP velociy are known, we can proceed to compute the transmitted power and the TL.

6.6 Sound transmission loss of a perforated panel in a baffle

Using the transmitted pressure $P^-(\lambda, \mu, z = 0)$ and the LAFP velocity $V_a(\lambda, \mu, z = 0)$ expressions derived in the previous section, we can evaluate the transmitted power due to the incidence of a plane acoustic wave on a perforated panel fixed in a baffle. The farfield transmitted power is [4]

$$W_t = \frac{1}{2}\,\mathrm{Re}\left\{\int_{-k}^{k} \int_{-\sqrt{k^2-\mu^2}}^{\sqrt{k^2-\mu^2}} P^-(\lambda, \mu, z = 0) V_a^*(\lambda, \mu, z = 0)\,\mathrm{d}\lambda\,\mathrm{d}\mu\right\}. \tag{6.48}$$

And the total power incident on the perforated panel is

$$W_i = \frac{|\tilde{P}_i|^2 \cos\theta\; ab}{2\rho_0 c}, \tag{6.49}$$

where θ is the polar angle. The sound transmission coefficient τ is the ratio of the transmitted to the incident sound powers and is

$$\tau = \frac{W_t}{W_i}. \tag{6.50}$$

And the sound transmission loss TL is

$$\mathrm{TL} = 10\log_{10}\left(\frac{1}{\tau}\right). \tag{6.51}$$

The effect of perforation (EP) is defined as the difference between the transmission loss of a perforated panel and that of an unperforated panel of the same size. Thus,

$$\mathrm{EP} = \mathrm{TL}_{\mathrm{perforated}} - \mathrm{TL}_{\mathrm{unperforated}}, \tag{6.52}$$

or

$$\mathrm{EP} = 10\log_{10}\left(\frac{W_{\mathrm{unperforated}}}{W_{\mathrm{perforated}}}\right).$$

6.7 Results

In this section, the TL of a finite perforated panel set in an unperforated baffle is computed for various system parameters. In all the forthcoming analyses the acoustic medium is air.

Panel dimensions	$a = 0.455$ m, $b = 0.546$ m and $h = 0.003$ m
Panel material properties (aluminum)	$E = 70$ GPa, $\rho_p = 2700$ kg/m^3 and $\nu = 0.33$
Properties of air	$\rho_0 = 1.204$ kg/m^3, $c = 343$ m/s and $\eta_0 = 1.8 \times 10^{-5}$ Ns/m^2

Table 6.1 The perforated panel dimensions and material properties.

The panel dimensions and the system properties are mentioned in Table 6.1. A harmonic plane wave of amplitude $\tilde{P}_i = 1$ is incident at a polar angle $\theta = 60^0$ and an azimuthal angle $\phi = 0^0$. Fig. 6.2 depicts the TL for panels with different perforation ratios. The different perforation ratios are achieved by varying the hole radius from $r_p = 0.5$ mm to $r_p = 5$ mm while keeping the total number of holes in the panel constant $N_0 = 750$. For comparison, the figure also shows the TL variation obtained using the uncoupled or the one-way coupled model presented in chapter 4.

In Fig. 6.2(a) the TL of a finite unperforated panel is shown (uncoupled and coupled cases). At low frequencies, the difference between the two cases (coupled and uncoupled) is significant. The inertial effect of the fluid-loading is significant at low frequencies reducing the panel response causing an increase in the TL. The infinite panel coupled

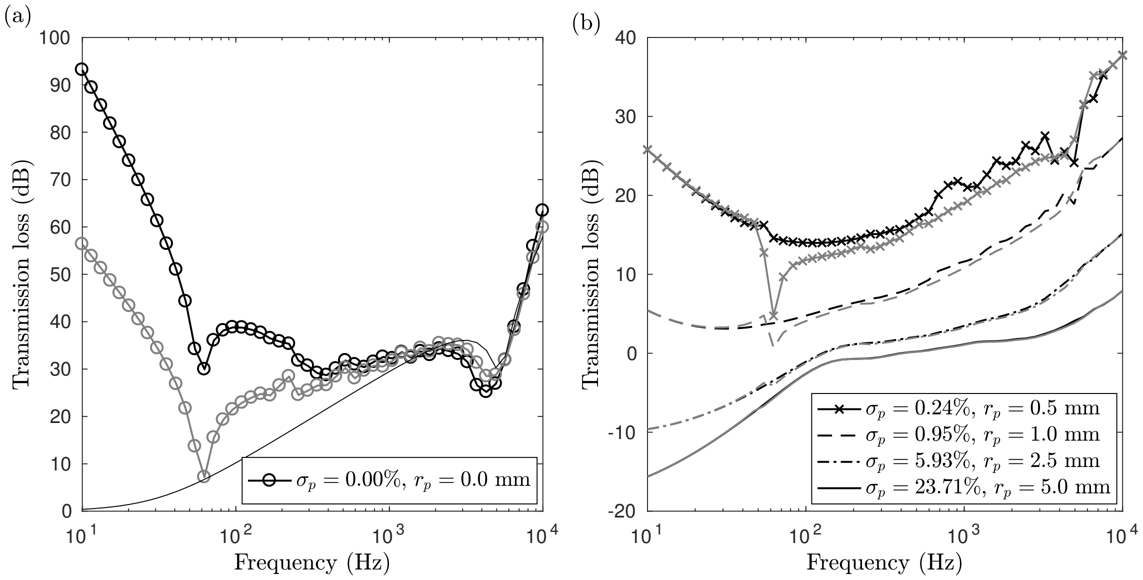

Fig. 6.2 Coupled and uncoupled TL of (a) unperforated panel (coupled: black marker, uncoupled: gray marker, infinite panel: black, no marker) and (b) perforated panels with different perforation ratios (coupled: black marker, uncoupled: gray marker). $N_0 = 750$. Unperforated baffle. $\theta = 60^0$ and $\phi = 0^0$.

case is plotted in the same figure. It can be seen that the two figures match at high frequencies. In the infinite case [7], at high frequencies, the panel stiffness begins to dominate over the fluid-loading. Also at high frequencies one can argue that the finite panel approaches the infinite panel condition. Thus, the same explanation holds here also. In fact, the transmitted power goes up with fluid density, as long as the panel stiffness dominates. It can also be seen that the fluid inertia drops the coincidence frequency (even though slightly).

Figure 6.2(b) shows the TL for finite perforated panels. Here, the difference between the uncoupled and coupled curves is small. In terms of computation, the panel velocity is differently computed between the coupled and uncoupled cases. For the coupled case, the effective panel impedance gets modified by the modal coupling coefficient. The panel velocity, however, remains negligible (in both the cases) as most of the transmission is through the perforations.

Figure 6.3 depicts the EP (Eq. 6.52) obtained for different perforation ratios of the panel using the coupled formulation. Note, that the unperforated TL for evaluating EP is also obtained using the coupled formulation. As the TL of a perforated panel is smaller than that of an unperforated one, EP is negative for all the cases. It can be noticed that as the perforation ratio increases TL decreases and hence the magnitude of EP ($\mathrm{EP_{abs}}$) increases.

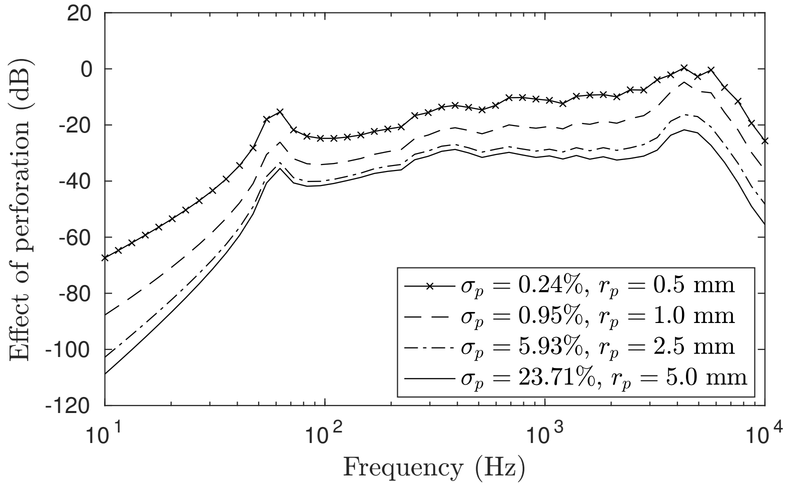

Fig. 6.3 Effect of perforation (EP) for panels of different perforation ratios. The coupled formulation is used here. $N_0 = 750$ in all the cases. $\theta = 60^0$ and $\phi = 0^0$. Baffle is unperforated.

Figures 6.4(a) and 6.4(b) show the absolute values of the perforate impedance and their break up into resistive and reactive components, respectively. In these figures, the perforation ratio is held a constant ($\sigma_p = 0.95\%$) by varying both the radii and the number of holes. The hole radius is varied from $r_p = 0.5$ mm to $r_p = 5.0$ mm, whereas the total number of holes is varied from $N_0 = 3000$ to $N_0 = 30$. In general, the reactance dominates over the resistance at high frequencies and decreases with decreasing frequency. At low frequencies, for small radii perforations, the resistive component becomes greater than the reactance. This character is predominant at sub-millimeter radii, i.e., for micro-perforated panels. This behavior reflects in the TL which is shown in Fig. 6.5. At low frequencies, the TL for $r_p = 0.5$ mm (which has a higher resistive component) is greater than that of $r_p = 5.0$ mm. The EP curves for different hole radii are plotted in Fig. 6.6. At higher frequencies, the $\mathrm{EP_{abs}}$ decreases with the increasing hole size (a larger hole is associated with a higher hole reactance and hence a higher TL). Whereas at lower frequencies, the smaller radius curve is seen to have a smaller $\mathrm{EP_{abs}}$ due to a higher hole resistance.

In all the previous analysis, the angle of incidence was kept constant ($\theta = 60^0$ and $\phi = 0^0$). Fig. 6.7(a) shows the variation in TL for different polar angles (θ), keeping $\phi = 0^0$. For all the cases $N_0 = 750$ and $r_p = 1$ mm with a resulting perforation ratio $\sigma_p = 0.95\%$. The two significant changes in TL brought by varying θ are (1) reduction in TL with increasing θ and (2) decrease in the coincidence frequency with increase in θ. The variation in transmitted power with θ is depicted in Fig. 6.7(b). It can be

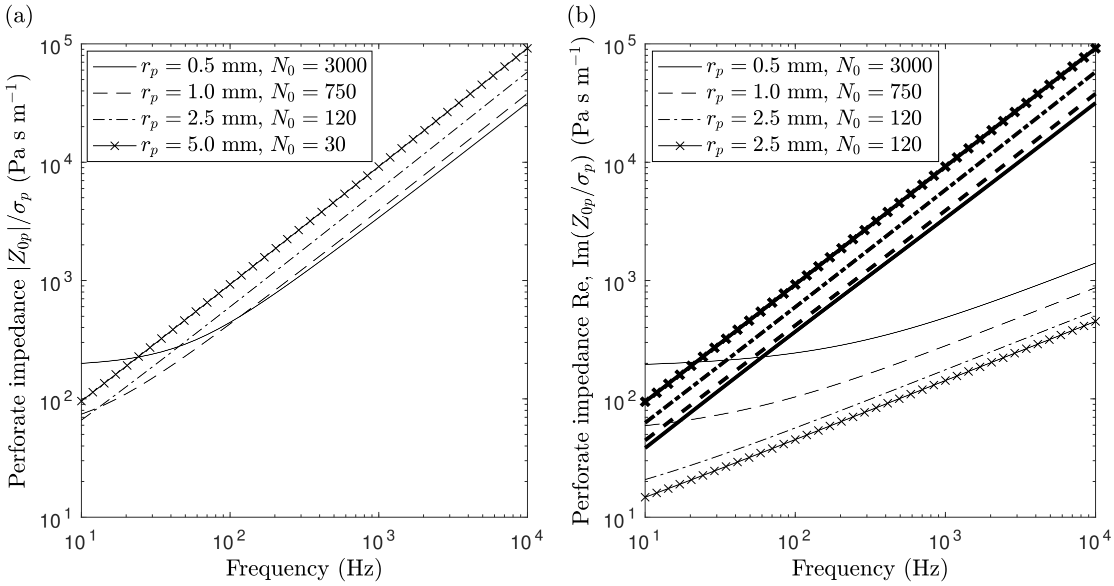

Fig. 6.4 Effect of radius on the perforate impedance. (a) Absolute perforate impedance and (b) components of perforate impedance. Resistive (thin line) and reactive (thick line). $\sigma_p = 0.95\%$ for all cases.

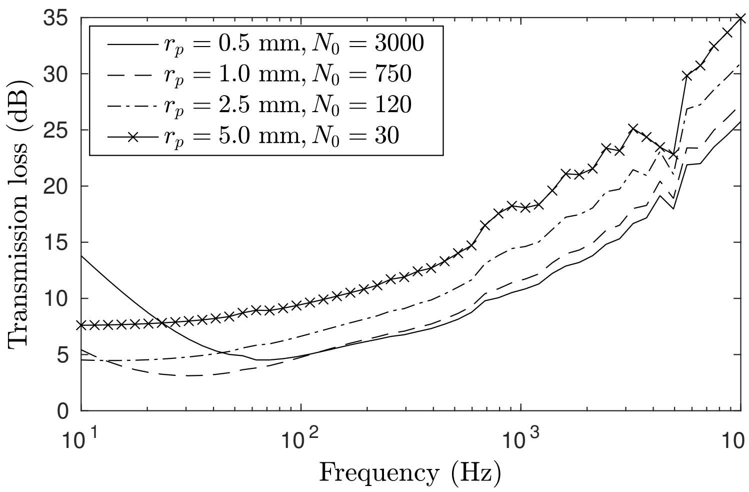

Fig. 6.5 TL of perforated panels with the same perforation ratio ($\sigma_p = 0.95\%$). The hole radius and the total number of holes are varied accordingly. Unperforated baffle. $\theta = 60^0$ and $\phi = 0^0$.

seen that the transmitted power does not vary significantly with θ (as the perforate impedance is independent of θ and the effect of the panel impedance is negligible in determining the transmitted power). However, the normal incident power decreases significantly with increasing angle of incidence (due to the $\cos\theta$ term in the numerator of Eq. (6.49)). Thus, although the transmitted power remains the same, the TL drops

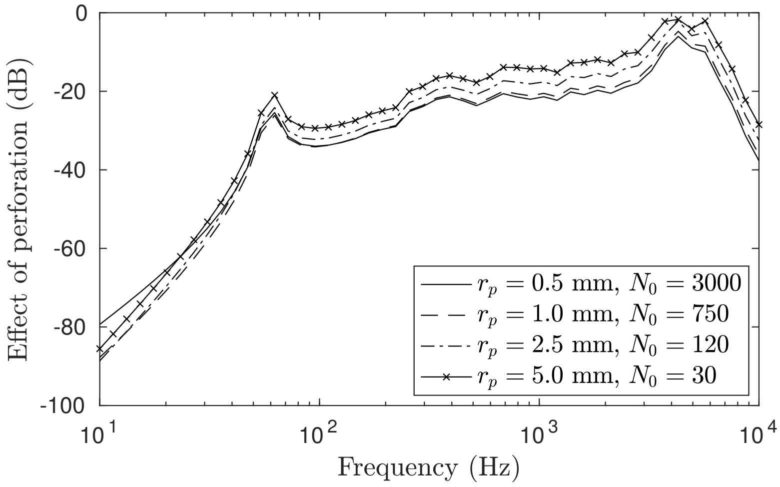

Fig. 6.6 Effect of perforation (EP) for panels with the same perforation ratio ($\sigma_p = 0.95\%$). The hole radius and the total number of holes are varied accordingly. Unperforated baffle. $\theta = 60^0$ and $\phi = 0^0$.

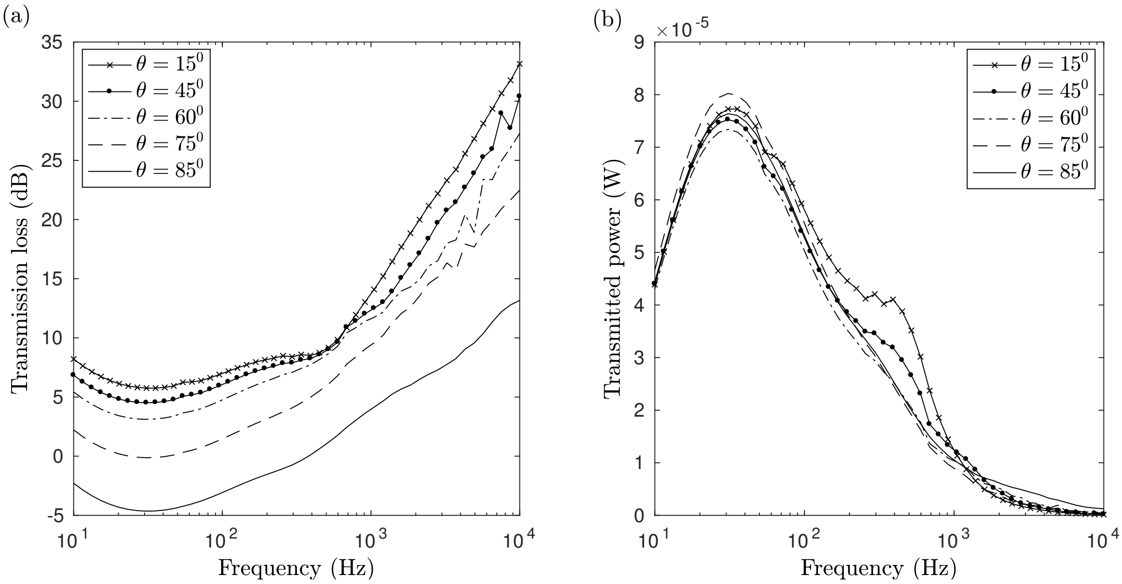

Fig. 6.7 (a) TL and (b) transmitted power of a perforated panel for different θ. For all the cases $\phi = 0^0$, $N_0 = 750$, $r_p = 1$ mm and $\sigma_p = 0.95\%$. Unperforated baffle.

as the angle of incidence increases. TL for the unperforated panel for different angles of incidence (θ) is evaluated and plotted in Fig. 6.8(a). These unperforated panel TL values are then used to find the EP for the perforated case ($r_p = 1$ mm and $N_0 = 750$) and are shown in Fig. 6.8(b). It can be observed that the $\mathrm{EP_{abs}}$ increases with the increasing angle of incidence. The variation in EP is largely due to the changes in the unperforated panel TL.

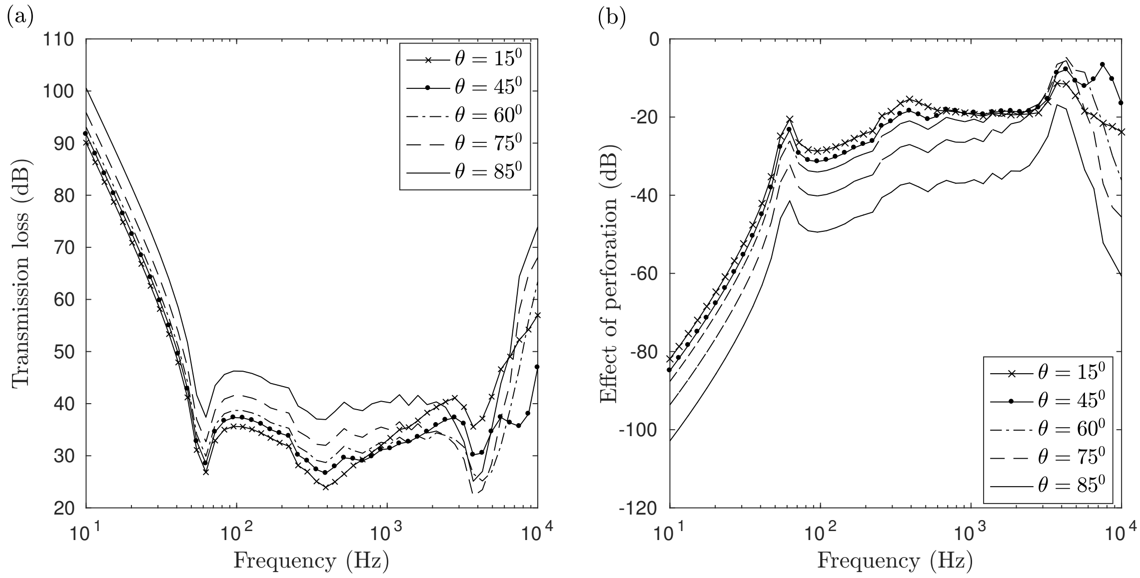

Fig. 6.8 (a) TL of an unperforated panel for different angles of incidence θ ($\phi = 0^0$ for all the cases). (b) Effect of perforation (EP) of a perforated panel for different θ. For all the cases $\phi = 0^0$, $N_0 = 750$, $r_p = 1$ mm and $\sigma_p = 0.95\%$. Unperforated baffle.

6.7.1 Negative transmission loss

It is observed from Fig. 6.2 that for larger perforation ratios ($\sigma_p = 5.93\%$ and 23.71%), the transmission loss is negative at lower frequencies. But, this behavior is unexpected for a passive system considered here. A negative TL implies a transmission coefficient (Eq. (6.50)) greater than unity and violates power conservation.

Similar cases of negative TL for sound transmission through apertures have been reported in the literature [69, 70]. And references [71, 54, 72] discuss about the absorption coefficient being greater than unity for micro-perforated panels backed by a cavity. In the above formulation, the incident power is a function of the incident pressure amplitude and its angle of incidence only. It is a frequency independent quantity. But, the actual power injected includes an additional term [71, 54] as shown below. Once this term is included, the TL remains positive throughout.

The reflected power normal to the panel surface is given by [54]

$$W_{\text{refl}} = \frac{1}{2}\,\text{Re}\left\{\iint_{A_p} [p_2(x,y,z=0) - p_i(x,y,z=0)] \times [v_a(x,y,z=0) - v_i(x,y,z=0)]^* \,\mathrm{d}A\right\},$$

where $v_i(x,y,z=0)$ is the normal velocity corresponding to the incident pressure field, A_p represents the panel area and all other variables are as defined above. The first square bracket represents the total reflected pressure and the second represents the total reflected velocity.

We know that $p_2(x,y,z=0) = 2p_i(x,y,z=0) + p^+(x,y,z=0)$ (from Eq. (6.24) and reference [7]), where $p^+(x,y,z=0)$ is the radiated pressure field on the incident side. Expanding the above equation

$$\begin{aligned} W_{\text{refl}} = -\frac{1}{2}\,\text{Re}&\left\{\iint_{A_p} -p_2(x,y,z=0)v_a^*(x,y,z=0)\,\mathrm{d}A\right\} \\ &+ \frac{1}{2}\,\text{Re}\left\{\iint_{A_p} -p_i(x,y,z=0)v_i^*(x,y,z=0)\,\mathrm{d}A\right\} \\ &+ \frac{1}{2}\,\text{Re}\left\{\iint_{A_p} \Big[-p_i(x,y,z=0)v_a^*(x,y,z=0) \right. \\ &\left. - p^+(x,y,z=0)v_i^*(x,y,z=0)\Big]\,\mathrm{d}A\right\}. \end{aligned} \tag{6.53}$$

The first term on the right hand side represents the power flow through the perforated panel (W_{flow}) and the second term denotes the incident power (W_i) as derived in Eq. (6.49). The third term is the additional term mentioned above. It is due to the diffraction caused by the discontinuity of perforate impedance at the panel-baffle boundary. It represents the power contribution due to cross coupling; the coupling of the in-phase components of the incident pressure and the radiated normal velocity, and the radiated pressure and the incident normal velocity. Denoting this term as $W_{\text{inc-rad}}$, the equation above can be written as

$$W_{\text{refl}} + W_{\text{flow}} = W_i + W_{\text{inc-rad}} = \tilde{W}_i, \tag{6.54}$$

where $\tilde{W}_i$ is the total power injected into the perforated panel (see Appendix K for details).

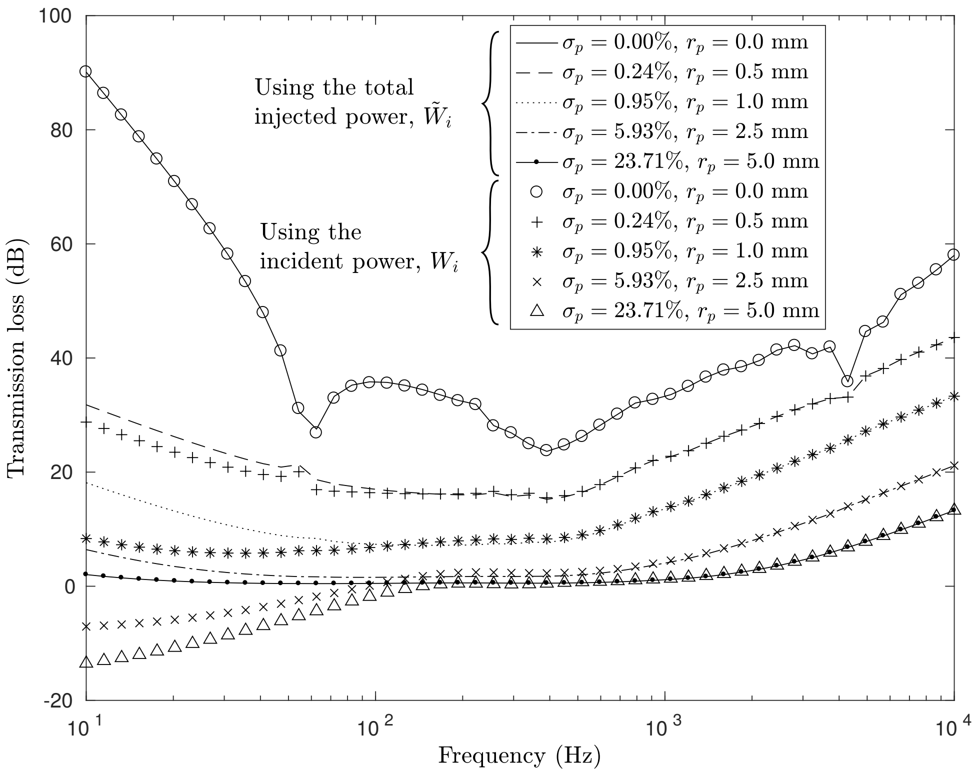

Fig. 6.9 Comparison of TL computed using $\tilde{W}_i$ (Eq. (K.8)) and that using W_i (Eq. (6.49)) for panels with different perforation ratios. In all the cases, the total number of holes in the panel is $N_0 = 750$. A normally incident plane wave is considered ($\theta = 0^0$ and $\phi = 0^0$).

Figure 6.9 shows the TL for panels with different perforation ratios under normal incidence of a plane wave of unit amplitude. The coupled formulation is used here. One set of curves uses $\tilde{W}_i$ (Eq. (K.8)), whereas the other set uses W_i (Eq. (6.49)). For the unperforated panel, there exists no discontinuity in the perforate impedance along the panel-baffle boundary and therefore the diffraction phenomenon does not occur. Thus, the TLs evaluated using both the methods are identical for the unperforated panel. As the perforation ratio increases, the diffraction effect becomes more significant at lower frequencies and $\tilde{W}_i$ differs from W_i. It can be seen from Fig. 6.9 that for all the cases in which $\tilde{W}_i$ is used, the TL is positive for the entire frequency range. At higher frequencies, the diffraction effect becomes negligible. Therefore, for a given perforation ratio, the TLs evaluated using both the methods are identical at higher frequencies. The corresponding EP values are plotted in Fig. 6.10. Here, the TLs of both the perforated and the unperforated panels are obtained using $\tilde{W}_i$.

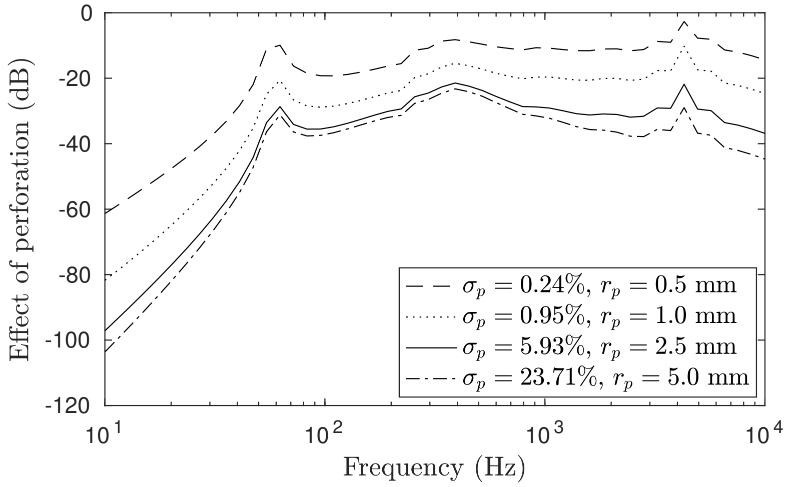

Fig. 6.10 Effect of perforation (EP) computed using $\tilde{W}_i$ (Eq. (K.8)) for panels with different perforation ratios. In all the cases, the total number of holes in the panel is $N_0 = 750$. A normally incident plane wave is considered ($\theta = 0^0$ and $\phi = 0^0$).

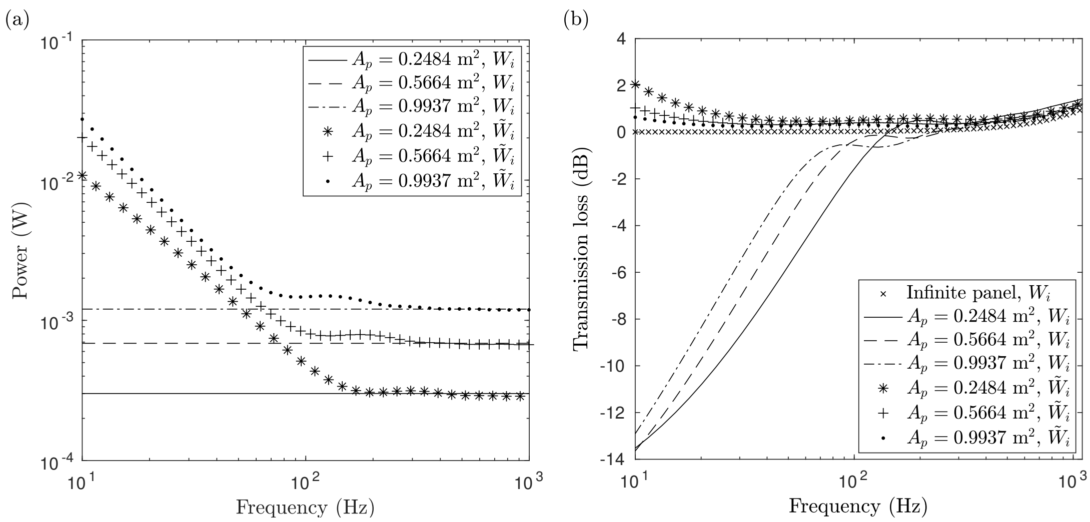

Fig. 6.11 Comparison of (a) Incident power $\tilde{W}_i$ (Eq. (K.8)) and W_i (Eq. (6.49)) and (b) TL computed using $\tilde{W}_i$ and that using W_i for panels of varying size. In all the cases, $r_p = 5$ mm and $\sigma_p = 23.71\%$. A normally incident plane wave is considered ($\theta = 0^0$ and $\phi = 0^0$).

We have seen that the diffraction phenomenon is caused by the discontinuity in the perforate impedance. It is also observed that at high frequencies the diffraction effect vanishes and the power carried by the incident plane wave alone is sufficient to evaluate TL correctly (see Appendix K). Thus, it suggests that the diffraction effect depends upon the relative size of the perforated panel with respect to the acoustic wavelength. Fig. 6.11 depicts the variation in the incident power (both $\tilde{W}_i$ and W_i) and the TL (evaluated using $\tilde{W}_i$ and W_i) for different panel sizes. For all the cases, the hole size and perforation ratio are the same ($r_p = 5$ mm and $\sigma_p = 23.71\%$). Fig. 6.11(b) also shows the TL for an infinite flexible perforated panel. The infinite perforated panel TL can be obtained in closed form using the equivalent circuit model as shown in Fig. 6.12 [1, 2, 7]. In the figure, z_p represents the wave impedance offered by the flexible perforated panel

$$z_p = \frac{\Delta p(x, z=0)}{v_p(x)} = \frac{\mathrm{i}}{\omega}\left[D^*(1-i\eta)k^4\sin^4\theta - m_p\omega^2\right], \tag{6.55}$$

$z_a = \dfrac{\rho c}{\cos\theta}$ is the specific acoustic impedance and $z_0 = \frac{Z_{0p}}{\sigma_p}$ is the perforate impedance. The transmission coefficient for the infinite panel can be obtained as

$$\tau(\theta) = \frac{|2z_a|^2}{\left|2z_a + \dfrac{1}{\left(\dfrac{1}{z_p/\zeta_I} + \dfrac{1}{z_0}\right)}\right|^2}. \tag{6.56}$$

Now, the TL can be obtained using Eq. (6.51).

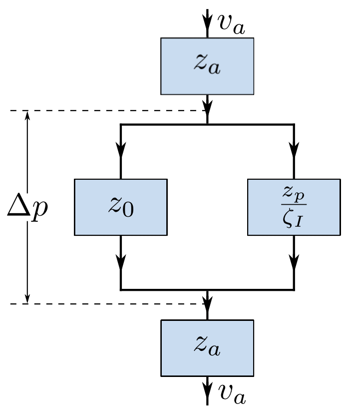

Fig. 6.12 Equivalent circuit representation of a flexible perforated panel of infinite extent.

As the panel area increases, the incident power (both $\tilde{W}_i$ and W_i) increases (see Fig. 6.11(a)). At lower frequencies, $\tilde{W}_i$ is higher than W_i for all the cases. This implies that the diffraction effect exists even for the largest panel considered here. However, the rate at which $\tilde{W}_i$ increases is lower than that of W_i, i.e., the diffraction effect reduces with increasing panel size. Consider the TL of the finite panel calculated using W_i (Fig. 6.11(b)). The TL decreases in magnitude with the increasing panel size and approaches that of the infinite panel, for which the TL is always positive. The TL considering $\tilde{W}_i$ is also seen to reduce in magnitude with the increasing panel size, but at a lower rate as compared to that computed using W_i. Thus, it is evident that the diffraction effect depends upon the area of the perforated panel - the larger the panel area, the effect of diffraction is smaller. This phenomenon is similar to the "area effect" in the sound absorption by finite absorbers [71, 73]. Also, it can be noticed from Fig. 6.11(b) that at higher frequencies, the finite panel TL approaches that of the infinite panel.

6.8 Conclusions

A fully coupled formulation in the 2-D wavenumber domain is used to model the sound transmission through a fluid-loaded finite perforated panel set in an infinite unperforated rigid baffle. A locally averaged fluid particle (LAFP) velocity is formulated as a combination of the sound transmission through the perforations and that due to the panel vibrations. The change in the resonances caused by the perforations is accounted for in the panel vibrations. Finally, the LAFP velocity is multiplied by the acoustic impedance resulting in the transmitted pressure. The formulation takes into account the self and cross modal coupling coefficients arising due to the fluid-loading effect. The transmission loss curves are plotted for various cases and the physics is discussed. Along the way the one-way coupled calculation is also presented for the sake of comparison. The results presented here are mainly for a light medium like air.

The perforate and the panel impedances are in parallel to each other. And for a light medium, the perforate impedance is lower than the panel impedance. Thus, the significant transmission happens through the perforations. The panel velocity contribution is insignificant and hence the one-way coupled calculation is adequate. For a heavy fluid (like water), the perforate impedance is higher than the panel impedance. Thus, a coupled calculation is needed.

In general, the absolute perforate impedance increases with increasing frequency. For a light medium, the TL curve matches this trend. At low frequencies, the absolute perforate impedance rises because the resistive component of the hole impedance increases. Thus, the TL curves rise at lower frequencies. This effect is prominent for sub-millimeter hole radii, i.e., for micro-perforations. Here, the increase in TL with the decreasing frequency begins at a higher frequency. Although, the perforate impedances rises at high and low frequencies, within the frequency range of interest, for air, it never compares with the panel impedance. These curves are also plotted in terms of the effect of perforations (EP).

Since for a light medium, the perforate impedance decides the TL, the transmitted power is independent of the angle of incidence of the plane wave. However, as the normal incident power depends on the incidence angle, the TL changes.

An important phenomenon observed in the TL curves at low frequencies is that the TL values become negative. This violates power conservation. The reason for this apparent violation is that the input power is defined solely based on the incident plane wave. In actuality, an additional component of power is incident onto the panel from the region above the baffle due to diffraction effects. This phenomenon is dominant at low frequencies and hence when it is ignored, the TL values become negative. An expression for this additional term is derived. Using this new definition of the incident power, the TL values remain positive throughout the frequency range. The intensity quiver plots that show the additional power component flowing from the baffle region onto the panel are also obtained. It is observed that the diffraction effect reduces with increasing panel size and the TL of a finite panel approaches that of the infinite panel.

It is observed that the fluid loading couples the *in vacuo* natural modes of the perforated panel. This coupling between the *in vacuo* modes is expressed as the modal coupling coefficient $\bar{\Theta}_{mnpq}$ in the coupled equation of motion of the perforated panel. The modal coupling coefficient is given in the form of a double integral in the wavenumber domain. So far, in chapters 5 and 6, the numerical integration method is used to evaluate this integral. In the next chapter, closed form solutions corresponding to different panel wavenumbers are obtained for this double integral.

Part IV

Closed form expressions for the modal coupling coefficient

Chapter 7

Closed form expressions for the modal coupling coefficient of a perforated panel

7.1 Introduction

The two-way coupled formulations for the radiation and the transmission problems result in the *in vacuo* modes getting coupled due to the fluid loading effect. This fluid loading effect is entirely captured by the modal coupling coefficient $\bar{\Theta}_{mnpq}$. In chapters 5 and 6, this modal coupling coefficient which ended up as a double integral was evaluated numerically. In this chapter, closed form expressions for the same modal coupling coefficient are derived.

7.2 The modal coupling coefficient

The term $\bar{\Theta}_{mnpq}$ in Eq. (5.34) is called the modal coupling coefficient. It is given by

$$\bar{\Theta}_{mnpq} = \int_{-\infty}^{\infty} \int_{-\infty}^{\infty} \frac{\Phi_{mn}(\lambda, \mu)\, \Phi_{pq}(-\lambda, -\mu)}{Z_a(\lambda, \mu)} \,\mathrm{d}\lambda \,\mathrm{d}\mu, \tag{7.1}$$

Before beginning to evaluate the above expression, a brief description is relevant here. The integrand of the coupling coefficient has a square root branch cut in addition to the regular singularities in the domain of integration. This makes it difficult to solve the integral exactly. In this chapter, approximate expressions are derived for all the types of modal interactions which can be significant at any given frequency. They are also applicable for any degree of fluid loading, be it light as for the case of air or be it heavy as for the case of water.

In the above equation, $\Phi_{mn}(\lambda,\mu)$ and $\Phi_{pq}(-\lambda,-\mu)$ can be obtained using Eq. (5.19) and $Z_a(\lambda,\mu) = \frac{\rho_0 ck}{\sqrt{k^2-\lambda^2-\mu^2}}$. It can be seen that the numerator of $\Phi_{mn}(\lambda,\mu)\,\Phi_{pq}(-\lambda,-\mu)$ has a multiplying factor in λ of the form $1+(-1)^{m+p}-(-1)^m\,\mathrm{e}^{\mathrm{i}\lambda a}-(-1)^p\,\mathrm{e}^{-\mathrm{i}\lambda a}$. When $m+p$ is odd this results in $\pm 2\mathrm{i}\sin\lambda a$ and since the rest of the integrand is even in λ, the integral over λ from $-\infty$ to ∞ vanishes. Similar is the case for the integral over μ when $n+q$ is odd. Thus, we can write

$$\bar{\Theta}_{mnpq} = 0, \qquad \text{if } m+p \text{ or } n+q \text{ is odd.} \tag{7.2}$$

On the other hand, when $m+p$ is even, we get $1+(-1)^{m+p}-(-1)^m\,\mathrm{e}^{\mathrm{i}\lambda a}-(-1)^p\,\mathrm{e}^{-\mathrm{i}\lambda a} = 2\,[1-(-1)^m\cos\lambda a]$. Similarly, when $n+q$ is even, $1+(-1)^{n+q}-(-1)^n\,\mathrm{e}^{\mathrm{i}\mu b}-(-1)^q\,\mathrm{e}^{-\mathrm{i}\mu b} = 2\,[1-(-1)^n\cos\mu b]$. Thus, we see that $\bar{\Theta}_{mnpq}$ is non-zero only when $m+p$ and $n+q$ are even, i.e., m and p and n and q have the same parity (either both odd or both even) [33]. Hence, each mode is coupled to at most only one quarter of all the other modes. Therefore, the nonzero components of $\bar{\Theta}_{mnpq}$ are given by (when $m+p$ and $n+q$ are even)

$$\bar{\Theta}_{mnpq} = \frac{4\,k_m\,k_n\,k_p\,k_q}{\rho_0 ck\,(2\pi)^2}\,I^{mnpq}, \tag{7.3}$$

where

$$I^{mnpq} = \int_{-\infty}^{\infty}\int_{-\infty}^{\infty} \frac{[1-(-1)^m\cos\lambda a]\;[1-(-1)^n\cos\mu b]\;\left(k^2-\lambda^2-\mu^2\right)^{1/2}}{\left(\lambda^2-k_m^2\right)\left(\lambda^2-k_p^2\right)\left(\mu^2-k_n^2\right)\left(\mu^2-k_q^2\right)}\,\mathrm{d}\lambda\,\mathrm{d}\mu. \tag{7.4}$$

In the equation above, the integral over λ is denoted as

$$I_1^{mp}(\mu) = \int_{-\infty}^{\infty} \frac{[1-(-1)^m\cos\lambda a]\;\left(k^2-\lambda^2-\mu^2\right)^{1/2}}{\left(\lambda^2-k_m^2\right)\left(\lambda^2-k_p^2\right)}\,\mathrm{d}\lambda, \tag{7.5}$$

and use the fact that for an even function $f(\lambda)$

$$\int_{-\infty}^{\infty} f(\lambda)\cos\lambda a\,\mathrm{d}\lambda = \int_{-\infty}^{\infty} f(\lambda)\,\mathrm{e}^{\mathrm{i}\lambda a}\,\mathrm{d}\lambda.$$

Thus

$$I_1^{mp}(\mu) = \int_{-\infty}^{\infty} \frac{\left[1-(-1)^m\,\mathrm{e}^{\mathrm{i}\lambda a}\right]\,\left(k^2-\lambda^2-\mu^2\right)^{1/2}}{\left(\lambda^2-k_m^2\right)\,\left(\lambda^2-k_p^2\right)}\,\mathrm{d}\lambda. \tag{7.6}$$

7.2.1 Branch points and branch cuts

The integrand of $I_1^{mp}(\mu)$ has square root branch points at

$$\lambda_{1,2} = \pm\left(k^2-\mu^2\right)^{1/2}.$$

Depending on the value of μ and hence the location of the branch points $\lambda_{1,2}$, $I_1^{mp}(\mu)$ has to be evaluated differently - **Case 1**: when $|\mu| < k$; $\lambda_{1,2} = \pm\sqrt{k^2-\mu^2}$, i.e., the branch points lie on the positive and the negative real axis and **Case 2**: when $|\mu| > k$; $\lambda_{1,2} = \pm\mathrm{i}\sqrt{\mu^2-k^2}$, i.e., the branch points lie on the positive and the negative imaginary axis.

Consider the first case in which $\lambda_{1,2}$ lie on the real axis, i.e.,

$$\lambda_1 = (k^2-\mu^2)^{1/2} \qquad \text{and} \qquad \lambda_2 = -\lambda_1.$$

For $z > 0$, the radiated pressure wave has the form $\mathrm{e}^{\mathrm{i}\xi z-\mathrm{i}\omega t}$ with $\xi = (k^2-\lambda^2-\mu^2)^{1/2} = (\lambda_1^2-\lambda^2)^{1/2}$. We know that for large values of λ, a growing wave is physically inadmissible and hence ξ must be positive imaginary.

$$\xi = \mathrm{i}(\lambda^2-\lambda_1^2)^{1/2} \qquad \text{for real } \lambda \text{ such that } |\lambda| > \lambda_1.$$

Thus, it is necessary that we choose a feasible definition for ξ so that a growing wave solution never occurs. We will now select an appropriate branch cut and definition for the function $(k^2-\lambda^2-\mu^2)^{1/2}$ by looking at it as a product of square roots, i.e.,

$$\left(\lambda_1^2-\lambda^2\right)^{1/2} = (\lambda_1-\lambda)^{1/2}\,(\lambda_1+\lambda)^{1/2} = |\lambda_1-\lambda|^{1/2}\,\mathrm{e}^{\mathrm{i}\,\gamma/2}\,|\lambda_1+\lambda|^{1/2}\,\mathrm{e}^{\mathrm{i}\,\theta/2}.$$

The complex functions $(\lambda_1-\lambda)$ and $(\lambda_1+\lambda)$ are shown in Figs. 7.1(a) and 7.1(b), respectively.

From Fig. 7.1(a), as γ varies from 0 to 2π, the resulting branch cut of $(\lambda_1-\lambda)^{1/2}$ runs along the real axis from λ_1 to $-\infty$ (see Fig. 7.2(a)). We may now select the following function definition for $(\lambda_1-\lambda)^{1/2}$ so that the branch cut modifies to an ‘L’

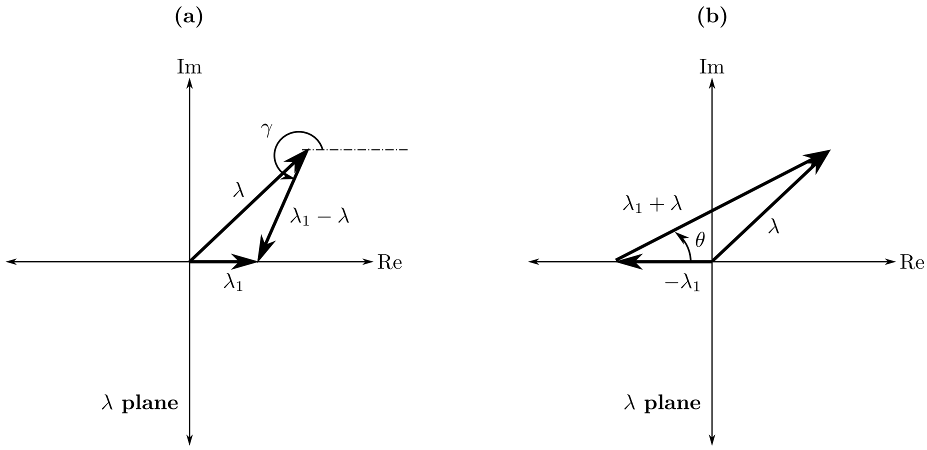

Fig. 7.1 Vectors of $\lambda_1 - \lambda$ and $\lambda_1 + \lambda$ (case 1) in the complex λ plane.

shaped one as shown Fig. 7.2(b):

$$(\lambda_1 - \lambda)^{1/2} = \begin{cases} |\lambda_1 - \lambda|^{1/2} \, \mathrm{e}^{\mathrm{i}\,\gamma/2} & \text{for } \mathrm{Re}(\lambda) > 0 \\ -\,|\lambda_1 - \lambda|^{1/2} \, \mathrm{e}^{\mathrm{i}\,\gamma/2} & \text{for } \mathrm{Re}(\lambda) < 0 \text{ and } \mathrm{Im}(\lambda) > 0 \\ |\lambda_1 - \lambda|^{1/2} \, \mathrm{e}^{\mathrm{i}\,\gamma/2} & \text{for } \mathrm{Re}(\lambda) < 0 \text{ and } \mathrm{Im}(\lambda) < 0. \end{cases} \tag{7.7}$$

It will be described later how the above modification of branch cut (and the one which will be explained next) prevent the function $(\lambda_1^2 - \lambda^2)^{1/2}$ from assuming any negative imaginary values for $|\mathrm{Re}(\lambda)| > \lambda_1$.

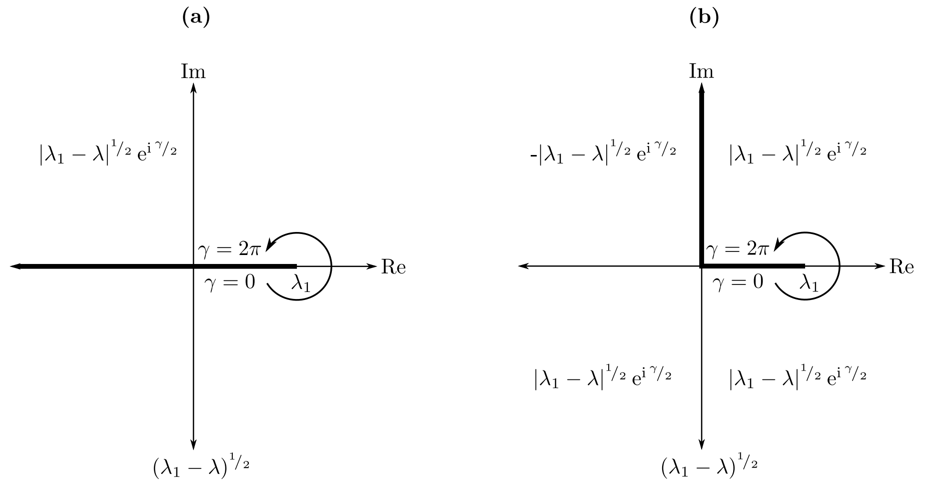

Fig. 7.2 (a) Initial and (b) modified branch cuts of $(\lambda_1 - \lambda)^{1/2}$ (case 1) in the complex λ plane.

Now assume that θ, the argument of $(\lambda_1+\lambda)$, varies from 0 to 2π. The resulting branch cut of $(\lambda_1+\lambda)^{1/2}$ extends from $-\lambda_1$ to ∞ along the real axis, as shown in Fig. 7.3(a). It is then modified to an 'L' shaped one by choosing the following function definition for $(\lambda_1+\lambda)^{1/2}$:

$$(\lambda_1+\lambda)^{1/2} = \begin{cases} |\lambda_1+\lambda|^{1/2}\ \mathrm{e}^{\mathrm{i}\,\theta/2} & \text{for } \mathrm{Re}(\lambda)<0 \\ -\,|\lambda_1+\lambda|^{1/2}\ \mathrm{e}^{\mathrm{i}\,\theta/2} & \text{for } \mathrm{Re}(\lambda)>0 \text{ and } \mathrm{Im}(\lambda)<0 \\ |\lambda_1+\lambda|^{1/2}\ \mathrm{e}^{\mathrm{i}\,\theta/2} & \text{for } \mathrm{Re}(\lambda)>0 \text{ and } \mathrm{Im}(\lambda)>0. \end{cases} \tag{7.8}$$

The modified branch cut is shown in Fig. 7.3(b).

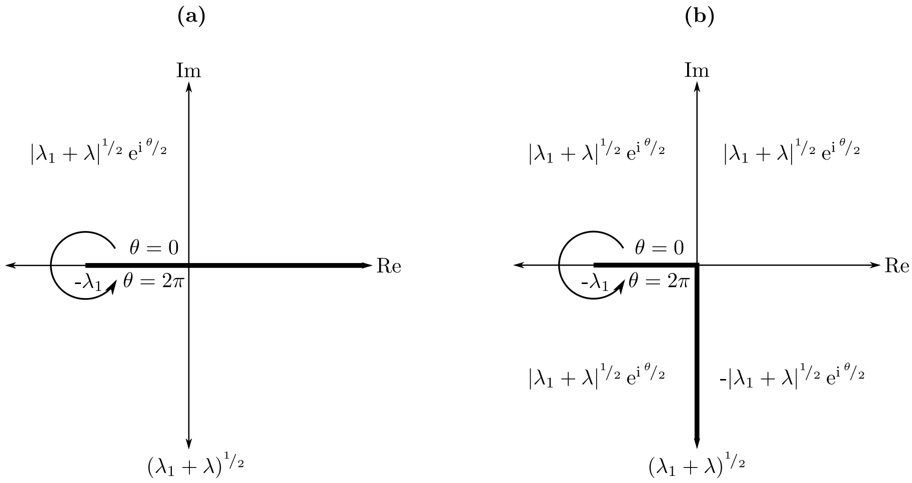

Fig. 7.3 (a) Initial and (b) modified branch cuts of $(\lambda_1+\lambda)^{1/2}$ (case 1) in the complex λ plane.

Combining the definitions of $(\lambda_1-\lambda)^{1/2}$ (Eq. (7.7)) and $(\lambda_1+\lambda)^{1/2}$ (Eq. (7.8)), $(\lambda_1^2-\lambda^2)^{1/2}$ can be defined as

$$\left(\lambda_1^2-\lambda^2\right)^{1/2} = \begin{cases} |\lambda_1-\lambda|^{1/2}\ |\lambda_1+\lambda|^{1/2}\ \mathrm{e}^{\mathrm{i}\,(\gamma+\theta)/2} & \text{for } \mathrm{Re}(\lambda)>0 \text{ and } \mathrm{Im}(\lambda)>0 \\ -\,|\lambda_1-\lambda|^{1/2}\ |\lambda_1+\lambda|^{1/2}\ \mathrm{e}^{\mathrm{i}\,(\gamma+\theta)/2} & \text{for } \mathrm{Re}(\lambda)<0 \text{ and } \mathrm{Im}(\lambda)>0 \\ |\lambda_1-\lambda|^{1/2}\ |\lambda_1+\lambda|^{1/2}\ \mathrm{e}^{\mathrm{i}\,(\gamma+\theta)/2} & \text{for } \mathrm{Re}(\lambda)<0 \text{ and } \mathrm{Im}(\lambda)<0 \\ -\,|\lambda_1-\lambda|^{1/2}\ |\lambda_1+\lambda|^{1/2}\ \mathrm{e}^{\mathrm{i}\,(\gamma+\theta)/2} & \text{for } \mathrm{Re}(\lambda)>0 \text{ and } \mathrm{Im}(\lambda)<0. \end{cases} \tag{7.9}$$

The arguments γ and θ varies from 0 to 2π. The resulting branch cut of $(\lambda_1^2-\lambda^2)^{1/2}$ is shown in Fig. 7.4.

Fig. 7.5 shows the values of arguments γ and θ along the real axis when $|\mathrm{Re}(\lambda)|>\lambda_1$. It can be found that for all the four cases, as shown in the figure, $(\lambda_1^2-\lambda^2)^{1/2} =$

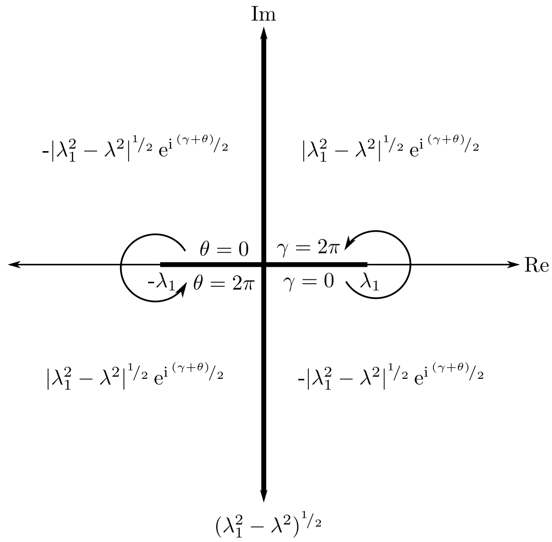

Fig. 7.4 Branch cut of $(\lambda_1^2-\lambda^2)^{1/2}$ (case 1) in the complex λ plane.

$\mathrm{i}\,|\lambda_1^2-\lambda^2|^{1/2}$. Hence the selected definition of $(\lambda_1^2-\lambda^2)^{1/2}$ and the associated branch cut result in an evanescent wave in the z direction for $|\mathrm{Re}(\lambda)|>\lambda_1$.

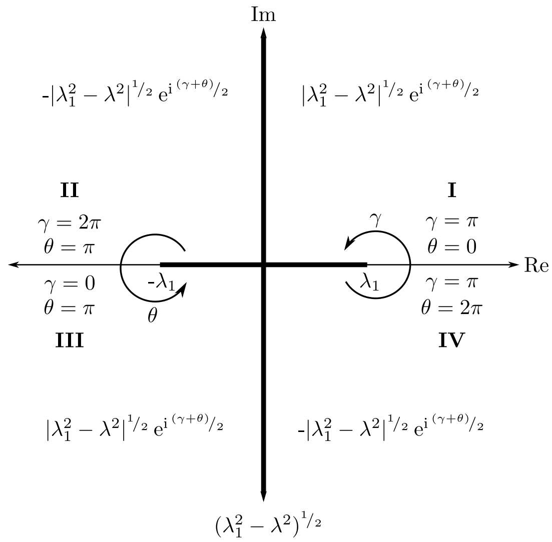

Fig. 7.5 Argument values of $(\lambda_1^2-\lambda^2)^{1/2}$ along the real axis when $|\mathrm{Re}(\lambda)|>\lambda_1$ (case 1).

Let us now consider the case 2 in which the branch points $\lambda_{1,2}$ lie on the imaginary axis of the complex λ plane.

$$\lambda_1=\mathrm{i}\left(\mu^2-k^2\right)^{1/2}\qquad\text{and}\qquad\lambda_2=-\lambda_1.$$

Again, $\xi = (k^2 - \lambda^2 - \mu^2)^{1/2}$ is the z wavenumber. For $z > 0$ and imaginary λ such that $|\mathrm{Im}(\lambda)| < \mathrm{Im}(\lambda_1)$, ξ must be positive imaginary and thus avoid z directional growing waves,

$$\xi = \mathrm{i}\left(\lambda_1'^2 - \lambda'^2\right)^{1/2} \qquad \text{for imaginary } \lambda \text{ such that } |\lambda'| < \lambda_1'.$$

Here the primed variables denote the imaginary part of the respective unprimed quantities. We will now select an appropriate branch cut and definition for the function $(k^2 - \lambda^2 - \mu^2)^{1/2}$ which satisfies the above condition.

As before, we have

$$\left(\lambda_1^2 - \lambda^2\right)^{1/2} = (\lambda_1 - \lambda)^{1/2}\,(\lambda_1 + \lambda)^{1/2} = |\lambda_1 - \lambda|^{1/2}\,\mathrm{e}^{\mathrm{i}\,\gamma/2}\,|\lambda_1 + \lambda|^{1/2}\,\mathrm{e}^{\mathrm{i}\,\theta/2}.$$

The complex functions $(\lambda_1 - \lambda)$ and $(\lambda_1 + \lambda)$ are shown in Fig. 7.6. As γ varies from

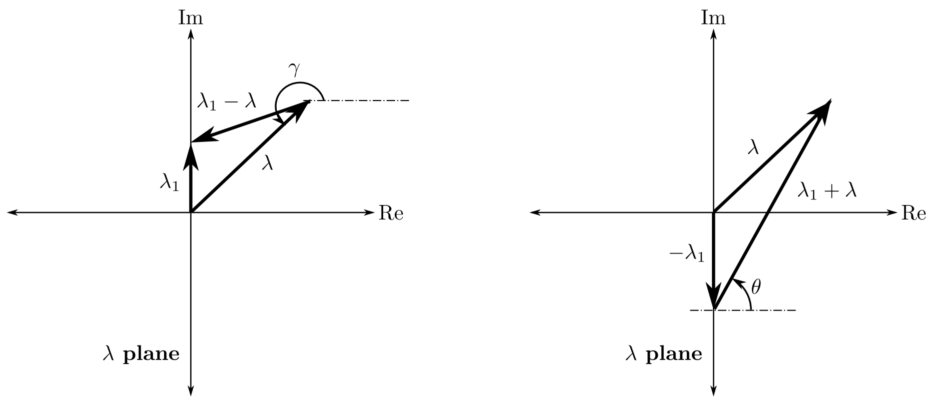

Fig. 7.6 Illustrations of $\lambda_1 - \lambda$ and $\lambda_1 + \lambda$ (case 2) in the complex λ plane.

$-\pi/2$ to $3\pi/2$, the resulting branch cut of $(\lambda_1 - \lambda)^{1/2}$ is along the imaginary axis from λ_1 to ∞, as shown in Fig. 7.7(a). Also as θ varies from $-\pi/2$ to $3\pi/2$, the branch cut of $(\lambda_1 + \lambda)^{1/2}$ is along the imaginary axis from $-\lambda_1$ to $-\infty$, as shown in Fig. 7.7(b). Thus, we have

$$\left(\lambda_1^2 - \lambda^2\right)^{1/2} = \left|\lambda_1^2 - \lambda^2\right|^{1/2}\,\mathrm{e}^{\mathrm{i}\,(\gamma+\theta)/2}, \tag{7.10}$$

where γ and θ vary from $-\pi/2$ to $3\pi/2$. The resulting branch cut is shown in Fig. 7.8. It can be seen that for $|\mathrm{Im}(\lambda)| < \lambda_1'$, along the imaginary axis, the argument values are $\gamma = \pi/2$ and $\theta = \pi/2$ and hence $(\lambda_1^2 - \lambda^2)^{1/2} = \mathrm{i}\,|\lambda_1^2 - \lambda^2|^{1/2}$. Thus, for case 2, by choosing the above definition of $(\lambda_1^2 - \lambda^2)^{1/2}$ we ensure an evanescent wave in the z direction when $|\mathrm{Im}(\lambda)| < \lambda_1'$.

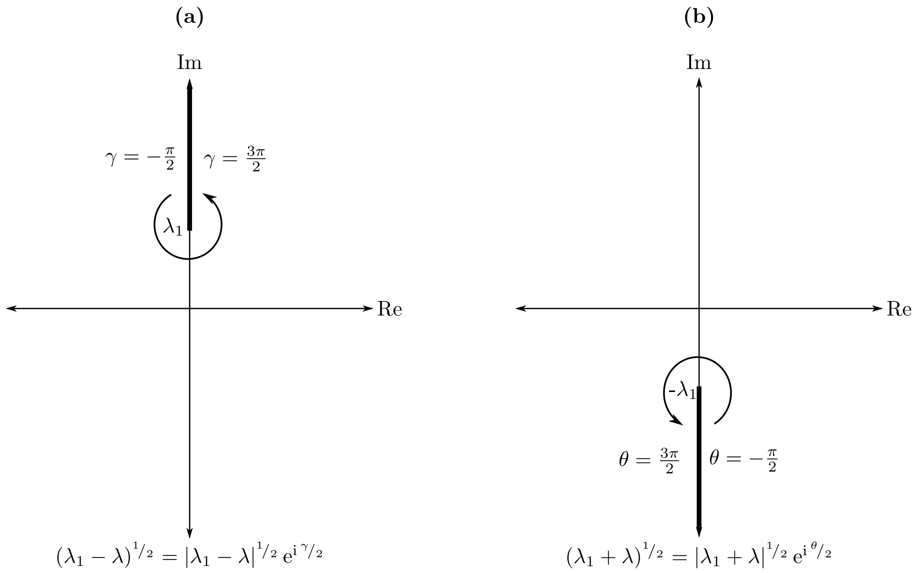

Fig. 7.7 Branch cuts of (a) $(\lambda_1 - \lambda)^{1/2}$ and (b) $(\lambda_1 + \lambda)^{1/2}$ for case 2 in the complex λ plane.

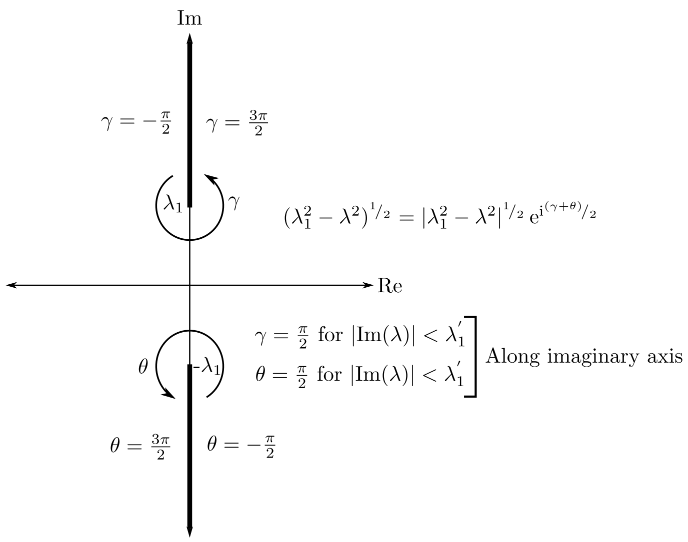

Fig. 7.8 Branch cut of $(\lambda_1^2 - \lambda^2)^{1/2}$ (case 2) as illustrated in the complex λ plane.

7.2.2 Integration contours for $I_1^{mp}(\mu)$ ($k_m, k_p > k$ and $m \neq p$)

The integral $I_1^{mp}(\mu)$, as defined in Eq. (7.6), can now be evaluated using the Cauchy residue theorem [67] along a contour in the complex λ plane. The contour is different for each of the cases as described before [34]. Consider a scenario of $k_m, k_p > k$, $m + p$ even and $m \neq p$.

Case 1 ($|\mu| < k$)

The poles, branch points, branch cuts and the integration contour for case 1 ($|\mu| < k$) are shown in Fig. 7.9.

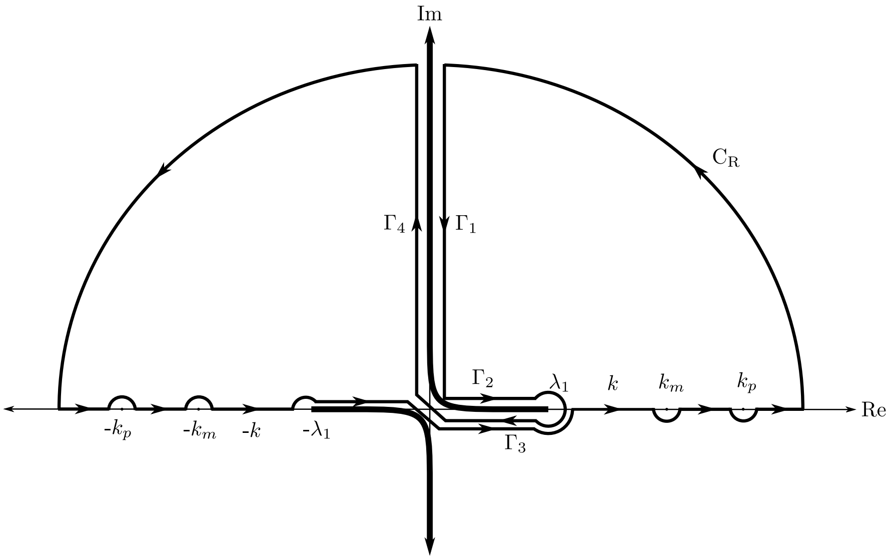

Fig. 7.9 Integration contour of $I_1^{mp}(\mu)$ for case 1 ($|\mu| < k$) when $k_m, k_p > k$ and $k_m \neq k_p$.

Using the Cauchy residue theorem we get

$$\begin{aligned}\mathrm{P}\left[I_1^{mp}(\mu)\right] = I_1^{mp}(\mu : |\mu| < k) = \pi\mathrm{i}\left[\mathrm{Res}(k_m) + \mathrm{Res}(k_p) + \mathrm{Res}(-k_m) + \mathrm{Res}(-k_p)\right] \\ - (\Gamma_1 + \Gamma_2 + \Gamma_3 + \Gamma_4),\end{aligned}$$

where P[∗] denotes the principal value of the integral and Res(∗) denotes the residue of the integrand at the specified poles. The integrals $\Gamma_1, \Gamma_2, \Gamma_3$ and Γ_4 are derived in detail in Appendix M and the final forms are given below:

$$\begin{aligned}
\Gamma_1 &= \mathrm{i}\int_0^\infty \frac{\left[1-(-1)^m\ \mathrm{e}^{-ay}\right]\left|\lambda_1^2+y^2\right|^{1/2}}{\left(y^2+k_m^2\right)\left(y^2+k_p^2\right)}\,\mathrm{d}y,\\
\Gamma_2 &= -\int_0^{\lambda_1} \frac{\left[1-(-1)^m\ \mathrm{e}^{\mathrm{i}ax}\right]\left|\lambda_1^2-x^2\right|^{1/2}}{\left(x^2-k_m^2\right)\left(x^2-k_p^2\right)}\,\mathrm{d}x,\\
\Gamma_3 &= -\int_0^{\lambda_1} \frac{\left[1-(-1)^m\ \mathrm{e}^{\mathrm{i}ax}\right]\left|\lambda_1^2-x^2\right|^{1/2}}{\left(x^2-k_m^2\right)\left(x^2-k_p^2\right)}\,\mathrm{d}x\\
\text{and}\quad \Gamma_4 &= \mathrm{i}\int_0^\infty \frac{\left[1-(-1)^m\ \mathrm{e}^{-ay}\right]\left|\lambda_1^2+y^2\right|^{1/2}}{\left(y^2+k_m^2\right)\left(y^2+k_p^2\right)}\,\mathrm{d}y.
\end{aligned} \tag{7.11}$$

It is shown in the Appendix M that the residues at simple poles $k_m, k_p, -k_m$ and $-k_p$ identically go to zero, i.e.,

$$\mathrm{Res}(k_m) = \mathrm{Res}(k_p) = \mathrm{Res}(-k_m) = \mathrm{Res}(-k_p) = 0. \tag{7.12}$$

Thus,

$$I_1^{mp}(\mu : |\mu| < k) = -(\Gamma_1 + \Gamma_2 + \Gamma_3 + \Gamma_4).$$

Substituting for $\Gamma_1, \Gamma_2, \Gamma_3$ and Γ_4 and grouping the real and imaginary terms we get

$$\begin{aligned}
I_1^{mp}(\mu : |\mu| < k) = 2\int_0^{\lambda_1} \frac{\left[1-(-1)^m\ \cos ax\right]\left|\lambda_1^2-x^2\right|^{1/2}}{\left(x^2-k_m^2\right)\left(x^2-k_p^2\right)}\,\mathrm{d}x\\
-2\,\mathrm{i}\left[\int_0^{\lambda_1} \frac{(-1)^m\ \sin ax\ \left|\lambda_1^2-x^2\right|^{1/2}}{\left(x^2-k_m^2\right)\left(x^2-k_p^2\right)}\,\mathrm{d}x + \int_0^\infty \frac{\left[1-(-1)^m\ \mathrm{e}^{-ay}\right]\left|\lambda_1^2+y^2\right|^{1/2}}{\left(y^2+k_m^2\right)\left(y^2+k_p^2\right)}\,\mathrm{d}y\right].
\end{aligned} \tag{7.13}$$

Case 2 ($|\mu| > k$)

The poles, branch points, branch cuts and the integration contour for case 2 ($|\mu| > k$) are shown in Fig. 7.10.

Now, using the Cauchy residue theorem we get

$$\begin{aligned}
\mathrm{P}\left[I_1^{mp}(\mu)\right] &= I_1^{mp}(\mu : |\mu| > k)\\
&= \pi\mathrm{i}\left[\mathrm{Res}(k_m) + \mathrm{Res}(k_p) + \mathrm{Res}(-k_m) + \mathrm{Res}(-k_p)\right] - (\Gamma_1 + \Gamma_2),
\end{aligned}$$

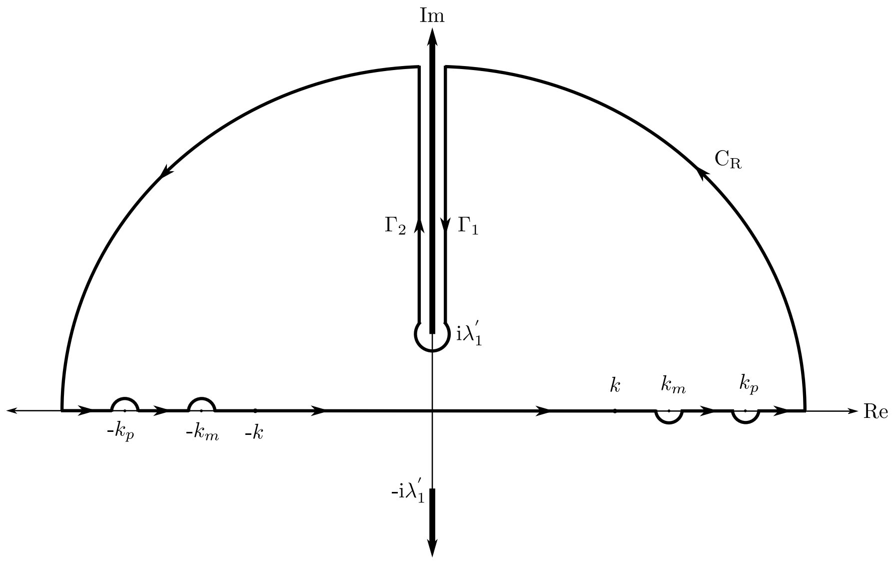

Fig. 7.10 Integration contour of $I_1^{mp}(\mu)$ for case 2 ($|\mu| > k$) when $k_m, k_p > k$ and $k_m \neq k_p$.

where P[$*$] denotes the principal value of the integral and Res($*$) denotes the residue of the integrand at the specified poles. The integrals Γ_1 and Γ_2 are different from those in case 1. They are derived in detail in Appendix N and the final forms are given below.

$$\Gamma_1 = \Gamma_2 = \mathrm{i} \int_{\lambda_1'}^{\infty} \frac{\left[1 - (-1)^m \; \mathrm{e}^{-ay}\right] \left|\lambda_1'^2 - y^2\right|^{1/2}}{\left(y^2 + k_m^2\right) \left(y^2 + k_p^2\right)} \, \mathrm{d}y. \tag{7.14}$$

The residues are also derived in Appendix N and are identically zero, i.e.,

$$\mathrm{Res}(k_m) = \mathrm{Res}(k_p) = \mathrm{Res}(-k_m) = \mathrm{Res}(-k_p) = 0.$$

We now have

$$I_1^{mp}(\mu : |\mu| > k) = -(\Gamma_1 + \Gamma_2).$$

Substituting for Γ_1 and Γ_2 we get

$$I_1^{mp}(\mu : |\mu| > k) = -2\,\mathrm{i} \int_{\lambda_1'}^{\infty} \frac{\left[1 - (-1)^m \; \mathrm{e}^{-ay}\right] \left|\lambda_1'^2 - y^2\right|^{1/2}}{\left(y^2 + k_m^2\right) \left(y^2 + k_p^2\right)} \, \mathrm{d}y. \tag{7.15}$$

Having obtained $I_1^{mp}(\mu)$ for $|\mu| < k$ and $|\mu| > k$, the I^{mnpq} integral (Eq. (7.4)) simplifies to

$$I^{mnpq} = 2\int_0^k \frac{[1-(-1)^n\cos\mu b]}{(\mu^2-k_n^2)\left(\mu^2-k_q^2\right)}\, I_1^{mp}(\mu : |\mu| < k)\,\mathrm{d}\mu + 2\int_k^\infty \frac{[1-(-1)^n\cos\mu b]}{(\mu^2-k_n^2)\left(\mu^2-k_q^2\right)}\, I_1^{mp}(\mu : |\mu| > k)\,\mathrm{d}\mu, \tag{7.16}$$

where $I_1^{mp}(\mu : |\mu| < k)$ and $I_1^{mp}(\mu : |\mu| > k)$ can be evaluated using Eqs. (7.13) and (7.15), respectively. This equation, however, can be used as a general expression for evaluating the modal coupling coefficient for the remaining types of modal interactions as well.

7.3 Derivation of the closed forms for I^{mnpq}

Based on the panel wavenumbers k_m and k_n, the modes of a vibrating panel can be classified into four categories: corner modes, X/Y edge (single edge) modes, XY edge (double edge) modes and acoustically fast (AF) modes [12, 33, 34]. The associated panel wavenumbers are given in Table 7.1.

Type	Panel wave numbers
Corner	$k_m > k, k_n > k$
X edge	$k_m < k, k_n > k$
Y edge	$k_m > k, k_n < k$
XY edge	$k_m < k, k_n < k, k_m^2 + k_n^2 > k^2$
Acoustically fast (AF)	$k_m < k, k_n < k, k_m^2 + k_n^2 < k^2$

Table 7.1 Types of panel modes based on the panel wavenumbers

The coupling coefficient $\bar{\Theta}_{mnpq}$ (Eq. (7.1)) quantifies the interaction between the panel modes ($(m,n)^{\text{th}}$ mode with $(p,q)^{\text{th}}$ mode) due to the fluid loading. In this study, approximate closed form expressions are obtained for $\bar{\Theta}_{mnpq}$ based on the type of interacting modes as listed in Table 7.1. It is readily known that there can be as many as 25 types of interactions. However, as the modal coupling coefficient is commutative (see Eq. (7.1)), it is only required to find the approximate expressions for 15 types of interactions: 1) corner - corner, 2) corner - X edge, 3) corner - Y edge, 4) corner - XY edge, 5) corner - AF, 6) X edge - X edge, 7) X edge - Y edge, 8) X edge - XY edge, 9) X edge - AF, 10) Y edge - Y edge, 11) Y edge - XY edge, 12) Y edge - AF, 13) XY edge - XY edge, 14) XY edge - AF and 15) AF - AF. Let us start by finding the closed form for the Y edge - Y edge coupling coefficient, which is the simplest of all. While finding the closed form expressions, only the dominant terms/contributions are taken into account. Approximations relevant to each of the cases are made at appropriate places in the derivation. The Mathematica numerical package [74] is used for the symbolic calculations.

7.3.1 Y edge - Y edge modes ($k_m, k_p > k$ and $k_n, k_q < k$)

The derivation of I^{mnpq} for the Y edge - Y edge case is outlined in Fig. 7.11 as a flow chart. Eq. (7.16) is used to evaluate I^{mnpq}, in which the inner integrals $I_1^{mp}(\mu : |\mu| < k)$ and $I_1^{mp}(\mu : |\mu| > k)$ are evaluated using Eqs. (7.13) and (7.15), respectively. Two cases are considered: 1) $k_m \neq k_p$ and $k_n = k_q$ and 2) $k_m = k_p$ and $k_n = k_q$.

$k_m \neq k_p$ **and** $k_n = k_q$

We have the following approximation by Kraichnan [75, 33, 34] (see Appendix P)

$$\left.\frac{[1-(-1)^n \cos \mu b]}{\left(\mu^2-k_n^2\right)\left(\mu^2-k_q^2\right)}\right|_{n=q} \approx \frac{\pi b}{4k_n^2}\,\delta(\mu-k_n). \tag{7.17}$$

Substituting this into Eq. (7.16) and knowing that $k_n < k$ we get

$$I^{mnpq} \approx \frac{\pi b}{2k_n^2}\, I_1^{mp}(k_n : k_n < k), \tag{7.18}$$

where $I_1^{mp}(k_n : k_n < k)$ can be evaluated using Eq. (7.13). The detailed derivation of I^{mnpq} when $k_m \neq k_p$ and $k_n = k_q$ is given in Appendix O.1. The result is given in the box below.

$$I^{mnpq} = I_R^{mnpq} + \mathrm{i}\, I_\chi^{mnpq}, \tag{7.19}$$

where the real part of I^{mnpq} is given by

$$I_R^{mnpq} \approx \frac{\pi^2 b}{2k_n^2}\left[\frac{k_p\sqrt{k_m^2-\lambda_1^2}-k_m\sqrt{k_p^2-\lambda_1^2}}{k_m^3 k_p - k_m k_p^3} - \frac{\lambda_1(-1)^m \mathrm{J}_1\left(a\lambda_1\right)}{a\left(\lambda_1^2-k_m^2\right)\left(\lambda_1^2-k_p^2\right)}\right]\delta_{nq}$$

and the imaginary part of I^{mnpq} is given by

$$I_\chi^{mnpq} \approx -\frac{\pi b}{k_n^2}(A+B+C)\,\delta_{nq}$$

with

$$A = \frac{\pi\lambda_1(-1)^m \mathrm{H}_1\left(a\lambda_1\right)}{2a\left(\lambda_1^2-k_m^2\right)\left(\lambda_1^2-k_p^2\right)},$$

$$B = \frac{2k\sqrt{2k^2-k_n^2}+(k^2-k_n^2)\log\left(\frac{\left(\sqrt{2k^2-k_n^2}+k\right)^2}{k^2-k_n^2}\right)}{4k_m^2 k_p^2} + \frac{\log\left(\frac{k^2+k_p^2}{k^2+k_m^2}\right)}{2\left(k_p^2-k_m^2\right)}$$

and $$C = \frac{(-1)^{m+1}}{12ak_m^2k_p^2}\left\{2\sqrt{\frac{1}{a^2}+k^2-k_n^2}-\left(k^2-k_n^2\right)\right.$$
$$\left.\times\left[-4a^2\sqrt{k^2-k_n^2}+4a^2\sqrt{\frac{1}{a^2}+k^2-k_n^2}-3a\log\left(\frac{\left(\sqrt{\frac{1}{a^2}+k^2-k_n^2}+\frac{1}{a}\right)^2}{k^2-k_n^2}\right)\right]\right\}.$$

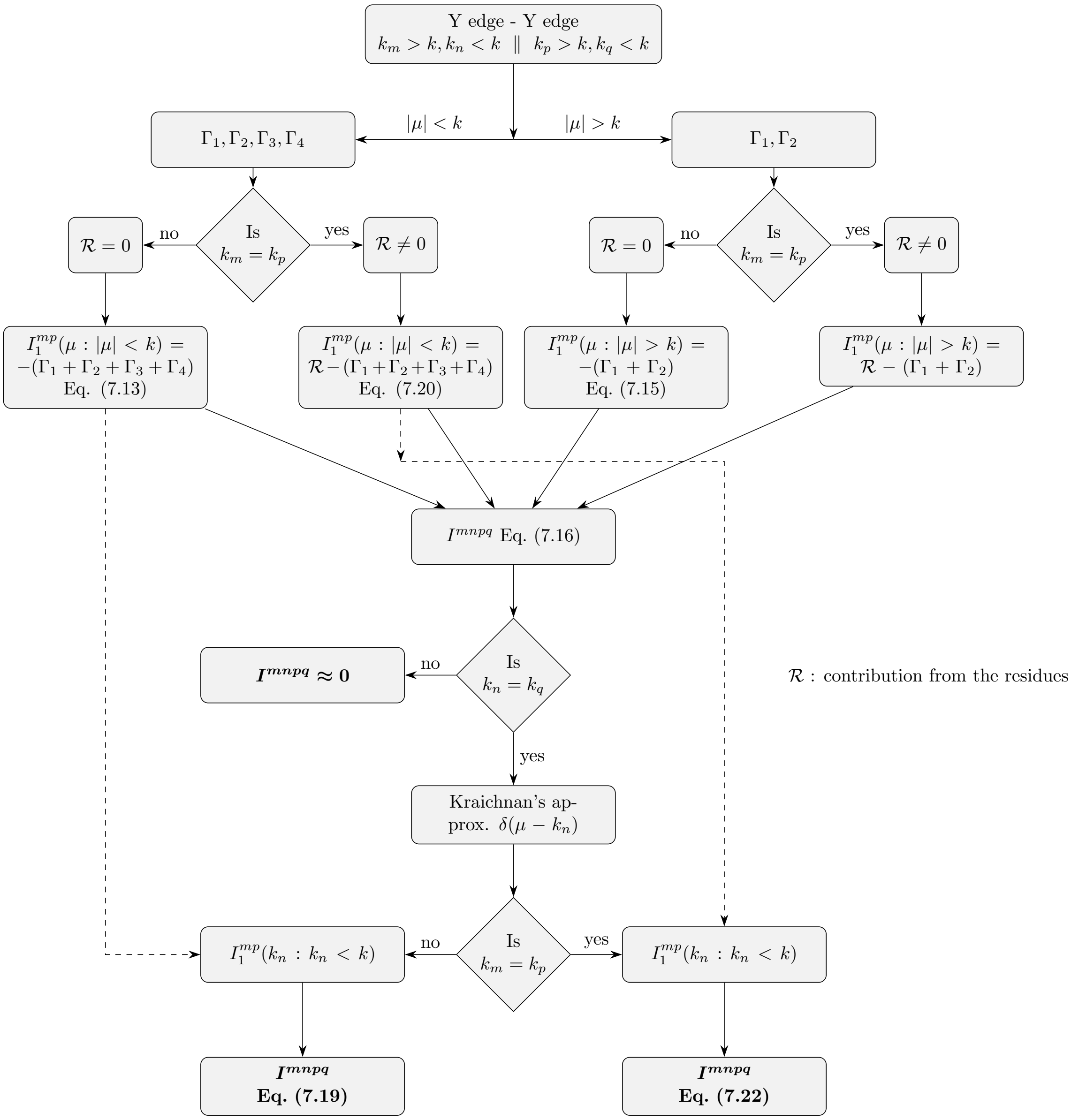

Fig. 7.11 A flow chart depicting the derivation of I^{mnpq} for the Y edge - Y dege interaction.

$k_m = k_p$ and $k_n = k_q$

In this case, the poles of the integrand of $I_1^{mp}(\mu)$ (Eq. (7.6)) are at $\lambda = \pm k_m$ and are of multiplicity two. The residues at the poles when $k_m = k_p$ are evaluated in the Appendix M and are given below.

$$\mathrm{Res}(-k_m) = \mathrm{Res}(k_m) = \frac{a\,\left|\lambda_1^2 - k_m^2\right|^{1/2}}{4\,k_m^2}.$$

Thus, for case 1, the contour integration around the branch cut as shown in Fig. 7.9 (note that for this case $k_m = k_p$ in the figure) results in

$$\mathrm{P}\left[I_1^{mp}(\mu)\right] = I_1^{mp}(\mu : |\mu| < k) = \pi\mathrm{i}\left[\mathrm{Res}(k_m) + \mathrm{Res}(-k_m)\right] - (\Gamma_1 + \Gamma_2 + \Gamma_3 + \Gamma_4).$$

Substituting for the residues and the Γ_i's from Eq. (7.11) we obtain

$$\begin{aligned} I_1^{mp}(\mu : |\mu| < k) = 2 \int_0^{\lambda_1} \frac{\left[1 - (-1)^m \cos ax\right] \left|\lambda_1^2 - x^2\right|^{1/2}}{\left(x^2 - k_m^2\right)^2} \,\mathrm{d}x \\ - 2\,\mathrm{i} \left[\frac{-\pi a \left|\lambda_1^2 - k_m^2\right|^{1/2}}{4\,k_m^2} + \int_0^{\lambda_1} \frac{(-1)^m \sin ax \left|\lambda_1^2 - x^2\right|^{1/2}}{\left(x^2 - k_m^2\right)^2} \,\mathrm{d}x \right. \\ \left. + \int_0^{\infty} \frac{\left[1 - (-1)^m \mathrm{e}^{-ay}\right] \left|\lambda_1^2 + y^2\right|^{1/2}}{\left(y^2 + k_m^2\right)^2} \,\mathrm{d}y \right]. \end{aligned} \tag{7.20}$$

Using Kraichnan's assumption (Eq. (7.17)) and knowing that $k_n < k$ we get

$$I^{mnpq} \approx \frac{\pi b}{2k_n^2}\, I_1^{mp}(k_n : k_n < k), \tag{7.21}$$

where $I_1^{mp}(k_n : k_n < k)$ is evaluated using Eq. (7.20). A detailed derivation of I^{mnpq} when $k_m = k_p$ and $k_n = k_q$ is given in Appendix O.1. The result is summarized below.

$$I^{mnpq} = I_R^{mnpq} + \mathrm{i}\, I_\chi^{mnpq}, \tag{7.22}$$

where the real part of I^{mnpq} is given by

$$I_R^{mnpq} \approx \frac{\pi^2 b}{2k_n^2}\left[\frac{\lambda_1^2}{2k_m^3\sqrt{k_m^2-\lambda_1^2}} - \frac{\lambda_1(-1)^m J_1\left(a\lambda_1\right)}{a\left(k_m^2-\lambda_1^2\right)^2}\right]\delta_{mp}\,\delta_{nq}$$

and the imaginary part of I^{mnpq} is given by

$$I_\chi^{mnpq} \approx \left[-\frac{\pi b}{k_n^2}(A+B+C)+D\right]\delta_{mp}\,\delta_{nq}$$

with

$$A = \frac{\pi\lambda_1(-1)^m \mathrm{H}_1\left(a\lambda_1\right)}{2a\left(\lambda_1^2-k_m^2\right)^2},$$

$$B = \frac{2k\sqrt{2k^2-k_n^2}+(k^2-k_n^2)\log\left(\frac{\left(\sqrt{2k^2-k_n^2}+k\right)^2}{k^2-k_n^2}\right)}{4k_m^4} + \frac{1}{2\left(k^2+k_m^2\right)},$$

$$C = \frac{(-1)^{m+1}}{12ak_m^4}\left\{2\sqrt{\frac{1}{a^2}+k^2-k_n^2} - \left(k^2-k_n^2\right)\right.$$
$$\left.\times\left[-4a^2\sqrt{k^2-k_n^2}+4a^2\sqrt{\frac{1}{a^2}+k^2-k_n^2}-3a\log\left(\frac{\left(\sqrt{\frac{1}{a^2}+k^2-k_n^2}+\frac{1}{a}\right)^2}{k^2-k_n^2}\right)\right]\right\}$$

$$\text{and } D = \frac{\pi^2 ab\sqrt{k_m^2-\lambda_1^2}}{4k_m^2k_n^2}.$$

For all the cases when $k_n \neq k_q$, it is assumed that $I^{mnpq} \approx 0$ (see Appendix P).

7.3.2 X edge - X edge modes ($k_m, k_p < k$ and $k_n, k_q > k$)

For the two instances, when $k_m = k_p < k$ and $k_n \neq k_q > k$ and when $k_m = k_p < k$ and $k_n = k_q > k$, the integral I^{mnpq} can be obtained from Eqs. (7.19) and (7.22), respectively, with the transformation rule

$$m \leftrightarrow n, p \leftrightarrow q \text{ and } a \leftrightarrow b.$$

And for all the cases, when $k_m \neq k_p$, it is assumed that $I^{mnpq} \approx 0$.

7.3.3 Acoustically fast (AF) - Y edge modes ($k_m, k_n, k_q < k$, $k_p > k$ and $k_m^2 + k_n^2 < k^2$)

The derivation of I^{mnpq} for the AF - Y edge interaction is outlined in Fig. 7.12. The integral I^{mnpq} can be evaluated using Eq. (7.16). Prior to this, integral forms of the terms $I_1^{mp}(\mu : |\mu| < k)$ (case 1) and $I_1^{mp}(\mu : |\mu| > k)$ (case 2) for the AF - Y edge interaction have to be obtained.

Case 1 ($|\mu| < k$)

The $|\mu| < k$ region is divided into two: (a) when $\lambda_1 < k_m$ and (b) when $\lambda_1 > k_m$, where $\lambda_1 = \sqrt{k^2 - \mu^2}$ [34].

(a) $\boldsymbol{\lambda_1 < k_m}$
$\lambda_1 < k_m$ implies that $k^2 - \mu^2 < k_m^2$, i.e., $\mu^2 > k^2 - k_m^2$. Therefore in this region

$$\sqrt{k^2 - k_m^2} < |\mu| < k.$$

As $\lambda_1 < k_m$, the integration contour for $I_1^{mp}(\mu)$ (Eq. (7.6)) is the same as that shown in Fig. 7.9, except that $\lambda_1 < k_m < k$. Therefore, using Eq. (7.13)

$$I_1^{mp}(\mu : \sqrt{k^2 - k_m^2} < |\mu| < k) = 2 \int_0^{\lambda_1} \frac{\left[1 - (-1)^m \cos ax\right] \left|\lambda_1^2 - x^2\right|^{1/2}}{\left(x^2 - k_m^2\right)\left(x^2 - k_p^2\right)} \mathrm{d}x$$
$$- 2\,\mathrm{i} \left[\int_0^{\lambda_1} \frac{(-1)^m \sin ax \left|\lambda_1^2 - x^2\right|^{1/2}}{\left(x^2 - k_m^2\right)\left(x^2 - k_p^2\right)} \mathrm{d}x + \int_0^{\infty} \frac{\left[1 - (-1)^m \mathrm{e}^{-ay}\right] \left|\lambda_1^2 + y^2\right|^{1/2}}{\left(y^2 + k_m^2\right)\left(y^2 + k_p^2\right)} \mathrm{d}y \right]. \quad (7.23)$$

(b) $\boldsymbol{\lambda_1 > k_m}$
$\lambda_1 > k_m$ implies that $k^2 - \mu^2 > k_m^2$, i.e., $\mu^2 < k^2 - k_m^2$. Therefore in this region

$$|\mu| < \sqrt{k^2 - k_m^2}$$

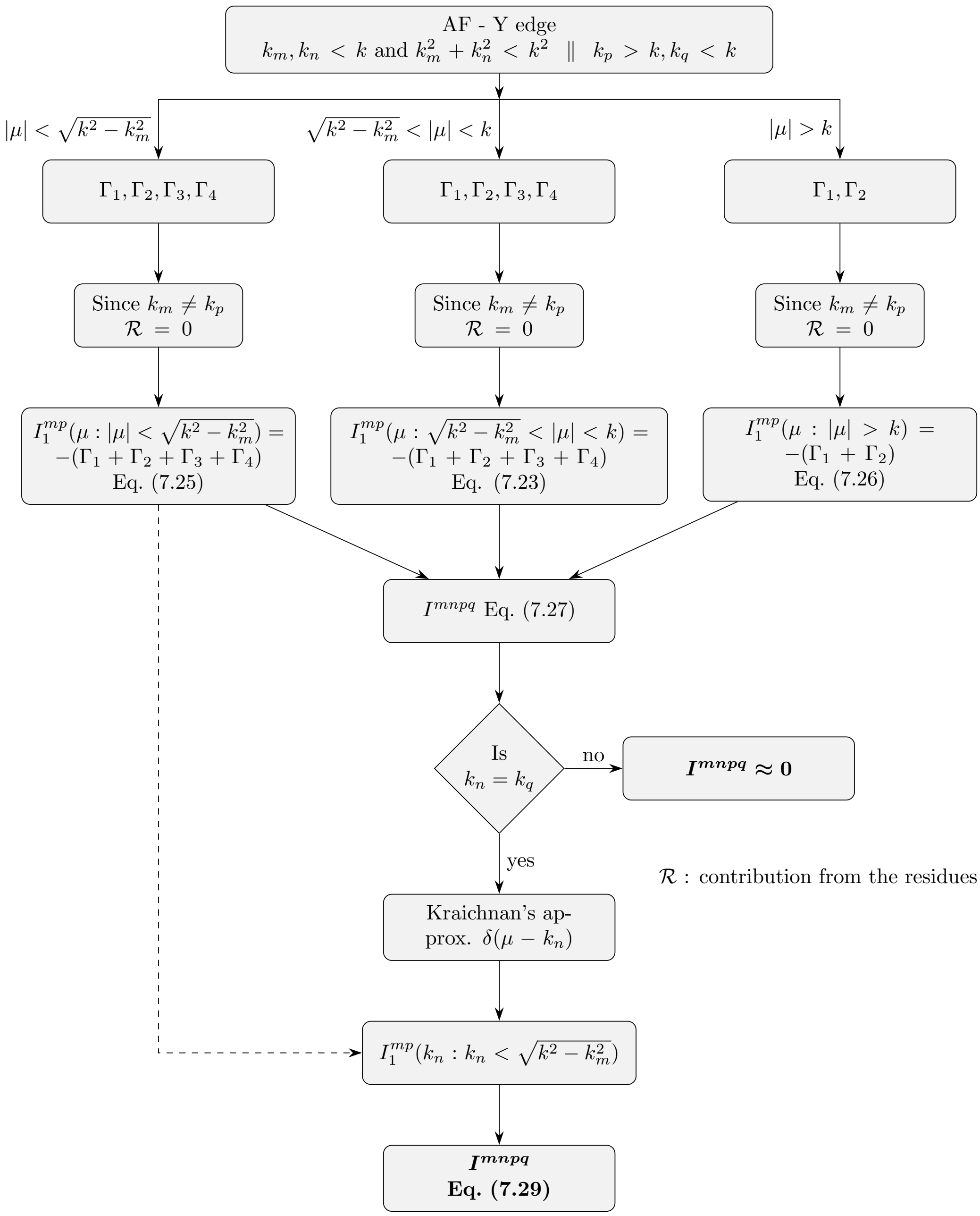

Fig. 7.12 A flow chart depicting the derivation of I^{mnpq} for the AF - Y edge interaction.

and since k_m is on the branch cut, Eq. (7.6) is used to evaluate $I_1^{mp}(\mu)$. The integration contour is shown in Fig. 7.13. Now, using the Cauchy residue theorem we get

$$\begin{aligned} \mathrm{P}\left[I_1^{mp}(\mu)\right] &= I_1^{mp}(\mu : |\mu| < \sqrt{k^2 - k_m^2}) \\ &= \pi\mathrm{i}\left[\mathrm{Res}(k_m) + \mathrm{Res}(k_p) + \mathrm{Res}(-k_m) + \mathrm{Res}(-k_p)\right] - (\Gamma_1 + \Gamma_2 + \Gamma_3 + \Gamma_4), \end{aligned}$$

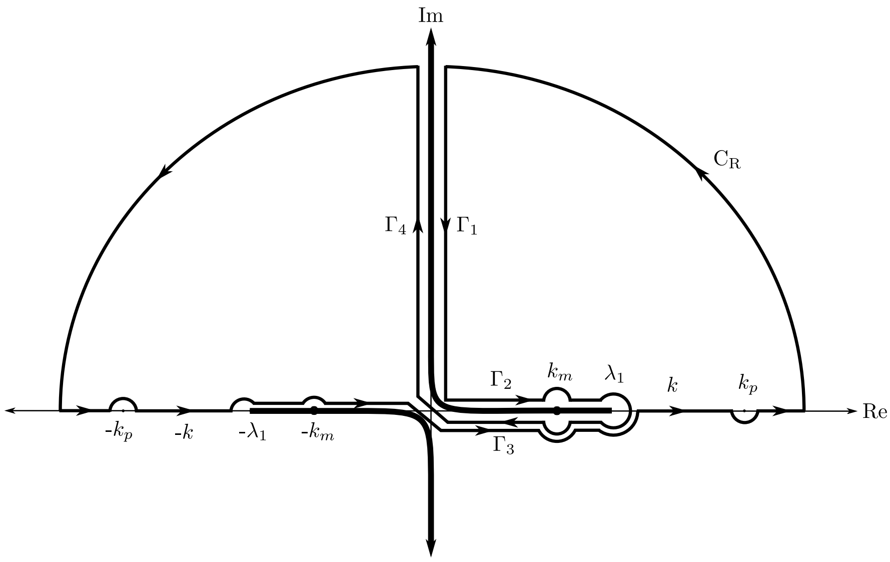

Fig. 7.13 Integration contour of $I_1^{mp}(\mu)$ for the AF - Y edge modal interaction when $k_m < \lambda_1 < k_p$.

where the residues are evaluated at the specified poles using the appropriate form of the square root function defined in Eq. (7.9). It is important to mention that for the residue at $\lambda = k_m$, the value of the square root function in the first quadrant ($\mathrm{Re}(\lambda) > 0$ and $\mathrm{Im}(\lambda) > 0$) is used and for residue at $\lambda = -k_m$, the value of the square root function in the second quadrant ($\mathrm{Re}(\lambda) < 0$ and $\mathrm{Im}(\lambda) > 0$) is used. The integrals $\Gamma_1, \Gamma_2, \Gamma_3$ and Γ_4 are derived in Appendix M and the final forms are given below.

$$
\begin{aligned}
\Gamma_1 &= \mathrm{i}\int_0^{\infty} \frac{\left[1-(-1)^m\ \mathrm{e}^{-ay}\right]\,\left|\lambda_1^2+y^2\right|^{1/2}}{\left(y^2+k_m^2\right)\,\left(y^2+k_p^2\right)}\,\mathrm{d}y,\\
\Gamma_2 &= -\mathrm{P}_{k_m}\int_0^{\lambda_1} \frac{\left[1-(-1)^m\ \mathrm{e}^{\mathrm{i}ax}\right]\,\left|\lambda_1^2-x^2\right|^{1/2}}{\left(x^2-k_m^2\right)\,\left(x^2-k_p^2\right)}\,\mathrm{d}x,\\
\Gamma_3 &= -\mathrm{P}_{k_m}\int_0^{\lambda_1} \frac{\left[1-(-1)^m\ \mathrm{e}^{\mathrm{i}ax}\right]\,\left|\lambda_1^2-x^2\right|^{1/2}}{\left(x^2-k_m^2\right)\,\left(x^2-k_p^2\right)}\,\mathrm{d}x\\
\text{and}\quad \Gamma_4 &= \mathrm{i}\int_0^{\infty} \frac{\left[1-(-1)^m\ \mathrm{e}^{-ay}\right]\,\left|\lambda_1^2+y^2\right|^{1/2}}{\left(y^2+k_m^2\right)\,\left(y^2+k_p^2\right)}\,\mathrm{d}y,
\end{aligned}
\tag{7.24}
$$

Note that while finding Γ_2 and Γ_3, the principal value of the integrals with respect to $x = k_m$ has to be considered and it is denoted as P_{k_m} in the above equation. It is shown in the Appendix M that when $k_m \neq k_p$, the residues at simple poles $k_m, k_p, -k_m$

and $-k_p$ identically goes to zero. Hence,

$$I_1^{mp}(\mu : |\mu| < \sqrt{k^2 - k_m^2}) = -(\Gamma_1 + \Gamma_2 + \Gamma_3 + \Gamma_4).$$

Substituting for $\Gamma_1, \Gamma_2, \Gamma_3$ and Γ_4 and rearranging we get

$$\begin{aligned} I_1^{mp}(\mu : |\mu| < \sqrt{k^2 - k_m^2}) &= 2\,\mathrm{P}_{k_m} \int_0^{\lambda_1} \frac{[1 - (-1)^m \cos ax]\, |\lambda_1^2 - x^2|^{1/2}}{(x^2 - k_m^2)\left(x^2 - k_p^2\right)}\, \mathrm{d}x \\ &- 2\,\mathrm{i} \left[\mathrm{P}_{k_m} \int_0^{\lambda_1} \frac{(-1)^m \sin ax\, |\lambda_1^2 - x^2|^{1/2}}{(x^2 - k_m^2)\left(x^2 - k_p^2\right)}\, \mathrm{d}x + \int_0^{\infty} \frac{[1 - (-1)^m\, \mathrm{e}^{-ay}]\, |\lambda_1^2 + y^2|^{1/2}}{(y^2 + k_m^2)\left(y^2 + k_p^2\right)}\, \mathrm{d}y \right]. \end{aligned} \tag{7.25}$$

Case 2 ($|\mu| > k$)

The integration contour for $I_1^{mp}(\mu)$ when $|\mu| > k$ is the same as that shown in Fig. 7.10, except that $k_m < k$. Therefore, using Eq. (7.15)

$$I_1^{mp}(\mu : |\mu| > k) = -2\,\mathrm{i} \int_{\lambda_1'}^{\infty} \frac{[1 - (-1)^m\, \mathrm{e}^{-ay}]\, \left|\lambda_1'^2 - y^2\right|^{1/2}}{(y^2 + k_m^2)\left(y^2 + k_p^2\right)}\, \mathrm{d}y. \tag{7.26}$$

Integral I^{mnpq}

I^{mnpq} (Eq. (7.16)) is now modified for the AF - Y edge interaction as

$$\begin{aligned} I^{mnpq} &= 2 \int_0^{\sqrt{k^2 - k_m^2}} \frac{[1 - (-1)^n \cos \mu b]}{(\mu^2 - k_n^2)\left(\mu^2 - k_q^2\right)}\, I_1^{mp}(\mu : |\mu| < \sqrt{k^2 - k_m^2})\, \mathrm{d}\mu \\ &+ 2 \int_{\sqrt{k^2 - k_m^2}}^{k} \frac{[1 - (-1)^n \cos \mu b]}{(\mu^2 - k_n^2)\left(\mu^2 - k_q^2\right)}\, I_1^{mp}(\mu : \sqrt{k^2 - k_m^2} < |\mu| < k)\, \mathrm{d}\mu \\ &+ 2 \int_k^{\infty} \frac{[1 - (-1)^n \cos \mu b]}{(\mu^2 - k_n^2)\left(\mu^2 - k_q^2\right)}\, I_1^{mp}(\mu : |\mu| > k)\, \mathrm{d}\mu, \end{aligned} \tag{7.27}$$

where $I_1^{mp}(\mu : |\mu| < \sqrt{k^2 - k_m^2})$, $I_1^{mp}(\mu : \sqrt{k^2 - k_m^2} < |\mu| < k)$ and $I_1^{mp}(\mu : |\mu| > k)$ can be evaluated using Eqs. (7.25), (7.23) and (7.26), respectively.

Assume that $k_n = k_q < k$, and we have $k_m < k$, $k_p > k$ and $k_m^2 + k_n^2 < k^2$. Now, substituting the Kraichnan's approximation (Eq. (7.17)) into Eq. (7.27) and using the fact that $\mu = k_n < \sqrt{k^2 - k_m^2}$ we find that only the first term applies, i.e.,

$$I^{mnpq} \approx \frac{\pi b}{2k_n^2} I_1^{mp}(k_n : k_n < \sqrt{k^2 - k_m^2}), \tag{7.28}$$

where $I_1^{mp}(k_n : k_n < \sqrt{k^2 - k_m^2})$ can be evaluated using Eq. (7.25). A detailed derivation of I^{mnpq} is given in Appendix O.2 and the result is given below.

$$I^{mnpq} \approx (A+B+C)\,\delta_{nq}, \tag{7.29}$$

where

$$A = -\frac{\pi b}{k_n^2}\left[\frac{\pi\lambda_1(-1)^m \mathrm{J}_1(a\lambda_1)}{2a\left(\lambda_1^2-k_m^2\right)\left(\lambda_1^2-k_p^2\right)} + \frac{\pi\left(k_m\sqrt{k_p^2-\lambda_1^2} - \mathrm{i}k_p\sqrt{\lambda_1^2-k_m^2}\right)}{2k_m^3 k_p - 2k_m k_p^3}\right],$$

$$B = \frac{\mathrm{i}\pi^2 b\lambda_1(-1)^{m+1}\mathrm{H}_1(a\lambda_1)}{2ak_n^2\left(\lambda_1^2-k_m^2\right)\left(\lambda_1^2-k_p^2\right)}$$

and

$$C = -\frac{\mathrm{i}\pi b}{k_n^2}\left[\frac{C_1 k_m + 2(\pi+C_2)\sqrt{k^2-k_m^2-k_n^2}}{4k_m k_p^2} + \frac{\log\left(\frac{k^2+k_p^2}{k^2+k_m^2}\right)}{2\left(k_p^2-k_m^2\right)} + \frac{(-1)^m C_3}{2k_m k_p^2} + \frac{(-1)^m\left(C_4 - aC_5\sqrt{k^2-k_m^2-k_n^2}\right)}{2k_p^2}\right]$$

with

$$C_1 = 2\tanh^{-1}\left(\frac{4kk_m^2\left(\sqrt{2k^2-k_n^2}+k\right)}{4k_m^2\left[k\left(\sqrt{2k^2-k_n^2}+2k\right)-k_n^2\right] + \left[k\left(2\sqrt{2k^2-k_n^2}+3k\right)-k_n^2\right]\left(k^2-k_n^2\right)}\right) + \log\left(\frac{-4k_m^2\left[k_n^2 - k\left(2\sqrt{2k^2-k_n^2}+3k\right)\right] - 2k\left(2\sqrt{2k^2-k_n^2}+5k\right)k_n^2}{\left(k^2-k_n^2\right)\left(k^2+4k_m^2-k_n^2\right)} + \frac{k^3\left(12\sqrt{2k^2-k_n^2}+17k\right)+k_n^4}{\left(k^2-k_n^2\right)\left(k^2+4k_m^2-k_n^2\right)}\right),$$

$$C_2 = -\mathrm{i}\,\log\left(\frac{k^4 - 2\mathrm{i}kk_m\sqrt{\left(k_n^2-2k^2\right)\left(-k^2+k_m^2+k_n^2\right)} - 3k^2k_m^2 - k^2k_n^2 + k_m^2k_n^2}{\left(k^2+k_m^2\right)\left(k^2-k_n^2\right)}\right),$$

$$C_3 = k_m\log\left(\frac{k^2-k_n^2}{\left(\sqrt{\frac{1}{a^2}+k^2-k_n^2}+\frac{1}{a}\right)^2}\right) - 2\pi\sqrt{k^2-k_m^2-k_n^2} + \mathrm{i}\sqrt{k^2-k_m^2-k_n^2}\,\log\left(\frac{2\mathrm{i}k_m\sqrt{\left(a^2k^2-a^2k_n^2+1\right)\left(k^2-k_m^2-k_n^2\right)}}{\left(k^2-k_n^2\right)\left(a^2k_m^2+1\right)} + \frac{k_m^2\left(a^2k^2-a^2k_n^2+2\right)-k^2+k_n^2}{\left(k^2-k_n^2\right)\left(a^2k_m^2+1\right)}\right),$$

$$C_4 = 2\left(\sqrt{a^2k^2-a^2k_n^2+1} - a\sqrt{k^2-k_n^2}\right)$$

and

$$C_5 = 2\log\left(\frac{k_m}{\sqrt{\left(k^2-k_n^2\right)\left(k^2-k_m^2-k_n^2\right)}+k^2-k_n^2}\right) + \log\left(\frac{\left(k^2-k_n^2\right)\left[a^2\left(2k^2-k_m^2-2k_n^2\right)+2a\sqrt{\left(a^2k^2-a^2k_n^2+1\right)\left(k^2-k_m^2-k_n^2\right)}+1\right]}{a^2k_m^2+1}\right).$$

For all the cases, when $k_n \neq k_q$, it is assumed that $I^{mnpq} \approx 0$.

7.3.4 Y edge - AF modes ($k_n, k_p, k_q < k$, $k_m > k$ and $k_p^2 + k_q^2 < k^2$)

When $k_n = k_q$, the integral I^{mnpq} can be obtained from Eq. (7.29) using the transformation rule $m \leftrightarrow p$. And for all the cases, when $k_n \neq k_q$, it is assumed that $I^{mnpq} \approx 0$.

7.3.5 AF - X edge modes ($k_m, k_n, k_p < k$, $k_q > k$ and $k_m^2 + k_n^2 < k^2$)

When $k_m = k_p$, the integral I^{mnpq} can be obtained from Eq. (7.29) using the transformation rules $m \leftrightarrow n$, $p \leftrightarrow q$ and $a \leftrightarrow b$. For all the cases, when $k_m \neq k_p$, it is assumed that $I^{mnpq} \approx 0$.

7.3.6 X edge - AF modes ($k_m, k_p, k_q < k$, $k_n > k$ and $k_p^2 + k_q^2 < k^2$)

When $k_m = k_p$, the integral I^{mnpq} can be obtained from Eq. (7.29) using the transformation rules $m \leftrightarrow q$, $p \leftrightarrow n$ and $a \leftrightarrow b$. For all the cases, when $k_m \neq k_p$, it is assumed that $I^{mnpq} \approx 0$.

7.3.7 Y edge - corner modes ($k_m, k_p, k_q > k$ and $k_n < k$)

The derivation of I^{mnpq} for the Y edge - corner interaction is outlined in Fig. 7.14. The general expression for the integral I^{mnpq} is given by Eq. (7.16) as

$$I^{mnpq} = 2\int_0^k \frac{\left[1 - (-1)^n \cos\mu b\right]}{\left(\mu^2 - k_n^2\right)\left(\mu^2 - k_q^2\right)} I_1^{mp}(\mu : |\mu| < k)\,\mathrm{d}\mu \\ + 2\int_k^\infty \frac{\left[1 - (-1)^n \cos\mu b\right]}{\left(\mu^2 - k_n^2\right)\left(\mu^2 - k_q^2\right)} I_1^{mp}(\mu : |\mu| > k)\,\mathrm{d}\mu,$$

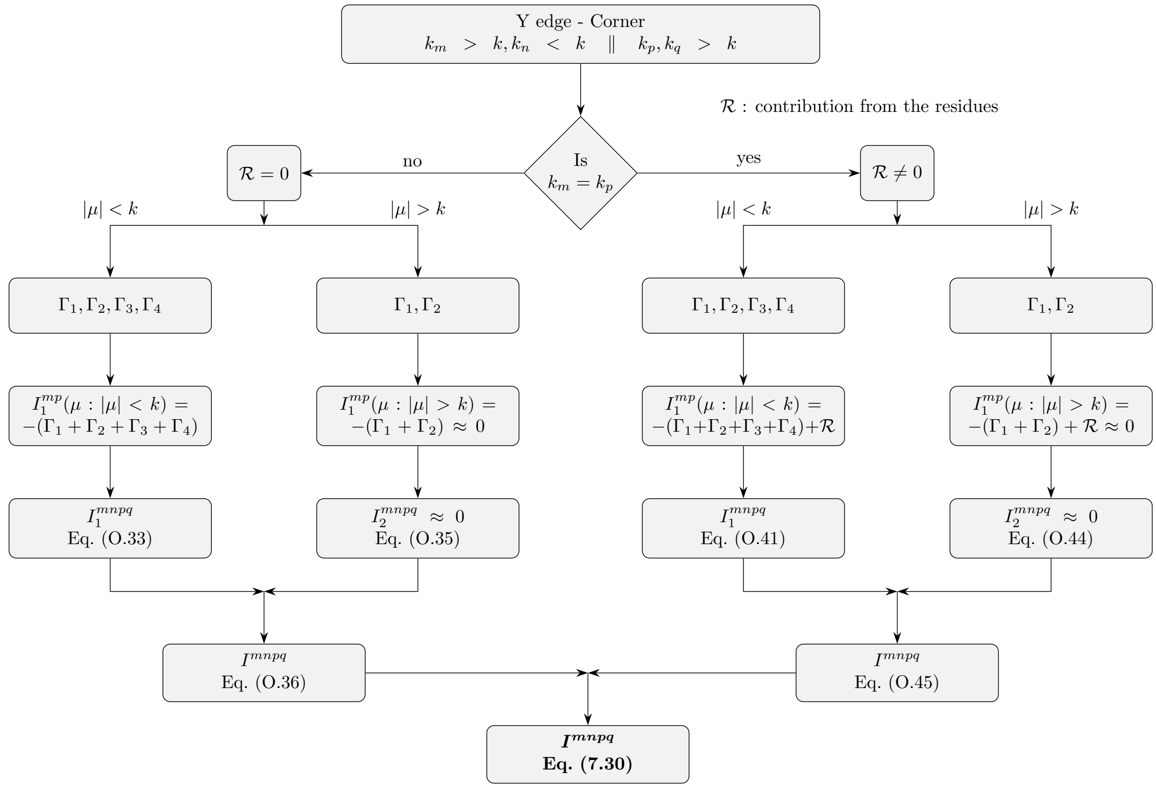

Fig. 7.14 A flow chart depicting the derivation of I^{mnpq} for the Y edge - corner interaction.

where $I_1^{mp}(\mu : |\mu| < k)$ is obtained from Eq. (7.13)

$$
\begin{aligned}
I_1^{mp}(\mu : |\mu| < k) &= 2 \int_0^{\lambda_1} \frac{\left[1 - (-1)^m \, \cos ax\right] \, \left|\lambda_1^2 - x^2\right|^{1/2}}{\left(x^2 - k_m^2\right) \left(x^2 - k_p^2\right)} \, \mathrm{d}x \\
&- 2\,\mathrm{i} \left[\int_0^{\lambda_1} \frac{(-1)^m \, \sin ax \, \left|\lambda_1^2 - x^2\right|^{1/2}}{\left(x^2 - k_m^2\right) \left(x^2 - k_p^2\right)} \, \mathrm{d}x + \int_0^{\infty} \frac{\left[1 - (-1)^m \, \mathrm{e}^{-ay}\right] \, \left|\lambda_1^2 + y^2\right|^{1/2}}{\left(y^2 + k_m^2\right) \left(y^2 + k_p^2\right)} \, \mathrm{d}y \right]
\end{aligned}
$$

and $I_1^{mp}(\mu : |\mu| > k)$ is evaluated using Eq. (7.15)

$$
I_1^{mp}(\mu : |\mu| > k) = -2\,\mathrm{i} \int_{\lambda_1'}^{\infty} \frac{\left[1 - (-1)^m \, \mathrm{e}^{-ay}\right] \, \left|{\lambda_1'}^2 - y^2\right|^{1/2}}{\left(y^2 + k_m^2\right) \left(y^2 + k_p^2\right)} \, \mathrm{d}y.
$$

Appendix O.3 presents a detailed derivation of I^{mnpq}. Expressions are obtained for two different cases: (a) when $k_m \neq k_p$ and (b) when $k_m = k_p$ and the results can be summarized as given below.

$$I^{mnpq} \approx A\,\delta_{mp} + B, \tag{7.30}$$

where

$$A = \frac{\pi a \left(\pi + 2\mathrm{i}\tanh^{-1}\left(\frac{k_n}{k}\right)\right)}{2k_m k_n k_q^2}$$

and

$$B = \frac{\pi\left[k^2\left(\log\left(\frac{k_n+k}{k-k_n}\right) - i\pi\right) + 2kk_n + k_n^2\left(\log\left(\frac{k-k_n}{k_n+k}\right) + i\pi\right)\right]}{2k_m^2 k_n k_p^2 k_q^2}.$$

7.3.8 X edge - corner modes ($k_n, k_p, k_q > k$ and $k_m < k$)

The integral I^{mnpq} can be obtained from Eq. (7.30) using the transformation rules $m \leftrightarrow n$, $p \leftrightarrow q$ and $a \leftrightarrow b$.

7.3.9 AF - AF modes ($k_m, k_n, k_q, k_p < k$, $k_m^2 + k_n^2 < k^2$ and $k_p^2 + k_q^2 < k^2$)

The derivation of I^{mnpq} for the AF - AF interaction is outlined in Fig. 7.15. I^{mnpq} can be evaluated using Eq. (7.16). For this, the integral forms of the terms $I_1^{mp}(\mu : |\mu| < k)$ (case 1) and $I_1^{mp}(\mu : |\mu| > k)$ (case 2) for the AF - AF interaction have to be obtained.

Case 1 ($|\mu| < k$)

The following derivation assumes that $k_m < k_p$. Further, the region $|\mu| < k$ is divided into three depending on the value of λ_1 $(= \sqrt{k^2 - \mu^2})$: (a) when $\lambda_1 < k_m$, (b) when $k_m < \lambda_1 < k_p$ and (c) when $\lambda_1 > k_p$.

(a) $\boldsymbol{\lambda_1 < k_m}$

$\lambda_1 < k_m$ implies that $k^2 - \mu^2 < k_m^2$, i.e., $\mu^2 > k^2 - k_m^2$. Therefore in this region

$$\sqrt{k^2 - k_m^2} < |\mu| < k.$$

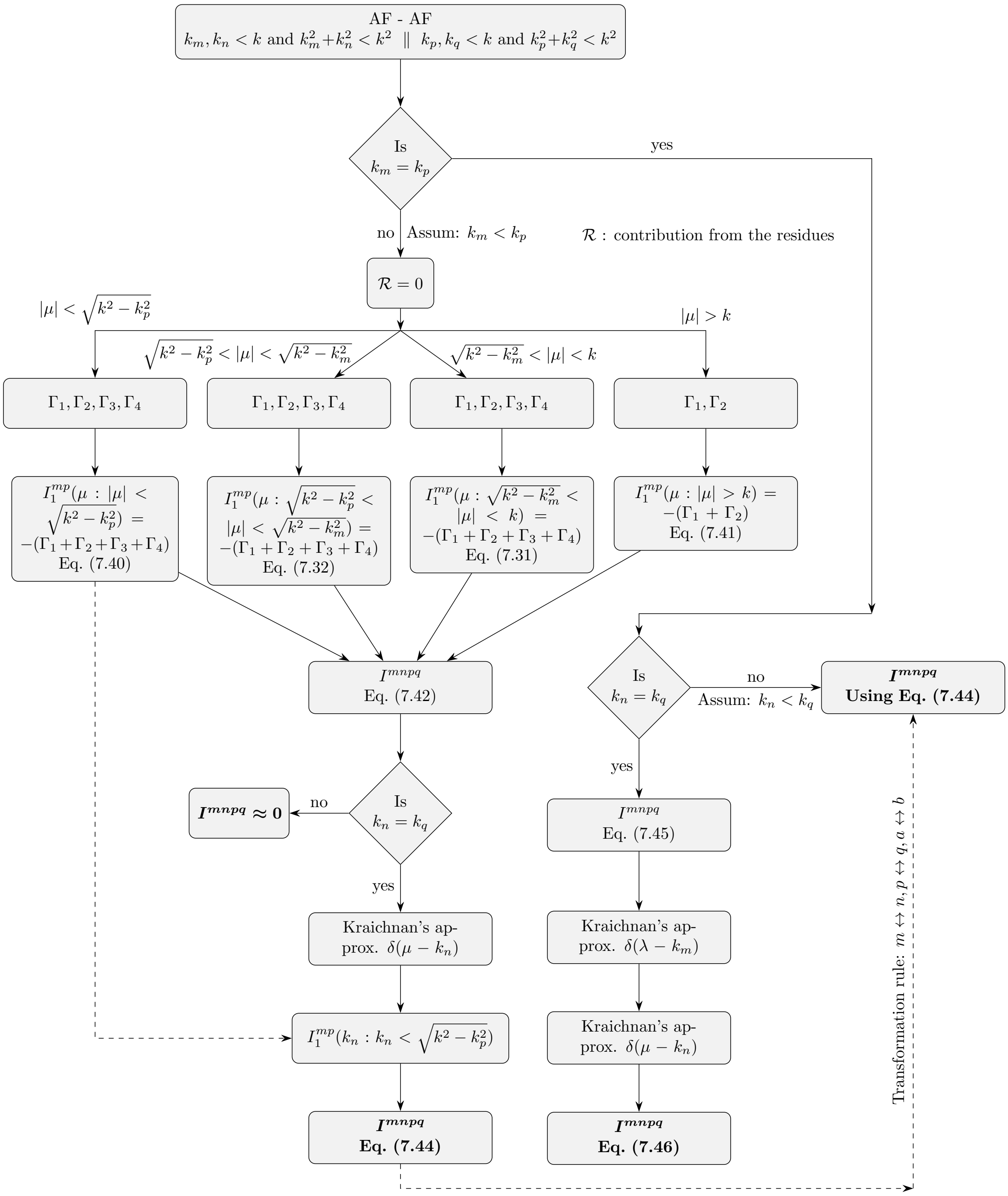

Fig. 7.15 A flow chart depicting the derivation of I^{mnpq} for the AF - AF interaction.

As $\lambda_1 < k_m$, the integration contour for $I_1^{mp}(\mu)$ (Eq. (7.6)) is the same as that shown in Fig. 7.9, except that $\lambda_1 < k_m, k_p < k$. Therefore, using Eq. (7.13)

$$I_1^{mp}(\mu : \sqrt{k^2 - k_m^2} < |\mu| < k) = 2 \int_0^{\lambda_1} \frac{\left[1 - (-1)^m \cos ax\right] \left|\lambda_1^2 - x^2\right|^{1/2}}{\left(x^2 - k_m^2\right)\left(x^2 - k_p^2\right)} \mathrm{d}x$$

$$- 2\,\mathrm{i} \left[\int_0^{\lambda_1} \frac{(-1)^m \sin ax \left|\lambda_1^2 - x^2\right|^{1/2}}{\left(x^2 - k_m^2\right)\left(x^2 - k_p^2\right)} \mathrm{d}x + \int_0^{\infty} \frac{\left[1 - (-1)^m \mathrm{e}^{-ay}\right] \left|\lambda_1^2 + y^2\right|^{1/2}}{\left(y^2 + k_m^2\right)\left(y^2 + k_p^2\right)} \mathrm{d}y \right]. \quad (7.31)$$

(b) $k_m < \lambda_1 < k_p$

$k_m < \lambda_1 < k_p$ implies that $k_m^2 < k^2 - \mu^2 < k_p^2$, i.e., $k^2 - k_p^2 < \mu^2 < k^2 - k_m^2$. Therefore in this region

$$\sqrt{k^2 - k_p^2} < |\mu| < \sqrt{k^2 - k_m^2}.$$

The integration contour for evaluating $I_1^{mp}(\mu)$ (Eq. (7.6)) is the same as that shown in Fig. 7.13, except that $\lambda_1 < k_p < k$. Therefore, using Eq. (7.25)

$$\begin{aligned} I_1^{mp}\left(\mu : \sqrt{k^2 - k_p^2} < |\mu| < \sqrt{k^2 - k_m^2}\right) &= 2\,\mathrm{P}_{k_m} \int_0^{\lambda_1} \frac{\left[1 - (-1)^m \cos ax\right] \left|\lambda_1^2 - x^2\right|^{1/2}}{\left(x^2 - k_m^2\right)\left(x^2 - k_p^2\right)}\,\mathrm{d}x \\ &- 2\,\mathrm{i}\left[\mathrm{P}_{k_m} \int_0^{\lambda_1} \frac{(-1)^m \sin ax \left|\lambda_1^2 - x^2\right|^{1/2}}{\left(x^2 - k_m^2\right)\left(x^2 - k_p^2\right)}\,\mathrm{d}x + \int_0^{\infty} \frac{\left[1 - (-1)^m\, \mathrm{e}^{-ay}\right] \left|\lambda_1^2 + y^2\right|^{1/2}}{\left(y^2 + k_m^2\right)\left(y^2 + k_p^2\right)}\,\mathrm{d}y\right]. \end{aligned} \tag{7.32}$$

(c) $\lambda_1 > k_p$

$\lambda_1 > k_p$ implies that $k^2 - \mu^2 > k_p^2$, i.e., $\mu^2 < k^2 - k_p^2$. Therefore in this region

$$|\mu| < \sqrt{k^2 - k_p^2},$$

and since k_m and k_p are on the branch cut, Eq. (7.6) is used to evaluate $I_1^{mp}(\mu)$. The integration contour is shown in Fig. 7.16. Now, using the Cauchy residue theorem we

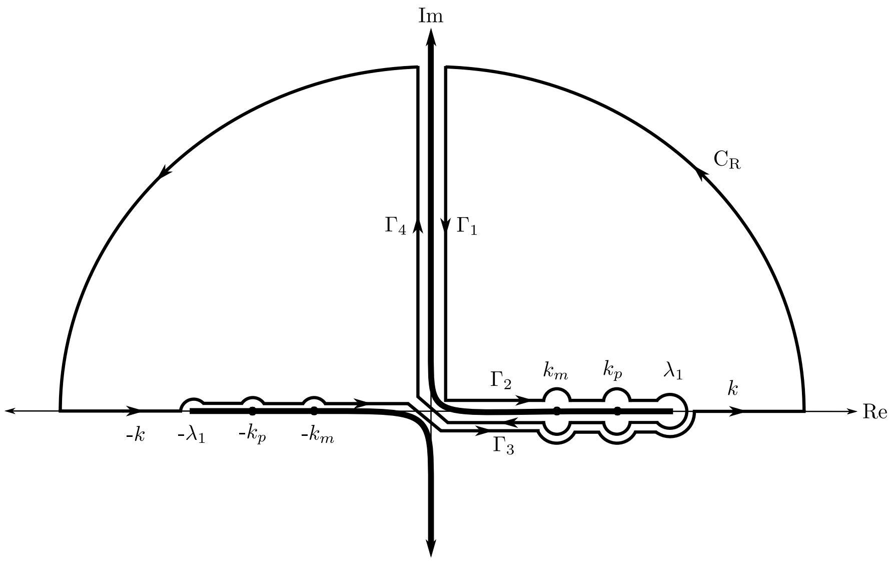

Fig. 7.16 Integration contour of $I_1^{mp}(\mu)$ for the AF - AF modal interaction when $k_m < k_p < \lambda_1$.

get

$$
\begin{aligned}
\mathrm{P}\left[I_1^{mp}(\mu)\right] &= I_1^{mp}\left(\mu : |\mu| < \sqrt{k^2 - k_p^2}\right) \\
&= \pi \mathrm{i}\left[\operatorname{Res}(k_m) + \operatorname{Res}(k_p) + \operatorname{Res}(-k_m) + \operatorname{Res}(-k_p)\right] - (\Gamma_1 + \Gamma_2 + \Gamma_3 + \Gamma_4), \quad (7.33)
\end{aligned}
$$

where the residues are evaluated at the specified poles using the appropriate form of the square root function defined in Eq. (7.9). Note that, while evaluating the residues at $\lambda = k_m$ and $\lambda = k_p$, the value of the square root function in the first quadrant ($\mathrm{Re}(\lambda) > 0$ and $\mathrm{Im}(\lambda) > 0$) is used and while evaluating the residues at $\lambda = -k_m$ and $\lambda = -k_p$, the value of the square root function in the second quadrant ($\mathrm{Re}(\lambda) < 0$ and $\mathrm{Im}(\lambda) > 0$) is used.

The residues are evaluated in the similar way as explained in the Appendix M. It can be deduced from Appendix M that when $k_m \neq k_p$, the residues at $\lambda = \pm k_m$ and $\lambda = \pm k_p$ are identically equal to zero. Therefore, when $k_m \neq k_p$

$$
\operatorname{Res}(k_m) + \operatorname{Res}(k_p) + \operatorname{Res}(-k_m) + \operatorname{Res}(-k_p) = 0. \quad (7.34)
$$

When $k_m = k_p$, the poles at $\lambda = \pm k_m$ are of order two. As mentioned before, while evaluating the residue at $\lambda = k_m$, the definition of the square root function in the first quadrant (from Eq. (7.9)) has to be used. It can be seen from Figs. 7.4 and 7.16 that near $\lambda = k_m$, $\gamma = 2\pi$ and $\theta = 0$. Thus,

$$
\left(\lambda_1^2 - \lambda^2\right)^{1/2} = \left|\lambda_1^2 - \lambda^2\right|^{1/2} \mathrm{e}^{\mathrm{i}\,(\gamma+\theta)/2} = -\left|\lambda_1^2 - \lambda^2\right|^{1/2}.
$$

Therefore,

$$
\operatorname{Res}(k_m) = -\frac{\mathrm{d}}{\mathrm{d}\lambda}\left[\frac{\left[1 - (-1)^m \,\mathrm{e}^{\mathrm{i}\lambda a}\right] \left|\lambda_1^2 - \lambda^2\right|^{1/2}}{(\lambda + k_m)^2}\right]\Bigg|_{\lambda = k_m}.
$$

Thus, knowing that $k_m = m\pi/a$ we get

$$
\operatorname{Res}(k_m) = \frac{\mathrm{i}a \left|\lambda_1^2 - k_m^2\right|^{1/2}}{4\,k_m^2}. \quad (7.35)
$$

Now, while evaluating the residue at $\lambda = -k_m$, the definition of the square root function in the second quadrant (from Eq. (7.9)) has to be used. Near $\lambda = -k_m$, we have $\gamma = 2\pi$ and $\theta = 0$ (see Figs. 7.4 and 7.16). Thus,

$$
\left(\lambda_1^2 - \lambda^2\right)^{1/2} = -\left|\lambda_1^2 - \lambda^2\right|^{1/2} \mathrm{e}^{\mathrm{i}\,(\gamma+\theta)/2} = \left|\lambda_1^2 - \lambda^2\right|^{1/2}.
$$

Therefore,

$$\mathrm{Res}(-k_m) = \frac{\mathrm{d}}{\mathrm{d}\lambda}\left[\frac{\left[1-(-1)^m\ \mathrm{e}^{\mathrm{i}\lambda a}\right]\ \left|\lambda_1^2-\lambda^2\right|^{1/2}}{(\lambda-k_m)^2}\right]\Bigg|_{\lambda=-k_m}.$$

Thus, knowing that $k_m = m\pi/a$ we get

$$\mathrm{Res}(-k_m) = -\frac{\mathrm{i}a\ \left|\lambda_1^2-k_m^2\right|^{1/2}}{4\,k_m^2}. \tag{7.36}$$

Therefore, when $k_m = k_p$ (using Eqs. (7.35) and (7.36))

$$\mathrm{Res}(k_m)+\mathrm{Res}(k_p)+\mathrm{Res}(-k_m)+\mathrm{Res}(-k_p) = \mathrm{Res}(k_m)+\mathrm{Res}(-k_m) = 0. \tag{7.37}$$

Hence, for all the cases ($k_m \neq k_p$ or $k_m = k_p$), Eq. (7.33) results in

$$I_1^{mp}\left(\mu : |\mu| < \sqrt{k^2-k_p^2}\right) = -(\Gamma_1+\Gamma_2+\Gamma_3+\Gamma_4), \tag{7.38}$$

where the integrals $\Gamma_1, \Gamma_2, \Gamma_3$ and Γ_4 are derived in Appendix M and the final forms are given below.

$$\begin{aligned}
\Gamma_1 &= \mathrm{i}\int_0^\infty \frac{\left[1-(-1)^m\ \mathrm{e}^{-ay}\right]\ \left|\lambda_1^2+y^2\right|^{1/2}}{\left(y^2+k_m^2\right)\left(y^2+k_p^2\right)}\,\mathrm{d}y,\\
\Gamma_2 &= -\mathrm{P}_{k_m,k_p}\int_0^{\lambda_1} \frac{\left[1-(-1)^m\ \mathrm{e}^{\mathrm{i}ax}\right]\ \left|\lambda_1^2-x^2\right|^{1/2}}{\left(x^2-k_m^2\right)\left(x^2-k_p^2\right)}\,\mathrm{d}x,\\
\Gamma_3 &= -\mathrm{P}_{k_m,k_p}\int_0^{\lambda_1} \frac{\left[1-(-1)^m\ \mathrm{e}^{\mathrm{i}ax}\right]\ \left|\lambda_1^2-x^2\right|^{1/2}}{\left(x^2-k_m^2\right)\left(x^2-k_p^2\right)}\,\mathrm{d}x\\
\text{and}\quad \Gamma_4 &= \mathrm{i}\int_0^\infty \frac{\left[1-(-1)^m\ \mathrm{e}^{-ay}\right]\ \left|\lambda_1^2+y^2\right|^{1/2}}{\left(y^2+k_m^2\right)\left(y^2+k_p^2\right)}\,\mathrm{d}y.
\end{aligned} \tag{7.39}$$

Note that, while finding Γ_2 and Γ_3, the principal value of the integrals with respect to $x = k_m$ and $x = k_p$ have to be considered and it is denoted as P_{k_m,k_p} in the above equation. Substituting for $\Gamma_1, \Gamma_2, \Gamma_3$ and Γ_4 and rearranging we get

$$I_1^{mp}\left(\mu : |\mu| < \sqrt{k^2 - k_p^2}\right) = 2\,\mathrm{P}_{k_m,k_p} \int\limits_0^{\lambda_1} \frac{\left[1 - (-1)^m \cos ax\right] \left|\lambda_1^2 - x^2\right|^{1/2}}{\left(x^2 - k_m^2\right)\left(x^2 - k_p^2\right)}\,\mathrm{d}x$$
$$-2\,\mathrm{i}\left[\mathrm{P}_{k_m,k_p} \int\limits_0^{\lambda_1} \frac{(-1)^m \sin ax \left|\lambda_1^2 - x^2\right|^{1/2}}{\left(x^2 - k_m^2\right)\left(x^2 - k_p^2\right)}\,\mathrm{d}x + \int\limits_0^{\infty} \frac{\left[1 - (-1)^m \mathrm{e}^{-ay}\right] \left|\lambda_1^2 + y^2\right|^{1/2}}{\left(y^2 + k_m^2\right)\left(y^2 + k_p^2\right)}\,\mathrm{d}y\right]. \tag{7.40}$$

Case 2 **($|\mu| > k$)**

The integration contour for $I_1^{mp}(\mu)$ when $|\mu| > k$ is the same as that shown in Fig. 7.10, except that $k_m, k_p < k$. Therefore, using Eq. (7.15)

$$I_1^{mp}(\mu : |\mu| > k) = -2\,\mathrm{i} \int\limits_{\lambda_1'}^{\infty} \frac{\left[1 - (-1)^m \mathrm{e}^{-ay}\right] \left|{\lambda_1'}^2 - y^2\right|^{1/2}}{\left(y^2 + k_m^2\right)\left(y^2 + k_p^2\right)}\,\mathrm{d}y, \tag{7.41}$$

where $\lambda_1' = \sqrt{\mu^2 - k^2}$.

Integral I^{mnpq}

Now, I^{mnpq} (Eq. (7.4)) for the AF - AF modal interaction can be written as

$$\begin{aligned} I^{mnpq} = 2 &\int\limits_0^{\sqrt{k^2-k_p^2}} \frac{\left[1 - (-1)^n \cos \mu b\right]}{\left(\mu^2 - k_n^2\right)\left(\mu^2 - k_q^2\right)}\, I_1^{mp}\left(\mu : |\mu| < \sqrt{k^2 - k_p^2}\right) \mathrm{d}\mu \\ + 2 &\int\limits_{\sqrt{k^2-k_p^2}}^{\sqrt{k^2-k_m^2}} \frac{\left[1 - (-1)^n \cos \mu b\right]}{\left(\mu^2 - k_n^2\right)\left(\mu^2 - k_q^2\right)}\, I_1^{mp}\left(\mu : \sqrt{k^2 - k_p^2} < |\mu| < \sqrt{k^2 - k_m^2}\right) \mathrm{d}\mu \\ + 2 &\int\limits_{\sqrt{k^2-k_m^2}}^{k} \frac{\left[1 - (-1)^n \cos \mu b\right]}{\left(\mu^2 - k_n^2\right)\left(\mu^2 - k_q^2\right)}\, I_1^{mp}\left(\mu : \sqrt{k^2 - k_m^2} < |\mu| < k\right) \mathrm{d}\mu \\ + 2 &\int\limits_{k}^{\infty} \frac{\left[1 - (-1)^n \cos \mu b\right]}{\left(\mu^2 - k_n^2\right)\left(\mu^2 - k_q^2\right)}\, I_1^{mp}(\mu : |\mu| > k)\, \mathrm{d}\mu, \end{aligned} \tag{7.42}$$

where the $I_1^{mp}(\mu)$ terms in the four integrals can be evaluated using Eqs. (7.40), (7.32), (7.31) and (7.41).

(a) $\boldsymbol{k_m \neq k_p}$ and $\boldsymbol{k_n = k_q}$
Assume that $k_n = k_q < k$, and $k_m \neq k_p < k$ ($k_m < k_p$), $k_m^2 + k_n^2 < k^2$ and $k_p^2 + k_q^2 < k^2$. Substituting the Kraichnan's assumption (Eq. (7.17)) into Eq. (7.42) and knowing that $k_n < \sqrt{k^2 - k_p^2}$ we get

$$I^{mnpq} \approx \frac{\pi b}{2k_n^2} I_1^{mp}\left(k_n : k_n < \sqrt{k^2 - k_p^2}\right), \tag{7.43}$$

where $I_1^{mp}\left(k_n : k_n < \sqrt{k^2 - k_p^2}\right)$ can be evaluated using Eq. (7.40). A detailed derivation of I^{mnpq} is given in Appendix O.4 and the result is given below.

$$I^{mnpq} \approx (A + B + C + D)\,\delta_{nq}, \tag{7.44}$$

where

$$A = \frac{\mathrm{i}\pi^2 b\left(k_p\sqrt{\lambda_1^2 - k_m^2} - k_m\sqrt{\lambda_1^2 - k_p^2}\right)}{2k_n^2\left(k_m^3 k_p - k_m k_p^3\right)},$$

$$B = -\frac{\mathrm{i}\pi b}{k_n^2}\left[\frac{\log\left(\frac{k_m^2+\lambda_1^2}{k_p^2+\lambda_1^2}\right)}{2k_m^2 - 2k_p^2} + \frac{\lambda_1\left(k_m\tan^{-1}\left(\frac{\lambda_1}{k_p}\right) - k_p\tan^{-1}\left(\frac{\lambda_1}{k_m}\right)\right)}{k_m^3 k_p - k_m k_p^3}\right],$$

$$C = \frac{\mathrm{i}\pi b\lambda_1(-1)^{m+1}}{2k_m k_n^2 k_p\left(k_m^2 - k_p^2\right)}\left[k_m\left(ak_p\log\left(\frac{k_m^2\left(k_p^2+\lambda_1^2\right)}{k_p^2\left(k_m^2+\lambda_1^2\right)}\right) - 2\tan^{-1}\left(\frac{\lambda_1}{k_p}\right)\right)\right.$$
$$\left. + 2k_p\tan^{-1}\left(\frac{\lambda_1}{k_m}\right)\right]$$

and

$$D = \frac{\mathrm{i}\pi b(-1)^{m+1}}{2k_n^2\left(k_m^2 - k_p^2\right)}\left[2ak_m\left(\tan^{-1}\left(\frac{k}{k_m}\right) - \tan^{-1}\left(\frac{\lambda_1}{k_m}\right)\right)\right.$$
$$\left. + 2ak_p\left(\tan^{-1}\left(\frac{\lambda_1}{k_p}\right) - \tan^{-1}\left(\frac{k}{k_p}\right)\right) + \log\left(\frac{\left(k^2+k_m^2\right)\left(k_p^2+\lambda_1^2\right)}{\left(k^2+k_p^2\right)\left(k_m^2+\lambda_1^2\right)}\right)\right].$$

If $k_m > k_p$ and $k_n = k_q$, I^{mnpq} can be obtained by using the transformation rule $m \leftrightarrow p$ and $n \leftrightarrow q$ on the above equation (remember that I^{mnpq} is symmetric).

(b) $\boldsymbol{k_m = k_p}$ and $\boldsymbol{k_n \neq k_q}$

When $k_m = k_p$ and $k_n \neq k_q$ ($k_n < k_q$), I^{mnpq} can be evaluated using

$$I^{mnpq} \approx \frac{\pi a}{2k_m^2}\, I_1^{nq}\left(k_m : k_m < \sqrt{k^2 - k_q^2}\right),$$

where $I_1^{nq}\left(k_m : k_m < \sqrt{k^2 - k_q^2}\right)$ is obtained from $I_1^{mp}\left(k_n : k_n < \sqrt{k^2 - k_p^2}\right)$ using the transformation rule $m \leftrightarrow n$, $p \leftrightarrow q$ and $a \leftrightarrow b$. The same transformation rule can be used with Eq. (7.44) to obtain the closed form for I^{mnpq}. When $k_n > k_q$ we can use the transformation rule $m \leftrightarrow q$, $p \leftrightarrow n$ and $a \leftrightarrow b$ in Eq. (7.44) instead.

(c) $\boldsymbol{k_m = k_p}$ and $\boldsymbol{k_n = k_q}$

Now, when $k_m = k_p$ and $k_n = k_q$, I^{mnpq} is evaluated using the Kraichnan's approximation [34] for both the λ and μ domains. We have from Eq. (7.4)

$$I^{mnpq} = 4 \int_0^\infty \int_0^\infty \frac{[1-(-1)^m \cos\lambda a]\ [1-(-1)^n \cos\mu b]\ \left(k^2-\lambda^2-\mu^2\right)^{1/2}}{\left(\lambda^2-k_m^2\right)\left(\lambda^2-k_p^2\right)\left(\mu^2-k_n^2\right)\left(\mu^2-k_q^2\right)}\, \mathrm{d}\lambda\, \mathrm{d}\mu. \quad (7.45)$$

When $k_m = k_p$, Kraichnan's assumption leads to

$$\left.\frac{[1-(-1)^m \cos\lambda a]}{\left(\lambda^2-k_m^2\right)\left(\lambda^2-k_p^2\right)}\right|_{m=p} \approx \frac{\pi a}{4k_m^2}\,\delta(\lambda - k_m).$$

Similarly, when $k_n = k_q$

$$\left.\frac{[1-(-1)^n \cos\mu b]}{\left(\mu^2-k_n^2\right)\left(\mu^2-k_q^2\right)}\right|_{n=q} \approx \frac{\pi b}{4k_n^2}\,\delta(\mu - k_n).$$

For $\lambda = k_m$ and $\mu = k_n$ ($k_n < k$ and $k_m < \sqrt{k^2 - k_n^2}$),

$$\left.\left(k^2-\lambda^2-\mu^2\right)^{1/2}\right|_{(\lambda,\mu)=(k_m,k_n)} = \left|k^2-k_m^2-k_n^2\right|^{1/2}.$$

In the above step, a positive sign is chosen for the square root in order to have a positive traveling wave in the z direction. Substituting the above results, Eq. (7.45) can be approximated as

$$\boxed{I^{mnpq} \approx \frac{\pi^2 ab}{4k_m^2 k_n^2}\left|k^2-k_m^2-k_n^2\right|^{1/2}\,\delta_{mp}\,\delta_{nq}. \quad (7.46)}$$

When $k_m \neq k_p$ and $k_n \neq k_q$, it is assumed that $I^{mnpq} \approx 0$ (a similar case for the Y edge - Y edge interaction is explained in Appendix P).

7.3.10 XY edge - XY edge modes ($k_m, k_n, k_p, k_q < k$, $k_m^2+k_n^2 > k^2$ and $k_p^2 + k_q^2 > k^2$)

The derivation of I^{mnpq} for the XY edge - XY edge interaction is outlined in Fig. 7.17.

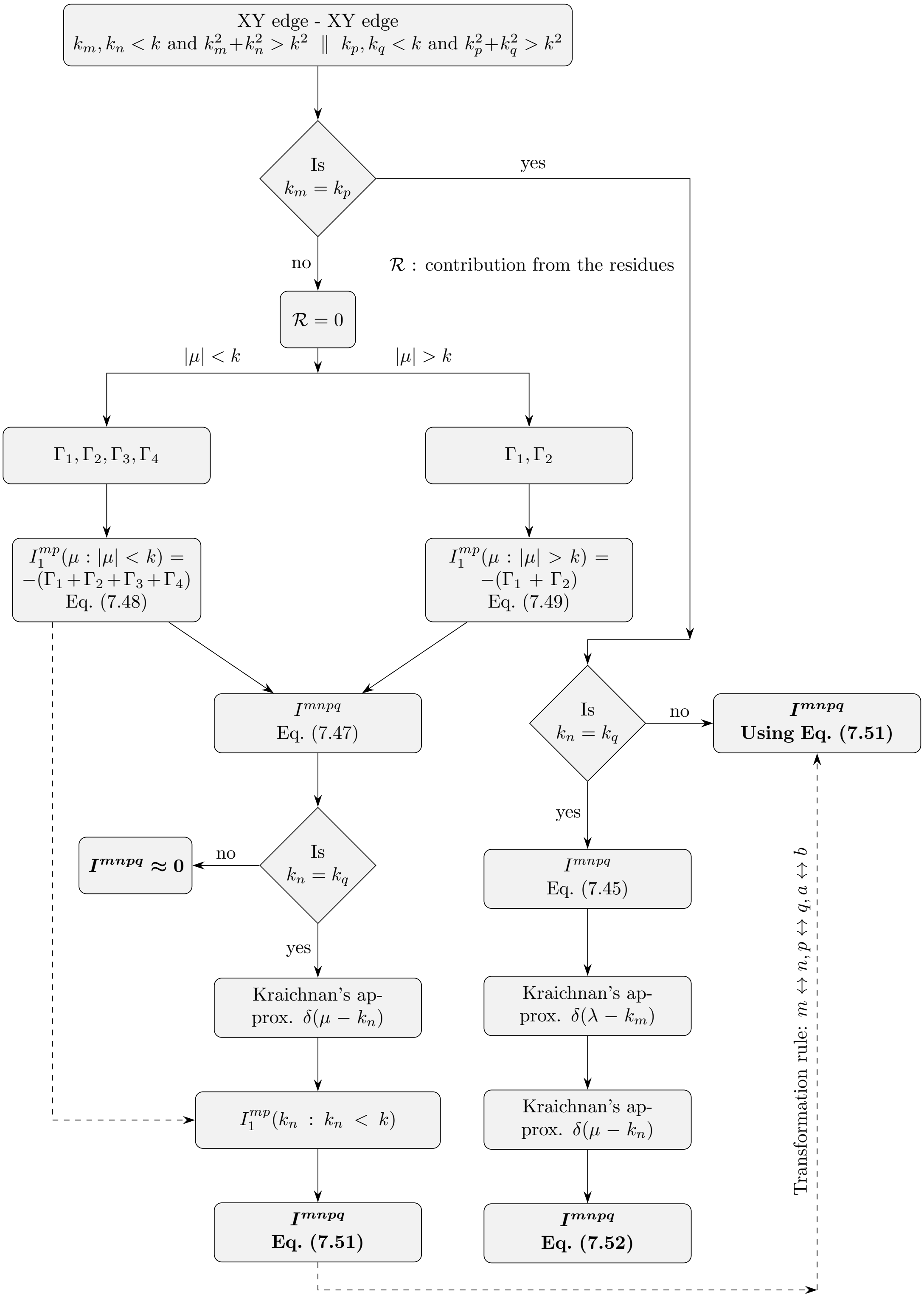

Fig. 7.17 A flow chart depicting the derivation of I^{mnpq} for the XY edge - XY edge interaction.

The working expression for the integral I^{mnpq} is given by (Eq. (7.16))

$$I^{mnpq} = 2 \int_0^k \frac{[1-(-1)^n \cos \mu b]}{(\mu^2 - k_n^2)\left(\mu^2 - k_q^2\right)} I_1^{mp}(\mu : |\mu| < k)\, \mathrm{d}\mu + 2 \int_k^\infty \frac{[1-(-1)^n \cos \mu b]}{(\mu^2 - k_n^2)\left(\mu^2 - k_q^2\right)} I_1^{mp}(\mu : |\mu| > k)\, \mathrm{d}\mu, \quad (7.47)$$

where $I_1^{mp}(\mu : |\mu| < k)$ can be obtained from Eq. (7.13) (assuming $k_m \neq k_p$ and hence the contribution from the poles is zero)

$$I_1^{mp}(\mu : |\mu| < k) = 2 \int_0^{\lambda_1} \frac{[1-(-1)^m \cos ax]\, \left|\lambda_1^2 - x^2\right|^{1/2}}{(x^2 - k_m^2)\left(x^2 - k_p^2\right)} \mathrm{d}x - 2\,\mathrm{i} \left[\int_0^{\lambda_1} \frac{(-1)^m \sin ax\, \left|\lambda_1^2 - x^2\right|^{1/2}}{(x^2 - k_m^2)\left(x^2 - k_p^2\right)} \mathrm{d}x + \int_0^\infty \frac{[1-(-1)^m \,\mathrm{e}^{-ay}]\, \left|\lambda_1^2 + y^2\right|^{1/2}}{(y^2 + k_m^2)\left(y^2 + k_p^2\right)} \mathrm{d}y \right], \quad (7.48)$$

where the first and second integrals on the right hand side have to be evaluated with due consideration of whether $k_m < \lambda_1$ and/or $k_p < \lambda_1$ ($\lambda_1^2 = k^2 - \mu^2$). The term $I_1^{mp}(\mu : |\mu| > k)$ in Eq. (7.47) can be evaluated using Eq. (7.15) (assuming $k_m \neq k_p$ and hence the contribution from the poles is zero)

$$I_1^{mp}(\mu : |\mu| > k) = -2\,\mathrm{i} \int_{\lambda_1'}^\infty \frac{[1-(-1)^m \,\mathrm{e}^{-ay}]\, \left|\lambda_1'^2 - y^2\right|^{1/2}}{(y^2 + k_m^2)\left(y^2 + k_p^2\right)} \mathrm{d}y, \quad (7.49)$$

where $\lambda_1'^2 = \mu^2 - k^2$.

(a) $k_m \neq k_p$ and $k_n = k_q$

Assume that $k_n = k_q < k$, and $k_m \neq k_p < k$. Substituting the Kraichnan's approximation (Eq. (7.17)) into Eq. (7.47) and knowing that $k_n < k$ we get

$$I^{mnpq} \approx \frac{\pi b}{2k_n^2} I_1^{mp}\left(k_n : k_n < k\right), \quad (7.50)$$

where $I_1^{mp}\left(k_n : k_n < k\right)$ can be evaluated using Eq. (7.48) by substituting $\mu = k_n$. Note that, since $k_m, k_p > \lambda_1$ $(= \sqrt{k^2 - k_n^2})$, there exist no regular singularities in the first and second integrals on the right hand side of Eq. (7.48). A detailed derivation of I^{mnpq} is given in Appendix O.5 and the result is given below.

$$I^{mnpq} = I_R^{mnpq} + \mathrm{i}\, I_\chi^{mnpq}, \tag{7.51}$$

where the real part of I^{mnpq} is given by

$$I_R^{mnpq} \approx \frac{\pi^2 b}{2k_n^2}\left[\frac{k_p\sqrt{k_m^2-\lambda_1^2} - k_m\sqrt{k_p^2-\lambda_1^2}}{k_m^3 k_p - k_m k_p^3} - \frac{\lambda_1(-1)^m \mathrm{J}_1\left(a\lambda_1\right)}{a k_m^2 k_p^2}\right]\delta_{nq}$$

and the imaginary part is

$$I_\chi^{mnpq} \approx -\frac{\pi b}{k_n^2}(A+B+C)\,\delta_{nq}$$

with

$$A = \frac{\pi\lambda_1(-1)^m \mathrm{H}_1\left(a\lambda_1\right)}{2a k_m^2 k_p^2},$$

$$B = \frac{2k\sqrt{2k^2-k_n^2} + (k^2-k_n^2)\log\left(\frac{\left(\sqrt{2k^2-k_n^2}+k\right)^2}{k^2-k_n^2}\right)}{4k_m^2 k_p^2} + \frac{\log\left(\frac{k^2+k_p^2}{k^2+k_m^2}\right)}{2\left(k_p^2-k_m^2\right)}$$

and

$$C = \frac{(-1)^{m+1}}{12 a k_m^2 k_p^2}\left\{2\sqrt{\frac{1}{a^2}+k^2-k_n^2} - \left(k^2-k_n^2\right)\right.$$
$$\left.\times\left[-4a^2\sqrt{k^2-k_n^2} + 4a^2\sqrt{\frac{1}{a^2}+k^2-k_n^2} - 3a\log\left(\frac{\left(\sqrt{\frac{1}{a^2}+k^2-k_n^2}+\frac{1}{a}\right)^2}{k^2-k_n^2}\right)\right]\right\}.$$

(b) $\boldsymbol{k_m = k_p}$ and $\boldsymbol{k_n \neq k_q}$

Similarly, when $k_m = k_p$ and $k_n \neq k_q$, I^{mnpq} can be evaluated using

$$I^{mnpq} \approx \frac{\pi a}{2k_m^2}\, I_1^{nq}\left(k_m : k_m < k\right),$$

where $I_1^{nq}\left(k_m : k_m < k\right)$ is obtained from $I_1^{mp}\left(k_n : k_n < k\right)$ using the transformation rule $m \leftrightarrow n$, $p \leftrightarrow q$ and $a \leftrightarrow b$. The same transformation rule can be used with Eq. (7.51) to obtain the closed form for I^{mnpq}.

(c) $\boldsymbol{k_m = k_p}$ and $\boldsymbol{k_n = k_q}$

When $k_m = k_p$ and $k_n = k_q$, I^{mnpq} is evaluated using the Kraichnan's approximation for both λ and μ domains. We have Eq. (7.45)

$$I^{mnpq} = 4 \int_0^\infty \int_0^\infty \frac{[1-(-1)^m \cos\lambda a]\,[1-(-1)^n \cos\mu b]\,\left(k^2-\lambda^2-\mu^2\right)^{1/2}}{\left(\lambda^2-k_m^2\right)\left(\lambda^2-k_p^2\right)\left(\mu^2-k_n^2\right)\left(\mu^2-k_q^2\right)}\,\mathrm{d}\lambda\,\mathrm{d}\mu.$$

When $k_m = k_p$, Kraichnan's assumption leads to

$$\left.\frac{[1-(-1)^m \cos\lambda a]}{\left(\lambda^2-k_m^2\right)\left(\lambda^2-k_p^2\right)}\right|_{m=p} \approx \frac{\pi a}{4k_m^2}\,\delta(\lambda-k_m).$$

Similarly, when $k_n = k_q$,

$$\left.\frac{[1-(-1)^n \cos\mu b]}{\left(\mu^2-k_n^2\right)\left(\mu^2-k_q^2\right)}\right|_{n=q} \approx \frac{\pi b}{4k_n^2}\,\delta(\mu-k_n).$$

For $\lambda = k_m$ and $\mu = k_n$ ($k_n < k$ and $k_m > \sqrt{k^2-k_n^2}$),

$$\left.\left(k^2-\lambda^2-\mu^2\right)^{1/2}\right|_{(\lambda,\mu)=(k_m,k_n)} = \mathrm{i}\,\left|k_m^2+k_n^2-k^2\right|^{1/2}.$$

Above, a positive imaginary solution is chosen in order to have an evanescent wave rather than a growing wave in the z direction. Substituting the above results into Eq. (7.45) we get

$$\boxed{I^{mnpq} \approx \frac{\mathrm{i}\pi^2 ab}{4k_m^2 k_n^2}\,\left|k_m^2+k_n^2-k^2\right|^{1/2}\,\delta_{mp}\,\delta_{nq}. \qquad (7.52)}$$

When $k_m \neq k_p$ and $k_n \neq k_q$, it is assumed that $I^{mnpq} \approx 0$ (a similar case for the Y edge - Y edge interaction is explained in Appendix P).

7.3.11 Corner - corner modes ($k_m, k_n, k_p, k_q > k$)

The derivation of I^{mnpq} for the corner - corner interaction is outlined in Fig. 7.18. The

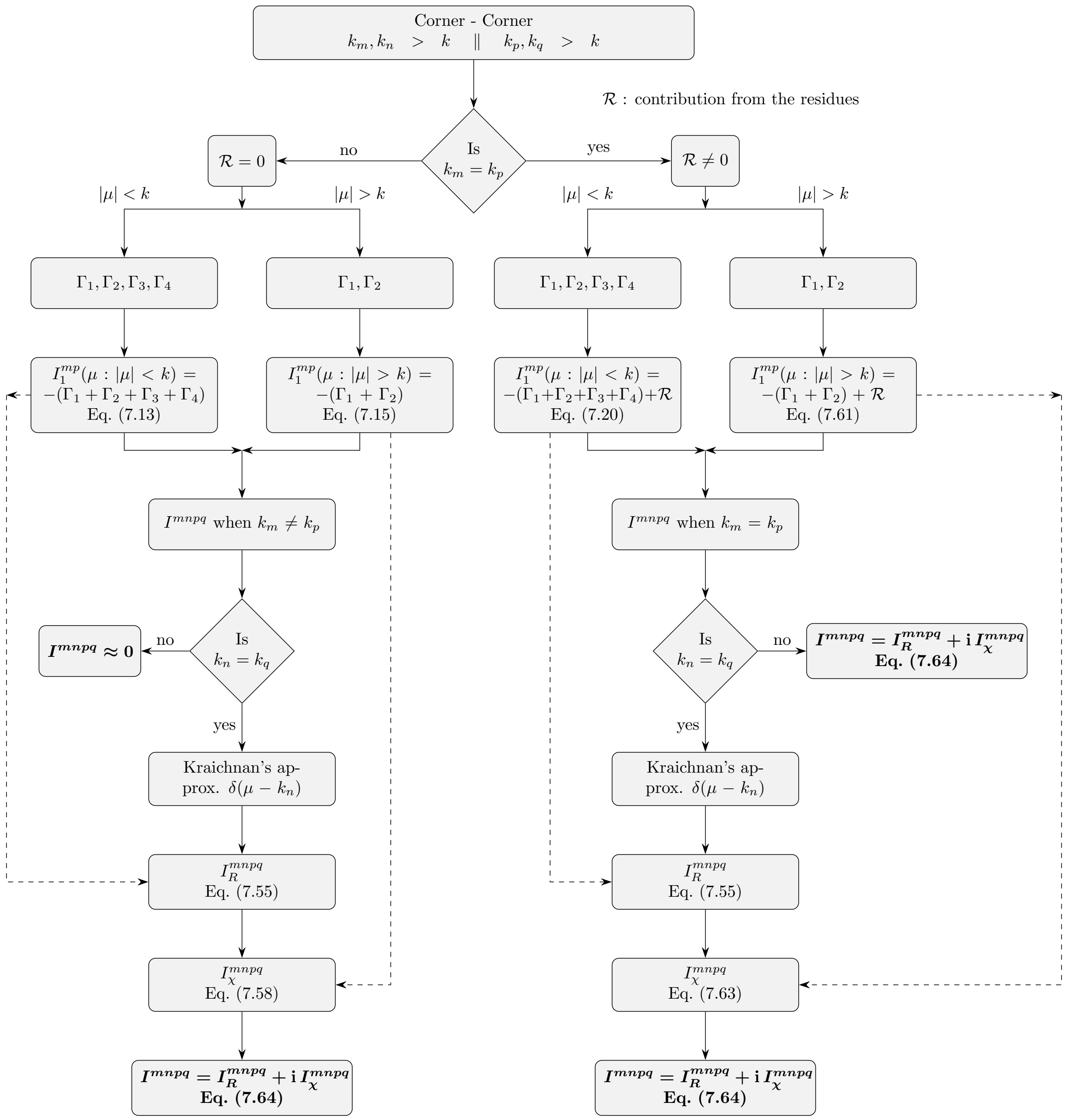

Fig. 7.18 A flow chart depicting the derivation of I^{mnpq} for the corner - corner interaction.

integral I^{mnpq} can be evaluated using Eq. (7.16)

$$I^{mnpq} = 2\int_0^k \frac{[1-(-1)^n \cos\mu b]}{(\mu^2-k_n^2)\left(\mu^2-k_q^2\right)}\, I_1^{mp}(\mu : |\mu| < k)\,\mathrm{d}\mu$$

$$+\,2\int_k^\infty \frac{[1-(-1)^n \cos\mu b]}{(\mu^2-k_n^2)\left(\mu^2-k_q^2\right)}\, I_1^{mp}(\mu : |\mu| > k)\,\mathrm{d}\mu,$$

where $I_1^{mp}(\mu : |\mu| < k)$ is evaluated using Eq. (7.13)

$$I_1^{mp}(\mu : |\mu| < k) = 2 \int_0^{\lambda_1} \frac{\left[1 - (-1)^m \; \cos ax\right] \, |\lambda_1^2 - x^2|^{1/2}}{\left(x^2 - k_m^2\right) \left(x^2 - k_p^2\right)} \, \mathrm{d}x$$

$$- 2\,\mathrm{i} \left[\int_0^{\lambda_1} \frac{(-1)^m \; \sin ax \; |\lambda_1^2 - x^2|^{1/2}}{\left(x^2 - k_m^2\right) \left(x^2 - k_p^2\right)} \, \mathrm{d}x + \int_0^{\infty} \frac{\left[1 - (-1)^m \; \mathrm{e}^{-ay}\right] \, |\lambda_1^2 + y^2|^{1/2}}{\left(y^2 + k_m^2\right) \left(y^2 + k_p^2\right)} \, \mathrm{d}y \right].$$

As $k_m, k_p > \lambda_1$ ($\lambda_1^2 = k^2 - \mu^2$), there exist no regular singularities in the above integrals. The term $I_1^{mp}(\mu : |\mu| > k)$ in Eq. (7.16) can be evaluated using Eq. (7.15)

$$I_1^{mp}(\mu : |\mu| > k) = -2\,\mathrm{i} \int_{\lambda_1'}^{\infty} \frac{\left[1 - (-1)^m \; \mathrm{e}^{-ay}\right] \, \left|{\lambda_1'}^2 - y^2\right|^{1/2}}{\left(y^2 + k_m^2\right) \left(y^2 + k_p^2\right)} \, \mathrm{d}y,$$

where ${\lambda_1'}^2 = \mu^2 - k^2$.

(a) $\boldsymbol{k_m \neq k_p}$ and $\boldsymbol{k_n = k_q}$

Assume that $k_m \neq k_p > k$, and $k_n = k_q > k$. Substituting the Kraichnan's approximation (Eq. (7.17)) into Eq. (7.16) and knowing that $k_n > k$ we get

$$I^{mnpq} \approx \frac{\pi b}{2k_n^2} \, I_1^{mp} \left(k_n : k_n > k\right), \tag{7.53}$$

where $I_1^{mp} \left(k_n : k_n > k\right)$ can be evaluated using Eq. (7.15) by substituting $\mu = k_n$, which is purely an imaginary quantity. However, for the corner - corner type of interaction, there must exist a real term, although small, associated with the radiation coupling in addition to the inertial coupling part (imaginary term) in the modal coupling coefficient [33, 34]. Here, the real part of I^{mnpq} can be evaluated using

$$I_R^{mnpq} = 2 \int_0^{k} \frac{\left[1 - (-1)^n \cos \mu b\right]}{\left(\mu^2 - k_n^2\right) \left(\mu^2 - k_q^2\right)} \, \mathrm{Re}\left[I_1^{mp}(\mu : |\mu| < k)\right] \, \mathrm{d}\mu. \tag{7.54}$$

From Eq. (7.13)

$$\mathrm{Re}\left[I_1^{mp}(\mu : |\mu| < k)\right] = 2 \int_0^{\lambda_1} \frac{\left[1 - (-1)^m \; \cos ax\right] \, |\lambda_1^2 - x^2|^{1/2}}{\left(x^2 - k_m^2\right) \left(x^2 - k_p^2\right)} \, \mathrm{d}x.$$

Therefore, by the approximation $(x^2 - k_m^2)\left(x^2 - k_p^2\right)(\mu^2 - k_n^2)\left(\mu^2 - k_q^2\right) \approx k_m^2\, k_n^2\, k_p^2\, k_q^2$ we get

$$I_R^{mnpq} \approx \frac{4}{k_m^2\, k_n^2\, k_p^2\, k_q^2} \int_0^k \int_0^{\sqrt{k^2-\mu^2}} [1 - (-1)^m \cos xa]\,[1 - (-1)^n \cos \mu b]\, \sqrt{k^2 - \mu^2 - x^2}\, \mathrm{d}x\, \mathrm{d}\mu.$$

After a few simplifications [34, 33],

$$I_R^{mnpq} \approx \frac{4}{k_m^2\, k_n^2\, k_p^2\, k_q^2} \left[\frac{\pi(-1)^m (ak\cos(ak) - \sin(ak))}{2a^3} + \frac{\pi(-1)^n (bk\cos(bk) - \sin(bk))}{2b^3} \right.$$
$$\left. + \frac{\pi(-1)^{m+n}\left(k\sqrt{a^2+b^2}\cos\left(k\sqrt{a^2+b^2}\right) - \sin\left(k\sqrt{a^2+b^2}\right)\right)}{2\left(a^2+b^2\right)^{3/2}} + \frac{\pi k^3}{6} \right]. \tag{7.55}$$

Now, the imaginary part of I^{mnpq} when $k_n = k_q$ and $k_m \neq k_p$ is given by Eq. (7.53)

$$I_\chi^{mnpq} \approx \frac{\pi b}{2k_n^2} \operatorname{Im}\left[I_1^{mp}\left(k_n : k_n > k\right)\right]. \tag{7.56}$$

As mentioned earlier, $I_1^{mp}\left(k_n : k_n > k\right)$ is purely an imaginary quantity (see Eq. (7.15)). A detailed derivation of $I_1^{mp}\left(k_n : k_n > k\right)$ is given in Appendix O.6 and the result is given below.

$$I_1^{mp}(k_n : k_n > k) \approx -\frac{\mathrm{i}\log\left(\frac{k^2+k_m^2}{k^2+k_p^2}\right)}{k_m^2 - k_p^2}\,\delta_{nq}. \tag{7.57}$$

Substituting this into Eq. (7.56) we get

$$I_\chi^{mnpq} \approx -\frac{\pi b\log\left(\frac{k^2+k_m^2}{k^2+k_p^2}\right)}{2k_n^2\left(k_m^2 - k_p^2\right)}\,\delta_{nq}. \tag{7.58}$$

(b) $\boldsymbol{k_m = k_p}$ and $\boldsymbol{k_n \neq k_q}$

The real part of I^{mnpq} can be obtained from Eq. (7.55) using the transformation rule $m \leftrightarrow n$, $p \leftrightarrow q$ and $a \leftrightarrow b$. The imaginary part of I^{mnpq} can be obtained from

$$I_\chi^{mnpq} \approx \frac{\pi a}{2k_m^2} \operatorname{Im}\left[I_1^{nq}\left(k_m : k_m > k\right)\right]. \tag{7.59}$$

Using the transformation rule $m \leftrightarrow n$, $p \leftrightarrow q$ and $a \leftrightarrow b$ in Eq. (7.58) we get

$$I_{\chi}^{mnpq} \approx -\frac{\pi a \log\left(\frac{k^2+k_n^2}{k^2+k_q^2}\right)}{2k_m^2\left(k_n^2-k_q^2\right)}\,\delta_{mp}. \tag{7.60}$$

(c) $\boldsymbol{k_m = k_p}$ and $\boldsymbol{k_n = k_q}$

The real part of I^{mnpq} can be evaluated using Eq. (7.54). When $k_m = k_p$ we have to include the contribution from the residues at $\pm k_m$ in the integral $I_1^{mp}(\mu : |\mu| < k)$. The resulting expression for $I_1^{mp}(\mu : |\mu| < k)$ is the same as given in Eq. (7.20). It can be seen that the contribution from the residues is purely imaginary. Hence, the residues do not contribute to the real part of I^{mnpq}. Therefore, the Eq. (7.55) for I_R^{mnpq} is still valid when $k_m = k_p$ and $k_n = k_q$.

When $k_m = k_p$ and $k_n = k_q$, either Eq. (7.56) or Eq. (7.59) can be used to evaluate I_{χ}^{mnpq}. Consider Eq. (7.56). When $k_m = k_p$, the integral $I_1^{mp}\,(k_n : k_n > k)$, given by Eq. (7.15), has to be modified to account for the poles of multiplicity two at $\pm k_m$. For the case 2 ($|\mu| > k$), the residues at the poles are (see Appendix N)

$$\mathrm{Res}(-k_m) = \mathrm{Res}(k_m) = \frac{a\,\left|\lambda_1^2 - k_m^2\right|^{1/2}}{4\,k_m^2},$$

where $\lambda_1 = \mathrm{i}\lambda_1' = \mathrm{i}\left(\mu^2 - k^2\right)^{1/2}$. Thus, the contour integration around the branch cut, as shown in Fig. 7.10 (note that for this case $k_m = k_p$ in the figure), results in

$$\mathrm{P}\left[I_1^{mp}(\mu)\right] = I_1^{mp}(\mu : |\mu| > k) = \pi\mathrm{i}\left[\mathrm{Res}(k_m) + \mathrm{Res}(-k_m)\right] - (\Gamma_1 + \Gamma_2).$$

Substituting for the residues and the Γ_i's from Eq. (7.14) we obtain

$$I_1^{mp}(\mu : |\mu| > k) = -2\,\mathrm{i}\left[\frac{-\pi a\left|\lambda_1^2 - k_m^2\right|^{1/2}}{4\,k_m^2} + \int\limits_{\lambda_1'}^{\infty} \frac{\left[1-(-1)^m\;\mathrm{e}^{-ay}\right]\,\left|\lambda_1'^2 - y^2\right|^{1/2}}{\left(y^2+k_m^2\right)^2}\,\mathrm{d}y\right]\delta_{mp}. \tag{7.61}$$

We obtain (see Appendix O.6)

$$I_1^{mp}(k_n : k_n > k) \approx \mathrm{i}\left[\frac{\pi a\,\left|k_m^2 + k_n^2 - k^2\right|^{1/2}}{2\,k_m^2} - \frac{1}{\left(k^2+k_m^2\right)}\right]\,\delta_{mp}. \tag{7.62}$$

Substituting the above equation into Eq. (7.56) we get

$$I_\chi^{mnpq} \approx \left[\frac{\pi^2 ab\, |k_m^2 + k_n^2 - k^2|^{1/2}}{4\, k_m^2\, k_n^2} - \frac{\pi b}{2\, k_n^2\, (k^2 + k_m^2)}\right] \delta_{mp}\, \delta_{nq}.$$

However, it is found that the above expression is a poor approximation when $k_m = k_p$ and $k_n = k_q$. A correction term $-\frac{\pi b}{2\, k_n^2 (k^2+k_m^2)}$, similar to the second term inside the square bracket, is added to the above expression. Thus, for $k_m = k_p$ and $k_n = k_q$, the imaginary part of I^{mnpq} is given by

$$I_\chi^{mnpq} \approx \left[\frac{\pi^2 ab\, |k_m^2 + k_n^2 - k^2|^{1/2}}{4\, k_m^2\, k_n^2} - \frac{\pi a}{2\, k_m^2\, (k^2 + k_n^2)} - \frac{\pi b}{2\, k_n^2\, (k^2 + k_m^2)}\right] \delta_{mp}\, \delta_{nq}. \quad (7.63)$$

Summarizing, using Eqs. (7.55), (7.58), (7.60) and (7.63),

$$I^{mnpq} = I_R^{mnpq} + \mathrm{i}\, I_\chi^{mnpq}, \quad (7.64)$$

where

$$I_R^{mnpq} \approx \frac{4}{k_m^2\, k_n^2\, k_p^2\, k_q^2}\left[\frac{\pi k^3}{6} + \frac{\pi(-1)^m(ak\cos(ak) - \sin(ak))}{2a^3} + \frac{\pi(-1)^n(bk\cos(bk) - \sin(bk))}{2b^3} + \frac{\pi(-1)^{m+n}\left(k\sqrt{a^2+b^2}\cos\left(k\sqrt{a^2+b^2}\right) - \sin\left(k\sqrt{a^2+b^2}\right)\right)}{2\,(a^2+b^2)^{3/2}}\right]$$

and

$$I_\chi^{mnpq} \approx A\, \delta_{mp} + B\, \delta_{nq} - (A+B)\, \delta_{mp}\, \delta_{nq} + C\, \delta_{mp}\, \delta_{nq}$$

with

$$A = -\frac{\pi a \log\left(\frac{k^2+k_n^2}{k^2+k_q^2}\right)}{2k_m^2\left(k_n^2 - k_q^2\right)},$$

$$B = -\frac{\pi b \log\left(\frac{k^2+k_m^2}{k^2+k_p^2}\right)}{2k_n^2\left(k_m^2 - k_p^2\right)}$$

and

$$C = \frac{\pi^2 ab\, |k_m^2 + k_n^2 - k^2|^{1/2}}{4\, k_m^2\, k_n^2} - \frac{\pi a}{2\, k_m^2\, (k^2 + k_n^2)} - \frac{\pi b}{2\, k_n^2\, (k^2 + k_m^2)}.$$

7.3.12 XY edge - Y edge modes ($k_m, k_n, k_q < k$, $k_p > k$ and $k_m^2 + k_n^2 > k^2$)

The derivation of I^{mnpq} for the XY edge - Y edge interaction is outlined in Fig. 7.19. The integral I^{mnpq} can be evaluated using Eq. (7.16). The integral forms of the terms

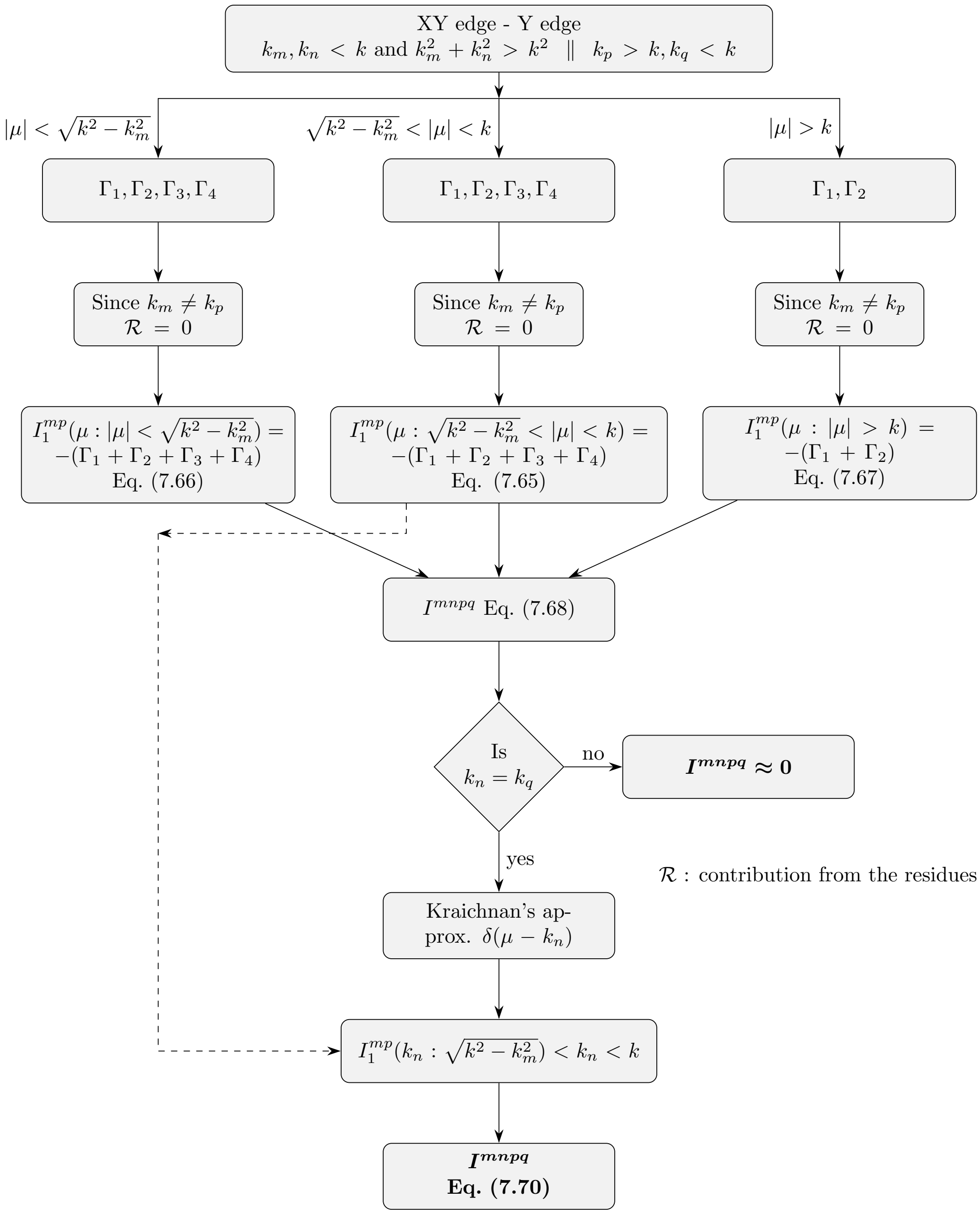

Fig. 7.19 A flow chart depicting the derivation of I^{mnpq} for the XY edge - Y edge interaction.

$I_1^{mp}(\mu : |\mu| < k)$ (case 1) and $I_1^{mp}(\mu : |\mu| > k)$ (case 2) are obtained below.

Case 1 ($|\mu| < k$)

The $|\mu| < k$ region can be divided into two: (a) when $\lambda_1 < k_m$ and (b) when $\lambda_1 > k_m$, where $\lambda_1 = \sqrt{k^2 - \mu^2}$.

(a) $\boldsymbol{\lambda_1 < k_m}$

$\lambda_1 < k_m$ implies that $k^2 - \mu^2 < k_m^2$, i.e., $\mu^2 > k^2 - k_m^2$. Therefore,

$$\sqrt{k^2 - k_m^2} < |\mu| < k.$$

For $\lambda_1 < k_m$, the integration contour for $I_1^{mp}(\mu)$ (Eq. (7.6)) is the same as that shown in Fig. 7.9, except that $\lambda_1 < k_m < k$. Therefore, $I_1^{mp}(\mu : \sqrt{k^2 - k_m^2} < |\mu| < k)$ is given by Eq. (7.13):

$$\begin{aligned} I_1^{mp}(\mu : \sqrt{k^2 - k_m^2} < |\mu| < k) &= 2 \int_0^{\lambda_1} \frac{[1 - (-1)^m \cos ax] \, |\lambda_1^2 - x^2|^{1/2}}{(x^2 - k_m^2)\left(x^2 - k_p^2\right)} \, \mathrm{d}x \\ - 2\,\mathrm{i} \left[\int_0^{\lambda_1} \frac{(-1)^m \sin ax \, |\lambda_1^2 - x^2|^{1/2}}{(x^2 - k_m^2)\left(x^2 - k_p^2\right)} \, \mathrm{d}x \right. &+ \left. \int_0^{\infty} \frac{[1 - (-1)^m \, \mathrm{e}^{-ay}] \, |\lambda_1^2 + y^2|^{1/2}}{(y^2 + k_m^2)\left(y^2 + k_p^2\right)} \, \mathrm{d}y \right]. \end{aligned} \tag{7.65}$$

(b) $\boldsymbol{\lambda_1 > k_m}$

$\lambda_1 > k_m$ implies that $k^2 - \mu^2 > k_m^2$, i.e., $\mu^2 < k^2 - k_m^2$. Therefore,

$$|\mu| < \sqrt{k^2 - k_m^2}.$$

The integration contour for evaluating $I_1^{mp}(\mu)$ (Eq. (7.6)) is shown in Fig. 7.13. Thus, $I_1^{mp}(\mu : |\mu| < \sqrt{k^2 - k_m^2})$ is given by Eq. (7.25):

$$\begin{aligned} I_1^{mp}(\mu : |\mu| < \sqrt{k^2 - k_m^2}) &= 2 \, \mathrm{P}_{k_m} \int_0^{\lambda_1} \frac{[1 - (-1)^m \cos ax] \, |\lambda_1^2 - x^2|^{1/2}}{(x^2 - k_m^2)\left(x^2 - k_p^2\right)} \, \mathrm{d}x \\ - 2\,\mathrm{i} \left[\mathrm{P}_{k_m} \int_0^{\lambda_1} \frac{(-1)^m \sin ax \, |\lambda_1^2 - x^2|^{1/2}}{(x^2 - k_m^2)\left(x^2 - k_p^2\right)} \, \mathrm{d}x \right. &+ \left. \int_0^{\infty} \frac{[1 - (-1)^m \, \mathrm{e}^{-ay}] \, |\lambda_1^2 + y^2|^{1/2}}{(y^2 + k_m^2)\left(y^2 + k_p^2\right)} \, \mathrm{d}y \right]. \end{aligned} \tag{7.66}$$

Case 2 ($|\mu| > k$)

The integration contour for $I_1^{mp}(\mu)$ when $|\mu| > k$ is the same as that shown in Fig. 7.10, except that $k_m < k$. Therefore, $I_1^{mp}(\mu : |\mu| > k)$ is given by Eq. (7.15):

$$I_1^{mp}(\mu : |\mu| > k) = -2\,\mathrm{i} \int\limits_{\lambda_1'}^{\infty} \frac{\left[1 - (-1)^m \,\mathrm{e}^{-ay}\right] \left|\lambda_1'^2 - y^2\right|^{1/2}}{\left(y^2 + k_m^2\right)\,\left(y^2 + k_p^2\right)} \,\mathrm{d}y. \tag{7.67}$$

Integral I^{mnpq}

The integral I^{mnpq} (Eq. (7.16)) can be modified for the XY edge - Y edge interaction as

$$\begin{aligned} I^{mnpq} = 2 &\int\limits_{0}^{\sqrt{k^2-k_m^2}} \frac{\left[1 - (-1)^n \cos \mu b\right]}{\left(\mu^2 - k_n^2\right)\,\left(\mu^2 - k_q^2\right)}\, I_1^{mp}\left(\mu : |\mu| < \sqrt{k^2 - k_m^2}\right) \mathrm{d}\mu \\ + 2 &\int\limits_{\sqrt{k^2-k_m^2}}^{k} \frac{\left[1 - (-1)^n \cos \mu b\right]}{\left(\mu^2 - k_n^2\right)\,\left(\mu^2 - k_q^2\right)}\, I_1^{mp}\left(\mu : \sqrt{k^2 - k_m^2} < |\mu| < k\right) \mathrm{d}\mu \\ + 2 &\int\limits_{k}^{\infty} \frac{\left[1 - (-1)^n \cos \mu b\right]}{\left(\mu^2 - k_n^2\right)\,\left(\mu^2 - k_q^2\right)}\, I_1^{mp}(\mu : |\mu| > k)\, \mathrm{d}\mu, \end{aligned} \tag{7.68}$$

where $I_1^{mp}(\mu : |\mu| < \sqrt{k^2 - k_m^2})$, $I_1^{mp}(\mu : \sqrt{k^2 - k_m^2} < |\mu| < k)$ and $I_1^{mp}(\mu : |\mu| > k)$ can be evaluated using Eqs. (7.66), (7.65) and (7.67), respectively.

Assuming $k_n = k_q < k$ and substituting the Kraichnan's approximation (Eq. (7.17)) into Eq. (7.68) while knowing that $\sqrt{k^2 - k_m^2} < k_n < k$ we get

$$I^{mnpq} \approx \frac{\pi b}{2k_n^2}\, I_1^{mp}\left(k_n : \sqrt{k^2 - k_m^2} < k_n < k\right), \tag{7.69}$$

where $I_1^{mp}(k_n : \sqrt{k^2 - k_m^2} < k_n < k)$ can be evaluated using Eq. (7.65) (corresponding to the $\lambda_1 < k_m$ case) after substituting $\mu = k_n$. As $k_m, k_p > \lambda_1$, $I_1^{mp}(k_n : \sqrt{k^2 - k_m^2} < k_n < k)$ can be approximated to $I_1^{mp}(k_n : k_n < k)$ of the Y edge -Y edge case (for $k_m \neq k_p$ and $k_n = k_q$). The derivation of $I_1^{mp}(k_n : k_n < k)$ is given in the Appendix O.1. It follows that the integral I^{mnpq} (Eq. (7.69)) is the same as that for the Y edge - Y edge interaction (see Eq. (7.18). Thus, using Eq. (7.19) we obtain

$$I^{mnpq} = I_R^{mnpq} + \mathrm{i}\, I_\chi^{mnpq}, \tag{7.70}$$

where the real part of I^{mnpq} is given by

$$I_R^{mnpq} \approx \frac{\pi^2 b}{2k_n^2}\left[\frac{k_p\sqrt{k_m^2-\lambda_1^2}-k_m\sqrt{k_p^2-\lambda_1^2}}{k_m^3 k_p - k_m k_p^3} - \frac{\lambda_1(-1)^m \mathrm{J}_1\left(a\lambda_1\right)}{a\left(\lambda_1^2-k_m^2\right)\left(\lambda_1^2-k_p^2\right)}\right]\delta_{nq}$$

and the imaginary part of I^{mnpq} is given by

$$I_\chi^{mnpq} \approx -\frac{\pi b}{k_n^2}(A+B+C)\,\delta_{nq}$$

with

$$A = \frac{\pi\lambda_1(-1)^m \mathrm{H}_1\left(a\lambda_1\right)}{2a\left(\lambda_1^2-k_m^2\right)\left(\lambda_1^2-k_p^2\right)},$$

$$B = \frac{2k\sqrt{2k^2-k_n^2}+\left(k^2-k_n^2\right)\log\left(\frac{\left(\sqrt{2k^2-k_n^2}+k\right)^2}{k^2-k_n^2}\right)}{4k_m^2k_p^2} + \frac{\log\left(\frac{k^2+k_p^2}{k^2+k_m^2}\right)}{2\left(k_p^2-k_m^2\right)}$$

and
$$C = \frac{(-1)^{m+1}}{12ak_m^2k_p^2}\left\{2\sqrt{\frac{1}{a^2}+k^2-k_n^2}-\left(k^2-k_n^2\right)\right.$$
$$\left.\times\left[-4a^2\sqrt{k^2-k_n^2}+4a^2\sqrt{\frac{1}{a^2}+k^2-k_n^2}-3a\log\left(\frac{\left(\sqrt{\frac{1}{a^2}+k^2-k_n^2}+\frac{1}{a}\right)^2}{k^2-k_n^2}\right)\right]\right\}.$$

It is assumed that when $k_n \neq k_q$, $I^{mnpq} \approx 0$.

7.3.13 XY edge - X edge modes ($k_m, k_n, k_p < k$, $k_q > k$ and $k_m^2 + k_n^2 > k^2$)

When $k_m = k_p$, the integral I^{mnpq} can be obtained from Eq. (7.70) using the transformation rules $m \leftrightarrow n$, $p \leftrightarrow q$ and $a \leftrightarrow b$. It is assumed that when $k_m \neq k_p$, $I^{mnpq} \approx 0$.

7.3.14 AF - XY edge modes ($k_m, k_n, k_q, k_p < k$, $k_m^2 + k_n^2 < k^2$ and $k_p^2 + k_q^2 > k^2$)

The derivation of I^{mnpq} for the AF - XY edge interaction is outlined in Fig. 7.20. The integral I^{mnpq} can be evaluated using Eq. (7.16), where the integral domain is classified into two regions: $|\mu| < k$ (case 1) and $|\mu| > k$ (case 2). However, as in the case of AF - AF interaction (section 7.3.9), the case 1 is further divided into three sub-regions depending on the value of μ and the resulting λ_1. An appropriate integral form of $I_1^{mp}(\mu)$ is defined in each of these regions/sub-regions.

Case 1 ($|\mu| < k$)

The following derivation assumes that $k_m < k_p$. The $|\mu| < k$ region can be divided into three depending on the value of λ_1 $(= \sqrt{k^2 - \mu^2})$: (a) when $\lambda_1 < k_m$, (b) when $k_m < \lambda_1 < k_p$ and (c) when $\lambda_1 > k_p$.

(a) $\boldsymbol{\lambda_1 < k_m}$
$\lambda_1 < k_m$ implies that $k^2 - \mu^2 < k_m^2$, i.e., $\mu^2 > k^2 - k_m^2$. Therefore in this region

$$\sqrt{k^2 - k_m^2} < |\mu| < k.$$

As $\lambda_1 < k_m$, the integration contour of $I_1^{mp}(\mu)$ (Eq. (7.6)) is the same as that shown in Fig. 7.9, except that $\lambda_1 < k_m, k_p < k$. Therefore, $I_1^{mp}(\mu : \sqrt{k^2 - k_m^2} < |\mu| < k)$ is given by Eq. (7.13):

$$\begin{aligned} I_1^{mp}(\mu : \sqrt{k^2 - k_m^2} < |\mu| < k) &= 2 \int_0^{\lambda_1} \frac{[1 - (-1)^m \cos ax] \left|\lambda_1^2 - x^2\right|^{1/2}}{(x^2 - k_m^2)\left(x^2 - k_p^2\right)} \mathrm{d}x \\ &- 2\mathrm{i} \left[\int_0^{\lambda_1} \frac{(-1)^m \sin ax \left|\lambda_1^2 - x^2\right|^{1/2}}{(x^2 - k_m^2)\left(x^2 - k_p^2\right)} \mathrm{d}x + \int_0^{\infty} \frac{[1 - (-1)^m \mathrm{e}^{-ay}] \left|\lambda_1^2 + y^2\right|^{1/2}}{(y^2 + k_m^2)\left(y^2 + k_p^2\right)} \mathrm{d}y \right]. \end{aligned} \quad (7.71)$$

(b) $\boldsymbol{k_m < \lambda_1 < k_p}$
$k_m < \lambda_1 < k_p$ implies that $k_m^2 < k^2 - \mu^2 < k_p^2$, i.e., $k^2 - k_p^2 < \mu^2 < k^2 - k_m^2$. Therefore in this region

$$\sqrt{k^2 - k_p^2} < |\mu| < \sqrt{k^2 - k_m^2}.$$

The integration contour for evaluating $I_1^{mp}(\mu)$ (Eq. (7.6)) is the same as that shown in Fig. 7.13, except that $\lambda_1 < k_p < k$. Therefore, $I_1^{mp}\left(\mu : \sqrt{k^2 - k_p^2} < |\mu| < \sqrt{k^2 - k_m^2}\right)$

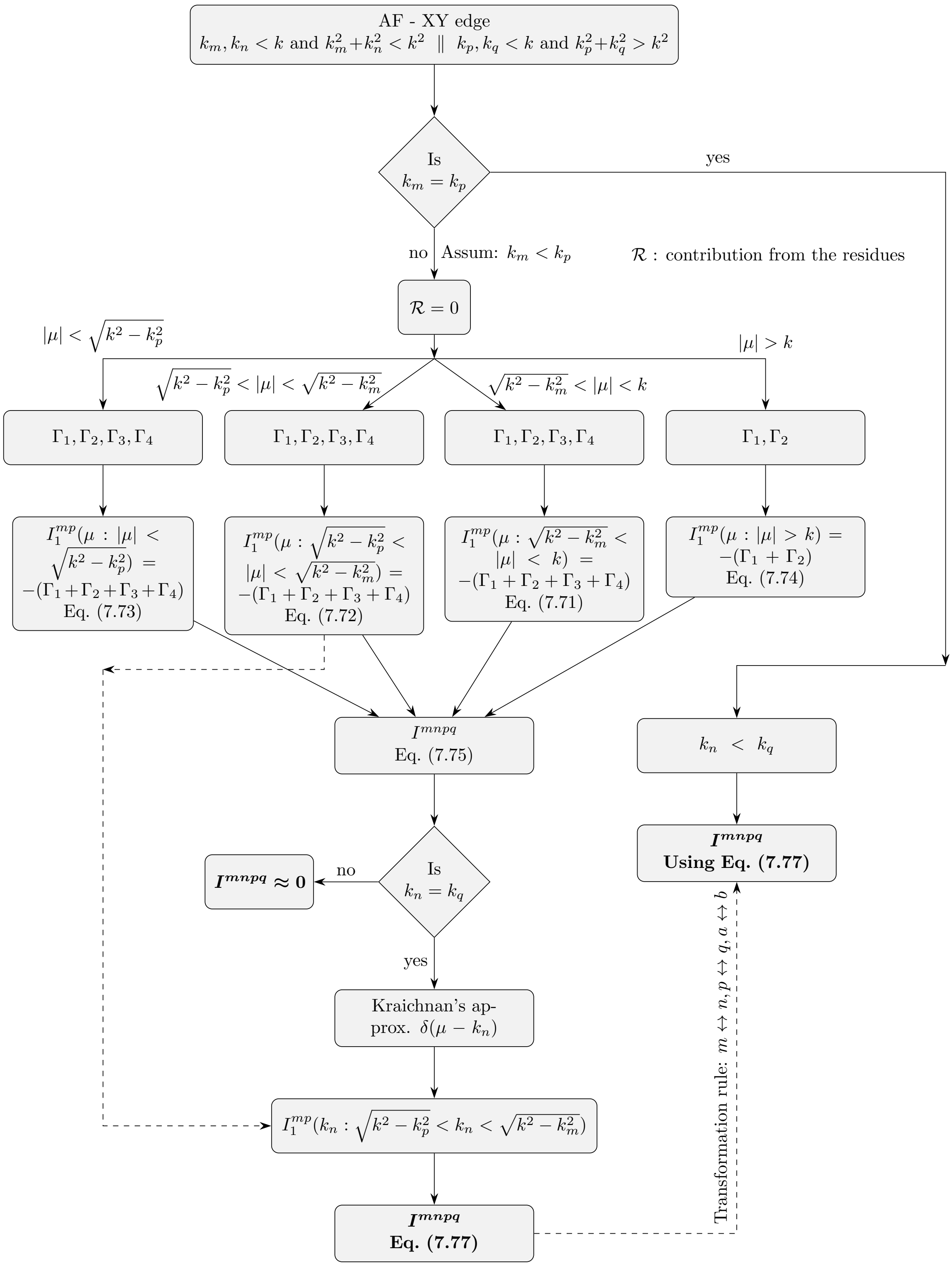

Fig. 7.20 A flow chart depicting the derivation of I^{mnpq} for the AF - XY edge interaction.

is given by Eq. (7.25):

$$I_1^{mp}\left(\mu : \sqrt{k^2-k_p^2} < |\mu| < \sqrt{k^2-k_m^2}\right) = 2\mathrm{P}_{k_m}\int_0^{\lambda_1}\frac{\left[1-(-1)^m\,\cos ax\right]\,\left|\lambda_1^2-x^2\right|^{1/2}}{\left(x^2-k_m^2\right)\,\left(x^2-k_p^2\right)}\,\mathrm{d}x$$
$$-\,2\,\mathrm{i}\left[\mathrm{P}_{k_m}\int_0^{\lambda_1}\frac{(-1)^m\,\sin ax\,\left|\lambda_1^2-x^2\right|^{1/2}}{\left(x^2-k_m^2\right)\,\left(x^2-k_p^2\right)}\,\mathrm{d}x+\int_0^{\infty}\frac{\left[1-(-1)^m\,\mathrm{e}^{-ay}\right]\,\left|\lambda_1^2+y^2\right|^{1/2}}{\left(y^2+k_m^2\right)\,\left(y^2+k_p^2\right)}\,\mathrm{d}y\right]. \tag{7.72}$$

(c) $\boldsymbol{\lambda_1 > k_p}$

$\lambda_1 > k_p$ implies that $k^2-\mu^2 > k_p^2$, i.e., $\mu^2 < k^2-k_p^2$. Therefore in this region

$$|\mu| < \sqrt{k^2-k_p^2}.$$

The integration contour for evaluating $I_1^{mp}(\mu)$ (Eq. (7.6)) is as shown in Fig. 7.16. The integral $I_1^{mp}\left(\mu : |\mu| < \sqrt{k^2-k_p^2}\right)$ is given by Eq. (7.40):

$$I_1^{mp}\left(\mu : |\mu| < \sqrt{k^2-k_p^2}\right) = 2\,\mathrm{P}_{k_m,k_p}\int_0^{\lambda_1}\frac{\left[1-(-1)^m\,\cos ax\right]\,\left|\lambda_1^2-x^2\right|^{1/2}}{\left(x^2-k_m^2\right)\,\left(x^2-k_p^2\right)}\,\mathrm{d}x$$
$$-\,2\,\mathrm{i}\left[\mathrm{P}_{k_m,k_p}\int_0^{\lambda_1}\frac{(-1)^m\,\sin ax\,\left|\lambda_1^2-x^2\right|^{1/2}}{\left(x^2-k_m^2\right)\,\left(x^2-k_p^2\right)}\,\mathrm{d}x+\int_0^{\infty}\frac{\left[1-(-1)^m\,\mathrm{e}^{-ay}\right]\,\left|\lambda_1^2+y^2\right|^{1/2}}{\left(y^2+k_m^2\right)\,\left(y^2+k_p^2\right)}\,\mathrm{d}y\right]. \tag{7.73}$$

Case 2 $(|\mu| > k)$

The integration contour for $I_1^{mp}(\mu)$ when $|\mu| > k$ is the same as that shown in Fig. 7.10, except that $k_m, k_p < k$. Therefore, $I_1^{mp}(\mu : |\mu| > k)$ is given by Eq. (7.15):

$$I_1^{mp}(\mu : |\mu| > k) = -2\,\mathrm{i}\int_{\lambda_1'}^{\infty}\frac{\left[1-(-1)^m\,\mathrm{e}^{-ay}\right]\,\left|\lambda_1'^2-y^2\right|^{1/2}}{\left(y^2+k_m^2\right)\,\left(y^2+k_p^2\right)}\,\mathrm{d}y, \tag{7.74}$$

where $\lambda_1' = \sqrt{\mu^2-k^2}$.

Integral I^{mnpq}

The integral I^{mnpq} (Eq. (7.4)) for the AF - XY edge modal interaction can be written as

$$
\begin{aligned}
I^{mnpq} = 2 \int_0^{\sqrt{k^2-k_p^2}} \frac{[1-(-1)^n \cos \mu b]}{(\mu^2-k_n^2)\left(\mu^2-k_q^2\right)} I_1^{mp}\left(\mu : |\mu| < \sqrt{k^2-k_p^2}\right) \mathrm{d}\mu \\
+ 2 \int_{\sqrt{k^2-k_p^2}}^{\sqrt{k^2-k_m^2}} \frac{[1-(-1)^n \cos \mu b]}{(\mu^2-k_n^2)\left(\mu^2-k_q^2\right)} I_1^{mp}\left(\mu : \sqrt{k^2-k_p^2} < |\mu| < \sqrt{k^2-k_m^2}\right) \mathrm{d}\mu \\
+ 2 \int_{\sqrt{k^2-k_m^2}}^{k} \frac{[1-(-1)^n \cos \mu b]}{(\mu^2-k_n^2)\left(\mu^2-k_q^2\right)} I_1^{mp}\left(\mu : \sqrt{k^2-k_m^2} < |\mu| < k\right) \mathrm{d}\mu \\
+ 2 \int_{k}^{\infty} \frac{[1-(-1)^n \cos \mu b]}{(\mu^2-k_n^2)\left(\mu^2-k_q^2\right)} I_1^{mp}(\mu : |\mu| > k) \,\mathrm{d}\mu,
\end{aligned}
\tag{7.75}
$$

where the $I_1^{mp}(\mu)$ terms in the four integrals can be evaluated using Eqs. (7.73), (7.72), (7.71) and (7.74).

(a) $k_m \neq k_p$ and $k_n = k_q$

Assume that $k_n = k_q < k$, and $k_m \neq k_p < k$ (for the AF - XY edge interaction, when $k_n = k_q$ it turns out that $k_m < k_p$). Substituting the Kraichnan's assumption (Eq. (7.17)) into Eq. (7.75) and knowing that $\sqrt{k^2-k_p^2} < k_n < \sqrt{k^2-k_m^2}$ we get

$$
I^{mnpq} \approx \frac{\pi b}{2k_n^2} I_1^{mp}\left(k_n : \sqrt{k^2-k_p^2} < k_n < \sqrt{k^2-k_m^2}\right), \tag{7.76}
$$

where $I_1^{mp}\left(k_n : \sqrt{k^2-k_p^2} < k_n < \sqrt{k^2-k_m^2}\right)$ can be evaluated using Eq. (7.72), for which, $k_m < \lambda_1 < k_p$. The integration contour of $I_1^{mp}\left(k_n : \sqrt{k^2-k_p^2} < k_n < \sqrt{k^2-k_m^2}\right)$ is similar to what appears in the evaluation of $I_1^{mp}(k_n : k_n < \sqrt{k^2-k_m^2})$ for the AF - Y edge type of interaction (see Eq. (7.25) and Fig. 7.13), except that $\lambda_1 < k_p < k$. Thus, $I_1^{mp}\left(k_n : \sqrt{k^2-k_p^2} < k_n < \sqrt{k^2-k_m^2}\right)$ can be approximated to $I_1^{mp}(k_n : k_n < \sqrt{k^2-k_m^2})$ of the AF - Y edge interaction presented in the Appendix O.2. It follows that the above expression for I^{mnpq} when $k_m \neq k_p$ and $k_n = k_q$ is also the same as that obtained in section 7.3.3 (see Eq. (7.28)). Therefore, Eq. (7.29) gives

$$I^{mnpq} \approx (A + B + C)\,\delta_{nq}, \tag{7.77}$$

where

$$A = -\frac{\pi b}{k_n^2}\left[\frac{\pi\lambda_1(-1)^m \mathrm{J}_1(a\lambda_1)}{2a\left(\lambda_1^2 - k_m^2\right)\left(\lambda_1^2 - k_p^2\right)} + \frac{\pi\left(k_m\sqrt{k_p^2-\lambda_1^2} - \mathrm{i}k_p\sqrt{\lambda_1^2 - k_m^2}\right)}{2k_m^3 k_p - 2k_m k_p^3}\right],$$

$$B = \frac{\mathrm{i}\pi^2 b\lambda_1(-1)^{m+1}\mathrm{H}_1(a\lambda_1)}{2ak_n^2\left(\lambda_1^2 - k_m^2\right)\left(\lambda_1^2 - k_p^2\right)}$$

and

$$C = -\frac{\mathrm{i}\pi b}{k_n^2}\left[\frac{C_1\,k_m + 2(\pi + C_2)\sqrt{k^2-k_m^2-k_n^2}}{4k_m k_p^2} + \frac{\log\left(\frac{k^2+k_p^2}{k^2+k_m^2}\right)}{2\left(k_p^2-k_m^2\right)}\right.$$
$$\left. + \frac{(-1)^m C_3}{2k_m k_p^2} + \frac{(-1)^m\left(C_4 - aC_5\sqrt{k^2-k_m^2-k_n^2}\right)}{2k_p^2}\right]$$

with

$$C_1 = 2\tanh^{-1}\left(\frac{4kk_m^2\left(\sqrt{2k^2-k_n^2}+k\right)}{4k_m^2\left[k\left(\sqrt{2k^2-k_n^2}+2k\right)-k_n^2\right]+\left[k\left(2\sqrt{2k^2-k_n^2}+3k\right)-k_n^2\right]\left(k^2-k_n^2\right)}\right)$$
$$+\log\left(\frac{-4k_m^2\left[k_n^2 - k\left(2\sqrt{2k^2-k_n^2}+3k\right)\right] - 2k\left(2\sqrt{2k^2-k_n^2}+5k\right)k_n^2}{\left(k^2-k_n^2\right)\left(k^2+4k_m^2-k_n^2\right)}\right.$$
$$\left. + \frac{k^3\left(12\sqrt{2k^2-k_n^2}+17k\right)+k_n^4}{\left(k^2-k_n^2\right)\left(k^2+4k_m^2-k_n^2\right)}\right),$$

$$C_2 = -\mathrm{i}\,\log\left(\frac{k^4 - 2\mathrm{i}kk_m\sqrt{\left(k_n^2-2k^2\right)\left(-k^2+k_m^2+k_n^2\right)} - 3k^2k_m^2 - k^2k_n^2 + k_m^2k_n^2}{\left(k^2+k_m^2\right)\left(k^2-k_n^2\right)}\right),$$

$$C_3 = k_m\log\left(\frac{k^2-k_n^2}{\left(\sqrt{\frac{1}{a^2}+k^2-k_n^2}+\frac{1}{a}\right)^2}\right) - 2\pi\sqrt{k^2-k_m^2-k_n^2}$$
$$+\mathrm{i}\sqrt{k^2-k_m^2-k_n^2}\,\log\left(\frac{2\mathrm{i}k_m\sqrt{\left(a^2k^2-a^2k_n^2+1\right)\left(k^2-k_m^2-k_n^2\right)}}{\left(k^2-k_n^2\right)\left(a^2k_m^2+1\right)}\right.$$
$$\left. + \frac{k_m^2\left(a^2k^2-a^2k_n^2+2\right)-k^2+k_n^2}{\left(k^2-k_n^2\right)\left(a^2k_m^2+1\right)}\right),$$

$$C_4 = 2\left(\sqrt{a^2k^2-a^2k_n^2+1} - a\sqrt{k^2-k_n^2}\right)$$

and

$$C_5 = 2\log\left(\frac{k_m}{\sqrt{\left(k^2-k_n^2\right)\left(k^2-k_m^2-k_n^2\right)}+k^2-k_n^2}\right)$$
$$+\log\left(\frac{\left(k^2-k_n^2\right)\left[a^2\left(2k^2-k_m^2-2k_n^2\right)+2a\sqrt{\left(a^2k^2-a^2k_n^2+1\right)\left(k^2-k_m^2-k_n^2\right)}+1\right]}{a^2k_m^2+1}\right).$$

(b) $\boldsymbol{k_m} = \boldsymbol{k_p}$ and $\boldsymbol{k_n} \neq \boldsymbol{k_q}$

When $k_m = k_p < k$ and $k_n \neq k_q < k$ ($k_n < k_q$), I^{mnpq} is given by

$$I^{mnpq} \approx \frac{\pi b}{2k_m^2} I_1^{nq} \left(k_m : \sqrt{k^2 - k_q^2} < k_m < \sqrt{k^2 - k_n^2} \right). \tag{7.78}$$

The approximate closed form can be obtained by applying the transformation rule $m \leftrightarrow n$, $p \leftrightarrow q$ and $a \leftrightarrow b$ in Eq. (7.77). It is assumed that when $k_m \neq k_p$ and $k_n \neq k_q$, $I^{mnpq} \approx 0$.

Since, both the AF (supersonic) and the corner (subsonic) types of radiation can rarely be significant at a given frequency, it is assumed that $I^{mnpq} \approx 0$ for the AF - corner type of modal coupling. This assumption is also applicable for the XY edge - corner interaction. The effect of any interaction between the X edge and the Y edge modes on the modal coupling coefficient is also neglected.

The right expression for $\bar{\Theta}_{mnpq}$ is chosen depending on the panel wavenumbers. Now, the response of the panel to a harmonic force excitation is obtained using Eq. (5.38) and the radiated pressure field is computed using Eq. (5.39). The expression for finding the radiation efficiency is presented in the next section.

7.4 The radiation efficiency

The far-field radiated power from the perforated panel set in an unperforated baffle is (see section 5.6)

$$W = \frac{1}{2}\mathrm{Re}\left\{ \int_{-k}^{k} \int_{-\sqrt{k^2-\mu^2}}^{\sqrt{k^2-\mu^2}} P^+(\lambda, \mu, z=0)\, V_a^*(\lambda, \mu)\, \mathrm{d}\lambda\, \mathrm{d}\mu \right\}. \tag{7.79}$$

In the above equation, only the far-field radiating components of the wavenumber spectrum ($k^2 > \lambda^2 + \mu^2$) are included . The integration is approximated by a sum over the range of discrete values of λ and μ.

Now, the radiation efficiency of the perforated panel [7]

$$\sigma = \frac{W}{\frac{1}{2}\rho_0 c a b < |v_p|^2 >}, \tag{7.80}$$

where W is the radiated power (Eq. (7.79)) and $< |v_p|^2 >$ is the spatially averaged squared velocity of the perforated panel defined as [7]

$$< |v_p|^2 >= \frac{1}{ab} \int\limits_{-b/2}^{b/2} \int\limits_{-a/2}^{a/2} |v_p(x,y)|^2 \, \mathrm{d}x \, \mathrm{d}y.$$

Using Eq. (5.38) and simplifying we get

$$< |v_p|^2 >= \frac{1}{4} \sum_{r,s} \sum_{m,n} B_r B_s^* U_{mnr} U_{mns}^*, \tag{7.81}$$

where * represents the complex conjugate. In a matrix form

$$< |v_p|^2 >= \frac{1}{4} \{B_r\}^T [U_{mn,r}]^T \left[U_{mn,s}^*\right] \{B_s^*\} . \tag{7.82}$$

Using Eqs. (7.79) and (7.81), the radiation efficiency of a perforated panel to a point harmonic excitation (Eq. (7.80)) is

$$\sigma = \frac{4}{\rho_0 cab \sum\limits_{r,s} \sum\limits_{m,n} B_r B_s^* U_{mnr} U_{mns}^*} \mathrm{Re} \left\{ \int\limits_{-k}^{k} \int\limits_{-\sqrt{k^2-\mu^2}}^{\sqrt{k^2-\mu^2}} P^+(\lambda, \mu, z=0) V_a^*(\lambda, \mu) \, \mathrm{d}\lambda \, \mathrm{d}\mu \right\}. \tag{7.83}$$

The radiation efficiencies and the resonance frequencies of fluid-loaded perforated panels are presented in the next section. Also, the characteristics of the modal coupling coefficient are discussed. Note, that the modal coupling coefficient is evaluated using the closed form expressions derived earlier.

7.5 Results

Panel dimensions	$a = 0.455$ m, $b = 0.546$ m and $h = 0.003$ m
Panel material properties (aluminum)	$E = 70$ GPa, $\rho_p = 2700$ kg/m^3 and $\nu = 0.33$
Properties of water	$\rho_0 = 998.2$ kg/m^3, $c = 1481$ m/s and $\eta_0 = 8.9 \times 10^{-4}$ Ns/m^2
Properties of air	$\rho_0 = 1.204$ kg/m^3, $c = 343$ m/s and $\eta_0 = 1.8 \times 10^{-5}$ Ns/m^2

Table 7.2 The perforated panel dimensions and material properties.

Consider a panel with dimensions and material properties as given in Table 7.2. All the *in vacuo* panel modes below 10,000 Hz are considered in the analysis. The panel is excited by a unit amplitude harmonic point force.

7.5.1 Radiation efficiency

Consider an unperforated panel of the above prescribed size, excited at the center. The radiation efficiencies of the panel are evaluated with air and water as the acoustic medium. Fig. 7.21 shows a comparison of the two results. The fluid loading essentially has both resistive and reactive characteristics, modeled as the real and the imaginary parts of the modal coupling coefficient. When the panel is immersed in water, it experiences greater resistive and reactive load from the acoustic medium than when it is immersed in air. Consequently, both the panel response and the radiated power reduce resulting in a lower radiation efficiency when the panel is immersed in water.

The radiation efficiency of perforated panels when they are immersed in water is shown in Fig. 7.22, where different perforation ratios are achieved by varying the hole radius from 0 mm to 5 mm; the total number of holes in the panel is kept constant at $N_0 = 750$. As the perforation ratio increases, the perforate impedance Z_{0p}/σ_p decreases and hence the propagation of acoustic waves through the perforations becomes easier. Accordingly, the radiated power decreases and hence the radiation efficiency also decreases. It is noted that when immersed in water, the radiation efficiency of the perforated panel is less than when it is immersed in air.

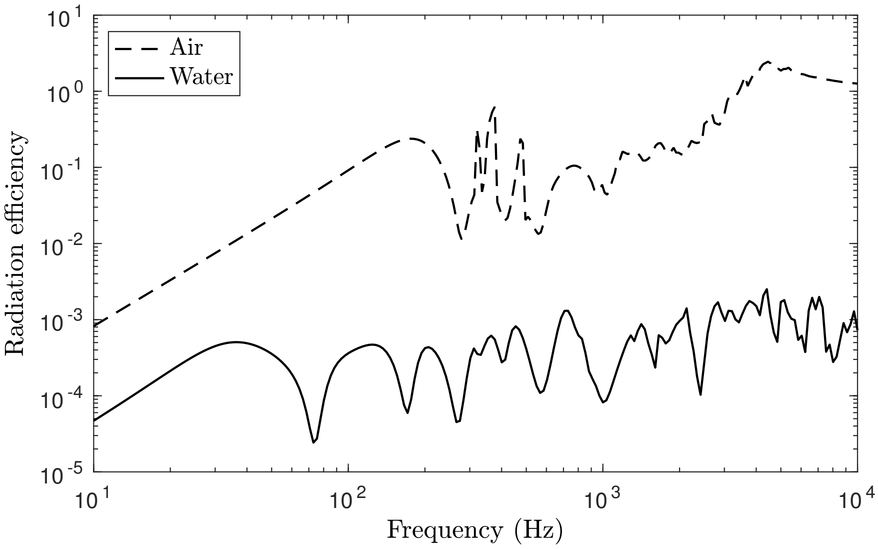

Fig. 7.21 Comparison of radiation efficiency of an unperforated panel when the acoustic medium is air vs. water. The excitation is at the center of the panel. The modal coupling coefficient is evaluated using the closed form expressions.

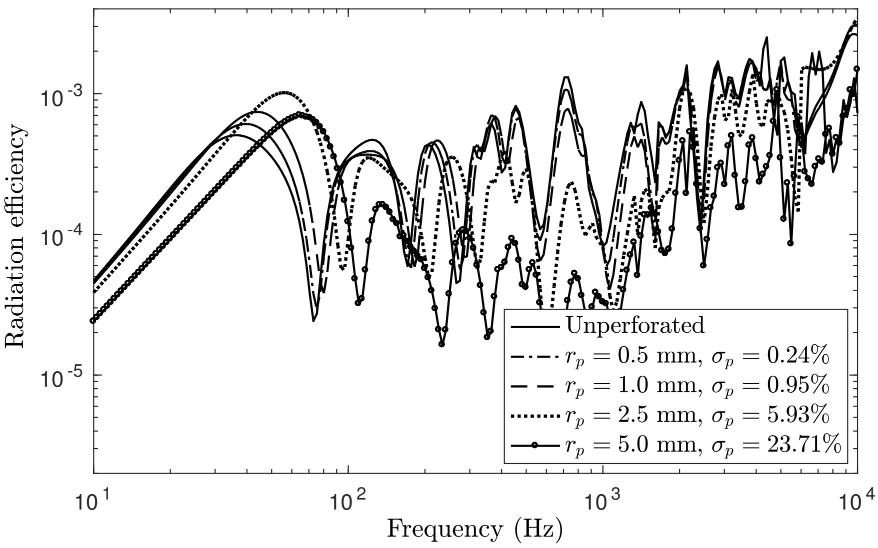

Fig. 7.22 Radiation efficiency of water-loaded panels for various perforation ratios. For all the cases, the excitation is at the center of the panel and the modal coupling coefficient is evaluated using the closed form expressions. In all the cases the total number of holes is $N_0 = 750$.

7.5.2 Mean quadratic velocity and natural frequencies

Consider the perforated panel immersed in water and excited by a simple harmonic force off from the center at (0.1, 0.1). The mean quadratic velocity of the panel is evaluated for different perforation ratios using the closed form analytical expressions of the modal coupling coefficient (mean quadratic velocity is equal to $\frac{<|v_p|^2>}{2}$ [37], see Eq. (7.82)). In Fig. 7.23, the mean quadratic velocities are compared with those obtained using the numerical integration. The natural frequencies of fluid-loaded panels can be identified from the peaks of mean quadratic velocity spectrum. The first four natural frequencies of the water-loaded panels (Fig. 7.23) are tabulated in Table 7.3 along with the corresponding *in vacuo* values. The natural frequencies computed using the closed form expressions of the modal coupling coefficient match very well with those obtained using the numerically computed coupling coefficient.

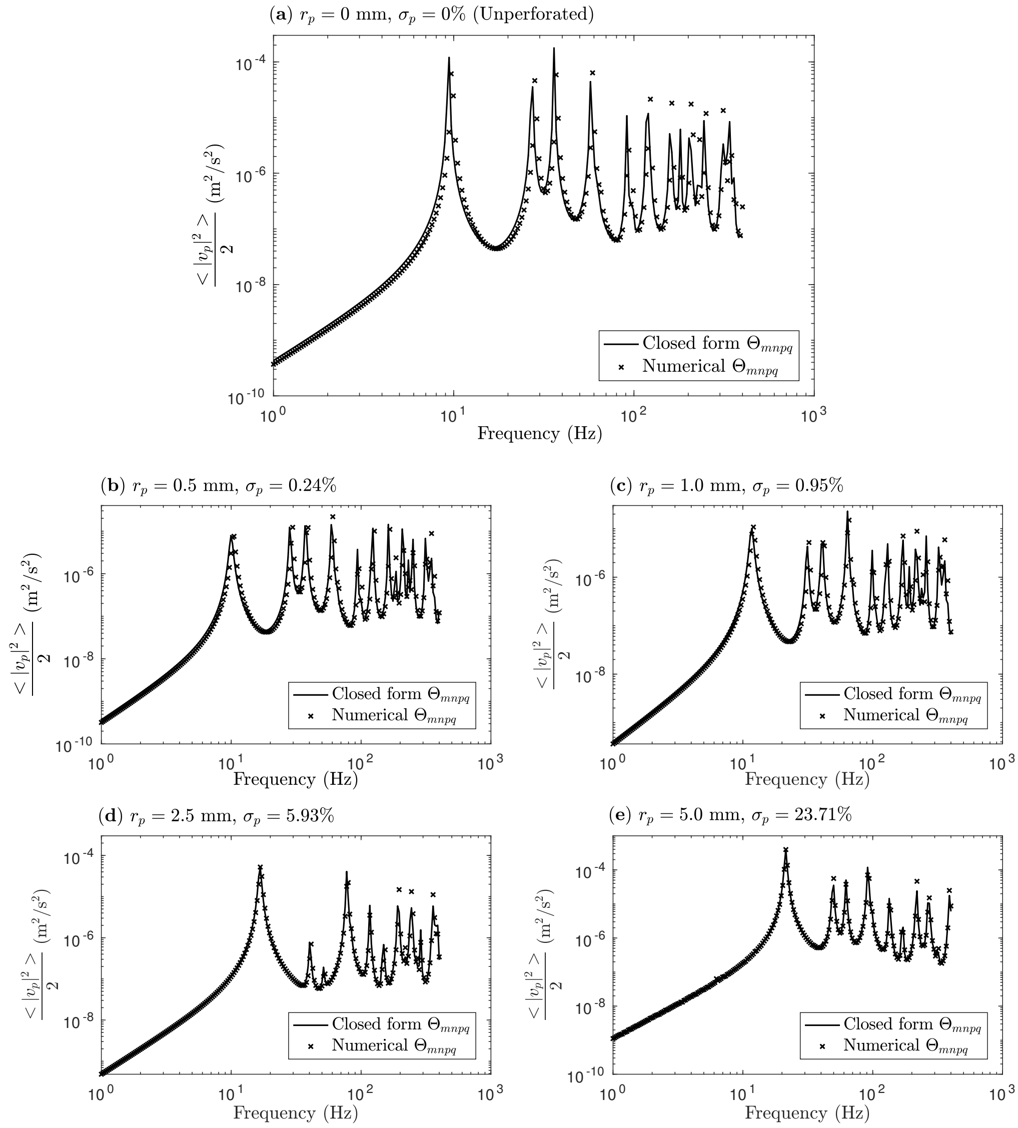

Fig. 7.23 Comparison of mean quadratic velocity ($\frac{<|v_p|^2>}{2}$) for various perforated panels under water-loading condition. Total number of holes in each of the panels is $N_0 = 750$. The panels are excited at (0.1,0.1). The peaks in the mean quadratic velocity plots correspond to the resonances.

The reactive part of the modal coupling coefficient arising due to the fluid loading, acts as virtual mass addition to the panel mass and thus causes a reduction in the natural frequencies from the respective *in vacuo* values. However, as the perforation ratio increases, both the stiffness and inertia of the panel reduces. In addition, there occurs a reduction in the virtual mass addition as a result of the reduction in the effective solid area of the panel. When the acoustic medium is water, the reduction in the total

(a) $\sigma_p = 0\%$

Mode order	*In vacuo*	Water-loaded (Fig. 7.23(a)) $\bar{\Theta}_{mnpq}$ evaluation: Numerical	Closed form
(1,1)	60.06	9.69	9.43
(1,2)	133.90	28.15	27.39
(2,1)	166.39	37.01	36.01
(2,2)	240.23	58.93	57.34

(b) $\sigma_p = 0.24\%$

Mode order	*In vacuo*	Water-loaded (Fig. 7.23(b)) $\bar{\Theta}_{mnpq}$ evaluation: Numerical	Closed form
(1,1)	59.95	10.52	9.96
(1,2)	133.66	29.74	28.15
(2,1)	166.09	39.10	37.01
(2,2)	239.80	60.57	58.93

(c) $\sigma_p = 0.95\%$

Mode order	*In vacuo*	Water-loaded (Fig. 7.23(c)) $\bar{\Theta}_{mnpq}$ evaluation: Numerical	Closed form
(1,1)	59.65	12.06	11.73
(1,2)	132.99	32.28	31.41
(2,1)	165.26	41.29	41.29
(2,2)	238.60	65.75	63.97

(d) $\sigma_p = 5.93\%$

Mode order	*In vacuo*	Water-loaded (Fig. 7.23(d)) $\bar{\Theta}_{mnpq}$ evaluation: Numerical	Closed form
(1,1)	57.85	16.74	16.74
(1,2)	128.98	41.29	40.18
(2,1)	160.28	52.82	51.40
(2,2)	231.40	79.62	77.48

(e) $\sigma_p = 23.71\%$

Mode order	*In vacuo*	Water-loaded (Fig. 7.23(e)) $\bar{\Theta}_{mnpq}$ evaluation: Numerical	Closed form
(1,1)	53.26	21.42	21.42
(1,2)	118.75	50.01	50.01
(2,1)	147.56	62.25	62.25
(2,2)	213.05	91.30	91.30

Table 7.3 Comparison of natural frequencies (in Hz) of panels with different perforation ratios under *in vacuo* and water-loaded conditions. The natural frequencies of water-loaded panels are computed using the mean quadratic velocity plots shown in Fig 7.23.

inertia loading is more than the reduction in the stiffness, which in turn results in the increase in the natural frequencies with perforation ratio. The radiation efficiencies of the water-loaded perforated panels are shown in Fig. 7.24. As the resonances of the water-loaded panels are relatively very close in the frequency spectrum, the reduction in the radiation efficiency with the perforation ratio is not evident in Fig. 7.24.

7.5.3 Modal coupling coefficient

As mentioned before, the fluid loading couples the *in vacuo* modes of the panel and is captured by the modal coupling coefficient. The vibrations of the $(m, n)^{\text{th}}$ mode of the panel generate an acoustic pressure field with wavenumber components spanning the whole spectrum. This acoustic pressure field influences the vibrations of the

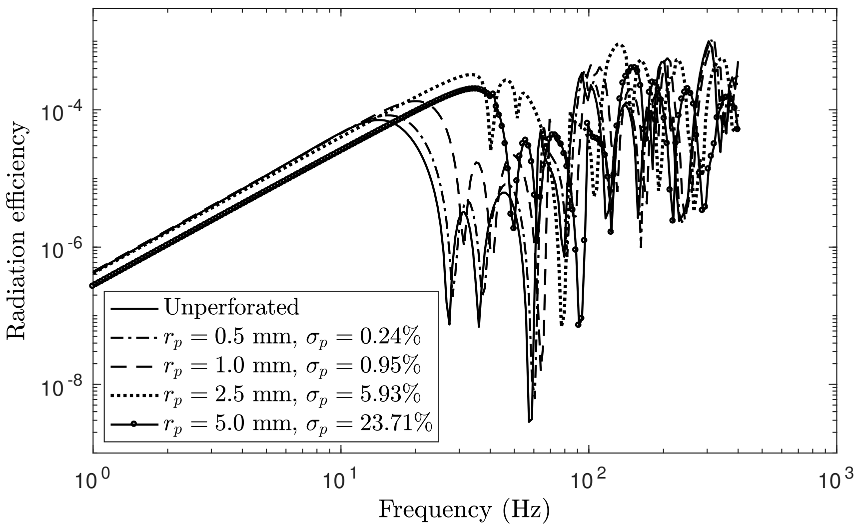

Fig. 7.24 Radiation efficiencies for water-loaded (in both the half-spaces) panels of different perforation ratios when the excitation is at an off-center location (0.1,0.1). Total number of holes in each of the panels is $N_0 = 750$. The modal coupling coefficient is evaluated using the closed form expressions.

$(p,q)^{\text{th}}$ mode of the panel. The modal coupling coefficient $\bar{\Theta}_{mnpq}$ signifies the effect of vibrations of the $(m,n)^{\text{th}}$ mode on that of the $(p,q)^{\text{th}}$ mode of the panel. At the same time, the pressure field generated by the $(p,q)^{\text{th}}$ mode influences the response by the $(m,n)^{\text{th}}$ mode of the panel as well.

This interaction between the two panel modes through the associated radiated pressure fields can be either resistive or reactive. For the resistive case, the pressure field generated by one mode dampens the vibrations of the other mode. Looking at differently, the pressure field of one mode offers resistive load on the vibrations of the other mode and thus, the energy from the acoustic field is transferred to the panel. On the other hand when the interaction is reactive, the acoustic field generated by one mode acts as a mass loading on the vibrations of the other mode and no net energy is transferred from the acoustic medium to the panel. This interaction between panel modes is shown in Fig. 7.25.

The modal coupling coefficient $\bar{\Theta}_{mnpq}$, as defined in Eq. (7.1) is a complex quantity. Its real part is termed as the radiation coupling coefficient as it represents the radiation loading offered by the surrounding acoustic medium to the panel vibration [33]. The radiation coupling coefficient acts along with the structural damping of the panel. The imaginary part of the modal coupling coefficient is termed as the inertia coupling coefficient, for it results in a virtual mass term to be added to the panel mass [33].

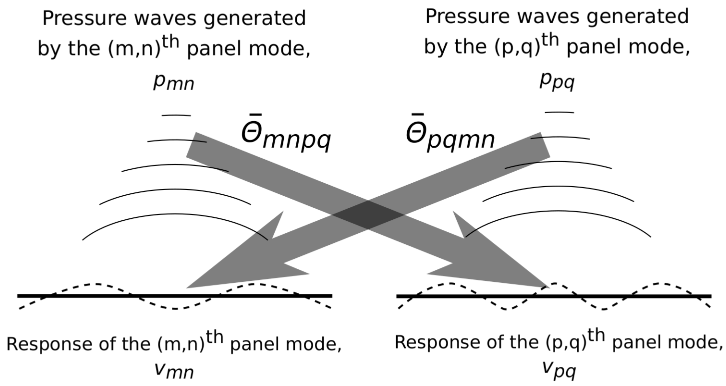

Fig. 7.25 Schematic of the panel modal interaction as a result of the fluid loading.

The combined effect of this radiation and inertia coupling terms causes a decrease in the vibration amplitude of a fluid-loaded panel from its *in vacuo* values. Consequently, a corresponding decrease in the radiated power and the radiation efficiency are also observed. This effect of fluid loading has been demonstrated in Fig. 7.21, however, between a light (air) and a heavy (water) fluid loading cases (we have observed in chapter 5 that for the case of air, the radiation efficiency match very well with that obtained using the one way coupled formulation).

For the wave motion in an infinite panel with subsonic phase velocities, the surrounding fluid acts as a virtual mass and hence no energy is transferred to the acoustic medium. Whereas, when the phase velocities in the panel are supersonic the surrounding fluid acts as a damper and the energy is transferred from the panel to the acoustic medium in the form of acoustic radiation [7, 33, 34]. For a finite panel, the 'uncancelled' components of the volume velocity at subsonic wave speeds cause the sound radiation [12] and therefore the modal coupling coefficient at subsonic wave speeds has a non-zero real part. The non-zero real term in the coupling coefficient was also derived by Davies [33] for the corner - corner interaction, which is the predominant form of coupling at subsonic wave speeds. However, Davies neglected the influence of the 'cross' inertia coupling terms in the radiated power.

We now look at the behavior of the modal coupling coefficient, which is classified according to the associated panel wavenumbers. It is assumed that the acoustic medium is air, since it is clear from Eq. (7.3) that for any other acoustic medium the modal coupling coefficient follows a similar behavior; the magnitude is inversely proportional to the density of the medium and the speed of sound in that medium. As $\bar{\Theta}_{mnpq}$ defined in Eq. (7.1) is general for panels of any given perforation ratio, it is sufficient we consider an unperforated panel to analyze the behavior of modal coupling coefficient. The characteristics are analyzed at different frequencies, viz., 100.77 Hz ($\omega/\omega_c = 0.03$), 507.79 Hz ($\omega/\omega_c = 0.13$), 3007.88 Hz ($\omega/\omega_c = 0.75$), 5000.31 Hz ($\omega/\omega_c = 1.25$) and 8312.51 Hz ($\omega/\omega_c = 2.07$), where ω_c denotes the critical frequency of the panel in air. They correspond to different regions which distinguish different types of panel radiation [12] (radiation efficiency of the unperforated panel with air as the acoustic medium is shown in Fig. 7.21). The real and the imaginary parts of the modal coupling coefficient at these frequencies are shown in Fig. 7.26. All types of modal interactions (based on the panel wavenumber/phase velocities) of a finite simply supported panel are included in this study. In brief, there are as many as eight different types of interactions which can be significant at any given frequency, namely, corner - corner (C-C), edge - corner (E-C), edge - edge (E-E), two edge - edge (XYE-E), two edge - two edge (XYE-XYE), acoustically fast - edge (AF-E), acoustically fast - two edge (AF-XYE) and acoustically fast - acoustically fast (AF-AF). The types of interactions which are present at a given frequency are also shown in Fig. 7.26. Each point in the figure corresponds to a specified type of interaction. The number of occurrences of a particular interaction is shown by the range which the interaction spans along the x axis.

(a) At 100.77 Hz ($\omega/\omega_c = 0.03$)

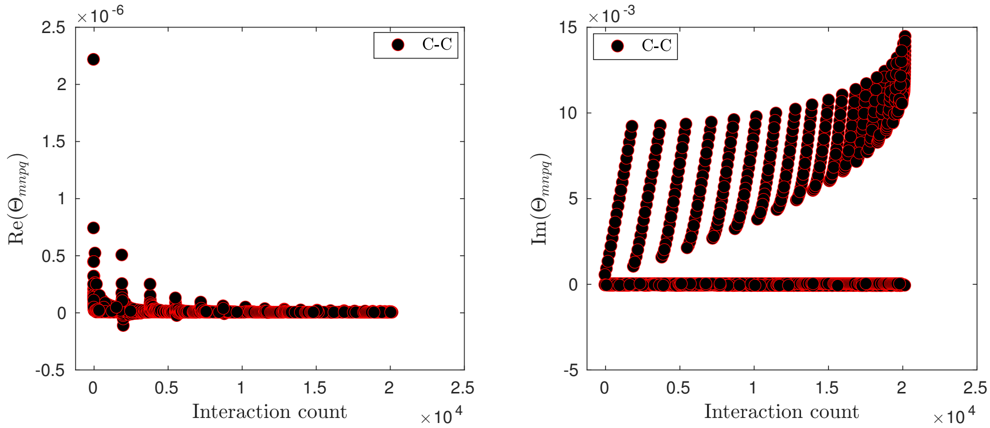

(b) At 507.79 Hz ($\omega/\omega_c = 0.13$)

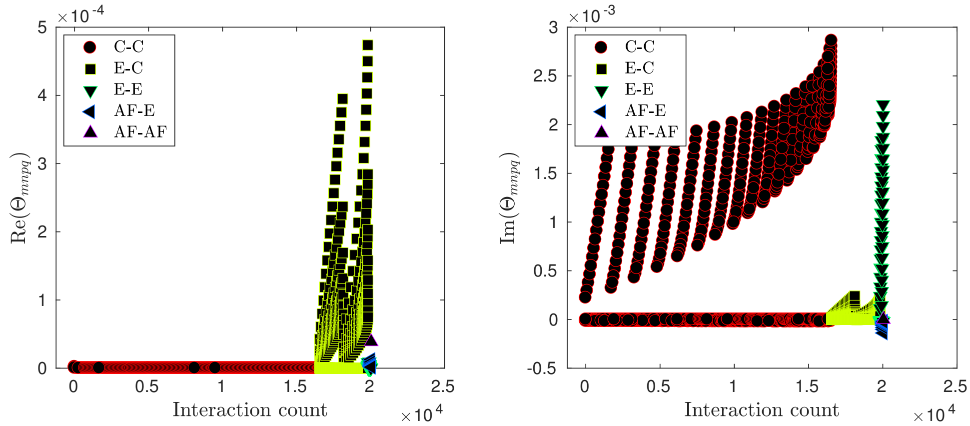

(c) At 3007.88 Hz ($\omega/\omega_c = 0.75$)

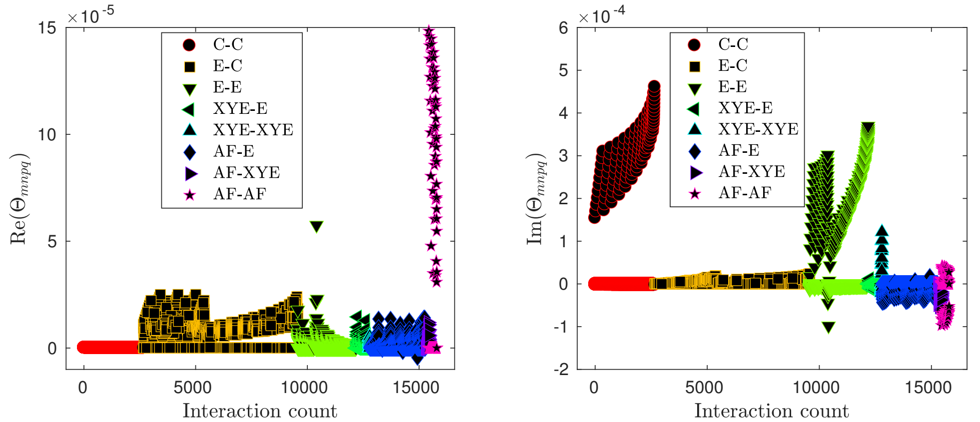

(d) At 5000.31 Hz ($\omega/\omega_c = 1.25$)

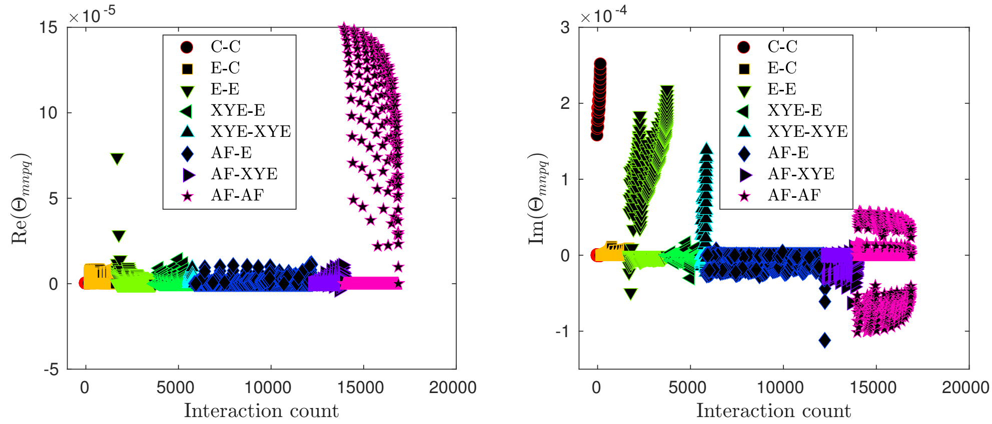

(e) At 8312.52 Hz ($\omega/\omega_c = 2.07$)

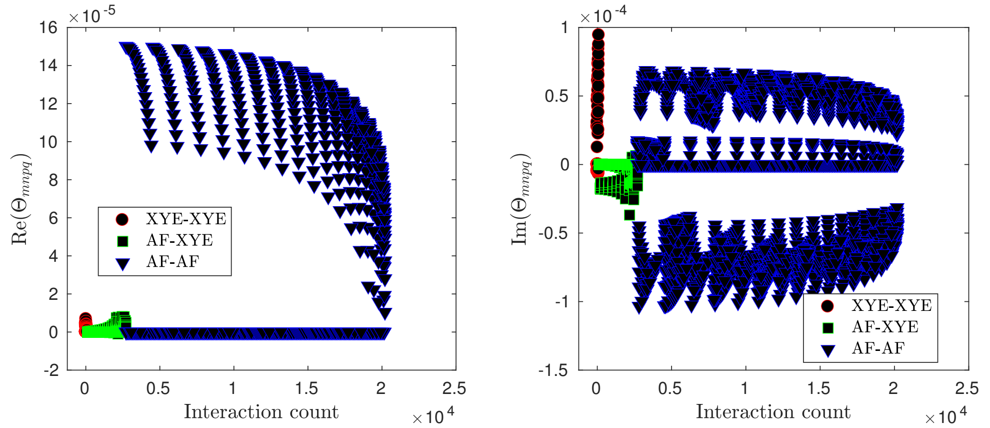

Fig. 7.26 Real and imaginary parts of the modal coupling coefficient ($\bar{\Theta}_{mnpq}$) of an unperforated simply supported panel with air in both the half-spaces and is excited at its center by a unit harmonic force at different frequencies.

It is evident from Fig. 7.26 that for the corner - corner interactions there exists a radiation term (real) in the modal coupling coefficient in addition to the inertia term (imaginary). This was also reported by Davies [33]. Note that in this study, the effect of 'cross' inertia coupling terms is taken into account while evaluating the panel response, which was neglected by Davies in his approximation. We know that at very low frequencies, the coupling is predominantly due to the modal interactions involving the subsonic modes. Although there exist non-zero real terms in the associated modal coupling coefficients, leading to the sound radiation in the acoustic medium, they are dominated by the inertia coupling terms (see Fig. 7.26a). This radiation behavior associated with the real part of the coupling coefficient is also seen for the other modal interactions involving corner type of panel modes (see Figs. 7.26a - 7.26d). With the increase in frequency, more panel modes become supersonic and hence the radiation coupling increases with the frequency. At the same time, as the frequency increases, the inertia coupling reduces and becomes less significant as compared to the radiation coupling (see Figs. 7.26d and 7.26e).

7.6 Conclusions

A two-way coupled formulation in the wavenumber domain is presented to study the sound radiation from a finite perforated panel set in baffle. The formulation is general and assumes arbitrary fluid loading on the panel. The fluid loading leads to a complex modal coupling coefficient in the coupled equation of motion. The modal coupling coefficient, defined in integral form, is different from that defined by Davies [33] and Pope [34] - the square root function now appears in the numerator of the integrand. The real part of the coupling coefficient acts as the radiation damping and the imaginary part offers virtual mass addition to the structure. Individual approximate expressions in closed form are obtained for the modal coupling coefficient based on the panel modal wavenumbers. The approximations are valid for the entire frequency range of interest and for any given fluid loading conditions.

It is found that the radiation efficiency of the panel immersed in water is less than when it is in air. The higher radiation damping and fluid inertia loading on the panel when it is in water reduces its vibration velocity amplitude. It is then reflected in the reduced radiated power and radiation efficiency of the panel immersed in water. The radiation efficiency of the water-loaded panel is found to decrease with the increasing perforation ratio. This behavior is due to the decrease in the perforate impedance with the increasing perforation ratio. Similar behavior was reported earlier while studying the panel sound radiation in air using the one-way coupled formulation.

The inertia coupling terms are responsible for the decrease in the natural frequencies of the panel when the fluid loading is taken into account. The natural frequencies of the perforated panels are obtained from the peaks of the mean quadratic velocity plots. The mean quadratic velocity and the natural frequencies of water-loaded panels are compared for various perforation ratios using either the closed form for the modal coupling coefficient or evaluating it using numerical integration technique. The closed form method is found to be in good agreement with the numerical scheme. It has been observed that under water loading conditions, the resonance frequency of a particular mode increases with the increase in the perforation ratio, as a result of the relatively larger reduction in the total inertia loading of the panel as compared to the reduction in its stiffness.

The real and the imaginary parts of the modal coupling coefficient are compared at different frequencies. It has been found that there are effectively only eight types of modal interactions that can be significant at any given frequency. These interactions are characterised by their modal wavenumbers. For any interaction involving subsonic modes there exists a small real term in the coupling coefficient which causes the sound radiation. This form of sound radiation by the subsonic modes are significant at low frequencies. However, at low frequencies, the dominant inertia coupling for the subsonic modal interaction offers significant inertia loading on the panel. As the frequency is increased more modes become supersonic and the interaction involving these modes are characterised by a larger real term in the coupling coefficient and results in the increased radiation damping at higher frequencies. At the same time, the inertia loading caused by these interactions at higher frequencies are small.

Chapter 8

Conclusions

The main work of this thesis relates to the sound radiation and transmission from a fluid loaded finite perforated panel set in an unperforated baffle. The work is presented in three parts: first, a one-way coupled analysis is presented followed by a complex two-way coupled formulation and in the last part, closed form expressions are derived for the modal coupling coefficient. In this chapter, a brief description of the mathematical models developed and the important results obtained is presented. Some of the directions in which this work can be further extended are also discussed in this chapter.

8.1 The one-way coupled analysis

In this part of the thesis (chapters 3 and 4), a one-way coupled formulation, neglecting the fluid loading on the panel is presented. Chapter 3 develops a model for the sound radiation from a flexible perforated panel set in an unperforated baffle. The panel is excited by a harmonic point force. This work extends the studies by Fahy and Thompson [5] and Putra and Thompson [4]. In this study, the *in vacuo* natural frequencies of the perforated panel are calculated using the Receptance method. Also, the discontinuity in the perforate impedance at the panel edges is modeled by an average velocity field (LAFP velocity) at the fluid-structure boundary. The model neglects the effect of radiated pressure on the panel response. However, the radiated pressure is taken into account while finding the LAFP velocity.

It is observed that for a given mode, the natural frequency of the perforated panel is less than that of the unperforated panel. Also, the natural frequency predictions agree very well with the finite element results. It is found that for a finite perforated panel the perforations reduces the radiation efficiency. In the monopole region at lower frequencies, the slope of the radiation efficiency curve is less than the 20 dB/decade slope of an unperforated panel.

The radiation efficiency is found to decrease with the decreasing perforate impedance. For a given hole radius, increasing the number of holes in the panel results in a lower perforate impedance and hence causes a reduction in the radiation efficiency. At low frequencies, for a panel with sub-millimeter hole radii, the sound radiation is more controlled by the resistive perforate impedance than the reactive component. A mean value of the radiation efficiency, averaged over all the forcing points on the panel surface, is also obtained for various perforation ratios.

Chapter 4 presents the one-way coupled model for the sound transmission through the finite perforated panel when a plane wave is incident upon it. The model predictions for the specific case of an unperforated panel are verified. The transmission loss decreases when perforations are made in the panel. A lower perforate impedance leads to a better transmission of sound through the perforations and hence in a lower transmission loss. The relatively higher resistive perforate impedance (as compared to the reactive impedance) at low frequencies brings about a high transmission loss for a panel with sub-millimeter size holes. It is found that the transmitted power does not vary significantly with the angle of incidence of the plane wave. Whereas, the incident power decreases with the increasing angle of incidence. Consequently, the transmission loss is also decreased.

8.2 The two-way coupled analysis

In this part of the thesis (chapters 5 and 6), a two-way coupled formulation is presented, which includes the effect of fluid loading on the panel response. The fluid loading invokes a coupling between the *in vacuo* natural modes of the perforated panel and is mathematically represented as a modal coupling coefficient in the equation of motion.

Chapter 5 develops the fully coupled model for the sound radiation from a flexible perforated panel set in an unperforated baffle, when the panel is excited by a harmonic point force. The formulation is presented as an extension of the work carried out in chapter 3. The model is also used to predict the natural frequencies of the fluid-loaded perforated panel. The natural frequencies of fluid-loaded panel are smaller than the corresponding *in vacuo* values. It is observed that when the panel is immersed in water, the natural frequency of a given mode increases with the increase in perforation ratio. As for the one-way coupled case, the perforate impedance influences the sound radiation more than the panel impedance, although the modal coupling coefficient alters the effective panel impedance. It is observed that the perforate impedance decreases with the increase in the perforation ratio, so is the radiation efficiency. Also, for a perforated panel immersed in water, the radiation efficiency is less than when it is immersed in air. It is observed that for light medium like air, the one-way coupled model is sufficient to predict the radiation efficiency.

In chapter 6, a fully coupled model for the sound transmission through the perforated panel under plane wave incidence is presented. The surrounding fluid load reduces the panel response. For an unperforated panel, the fluid loading causes an increase in the transmission loss as compared to the one-way coupled prediction. For a perforated panel, the perforate impedance controls the transmission through the perforated panel - the influence of the panel vibration is negligible, even after including the fluid loading effect. As a result, the transmission loss decreases with the increase in the perforation ratio. It is observed that when the acoustic medium is light, the one-way coupled model is sufficient to predict the transmission loss of a perforated panel.

It is observed that at low frequencies, the transmission loss of a perforated panel becomes negative. This apparent violation of the conservation of power is related to the definition of the incident power, which considered only the power carried by the incident plane wave. There exists an additional component in the incident power owing to the discontinuous perforate impedance at the panel-baffle boundary. And this additional incident power on the panel surface comes from above the baffle region by the diffraction effect. Further, an expression for this additional incident power is derived. The new transmission loss, calculated after including the diffracted component, remains positive in the entire frequency range.

8.3 Closed form expressions for the modal coupling coefficient

In this part (chapter 7), approximate expressions for the modal coupling coefficient are obtained based on the associated panel wavenumbers using the contour integration technique. The closed form expressions are then used to compute the resonance frequencies and the radiation efficiency of the finite flexible perforated panel. The results are in close agreement with that reported in chapter 5, where the modal coupling coefficient is evaluated using the numerical integration technique. The derived expressions for the modal coupling coefficient are valid for the entire frequency range and for any fluid loading conditions; for a given acoustic medium the coupling coefficient is inversely proportional to the density of the medium and the speed of sound in that medium. Also, the closed form expressions can be used for any given perforation ratio.

The modal coupling coefficient represents the interaction between different *in vacuo* panel modes. It is a complex quantity - the real part represents the radiation damping and acts along with the structural damping, whereas the imaginary part represents the inertia loading on the perforated panel. The combined effect of the radiation and the inertia coupling terms causes a reduction in the panel response from its *in vacuo* values. Therefore, the radiation efficiency also gets reduced when the fluid loading is included in the analysis. The inertia coupling term is responsible for the decrease in the resonance frequencies of the fluid-loaded panel. It is observed that of the fifteen different modal interactions only eight are significant at any given frequency, namely, corner - corner (C-C), edge - corner (E-C), edge - edge (E-E), two edge - edge (XYE-E), two edge - two edge (XYE-XYE), acoustically fast - edge (AF-E), acoustically fast - two edge (AF-XYE) and acoustically fast - acoustically fast (AF-AF) interactions.

At very low frequencies, the coupling is predominantly due to the interaction between the subsonic modes. The corresponding modal coupling coefficient has a large reactive part (inertia coupling). The real part (radiation coupling), although very small, is responsible for the sound radiation by these subsonic panel modes. As the frequency increases, more panel modes become supersonic and the radiation coupling increases with frequency. And at higher frequencies, the radiation coupling dominates over the inertia coupling.

Thus, the novelty of this work lies in modeling the sound radiation and transmission through a finite flexible perforated panel set in an infinite rigid unperforated baffle using the one-way and the two-way coupled formulations and also in finding the resonance frequencies of a fluid-loaded perforated panel. The novelty is also due to the closed form expressions of the modal coupling coefficient for different types of modal interactions of the fluid-loaded perforated panel.

8.4 Design guidelines

The use of perforated panel as a sound barrier can achieve sound reduction at the receiver side. The sound reduction can be computed from the sound transmission loss (TL) across the perforated panel. The objective of a noise control engineer using perforated panel is to achieve maximum TL in a specific frequency band. The following guidelines are drawn from the present study and can be useful in the design of perforated panel for the sound transmission applications:

- A smaller size perforation can achieve the highest TL threshold (the required minimum of TL in the whole frequency range). For example, if the required minimum TL is 15 dB for a perforated panel with dimensions 0.455 m $\times$ 0.546 m, the hole radius should be $\leq$ 0.5 mm (see Fig. 6.9 for the constant number of holes case). For the panel with 0.5 mm hole radius, the minimum TL of 15 dB occurs at 390 Hz. In comparison, for the panel with 1 mm hole radius, the minimum TL is 7 dB and it occurs at 145 Hz.

- At low frequencies, a perforated panel with a smaller hole size (radius $<$ 0.5 mm) is preferred as it can provide the maximum TL (see Fig. 6.5 for constant perforation ratio and Fig. 6.9 for constant number of holes cases). For the 0.5 mm radius case shown in Fig. 6.9, the TL at 10 Hz is 32 dB, whereas for the 1 mm radius case, it is 18 dB at the same frequency.

- Panels with larger holes (radius $>$ 2 mm) have very low TL at low frequencies. The TL will increase only at high frequencies. For example, in the present study, the panel with 2.5 mm radius holes has TL $<$ 10 dB up to 2000 Hz; TL reaches the 20 dB level only at 10000 Hz (see Fig. 6.9 for the constant number of holes case).

Perforated panels are used in machine casings. In such applications, the perforation helps to reduce the noise generated by panel vibrations. In this thesis, the sound generated by the vibrating perforated panel is measured in terms of the sound radiation efficiency (σ). The objective of a design engineer is to achieve a minimum radiation efficiency in the operating frequency range. The following guidelines are proposed to ensure minimum radiation efficiency from the perforated panel:

- A lower radiation efficiency can be achieved by increasing the perforation ratio. For small perforation ratios, the radiation efficiency is very close to that of an unperforated panel. As shown in Fig. 5.9, the radiation efficiency of panels with perforation ratio 0.24% and 0.95% is very close to unperforated panel radiation efficiency.

- The reduction in radiation efficiency with larger perforation ratio is significant only up to the coincidence frequency (see Figs. 3.8, 3.10 and 5.9). At high frequencies, the perforated panel acts as a perfect sound radiator. Therefore, the panel should be designed such that its coincidence frequency must be greater than the operating frequency range of the machinery.

- For low frequency applications, perforations with large hole size (radius > 2 mm) is suggested. For small holes, the resistive impedance is significant at low frequencies, resulting in a higher radiation efficiency (see Figs. 3.12 and 3.13).

8.5 Future research directions

- In this thesis, the hole size is assumed to be relatively small compared to the acoustic wavelength so that the acoustic field of one hole does not affect the pressure field at the other holes. Also, it is assumed that the hole separation is small with respect to the acoustic wavelength. This assumption is necessary to derive the acoustic impedance of an array of holes (perforate impedance) from that of one hole [2]. It will be interesting to test the validity of these assumptions for the flexible panel by studying the interaction between two adjacent holes and incorporating it in the perforate impedance expression.

- Li et al. [3] derived the hole impedance model for a micro-perforated membrane by including the no-slip condition for the fluid particle at the hole wall boundary. In line with this development, an improved expression for the perforate impedance using the thin plate theory can be developed and implemented in the model developed in this thesis.

- In finding the *in vacuo* natural frequencies and modeshapes of the perforated panel, the holes are considered as point mass voids, without accounting for the area effect. The present study can be further extended to include the area effect of the holes in the panel modal behavior.

- In this thesis, only two types of external excitations on the perforated panel are considered, viz., the point force and the plane wave excitations. However, the methodology presented here can be further modified to study the perforated panel response to line force and turbulent boundary layer excitations.

- In many practical applications of the perforated panel, it is backed by a finite cavity, with rigid or flexible walls. A one-way coupled analysis of a similar system was performed by Bravo et al. [55]. A fully coupled analysis including the fluid loading effects, as implemented in this thesis, along with the backing cavity dynamics will certainly help to achieve a better design of the perforated panel for greater sound absorption.

- The modal coefficient γ_{pq} arising due to the external excitation is evaluated numerically in this thesis. An analytical solution to the underlying integral will help to understand the physics of interaction between different external excitations and the *in vacuo* modes of the perforated panel.

- Developing a fully coupled model which includes the effect of mean fluid flow over the perforated panel will be an exciting problem to solve. This can be further extended to investigate more complex problems involving turbulent flows.

References

[1] Dah-You Maa. Potential of microperforated panel absorber. *The Journal of the Acoustical Society of America*, 104(5):2861–2866, 1998.

[2] D. Takahashi and M. Tanaka. Flexural vibration of perforated plates and porous elastic materials under acoustic loading. *The Journal of the Acoustical Society of America*, 112(4):1456–1464, 2002.

[3] Chenxi Li, Ben Cazzolato, and Anthony Zander. Acoustic impedance of micro perforated membranes: Velocity continuity condition at the perforation boundary. *The Journal of the Acoustical Society of America*, 139(1):93–103, 2016.

[4] A. Putra and D. J. Thompson. Sound radiation from perforated plates. *Journal of Sound and Vibration*, 329(20):4227–4250, 2010.

[5] F. J. Fahy and D. J. Thompson. The effect of perforation on the radiation efficiency of vibrating plates. *Proceedings of the Institute of Acoustics*, 26, 2004.

[6] L. Cremer, M. Heckl, and B.A.T. Petersson. *Structure-Borne Sound: Structural Vibrations and Sound Radiation at Audio Frequencies.* Springer, Berlin, Heidelberg, 3 edition, 2005.

[7] Frank Fahy and Paolo Gardonio. *Sound and Structural Vibration - Radiation, Transmission and Response.* Academic Press, UK, second edition, 2007.

[8] L. Meirovitch. *Fundamentals of Vibration.* Mcgraw-Hill Publ.Comp., 2003.

[9] Abhijit Sarkar. *Asymptotic analysis of the dispersion characteristics of structural acoustic waveguides.* PhD thesis, Indian Institute of Science, Bangalore, India, January 2009.

[10] Miguel C. Junger. Approaches to acoustic fluid–elastic structure interactions. *The Journal of the Acoustical Society of America*, 82(4):1115–1121, 1987.

[11] G. Xie, D. J. Thompson, and C. J. C. Jones. The radiation efficiency of baffled plates and strips. *Journal of Sound and Vibration*, 280(1–2):181–209, 2005.

[12] Gideon Maidanik. Response of ribbed panels to reverberant acoustic fields. *The Journal of the Acoustical Society of America*, 34(6):809–826, 1962.

[13] C. E. Wallace. Radiation resistance of a rectangular panel. *The Journal of the Acoustical Society of America*, 51(3B):946–952, 1972.

[14] M. C. Gomperts. Sound radiation from baffled, thin, rectangular plates. *Acta Acustica united with Acustica*, 37(2):93–102, 1977.

[15] M. C. Gomperts. Radiation from rigid baffled, rectangular plates with general boundary conditions. *Acta Acustica united with Acustica*, 30(6):320–327, 1974.

[16] Gideon Maidanik. Radiation efficiency of panels. *The Journal of the Acoustical Society of America*, 35(1):115–115, 1963.

[17] F. G. Leppington, E. G. Broadbent, and K. H. Heron. Acoustic radiation from rectangular panels with constrained edges. *Proceedings of the Royal Society of London. Series A, Mathematical and Physical Sciences*, 393(1804):67–84, 1984.

[18] Earl G. Williams. A series expansion of the acoustic power radiated from planar sources. *The Journal of the Acoustical Society of America*, 73(5):1520–1524, 1983.

[19] Alain Berry, Louis Guyader, Jean, and Jean Nicolas. A general formulation for the sound radiation from rectangular, baffled plates with arbitrary boundary conditions. *The Journal of the Acoustical Society of America*, 88(6):2792–2802, 1990.

[20] Xuefeng Zhang and Wen L. Li. A unified approach for predicting sound radiation from baffled rectangular plates with arbitrary boundary conditions. *Journal of Sound and Vibration*, 329(25):5307–5320, 2010.

[21] R. F. Keltie. The effects of modal coupling on the acoustic power radiation from panels. *Journal of Vibration, Acoustics, Stress, and Reliability in Design*, 109(48):1048–9002, 1987.

[22] W.L. Li and H.J. Gibeling. Determination of the mutual radiation resistances of a rectangular plate and their impact on the radiated sound power. *Journal of Sound and Vibration*, 229(5):1213–1233, 2000.

[23] W.L. Li. An analytical solution for the self- and mutual radiation resistances of a rectangular plate. *Journal of Sound and Vibration*, 245(1):1–16, 2001.

[24] F. G. Leppington, F. R. S. E. G. Broadbent, K. H. Heron, and Susan M. Mead. Resonant and non-resonant acoustic properties of elastic panels. i. the radiation problem. *Proceedings of the Royal Society of London A: Mathematical, Physical and Engineering Sciences*, 406(1831):139–171, 1986.

[25] W.A. Utley. Single leaf transmission loss at low frequencies. *Journal of Sound and Vibration*, 8(2):256–261, 1968.

[26] A. Brekke. Calculation methods for the transmission loss of single, double and triple partitions. *Applied Acoustics*, 14(3):225–240, 1981.

[27] A. Pellicier and N. Trompette. A review of analytical methods, based on the wave approach, to compute partitions transmission loss. *Applied Acoustics*, 68(10):1192–1212, 2007.

[28] Louis A. Roussos. Noise transmission loss of a rectangular plate in an infinite baffle. Technical paper NASA-TP-2398, L-15861, NAS 1.60:2398, NASA, 1985.

[29] Sten Ljunggren. Airborne sound insulation of thin walls. *The Journal of the Acoustical Society of America*, 89(5):2324–2337, 1991.

[30] M. Villot, C. Guigou, and L. Gagliardini. Predicting the acoustical radiation of finite size multi-layered structures by applying spatial windowing on infinite structures. *Journal of Sound and Vibration*, 245(3):433–455, 2001.

[31] John L. Davy. Predicting the sound insulation of single leaf walls: Extension of cremer's model. *The Journal of the Acoustical Society of America*, 126(4):1871–1877, 2009.

[32] Jonas Brunskog. The forced sound transmission of finite single leaf walls using a variational technique. *The Journal of the Acoustical Society of America*, 132(3):1482–1493, 2012.

[33] H. G. Davies. Low frequency random excitation of water-loaded rectangular plates. *Journal of Sound and Vibration*, 15(1):107–126, 1971.

[34] Larry D. Pope and Ralph C. Leibowitz. Intermodal coupling coefficients for a fluid-loaded rectangular plate. *The Journal of the Acoustical Society of America*, 56(2):408–415, 1974.

[35] B. E. Sandman. Fluid-loaded vibration of an elastic plate carrying a concentrated mass. *The Journal of the Acoustical Society of America*, 61(6):1503–1510, 1977.

[36] N. S. Lomas and S. I. Hayek. Vibration and acoustic radiation of elastically supported rectangular plates. *Journal of Sound and Vibration*, 52(1):1–25, 1977.

[37] Alain Berry. A new formulation for the vibrations and sound radiation of fluid-loaded plates with elastic boundary conditions. *The Journal of the Acoustical Society of America*, 96(2):889–901, 1994.

[38] W. R. Graham. High-frequency vibration and acoustic radiation of fluid-loaded plates. *Philosophical Transactions of the Royal Society of London A: Mathematical, Physical and Engineering Sciences*, 352(1698):1–43, 1995.

[39] W. R. Graham. Analytical approximations for the modal acoustic impedances of simply supported, rectangular plates. *The Journal of the Acoustical Society of America*, 122(2):719–730, 2007.

[40] D.G. Crighton and D. Innes. Low frequency acoustic radiation and vibration response of locally excited fluid-loaded structures. *Journal of Sound and Vibration*, 91(2):293–314, 1983.

[41] G.P. Eatwell and D. Butler. The response of a fluid-loaded, beam-stiffened plate. *Journal of Sound and Vibration*, 84(3):371–388, 1982.

[42] Denys J. Mead. Plates with regular stiffening in acoustic media: Vibration and radiation. *The Journal of the Acoustical Society of America*, 88(1):391–401, 1990.

[43] E. C. Sewell. Transmission of reverberant sound through single-leaf partition surrounded by an infinite rigid baffle. *Journal of Sound and Vibration*, 12(1):21–32, 1970.

[44] K. A. Mulholland and R. H. Lyon. Sound insulation at low frequencies. *The Journal of the Acoustical Society of America*, 54(4):867–878, 1973.

[45] F. G. Leppington, K. H. Heron, F. R. S. E. G. Broadbent, and Susan M. Mead. Resonant and non-resonant acoustic properties of elastic panels. ii. the transmission problem. *Proceedings of the Royal Society of London A: Mathematical, Physical and Engineering Sciences*, 412(1843):309–337, 1987.

[46] D. Takahashi. Effects of panel boundedness on sound transmission problems. *The Journal of the Acoustical Society of America*, 98(5):2598–2606, 1995.

[47] Jong-Hwa Lee and Jeong-Guon Ih. Significance of resonant sound transmission in finite single partitions. *Journal of Sound and Vibration*, 277(4):881–893, 2004.

[48] Chong Wang. Modal sound transmission loss of a single leaf panel: Effects of inter-modal coupling. *The Journal of the Acoustical Society of America*, 137(6):3514–3522, 2015.

[49] Chong Wang. Modal sound transmission loss of a single leaf panel: Asymptotic solutions. *The Journal of the Acoustical Society of America*, 138(6):3964–3975, 2015.

[50] Ran Zhou and Malcolm J. Crocker. Boundary element analyses for sound transmission loss of panels. *The Journal of the Acoustical Society of America*, 127(2):829–840, 2010.

[51] Raymond Panneton and Noureddine Atalla. Numerical prediction of sound transmission through finite multilayer systems with poroelastic materials. *The Journal of the Acoustical Society of America*, 100(1):346–354, 1996.

[52] Jean-Daniel Chazot and Jean-Louis Guyader. Prediction of transmission loss of double panels with a patch-mobility method. *The Journal of the Acoustical Society of America*, 121(1):267–278, 2007.

[53] A. Putra. *Sound radiation from perforated plates*. PhD thesis, ISVR, University of Southampton, June 2008.

[54] Teresa Bravo, Cic Maury, and Cic Pinh. Sound absorption and transmission through flexible micro-perforated panels backed by an air layer and a thin plate. *The Journal of the Acoustical Society of America*, 131(5):3853–3863, 2012.

[55] Teresa Bravo, Cic Maury, and Cic Pinh. Vibroacoustic properties of thin micro-perforated panel absorbers. *The Journal of the Acoustical Society of America*, 132(2):789–798, 2012.

[56] Stuart Bolton and Nicholas Kim. Use of cfd to calculate the dynamic resistive end correction for microperforated materials. *Acoustics Australia*, 38(3):134–139, 2010.

[57] Thomas Herdtle, J. Stuart Bolton, Nicholas N. Kim, Jonathan H. Alexander, and Ronald W. Gerdes. Transfer impedance of microperforated materials with tapered holes. *The Journal of the Acoustical Society of America*, 134(6):4752–4762, 2013.

[58] Masahiro Toyoda and Daiji Takahashi. Reduction of acoustic radiation by impedance control with a perforated absorber system. *Journal of Sound and Vibration*, 286(3):601–614, 2005.

[59] Masahiro Toyoda, Mikito Tanaka, and Daiji Takahashi. Reduction of acoustic radiation by perforated board and honeycomb layer systems. *Applied Acoustics*, 68(1):71–85, 2007.

[60] A. Putra and D.J. Thompson. Radiation efficiency of unbaffled and perforated plates near a rigid reflecting surface. *Journal of Sound and Vibration*, 330(22):5443–5459, 2011.

[61] Kimihiro Sakagami, Tomohito Nakamori, Masayuki Morimoto, and Motoki Yairi. Double-leaf microperforated panel space absorbers: A revised theory and detailed analysis. *Applied Acoustics*, 70(5):703–709, 2009.

[62] T. Dupont, G. Pavic, and B. Laulagnet. Acoustic properties of lightweight micro-perforated plate systems. *Acta Acustica united with Acustica*, 89(2):201–212, 2003.

[63] Y.Y. Lee, E.W.M. Lee, and C.F. Ng. Sound absorption of a finite flexible micro-perforated panel backed by an air cavity. *Journal of Sound and Vibration*, 287(1–2):227–243, 2005.

[64] Frank M. White. *Fluid Mechanics*. McGraw-Hill series in mechanical engineering. McGraw-Hill, 7 edition, 2011.

[65] Werner Soedel. *Vibrations of Shells and Plates*. Marcel Dekker, Inc., New York, 2004.

[66] V. R. Sonti. Sound radiation from a baffled rectangular plate under a variable line constraint. *Journal of Sound and Vibration*, 265(1):235–243, 2003.

[67] Mark J. Ablowitz and Athanassios S. Fokas. *Complex Variables: Introduction and Applications*. Cambridge Texts in Applied Mathematics. Cambridge University Press, 2 edition, 2003.

[68] A. I. Soler and W. S. Hill. Effective bending properties for stress analysis of rectangular tubesheets. *Journal of Engineering for Power*, 99(3):365–370, 1977.

[69] George P. Wilson and Walter W. Soroka. Approximation to the diffraction of sound by a circular aperture in a rigid wall of finite thickness. *The Journal of the Acoustical Society of America*, 37(2):286–297, 1965.

[70] Hyun H. Park and Hyo J. Eom. Acoustic scattering from a rectangular aperture in a thick hard screen. *The Journal of the Acoustical Society of America*, 101(1):595–598, 1997.

[71] L. Maxit, C. Yang, L. Cheng, and J.-L. Guyader. Modeling of micro-perforated panels in a complex vibro-acoustic environment using patch transfer function approach. *The Journal of the Acoustical Society of America*, 131(3):2118–2130, 2012.

[72] Cheng Yang, Li Cheng, and Jie Pan. Absorption of oblique incidence sound by a finite micro-perforated panel absorber. *The Journal of the Acoustical Society of America*, 133(1):201–209, 2013.

[73] Eric D. Daniel. On the dependence of absorption coefficients upon the area of the absorbent material. *The Journal of the Acoustical Society of America*, 35(4):571–573, 1963.

[74] Wolfram Research, Inc. Mathematica, Version 11.3. Champaign, IL, 2018.

[75] Robert H. Kraichnan. Noise transmission from boundary layer pressure fluctuations. *The Journal of the Acoustical Society of America*, 29(1):65–80, 1957.

Appendix A

Numerical evaluation of the Fourier transform of the LAFP velocity

The Fourier transform of the LAFP velocity can be obtained by solving Eq. (3.27) numerically. Eq. (3.27) is given by

$$\left[1 + \frac{2\sigma_b}{Z_{0b}} Z_a(\lambda,\mu)\right] V_a(\lambda,\mu,z=0) = \zeta_I V_p(\lambda,\mu) + \frac{ab}{2\pi^2}\left[\frac{\sigma_b}{Z_{0b}} - \frac{\sigma_p}{Z_{0p}}\right]$$
$$\times \left\{ \int_{-\infty}^{\infty}\int_{-\infty}^{\infty} Z_a(\lambda',\mu') V_a(\lambda',\mu',z=0)\,\mathrm{sinc}\left[\frac{(\lambda-\lambda')a}{2}\right]\,\mathrm{sinc}\left[\frac{(\mu-\mu')b}{2}\right]\,\mathrm{d}\lambda'\,\mathrm{d}\mu' \right\}.$$

We select a finite 2-D wavenumber domain for λ and μ and discretize it into $N_{\lambda\mu}$ (=N_λ $\times$ N_μ) smaller sub-domains of size d$\lambda \times$ dμ. Further, we identify each sub-domains with the corresponding (λ_i, μ_i) values. Thus, the above equation can be represented as

$$\left[1 + \frac{2\sigma_b}{Z_{0b}} Z_a(\lambda_i,\mu_i)\right] V_a(\lambda_i,\mu_i,z=0) = \zeta_I V_p(\lambda_i,\mu_i) + \frac{ab}{2\pi^2}\left[\frac{\sigma_b}{Z_{0b}} - \frac{\sigma_p}{Z_{0p}}\right]$$
$$\times \left\{ \sum_{j=1}^{N_\lambda \times N_\mu} Z_a(\lambda_j,\mu_j) V_a(\lambda_j,\mu_j,z=0)\,\mathrm{sinc}\left[\frac{(\lambda_i-\lambda_j)a}{2}\right]\,\mathrm{sinc}\left[\frac{(\mu_i-\mu_j)b}{2}\right]\,\mathrm{d}\lambda\,\mathrm{d}\mu \right\}. \tag{A.1}$$

Note, that the integral over the infinite 2-D wavenumber domain is approximated by a sum over a discretized, finite 2-D wavenumber domain. Now, define vectors: $\{V_a\}_{N_{\lambda\mu}\times 1}$, $\{V_p\}_{N_{\lambda\mu}\times 1}$ and $\{Z_a\}_{N_{\lambda\mu}\times 1}$ and matrices: $[Z_{ad}]_{N_{\lambda\mu}\times N_{\lambda\mu}}$ and $\left[\bar{Z}_a\right]_{N_{\lambda\mu}\times N_{\lambda\mu}}$, whose elements are given by

$$\begin{aligned} V_{a\,i} &= V_a(\lambda_i, \mu_i, z = 0), \\ V_{p\,i} &= V_p(\lambda_i, \mu_i), \\ Z_{a\,i} &= Z_a(\lambda_i, \mu_i), \\ Z_{ad\,ij} &= Z_a(\lambda_i, \mu_i)\delta_{ij} \end{aligned}$$

and

$$\bar{Z}_{a\,ij} = Z_a(\lambda_j, \mu_j)\,\mathrm{sinc}\left[\frac{(\lambda_i - \lambda_j)a}{2}\right]\,\mathrm{sinc}\left[\frac{(\mu_i - \mu_j)b}{2}\right]\,\mathrm{d}\lambda\,\mathrm{d}\mu,$$

Now, Eq. (A.1) can be expressed in matrix form as given below.

$$\left[[I] + \frac{2\sigma_b}{Z_{0b}}\,[Z_{ad}]\right]\{V_a\} = \zeta_I\,\{V_p\} + \frac{ab}{2\pi^2}\left(\frac{\sigma_b}{Z_{0b}} - \frac{\sigma_p}{Z_{0p}}\right)\left[\bar{Z}_a\right]\{V_a\}\,,$$

where $[I]$ is an identity matrix of order $N_{\lambda\mu} \times N_{\lambda\mu}$. Rearranging the above equation, we obtain

$$\left[[I] + \frac{2\sigma_b}{Z_{0b}}\,[Z_{ad}] - \frac{ab}{2\pi^2}\left(\frac{\sigma_b}{Z_{0b}} - \frac{\sigma_p}{Z_{0p}}\right)\left[\bar{Z}_a\right]\right]\{V_a\} = \zeta_I\,\{V_p\}\,. \tag{A.2}$$

Above equation can be solved for $\{V_a\}$ using matrix inversion.

Appendix B

Modal average radiation efficiency: similarly perforated panel and baffle

Consider a simply supported perforated panel ($-a/2 \leq x \leq a/b$, $-b/2 \leq y \leq b/2$) of perforation ratio σ_p set in a perforated baffle of same perforation ratio. A harmonic point force of magnitude F and angular frequency ω is applied at (x_i, y_i) on the panel. It is assumed that the perforations do not affect the modal characteristics of the panel. Hence, the response of the perforated panel at point (x, y) can be obtained from the modal sum of the unperforated panel and is given by [11]

$$v_p(x, y) = \sum_{m=1}^{\infty} \sum_{n=1}^{\infty} U_{mn} \phi_{mn}(x, y), \tag{B.1}$$

where

$$U_{mn} = \frac{-i\omega\phi_{mn}(x_i, y_i)F}{M_{mn}[\omega_{mn}^2(1 - i\eta) - \omega^2]}, \tag{B.2}$$

$$\phi_{mn}(x, y) = \sin\frac{m\pi(x + a/2)}{a} \sin\frac{n\pi(y + b/2)}{b}. \tag{B.3}$$

In the above equations, $\phi_{mn}(x, y)$ denotes the modeshape for the mode (m, n) and U_{mn} is the corresponding modal coefficient of an unperforated simply supported panel. η represents the damping loss factor and M_{mn} is known as the modal mass as given below.

$$M_{mn} = \int_{-b/2}^{b/2} \int_{-a/2}^{a/2} \rho_p h \phi_{mn}^2(x, y)\, \mathrm{d}x\, \mathrm{d}y = \frac{\rho_p hab}{4}. \tag{B.4}$$

Now, the spatial Fourier transform of the panel velocity is given by

$$V_p(\lambda, \mu) = \sum_{m=1}^{\infty} \sum_{n=1}^{\infty} U_{mn} \Phi_{mn}(\lambda, \mu), \tag{B.5}$$

where

$$\Phi_{mn}(\lambda, \mu) = \frac{1}{2\pi} \int_{-b/2}^{b/2} \int_{-a/2}^{a/2} \sin \frac{m\pi(x + a/2)}{a} \sin \frac{n\pi(y + b/2)}{b} e^{i\lambda x + i\mu y} \, \mathrm{d}x \, \mathrm{d}y.$$

Note that the integration is truncated to the panel area alone as the panel velocity $v_p(x, y)$ is zero over the baffle region. Thus,

$$\Phi_{mn}(\lambda, \mu) = \frac{a_m b_n}{2\pi} \frac{\left[(-1)^m e^{i\lambda a/2} - e^{-i\lambda a/2}\right]}{[\lambda^2 - a_m^2]} \frac{\left[(-1)^n e^{i\mu b/2} - e^{-i\mu b/2}\right]}{[\mu^2 - b_n^2]}, \tag{B.6}$$

with $a_m = \frac{m\pi}{a}$ and $b_n = \frac{n\pi}{b}$. The Fourier transform of the LAFP velocity over the perforated panel, for a similarly perforated baffle case is given by Eq. (3.30).

$$V_a(\lambda, \mu, z = 0) = \frac{\zeta_I}{\left[1 + \frac{2\sigma_p}{Z_{0p}} Z_a(\lambda, \mu)\right]} V_p(\lambda, \mu).$$

B.1 Average radiated power

The radiated power from the perforated panel is given by Eq. (3.31).

$$W = \frac{1}{2} \mathrm{Re} \left\{ \int_{-\infty}^{\infty} \int_{-\infty}^{\infty} P^+(\lambda, \mu, z = 0) V_a^*(\lambda, \mu) \, \mathrm{d}\lambda \, \mathrm{d}\mu \right\}.$$

In the above equation, the average fluid particle velocity due to panel motion and flow of fluid through the perforate is used to evaluate the radiated power. Substituting for $P^+(\lambda, \mu, z = 0)$ from Eq. (3.13) we get

$$W = \frac{1}{2} \mathrm{Re} \left\{ \int_{-\infty}^{\infty} \int_{-\infty}^{\infty} Z_a(\lambda, \mu) |V_a(\lambda, \mu, z = 0)|^2 \, \mathrm{d}\lambda \, \mathrm{d}\mu \right\}. \tag{B.7}$$

In order to find a mean value of radiated power, let us take an average over all forcing locations [11]. The average radiated power is defined as

$$\overline{W} = \frac{1}{ab} \int_{-b/2}^{b/2} \int_{-a/2}^{a/2} W(x_i, y_i) \, \mathrm{d}x_i \, \mathrm{d}y_i. \tag{B.8}$$

Substituting for W from Eq. (B.7) and rearranging the order of integration we obtain

$$\overline{W} = \frac{1}{2} \mathrm{Re} \left\{ \int_{-\infty}^{\infty} \int_{-\infty}^{\infty} Z_a(\lambda, \mu) \left[\frac{1}{ab} \int_{-b/2}^{b/2} \int_{-a/2}^{a/2} |V_a(\lambda, \mu, z = 0)|^2 \, \mathrm{d}x_i \, \mathrm{d}y_i \right] \mathrm{d}\lambda \, \mathrm{d}\mu \right\}. \tag{B.9}$$

The equation above is the power radiated by the entire panel at a given frequency (hence responding in several modes) averaged over all the force locations. Let the integral inside the square bracket be denoted as

$$\overline{|V_a(\lambda, \mu, z = 0)|^2} = \frac{1}{ab} \int_{-b/2}^{b/2} \int_{-a/2}^{a/2} |V_a(\lambda, \mu, z = 0)|^2 \, \mathrm{d}x_i \, \mathrm{d}y_i. \tag{B.10}$$

Using the equation for $V_a(\lambda, \mu, z = 0)$ (Eq. (3.30)), the integral on the right hand side is evaluated as below.

$$\begin{aligned}
\overline{|V_a(\lambda, \mu, z = 0)|^2} &= \frac{|\zeta_I|^2}{\left|1 + \frac{2\sigma_p}{Z_{0p}} Z_a(\lambda, \mu)\right|^2} \left[\frac{1}{ab} \int_{-b/2}^{b/2} \int_{-a/2}^{a/2} |V_p(\lambda, \mu)|^2 \, \mathrm{d}x_i \, \mathrm{d}y_i \right] \\
&= \frac{|\zeta_I|^2}{\left|1 + \frac{2\sigma_p}{Z_{0p}} Z_a(\lambda, \mu)\right|^2} \\
&\quad \times \left[\frac{1}{ab} \int_{-b/2}^{b/2} \int_{-a/2}^{a/2} \sum_{m=1}^{\infty} \sum_{n=1}^{\infty} \sum_{p=1}^{\infty} \sum_{q=1}^{\infty} U_{mn} U_{pq}^{*} \Phi_{mn}(\lambda, \mu) \Phi_{pq}^{*}(\lambda, \mu) \, \mathrm{d}x_i \, \mathrm{d}y_i \right] \\
&= \frac{|\zeta_I|^2}{\left|1 + \frac{2\sigma_p}{Z_{0p}} Z_a(\lambda, \mu)\right|^2} \\
&\quad \times \sum_{m=1}^{\infty} \sum_{n=1}^{\infty} \sum_{p=1}^{\infty} \sum_{q=1}^{\infty} \left[\frac{1}{ab} \int_{-b/2}^{b/2} \int_{-a/2}^{a/2} U_{mn} U_{pq}^{*} \, \mathrm{d}x_i \, \mathrm{d}y_i \right] \Phi_{mn}(\lambda, \mu) \Phi_{pq}^{*}(\lambda, \mu).
\end{aligned}$$

Due to orthogonality property of eigenfunctions, the summation over cross modal terms ($m \neq p$ or $n \neq q$) vanish. Hence, we get

$$\overline{|V_a(\lambda, \mu, z=0)|^2} = \sum_{m=1}^{\infty}\sum_{n=1}^{\infty} \frac{|\zeta_I|^2 |\Phi_{mn}(\lambda, \mu)|^2}{\left|1 + \frac{2\sigma_p}{Z_{0p}} Z_a(\lambda, \mu)\right|^2} \left[\frac{1}{ab} \int_{-b/2}^{b/2}\int_{-a/2}^{a/2} |U_{mn}|^2 \, \mathrm{d}x_i \, \mathrm{d}y_i\right].$$

Let,

$$\overline{|U_{mn}|^2} = \frac{1}{ab} \int_{-b/2}^{b/2}\int_{-a/2}^{a/2} |U_{mn}|^2 \, \mathrm{d}x_i \, \mathrm{d}y_i.$$

Now, using the expression for U_{mn} (Eq. (B.2)),

$$\overline{|U_{mn}|^2} = \frac{\omega^2 |F|^2}{4M_{mn}^2 \left|\omega_{mn}^2(1 - i\eta) - \omega^2\right|^2}. \tag{B.11}$$

Therefore,

$$\overline{|V_a(\lambda, \mu, z=0)|^2} = \sum_{m=1}^{\infty}\sum_{n=1}^{\infty} \frac{|\zeta_I|^2}{\left|1 + \frac{2\sigma_p}{Z_{0p}} Z_a(\lambda, \mu)\right|^2} \overline{|U_{mn}|^2} \, |\Phi_{mn}(\lambda, \mu)|^2. \tag{B.12}$$

Hence, the average radiated power is obtained as

$$\overline{W} = \sum_{m=1}^{\infty}\sum_{n=1}^{\infty} \frac{\overline{|U_{mn}|^2}}{2} \operatorname{Re}\left\{\int_{-\infty}^{\infty}\int_{-\infty}^{\infty} \frac{Z_a(\lambda, \mu) \, |\zeta_I|^2}{\left|1 + \frac{2\sigma_p}{Z_{0p}} Z_a(\lambda, \mu)\right|^2} \, |\Phi_{mn}(\lambda, \mu)|^2 \, \mathrm{d}\lambda \, \mathrm{d}\mu\right\}.$$

where, $\Phi_{mn}(\lambda, \mu)$ and $\overline{|U_{mn}|^2}$ are given by Eqs. (B.6) and (B.11) respectively. In the above equation, only the wavenumber components satisfying the equation $k^2 > \lambda^2 + \mu^2$ will radiate into the far field. Hence, for the average power radiated into the far field, the limits of integration is truncated as shown below.

$$\overline{W} = \sum_{m=1}^{\infty}\sum_{n=1}^{\infty} \frac{\overline{|U_{mn}|^2}}{2} \operatorname{Re}\left\{\int_{-k}^{k}\int_{-\sqrt{k^2-\mu^2}}^{\sqrt{k^2-\mu^2}} \frac{Z_a(\lambda, \mu) \, |\zeta_I|^2}{\left|1 + \frac{2\sigma_p}{Z_{0p}} Z_a(\lambda, \mu)\right|^2} \, |\Phi_{mn}(\lambda, \mu)|^2 \, \mathrm{d}\lambda \, \mathrm{d}\mu\right\}. \tag{B.13}$$

Before finding the average radiation efficiency, let's look at the average radiated power in detail. Let, $\overline{W_{mn}}$ be the average modal radiated power for the perforated panel.

This is defined as (using Eq. (B.8))

$$\overline{W_{mn}} = \frac{1}{ab} \int_{-b/2}^{b/2} \int_{-a/2}^{a/2} W_{mn}(x_i, y_i) \, \mathrm{d}x_i \, \mathrm{d}y_i. \tag{B.14}$$

Substituting for W_{mn}, we obtain

$$\overline{W_{mn}} = \frac{1}{2} \mathrm{Re} \left\{ \int_{-k}^{k} \int_{-\sqrt{k^2-\mu^2}}^{\sqrt{k^2-\mu^2}} Z_a(\lambda, \mu) \overline{|V_{a,mn}(\lambda, \mu, z=0)|^2} \, \mathrm{d}\lambda \, \mathrm{d}\mu \right\},$$

where $\overline{|V_{a,mn}(\lambda, \mu, z=0)|^2}$ is the modulus squared average fluid particle velocity for the mode (m, n), averaged over all forcing locations on the panel. Using Eqs. (B.10) and (B.12), we get

$$\overline{|V_{a,mn}(\lambda, \mu, z=0)|^2} = \frac{|\zeta_I|^2}{\left| 1 + \frac{2\sigma_p}{Z_{0p}} Z_a(\lambda, \mu) \right|^2} \overline{|U_{mn}|^2} \, |\Phi_{mn}(\lambda, \mu)|^2.$$

Therefore, the averaged modal radiated power is

$$\overline{W_{mn}} = \frac{\overline{|U_{mn}|^2}}{2} \mathrm{Re} \left\{ \int_{-k}^{k} \int_{-\sqrt{k^2-\mu^2}}^{\sqrt{k^2-\mu^2}} \frac{Z_a(\lambda, \mu) \, |\zeta_I|^2}{\left| 1 + \frac{2\sigma_p}{Z_{0p}} Z_a(\lambda, \mu) \right|^2} \, |\Phi_{mn}(\lambda, \mu)|^2 \, \mathrm{d}\lambda \, \mathrm{d}\mu \right\}. \tag{B.15}$$

Comparing Eqs. (B.13) and (B.15), we obtain

$$\overline{W} = \sum_{m=1}^{\infty} \sum_{n=1}^{\infty} \overline{W_{mn}}. \tag{B.16}$$

Thus, the average radiated power is the sum of averaged modal radiated powers [11, 4].

B.2 Average radiation efficiency

The average modal radiation efficiency is given by [11]

$$\sigma_{mn} = \frac{\overline{W_{mn}}}{\frac{1}{2} \rho_0 c a b \overline{< |v_{mn}|^2 >}}, \tag{B.17}$$

where $\overline{W_{mn}}$ is given by Eq. (B.15) and $\overline{<|v_{mn}|^2>}$ is the spatially averaged squared velocity amplitude in mode (m, n) averaged over all forcing locations. The spatially averaged squared modal velocity is given by

$$<|v_{mn}|^2>= \frac{1}{ab} \int_{-b/2}^{b/2} \int_{-a/2}^{a/2} |v_{mn}(x, y)|^2 \,\mathrm{d}x \,\mathrm{d}y. \tag{B.18}$$

Substituting for the panel velocity of mode (m, n)

$$<|v_{mn}|^2>= \frac{1}{ab} \int_{-b/2}^{b/2} \int_{-a/2}^{a/2} |U_{mn}|^2 \phi_{mn}^2(x, y) \,\mathrm{d}x \,\mathrm{d}y.$$

But we know that

$$\int_{-b/2}^{b/2} \int_{-a/2}^{a/2} \phi_{mn}^2(x, y) \,\mathrm{d}x \,\mathrm{d}y = \frac{ab}{4}. \tag{B.19}$$

Therefore,

$$<|v_{mn}|^2>= \frac{|U_{mn}|^2}{4}.$$

Now, averaging over all the forcing locations,

$$\overline{<|v_{mn}|^2>} = \frac{1}{ab} \int_{-b/2}^{b/2} \int_{-a/2}^{a/2} <|v_{mn}(x_i, y_i)|^2> \,\mathrm{d}x_i \,\mathrm{d}y_i.$$

or

$$\overline{<|v_{mn}|^2>} = \frac{\overline{|U_{mn}|^2}}{4}, \tag{B.20}$$

where $\overline{|U_{mn}|^2}$ is given by Eq. (B.11). Therefore, using Eq. (B.15), the average modal radiation efficiency Eq. (B.17) is given by

$$\sigma_{mn} = \frac{4}{\rho_0 cab} \operatorname{Re} \left\{ \int_{-k}^{k} \int_{-\sqrt{k^2-\mu^2}}^{\sqrt{k^2-\mu^2}} \frac{Z_a(\lambda, \mu) \, |\zeta_I|^2}{\left| 1 + \frac{2\sigma_p}{Z_{0p}} Z_a(\lambda, \mu) \right|^2} \, |\Phi_{mn}(\lambda, \mu)|^2 \,\mathrm{d}\lambda \,\mathrm{d}\mu \right\}. \tag{B.21}$$

The average radiation efficiency is defined as

$$\sigma = \frac{\overline{W}}{\frac{1}{2}\rho_0 cab\overline{<|v_p|^2>}}, \tag{B.22}$$

where $\overline{W}$ is the average radiated power given by Eq. (B.13) and $\overline{<|v_p|^2>}$ is the spatially mean squared panel velocity averaged over all forcing locations. The spatially mean squared panel velocity is given by

$$<|v_p|^2>= \frac{1}{ab}\int\limits_{-b/2}^{b/2}\int\limits_{-a/2}^{a/2} |v_p(x,y)|^2 \, \mathrm{d}x \, \mathrm{d}y. \tag{B.23}$$

Substituting for panel velocity $v_p(x, y)$ and rearranging,

$$<|v_p|^2>= \sum_{m=1}^{\infty}\sum_{n=1}^{\infty}\sum_{p=1}^{\infty}\sum_{q=1}^{\infty} U_{mn}U_{pq}^* \frac{1}{ab}\int\limits_{-b/2}^{b/2}\int\limits_{-a/2}^{a/2} \phi_{mn}(x,y)\phi_{pq}(x,y) \, \mathrm{d}x \, \mathrm{d}y.$$

Substitute for $\phi_{mn}(x, y)$ in the above equation and knowing that

$$\int\limits_{-b/2}^{b/2}\int\limits_{-a/2}^{a/2} \sin\frac{m\pi(x+a/2)}{a}\sin\frac{n\ pi(y+b/2)}{b}\sin\frac{p\pi(x+a/2)}{a}\sin\frac{q\pi(y+b/2)}{b}\,\mathrm{d}x\,\mathrm{d}y$$
$$= \begin{cases} \dfrac{ab}{4} & \text{when } m = p \text{ and } n = q \\ 0 & \text{otherwise} \end{cases}$$

we get,

$$<|v_p|^2>= \sum_{m=1}^{\infty}\sum_{n=1}^{\infty} \frac{|U_{mn}|^2}{4}.$$

Averaging over all the forcing locations,

$$\overline{<|v_p|^2>} = \frac{1}{ab}\int\limits_{-b/2}^{b/2}\int\limits_{-a/2}^{a/2} <|v_p(x_i,y_i)|^2> \, \mathrm{d}x_i \, \mathrm{d}y_i.$$

Thus,

$$\overline{<|v_p|^2>} = \sum_{m=1}^{\infty}\sum_{n=1}^{\infty} \frac{\overline{|U_{mn}|^2}}{4} = \sum_{m=1}^{\infty}\sum_{n=1}^{\infty} \overline{<|v_{mn}|^2>}. \tag{B.24}$$

Hence, the average radiation efficiency of the perforated panel set in a similarly perforated baffle can be written as

$$\sigma = \frac{\sum_{m=1}^{\infty}\sum_{n=1}^{\infty}\overline{W_{mn}}}{\frac{1}{2}\rho_0 cab\sum_{m=1}^{\infty}\sum_{n=1}^{\infty}\overline{<|v_{mn}|^2>}}. \tag{B.25}$$

The integrals are evaluated numerically for discrete values of λ and μ.

Appendix C

Expression for M_r

We have

$$M_r = \int_{-b/2}^{b/2} \int_{-a/2}^{a/2} \rho_p h \psi_r^2(x, y)\,\mathrm{d}x\,\mathrm{d}y, \tag{C.1}$$

where ρ_p, h and $\psi_r(x, y)$ are the density, thickness and r^{th} mode shape of perforated panel respectively. We know that

$$\psi_r(x, y) = \sum_{m=1}^{\infty} \sum_{n=1}^{\infty} U_{mnr} \sin \frac{m\pi(x + a/2)}{a} \sin \frac{n\pi(y + b/2)}{b}. \tag{C.2}$$

Therefore,

$$\begin{aligned} M_r = \int_{-b/2}^{b/2} \int_{-a/2}^{a/2} \rho_p h \sum_{m=1}^{\infty} \sum_{n=1}^{\infty} U_{mnr} \sin \frac{m\pi(x + a/2)}{a} \sin \frac{n\pi(y + b/2)}{b} & \\ \times \sum_{p=1}^{\infty} \sum_{q=1}^{\infty} U_{pqr}^{*} \sin \frac{p\pi(x + a/2)}{a} \sin \frac{q\pi(y + b/2)}{b}\,\mathrm{d}x\,\mathrm{d}y & \end{aligned}$$

$$\begin{aligned} \Rightarrow\ M_r = \sum_{m=1}^{\infty} \sum_{n=1}^{\infty} \sum_{p=1}^{\infty} \sum_{q=1}^{\infty} \rho_p h U_{mnr} U_{pqr}^{*} & \\ \times \int_{-b/2}^{b/2} \int_{-a/2}^{a/2} \sin \frac{m\pi(x + a/2)}{a} \sin \frac{n\pi(y + b/2)}{b} \sin \frac{p\pi(x + a/2)}{a} \sin \frac{q\pi(y + b/2)}{b}\,\mathrm{d}x\,\mathrm{d}y. & \end{aligned}$$

But the integral

$$\int_{-b/2}^{b/2}\int_{-a/2}^{a/2} \sin\frac{m\pi(x+a/2)}{a}\sin\frac{n\pi(y+b/2)}{b}\sin\frac{p\pi(x+a/2)}{a}\sin\frac{q\pi(y+b/2)}{b}\,\mathrm{d}x\,\mathrm{d}y$$

$$= \begin{cases} \dfrac{ab}{4} & \text{when } m = p \text{ and } n = q \\ 0 & \text{otherwise} \end{cases}$$

Therefore,

$$M_r = \frac{\rho_p hab}{4}\sum_{m=1}^{\infty}\sum_{n=1}^{\infty}|U_{mnr}|^2. \tag{C.3}$$

Appendix D

Expression for $\Phi_{mn}\left(\lambda, \mu\right)$

The $(m, n)^{\text{th}}$ modeshape of an unperforated simply supported panel $\phi_{mn}(x, y)$ is

$$\phi_{mn}(x, y) = \sin\frac{m\pi(x + a/2)}{a}\sin\frac{n\pi(y + b/2)}{b}, \tag{D.1}$$

where a and b are the panel dimensions. Taking the double Fourier transform

$$\begin{aligned}\Phi_{mn}(\lambda, \mu) &= \frac{1}{2\pi}\int\limits_{-b/2}^{b/2}\int\limits_{-a/2}^{a/2}\phi_{mn}(x, y)\, e^{i\lambda x + i\mu y}\,\mathrm{d}x\,\mathrm{d}y \\ &= \frac{1}{2\pi}\int\limits_{-b/2}^{b/2}\int\limits_{-a/2}^{a/2}\sin\frac{m\pi(x + a/2)}{a}\sin\frac{n\pi(y + b/2)}{b}\, e^{i\lambda x + i\mu y}\,\mathrm{d}x\,\mathrm{d}y.\end{aligned} \tag{D.2}$$

Considering the integral in the x direction

$$\begin{aligned}\int\limits_{-a/2}^{a/2}\sin\frac{m\pi(x + a/2)}{a}\, e^{i\lambda x}\,\mathrm{d}x &= \int\limits_{-a/2}^{a/2}\frac{1}{2i}\left[e^{\frac{im\pi(x+a/2)}{a}} - e^{\frac{-im\pi(x+a/2)}{a}}\right] e^{i\lambda x}\,\mathrm{d}x \\ &= \frac{1}{2i}\int\limits_{-a/2}^{a/2} e^{im\pi/2}\, e^{i(\lambda + m\pi/a)x}\,\mathrm{d}x - \frac{1}{2i}\int\limits_{-a/2}^{a/2} e^{-im\pi/2}\, e^{i(\lambda - m\pi/a)x}\,\mathrm{d}x.\end{aligned}$$

But we know that

$$\int\limits_{-a/2}^{a/2} e^{i(\lambda + m\pi/a)x}\,\mathrm{d}x = a\,\mathrm{sinc}\left[\frac{(\lambda + m\pi/a)\,a}{2}\right]$$

and

$$\int_{-a/2}^{a/2} e^{i(\lambda - m\pi/a)x}\,\mathrm{d}x = a\,\mathrm{sinc}\left[\frac{(\lambda - m\pi/a)\,a}{2}\right].$$

Therefore

$$\int_{-a/2}^{a/2} \sin\frac{m\pi(x+a/2)}{a}\,e^{i\lambda x}\,\mathrm{d}x = \frac{a}{2i}\left\{e^{im\pi/2}\,\mathrm{sinc}\left[\frac{(\lambda + m\pi/a)\,a}{2}\right]\right.$$
$$\left. - \,e^{-im\pi/2}\,\mathrm{sinc}\left[\frac{(\lambda - m\pi/a)\,a}{2}\right]\right\}. \quad \text{(D.3)}$$

Similarly the integral over the y space yields

$$\int_{-b/2}^{b/2} \sin\frac{n\pi(y+b/2)}{b}\,e^{i\mu y}\,\mathrm{d}y = \frac{b}{2i}\left\{e^{in\pi/2}\,\mathrm{sinc}\left[\frac{(\mu + n\pi/b)\,b}{2}\right]\right.$$
$$\left. - \,e^{-in\pi/2}\,\mathrm{sinc}\left[\frac{(\mu - n\pi/b)\,b}{2}\right]\right\}. \quad \text{(D.4)}$$

Therefore, using Eqs. (D.3) and (D.4), Eq. (D.2) turns out to be

$$\Phi_{mn}(\lambda, \mu) = -\frac{ab}{8\pi}\left\{e^{im\pi/2}\,\mathrm{sinc}\left[\frac{(\lambda + m\pi/a)\,a}{2}\right] - e^{-im\pi/2}\,\mathrm{sinc}\left[\frac{(\lambda - m\pi/a)\,a}{2}\right]\right\}$$
$$\times\left\{e^{in\pi/2}\,\mathrm{sinc}\left[\frac{(\mu + n\pi/b)\,b}{2}\right] - e^{-in\pi/2}\,\mathrm{sinc}\left[\frac{(\mu - n\pi/b)\,b}{2}\right]\right\}.$$

Appendix E

Integral $\int\limits_{-\infty}^{\infty} \int\limits_{-\infty}^{\infty} \Phi_{mn}(\lambda, \mu)\, \Phi_{pq}(-\lambda, -\mu)\, \mathrm{d}\lambda\, \mathrm{d}\mu$

Using the double Fourier transform, we can write

$$\int\limits_{-\infty}^{\infty} \int\limits_{-\infty}^{\infty} \Phi_{mn}(\lambda, \mu)\Phi_{pq}(-\lambda, -\mu)\, \mathrm{d}\lambda\, \mathrm{d}\mu = \int\limits_{-\infty}^{\infty} \int\limits_{-\infty}^{\infty} \left[\frac{1}{2\pi} \int\limits_{-b/2}^{b/2} \int\limits_{-a/2}^{a/2} \phi_{mn}(x, y)\, e^{i\lambda x + i\mu y}\, \mathrm{d}x\, \mathrm{d}y \right]$$
$$\times \left[\frac{1}{2\pi} \int\limits_{-b/2}^{b/2} \int\limits_{-a/2}^{a/2} \phi_{pq}(x', y')\, e^{-i\lambda x' - i\mu y'}\, \mathrm{d}x'\, \mathrm{d}y' \right] \mathrm{d}\lambda\, \mathrm{d}\mu.$$

Rearranging the integrals, we get

$$\int\limits_{-\infty}^{\infty} \int\limits_{-\infty}^{\infty} \Phi_{mn}(\lambda, \mu)\Phi_{pq}(-\lambda, -\mu)\, \mathrm{d}\lambda\, \mathrm{d}\mu = \frac{1}{4\pi^2} \int\limits_{-b/2}^{b/2} \int\limits_{-a/2}^{a/2} \int\limits_{-b/2}^{b/2} \int\limits_{-a/2}^{a/2} \phi_{mn}(x, y)\, \phi_{pq}(x', y')$$
$$\times \left[\int\limits_{-\infty}^{\infty} \int\limits_{-\infty}^{\infty} e^{i\lambda(x - x') + i\mu(y - y')}\, \mathrm{d}\lambda\, \mathrm{d}\mu \right] \mathrm{d}x\, \mathrm{d}y\, \mathrm{d}x'\, \mathrm{d}y'.$$

But, we know that

$$\int\limits_{-\infty}^{\infty} \int\limits_{-\infty}^{\infty} e^{i\lambda(x - x') + i\mu(y - y')}\, \mathrm{d}\lambda\, \mathrm{d}\mu = 4\pi^2\, \delta(x - x')\, \delta(y - y').$$

Therefore

$$\int_{-\infty}^{\infty}\int_{-\infty}^{\infty} \Phi_{mn}(\lambda,\mu)\Phi_{pq}(-\lambda,-\mu)\,\mathrm{d}\lambda\,\mathrm{d}\mu = \int_{-b/2}^{b/2}\int_{-a/2}^{a/2}\int_{-b/2}^{b/2}\int_{-a/2}^{a/2} \phi_{mn}(x,y)\,\phi_{pq}(x',y')\,\delta(x-x')\,\delta(y-y')\,\mathrm{d}x\,\mathrm{d}y\,\mathrm{d}x'\,\mathrm{d}y'.$$

Consider the integral over the $x'-y'$ space. We know that $\phi_{pq}(x',y')$ is defined only over the panel area, everywhere else it equals to zero. Now, define two rect() functions, such that

$$\mathrm{rect}\left(\frac{x'}{a}\right) = \begin{cases} 1 & -a/2 \le x' \le a/2 \\ 0 & \text{otherwise} \end{cases} \tag{E.1}$$

and

$$\mathrm{rect}\left(\frac{y'}{b}\right) = \begin{cases} 1 & -b/2 \le y' \le b/2 \\ 0 & \text{otherwise} \end{cases}. \tag{E.2}$$

Using rect() functions, the integral over $x'-y'$ domain can be written as

$$\begin{aligned}
&\int_{-b/2}^{b/2}\int_{-a/2}^{a/2} \phi_{pq}(x',y')\,\delta(x-x')\,\delta(y-y')\,\mathrm{d}x'\,\mathrm{d}y' \\
&\quad= \int_{-\infty}^{\infty}\int_{-\infty}^{\infty} \phi_{pq}(x',y')\,\delta(x-x')\,\delta(y-y')\,\mathrm{rect}\left(\frac{x'}{a}\right)\,\mathrm{rect}\left(\frac{y'}{b}\right)\,\mathrm{d}x'\,\mathrm{d}y' \\
&\quad= \phi_{pq}(x,y)\,\mathrm{rect}\left(\frac{x}{a}\right)\,\mathrm{rect}\left(\frac{y}{b}\right).
\end{aligned}$$

Therefore

$$\int_{-\infty}^{\infty}\int_{-\infty}^{\infty} \Phi_{mn}(\lambda,\mu)\Phi_{pq}(-\lambda,-\mu)\,\mathrm{d}\lambda\,\mathrm{d}\mu = \int_{-b/2}^{b/2}\int_{-a/2}^{a/2} \phi_{mn}(x,y)\,\phi_{pq}(x,y) \times \mathrm{rect}\left(\frac{x}{a}\right)\,\mathrm{rect}\left(\frac{y}{b}\right)\,\mathrm{d}x\,\mathrm{d}y.$$

Using the definition of rect() function (Eqs. (E.1) and (E.2)), we can write

$$\int_{-\infty}^{\infty}\int_{-\infty}^{\infty} \Phi_{mn}(\lambda,\mu)\Phi_{pq}(-\lambda,-\mu)\,\mathrm{d}\lambda\,\mathrm{d}\mu = \int_{-b/2}^{b/2}\int_{-a/2}^{a/2} \phi_{mn}(x,y)\,\phi_{pq}(x,y)\,\mathrm{d}x\,\mathrm{d}y. \tag{E.3}$$

We have

$$\phi_{mn}(x, y) = \sin \frac{m\pi(x + a/2)}{a} \sin \frac{n\pi(y + b/2)}{b}$$

and it can be found out that

$$\int_{-b/2}^{b/2} \int_{-a/2}^{a/2} \sin \frac{m\pi(x + a/2)}{a} \sin \frac{n\pi(y + b/2)}{b} \sin \frac{p\pi(x + a/2)}{a} \sin \frac{q\pi(y + b/2)}{b} \, \mathrm{d}x \, \mathrm{d}y$$

$$= \begin{cases} \dfrac{ab}{4} & \text{if } m = p \text{ and } n = q \\ 0 & \text{otherwise} \end{cases}. \tag{E.4}$$

Thus, Eq. (E.3) turns out to be

$$\int_{-\infty}^{\infty} \int_{-\infty}^{\infty} \Phi_{mn}(\lambda, \mu) \Phi_{pq}(-\lambda, -\mu) \, \mathrm{d}\lambda \, \mathrm{d}\mu = \frac{ab}{4} \, \delta_{mp} \, \delta_{nq}. \tag{E.5}$$

Appendix F

Numerical evaluation of the Fourier transform of the LAFP velocity

The Fourier transform of the LAFP velocity can be obtained by solving Eq. (4.31) numerically. Knowing $P^{-}(\lambda, \mu, z = 0) = -Z_a(\lambda, \mu)\, V_a(\lambda, \mu, z = 0)$ (Eq. (4.12)), Eq. (4.31) turns out to be

$$\begin{aligned}
\left[1 + \frac{2\sigma_b}{Z_{0b}}\, Z_a(\lambda, \mu)\right] V_a(\lambda, \mu, z = 0) \;=\; & \zeta_I V_p(\lambda, \mu) - 2\pi \tilde{P}_i \frac{2\sigma_b}{Z_{0b}}\, \delta(\lambda + k_x)\, \delta(\mu + k_y) \\
& - \left[\frac{2\sigma_p}{Z_{0p}} - \frac{2\sigma_b}{Z_{0b}}\right] \frac{ab}{4\pi^2} \int\limits_{-\infty}^{\infty} \int\limits_{-\infty}^{\infty} Z_a(\lambda', \mu')\, V_a(\lambda', \mu', z = 0) \\
& \times \operatorname{sinc}\left[\frac{(\lambda - \lambda')a}{2}\right] \operatorname{sinc}\left[\frac{(\mu - \mu')b}{2}\right] \mathrm{d}\lambda'\, \mathrm{d}\mu' \\
& - \left[\frac{2\sigma_p}{Z_{0p}} - \frac{2\sigma_b}{Z_{0b}}\right] \frac{\tilde{P}_i ab}{2\pi} \operatorname{sinc}\left[\frac{(\lambda + k_x)a}{2}\right] \operatorname{sinc}\left[\frac{(\mu + k_y)b}{2}\right],
\end{aligned}$$

We select a finite 2-D wavenumber domain for λ and μ, and discretize it into $N_{\lambda\mu}$ ($= N_\lambda \times N_\mu$) smaller sub-domains of size $\mathrm{d}\lambda \times \mathrm{d}\mu$. Further, we identify each sub-domain with the corresponding (λ_i, μ_i) values. Thus, the above equation can be represented as

$$\begin{aligned}
\left[1+\frac{2\sigma_b}{Z_{0b}}\,Z_a(\lambda_i,\mu_i)\right] V_a(\lambda_i,\mu_i,z=0) \;&=\; \zeta_I V_p(\lambda_i,\mu_i) - 2\pi\tilde{P}_i\,\frac{2\sigma_b}{Z_{0b}}\,\delta_{\lambda_i\,k_x}\,\delta_{\mu_i\,k_y} \\
&- \left[\frac{2\sigma_p}{Z_{0p}}-\frac{2\sigma_b}{Z_{0b}}\right]\frac{ab}{4\pi^2}\sum_{j=1}^{N_{\lambda\mu}} Z_a(\lambda_j,\mu_j)\,V_a\left(\lambda_j,\mu_j,z=0\right)\,\mathrm{sinc}\left[\frac{(\lambda_i-\lambda_j)a}{2}\right] \\
&\qquad\times\mathrm{sinc}\left[\frac{(\mu_i-\mu_j)b}{2}\right]\,\mathrm{d}\lambda\,\mathrm{d}\mu \\
&- \left[\frac{2\sigma_p}{Z_{0p}}-\frac{2\sigma_b}{Z_{0b}}\right]\frac{\tilde{P}_i ab}{2\pi}\,\mathrm{sinc}\left[\frac{(\lambda_i+k_x)a}{2}\right]\,\mathrm{sinc}\left[\frac{(\mu_i+k_y)b}{2}\right], \qquad \text{(F.1)}
\end{aligned}$$

Note, that the integral over the infinite 2-D wavenumber domain is approximated by a sum over a discretized finite 2-D wavenumber domain. Now, define the following vectors: $\{V_a\}_{N_{\lambda\mu}\times 1}$, $\{V_p\}_{N_{\lambda\mu}\times 1}$, $\{Z_a\}_{N_{\lambda\mu}\times 1}$, $\{C_1\}_{N_{\lambda\mu}\times 1}$ and $\{C_2\}_{N_{\lambda\mu}\times 1}$ and matrices: $[Z_{ad}]_{N_{\lambda\mu}\times N_{\lambda\mu}}$ and $\left[\bar{Z}_a\right]_{N_{\lambda\mu}\times N_{\lambda\mu}}$, whose elements are given by

$$\begin{aligned}
V_{a\,i} &= V_a(\lambda_i,\mu_i,z=0), \\
V_{p\,i} &= V_p(\lambda_i,\mu_i), \\
Z_{a\,i} &= Z_a(\lambda_i,\mu_i), \\
C_{1\,i} &= \mathrm{sinc}\left[\frac{(\lambda_i+k_x)a}{2}\right]\,\mathrm{sinc}\left[\frac{(\mu_i+k_y)b}{2}\right], \\
C_{2\,i} &= \delta_{\lambda_i\,k_x}\,\delta_{\mu_i\,k_y}, \\
Z_{ad\,ij} &= Z_a(\lambda_i,\mu_i)\,\delta_{ij}
\end{aligned}$$

and

$$\bar{Z}_{a\,ij} = Z_a(\lambda_j,\mu_j)\,\mathrm{sinc}\left[\frac{(\lambda_i-\lambda_j)a}{2}\right]\,\mathrm{sinc}\left[\frac{(\mu_i-\mu_j)b}{2}\right]\,\mathrm{d}\lambda\,\mathrm{d}\mu,$$

Next, Eq. (F.1) can be expressed in a matrix form as

$$\begin{aligned}
\left[[I]+\frac{2\sigma_b}{Z_{0b}}\,[Z_{ad}]\right]\{V_a\} = \zeta_I\,\{V_p\} - \frac{ab}{2\pi^2}\left(\frac{\sigma_p}{Z_{0p}}-\frac{\sigma_b}{Z_{0b}}\right)\left[\bar{Z}_a\right]\{V_a\} \\
- \frac{\tilde{P}_i\,ab}{\pi}\left(\frac{\sigma_p}{Z_{0p}}-\frac{\sigma_b}{Z_{0b}}\right)\{C_1\} - 4\pi\,\tilde{P}_i\,\frac{\sigma_b}{Z_{0b}}\,\{C_2\}\,,
\end{aligned}$$

where $[I]$ is an identity matrix of order $N_{\lambda\mu} \times N_{\lambda\mu}$. Rearranging the above equation

$$\left[[I] + \frac{2\sigma_b}{Z_{0b}}[Z_{ad}] + \frac{ab}{2\pi^2}\left(\frac{\sigma_p}{Z_{0p}} - \frac{\sigma_b}{Z_{0b}}\right)[\bar{Z}_a]\right]\{V_a\}$$

$$= \zeta_I\{V_p\} - \frac{\tilde{P}_i\, ab}{\pi}\left(\frac{\sigma_p}{Z_{0p}} - \frac{\sigma_b}{Z_{0b}}\right)\{C_1\} - 4\pi\,\tilde{P}_i\,\frac{\sigma_b}{Z_{0b}}\{C_2\}\,, \quad \text{(F.2)}$$

The above equation can be solved for $\{V_a\}$ using matrix inversion.

Appendix G

The transmitted power

G.1 Transmitted power through a perforated panel set in an unperforated baffle

Let start by assuming an unperforated panel. Given the panel velocity, $v_p(x,y)$, the transmitted power is given by

$$W_t = \frac{1}{2}\mathrm{Re}\left\{ \int_{-b/2}^{b/2} \int_{-a/2}^{a/2} p^-(x,y,z=0) v_p^*(x,y)\,\mathrm{d}x\,\mathrm{d}y \right\}, \tag{G.1}$$

where $p^-(x,y,z=0)$ is the transmitted pressure field on the panel-baffle surface. Using the inverse Fourier transform

$$W_t = \frac{1}{2}\mathrm{Re}\left\{ \int_{-b/2}^{b/2} \int_{-a/2}^{a/2} \left[\frac{1}{2\pi} \int_{-\infty}^{\infty} \int_{-\infty}^{\infty} P^-(\lambda,\mu,z=0) e^{-i\lambda x - i\mu y}\,\mathrm{d}\lambda\,\mathrm{d}\mu \right] \right.$$
$$\left. \times \left[\frac{1}{2\pi} \int_{-\infty}^{\infty} \int_{-\infty}^{\infty} V_p^*(\lambda',\mu') e^{i\lambda' x + i\mu' y}\,\mathrm{d}\lambda'\,\mathrm{d}\mu' \right] \mathrm{d}x\,\mathrm{d}y \right\}.$$

Rearranging, we get

$$W_t = \frac{1}{8\pi^2}\mathrm{Re}\left\{\int_{-\infty}^{\infty}\int_{-\infty}^{\infty}\int_{-\infty}^{\infty}\int_{-\infty}^{\infty} P^-(\lambda,\mu,z=0)\,V_p^*(\lambda',\mu') \times\left[\int_{-b/2}^{b/2}\int_{-a/2}^{a/2} e^{i(\lambda'-\lambda)x+i(\mu'-\mu)y}\,\mathrm{d}x\,\mathrm{d}y\right]\mathrm{d}\lambda\,\mathrm{d}\mu\,\mathrm{d}\lambda'\,\mathrm{d}\mu'\right\}. \tag{G.2}$$

In fact, the panel velocity $v_p(x, y)$ is zero in the baffle region of $z = 0$ plane. Hence, it is possible to extend the integral over the finite panel region in Eq. (G.1) to an infinite one (infinite panel-baffle plane). Thus

$$W_t = \frac{1}{8\pi^2}\mathrm{Re}\left\{\int_{-\infty}^{\infty}\int_{-\infty}^{\infty}\int_{-\infty}^{\infty}\int_{-\infty}^{\infty} P^-(\lambda,\mu,z=0)\,V_p^*(\lambda',\mu') \times\left[\int_{-\infty}^{\infty}\int_{-\infty}^{\infty} e^{i(\lambda'-\lambda)x+i(\mu'-\mu)y}\,\mathrm{d}x\,\mathrm{d}y\right]\mathrm{d}\lambda\,\mathrm{d}\mu\,\mathrm{d}\lambda'\,\mathrm{d}\mu'\right\}. \tag{G.3}$$

But we know that

$$\int_{-\infty}^{\infty}\int_{-\infty}^{\infty} e^{i(\lambda'-\lambda)x+i(\mu'-\mu)y}\,\mathrm{d}x\,\mathrm{d}y = 4\pi^2\,\delta(\lambda'-\lambda)\,\delta(\mu'-\mu). \tag{G.4}$$

Therefore

$$W_t = \frac{1}{2}\mathrm{Re}\left\{\int_{-\infty}^{\infty}\int_{-\infty}^{\infty} P^-(\lambda,\mu,z=0)V_p^*(\lambda,\mu)\,\mathrm{d}\lambda\,\mathrm{d}\mu\right\}. \tag{G.5}$$

However, for the case of a perforated panel fixed in a baffle, we can replace the panel velocity $V_p(\lambda, \mu)$ with the LAFP velocity $V_a(\lambda, \mu, z = 0)$, provided the baffle is unperforated.

$$W_t = \frac{1}{2}\mathrm{Re}\left\{\int_{-\infty}^{\infty}\int_{-\infty}^{\infty} P^-(\lambda,\mu,z=0)V_a^*(\lambda,\mu,z=0)\,\mathrm{d}\lambda\,\mathrm{d}\mu\right\}. \tag{G.6}$$

where $P^-(\lambda, \mu, z = 0) = -Z_a(\lambda, \mu)V_a(\lambda, \mu, z = 0)$. If the baffle is perforated, the LAFP velocity $v_a(x, y, z = 0)$ over the baffle region is nonzero and hence the assumption in arriving at Eq. (G.3) is violated. In the next section, an expression for the transmitted power through a perforated panel set in a perforated baffle is derived.

G.2 Transmitted power through a perforated panel set in a perforated baffle

Let us start with Eq. (G.2) with the LAFP velocity $V_a(\lambda, \mu, z=0)$ in the place of panel velocity $V_p(\lambda, \mu)$ as shown below.

$$W_t = \frac{1}{8\pi^2}\mathrm{Re}\left\{\int_{-\infty}^{\infty}\int_{-\infty}^{\infty}\int_{-\infty}^{\infty}\int_{-\infty}^{\infty} P^-(\lambda, \mu, z=0)\, V_a^*(\lambda', \mu', z=0) \times \left[\int_{-b/2}^{b/2}\int_{-a/2}^{a/2} e^{i(\lambda'-\lambda)x + i(\mu'-\mu)y}\, \mathrm{d}x\, \mathrm{d}y\right] \mathrm{d}\lambda\, \mathrm{d}\mu\, \mathrm{d}\lambda'\, \mathrm{d}\mu'\right\}.$$

In the next step we will not make an assumption of zero fluid particle velocity as we have done before. We know that

$$\int_{-b/2}^{b/2}\int_{-a/2}^{a/2} e^{i(\lambda'-\lambda)x + i(\mu'-\mu)y}\, \mathrm{d}x\, \mathrm{d}y = ab\,\mathrm{sinc}\left[\frac{(\lambda'-\lambda)a}{2}\right] \mathrm{sinc}\left[\frac{(\mu'-\mu)b}{2}\right]. \tag{G.7}$$

Thus

$$W_t = \frac{ab}{8\pi^2}\mathrm{Re}\left\{\int_{-\infty}^{\infty}\int_{-\infty}^{\infty}\int_{-\infty}^{\infty}\int_{-\infty}^{\infty} P^-(\lambda, \mu, z=0)\, V_a^*(\lambda', \mu', z=0) \times \mathrm{sinc}\left[\frac{(\lambda'-\lambda)a}{2}\right] \mathrm{sinc}\left[\frac{(\mu'-\mu)b}{2}\right] \mathrm{d}\lambda\, \mathrm{d}\mu\, \mathrm{d}\lambda'\, \mathrm{d}\mu'\right\}. \tag{G.8}$$

The above equation is applicable in any case irrespective of whether the baffle is perforated or unperforated. Thus it can rather be called as a general expression for the power transmitted through a panel set in a baffle whose perforation ratios may differ. The integral in the above equation has to be evaluated numerically as a sum over a finite wavenumber domain using discrete values of λ and μ. The numerical scheme is presented below.

G.2.1 A numerical scheme to evaluate the transmitted power for the perforated baffle case

We select a finite 2-D wavenumber domain for λ and μ and discretize it into $N_{\lambda\mu}$ ($= N_\lambda \times N_\mu$) smaller sub-domains of size $\mathrm{d}\lambda \times \mathrm{d}\mu$. Further, we identify each sub-domains with the corresponding (λ_i, μ_i) values. Thus, the above equation can be represented as

$$W_t = \frac{ab}{8\pi^2} \mathrm{Re} \left\{ \sum_{i=1}^{N_{\lambda\mu}} \sum_{j=1}^{N_{\lambda\mu}} -Z_a(\lambda_i, \mu_i) V_a(\lambda_i, \mu_i, z=0)\, V_a^*(\lambda_j, \mu_j, z=0) \right. \\ \left. \times \mathrm{sinc}\left[\frac{(\lambda_j - \lambda_i)a}{2}\right] \mathrm{sinc}\left[\frac{(\mu_j - \mu_i)b}{2}\right] (\mathrm{d}\lambda\, \mathrm{d}\mu)^2 \right\}. \tag{G.9}$$

Note, that the integral over the infinite 2-D wavenumber domain is approximated by a sum over a discretized, finite 2-D wavenumber domain. Now, define vector $\{V_a\}_{N_{\lambda\mu}\times 1}$ and matrices: $[Z_{ad}]_{N_{\lambda\mu}\times N_{\lambda\mu}}$ and $[C]_{N_{\lambda\mu}\times N_{\lambda\mu}}$, whose elements are given by

$$V_{a\,i} = V_a(\lambda_i, \mu_i, z=0),$$

$$Z_{ad\,ij} = Z_a(\lambda_i, \mu_i)\delta_{ij}$$

and

$$C_{ij} = \mathrm{sinc}\left[\frac{(\lambda_j - \lambda_i)a}{2}\right] \mathrm{sinc}\left[\frac{(\mu_j - \mu_i)b}{2}\right] (\mathrm{d}\lambda\, \mathrm{d}\mu)^2.$$

Therefore the transmitted power (Eq. (G.9)) can be written in matrix form as

$$W_t = \frac{ab}{8\pi^2} \mathrm{Re}\left\{ -\{[Z_{ad}]\{V_a\}\}^T [C] \{V_a^*\} \right\},$$

$$= \frac{ab}{8\pi^2} \mathrm{Re}\left\{ -\{V_a\}^T [Z_{ad}]^T [C] \{V_a^*\} \right\}.$$

But $[Z_{ad}]^T = [Z_{ad}]$. Therefore the transmitted power is given by

$$W_t = \frac{ab}{8\pi^2} \mathrm{Re}\left\{ -\{V_a\}^T [Z_{ad}] [C] \{V_a^*\} \right\}. \tag{G.10}$$

Appendix H

Simplification of the coupled equation

Eq. (5.23) is repeated here for convenience,

$$\left[1+\frac{2\sigma_b}{Z_{0b}}Z_a(\lambda,\mu)\right]\left[\frac{1}{2i\omega Z_a\left(\lambda,\mu\right)}\sum_{r,m,n}B_r\bar{U}_{mnr}\Phi_{mn}(\lambda,\mu)+\frac{\tilde{F}}{4\pi Z_a\left(\lambda,\mu\right)}\,e^{i\lambda x_0+i\mu y_0}\right]$$

$$=\ \zeta_I\sum_{r,m,n}B_rU_{mnr}\Phi_{mn}(\lambda,\mu)$$

$$-\ \frac{ab}{2\pi^2}\left[\frac{\sigma_p}{Z_{0p}}-\frac{\sigma_b}{Z_{0b}}\right]\int\limits_{-\infty}^{\infty}\int\limits_{-\infty}^{\infty}\left[\frac{1}{2i\omega}\sum_{r,m,n}B_r\bar{U}_{mnr}\Phi_{mn}(\lambda',\mu')+\frac{\tilde{F}}{4\pi}\,e^{i\lambda' x_0+i\mu' y_0}\right]$$

$$\times\ \mathrm{sinc}\left[\frac{(\lambda-\lambda')a}{2}\right]\ \mathrm{sinc}\left[\frac{(\mu-\mu')b}{2}\right]\ \mathrm{d}\lambda'\,\mathrm{d}\mu',$$

where

$$\bar{U}_{mnr}=\left[D^*(1-i\eta)\left\{\left(\frac{m\pi}{a}\right)^2+\left(\frac{n\pi}{b}\right)^2\right\}^2-m_p\omega^2\right]U_{mnr}.$$

Expanding

$$\frac{1}{2i\omega}\left[1+\frac{2\sigma_b}{Z_{0b}}Z_a(\lambda,\mu)\right]\sum_{r,m,n}B_r\bar{U}_{mnr}\Theta_{mn}(\lambda,\mu)\;+\;\frac{\tilde{F}}{4\pi}\left[1+\frac{2\sigma_b}{Z_{0b}}Z_a(\lambda,\mu)\right]\frac{e^{i\lambda x_0+i\mu y_0}}{Z_a\left(\lambda,\mu\right)}$$

$$=\;\zeta_I\sum_{r,m,n}B_rU_{mnr}\Phi_{mn}(\lambda,\mu)\;-\;\frac{ab}{2\pi^2}\left[\frac{\sigma_p}{Z_{0p}}-\frac{\sigma_b}{Z_{0b}}\right]\frac{1}{2i\omega}\sum_{r,m,n}B_r\bar{U}_{mnr}X_{mn}(\lambda,\mu)$$

$$-\;\frac{\tilde{F}ab}{8\pi^3}\left[\frac{\sigma_p}{Z_{0p}}-\frac{\sigma_b}{Z_{0b}}\right]\int_{-\infty}^{\infty}\int_{-\infty}^{\infty}\operatorname{sinc}\left[\frac{(\lambda-\lambda')a}{2}\right]\,\operatorname{sinc}\left[\frac{(\mu-\mu')b}{2}\right]\,e^{i\lambda' x_0+i\mu' y_0}\,\mathrm{d}\lambda'\,\mathrm{d}\mu', \tag{H.1}$$

where

$$\Theta_{mn}(\lambda,\mu)=\frac{\Phi_{mn}(\lambda,\mu)}{Z_a(\lambda,\mu)} \tag{H.2}$$

and

$$X_{mn}(\lambda,\mu)=\int_{-\infty}^{\infty}\int_{-\infty}^{\infty}\Phi_{mn}(\lambda',\mu')\operatorname{sinc}\left[\frac{(\lambda-\lambda')a}{2}\right]\,\operatorname{sinc}\left[\frac{(\mu-\mu')b}{2}\right]\,\mathrm{d}\lambda'\,\mathrm{d}\mu'. \tag{H.3}$$

We know that

$$\int_{-\infty}^{\infty}\operatorname{sinc}\left[\frac{\lambda}{2}\right]\,e^{-i\lambda x}\,\mathrm{d}\lambda=2\pi\,\operatorname{rect}(x), \tag{H.4}$$

where

$$\operatorname{rect}(x)=\begin{cases}1 & -1/2\le x\le 1/2\\ 0 & \text{otherwise}\end{cases}. \tag{H.5}$$

Consider a function of λ', $f\left(\frac{\alpha-\beta\lambda'}{2}\right)$ with α and β are constants. Now

$$\int_{-\infty}^{\infty}f\left(\frac{\alpha-\beta\lambda'}{2}\right)\,e^{i\lambda' x_0}\,\mathrm{d}\lambda'=-\frac{1}{\beta}\int_{-\infty}^{\infty}f\left(\frac{\bar{\lambda}}{2}\right)\,e^{\frac{i\left(\alpha-\bar{\lambda}\right)}{\beta}x_0}\,\mathrm{d}\bar{\lambda},$$

where the transformed variable $\bar{\lambda}$ is given by

$$\bar{\lambda}=\alpha-\beta\lambda'.$$

Expanding the above integral

$$\int_{-\infty}^{\infty} f\left(\frac{\alpha-\beta\lambda'}{2}\right)\, e^{i\lambda' x_0}\,\mathrm{d}\lambda' = -\frac{1}{\beta}\int_{-\infty}^{\infty} f\left(\frac{\bar{\lambda}}{2}\right)\, e^{-i\bar{\lambda}(x_0/\beta)}\, e^{i\alpha x_0/\beta}\,\mathrm{d}\bar{\lambda}.$$

Thus,

$$\int_{-\infty}^{\infty} f\left(\frac{\alpha-\beta\lambda'}{2}\right)\, e^{i\lambda' x_0}\,\mathrm{d}\lambda' = -\frac{1}{\beta}\, e^{i\alpha x_0/\beta}\int_{-\infty}^{\infty} f\left(\frac{\bar{\lambda}}{2}\right)\, e^{-i\bar{\lambda}(x_0/\beta)}\,\mathrm{d}\bar{\lambda}. \tag{H.6}$$

Now consider the integral

$$\int_{-\infty}^{\infty} \mathrm{sinc}\left[\frac{(\lambda-\lambda')a}{2}\right]\, e^{i\lambda' x_0}\,\mathrm{d}\lambda'.$$

On comparing with Eq. (H.6), we can find that

$$\int_{-\infty}^{\infty} \mathrm{sinc}\left[\frac{(\lambda-\lambda')a}{2}\right]\, e^{i\lambda' x_0}\,\mathrm{d}\lambda' = -\frac{1}{a}\, e^{i\lambda' x_0}\int_{-\infty}^{\infty} \mathrm{sinc}\left[\frac{\bar{\lambda}}{2}\right]\, e^{-i\bar{\lambda}(x_0/a)}\,\mathrm{d}\bar{\lambda}.$$

Using Eq. (H.4)

$$\int_{-\infty}^{\infty} \mathrm{sinc}\left[\frac{(\lambda-\lambda')a}{2}\right]\, e^{i\lambda' x_0}\,\mathrm{d}\lambda' = -\frac{2\pi}{a}\,\mathrm{rect}\left(\frac{x_0}{a}\right)\, e^{i\lambda x_0}. \tag{H.7}$$

Similarly

$$\int_{-\infty}^{\infty} \mathrm{sinc}\left[\frac{(\mu-\mu')b}{2}\right]\, e^{i\mu' y_0}\,\mathrm{d}\mu' = -\frac{2\pi}{b}\,\mathrm{rect}\left(\frac{y_0}{b}\right)\, e^{i\mu y_0}. \tag{H.8}$$

Therefore

$$\int_{-\infty}^{\infty}\int_{-\infty}^{\infty} \mathrm{sinc}\left[\frac{(\lambda-\lambda')a}{2}\right]\,\mathrm{sinc}\left[\frac{(\mu-\mu')b}{2}\right]\, e^{i\lambda' x_0+i\mu' y_0}\,\mathrm{d}\lambda'\,\mathrm{d}\mu'$$

$$= \frac{4\pi^2}{ab}\,\mathrm{rect}\left(\frac{x_0}{a}\right)\,\mathrm{rect}\left(\frac{y_0}{b}\right)\, e^{i\lambda x_0+i\mu y_0}.$$

But we know that if $-a/2 \le x_0 \le a/2$ and $-b/2 \le y_0 \le b/2$, $\mathrm{rect}\left(\frac{x_0}{a}\right) = \mathrm{rect}\left(\frac{y_0}{b}\right) = 1$. Therefore

$$\int_{-\infty}^{\infty}\int_{-\infty}^{\infty} \mathrm{sinc}\left[\frac{(\lambda-\lambda')a}{2}\right] \mathrm{sinc}\left[\frac{(\mu-\mu')b}{2}\right] e^{i\lambda' x_0 + i\mu' y_0} \,\mathrm{d}\lambda' \,\mathrm{d}\mu' = \frac{4\pi^2}{ab} e^{i\lambda x_0 + i\mu y_0}. \tag{H.9}$$

Substituting Eq. (H.9) in Eq. (H.1)

$$\begin{aligned} &\frac{1}{2i\omega}\left[1+\frac{2\sigma_b}{Z_{0b}}Z_a(\lambda,\mu)\right]\sum_{r,m,n} B_r \bar{U}_{mnr}\Theta_{mn}(\lambda,\mu) + \frac{\tilde{F}}{4\pi}\left[1+\frac{2\sigma_b}{Z_{0b}}Z_a(\lambda,\mu)\right]\frac{e^{i\lambda x_0+i\mu y_0}}{Z_a(\lambda,\mu)} \\ &\quad = \zeta_I \sum_{r,m,n} B_r U_{mnr}\Phi_{mn}(\lambda,\mu) - \frac{ab}{2\pi^2}\left[\frac{\sigma_p}{Z_{0p}} - \frac{\sigma_b}{Z_{0b}}\right]\frac{1}{2i\omega}\sum_{r,m,n} B_r \bar{U}_{mnr} X_{mn}(\lambda,\mu) \\ &\qquad - \frac{\tilde{F}}{2\pi}\left[\frac{\sigma_p}{Z_{0p}} - \frac{\sigma_b}{Z_{0b}}\right] e^{i\lambda x_0+i\mu y_0}. \end{aligned}$$

After removing the identical terms

$$\begin{aligned} &\frac{1}{2i\omega}\left[1+\frac{2\sigma_b}{Z_{0b}}Z_a(\lambda,\mu)\right]\sum_{r,m,n} B_r \bar{U}_{mnr}\Theta_{mn}(\lambda,\mu) + \frac{\tilde{F}}{4\pi}\frac{e^{i\lambda x_0+i\mu y_0}}{Z_a(\lambda,\mu)} \\ &\quad = \zeta_I \sum_{r,m,n} B_r U_{mnr}\Phi_{mn}(\lambda,\mu) - \frac{ab}{2\pi^2}\left[\frac{\sigma_p}{Z_{0p}} - \frac{\sigma_b}{Z_{0b}}\right]\frac{1}{2i\omega}\sum_{r,m,n} B_r \bar{U}_{mnr} X_{mn}(\lambda,\mu) \\ &\qquad - \frac{\tilde{F}}{2\pi}\frac{\sigma_p}{Z_{0p}} e^{i\lambda x_0+i\mu y_0}. \end{aligned}$$

Rearranging gives

$$\begin{aligned} &\frac{1}{2i\omega}\left[1+\frac{2\sigma_b}{Z_{0b}}Z_a(\lambda,\mu)\right]\sum_{r,m,n} B_r \bar{U}_{mnr}\Theta_{mn}(\lambda,\mu) - \zeta_I \sum_{r,m,n} B_r U_{mnr}\Phi_{mn}(\lambda,\mu) \\ &+\frac{ab}{8\pi^2 i\omega}\left[\frac{2\sigma_p}{Z_{0p}} - \frac{2\sigma_b}{Z_{0b}}\right]\sum_{r,m,n} B_r \bar{U}_{mnr} X_{mn}(\lambda,\mu) = -\frac{\tilde{F}}{4\pi}\frac{2\sigma_p}{Z_{0p}} e^{i\lambda x_0+i\mu y_0} - \frac{\tilde{F}}{4\pi}\frac{e^{i\lambda x_0+i\mu y_0}}{Z_a(\lambda,\mu)}. \end{aligned}$$

Appendix I

Integrals in the coupled equation

I.1 Integral $\int\limits_{-\infty}^{\infty} \int\limits_{-\infty}^{\infty} \Theta_{mn}(\lambda,\mu)\Phi_{pq}(-\lambda,-\mu)\,\mathrm{d}\lambda\,\mathrm{d}\mu$

We have

$$\Theta_{mn}(\lambda,\mu) = \frac{\Phi_{mn}(\lambda,\mu)}{Z_a(\lambda,\mu)}.$$

Therefore

$$\bar{\Theta}_{mnpq} = \int\limits_{-\infty}^{\infty} \int\limits_{-\infty}^{\infty} \Theta_{mn}(\lambda,\mu)\Phi_{pq}(-\lambda,-\mu)\,\mathrm{d}\lambda\,\mathrm{d}\mu = \int\limits_{-\infty}^{\infty} \int\limits_{-\infty}^{\infty} \frac{\Phi_{mn}(\lambda,\mu)\Phi_{pq}(-\lambda,-\mu)}{Z_a(\lambda,\mu)}\,\mathrm{d}\lambda\,\mathrm{d}\mu. \tag{I.1}$$

The above integral is evaluated numerically. The integral over the infinite 2-D wavenumber domain is approximated by a sum over a finite discretized wavenumber domain.

I.2 Integral $\int\limits_{-\infty}^{\infty} \int\limits_{-\infty}^{\infty} \Phi_{mn}(\lambda,\mu)\Phi_{pq}(-\lambda,-\mu)\,\mathrm{d}\lambda\,\mathrm{d}\mu$

Using the double Fourier transform

$$\int\limits_{-\infty}^{\infty} \int\limits_{-\infty}^{\infty} \Phi_{mn}(\lambda,\mu)\Phi_{pq}(-\lambda,-\mu)\,\mathrm{d}\lambda\,\mathrm{d}\mu = \int\limits_{-\infty}^{\infty} \int\limits_{-\infty}^{\infty} \left[\frac{1}{2\pi} \int\limits_{-b/2}^{b/2} \int\limits_{-a/2}^{a/2} \phi_{mn}(x,y)\, e^{i\lambda x + i\mu y}\,\mathrm{d}x\,\mathrm{d}y\right]$$

$$\times \left[\frac{1}{2\pi} \int\limits_{-b/2}^{b/2} \int\limits_{-a/2}^{a/2} \phi_{pq}(x',y')\, e^{-i\lambda x' - i\mu y'}\,\mathrm{d}x'\,\mathrm{d}y'\right] \mathrm{d}\lambda\,\mathrm{d}\mu.$$

Rearranging the integrals

$$\int_{-\infty}^{\infty}\int_{-\infty}^{\infty}\Phi_{mn}(\lambda,\mu)\Phi_{pq}(-\lambda,-\mu)\,\mathrm{d}\lambda\,\mathrm{d}\mu = \frac{1}{4\pi^2}\int_{-b/2}^{b/2}\int_{-a/2}^{a/2}\int_{-b/2}^{b/2}\int_{-a/2}^{a/2}\phi_{mn}(x,y)\,\phi_{pq}(x',y')$$
$$\times\left[\int_{-\infty}^{\infty}\int_{-\infty}^{\infty} e^{i\lambda(x-x')+i\mu(y-y')}\,\mathrm{d}\lambda\,\mathrm{d}\mu\right]\,\mathrm{d}x\,\mathrm{d}y\,\mathrm{d}x'\,\mathrm{d}y'.$$

But we know that

$$\int_{-\infty}^{\infty}\int_{-\infty}^{\infty} e^{i\lambda(x-x')+i\mu(y-y')}\,\mathrm{d}\lambda\,\mathrm{d}\mu = 4\pi^2\,\delta(x-x')\,\delta(y-y').$$

Therefore

$$\int_{-\infty}^{\infty}\int_{-\infty}^{\infty}\Phi_{mn}(\lambda,\mu)\Phi_{pq}(-\lambda,-\mu)\,\mathrm{d}\lambda\,\mathrm{d}\mu$$
$$= \int_{-b/2}^{b/2}\int_{-a/2}^{a/2}\int_{-b/2}^{b/2}\int_{-a/2}^{a/2}\phi_{mn}(x,y)\,\phi_{pq}(x',y')\,\delta(x-x')\,\delta(y-y')\,\mathrm{d}x\,\mathrm{d}y\,\mathrm{d}x'\,\mathrm{d}y'.$$

We know that $\phi_{pq}(x',y')$ is defined only over the panel area and on the baffle surface it is equal to zero. Now define two rect() functions such that

$$\mathrm{rect}\left(\frac{x'}{a}\right) = \begin{cases} 1 & -a/2 \le x' \le a/2 \\ 0 & \text{otherwise} \end{cases} \tag{I.2}$$

and

$$\mathrm{rect}\left(\frac{y'}{b}\right) = \begin{cases} 1 & -b/2 \le y' \le b/2 \\ 0 & \text{otherwise} \end{cases}. \tag{I.3}$$

Using rect() functions, the integral over $x'-y'$ domain can be written as

$$\begin{aligned}
&\int\limits_{-b/2}^{b/2}\int\limits_{-a/2}^{a/2}\phi_{pq}(x',y')\,\delta(x-x')\,\delta(y-y')\,\mathrm{d}x'\,\mathrm{d}y' \\
&\qquad = \int\limits_{-\infty}^{\infty}\int\limits_{-\infty}^{\infty}\phi_{pq}(x',y')\,\delta(x-x')\,\delta(y-y')\,\mathrm{rect}\left(\frac{x'}{a}\right)\,\mathrm{rect}\left(\frac{y'}{b}\right)\,\mathrm{d}x'\,\mathrm{d}y' \\
&\qquad = \phi_{pq}(x,y)\,\mathrm{rect}\left(\frac{x}{a}\right)\,\mathrm{rect}\left(\frac{y}{b}\right).
\end{aligned}$$

Therefore

$$\begin{aligned}
&\int\limits_{-\infty}^{\infty}\int\limits_{-\infty}^{\infty}\Phi_{mn}(\lambda,\mu)\Phi_{pq}(-\lambda,-\mu)\,\mathrm{d}\lambda\,\mathrm{d}\mu \\
&\qquad = \int\limits_{-b/2}^{b/2}\int\limits_{-a/2}^{a/2}\phi_{mn}(x,y)\,\phi_{pq}(x,y)\,\mathrm{rect}\left(\frac{x}{a}\right)\,\mathrm{rect}\left(\frac{y}{b}\right)\,\mathrm{d}x\,\mathrm{d}y.
\end{aligned}$$

Using the definition of rect() function (Eqs. (I.2) and (I.3))

$$\int\limits_{-\infty}^{\infty}\int\limits_{-\infty}^{\infty}\Phi_{mn}(\lambda,\mu)\Phi_{pq}(-\lambda,-\mu)\,\mathrm{d}\lambda\,\mathrm{d}\mu = \int\limits_{-b/2}^{b/2}\int\limits_{-a/2}^{a/2}\phi_{mn}(x,y)\,\phi_{pq}(x,y)\,\mathrm{d}x\,\mathrm{d}y. \tag{I.4}$$

We have

$$\phi_{mn}(x,y) = \sin\frac{m\pi(x+a/2)}{a}\sin\frac{n\pi(y+b/2)}{b}$$

and it can be seen that

$$\begin{aligned}
&\int\limits_{-b/2}^{b/2}\int\limits_{-a/2}^{a/2}\sin\frac{m\pi(x+a/2)}{a}\sin\frac{n\pi(y+b/2)}{b}\sin\frac{p\pi(x+a/2)}{a}\sin\frac{q\pi(y+b/2)}{b}\,\mathrm{d}x\,\mathrm{d}y \\
&\qquad = \begin{cases}\dfrac{ab}{4} & \text{if } m=p \text{ and } n=q \\ 0 & \text{otherwise}\end{cases}.
\end{aligned} \tag{I.5}$$

Thus, Eq. (I.4) turns out to be

$$\int_{-\infty}^{\infty}\int_{-\infty}^{\infty}\Phi_{mn}(\lambda,\mu)\Phi_{pq}(-\lambda,-\mu)\,\mathrm{d}\lambda\,\mathrm{d}\mu = \frac{ab}{4}\,\delta_{mp}\,\delta_{nq}. \tag{I.6}$$

I.3 Integral $\int_{-\infty}^{\infty}\int_{-\infty}^{\infty} X_{mn}(\lambda,\mu)\Phi_{pq}(-\lambda,-\mu)\,\mathrm{d}\lambda\,\mathrm{d}\mu$

We have

$$X_{mn}(\lambda,\mu) = \int_{-\infty}^{\infty}\int_{-\infty}^{\infty}\Phi_{mn}(\lambda',\mu')\,\mathrm{sinc}\left[\frac{(\lambda-\lambda')a}{2}\right]\,\mathrm{sinc}\left[\frac{(\mu-\mu')b}{2}\right]\,\mathrm{d}\lambda'\,\mathrm{d}\mu'.$$

Using the double Fourier transform

$$\int_{-\infty}^{\infty}\int_{-\infty}^{\infty} X_{mn}(\lambda,\mu)\Phi_{pq}(-\lambda,-\mu)\,\mathrm{d}\lambda\,\mathrm{d}\mu$$

$$= \int_{-\infty}^{\infty}\int_{-\infty}^{\infty}\int_{-\infty}^{\infty}\int_{-\infty}^{\infty}\left[\frac{1}{2\pi}\int_{-b/2}^{b/2}\int_{-a/2}^{a/2}\phi_{mn}(x',y')\,e^{i\lambda'x'+i\mu'y'}\,\mathrm{d}x'\,\mathrm{d}y'\right]$$

$$\times\left[\frac{1}{2\pi}\int_{-b/2}^{b/2}\int_{-a/2}^{a/2}\phi_{pq}(x,y)\,e^{-i\lambda x-i\mu y}\,\mathrm{d}x\,\mathrm{d}y\right]\mathrm{sinc}\left[\frac{(\lambda-\lambda')a}{2}\right]\,\mathrm{sinc}\left[\frac{(\mu-\mu')b}{2}\right]\,\mathrm{d}\lambda\,\mathrm{d}\mu\,\mathrm{d}\lambda'\,\mathrm{d}\mu'.$$

Rearranging the integrals

$$\int_{-\infty}^{\infty}\int_{-\infty}^{\infty} X_{mn}(\lambda,\mu)\Phi_{pq}(-\lambda,-\mu)\,\mathrm{d}\lambda\,\mathrm{d}\mu = \frac{1}{4\pi^2}\int_{-b/2}^{b/2}\int_{-a/2}^{a/2}\int_{-b/2}^{b/2}\int_{-a/2}^{a/2} \phi_{mn}(x',y')\,\phi_{pq}(x,y)$$
$$\times\left[\int_{-\infty}^{\infty}\int_{-\infty}^{\infty} e^{i\lambda' x' - i\lambda x}\operatorname{sinc}\left[\frac{(\lambda-\lambda')a}{2}\right]\mathrm{d}\lambda\,\mathrm{d}\lambda'\right]$$
$$\times\left[\int_{-\infty}^{\infty}\int_{-\infty}^{\infty} e^{i\mu' y' - i\mu y}\operatorname{sinc}\left[\frac{(\mu-\mu')b}{2}\right]\mathrm{d}\mu\,\mathrm{d}\mu'\right]\mathrm{d}x\,\mathrm{d}y\,\mathrm{d}x'\,\mathrm{d}y'. \quad \text{(I.7)}$$

We know that

$$\int_{-\infty}^{\infty}\operatorname{sinc}\left[\frac{\lambda}{2}\right] e^{-i\lambda x}\,\mathrm{d}\lambda = 2\pi\operatorname{rect}(x), \quad \text{(I.8)}$$

where

$$\operatorname{rect}(x) = \begin{cases} 1 & -1/2 \le x \le 1/2 \\ 0 & \text{otherwise} \end{cases}. \quad \text{(I.9)}$$

Now, $f\left(\frac{\alpha\lambda-\beta}{2}\right)$ is a function of λ with α and β as constants

$$\int_{-\infty}^{\infty} f\left(\frac{\alpha\lambda-\beta}{2}\right) e^{-i\lambda x}\,\mathrm{d}\lambda = \frac{1}{\alpha}\int_{-\infty}^{\infty} f\left(\frac{\bar{\lambda}}{2}\right) e^{\frac{-i\left(\bar{\lambda}+\beta\right)}{\alpha}x}\,\mathrm{d}\bar{\lambda},$$

where the transformed variable $\bar{\lambda}$ is given by

$$\bar{\lambda} = \alpha\lambda - \beta.$$

Expanding the integrand we get

$$\int_{-\infty}^{\infty} f\left(\frac{\alpha\lambda-\beta}{2}\right) e^{-i\lambda x}\,\mathrm{d}\lambda = \frac{1}{\alpha}\int_{-\infty}^{\infty} f\left(\frac{\bar{\lambda}}{2}\right) e^{-i\bar{\lambda}(x/\alpha)}\, e^{-i\beta x/\alpha}\,\mathrm{d}\bar{\lambda}.$$

Thus,

$$\int_{-\infty}^{\infty} f\left(\frac{\alpha\lambda-\beta}{2}\right) e^{-i\lambda x}\,\mathrm{d}\lambda = \frac{1}{\alpha}\, e^{-i\beta x/\alpha}\int_{-\infty}^{\infty} f\left(\frac{\bar{\lambda}}{2}\right) e^{-i\bar{\lambda}(x/\alpha)}\,\mathrm{d}\bar{\lambda}. \quad \text{(I.10)}$$

Now, consider the integral

$$\int_{-\infty}^{\infty} \operatorname{sinc}\left[\frac{(\lambda-\lambda')a}{2}\right]\, e^{-i\lambda x}\,\mathrm{d}\lambda.$$

On comparing with Eq. (I.10) we can find that

$$\int_{-\infty}^{\infty} \operatorname{sinc}\left[\frac{(\lambda-\lambda')a}{2}\right]\, e^{-i\lambda x}\,\mathrm{d}\lambda = \frac{1}{a}\, e^{-i\lambda' x} \int_{-\infty}^{\infty} \operatorname{sinc}\left[\frac{\bar{\lambda}}{2}\right]\, e^{-i\bar{\lambda}(x/a)}\,\mathrm{d}\bar{\lambda}.$$

Using Eq. (I.8) we get

$$\int_{-\infty}^{\infty} \operatorname{sinc}\left[\frac{(\lambda-\lambda')a}{2}\right]\, e^{-i\lambda x}\,\mathrm{d}\lambda = \frac{2\pi}{a}\operatorname{rect}\left(\frac{x}{a}\right)\, e^{-i\lambda' x}. \tag{I.11}$$

Now, the integral in Eq. (I.7) turns out to be

$$\int_{-\infty}^{\infty}\int_{-\infty}^{\infty} e^{i\lambda' x' - i\lambda x} \operatorname{sinc}\left[\frac{(\lambda-\lambda')a}{2}\right]\,\mathrm{d}\lambda\,\mathrm{d}\lambda' = \frac{2\pi}{a}\operatorname{rect}\left(\frac{x}{a}\right) \int_{-\infty}^{\infty} e^{i\lambda' x' - i\lambda' x}\,\mathrm{d}\lambda'.$$

But we know that

$$\int_{-\infty}^{\infty} e^{i\lambda' x' - i\lambda' x}\,\mathrm{d}\lambda' = 2\pi\,\delta(x'-x).$$

Therefore

$$\int_{-\infty}^{\infty}\int_{-\infty}^{\infty} e^{i\lambda' x' - i\lambda x} \operatorname{sinc}\left[\frac{(\lambda-\lambda')a}{2}\right]\,\mathrm{d}\lambda\,\mathrm{d}\lambda' = \frac{4\pi^2}{a}\operatorname{rect}\left(\frac{x}{a}\right)\,\delta(x'-x). \tag{I.12}$$

Similarly,

$$\int_{-\infty}^{\infty}\int_{-\infty}^{\infty} e^{i\mu' y' - i\mu y} \operatorname{sinc}\left[\frac{(\mu-\mu')b}{2}\right]\,\mathrm{d}\mu\,\mathrm{d}\mu' = \frac{4\pi^2}{b}\operatorname{rect}\left(\frac{y}{b}\right)\,\delta(y'-y). \tag{I.13}$$

Using Eqs. (I.12) and (I.13) we can rewrite Eq. (I.7) as

$$\int\limits_{-\infty}^{\infty}\int\limits_{-\infty}^{\infty} X_{mn}(\lambda,\mu)\Phi_{pq}(-\lambda,-\mu)\,\mathrm{d}\lambda\,\mathrm{d}\mu = \frac{4\pi^2}{ab}\int\limits_{-b/2}^{b/2}\int\limits_{-a/2}^{a/2}\int\limits_{-b/2}^{b/2}\int\limits_{-a/2}^{a/2}\phi_{mn}(x',y')\,\phi_{pq}(x,y)$$
$$\times\,\mathrm{rect}\left(\frac{x}{a}\right)\,\mathrm{rect}\left(\frac{y}{b}\right)\,\delta(x'-x)\,\delta(y'-y)\,\mathrm{d}x\,\mathrm{d}y\,\mathrm{d}x'\,\mathrm{d}y'.$$

The presence of the rect() function allows us to extend the integral limits to infinity. Thus,

$$\int\limits_{-\infty}^{\infty}\int\limits_{-\infty}^{\infty} X_{mn}(\lambda,\mu)\Phi_{pq}(-\lambda,-\mu)\,\mathrm{d}\lambda\,\mathrm{d}\mu = \frac{4\pi^2}{ab}\int\limits_{-b/2}^{b/2}\int\limits_{-a/2}^{a/2}\phi_{mn}(x',y')\int\limits_{-\infty}^{\infty}\int\limits_{-\infty}^{\infty}\phi_{pq}(x,y)$$
$$\times\,\mathrm{rect}\left(\frac{x}{a}\right)\,\mathrm{rect}\left(\frac{y}{b}\right)\,\delta(x'-x)\,\delta(y'-y)\,\mathrm{d}x\,\mathrm{d}y\,\mathrm{d}x'\,\mathrm{d}y'$$
$$= \frac{4\pi^2}{ab}\int\limits_{-b/2}^{b/2}\int\limits_{-a/2}^{a/2}\phi_{mn}(x',y')\,\phi_{pq}(x',y')\,\mathrm{rect}\left(\frac{x'}{a}\right)\,\mathrm{rect}\left(\frac{y'}{b}\right)\,\mathrm{d}x'\,\mathrm{d}y'.$$

However, by the definition of rect() functions (Eqs. (I.2) and (I.3)), we get

$$\int\limits_{-\infty}^{\infty}\int\limits_{-\infty}^{\infty} X_{mn}(\lambda,\mu)\Phi_{pq}(-\lambda,-\mu)\,\mathrm{d}\lambda\,\mathrm{d}\mu = \frac{4\pi^2}{ab}\int\limits_{-b/2}^{b/2}\int\limits_{-a/2}^{a/2}\phi_{mn}(x',y')\,\phi_{pq}(x',y')\,\mathrm{d}x'\,\mathrm{d}y'.$$

We have

$$\phi_{mn}(x,y) = \sin\frac{m\pi(x+a/2)}{a}\sin\frac{n\pi(y+b/2)}{b}.$$

And using Eq. (I.5) we can find that

$$\int\limits_{-\infty}^{\infty}\int\limits_{-\infty}^{\infty} X_{mn}(\lambda,\mu)\Phi_{pq}(-\lambda,-\mu)\,\mathrm{d}\lambda\,\mathrm{d}\mu = \pi^2\,\delta_{mp}\,\delta_{nq}. \tag{I.14}$$

I.4 Integral $\int\limits_{-\infty}^{\infty}\int\limits_{-\infty}^{\infty}\frac{\Phi_{pq}(-\lambda,-\mu)}{Z_a(\lambda,\mu)}\,e^{i\lambda x_0+i\mu y_0}\,\mathrm{d}\lambda\,\mathrm{d}\mu$

$$\gamma_{pq}\left(x_0,y_0\right)=\int\limits_{-\infty}^{\infty}\int\limits_{-\infty}^{\infty}\frac{\Phi_{pq}(-\lambda,-\mu)}{Z_a\left(\lambda,\mu\right)}\,e^{i\lambda x_0+i\mu y_0}\,\mathrm{d}\lambda\,\mathrm{d}\mu. \tag{I.15}$$

The above integral is evaluated numerically. The integral over the infinite 2-D wavenumber domain is approximated by a sum over a finite discretized wavenumber domain.

I.5 Integral $\int\limits_{-\infty}^{\infty}\int\limits_{-\infty}^{\infty}\Phi_{pq}(-\lambda,-\mu)\,e^{i\lambda x_0+i\mu y_0}\,\mathrm{d}\lambda\,\mathrm{d}\mu$

Let $\bar{\lambda}=-\lambda$ and $\bar{\mu}=-\mu$. Therefore

$$\begin{aligned}\int\limits_{-\infty}^{\infty}\int\limits_{-\infty}^{\infty}\Phi_{pq}(-\lambda,-\mu)\,e^{i\lambda x_0+i\mu y_0}\,\mathrm{d}\lambda\,\mathrm{d}\mu &=\int\limits_{-\infty}^{\infty}\int\limits_{-\infty}^{\infty}\Phi_{pq}(\bar{\lambda},\bar{\mu})\,e^{-i\bar{\lambda}x_0-i\bar{\mu}y_0}\,\mathrm{d}\bar{\lambda}\,\mathrm{d}\bar{\mu}\\ &=2\pi\,\phi_{pq}\left(x_0,y_0\right).\end{aligned} \tag{I.16}$$

The last deduction uses the definition of inverse Fourier transforms.

Appendix J

Simplifying the coupled equation

The initial form of the coupled equation is (Eq. (6.35))

$$\left[1+\frac{2\sigma_b}{Z_{0b}}Z_a(\lambda,\mu)\right]\left[\frac{1}{2\mathrm{i}\omega Z_a\left(\lambda,\mu\right)}\sum_{r,m,n}B_r\bar{U}_{mnr}\Phi_{mn}(\lambda,\mu)-\frac{2\pi\tilde{P}_i}{Z_a\left(\lambda,\mu\right)}\delta(\lambda+k_x)\,\delta(\mu+k_y)\right]$$

$$\begin{aligned}
&= \zeta_I\sum_{r,m,n}B_rU_{mnr}\Phi_{mn}(\lambda,\mu)-\frac{2\sigma_b}{Z_{0b}}\,2\pi\tilde{P}_i\,\delta(\lambda+k_x)\,\delta(\mu+k_y)\\
&- \left[\frac{2\sigma_p}{Z_{0p}}-\frac{2\sigma_b}{Z_{0b}}\right]\frac{\tilde{P}_iab}{2\pi}\operatorname{sinc}\left[\frac{(\lambda+k_x)a}{2}\right]\operatorname{sinc}\left[\frac{(\mu+k_y)b}{2}\right]
\end{aligned}$$

$$-\left[\frac{2\sigma_p}{Z_{0p}}-\frac{2\sigma_b}{Z_{0b}}\right]\frac{ab}{4\pi^2}\int\limits_{-\infty}^{\infty}\int\limits_{-\infty}^{\infty}\left[\frac{1}{2\mathrm{i}\omega}\sum_{r,m,n}B_r\bar{U}_{mnr}\Phi_{mn}(\lambda',\mu')-2\pi\tilde{P}_i\,\delta(\lambda'+k_x)\,\delta(\mu'+k_y)\right]$$

$$\times\operatorname{sinc}\left[\frac{(\lambda-\lambda')a}{2}\right]\operatorname{sinc}\left[\frac{(\mu-\mu')b}{2}\right]\,\mathrm{d}\lambda'\,\mathrm{d}\mu',$$

where

$$\bar{U}_{mnr}=\left[D^*(1-\mathrm{i}\eta)\left\{\left(\frac{m\pi}{a}\right)^2+\left(\frac{n\pi}{b}\right)^2\right\}^2-m_p\omega^2\right]U_{mnr}.$$

Expanding

$$\left[1+\frac{2\sigma_b}{Z_{0b}}Z_a(\lambda,\mu)\right]\frac{1}{2\mathrm{i}\omega}\sum_{r,m,n}B_r\bar{U}_{mnr}\Theta_{mn}(\lambda,\mu)$$

$$-\frac{2\pi\tilde{P}_i}{Z_a\,(\lambda,\mu)}\,\delta(\lambda+k_x)\,\delta(\mu+k_y)-\frac{2\sigma_b}{Z_{0b}}\,2\pi\tilde{P}_i\,\delta(\lambda+k_x)\,\delta(\mu+k_y)$$

$$=\;\zeta_I\sum_{r,m,n}B_rU_{mnr}\Phi_{mn}(\lambda,\mu)-\frac{2\sigma_b}{Z_{0b}}\,2\pi\tilde{P}_i\,\delta(\lambda+k_x)\,\delta(\mu+k_y)$$

$$-\;\left[\frac{2\sigma_p}{Z_{0p}}-\frac{2\sigma_b}{Z_{0b}}\right]\frac{\tilde{P}_iab}{2\pi}\,\mathrm{sinc}\left[\frac{(\lambda+k_x)a}{2}\right]\,\mathrm{sinc}\left[\frac{(\mu+k_y)b}{2}\right]$$

$$-\;\left[\frac{2\sigma_p}{Z_{0p}}-\frac{2\sigma_b}{Z_{0b}}\right]\frac{ab}{4\pi^2}\,\frac{1}{2\mathrm{i}\omega}\sum_{r,m,n}B_r\bar{U}_{mnr}X_{mn}(\lambda,\mu)$$

$$+\;\left[\frac{2\sigma_p}{Z_{0p}}-\frac{2\sigma_b}{Z_{0b}}\right]\frac{\tilde{P}_iab}{2\pi}\,\mathrm{sinc}\left[\frac{(\lambda+k_x)a}{2}\right]\,\mathrm{sinc}\left[\frac{(\mu+k_y)b}{2}\right],$$

where

$$\Theta_{mn}(\lambda,\mu)=\frac{\Phi_{mn}(\lambda,\mu)}{Z_a(\lambda,\mu)}\tag{J.1}$$

and

$$X_{mn}(\lambda,\mu)=\int_{-\infty}^{\infty}\int_{-\infty}^{\infty}\Phi_{mn}(\lambda',\mu')\,\mathrm{sinc}\left[\frac{(\lambda-\lambda')a}{2}\right]\,\mathrm{sinc}\left[\frac{(\mu-\mu')b}{2}\right]\,\mathrm{d}\lambda'\,\mathrm{d}\mu'.\tag{J.2}$$

After removing the identical terms we get

$$\left[1+\frac{2\sigma_b}{Z_{0b}}Z_a(\lambda,\mu)\right]\frac{1}{2\mathrm{i}\omega}\sum_{r,m,n}B_r\bar{U}_{mnr}\Theta_{mn}(\lambda,\mu)-\frac{2\pi\tilde{P}_i}{Z_a\,(\lambda,\mu)}\,\delta(\lambda+k_x)\,\delta(\mu+k_y)$$

$$=\;\zeta_I\sum_{r,m,n}B_rU_{mnr}\Phi_{mn}(\lambda,\mu)\;-\;\left[\frac{2\sigma_p}{Z_{0p}}-\frac{2\sigma_b}{Z_{0b}}\right]\frac{ab}{4\pi^2}\,\frac{1}{2\mathrm{i}\omega}\sum_{r,m,n}B_r\bar{U}_{mnr}X_{mn}(\lambda,\mu).$$

Rearranging

$$\frac{1}{2\mathrm{i}\omega}\left[1+\frac{2\sigma_b}{Z_{0b}}Z_a(\lambda,\mu)\right]\sum_{r,m,n}B_r\bar{U}_{mnr}\Theta_{mn}(\lambda,\mu)-\zeta_I\sum_{r,m,n}B_rU_{mnr}\Phi_{mn}(\lambda,\mu)$$
$$+\frac{ab}{8\pi^2\mathrm{i}\omega}\left[\frac{2\sigma_p}{Z_{0p}}-\frac{2\sigma_b}{Z_{0b}}\right]\sum_{r,m,n}B_r\bar{U}_{mnr}X_{mn}(\lambda,\mu) \;=\; \frac{2\pi\tilde{P}_i}{Z_a\,(\lambda,\mu)}\,\delta(\lambda+k_x)\,\delta(\mu+k_y). \tag{J.3}$$

Appendix K

Negative transmission loss

The power balance equation (Eq. (6.53)) is written as

$$W_{\text{refl}} + W_{\text{flow}} = W_i + W_{\text{inc-rad}} = \tilde{W}_i. \tag{K.1}$$

Let us now find the expression for $W_{\text{inc-rad}}$ in terms of the pressure and velocity fields in the wavenumber domain given that

$$W_{\text{inc-rad}} = -\frac{1}{2}\,\mathrm{Re}\left\{\iint_{A_p}\Big[p_i(x,y,z=0)v_a^*(x,y,z=0) + p^+(x,y,z=0)v_i^*(x,y,z=0)\Big]\,\mathrm{d}A\right\}. \tag{K.2}$$

First, consider the integral

$$T^1_{\text{inc-rad}} = \iint_{A_p} p_i(x,y,z=0)v_a^*(x,y,z=0)\;\mathrm{d}A. \tag{K.3}$$

Using Eq. (6.1) and the definition of inverse double Fourier transform

$$T^1_{\text{inc-rad}} = \int\limits_{-b/2}^{b/2}\int\limits_{-a/2}^{a/2} \tilde{P}_i\,\mathrm{e}^{\mathrm{i}k_x x + \mathrm{i}k_y y}\left[\frac{1}{2\pi}\int\limits_{-\infty}^{\infty}\int\limits_{-\infty}^{\infty} V_a^*(\lambda,\mu,z=0)\;\mathrm{e}^{\mathrm{i}\lambda x + \mathrm{i}\mu y}\,\mathrm{d}\lambda\,\mathrm{d}\mu\right]\mathrm{d}x\,\mathrm{d}y.$$

We know that $v_a(x,y,z=0) = 0$ on the baffle region if the baffle is unperforated. We may now extend the surface integral over the entire $z=0$ plane. Thus, after rearranging the integrals we get

$$T^1_{\text{inc-rad}} = \frac{\tilde{P}_i}{2\pi} \int_{-\infty}^{\infty} \int_{-\infty}^{\infty} V_a^* \left(\lambda, \mu, z = 0\right) \left[\int_{-\infty}^{\infty} \int_{-\infty}^{\infty} \mathrm{e}^{\mathrm{i}(\lambda + k_x)x + \mathrm{i}(\mu + k_y)y} \, \mathrm{d}x \, \mathrm{d}y \right] \mathrm{d}\lambda \, \mathrm{d}\mu.$$

Also

$$\int_{-\infty}^{\infty} \int_{-\infty}^{\infty} \mathrm{e}^{\mathrm{i}(\lambda + k_x)x + \mathrm{i}(\mu + k_y)y} \, \mathrm{d}x \, \mathrm{d}y = 4\pi^2 \, \delta(\lambda + k_x) \, \delta(\mu + k_y).$$

Therefore

$$T^1_{\text{inc-rad}} = 2\pi \, \tilde{P}_i \, V_a^* \left(-k_x, -k_y, z = 0\right). \tag{K.4}$$

Next, consider the integral

$$T^2_{\text{inc-rad}} = \iint_{A_p} p^+(x, y, z = 0) v_i^* \left(x, y, z = 0\right) \, \mathrm{d}A, \tag{K.5}$$

where the normal velocity of the incident plane wave is $v_i(x, y, z = 0) = -\frac{\cos\theta}{\rho_0 c} \tilde{P}_i \mathrm{e}^{\mathrm{i}k_x x + \mathrm{i}k_y y}$. Using the inverse double Fourier transform we get

$$T^2_{\text{inc-rad}} = \int_{-b/2}^{b/2} \int_{-a/2}^{a/2} \frac{-\cos\theta}{\rho_0 c} \tilde{P}_i^* \, \mathrm{e}^{-\mathrm{i}k_x x - \mathrm{i}k_y y}$$
$$\times \left[\frac{1}{2\pi} \int_{-\infty}^{\infty} \int_{-\infty}^{\infty} P^+ \left(\lambda, \mu, z = 0\right) \, \mathrm{e}^{-\mathrm{i}\lambda x - \mathrm{i}\mu y} \, \mathrm{d}\lambda \, \mathrm{d}\mu \right] \mathrm{d}x \, \mathrm{d}y.$$

From Eq. (6.24) we know that

$$P^+(\lambda, \mu, z = 0) = Z_a(\lambda, \mu) V_a \left(\lambda, \mu, z = 0\right).$$

After rearranging the integrals in $T^2_{\text{inc-rad}}$ and substituting for $P^+(\lambda, \mu, z = 0)$

$$T^2_{\text{inc-rad}} = \frac{-\tilde{P}_i^* \cos\theta}{2\pi \, \rho_0 c} \int_{-\infty}^{\infty} \int_{-\infty}^{\infty} Z_a(\lambda, \mu) V_a \left(\lambda, \mu, z = 0\right)$$
$$\times \left[\int_{-b/2}^{b/2} \int_{-a/2}^{a/2} \mathrm{e}^{-\mathrm{i}(\lambda + k_x)x - \mathrm{i}(\mu + k_y)y} \, \mathrm{d}x \, \mathrm{d}y \right] \mathrm{d}\lambda \, \mathrm{d}\mu.$$

Also

$$\int_{-b/2}^{b/2}\int_{-a/2}^{a/2} \mathrm{e}^{-\mathrm{i}(\lambda+k_x)x-\mathrm{i}(\mu+k_y)y}\,\mathrm{d}x\,\mathrm{d}y = ab\,\mathrm{sinc}\left[\frac{(\lambda+k_x)a}{2}\right]\,\mathrm{sinc}\left[\frac{(\mu+k_y)b}{2}\right].$$

Therefore

$$T^2_{\text{inc-rad}} = \frac{-\tilde{P}_i^*\cos\theta\,ab}{2\pi\,\rho_0 c}\int_{-\infty}^{\infty}\int_{-\infty}^{\infty} Z_a(\lambda,\mu)V_a\left(\lambda,\mu,z=0\right) \times \mathrm{sinc}\left[\frac{(\lambda+k_x)a}{2}\right]\,\mathrm{sinc}\left[\frac{(\mu+k_y)b}{2}\right]\,\mathrm{d}\lambda\,\mathrm{d}\mu. \quad \text{(K.6)}$$

The above integral can be evaluated numerically.

Now, using Eqs. (K.3) to (K.6), Eq. (K.2) becomes

$$W_{\text{inc-rad}} = \frac{1}{2}\,\mathrm{Re}\left\{\frac{\tilde{P}_i^*\cos\theta\,ab}{2\pi\,\rho_0 c} \times \int_{-\infty}^{\infty}\int_{-\infty}^{\infty} Z_a(\lambda,\mu)V_a\left(\lambda,\mu,z=0\right)\mathrm{sinc}\left[\frac{(\lambda+k_x)a}{2}\right]\,\mathrm{sinc}\left[\frac{(\mu+k_y)b}{2}\right]\,\mathrm{d}\lambda\,\mathrm{d}\mu - 2\pi\,\tilde{P}_i\,V_a^*\left(-k_x,-k_y,z=0\right)\right\}. \quad \text{(K.7)}$$

And therefore the total power injected into the perforated panel $\tilde{W}_i$ is obtained as (W_i is given by Eq. (6.49))

$$\tilde{W}_i = \frac{|\tilde{P}_i|^2\cos\theta\;ab}{2\rho_0 c} + \frac{1}{2}\,\mathrm{Re}\left\{\frac{\tilde{P}_i^*\cos\theta\,ab}{2\pi\,\rho_0 c} \times \int_{-\infty}^{\infty}\int_{-\infty}^{\infty} Z_a(\lambda,\mu)V_a\left(\lambda,\mu,z=0\right)\mathrm{sinc}\left[\frac{(\lambda+k_x)a}{2}\right]\,\mathrm{sinc}\left[\frac{(\mu+k_y)b}{2}\right]\,\mathrm{d}\lambda\,\mathrm{d}\mu - 2\pi\,\tilde{P}_i\,V_a^*\left(-k_x,-k_y,z=0\right)\right\}. \quad \text{(K.8)}$$

Let us consider the case of negative TL for the panel with $r_p = 2.5$ mm and $\sigma_p = 5.93\%$. The panel dimensions and material properties are the same as before.

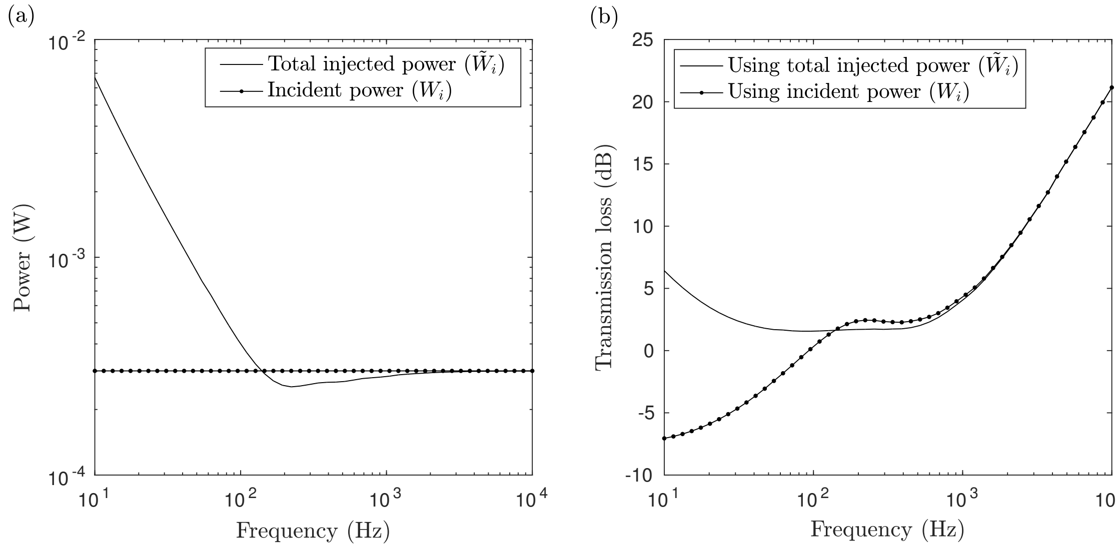

Fig. K.1 (a) Comparison between the total injected power normal to the perforated panel (Eq. (K.8)) and the power carried by the incident plane wave normal to the panel area (Eq. (6.49)). (b) Comparison of TL evaluated using the total injected power with that computed using the normal incident power. The panel has a perforation ratio of $\sigma_p = 5.93\%$ with hole radius $r_p = 2.5$ mm. A normally incident plane wave is considered ($\theta = 0^0$ and $\phi = 0^0$).

For normal incidence of the plane wave ($\theta = 0^0$ and $\phi = 0^0$), Fig. K.1(a) compares $\tilde{W}_i$ (Eq. (K.8)) with W_i (Eq. (6.49)). And Fig. K.1(b) compares the corresponding TLs. The coupled formulation is used here.

$\tilde{W}_i$, as shown in Fig. K.1(a), has a frequency dependent behavior and is much greater than W_i at lower frequencies. This implies that more power is incident upon the panel than the power carried by the incident plane wave alone. Thus, at lower frequencies, evaluating TL using W_i (Eq. (6.49)) alone results in an underestimation of the actual incident power and causes a negative TL (dotted line in Fig. K.1(b)). The two terms of $W_{\text{inc-rad}}$ (Eq. (K.7)) have opposite signs. And at lower frequencies, a significant contribution to $W_{\text{inc-rad}}$ comes from the in-phase components of the incident pressure and the radiated velocity ($T^1_{\text{inc-rad}}$ as given in Eq. (K.4)). As the frequency increases, both the terms reduce in magnitude. And at higher frequencies, they cancel out each other and $\tilde{W}_i$ approaches W_i.

The discontinuity in the perforate impedance at the panel-baffle boundary results in the diffraction of sound waves [71]. The diffraction is significant at lower frequencies so as to cause an increase in the power drawn towards the perforated panel surface. In order to visualize this effect, the total sound intensity field (averaged over time) on the incident side of the perforated panel is plotted in Fig. K.2 for 71.97 Hz, 222.3 Hz

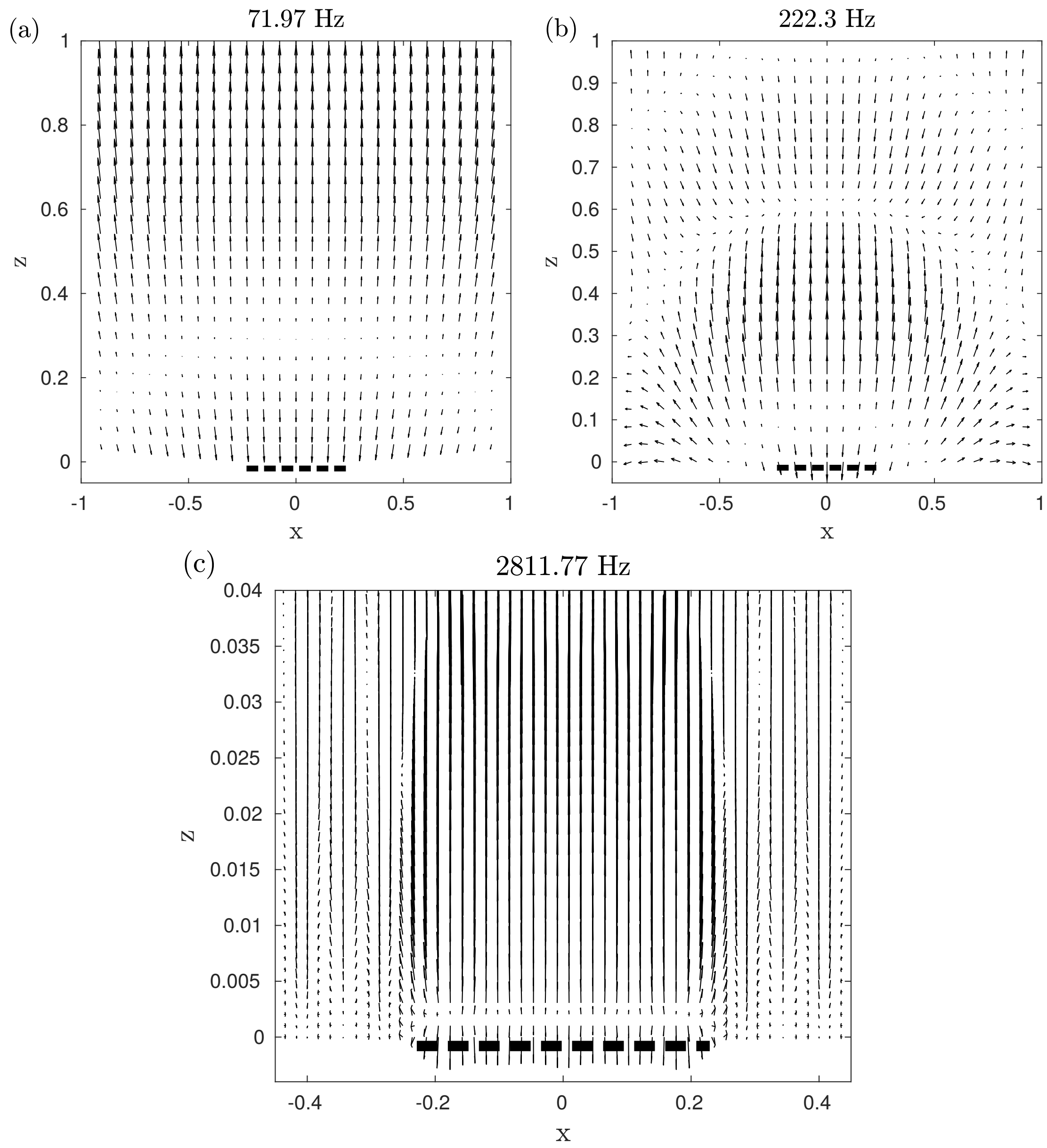

Fig. K.2 The total sound intensity field on the incident side of the perforated panel (in the $y = 0$ plane) at different frequencies: (a) 71.97 Hz, (b) 222.3 Hz and (c) 2811.77 Hz. The panel has a perforation ratio of $\sigma_p = 5.93\%$ with hole radius $r_p = 2.5$ mm. A normally incident plane wave is considered ($\theta = 0^0$ and $\phi = 0^0$).

and 2811.77 Hz. The sound intensity on the incident side is derived in L. 71.97 Hz corresponds to $\tilde{W}_i > W_i$ (see Fig. K.1(a)); 222.3 Hz corresponds to $\tilde{W}_i < W_i$ and 2811.77 Hz, $\tilde{W}_i \approx W_i$. In the intensity plots, at a given point, the vector length is proportional to the magnitude of intensity and the arrow heads point in the direction of power flow. In Fig. K.2, the perforated panel is shown as a thick dashed line. At

71.97 Hz (Fig. K.2(a)), the sound energy is directed towards the perforated panel from a wide region around it; not only from above the panel surface (due to the incident plane wave), but also from the sides (due to the diffraction phenomenon). On the other hand, at higher frequencies, the power is drawn mostly from the front of the perforated panel and the power drawn from the sides due to the diffraction becomes more negligible, as seen in Figs. K.2(b) and K.2(c). Here, the term $W_{\text{inc-rad}}$ (Eq. (K.7)) represents the additional power drawn from the sides due to the diffraction phenomenon, which becomes negligible at higher frequencies. Note, that at certain frequencies, the diffraction results in a total injected power which is lower than the normal incident power, as is evident from the smaller arrows above the perforated panel in Fig. K.2(b). It is attributed to a larger in-phase component of the radiated pressure and the incident velocity ($T^2_{\text{inc-rad}}$ as given in Eq. (K.6)) in the expression for $W_{\text{inc-rad}}$ (Eq. (K.7)).

Appendix L

Sound intensity field on the incident side of the perforated panel

L.1 Pressure and velocity fields on the incident side

We know that the total pressure field (in the wavenumber domain) on the incident side of the panel is (Eq. (6.23))

$$P_2\left(\lambda,\mu,z\right) = Z_a(\lambda,\mu)V_a\left(\lambda,\mu,z=0\right)\,\mathrm{e}^{\mathrm{i}\sqrt{k^2-\lambda^2-\mu^2}z} + 4\pi\tilde{P}_i\,\delta(\lambda+k_x)\,\delta(\mu+k_y)\,\cos k_z z, \tag{L.1}$$

where $Z_a(\lambda,\mu) = \frac{\rho_0 ck}{\sqrt{k^2-\lambda^2-\mu^2}}$. Using the Euler equation in the x direction

$$\frac{\partial p_2(x,y,z)}{\partial x} = \mathrm{i}\rho_0\omega\, v_{2x}(x,y,z). \tag{L.2}$$

Taking the double Fourier transform on both the sides

$$-\mathrm{i}\lambda\, P_2(\lambda,\mu,z) = \mathrm{i}\rho_0 ck\, V_{2x}(\lambda,\mu,z).$$

Therefore

$$V_{2x}(\lambda,\mu,z) = -\frac{\lambda}{\rho_0 ck}\, P_2(\lambda,\mu,z). \tag{L.3}$$

Now, using the Euler equation in the z direction

$$\frac{\partial p_2(x,y,z)}{\partial z} = \mathrm{i}\rho_0\omega\, v_{2z}(x,y,z). \tag{L.4}$$

Taking the double Fourier transform we get

$$\frac{\partial P_2(\lambda,\mu,z)}{\partial z} = \mathrm{i}\rho_0\omega\, V_{2z}(\lambda,\mu,z). \tag{L.5}$$

Substituting for $P_2(\lambda,\mu,z)$ from Eq. (L.1)

$$\begin{aligned}\mathrm{i}\sqrt{k^2-\lambda^2-\mu^2}\, Z_a(\lambda,\mu) V_a\,(\lambda,\mu,z=0)\ \mathrm{e}^{\mathrm{i}\sqrt{k^2-\lambda^2-\mu^2}z}& \\ - k_z\, 4\pi\tilde{P}_i\,\delta(\lambda+k_x)\,\delta(\mu+k_y)\ \sin k_z z &= \mathrm{i}\rho_0\omega\, V_{2z}(\lambda,\mu,z).\end{aligned}$$

Therefore

$$V_{2z}(\lambda,\mu,z) = V_a\,(\lambda,\mu,z=0)\ \mathrm{e}^{\mathrm{i}\sqrt{k^2-\lambda^2-\mu^2}z} + \frac{\mathrm{i}\cos\theta}{\rho_0 c} 4\pi\tilde{P}_i\,\delta(\lambda+k_x)\,\delta(\mu+k_y)\ \sin k_z z. \tag{L.6}$$

L.2 Total intensity on the incident side

The x component of the total intensity on the incident side is given by

$$I_{2x} = \frac{1}{2}\,\mathrm{Re}\left\{p_2(x,y,z)\, v_{2x}^*(x,y,z)\right\}. \tag{L.7}$$

Using the inverse Fourier transform we can write

$$\begin{aligned}I_{2x} = \frac{1}{8\pi^2}\,\mathrm{Re}\Bigg\{&\left[\int_{-\infty}^{\infty}\int_{-\infty}^{\infty} P_2(\lambda,\mu,z)\,\mathrm{e}^{-\mathrm{i}\lambda x-\mathrm{i}\mu y}\,\mathrm{d}\lambda\,\mathrm{d}\mu\right] \\ &\times\left[\int_{-\infty}^{\infty}\int_{-\infty}^{\infty} V_{2x}^*(\lambda',\mu',z)\,\mathrm{e}^{\mathrm{i}\lambda' x+\mathrm{i}\mu' y}\,\mathrm{d}\lambda'\,\mathrm{d}\mu'\right]\Bigg\}.\end{aligned} \tag{L.8}$$

Substituting $P_2(\lambda, \mu, z)$ from Eq. (L.1) into the first integral

$$\int_{-\infty}^{\infty}\int_{-\infty}^{\infty} P_2(\lambda, \mu, z)\, \mathrm{e}^{-\mathrm{i}\lambda x - \mathrm{i}\mu y}\, \mathrm{d}\lambda\, \mathrm{d}\mu = \int_{-\infty}^{\infty}\int_{-\infty}^{\infty} P_2^1(\lambda, \mu, z)\, \mathrm{e}^{-\mathrm{i}\lambda x - \mathrm{i}\mu y}\, \mathrm{d}\lambda\, \mathrm{d}\mu + 4\pi \tilde{P}_i\, \mathrm{e}^{\mathrm{i}k_x x + \mathrm{i}k_y y} \cos k_z z, \quad \text{(L.9)}$$

where

$$P_2^1(\lambda, \mu, z) = Z_a(\lambda, \mu) V_a\,(\lambda, \mu, z = 0)\, \mathrm{e}^{\mathrm{i}\sqrt{k^2 - \lambda^2 - \mu^2} z}. \quad \text{(L.10)}$$

The integral on the right hand side of Eq. (L.9) can be evaluated numerically.

Substituting $V_{2x}(\lambda, \mu, z)$ from Eq. (L.3) into the second integral of Eq. (L.8)

$$\int_{-\infty}^{\infty}\int_{-\infty}^{\infty} V_{2x}^*(\lambda', \mu', z)\, \mathrm{e}^{\mathrm{i}\lambda' x + \mathrm{i}\mu' y}\, \mathrm{d}\lambda'\, \mathrm{d}\mu' = \int_{-\infty}^{\infty}\int_{-\infty}^{\infty} -\frac{\lambda'}{\rho_0 c k} P_2^1(\lambda', \mu', z)\, \mathrm{e}^{\mathrm{i}\lambda' x + \mathrm{i}\mu' y}\, \mathrm{d}\lambda'\, \mathrm{d}\mu' + \frac{\sin\theta\cos\phi}{\rho_0 c} 4\pi \tilde{P}_i^*\, \mathrm{e}^{-\mathrm{i}k_x x - \mathrm{i}k_y y} \cos k_z z, \quad \text{(L.11)}$$

where $P_2^1(\lambda, \mu, z)$ is given by Eq. (L.10). The integral on the right hand side of the above equation can be evaluated numerically.

Now, using Eqs. (L.9) and (L.11), we can evaluate the total intensity in the x direction on the incident side (given by Eq. (L.8)).

The z component of the total intensity on the incident side is given by

$$I_{2z} = \frac{1}{2} \operatorname{Re}\left\{p_2(x, y, z)\, v_{2z}^*(x, y, z)\right\}. \quad \text{(L.12)}$$

Using the inverse Fourier transform we can write

$$I_{2z} = \frac{1}{8\pi^2} \operatorname{Re}\left\{\left[\int_{-\infty}^{\infty}\int_{-\infty}^{\infty} P_2(\lambda, \mu, z)\, \mathrm{e}^{-\mathrm{i}\lambda x - \mathrm{i}\mu y}\, \mathrm{d}\lambda\, \mathrm{d}\mu\right] \times \left[\int_{-\infty}^{\infty}\int_{-\infty}^{\infty} V_{2z}^*(\lambda', \mu', z)\, \mathrm{e}^{\mathrm{i}\lambda' x + \mathrm{i}\mu' y}\, \mathrm{d}\lambda'\, \mathrm{d}\mu'\right]\right\}. \quad \text{(L.13)}$$

The first integral on the right hand side is given by Eq. (L.9). Substituting $V_{2z}(\lambda, \mu, z)$ from Eq. (L.6) into the second integral

$$\int_{-\infty}^{\infty}\int_{-\infty}^{\infty} V_{2z}^{*}(\lambda', \mu', z)\,\mathrm{e}^{\mathrm{i}\lambda' x+\mathrm{i}\mu' y}\,\mathrm{d}\lambda'\,\mathrm{d}\mu' = \int_{-\infty}^{\infty}\int_{-\infty}^{\infty} V_{2z}^{1*}(\lambda', \mu', z)\,\mathrm{e}^{\mathrm{i}\lambda' x+\mathrm{i}\mu' y}\,\mathrm{d}\lambda'\,\mathrm{d}\mu' + \frac{\mathrm{i}\cos\theta}{\rho_0 c} 4\pi \tilde{P}_i^{*}\,\mathrm{e}^{-\mathrm{i}k_x x-\mathrm{i}k_y y}\,\sin k_z z, \quad \text{(L.14)}$$

where

$$V_{2z}^{1}(\lambda', \mu', z) = V_a(\lambda', \mu', z=0)\,\mathrm{e}^{\mathrm{i}\sqrt{k^2-\lambda'^2-\mu'^2}z}. \quad \text{(L.15)}$$

The first integral on the right hand side of Eq. (L.14) is evaluated numerically. Using Eqs. (L.9) and (L.14), we can now find the total intensity in the z direction on the incident side of the panel (given by Eq. (L.13)).

Appendix M

Line integrals and residues in $I_1^{mp}(\mu : |\mu| < k)$ (case 1)

M.1 Line integrals of $\Gamma_1, \Gamma_2, \Gamma_3$ and Γ_4

Consider the contour integrals of case 1 as shown in Fig. 7.9.

$$\begin{aligned} \Gamma_1 &= \int_{\mathrm{i}\infty}^{0} \frac{\left[1-(-1)^m\ \mathrm{e}^{\mathrm{i}\lambda a}\right]\ \left(\lambda_1^2-\lambda^2\right)^{1/2}}{\left(\lambda^2-k_m^2\right)\ \left(\lambda^2-k_p^2\right)}\,\mathrm{d}\lambda, \\ \Gamma_2 &= \int_{0}^{\lambda_1} \frac{\left[1-(-1)^m\ \mathrm{e}^{\mathrm{i}\lambda a}\right]\ \left(\lambda_1^2-\lambda^2\right)^{1/2}}{\left(\lambda^2-k_m^2\right)\ \left(\lambda^2-k_p^2\right)}\,\mathrm{d}\lambda, \\ \Gamma_3 &= \int_{\lambda_1}^{0} \frac{\left[1-(-1)^m\ \mathrm{e}^{\mathrm{i}\lambda a}\right]\ \left(\lambda_1^2-\lambda^2\right)^{1/2}}{\left(\lambda^2-k_m^2\right)\ \left(\lambda^2-k_p^2\right)}\,\mathrm{d}\lambda, \\ \text{and}\quad \Gamma_4 &= \int_{0}^{\mathrm{i}\infty} \frac{\left[1-(-1)^m\ \mathrm{e}^{\mathrm{i}\lambda a}\right]\ \left(\lambda_1^2-\lambda^2\right)^{1/2}}{\left(\lambda^2-k_m^2\right)\ \left(\lambda^2-k_p^2\right)}\,\mathrm{d}\lambda. \end{aligned} \tag{M.1}$$

We have from Eq. (7.9)

$$\left(\lambda_1^2-\lambda^2\right)^{1/2} = \begin{cases} |\lambda_1-\lambda|^{1/2}\ |\lambda_1+\lambda|^{1/2}\ \mathrm{e}^{\mathrm{i}\,(\gamma+\theta)/2} & \text{for } \mathrm{Re}(\lambda) > 0 \text{ and } \mathrm{Im}(\lambda) > 0 \\ -|\lambda_1-\lambda|^{1/2}\ |\lambda_1+\lambda|^{1/2}\ \mathrm{e}^{\mathrm{i}\,(\gamma+\theta)/2} & \text{for } \mathrm{Re}(\lambda) < 0 \text{ and } \mathrm{Im}(\lambda) > 0 \\ |\lambda_1-\lambda|^{1/2}\ |\lambda_1+\lambda|^{1/2}\ \mathrm{e}^{\mathrm{i}\,(\gamma+\theta)/2} & \text{for } \mathrm{Re}(\lambda) < 0 \text{ and } \mathrm{Im}(\lambda) < 0 \\ -|\lambda_1-\lambda|^{1/2}\ |\lambda_1+\lambda|^{1/2}\ \mathrm{e}^{\mathrm{i}\,(\gamma+\theta)/2} & \text{for } \mathrm{Re}(\lambda) > 0 \text{ and } \mathrm{Im}(\lambda) < 0 \end{cases}$$

where γ and θ vary from 0 to 2π.

It can be seen that along the contour Γ_1, $\gamma+\theta = 2\pi$ (Fig. 7.4) and $\lambda = \mathrm{i}y$. Therefore,

$$\left(\lambda_1^2 - \lambda^2\right)^{1/2} = \left|\lambda_1^2 - \lambda^2\right|^{1/2} \mathrm{e}^{\mathrm{i}(\gamma+\theta)/2} = -\left|\lambda_1^2 + y^2\right|^{1/2}.$$

Thus,

$$\Gamma_1 = \mathrm{i}\int_0^\infty \frac{\left[1-(-1)^m\,\mathrm{e}^{-ay}\right]\,\left|\lambda_1^2+y^2\right|^{1/2}}{\left(y^2+k_m^2\right)\left(y^2+k_p^2\right)}\,\mathrm{d}y. \tag{M.2}$$

Now, along the contour of Γ_2, $\gamma = 2\pi$, $\theta = 0$ (Fig. 7.4) and $\lambda = x$. Therefore,

$$\left(\lambda_1^2 - \lambda^2\right)^{1/2} = \left|\lambda_1^2 - \lambda^2\right|^{1/2} \mathrm{e}^{\mathrm{i}(\gamma+\theta)/2} = -\left|\lambda_1^2 - x^2\right|^{1/2}.$$

Thus,

$$\Gamma_2 = -\int_0^{\lambda_1} \frac{\left[1-(-1)^m\,\mathrm{e}^{\mathrm{i}ax}\right]\,\left|\lambda_1^2-x^2\right|^{1/2}}{\left(x^2-k_m^2\right)\left(x^2-k_p^2\right)}\,\mathrm{d}x. \tag{M.3}$$

Along the contour of Γ_3, $\gamma = 0$, $\theta = 2\pi$ (Fig. 7.4) and $\lambda = x$. Therefore,

$$\left(\lambda_1^2 - \lambda^2\right)^{1/2} = -\left|\lambda_1^2 - \lambda^2\right|^{1/2} \mathrm{e}^{\mathrm{i}(\gamma+\theta)/2} = \left|\lambda_1^2 - x^2\right|^{1/2}.$$

Thus,

$$\Gamma_3 = -\int_0^{\lambda_1} \frac{\left[1-(-1)^m\,\mathrm{e}^{\mathrm{i}ax}\right]\,\left|\lambda_1^2-x^2\right|^{1/2}}{\left(x^2-k_m^2\right)\left(x^2-k_p^2\right)}\,\mathrm{d}x. \tag{M.4}$$

And along the contour of Γ_4, $\gamma+\theta = 2\pi$ (Fig. 7.4) and $\lambda = \mathrm{i}y$. Therefore,

$$\left(\lambda_1^2 - \lambda^2\right)^{1/2} = -\left|\lambda_1^2 - \lambda^2\right|^{1/2} \mathrm{e}^{\mathrm{i}(\gamma+\theta)/2} = \left|\lambda_1^2 + y^2\right|^{1/2}.$$

Thus,

$$\Gamma_4 = \mathrm{i}\int_0^\infty \frac{\left[1-(-1)^m\,\mathrm{e}^{-ay}\right]\,\left|\lambda_1^2+y^2\right|^{1/2}}{\left(y^2+k_m^2\right)\left(y^2+k_p^2\right)}\,\mathrm{d}y. \tag{M.5}$$

M.2 The small circular contour around λ_1

Consider the small circular contour C_ϵ connecting Γ_2 and Γ_3 in Fig. 7.9. Along the contour

$$\lambda = \lambda_1 + \epsilon\,\mathrm{e}^{\mathrm{i}\phi},$$

where $\epsilon \to 0$ is a small real quantity and $\phi : \pi$ to $-\pi$. Along the contour

$$\left(\lambda_1^2 - \lambda^2\right)^{1/2} = \left|\lambda_1^2 - \lambda^2\right|^{1/2} \mathrm{e}^{\mathrm{i}\,(\gamma+\theta)/2},$$

where γ and θ can vary from 0 to 2π. The integral around the contour is

$$I_{\mathrm{C}_\epsilon} = \lim_{\epsilon\to 0} \int_{\mathrm{C}_\epsilon} \underbrace{\frac{\left[1-(-1)^m\, \mathrm{e}^{\mathrm{i}\lambda a}\right]\, \left(\lambda_1^2 - \lambda^2\right)^{1/2}}{\left(\lambda^2 - k_m^2\right)\, \left(\lambda^2 - k_p^2\right)}}_{f(\lambda)}\, \mathrm{d}\lambda. \tag{M.6}$$

Now evaluating $|\,(\lambda-\lambda_1)\, f(\lambda)|$ in the limit $\epsilon \to 0$,

$$\begin{aligned}\lim_{\epsilon\to 0} |\,(\lambda-\lambda_1)\, f(\lambda)| &= \lim_{\epsilon\to 0} \left|\frac{\epsilon\, \mathrm{e}^{\mathrm{i}\phi}\left[1-(-1)^m\, \mathrm{e}^{\mathrm{i}\lambda_1 a}\right] \left|\lambda_1^2 - \left(\lambda_1 + \epsilon\, \mathrm{e}^{\mathrm{i}\phi}\right)^2\right|^{1/2} \mathrm{e}^{\mathrm{i}\,(\gamma+\theta)/2}}{\left(\lambda_1^2 - k_m^2\right)\, \left(\lambda_1^2 - k_p^2\right)}\right| \\ &= 0.\end{aligned}$$

Therefore [67]

$$\lim_{\epsilon\to 0} \int_{\mathrm{C}_\epsilon} f(\lambda)\, \mathrm{d}\lambda = 0.$$

Thus,

$$I_{\mathrm{C}_\epsilon} = 0. \tag{M.7}$$

M.3 Residues at the simple poles when $k_m \neq k_p$

The integrand of case 1 can be obtained from Eq. (7.6) as

$$f(\lambda) = \frac{\left[1-(-1)^m\, \mathrm{e}^{\mathrm{i}\lambda a}\right]\, \left(\lambda_1^2 - \lambda^2\right)^{1/2}}{\left(\lambda^2 - k_m^2\right)\, \left(\lambda^2 - k_p^2\right)}.$$

The poles are at $\lambda = \pm k_m$ and $\pm\, k_p$, where $k_m = m\pi/a$ and $k_p = p\pi/a$. The residue at k_m can be obtained as

$$\mathrm{Res}(k_m) = \left.(\lambda - k_m)\, f(\lambda)\right|_{\lambda = k_m} = \frac{\left[1-(-1)^{2m}\right]\, \left(\lambda_1^2 - k_m^2\right)^{1/2}}{2\, k_m\, \left(k_m^2 - k_p^2\right)}$$

which is equal to zero. Thus,

$$\mathrm{Res}(k_m) = 0. \tag{M.8}$$

Similarly, we can also arrive at

$$\mathrm{Res}(-k_m) = \mathrm{Res}(k_p) = \mathrm{Res}(-k_p) = 0. \tag{M.9}$$

M.4 Residues at the poles when $k_m = k_p$

When $k_m = k_p$, the integrand of case 1 is

$$f(\lambda) = \frac{\left[1 - (-1)^m \, \mathrm{e}^{\mathrm{i}\lambda a}\right] \, (\lambda_1^2 - \lambda^2)^{1/2}}{(\lambda^2 - k_m^2)^2}.$$

The poles at $\lambda = \pm k_m$ are of multiplicity two. The residue at $\lambda = k_m$ can be obtained from

$$\mathrm{Res}(k_m) = \frac{\mathrm{d}}{\mathrm{d}\lambda} \left[(\lambda - k_m)^2 f(\lambda)\right]\bigg|_{\lambda = k_m}.$$

We see from Figs. 7.4 and 7.9 that near $\lambda = k_m$, $\gamma = \pi$ and $\theta = 0$. Thus, the square root function

$$\left(\lambda_1^2 - \lambda^2\right)^{1/2} = \left|\lambda_1^2 - \lambda^2\right|^{1/2} \mathrm{e}^{\mathrm{i}\,(\gamma+\theta)/2} = \mathrm{i}\,\left|\lambda_1^2 - \lambda^2\right|^{1/2}.$$

Therefore,

$$\mathrm{Res}(k_m) = \frac{\mathrm{d}}{\mathrm{d}\lambda} \left[\frac{\left[1 - (-1)^m \, \mathrm{e}^{\mathrm{i}\lambda a}\right] \, \mathrm{i}\, |\lambda_1^2 - \lambda^2|^{1/2}}{(\lambda + k_m)^2}\right]\Bigg|_{\lambda = k_m}.$$

Thus, knowing that $k_m = m\pi/a$ we get

$$\mathrm{Res}(k_m) = \frac{a \, |\lambda_1^2 - k_m^2|^{1/2}}{4\, k_m^2}. \tag{M.10}$$

Similarly, the residue at $\lambda = -k_m$ can be obtained from

$$\mathrm{Res}(-k_m) = \frac{\mathrm{d}}{\mathrm{d}\lambda} \left[(\lambda + k_m)^2 f(\lambda)\right]\bigg|_{\lambda = -k_m}.$$

Near $\lambda = -k_m$, $\gamma = 2\pi$ and $\theta = \pi$. Thus, the square root function

$$\left(\lambda_1^2 - \lambda^2\right)^{1/2} = -\left|\lambda_1^2 - \lambda^2\right|^{1/2} \mathrm{e}^{\mathrm{i}\,(\gamma+\theta)/2} = \mathrm{i}\,\left|\lambda_1^2 - \lambda^2\right|^{1/2}.$$

Therefore,

$$\mathrm{Res}(-k_m) = \frac{\mathrm{d}}{\mathrm{d}\lambda}\left[\frac{\left[1-(-1)^m\ \mathrm{e}^{\mathrm{i}\lambda a}\right]\ \mathrm{i}\ \left|\lambda_1^2-\lambda^2\right|^{1/2}}{(\lambda-k_m)^2}\right]\Bigg|_{\lambda=-k_m}.$$

And by knowing that $k_m = m\pi/a$ we arrive at

$$\mathrm{Res}(-k_m) = \frac{a\ \left|\lambda_1^2-k_m^2\right|^{1/2}}{4\,k_m^2}. \tag{M.11}$$

Appendix N

Line integrals and residues in $I_1^{mp}(\mu : |\mu| > k)$ (case 2)

N.1 Line integrals of Γ_1 and Γ_2

The integrals Γ_1 and Γ_2, along the contours as shown in Fig. 7.10, are given by

$$\begin{aligned} \Gamma_1 &= \int_{\mathrm{i}\infty}^{\lambda_1} \frac{\left[1-(-1)^m\ \mathrm{e}^{\mathrm{i}\lambda a}\right]\ \left(\lambda_1^2-\lambda^2\right)^{1/2}}{\left(\lambda^2-k_m^2\right)\ \left(\lambda^2-k_p^2\right)}\,\mathrm{d}\lambda, \\ \text{and} \quad \Gamma_2 &= \int_{\lambda_1}^{\mathrm{i}\infty} \frac{\left[1-(-1)^m\ \mathrm{e}^{\mathrm{i}\lambda a}\right]\ \left(\lambda_1^2-\lambda^2\right)^{1/2}}{\left(\lambda^2-k_m^2\right)\ \left(\lambda^2-k_p^2\right)}\,\mathrm{d}\lambda, \end{aligned} \tag{N.1}$$

where $\lambda_1 = \mathrm{i}\lambda_1'$. We have from Eq. (7.10)

$$\left(\lambda_1^2-\lambda^2\right)^{1/2} = \left|\lambda_1^2-\lambda^2\right|^{1/2}\ \mathrm{e}^{\mathrm{i}\,(\gamma+\theta)/2},$$

where γ and θ vary from $-\pi/2$ to $3\pi/2$.

We can see that along Γ_1, $\gamma = 3\pi/2$ and $\theta = \pi/2$ (Fig. 7.8) and $\lambda = \mathrm{i}y$. Therefore

$$\left(\lambda_1^2-\lambda^2\right)^{1/2} = \left|\lambda_1^2-\lambda^2\right|^{1/2}\ \mathrm{e}^{\mathrm{i}\,(\gamma+\theta)/2} = -\left|\lambda_1'^2-y^2\right|^{1/2}.$$

Thus,

$$\Gamma_1 = \mathrm{i}\int_{\lambda_1'}^{\infty} \frac{\left[1-(-1)^m\ \mathrm{e}^{-ay}\right]\ \left|\lambda_1'^2-y^2\right|^{1/2}}{\left(y^2+k_m^2\right)\ \left(y^2+k_p^2\right)}\,\mathrm{d}y. \tag{N.2}$$

Similarly, along Γ_2, $\gamma = -\pi/2$ and $\theta = \pi/2$ (Fig. 7.8) and $\lambda = \mathrm{i}y$. Therefore

$$\left(\lambda_1^2 - \lambda^2\right)^{1/2} = \left|\lambda_1^2 - \lambda^2\right|^{1/2} \mathrm{e}^{\mathrm{i}\,(\gamma+\theta)/2} = \left|\lambda_1'^2 - y^2\right|^{1/2}.$$

Thus,

$$\Gamma_2 = \mathrm{i} \int\limits_{\lambda_1'}^{\infty} \frac{\left[1 - (-1)^m\, \mathrm{e}^{-ay}\right] \left|\lambda_1'^2 - y^2\right|^{1/2}}{\left(y^2 + k_m^2\right)\left(y^2 + k_p^2\right)}\, \mathrm{d}y. \tag{N.3}$$

N.2 The small circular contour around λ_1

Consider the small circular contour C_ϵ connecting Γ_1 and Γ_2 in Fig. 7.10. Along the contour

$$\lambda = \lambda_1 + \epsilon\, \mathrm{e}^{\mathrm{i}\phi},$$

where $\epsilon \to 0$ is a small real quantity and $\phi : \pi/2$ to $-3\pi/2$. Also, along the contour

$$\left(\lambda_1^2 - \lambda^2\right)^{1/2} = \left|\lambda_1^2 - \lambda^2\right|^{1/2} \mathrm{e}^{\mathrm{i}\,(\gamma+\theta)/2},$$

where γ and θ can vary from $-\pi/2$ to $3\pi/2$.

The integral around the contour is

$$I_{\mathrm{C}_\epsilon} = \lim_{\epsilon\to 0} \int\limits_{\mathrm{C}_\epsilon} \underbrace{\frac{\left[1 - (-1)^m\, \mathrm{e}^{\mathrm{i}\lambda a}\right] \left(\lambda_1^2 - \lambda^2\right)^{1/2}}{\left(\lambda^2 - k_m^2\right)\left(\lambda^2 - k_p^2\right)}}_{f(\lambda)}\, \mathrm{d}\lambda. \tag{N.4}$$

Now evaluating $|(\lambda - \lambda_1)\, f(\lambda)|$ in the limit $\epsilon \to 0$,

$$\begin{aligned}\lim_{\epsilon\to 0} |(\lambda - \lambda_1)\, f(\lambda)| &= \lim_{\epsilon\to 0} \left| \frac{\epsilon\, \mathrm{e}^{\mathrm{i}\phi} \left[1 - (-1)^m\, \mathrm{e}^{\mathrm{i}\lambda_1 a}\right] \left|\lambda_1^2 - \left(\lambda_1 + \epsilon\, \mathrm{e}^{\mathrm{i}\phi}\right)^2\right|^{1/2} \mathrm{e}^{\mathrm{i}\,(\gamma+\theta)/2}}{\left(\lambda_1^2 - k_m^2\right)\left(\lambda_1^2 - k_p^2\right)} \right| \\ &= 0.\end{aligned}$$

Therefore [67]

$$\lim_{\epsilon\to 0} \int\limits_{\mathrm{C}_\epsilon} f(\lambda)\, \mathrm{d}\lambda = 0.$$

Thus,

$$I_{\mathrm{C}_\epsilon} = 0. \tag{N.5}$$

N.3 Residues at the simple poles when $k_m \neq k_p$

The integrand of case 2 is (from Eq. (7.6))

$$f(\lambda) = \frac{\left[1 - (-1)^m \, \mathrm{e}^{\mathrm{i}\lambda a}\right] \, \left(\lambda_1^2 - \lambda^2\right)^{1/2}}{\left(\lambda^2 - k_m^2\right) \, \left(\lambda^2 - k_p^2\right)}.$$

The poles are at $\lambda = \pm k_m$ and $\pm\, k_p$, where $k_m = m\pi/a$ and $k_p = p\pi/a$. Now, the residue at k_m is given by

$$\mathrm{Res}(k_m) = \left.(\lambda - k_m)\, f(\lambda)\right|_{\lambda = k_m} = \frac{\left[1 - (-1)^{2m}\right] \, \left(\lambda_1^2 - k_m^2\right)^{1/2}}{2\, k_m \, \left(k_m^2 - k_p^2\right)}$$

which is equal to zero. Thus,

$$\mathrm{Res}(k_m) = 0. \tag{N.6}$$

Similarly, we find that

$$\mathrm{Res}(-k_m) = \mathrm{Res}(k_p) = \mathrm{Res}(-k_p) = 0. \tag{N.7}$$

N.4 Residues at the poles when $k_m = k_p$

When $k_m = k_p$ the integrand of case 2 is

$$f(\lambda) = \frac{\left[1 - (-1)^m \, \mathrm{e}^{\mathrm{i}\lambda a}\right] \, \left(\lambda_1^2 - \lambda^2\right)^{1/2}}{\left(\lambda^2 - k_m^2\right)^2}.$$

The poles at $\lambda = \pm k_m$ are of multiplicity two. Fig. N.1 illustrates $\lambda_1 - \lambda$ and $\lambda_1 + \lambda$ near these poles. It can be seen that along the real axis $\gamma + \theta = \pi$. Therefore, the value of the square root function (as given by Eq. (7.10)) along the real axis is

$$\left(\lambda_1^2 - \lambda^2\right)^{1/2} = \left|\lambda_1^2 - \lambda^2\right|^{1/2} \, \mathrm{e}^{\mathrm{i}\,(\gamma+\theta)/2} = \mathrm{i}\, \left|\lambda_1^2 - \lambda^2\right|^{1/2}.$$

Now, the residue at $\lambda = k_m$ can be obtained from (see Fig. N.1a)

$$\mathrm{Res}(k_m) = \left.\frac{\mathrm{d}}{\mathrm{d}\lambda} \left[(\lambda - k_m)^2 \, f(\lambda)\right]\right|_{\lambda = k_m}.$$

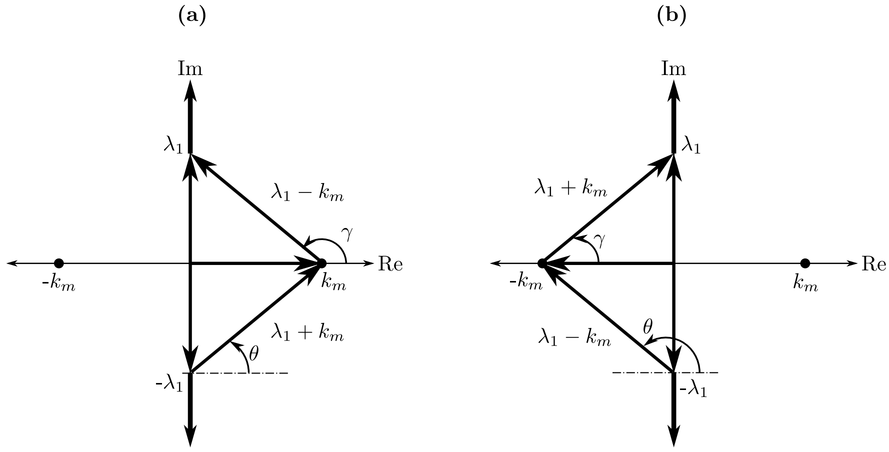

Fig. N.1 Illustrations of $\lambda_1 - \lambda$ and $\lambda_1 + \lambda$ near the poles $\lambda = \pm k_m$ in the complex λ plane (case 2).

Substituting for $f(\lambda)$ with the appropriate square root term we obtain

$$\mathrm{Res}(k_m) = \frac{\mathrm{d}}{\mathrm{d}\lambda}\left[\frac{\left[1-(-1)^m\ \mathrm{e}^{\mathrm{i}\lambda a}\right]\ \mathrm{i}\ |\lambda_1^2 - \lambda^2|^{1/2}}{(\lambda + k_m)^2}\right]\Bigg|_{\lambda = k_m} .$$

Thus, knowing that $k_m = m\pi/a$ we get

$$\mathrm{Res}(k_m) = \frac{a\ |\lambda_1^2 - k_m^2|^{1/2}}{4\,k_m^2}. \tag{N.8}$$

Similarly, the residue at $\lambda = -k_m$ can be obtained from (see Fig. N.1b)

$$\mathrm{Res}(-k_m) = \frac{\mathrm{d}}{\mathrm{d}\lambda}\left[(\lambda + k_m)^2 f(\lambda)\right]\Big|_{\lambda=-k_m} = \frac{\mathrm{d}}{\mathrm{d}\lambda}\left[\frac{\left[1-(-1)^m\ \mathrm{e}^{\mathrm{i}\lambda a}\right]\ \mathrm{i}\ |\lambda_1^2 - \lambda^2|^{1/2}}{(\lambda - k_m)^2}\right]\Bigg|_{\lambda = -k_m} .$$

And by knowing that $k_m = m\pi/a$ we arrive at

$$\mathrm{Res}(-k_m) = \frac{a\ |\lambda_1^2 - k_m^2|^{1/2}}{4\,k_m^2}. \tag{N.9}$$

Appendix O

Detailed derivation of I^{mnpq} in closed form for various modal interactions

O.1 Y edge - Y edge

In this case $k_m, k_p > k$ and $k_n, k_q < k$.

O.1.1 $k_m \neq k_p$ and $k_n = k_q$

Eq. (7.13) is rewritten here

$$I_1^{mp}(\mu : |\mu| < k) = 2 \underbrace{\int_0^{\lambda_1} \frac{\left[1 - (-1)^m \cos ax\right] \left|\lambda_1^2 - x^2\right|^{1/2}}{\left(x^2 - k_m^2\right)\left(x^2 - k_p^2\right)} \,\mathrm{d}x}_{T_1(\mu)}$$

$$- 2\,\mathrm{i} \left[\underbrace{\int_0^{\lambda_1} \frac{(-1)^m \sin ax \left|\lambda_1^2 - x^2\right|^{1/2}}{\left(x^2 - k_m^2\right)\left(x^2 - k_p^2\right)} \,\mathrm{d}x}_{T_2(\mu)} + \underbrace{\int_0^{\infty} \frac{\left[1 - (-1)^m \mathrm{e}^{-ay}\right] \left|\lambda_1^2 + y^2\right|^{1/2}}{\left(y^2 + k_m^2\right)\left(y^2 + k_p^2\right)} \,\mathrm{d}y}_{T_3(\mu)} \right].$$

This can be used to evaluate $I_1^{mp}(k_n : k_n < k)$, by substituting $\mu = k_n$. In the following, closed form expressions are obtained for each of the integrals appearing in the above equation when $\mu = k_n$.

Integral $\boldsymbol{T_1(\mu : \mu = k_n)}$

Consider first the integral

$$\int_0^{\lambda_1} \frac{\left[1-(-1)^m \cos ax\right] \left|\lambda_1^2 - x^2\right|^{1/2}}{\left(x^2-k_m^2\right)\left(x^2-k_p^2\right)} \,\mathrm{d}x.$$

The integrand can be written as

$$\frac{\left[1-(-1)^m \cos ax\right] \left|\lambda_1^2 - x^2\right|^{1/2}}{\left(x^2-k_m^2\right)\left(x^2-k_p^2\right)} = \frac{(-1)^{m+1}\sqrt{\lambda_1^2-x^2}\cos ax}{\left(x^2-k_m^2\right)\left(x^2-k_p^2\right)} + \frac{\sqrt{\lambda_1^2-x^2}}{\left(x^2-k_m^2\right)\left(x^2-k_p^2\right)}. \tag{O.1}$$

Since $k_m, k_p > \lambda_1$, the following approximation is used in the first term [34] (see Appendix Q)

$$\left(x^2-k_m^2\right)\left(x^2-k_p^2\right) \approx \left(k_m^2-\lambda_1^2\right)\left(k_p^2-\lambda_1^2\right). \tag{O.2}$$

Now integrating

$$\int_0^{\lambda_1} \frac{(-1)^{m+1}\sqrt{\lambda_1^2-x^2}\cos ax}{\left(x^2-k_m^2\right)\left(x^2-k_p^2\right)} \,\mathrm{d}x \approx -\frac{\pi\lambda_1(-1)^m \mathrm{J}_1\left(a\lambda_1\right)}{2a\left(\lambda_1^2-k_m^2\right)\left(\lambda_1^2-k_p^2\right)},$$

where $\mathrm{J}_1(*)$ represents the Bessel function of the first kind and first order. Integrating the second term in Eq. (O.1) without any approximations yields

$$\int_0^{\lambda_1} \frac{\sqrt{\lambda_1^2-x^2}}{\left(x^2-k_m^2\right)\left(x^2-k_p^2\right)} \,\mathrm{d}x = \frac{\pi\left(k_p\sqrt{k_m^2-\lambda_1^2} - k_m\sqrt{k_p^2-\lambda_1^2}\right)}{2k_m^3 k_p - 2k_m k_p^3}.$$

Therefore

$$\int_0^{\lambda_1} \frac{\left[1-(-1)^m \cos ax\right] \left|\lambda_1^2 - x^2\right|^{1/2}}{\left(x^2-k_m^2\right)\left(x^2-k_p^2\right)} \,\mathrm{d}x \approx -\frac{\pi\lambda_1(-1)^m \mathrm{J}_1\left(a\lambda_1\right)}{2a\left(\lambda_1^2-k_m^2\right)\left(\lambda_1^2-k_p^2\right)} + \frac{\pi\left(k_p\sqrt{k_m^2-\lambda_1^2} - k_m\sqrt{k_p^2-\lambda_1^2}\right)}{2k_m^3 k_p - 2k_m k_p^3}. \tag{O.3}$$

Integral $T_2(\mu : \mu = k_n)$

Consider the integral

$$\int_0^{\lambda_1} \frac{(-1)^m \sin ax \, |\lambda_1^2 - x^2|^{1/2}}{(x^2 - k_m^2)\left(x^2 - k_p^2\right)} \, \mathrm{d}x.$$

Using the approximation Eq. (O.2) and integrating we get

$$\int_0^{\lambda_1} \frac{(-1)^m \sin ax \, |\lambda_1^2 - x^2|^{1/2}}{(x^2 - k_m^2)\left(x^2 - k_p^2\right)} \, \mathrm{d}x \approx \frac{\pi \lambda_1 (-1)^m \mathrm{H}_1 (a\lambda_1)}{2a\left(\lambda_1^2 - k_m^2\right)\left(\lambda_1^2 - k_p^2\right)}, \tag{O.4}$$

where $\mathrm{H}_1(*)$ is the Struve function of the first order.

Integral $T_3(\mu : \mu = k_n)$

Consider the integral

$$\int_0^{\infty} \frac{\left[1 - (-1)^m \, \mathrm{e}^{-ay}\right] |\lambda_1^2 + y^2|^{1/2}}{(y^2 + k_m^2)\left(y^2 + k_p^2\right)} \, \mathrm{d}y.$$

For $\mu = k_n$ and $\lambda_1^2 = k^2 - k_n^2$, the integral can be written as

$$\int_0^{\infty} \frac{\left[1 - (-1)^m \, \mathrm{e}^{-ay}\right] |\lambda_1^2 + y^2|^{1/2}}{(y^2 + k_m^2)\left(y^2 + k_p^2\right)} \, \mathrm{d}y = \underbrace{\int_0^{\infty} \frac{\sqrt{k^2 - k_n^2 + y^2}}{(k_m^2 + y^2)\left(k_p^2 + y^2\right)} \, \mathrm{d}y}_{T_3^1(k_n)} + \underbrace{\int_0^{\infty} \frac{(-1)^{m+1} \mathrm{e}^{-ay} \sqrt{k^2 - k_n^2 + y^2}}{(k_m^2 + y^2)\left(k_p^2 + y^2\right)} \, \mathrm{d}y}_{T_3^2(k_n)}. \tag{O.5}$$

Here, the integration domain can be divided into two parts: $\int_0^\infty = \int_0^k + \int_k^\infty$.

Integral $T_3^1(k_n)$

Consider the integration from 0 to k of $T_3^1(k_n)$. Since $y < k$ and $k_m, k_p > k$, the following approximation holds (see Appendix Q)

$$\int_0^k \frac{\sqrt{k^2-k_n^2+y^2}}{\left(k_m^2+y^2\right)\left(k_p^2+y^2\right)}\,\mathrm{d}y \approx \int_0^k \frac{\sqrt{k^2-k_n^2+y^2}}{k_m^2 k_p^2}\,\mathrm{d}y.$$

Integrating and simplifying we get

$$\int_0^k \frac{\sqrt{k^2-k_n^2+y^2}}{\left(k_m^2+y^2\right)\left(k_p^2+y^2\right)}\,\mathrm{d}y \approx \frac{2k\sqrt{2k^2-k_n^2}+\left(k^2-k_n^2\right)\log\left(\frac{\left(\sqrt{2k^2-k_n^2}+k\right)^2}{k^2-k_n^2}\right)}{4k_m^2k_p^2}. \tag{O.6}$$

Now, for the integration from k to ∞, $y \gg k^2-k_n^2$. Therefore, we may approximate $\sqrt{k^2-k_n^2+y^2} \approx y$. Hence (see Appendix Q),

$$\int_k^\infty \frac{\sqrt{k^2-k_n^2+y^2}}{\left(k_m^2+y^2\right)\left(k_p^2+y^2\right)}\,\mathrm{d}y \approx \int_k^\infty \frac{y}{\left(k_m^2+y^2\right)\left(k_p^2+y^2\right)}\,\mathrm{d}y.$$

Thus,

$$\int_k^\infty \frac{\sqrt{k^2-k_n^2+y^2}}{\left(k_m^2+y^2\right)\left(k_p^2+y^2\right)}\,\mathrm{d}y \approx \frac{\log\left(\frac{k^2+k_p^2}{k^2+k_m^2}\right)}{2\left(k_p^2-k_m^2\right)}. \tag{O.7}$$

Therefore using Eqs. (O.6) and (O.7) we obtain

$$\begin{aligned}\int_0^\infty \frac{\sqrt{k^2-k_n^2+y^2}}{\left(k_m^2+y^2\right)\left(k_p^2+y^2\right)}\,\mathrm{d}y \approx{}& \frac{\log\left(\frac{k^2+k_p^2}{k^2+k_m^2}\right)}{2\left(k_p^2-k_m^2\right)} \\ &+\frac{2k\sqrt{2k^2-k_n^2}+\left(k^2-k_n^2\right)\log\left(\frac{\left(\sqrt{2k^2-k_n^2}+k\right)^2}{k^2-k_n^2}\right)}{4k_m^2k_p^2}.\end{aligned} \tag{O.8}$$

Integral $T_3^2(k_n)$

Consider the following first order approximation for the exponential function

$$\mathrm{e}^{-ay} \approx \begin{cases} 1-ay & \text{when } ay<1 \\ 0 & \text{when } ay \geq 1. \end{cases} \tag{O.9}$$

If $ak \geq \pi$, $\mathrm{e}^{-ay} \approx 0$, $\forall\, y \geq k$ (see Appendix Q). Therefore

$$\int_{k}^{\infty} \frac{(-1)^{m+1}\mathrm{e}^{-ay}\sqrt{k^2-k_n^2+y^2}}{\left(k_m^2+y^2\right)\left(k_p^2+y^2\right)}\,\mathrm{d}y \approx 0.$$

The integration from 0 to k can be expressed as $\int_0^k = \int_0^{1/a} + \int_{1/a}^k$. When $y > 1/a$, i.e., $ay > 1$, we have the approximation $\mathrm{e}^{-ay} \approx 0$. Hence, one can neglect the integration from $1/a$ to k. Thus, by noting that $1/a < k$ and $k_m, k_p > k$ the integral can be approximated as

$$\int_{0}^{\infty} \frac{(-1)^{m+1}\mathrm{e}^{-ay}\sqrt{k^2-k_n^2+y^2}}{\left(k_m^2+y^2\right)\left(k_p^2+y^2\right)}\,\mathrm{d}y \approx \int_{0}^{1/a} \frac{(-1)^{m+1}(1-ay)\sqrt{k^2-k_n^2+y^2}}{k_m^2k_p^2}\,\mathrm{d}y.$$

Integrating we obtain

$$\int_{0}^{\infty} \frac{(-1)^{m+1}\mathrm{e}^{-ay}\sqrt{k^2-k_n^2+y^2}}{\left(k_m^2+y^2\right)\left(k_p^2+y^2\right)}\,\mathrm{d}y \approx \frac{(-1)^{m+1}}{12ak_m^2k_p^2}\left\{2\sqrt{\frac{1}{a^2}+k^2-k_n^2}-\left(k^2-k_n^2\right)\right.$$
$$\left.\times\left[-4a^2\sqrt{k^2-k_n^2}+4a^2\sqrt{\frac{1}{a^2}+k^2-k_n^2}-3a\log\left(\frac{\left(\sqrt{\frac{1}{a^2}+k^2-k_n^2}+\frac{1}{a}\right)^2}{k^2-k_n^2}\right)\right]\right\}. \tag{O.10}$$

Thus, combining Eqs. (O.8) and (O.10) we get

$$\int_{0}^{\infty} \frac{\left[1-(-1)^m\ \mathrm{e}^{-ay}\right]\left|\lambda_1^2+y^2\right|^{1/2}}{\left(y^2+k_m^2\right)\left(y^2+k_p^2\right)}\,\mathrm{d}y \approx \frac{\log\left(\frac{k^2+k_p^2}{k^2+k_m^2}\right)}{2\left(k_p^2-k_m^2\right)}+\frac{2k\sqrt{2k^2-k_n^2}}{4k_m^2k_p^2}$$
$$+\frac{\left(k^2-k_n^2\right)\log\left(\frac{\left(\sqrt{2k^2-k_n^2}+k\right)^2}{k^2-k_n^2}\right)}{4k_m^2k_p^2}+\frac{(-1)^{m+1}}{12ak_m^2k_p^2}\left\{2\sqrt{\frac{1}{a^2}+k^2-k_n^2}-\left(k^2-k_n^2\right)\right.$$
$$\left.\times\left[-4a^2\sqrt{k^2-k_n^2}+4a^2\sqrt{\frac{1}{a^2}+k^2-k_n^2}-3a\log\left(\frac{\left(\sqrt{\frac{1}{a^2}+k^2-k_n^2}+\frac{1}{a}\right)^2}{k^2-k_n^2}\right)\right]\right\}. \tag{O.11}$$

Integral I^{mnpq}

We can now evaluate I^{mnpq} from Eq. (7.18). Using Eqs. (7.13), (O.3), (O.4) and (O.11) we obtain

$$I^{mnpq} \approx \frac{\pi b}{2k_n^2}\, I_1^{mp}(k_n : k_n < k) = I_R^{mnpq} + \mathrm{i}\, I_\chi^{mnpq}, \tag{O.12}$$

where the real part of I^{mnpq} is given by

$$I_R^{mnpq} = \frac{\pi^2 b}{2k_n^2}\left[\frac{k_p\sqrt{k_m^2-\lambda_1^2} - k_m\sqrt{k_p^2-\lambda_1^2}}{k_m^3 k_p - k_m k_p^3} - \frac{\lambda_1(-1)^m \mathrm{J}_1\left(a\lambda_1\right)}{a\left(\lambda_1^2-k_m^2\right)\left(\lambda_1^2-k_p^2\right)}\right]\delta_{nq}$$

and the imaginary part of I^{mnpq} is given by

$$I_\chi^{mnpq} = -\frac{\pi b}{k_n^2}(A+B+C)\,\delta_{nq}$$

with

$$A = \frac{\pi\lambda_1(-1)^m \mathrm{H}_1\left(a\lambda_1\right)}{2a\left(\lambda_1^2-k_m^2\right)\left(\lambda_1^2-k_p^2\right)},$$

$$B = \frac{2k\sqrt{2k^2-k_n^2} + (k^2-k_n^2)\log\left(\frac{\left(\sqrt{2k^2-k_n^2}+k\right)^2}{k^2-k_n^2}\right)}{4k_m^2 k_p^2} + \frac{\log\left(\frac{k^2+k_p^2}{k^2+k_m^2}\right)}{2\left(k_p^2-k_m^2\right)}$$

and $$C = \frac{(-1)^{m+1}}{12ak_m^2 k_p^2}\left\{2\sqrt{\frac{1}{a^2}+k^2-k_n^2} - \left(k^2-k_n^2\right)\right.$$

$$\left.\times\left[-4a^2\sqrt{k^2-k_n^2} + 4a^2\sqrt{\frac{1}{a^2}+k^2-k_n^2} - 3a\log\left(\frac{\left(\sqrt{\frac{1}{a^2}+k^2-k_n^2}+\frac{1}{a}\right)^2}{k^2-k_n^2}\right)\right]\right\}.$$

O.1.2 $k_m = k_p$ and $k_n = k_q$

When $k_m = k_p$, $I_1^{mp}(\mu : |\mu| < k)$ can be obtained from Eq. (7.20)

$$I_1^{mp}(\mu : |\mu| < k) = 2 \underbrace{\int_0^{\lambda_1} \frac{\left[1 - (-1)^m \, \cos ax\right] \, \left|\lambda_1^2 - x^2\right|^{1/2}}{\left(x^2 - k_m^2\right)^2} \, \mathrm{d}x}_{T_1(\mu)}$$
$$- 2\,\mathrm{i} \left[\frac{-\pi a \, \left|\lambda_1^2 - k_m^2\right|^{1/2}}{4\,k_m^2} + \underbrace{\int_0^{\lambda_1} \frac{(-1)^m \, \sin ax \, \left|\lambda_1^2 - x^2\right|^{1/2}}{\left(x^2 - k_m^2\right)^2} \, \mathrm{d}x}_{T_2(\mu)} \right.$$
$$\left. + \underbrace{\int_0^{\infty} \frac{\left[1 - (-1)^m \, \mathrm{e}^{-ay}\right] \, \left|\lambda_1^2 + y^2\right|^{1/2}}{\left(y^2 + k_m^2\right)^2} \, \mathrm{d}y}_{T_3(\mu)} \right] .$$

$I_1^{mp}(k_n : k_n < k)$ for $k_m = k_p$ can be evaluated from the above equation by substituting $\mu = k_n$. A similar derivation as presented in the $k_m \neq k_p$ and $k_n = k_q$ case is followed for each of the integrals on the right hand side.

Integral $T_1(\mu : \mu = k_n)$

While evaluating the integral

$$\int_0^{\lambda_1} \frac{\left[1 - (-1)^m \, \cos ax\right] \, \left|\lambda_1^2 - x^2\right|^{1/2}}{\left(x^2 - k_m^2\right)^2} \, \mathrm{d}x$$

we get the following results

$$\int_0^{\lambda_1} \frac{(-1)^{m+1}\sqrt{\lambda_1^2 - x^2} \cos ax}{\left(x^2 - k_m^2\right)^2} \, \mathrm{d}x \approx -\frac{\pi\lambda_1(-1)^m \mathrm{J}_1\left(a\lambda_1\right)}{2a\left(k_m^2 - \lambda_1^2\right)^2}$$

and

$$\int_0^{\lambda_1} \frac{\sqrt{\lambda_1^2 - x^2}}{\left(x^2 - k_m^2\right)^2} \, \mathrm{d}x = \frac{\pi\lambda_1^2}{4k_m^3\sqrt{k_m^2 - \lambda_1^2}}.$$

Therefore

$$\int_0^{\lambda_1} \frac{[1-(-1)^m \cos ax]\, |\lambda_1^2 - x^2|^{1/2}}{(x^2-k_m^2)^2}\,\mathrm{d}x \approx -\frac{\pi\lambda_1(-1)^m \mathrm{J}_1(a\lambda_1)}{2a\,(k_m^2-\lambda_1^2)^2} + \frac{\pi\lambda_1^2}{4k_m^3\sqrt{k_m^2-\lambda_1^2}}. \tag{O.13}$$

Integral $T_2(\mu : \mu = k_n)$

Similarly, we can also arrive at

$$\int_0^{\lambda_1} \frac{(-1)^m \sin ax\, |\lambda_1^2 - x^2|^{1/2}}{(x^2-k_m^2)^2}\,\mathrm{d}x \approx \frac{\pi\lambda_1(-1)^m \mathrm{H}_1(a\lambda_1)}{2a\,(\lambda_1^2-k_m^2)^2}. \tag{O.14}$$

Integral $T_3(\mu : \mu = k_n)$

We can derive that

$$\int_0^{\infty} \frac{\sqrt{k^2-k_n^2+y^2}}{(k_m^2+y^2)^2}\,\mathrm{d}y \approx \frac{1}{2\,(k^2+k_m^2)} + \frac{2k\sqrt{2k^2-k_n^2} + (k^2-k_n^2)\log\left(\frac{\left(\sqrt{2k^2-k_n^2}+k\right)^2}{k^2-k_n^2}\right)}{4k_m^4}$$

and

$$\int_0^{\infty} \frac{(-1)^{m+1}\mathrm{e}^{-ay}\sqrt{k^2-k_n^2+y^2}}{(k_m^2+y^2)^2}\,\mathrm{d}y \approx \frac{(-1)^{m+1}}{12ak_m^4}\left\{2\sqrt{\frac{1}{a^2}+k^2-k_n^2} - \left(k^2-k_n^2\right)\right.$$
$$\left. \times\left[-4a^2\sqrt{k^2-k_n^2} + 4a^2\sqrt{\frac{1}{a^2}+k^2-k_n^2} - 3a\log\left(\frac{\left(\sqrt{\frac{1}{a^2}+k^2-k_n^2}+\frac{1}{a}\right)^2}{k^2-k_n^2}\right)\right]\right\}.$$

Thus,

$$\int_0^\infty \frac{\left[1-(-1)^m\ \mathrm{e}^{-ay}\right]\ \left|\lambda_1^2+y^2\right|^{1/2}}{\left(y^2+k_m^2\right)^2}\,\mathrm{d}y \approx \frac{2k\sqrt{2k^2-k_n^2}+(k^2-k_n^2)\log\left(\frac{\left(\sqrt{2k^2-k_n^2}+k\right)^2}{k^2-k_n^2}\right)}{4k_m^4}$$
$$+\frac{1}{2\left(k^2+k_m^2\right)}+\frac{(-1)^{m+1}}{12ak_m^4}\left\{2\sqrt{\frac{1}{a^2}+k^2-k_n^2}-\left(k^2-k_n^2\right)\right.$$
$$\left.\times\left[-4a^2\sqrt{k^2-k_n^2}+4a^2\sqrt{\frac{1}{a^2}+k^2-k_n^2}-3a\log\left(\frac{\left(\sqrt{\frac{1}{a^2}+k^2-k_n^2}+\frac{1}{a}\right)^2}{k^2-k_n^2}\right)\right]\right\}. \tag{O.15}$$

Integral I^{mnpq}

Now, I^{mnpq} (Eq. (7.21)) can be obtained using Eqs. (7.20), (O.13), (O.14) and (O.15) as

$$I^{mnpq} \approx \frac{\pi b}{2k_n^2}\, I_1^{mp}(k_n : k_n < k) = I_R^{mnpq} + \mathrm{i}\, I_\chi^{mnpq}, \tag{O.16}$$

where the real part of I^{mnpq} is given by

$$I_R^{mnpq} = \frac{\pi^2 b}{2k_n^2}\left[\frac{\lambda_1^2}{2k_m^3\sqrt{k_m^2-\lambda_1^2}}-\frac{\lambda_1(-1)^m J_1\left(a\lambda_1\right)}{a\left(k_m^2-\lambda_1^2\right)^2}\right]\delta_{mp}\,\delta_{nq}$$

and the imaginary part of I^{mnpq} is given by

$$I_\chi^{mnpq} = \left[-\frac{\pi b}{k_n^2}(A+B+C)+D\right]\delta_{mp}\,\delta_{nq}$$

with

$$A = \frac{\pi\lambda_1(-1)^m \mathrm{H}_1\left(a\lambda_1\right)}{2a\left(\lambda_1^2-k_m^2\right)^2},$$

$$B = \frac{2k\sqrt{2k^2-k_n^2}+(k^2-k_n^2)\log\left(\frac{\left(\sqrt{2k^2-k_n^2}+k\right)^2}{k^2-k_n^2}\right)}{4k_m^4}+\frac{1}{2\left(k^2+k_m^2\right)},$$

$$C = \frac{(-1)^{m+1}}{12ak_m^4}\left\{2\sqrt{\frac{1}{a^2}+k^2-k_n^2} - \left(k^2-k_n^2\right)\right.$$

$$\left.\times\left[-4a^2\sqrt{k^2-k_n^2} + 4a^2\sqrt{\frac{1}{a^2}+k^2-k_n^2} - 3a\log\left(\frac{\left(\sqrt{\frac{1}{a^2}+k^2-k_n^2}+\frac{1}{a}\right)^2}{k^2-k_n^2}\right)\right]\right\}$$

and $D = \dfrac{\pi^2 ab\sqrt{k_m^2-\lambda_1^2}}{4k_m^2k_n^2}$.

O.2 Acoustically fast (AF) - Y edge

In this case, $k_m, k_n, k_q < k$, $k_p > k$ and $k_m^2 + k_n^2 < k^2$. We have the equation (Eq. (7.25))

$$I_1^{mp}(\mu : |\mu| < \sqrt{k^2 - k_m^2}) = 2\ \underbrace{\mathrm{P}_{k_m} \int_0^{\lambda_1} \frac{\left[1 - (-1)^m \cos ax\right] \left|\lambda_1^2 - x^2\right|^{1/2}}{\left(x^2 - k_m^2\right)\left(x^2 - k_p^2\right)}\, \mathrm{d}x}_{T_1(\mu)}$$

$$- 2\,\mathrm{i} \left[\underbrace{\mathrm{P}_{k_m} \int_0^{\lambda_1} \frac{(-1)^m \sin ax \left|\lambda_1^2 - x^2\right|^{1/2}}{\left(x^2 - k_m^2\right)\left(x^2 - k_p^2\right)}\, \mathrm{d}x}_{T_2(\mu)} + \underbrace{\int_0^{\infty} \frac{\left[1 - (-1)^m \mathrm{e}^{-ay}\right] \left|\lambda_1^2 + y^2\right|^{1/2}}{\left(y^2 + k_m^2\right)\left(y^2 + k_p^2\right)}\, \mathrm{d}y}_{T_3(\mu)}\right].$$

The above equation is used to evaluate $I_1^{mp}(k_n : k_n < \sqrt{k^2 - k_m^2})$. The closed form expressions for each of the above integrals are obtained next.

Integral $T_1(\mu : \mu = k_n)$

We have the integral

$$\mathrm{P}_{k_m} \int_0^{\lambda_1} \frac{\left[1 - (-1)^m \cos ax\right] \left|\lambda_1^2 - x^2\right|^{1/2}}{\left(x^2 - k_m^2\right)\left(x^2 - k_p^2\right)}\, \mathrm{d}x = \mathrm{P}_{k_m} \int_0^{\lambda_1} \frac{\left|\lambda_1^2 - x^2\right|^{1/2}}{\left(x^2 - k_m^2\right)\left(x^2 - k_p^2\right)}\, \mathrm{d}x$$
$$+ \mathrm{P}_{k_m} \int_0^{\lambda_1} \frac{-(-1)^m \cos ax \left|\lambda_1^2 - x^2\right|^{1/2}}{\left(x^2 - k_m^2\right)\left(x^2 - k_p^2\right)}\, \mathrm{d}x.$$

The first integral on the right hand side is evaluated exactly. While evaluating the second integral on the right hand side, we use the approximation [34] (see Appendix Q)

$$\left(x^2 - k_m^2\right)\left(x^2 - k_p^2\right) \approx \left(\lambda_1^2 - k_m^2\right)\left(\lambda_1^2 - k_p^2\right).$$

Thus we obtain

$$\mathrm{P}_{k_m}\int_0^{\lambda_1}\frac{\left[1-(-1)^m\,\cos ax\right]\,\left|\lambda_1^2-x^2\right|^{1/2}}{\left(x^2-k_m^2\right)\left(x^2-k_p^2\right)}\,\mathrm{d}x \approx -\frac{\pi\lambda_1(-1)^m\mathrm{J}_1\left(a\lambda_1\right)}{2a\left(\lambda_1^2-k_m^2\right)\left(\lambda_1^2-k_p^2\right)} - \frac{\pi\left(k_m\sqrt{k_p^2-\lambda_1^2}-ik_p\sqrt{\lambda_1^2-k_m^2}\right)}{2k_m^3k_p-2k_mk_p^3}. \tag{O.17}$$

Integral $T_2(\mu : \mu = k_n)$

Following the similar derivation as that of $T_1(\mu : \mu = k_n)$ we get

$$\mathrm{P}_{k_m}\int_0^{\lambda_1}\frac{(-1)^m\,\sin ax\,\left|\lambda_1^2-x^2\right|^{1/2}}{\left(x^2-k_m^2\right)\left(x^2-k_p^2\right)}\,\mathrm{d}x \approx \frac{\pi\lambda_1(-1)^m\mathrm{H}_1\left(a\lambda_1\right)}{2a\left(\lambda_1^2-k_m^2\right)\left(\lambda_1^2-k_p^2\right)}. \tag{O.18}$$

Integral $T_3(\mu : \mu = k_n)$

Next, consider the integral

$$\int_0^{\infty}\frac{\left[1-(-1)^m\,\mathrm{e}^{-ay}\right]\,\left|\lambda_1^2+y^2\right|^{1/2}}{\left(y^2+k_m^2\right)\left(y^2+k_p^2\right)}\,\mathrm{d}y.$$

For $\mu = k_n$, $\lambda_1^2 = k^2 - k_n^2$. The integral can be written as

$$\int_0^{\infty}\frac{\left[1-(-1)^m\,\mathrm{e}^{-ay}\right]\,\left|\lambda_1^2+y^2\right|^{1/2}}{\left(y^2+k_m^2\right)\left(y^2+k_p^2\right)}\,\mathrm{d}y = \underbrace{\int_0^{\infty}\frac{\sqrt{k^2-k_n^2+y^2}}{\left(k_m^2+y^2\right)\left(k_p^2+y^2\right)}\,\mathrm{d}y}_{T_3^1(k_n)} + \underbrace{\int_0^{\infty}\frac{(-1)^{m+1}\mathrm{e}^{-ay}\sqrt{k^2-k_n^2+y^2}}{\left(k_m^2+y^2\right)\left(k_p^2+y^2\right)}\,\mathrm{d}y}_{T_3^2(k_n)}. \tag{O.19}$$

And the integration domain can be divided into two parts: $\int_0^{\infty} = \int_0^{k} + \int_k^{\infty}$.

Integral $T_3^1(k_n)$

Since $y < k$ and $k_p > k$ for a Y edge mode, the following approximation holds (see

Appendix Q)

$$\int_0^k \frac{\sqrt{k^2 - k_n^2 + y^2}}{\left(k_m^2 + y^2\right)\left(k_p^2 + y^2\right)}\,\mathrm{d}y \approx \int_0^k \frac{\sqrt{k^2 - k_n^2 + y^2}}{\left(k_m^2 + y^2\right)k_p^2}\,\mathrm{d}y.$$

Integrating and simplifying we get

$$\int_0^k \frac{\sqrt{k^2 - k_n^2 + y^2}}{\left(k_m^2 + y^2\right)\left(k_p^2 + y^2\right)}\,\mathrm{d}y \approx \frac{A\,k_m + 2(\pi + B)\sqrt{k^2 - k_m^2 - k_n^2}}{4k_m k_p^2}, \tag{O.20}$$

where

$$A = 2\tanh^{-1}\left(\frac{4kk_m^2\left(\sqrt{2k^2 - k_n^2} + k\right)}{4k_m^2\left[k\left(\sqrt{2k^2 - k_n^2} + 2k\right) - k_n^2\right] + \left[k\left(2\sqrt{2k^2 - k_n^2} + 3k\right) - k_n^2\right]\left(k^2 - k_n^2\right)}\right)$$
$$+ \log\left(\frac{-4k_m^2\left[k_n^2 - k\left(2\sqrt{2k^2 - k_n^2} + 3k\right)\right] - 2k\left(2\sqrt{2k^2 - k_n^2} + 5k\right)k_n^2}{\left(k^2 - k_n^2\right)\left(k^2 + 4k_m^2 - k_n^2\right)}\right.$$
$$\left. + \frac{k^3\left(12\sqrt{2k^2 - k_n^2} + 17k\right) + k_n^4}{\left(k^2 - k_n^2\right)\left(k^2 + 4k_m^2 - k_n^2\right)}\right)$$

and

$$B = -\mathrm{i}\,\log\left(\frac{k^4 - 2\mathrm{i}kk_m\sqrt{\left(k_n^2 - 2k^2\right)\left(-k^2 + k_m^2 + k_n^2\right)} - 3k^2k_m^2 - k^2k_n^2 + k_m^2k_n^2}{\left(k^2 + k_m^2\right)\left(k^2 - k_n^2\right)}\right). \tag{O.21}$$

Now for the integration from k to ∞, $y >> k^2 - k_n^2$. Therefore, we may approximate $\sqrt{k^2 - k_n^2 + y^2} \approx y$. Hence (see Appendix Q),

$$\int_k^\infty \frac{\sqrt{k^2 - k_n^2 + y^2}}{\left(k_m^2 + y^2\right)\left(k_p^2 + y^2\right)}\,\mathrm{d}y \approx \int_k^\infty \frac{y}{\left(k_m^2 + y^2\right)\left(k_p^2 + y^2\right)}\,\mathrm{d}y.$$

Thus,

$$\int_k^\infty \frac{\sqrt{k^2 - k_n^2 + y^2}}{\left(k_m^2 + y^2\right)\left(k_p^2 + y^2\right)}\,\mathrm{d}y \approx \frac{\log\left(\frac{k^2 + k_p^2}{k^2 + k_m^2}\right)}{2\left(k_p^2 - k_m^2\right)}. \tag{O.22}$$

Therefore, using Eqs. (O.20) and (O.22) we obtain

$$\int_0^\infty \frac{\sqrt{k^2-k_n^2+y^2}}{\left(k_m^2+y^2\right)\left(k_p^2+y^2\right)}\,\mathrm{d}y \approx \frac{A\,k_m+2(\pi+B)\sqrt{k^2-k_m^2-k_n^2}}{4k_mk_p^2}+\frac{\log\left(\frac{k^2+k_p^2}{k^2+k_m^2}\right)}{2\left(k_p^2-k_m^2\right)}, \tag{O.23}$$

where A and B are given by Eqs. (O.2) and (O.21), respectively.

Integral $T_3^2(k_n)$

Using the first order approximation for the exponential function defined in Eq. (O.9) and assuming that $ak \geq \pi$ we get $\mathrm{e}^{-ay} \approx 0$, $\forall\, y \geq k$ (see Appendix Q). Therefore,

$$\int_k^\infty \frac{(-1)^{m+1}\mathrm{e}^{-ay}\sqrt{k^2-k_n^2+y^2}}{\left(k_m^2+y^2\right)\left(k_p^2+y^2\right)}\,\mathrm{d}y \approx 0.$$

The integration from 0 to k can be expressed as $\int_0^k=\int_0^{1/a}+\int_{1/a}^k$. When $y>1/a$, i.e., $ay>1$, It is assumed that $\mathrm{e}^{-ay}\approx 0$. Hence, one can neglect the integration from $1/a$ to k. Thus, by noting that $1/a<k$ and $k_p>k$ the integral can be approximated as

$$\int_0^\infty \frac{(-1)^{m+1}\mathrm{e}^{-ay}\sqrt{k^2-k_n^2+y^2}}{\left(k_m^2+y^2\right)\left(k_p^2+y^2\right)}\,\mathrm{d}y \approx \int_0^{1/a} \frac{(-1)^{m+1}(1-ay)\sqrt{k^2-k_n^2+y^2}}{\left(k_m^2+y^2\right)k_p^2}\,\mathrm{d}y.$$

Integrating we obtain

$$\int_0^\infty \frac{(-1)^{m+1}\mathrm{e}^{-ay}\sqrt{k^2-k_n^2+y^2}}{\left(k_m^2+y^2\right)\left(k_p^2+y^2\right)}\,\mathrm{d}y \approx \frac{(-1)^m\,C}{2k_mk_p^2}+\frac{(-1)^m\left(D-aE\sqrt{k^2-k_m^2-k_n^2}\right)}{2k_p^2}, \tag{O.24}$$

where

$$\begin{aligned}C = {} & k_m\log\left(\frac{k^2-k_n^2}{\left(\sqrt{\frac{1}{a^2}+k^2-k_n^2}+\frac{1}{a}\right)^2}\right)-2\pi\sqrt{k^2-k_m^2-k_n^2}\\ & +\mathrm{i}\sqrt{k^2-k_m^2-k_n^2}\,\log\left(\frac{2\mathrm{i}k_m\sqrt{\left(a^2k^2-a^2k_n^2+1\right)\left(k^2-k_m^2-k_n^2\right)}}{\left(k^2-k_n^2\right)\left(a^2k_m^2+1\right)}\right.\\ & \left.+\frac{k_m^2\left(a^2k^2-a^2k_n^2+2\right)-k^2+k_n^2}{\left(k^2-k_n^2\right)\left(a^2k_m^2+1\right)}\right),\end{aligned} \tag{O.25}$$

$$D = 2\left(\sqrt{a^2k^2 - a^2k_n^2 + 1} - a\sqrt{k^2 - k_n^2}\right) \tag{O.26}$$

and

$$E = 2\log\left(\frac{k_m}{\sqrt{\left(k^2 - k_n^2\right)\left(k^2 - k_m^2 - k_n^2\right)} + k^2 - k_n^2}\right)$$
$$+\log\left(\frac{\left(k^2 - k_n^2\right)\left[a^2\left(2k^2 - k_m^2 - 2k_n^2\right) + 2a\sqrt{\left(a^2k^2 - a^2k_n^2 + 1\right)\left(k^2 - k_m^2 - k_n^2\right)} + 1\right]}{a^2k_m^2 + 1}\right). \tag{O.27}$$

Thus, by combining Eqs. (O.23) and (O.24) we get

$$\int_0^\infty \frac{\left[1 - (-1)^m\,\mathrm{e}^{-ay}\right]\left|\lambda_1^2 + y^2\right|^{1/2}}{\left(y^2 + k_m^2\right)\left(y^2 + k_p^2\right)}\,\mathrm{d}y \approx \frac{A\,k_m + 2(\pi + B)\sqrt{k^2 - k_m^2 - k_n^2}}{4k_mk_p^2} + \frac{\log\left(\frac{k^2 + k_p^2}{k^2 + k_m^2}\right)}{2\left(k_p^2 - k_m^2\right)}$$
$$+ \frac{(-1)^m\,C}{2k_mk_p^2} + \frac{(-1)^m\left(D - aE\sqrt{k^2 - k_m^2 - k_n^2}\right)}{2k_p^2}, \tag{O.28}$$

where A, B, C, D and E are given by Eqs. (O.2), (O.21), (O.25), (O.26) and (O.27), respectively.

Integral I^{mnpq}

Now, we can find the closed form approximation for I^{mnpq} (Eq. (7.28)). Using Eqs. (7.25), (O.17), (O.18) and (O.28) we obtain

$$I^{mnpq} \approx \frac{\pi b}{2k_n^2}\,I_1^{mp}\left(k_n : k_n < \sqrt{k^2 - k_m^2}\right) = (A + B + C)\,\delta_{nq}, \tag{O.29}$$

where

$$A = -\frac{\pi b}{k_n^2}\left[\frac{\pi\lambda_1(-1)^m \mathrm{J}_1\left(a\lambda_1\right)}{2a\left(\lambda_1^2 - k_m^2\right)\left(\lambda_1^2 - k_p^2\right)} + \frac{\pi\left(k_m\sqrt{k_p^2 - \lambda_1^2} - \mathrm{i}k_p\sqrt{\lambda_1^2 - k_m^2}\right)}{2k_m^3k_p - 2k_mk_p^3}\right],$$
$$B = \frac{\mathrm{i}\pi^2 b\lambda_1(-1)^{m+1}\mathrm{H}_1\left(a\lambda_1\right)}{2ak_n^2\left(\lambda_1^2 - k_m^2\right)\left(\lambda_1^2 - k_p^2\right)}$$

and

$$C = -\frac{\mathrm{i}\pi b}{k_n^2}\left[\frac{C_1\, k_m + 2(\pi + C_2)\sqrt{k^2 - k_m^2 - k_n^2}}{4k_m k_p^2} + \frac{\log\left(\frac{k^2+k_p^2}{k^2+k_m^2}\right)}{2\left(k_p^2 - k_m^2\right)}\right.$$
$$\left. + \frac{(-1)^m\, C_3}{2k_m k_p^2} + \frac{(-1)^m\left(C_4 - aC_5\sqrt{k^2 - k_m^2 - k_n^2}\right)}{2k_p^2}\right]$$

with

$$C_1 = 2\tanh^{-1}\left(\frac{4kk_m^2\left(\sqrt{2k^2 - k_n^2} + k\right)}{4k_m^2\left[k\left(\sqrt{2k^2 - k_n^2} + 2k\right) - k_n^2\right] + \left[k\left(2\sqrt{2k^2 - k_n^2} + 3k\right) - k_n^2\right](k^2 - k_n^2)}\right)$$
$$+ \log\left(\frac{-4k_m^2\left[k_n^2 - k\left(2\sqrt{2k^2 - k_n^2} + 3k\right)\right] - 2k\left(2\sqrt{2k^2 - k_n^2} + 5k\right)k_n^2}{(k^2 - k_n^2)(k^2 + 4k_m^2 - k_n^2)}\right.$$
$$\left. + \frac{k^3\left(12\sqrt{2k^2 - k_n^2} + 17k\right) + k_n^4}{(k^2 - k_n^2)(k^2 + 4k_m^2 - k_n^2)}\right),$$

$$C_2 = -\mathrm{i}\,\log\left(\frac{k^4 - 2\mathrm{i}kk_m\sqrt{(k_n^2 - 2k^2)(-k^2 + k_m^2 + k_n^2)} - 3k^2k_m^2 - k^2k_n^2 + k_m^2k_n^2}{(k^2 + k_m^2)(k^2 - k_n^2)}\right),$$

$$C_3 = k_m \log\left(\frac{k^2 - k_n^2}{\left(\sqrt{\frac{1}{a^2} + k^2 - k_n^2} + \frac{1}{a}\right)^2}\right) - 2\pi\sqrt{k^2 - k_m^2 - k_n^2}$$
$$+ \mathrm{i}\sqrt{k^2 - k_m^2 - k_n^2}\,\log\left(\frac{2\mathrm{i}k_m\sqrt{(a^2k^2 - a^2k_n^2 + 1)(k^2 - k_m^2 - k_n^2)}}{(k^2 - k_n^2)(a^2k_m^2 + 1)}\right.$$
$$\left. + \frac{k_m^2(a^2k^2 - a^2k_n^2 + 2) - k^2 + k_n^2}{(k^2 - k_n^2)(a^2k_m^2 + 1)}\right),$$

$$C_4 = 2\left(\sqrt{a^2k^2 - a^2k_n^2 + 1} - a\sqrt{k^2 - k_n^2}\right)$$

and

$$C_5 = 2\log\left(\frac{k_m}{\sqrt{\left(k^2-k_n^2\right)\left(k^2-k_m^2-k_n^2\right)}+k^2-k_n^2}\right)$$
$$+\log\left(\frac{\left(k^2-k_n^2\right)\left[a^2\left(2k^2-k_m^2-2k_n^2\right)+2a\sqrt{\left(a^2k^2-a^2k_n^2+1\right)\left(k^2-k_m^2-k_n^2\right)}+1\right]}{a^2k_m^2+1}\right).$$

It is assumed that $I^{mnpq} \approx 0$ for all the cases when $n \neq q$.

O.3 Y edge - corner

In this case $k_m, k_p, k_q > k$ and $k_n < k$. The general expression for the integral I^{mnpq} is given by Eq. (7.16) as

$$I^{mnpq} = \underbrace{2\int_0^k \frac{[1-(-1)^n\cos\mu b]}{(\mu^2-k_n^2)\left(\mu^2-k_q^2\right)}\, I_1^{mp}(\mu : |\mu| < k)\,\mathrm{d}\mu}_{I_1^{mnpq}} + \underbrace{2\int_k^\infty \frac{[1-(-1)^n\cos\mu b]}{(\mu^2-k_n^2)\left(\mu^2-k_q^2\right)}\, I_1^{mp}(\mu : |\mu| > k)\,\mathrm{d}\mu}_{I_2^{mnpq}}, \quad \text{(O.30)}$$

where $I_1^{mp}(\mu : |\mu| < k)$ and $I_1^{mp}(\mu : |\mu| > k)$ represent the integral given in Eq. (7.6) evaluated when $|\mu| < k$ and $|\mu| > k$, respectively. The above integral is computed for two cases (collectively exhaustive): (a) $k_m \neq k_p$ and (b) $k_m = k_p$.

O.3.1 $k_m \neq k_p$

Integral I_1^{mnpq}

Consider the first term on the right hand side of the above equation

$$I_1^{mnpq} = 2\int_0^k \frac{[1-(-1)^n\cos\mu b]}{(\mu^2-k_n^2)\left(\mu^2-k_q^2\right)}\, I_1^{mp}(\mu : |\mu| < k)\,\mathrm{d}\mu, \quad \text{(O.31)}$$

where $I_1^{mp}(\mu : |\mu| < k)$ can be evaluated using Eq. (7.13),

$$I_1^{mp}(\mu : |\mu| < k) = 2\int_0^{\lambda_1} \frac{[1-(-1)^m\ \cos ax]\ \left|\lambda_1^2 - x^2\right|^{1/2}}{(x^2-k_m^2)\left(x^2-k_p^2\right)}\,\mathrm{d}x$$
$$- 2\,\mathrm{i}\left[\int_0^{\lambda_1} \frac{(-1)^m\ \sin ax\ \left|\lambda_1^2-x^2\right|^{1/2}}{(x^2-k_m^2)\left(x^2-k_p^2\right)}\,\mathrm{d}x + \int_0^\infty \frac{[1-(-1)^m\ \mathrm{e}^{-ay}]\ \left|\lambda_1^2+y^2\right|^{1/2}}{(y^2+k_m^2)\left(y^2+k_p^2\right)}\,\mathrm{d}y\right].$$

In the above equation, the contributions from the oscillatory $\cos ax$ and $\sin ax$ terms are neglected (see Appendix Q). Also, the contribution from the third integral on the right hand side is neglected due to the exponentially decaying function and the large values of k_m and k_p [34]. Therefore

$$I_1^{mp}(\mu : |\mu| < k) \approx 2 \int_0^{\lambda_1} \frac{\sqrt{\lambda_1^2 - x^2}}{(x^2 - k_m^2)\left(x^2 - k_p^2\right)} \, \mathrm{d}x.$$

Since $x < \lambda_1 \, (= \sqrt{k^2 - \mu^2})$ and $k_m, k_p > k$, the following approximation holds

$$I_1^{mp}(\mu : |\mu| < k) \approx 2 \int_0^{\lambda_1} \frac{\sqrt{\lambda_1^2 - x^2}}{k_m^2 k_p^2} \, \mathrm{d}x.$$

Thus we obtain

$$I_1^{mp}(\mu : |\mu| < k) \approx \frac{\pi \lambda_1^2}{2 k_m^2 k_p^2}. \tag{O.32}$$

Substituting this into Eq. (O.31) and approximating $\mu^2 - k_q^2 \approx -k_q^2$ (since $k_q > k$ and μ varies from 0 to k) we get

$$I_1^{mnpq} \approx -2 \int_0^{k} \frac{\pi \left(k^2 - \mu^2\right)}{2 k_m^2 k_p^2 k_q^2 \left(\mu^2 - k_n^2\right)} \, \mathrm{d}\mu.$$

In order to arrive at the above approximation, the contribution from the $\cos \mu b$ term is assumed to be negligible. Integrating we obtain

$$I_1^{mnpq} \approx \frac{\pi \left[k^2 \left(\log\left(\frac{k_n + k}{k - k_n}\right) - \mathrm{i}\pi\right) + 2 k k_n + k_n^2 \left(\log\left(\frac{k - k_n}{k_n + k}\right) + \mathrm{i}\pi\right)\right]}{2 k_m^2 k_n k_p^2 k_q^2}. \tag{O.33}$$

Integral I_2^{mnpq}

Now, consider the second term on the right hand side of the Eq. (O.30)

$$I_2^{mnpq} = 2 \int_k^{\infty} \frac{\left[1 - (-1)^n \cos \mu b\right]}{\left(\mu^2 - k_n^2\right)\left(\mu^2 - k_q^2\right)} \, I_1^{mp}(\mu : |\mu| > k) \, \mathrm{d}\mu, \tag{O.34}$$

where $I_1^{mp}(\mu : |\mu| > k)$ can be obtained using Eq. (7.15),

$$I_1^{mp}(\mu : |\mu| > k) = -2\,\mathrm{i} \int_{\lambda_1'}^{\infty} \frac{\left[1 - (-1)^m \, \mathrm{e}^{-ay}\right] \left|\lambda_1'^2 - y^2\right|^{1/2}}{\left(y^2 + k_m^2\right)\left(y^2 + k_p^2\right)} \, \mathrm{d}y.$$

Owing to the large values of k_m, k_p and μ (μ varies from k to ∞), the contribution from the integral $I_1^{mp}(\mu : |\mu| > k)$ is neglected. Hence,

$$I_2^{mnpq} \approx 0. \tag{O.35}$$

Integral I^{mnpq}

Using Eqs. (O.30), (O.33) and (O.35),

$$I^{mnpq} = I_1^{mnpq} + I_2^{mnpq} \approx \frac{\pi\left[k^2\left(\log\left(\frac{k_n+k}{k-k_n}\right) - \mathrm{i}\pi\right) + 2kk_n + k_n^2\left(\log\left(\frac{k-k_n}{k_n+k}\right) + \mathrm{i}\pi\right)\right]}{2k_m^2 k_n k_p^2 k_q^2}. \tag{O.36}$$

O.3.2 $k_m = k_p$

Integral $I_1^{mp}(\mu : |\mu| < k)$

The poles of the integrand in $I_1^{mp}(\mu)$ (Eq. (7.6)) are at $\lambda = \pm k_m$ and are of multiplicity two. The residues at the poles for $|\mu| < k$ (case 1) and $|\mu| > k$ (case 2) are evaluated in the Appendices M and N, respectively. For the case 1, they are

$$\mathrm{Res}(-k_m) = \mathrm{Res}(k_m) = \frac{a\,\left|\lambda_1^2 - k_m^2\right|^{1/2}}{4\,k_m^2},$$

where $\lambda_1 = \left(k^2 - \mu^2\right)^{1/2}$. Thus, for case 1, the contour integration around the branch cut as shown in Fig. 7.9 (note that for this case $k_m = k_p$ in the figure) results in

$$\mathrm{P}\left[I_1^{mp}(\mu)\right] = I_1^{mp}(\mu : |\mu| < k) = \pi\mathrm{i}\left[\mathrm{Res}(k_m) + \mathrm{Res}(-k_m)\right] - (\Gamma_1 + \Gamma_2 + \Gamma_3 + \Gamma_4).$$

Substituting for the residues and the Γ_i's from Eq. (7.11) we obtain

$$\begin{aligned} I_1^{mp}(\mu : |\mu| < k) = 2\int_0^{\lambda_1} & \frac{\left[1 - (-1)^m\,\cos ax\right]\,\left|\lambda_1^2 - x^2\right|^{1/2}}{\left(x^2 - k_m^2\right)^2}\,\mathrm{d}x \\ & - 2\,\mathrm{i}\left[\frac{-\pi a\,\left|\lambda_1^2 - k_m^2\right|^{1/2}}{4\,k_m^2} + \int_0^{\lambda_1}\frac{(-1)^m\,\sin ax\,\left|\lambda_1^2 - x^2\right|^{1/2}}{\left(x^2 - k_m^2\right)^2}\,\mathrm{d}x \right. \\ & \left. + \int_0^{\infty}\frac{\left[1 - (-1)^m\,\mathrm{e}^{-ay}\right]\,\left|\lambda_1^2 + y^2\right|^{1/2}}{\left(y^2 + k_m^2\right)^2}\,\mathrm{d}y\right]. \end{aligned} \tag{O.37}$$

Integral I_1^{mnpq}

Let us now consider the first term on the right hand side of Eq. (O.30),

$$I_1^{mnpq} = 2\int\limits_0^k \frac{[1-(-1)^n \cos\mu b]}{(\mu^2 - k_n^2)\left(\mu^2 - k_q^2\right)} I_1^{mp}(\mu : |\mu| < k)\,\mathrm{d}\mu, \tag{O.38}$$

where $I_1^{mp}(\mu : |\mu| < k)$ is given by Eq. (O.37) above. The contributions from the terms of $I_1^{mp}(\mu : |\mu| < k)$, except the residue term, can be obtained by substituting $k_m = k_p$ in Eq. (O.33). Thus,

$$I_{1\,\mathrm{NR}}^{mnpq} \approx \frac{\pi\left[k^2\left(\log\left(\frac{k_n+k}{k-k_n}\right) - \mathrm{i}\pi\right) + 2kk_n + k_n^2\left(\log\left(\frac{k-k_n}{k_n+k}\right) + \mathrm{i}\pi\right)\right]}{2k_m^4 k_n k_q^2}. \tag{O.39}$$

Now, the contribution from the residue term can be evaluated from

$$I_{1\,\mathrm{R}}^{mnpq} = 2\int\limits_0^k \frac{[1-(-1)^n \cos\mu b]}{(\mu^2 - k_n^2)\left(\mu^2 - k_q^2\right)} \frac{i\pi a\sqrt{k_m^2 - \lambda_1^2}}{2k_m^2}\,\mathrm{d}\mu.$$

Knowing that $\lambda_1^2 = k^2 - \mu^2$ and approximating $\mu^2 - k_q^2 \approx -k_q^2$ (since $k_q > k$ and μ varies from 0 to k) and $\sqrt{k_m^2 + \mu^2 - k^2} \approx k_m$ (since $k_m > k$ and μ varies from 0 to k) we get

$$I_{1\,\mathrm{R}}^{mnpq} \approx \int\limits_0^k \frac{i\pi a}{k_m k_q^2\left(\mu^2 - k_n^2\right)}\,\mathrm{d}\mu.$$

As the contribution from the $\cos\mu b$ oscillatory term is negligible, it is neglected while arriving at the above approximation. Integrating the above equation we obtain

$$I_{1\,\mathrm{R}}^{mnpq} \approx \frac{\pi a\left(\pi + 2\mathrm{i}\tanh^{-1}\left(\frac{k_n}{k}\right)\right)}{2k_m k_n k_q^2}. \tag{O.40}$$

Therefore, using Eqs. (O.38)-(O.40),

$$\begin{aligned} I_1^{mnpq} \approx{}& \frac{\pi a\left(\pi + 2\mathrm{i}\tanh^{-1}\left(\frac{k_n}{k}\right)\right)}{2k_m k_n k_q^2} \\ &+ \frac{\pi\left[k^2\left(\log\left(\frac{k_n+k}{k-k_n}\right) - \mathrm{i}\pi\right) + 2kk_n + k_n^2\left(\log\left(\frac{k-k_n}{k_n+k}\right) + \mathrm{i}\pi\right)\right]}{2k_m^4 k_n k_q^2}. \end{aligned} \tag{O.41}$$

Integral $I_1^{mp}(\mu : |\mu| > k)$

Now, for the case 2 ($|\mu| > k$), the residues at the poles are (see Appendix N)

$$\mathrm{Res}(-k_m) = \mathrm{Res}(k_m) = \frac{a\,\left|\lambda_1^2 - k_m^2\right|^{1/2}}{4\,k_m^2},$$

where $\lambda_1 = \mathrm{i}\lambda_1' = \mathrm{i}\,(\mu^2 - k^2)^{1/2}$. Thus, the contour integration around the branch cut as shown in Fig. 7.10 (note that for this case $k_m = k_p$ in the figure) results in

$$\mathrm{P}\left[I_1^{mp}(\mu)\right] = I_1^{mp}(\mu : |\mu| > k) = \pi\mathrm{i}\left[\mathrm{Res}(k_m) + \mathrm{Res}(-k_m)\right] - (\Gamma_1 + \Gamma_2).$$

Substituting for the residues and the Γ_i's from Eq. (7.14) we obtain

$$I_1^{mp}(\mu : |\mu| > k) = -2\,\mathrm{i}\left[\frac{-\pi a\,\left|\lambda_1^2 - k_m^2\right|^{1/2}}{4\,k_m^2} + \int_{\lambda_1'}^{\infty} \frac{\left[1 - (-1)^m\ \mathrm{e}^{-ay}\right]\left|\lambda_1'^2 - y^2\right|^{1/2}}{(y^2 + k_m^2)^2}\,\mathrm{d}y\right]. \tag{O.42}$$

Integral I_2^{mnpq}

Consider the second term on the right hand side of the Eq. (O.30)

$$I_2^{mnpq} = 2\int_{k}^{\infty} \frac{\left[1 - (-1)^n \cos\mu b\right]}{(\mu^2 - k_n^2)\left(\mu^2 - k_q^2\right)}\, I_1^{mp}(\mu : |\mu| > k)\,\mathrm{d}\mu, \tag{O.43}$$

where $I_1^{mp}(\mu : |\mu| > k)$ is given by Eq. (O.42). But, the contribution from the integral $I_1^{mp}(\mu : |\mu| > k)$ is negligible owing to the large value of k_m and μ (μ varies from k to ∞). Hence,

$$I_2^{mnpq} \approx 0. \tag{O.44}$$

Integral I^{mnpq}

Using Eqs. (O.30), (O.41) and (O.44),

$$\begin{aligned} I^{mnpq} = I_1^{mnpq} + I_2^{mnpq} &\approx \frac{\pi a\left(\pi + 2\mathrm{i}\tanh^{-1}\left(\frac{k_n}{k}\right)\right)}{2k_m k_n k_q^2} \\ &+ \frac{\pi\left[k^2\left(\log\left(\frac{k_n+k}{k-k_n}\right) - \mathrm{i}\pi\right) + 2kk_n + k_n^2\left(\log\left(\frac{k-k_n}{k_n+k}\right) + \mathrm{i}\pi\right)\right]}{2k_m^4 k_n k_q^2}. \end{aligned} \tag{O.45}$$

Summarizing, for the Y edge - corner mode interaction

$$I^{mnpq} \approx A\,\delta_{mp} + B, \tag{O.46}$$

where

$$A = \frac{\pi a \left(\pi + 2\mathrm{i}\tanh^{-1}\left(\frac{k_n}{k}\right)\right)}{2k_m k_n k_q^2}$$

and

$$B = \frac{\pi\left[k^2\left(\log\left(\frac{k_n+k}{k-k_n}\right) - i\pi\right) + 2kk_n + k_n^2\left(\log\left(\frac{k-k_n}{k_n+k}\right) + i\pi\right)\right]}{2k_m^2 k_n k_p^2 k_q^2}.$$

O.4 Acoustically fast - acoustically fast (AF - AF)

In this case, $k_m, k_n, k_p, k_q < k$, $k_m^2 + k_n^2 < k^2$ and $k_p^2 + k_q^2 < k^2$. For the case $k_n = k_q$ (and $k_m < k_p$), I^{mnpq} is given by Eq. (7.43).

$$I^{mnpq} = \frac{\pi b}{2k_n^2}\, I_1^{mp}\left(k_n : k_n < \sqrt{k^2 - k_p^2}\right),$$

where $I_1^{mp}\left(k_n : k_n < \sqrt{k^2 - k_p^2}\right)$ can be obtained from Eq. (7.40)

$$I_1^{mp}\left(\mu : |\mu| < \sqrt{k^2 - k_p^2}\right) = 2\,\mathrm{P}_{k_m,k_p}\int_0^{\lambda_1} \frac{\left[1 - (-1)^m\, \cos ax\right]\, \left|\lambda_1^2 - x^2\right|^{1/2}}{\left(x^2 - k_m^2\right)\,\left(x^2 - k_p^2\right)}\,\mathrm{d}x$$
$$- 2\,\mathrm{i}\left[\mathrm{P}_{k_m,k_p}\int_0^{\lambda_1} \frac{(-1)^m\, \sin ax\, \left|\lambda_1^2 - x^2\right|^{1/2}}{\left(x^2 - k_m^2\right)\,\left(x^2 - k_p^2\right)}\,\mathrm{d}x + \int_0^{\infty} \frac{\left[1 - (-1)^m\, \mathrm{e}^{-ay}\right]\, \left|\lambda_1^2 + y^2\right|^{1/2}}{\left(y^2 + k_m^2\right)\,\left(y^2 + k_p^2\right)}\,\mathrm{d}y\right]$$

by substituting $\mu = k_n$.

In the above equation, the contributions from the oscillatory $\cos ax$ and $\sin ax$ terms are neglected. Hence,

$$I_1^{mp}\left(k_n : k_n < \sqrt{k^2 - k_p^2}\right) \approx 2\,\underbrace{\mathrm{P}_{k_m,k_p}\int_0^{\lambda_1} \frac{\left|\lambda_1^2 - x^2\right|^{1/2}}{\left(x^2 - k_m^2\right)\,\left(x^2 - k_p^2\right)}\,\mathrm{d}x}_{T_1(k_n)}$$
$$- 2\,\mathrm{i}\,\underbrace{\int_0^{\infty} \frac{\left[1 - (-1)^m\, \mathrm{e}^{-ay}\right]\, \left|\lambda_1^2 + y^2\right|^{1/2}}{\left(y^2 + k_m^2\right)\,\left(y^2 + k_p^2\right)}\,\mathrm{d}y}_{T_2(k_n)}, \quad \text{(O.47)}$$

where $\lambda_1^2 = k^2 - k_n^2$.

Integral $T_1(k_n)$

We can find that

$$\mathrm{P}_{k_m,k_p}\int_0^{\lambda_1} \frac{\left|\lambda_1^2 - x^2\right|^{1/2}}{\left(x^2 - k_m^2\right)\,\left(x^2 - k_p^2\right)}\,\mathrm{d}x = \frac{\mathrm{i}\pi\left(k_p\sqrt{\lambda_1^2 - k_m^2} - k_m\sqrt{\lambda_1^2 - k_p^2}\right)}{2k_m^3 k_p - 2k_m k_p^3}. \quad \text{(O.48)}$$

Integral $T_2(k_n)$

The integral can be written as

$$\int_0^\infty \frac{\left[1-(-1)^m \,\mathrm{e}^{-ay}\right] \left|\lambda_1^2+y^2\right|^{1/2}}{\left(y^2+k_m^2\right)\left(y^2+k_p^2\right)}\,\mathrm{d}y = \underbrace{\int_0^\infty \frac{\sqrt{\lambda_1^2+y^2}}{\left(k_m^2+y^2\right)\left(k_p^2+y^2\right)}\,\mathrm{d}y}_{T_2^1(k_n)} + \underbrace{\int_0^\infty \frac{(-1)^{m+1}\mathrm{e}^{-ay}\sqrt{\lambda_1^2+y^2}}{\left(k_m^2+y^2\right)\left(k_p^2+y^2\right)}\,\mathrm{d}y}_{T_2^2(k_n)}\,. \quad \text{(O.49)}$$

Integral $T_2^1(k_n)$

We can use the approximation

$$\int_0^\infty \frac{\sqrt{\lambda_1^2+y^2}}{\left(k_m^2+y^2\right)\left(k_p^2+y^2\right)}\,\mathrm{d}y \approx \int_0^{\lambda_1} \frac{\lambda_1}{\left(k_m^2+y^2\right)\left(k_p^2+y^2\right)}\,\mathrm{d}y + \int_{\lambda_1}^\infty \frac{y}{\left(k_m^2+y^2\right)\left(k_p^2+y^2\right)}\,\mathrm{d}y.$$

Integrating, we get

$$\int_0^\infty \frac{\sqrt{\lambda_1^2+y^2}}{\left(k_m^2+y^2\right)\left(k_p^2+y^2\right)}\,\mathrm{d}y \approx \frac{\lambda_1\left(k_m \tan^{-1}\left(\frac{\lambda_1}{k_p}\right) - k_p \tan^{-1}\left(\frac{\lambda_1}{k_m}\right)\right)}{k_m^3 k_p - k_m k_p^3} + \frac{\log\left(\frac{k_m^2+\lambda_1^2}{k_p^2+\lambda_1^2}\right)}{2k_m^2-2k_p^2}. \quad \text{(O.50)}$$

Integral $T_2^2(k_n)$

Using the first order approximation for the exponential function defined in Eq. (O.9) and assuming that $ak \geq \pi$ we get $\mathrm{e}^{-ay} \approx 0,\ \forall\, y \geq k$. Therefore,

$$\int_k^\infty \frac{(-1)^{m+1}\mathrm{e}^{-ay}\sqrt{\lambda_1^2+y^2}}{\left(k_m^2+y^2\right)\left(k_p^2+y^2\right)}\,\mathrm{d}y \approx 0.$$

Thus, we can approximate

$$\int_0^{\infty} \frac{(-1)^{m+1}\mathrm{e}^{-ay}\sqrt{\lambda_1^2+y^2}}{\left(k_m^2+y^2\right)\left(k_p^2+y^2\right)}\,\mathrm{d}y \approx \int_0^{\lambda_1} \frac{(-1)^{m+1}\left(1-ay\right)\lambda_1}{\left(k_m^2+y^2\right)\left(k_p^2+y^2\right)}\,\mathrm{d}y + \int_{\lambda_1}^{k} \frac{(-1)^{m+1}\left(1-ay\right)y}{\left(k_m^2+y^2\right)\left(k_p^2+y^2\right)}\,\mathrm{d}y.$$

We can find that

$$\int_0^{\lambda_1} \frac{(-1)^{m+1}\left(1-ay\right)\lambda_1}{\left(k_m^2+y^2\right)\left(k_p^2+y^2\right)}\,\mathrm{d}y = \frac{\lambda_1(-1)^m k_m\left(ak_p\log\left(\frac{k_m^2\left(k_p^2+\lambda_1^2\right)}{k_p^2\left(k_m^2+\lambda_1^2\right)}\right)-2\tan^{-1}\left(\frac{\lambda_1}{k_p}\right)\right)}{2k_mk_p\left(k_m^2-k_p^2\right)} + \frac{2\lambda_1(-1)^m k_p\tan^{-1}\left(\frac{\lambda_1}{k_m}\right)}{2k_mk_p\left(k_m^2-k_p^2\right)} \tag{O.51}$$

and

$$\int_{\lambda_1}^{k} \frac{(-1)^{m+1}\left(1-ay\right)y}{\left(k_m^2+y^2\right)\left(k_p^2+y^2\right)}\,\mathrm{d}y = \frac{(-1)^m}{2\left(k_m^2-k_p^2\right)}\left[2ak_m\left(\tan^{-1}\left(\frac{k}{k_m}\right)-\tan^{-1}\left(\frac{\lambda_1}{k_m}\right)\right) +2ak_p\left(\tan^{-1}\left(\frac{\lambda_1}{k_p}\right)-\tan^{-1}\left(\frac{k}{k_p}\right)\right)+\log\left(\frac{\left(k^2+k_m^2\right)\left(k_p^2+\lambda_1^2\right)}{\left(k^2+k_p^2\right)\left(k_m^2+\lambda_1^2\right)}\right)\right]. \tag{O.52}$$

Integral I^{mnpq}

Now we can find the closed form approximation for I^{mnpq} (Eq. (7.43)). Using Eqs. (O.47)-(O.52) we get

$$I^{mnpq} \approx \left(A+B+C+D\right)\delta_{nq}, \tag{O.53}$$

where

$$A = \frac{\mathrm{i}\pi^2 b\left(k_p\sqrt{\lambda_1^2-k_m^2}-k_m\sqrt{\lambda_1^2-k_p^2}\right)}{2k_n^2\left(k_m^3k_p-k_mk_p^3\right)},$$

$$B = -\frac{\mathrm{i}\pi b}{k_n^2}\left[\frac{\log\left(\frac{k_m^2+\lambda_1^2}{k_p^2+\lambda_1^2}\right)}{2k_m^2-2k_p^2}+\frac{\lambda_1\left(k_m\tan^{-1}\left(\frac{\lambda_1}{k_p}\right)-k_p\tan^{-1}\left(\frac{\lambda_1}{k_m}\right)\right)}{k_m^3k_p-k_mk_p^3}\right],$$

$$C = \frac{\mathrm{i}\pi b\lambda_1(-1)^{m+1}}{2k_m k_n^2 k_p\left(k_m^2 - k_p^2\right)}\left[k_m\left(ak_p\log\left(\frac{k_m^2\left(k_p^2+\lambda_1^2\right)}{k_p^2\left(k_m^2+\lambda_1^2\right)}\right) - 2\tan^{-1}\left(\frac{\lambda_1}{k_p}\right)\right)\right.$$
$$\left. + 2k_p\tan^{-1}\left(\frac{\lambda_1}{k_m}\right)\right]$$

and

$$D = \frac{\mathrm{i}\pi b(-1)^{m+1}}{2k_n^2\left(k_m^2-k_p^2\right)}\left[2ak_m\left(\tan^{-1}\left(\frac{k}{k_m}\right) - \tan^{-1}\left(\frac{\lambda_1}{k_m}\right)\right)\right.$$
$$\left. + 2ak_p\left(\tan^{-1}\left(\frac{\lambda_1}{k_p}\right) - \tan^{-1}\left(\frac{k}{k_p}\right)\right) + \log\left(\frac{\left(k^2+k_m^2\right)\left(k_p^2+\lambda_1^2\right)}{\left(k^2+k_p^2\right)\left(k_m^2+\lambda_1^2\right)}\right)\right].$$

O.5 XY edge - XY edge

In this case, $k_m, k_n, k_p, k_q < k$, $k_m^2 + k_n^2 > k^2$ and $k_p^2 + k_q^2 > k^2$. The coupling coefficient for the case $k_n = k_q$ and $k_m \neq k_p$ is given by Eq. (7.50).

$$I^{mnpq} = \frac{\pi b}{2k_n^2} I_1^{mp}(k_n : k_n < k),$$

where $I_1^{mp}(k_n : k_n < k)$ can be obtained from Eq. (7.48)

$$I_1^{mp}(\mu : |\mu| < k) = 2 \underbrace{\int_0^{\lambda_1} \frac{[1 - (-1)^m \cos ax] \, |\lambda_1^2 - x^2|^{1/2}}{(x^2 - k_m^2)(x^2 - k_p^2)} \, \mathrm{d}x}_{T_1(\mu)}$$

$$- 2\,\mathrm{i} \left[\underbrace{\int_0^{\lambda_1} \frac{(-1)^m \sin ax \, |\lambda_1^2 - x^2|^{1/2}}{(x^2 - k_m^2)(x^2 - k_p^2)} \, \mathrm{d}x}_{T_2(\mu)} + \underbrace{\int_0^{\infty} \frac{[1 - (-1)^m \, \mathrm{e}^{-ay}] \, |\lambda_1^2 + y^2|^{1/2}}{(y^2 + k_m^2)(y^2 + k_p^2)} \, \mathrm{d}y}_{T_3(\mu)} \right],$$

by substituting $\mu = k_n$. Here, a similar procedure as detailed in O.1 is followed.

Integral $T_1(\mu : \mu = k_n)$

Consider the first integral on the right hand side of the above equation

$$\int_0^{\lambda_1} \frac{[1 - (-1)^m \cos ax] \, |\lambda_1^2 - x^2|^{1/2}}{(x^2 - k_m^2)(x^2 - k_p^2)} \, \mathrm{d}x = \int_0^{\lambda_1} \frac{(-1)^{m+1} \sqrt{\lambda_1^2 - x^2} \cos ax}{(x^2 - k_m^2)(x^2 - k_p^2)} \, \mathrm{d}x + \int_0^{\lambda_1} \frac{\sqrt{\lambda_1^2 - x^2}}{(x^2 - k_m^2)(x^2 - k_p^2)} \, \mathrm{d}x. \quad \text{(O.54)}$$

Since $k_m, k_p > \lambda_1 (= \sqrt{k^2 - k_n^2})$, the following approximation [34] is used in the first integral on the right hand side

$$(x^2 - k_m^2)(x^2 - k_p^2) \approx k_m^2 k_p^2. \quad \text{(O.55)}$$

Thus,

$$\int_0^{\lambda_1} \frac{(-1)^{m+1}\sqrt{\lambda_1^2 - x^2}\cos ax}{\left(x^2 - k_m^2\right)\left(x^2 - k_p^2\right)}\,\mathrm{d}x \approx -\frac{\pi\lambda_1(-1)^m \mathrm{J}_1\left(a\lambda_1\right)}{2ak_m^2k_p^2},$$

where $\mathrm{J}_1(*)$ represents Bessel function of the first kind and first order. The second integral on the right hand side of Eq. (O.54) yields (without any approximations)

$$\int_0^{\lambda_1} \frac{\sqrt{\lambda_1^2 - x^2}}{\left(x^2 - k_m^2\right)\left(x^2 - k_p^2\right)}\,\mathrm{d}x = \frac{\pi\left(k_p\sqrt{k_m^2 - \lambda_1^2} - k_m\sqrt{k_p^2 - \lambda_1^2}\right)}{2k_m^3k_p - 2k_mk_p^3}.$$

Therefore

$$\int_0^{\lambda_1} \frac{\left[1 - (-1)^m\ \cos ax\right]\left|\lambda_1^2 - x^2\right|^{1/2}}{\left(x^2 - k_m^2\right)\left(x^2 - k_p^2\right)}\,\mathrm{d}x \approx -\frac{\pi\lambda_1(-1)^m \mathrm{J}_1\left(a\lambda_1\right)}{2ak_m^2k_p^2} + \frac{\pi\left(k_p\sqrt{k_m^2 - \lambda_1^2} - k_m\sqrt{k_p^2 - \lambda_1^2}\right)}{2k_m^3k_p - 2k_mk_p^3}. \quad \text{(O.56)}$$

Integral $T_2(\mu : \mu = k_n)$

Now, consider the second integral on the right hand side of Eq. (7.48). Using the approximation Eq. (O.55) we get

$$\int_0^{\lambda_1} \frac{(-1)^m\ \sin ax\ \left|\lambda_1^2 - x^2\right|^{1/2}}{\left(x^2 - k_m^2\right)\left(x^2 - k_p^2\right)}\,\mathrm{d}x \approx \frac{\pi\lambda_1(-1)^m \mathrm{H}_1\left(a\lambda_1\right)}{2ak_m^2k_p^2}, \quad \text{(O.57)}$$

where $\mathrm{H}_1(*)$ is the Struve function of first order.

Integral $T_3(\mu : \mu = k_n)$

For $\mu = k_n$ and $\lambda_1^2 = k^2 - k_n^2$, the third integral on the right hand side of Eq. (7.48) can be written as

$$\int_0^\infty \frac{\left[1-(-1)^m\ \mathrm{e}^{-ay}\right]\left|\lambda_1^2+y^2\right|^{1/2}}{\left(y^2+k_m^2\right)\left(y^2+k_p^2\right)}\,\mathrm{d}y = \underbrace{\int_0^\infty \frac{\sqrt{k^2-k_n^2+y^2}}{\left(k_m^2+y^2\right)\left(k_p^2+y^2\right)}\,\mathrm{d}y}_{T_3^1(k_n)} + \underbrace{\int_0^\infty \frac{(-1)^{m+1}\mathrm{e}^{-ay}\sqrt{k^2-k_n^2+y^2}}{\left(k_m^2+y^2\right)\left(k_p^2+y^2\right)}\,\mathrm{d}y}_{T_3^2(k_n)}\,. \quad \text{(O.58)}$$

Here, the integration domain can be divided into two parts: $\int_0^\infty = \int_0^k + \int_k^\infty$.

Integral $T_3^1(k_n)$

Consider the integration from 0 to k of $T_3^1(k_n)$. Since $y < k$ and $k_m, k_p \approx k$ for the two-edge modes, the following approximation holds

$$\int_0^k \frac{\sqrt{k^2-k_n^2+y^2}}{\left(k_m^2+y^2\right)\left(k_p^2+y^2\right)}\,\mathrm{d}y \approx \int_0^k \frac{\sqrt{k^2-k_n^2+y^2}}{k_m^2 k_p^2}\,\mathrm{d}y.$$

Integrating and simplifying we get

$$\int_0^k \frac{\sqrt{k^2-k_n^2+y^2}}{\left(k_m^2+y^2\right)\left(k_p^2+y^2\right)}\,\mathrm{d}y \approx \frac{2k\sqrt{2k^2-k_n^2}+\left(k^2-k_n^2\right)\log\left(\frac{\left(\sqrt{2k^2-k_n^2}+k\right)^2}{k^2-k_n^2}\right)}{4k_m^2 k_p^2}. \quad \text{(O.59)}$$

Now for the integration from k to ∞, $y \gg k^2 - k_n^2$. Therefore, we can approximate $\sqrt{k^2-k_n^2+y^2} \approx y$. Hence,

$$\int_k^\infty \frac{\sqrt{k^2-k_n^2+y^2}}{\left(k_m^2+y^2\right)\left(k_p^2+y^2\right)}\,\mathrm{d}y \approx \int_k^\infty \frac{y}{\left(k_m^2+y^2\right)\left(k_p^2+y^2\right)}\,\mathrm{d}y.$$

Thus,

$$\int_k^\infty \frac{\sqrt{k^2-k_n^2+y^2}}{\left(k_m^2+y^2\right)\left(k_p^2+y^2\right)}\,\mathrm{d}y \approx \frac{\log\left(\frac{k^2+k_p^2}{k^2+k_m^2}\right)}{2\left(k_p^2-k_m^2\right)}. \quad \text{(O.60)}$$

Therefore using Eqs. (O.59) and (O.60) we obtain

$$\int_0^\infty \frac{\sqrt{k^2-k_n^2+y^2}}{\left(k_m^2+y^2\right)\left(k_p^2+y^2\right)}\,\mathrm{d}y \approx \frac{\log\left(\frac{k^2+k_p^2}{k^2+k_m^2}\right)}{2\left(k_p^2-k_m^2\right)} + \frac{2k\sqrt{2k^2-k_n^2}+\left(k^2-k_n^2\right)\log\left(\frac{\left(\sqrt{2k^2-k_n^2}+k\right)^2}{k^2-k_n^2}\right)}{4k_m^2k_p^2}. \tag{O.61}$$

Integral $\boldsymbol{T_3^2(k_n)}$

Consider the first order approximation for the exponential function (Eq. (O.9))

$$\mathrm{e}^{-ay} \approx \begin{cases} 1-ay & \text{when } ay<1 \\ 0 & \text{when } ay\geq 1. \end{cases}$$

If $ak\geq\pi$, $\mathrm{e}^{-ay}\approx 0$, $\forall\, y\geq k$. Therefore

$$\int_k^\infty \frac{(-1)^{m+1}\mathrm{e}^{-ay}\sqrt{k^2-k_n^2+y^2}}{\left(k_m^2+y^2\right)\left(k_p^2+y^2\right)}\,\mathrm{d}y \approx 0.$$

The integration from 0 to k can be expressed as $\int_0^k = \int_0^{1/a} + \int_{1/a}^k$. When $y>1/a$, i.e., $ay>1$, we have the approximation $\mathrm{e}^{-ay}\approx 0$. Hence, one can neglect the integration from $1/a$ to k. Thus, by noting that $1/a<k$ and $k_m, k_p\approx k$ the integral can be approximated as

$$\int_0^\infty \frac{(-1)^{m+1}\mathrm{e}^{-ay}\sqrt{k^2-k_n^2+y^2}}{\left(k_m^2+y^2\right)\left(k_p^2+y^2\right)}\,\mathrm{d}y \approx \int_0^{1/a} \frac{(-1)^{m+1}(1-ay)\sqrt{k^2-k_n^2+y^2}}{k_m^2k_p^2}\,\mathrm{d}y.$$

Integrating we obtain

$$\int_0^\infty \frac{(-1)^{m+1}\mathrm{e}^{-ay}\sqrt{k^2-k_n^2+y^2}}{\left(k_m^2+y^2\right)\left(k_p^2+y^2\right)}\,\mathrm{d}y \approx \frac{(-1)^{m+1}}{12ak_m^2k_p^2}\left\{2\sqrt{\frac{1}{a^2}+k^2-k_n^2}-\left(k^2-k_n^2\right)\right. \times\left.\left[-4a^2\sqrt{k^2-k_n^2}+4a^2\sqrt{\frac{1}{a^2}+k^2-k_n^2}-3a\log\left(\frac{\left(\sqrt{\frac{1}{a^2}+k^2-k_n^2}+\frac{1}{a}\right)^2}{k^2-k_n^2}\right)\right]\right\}. \tag{O.62}$$

Thus, combining Eqs. (O.61) and (O.62) we get

$$\int_0^\infty \frac{\left[1-(-1)^m \,\mathrm{e}^{-ay}\right]\,\left|\lambda_1^2+y^2\right|^{1/2}}{\left(y^2+k_m^2\right)\,\left(y^2+k_p^2\right)}\,\mathrm{d}y \approx \frac{\log\left(\frac{k^2+k_p^2}{k^2+k_m^2}\right)}{2\left(k_p^2-k_m^2\right)} + \frac{2k\sqrt{2k^2-k_n^2}}{4k_m^2k_p^2}$$
$$+\frac{(k^2-k_n^2)\,\log\left(\frac{\left(\sqrt{2k^2-k_n^2}+k\right)^2}{k^2-k_n^2}\right)}{4k_m^2k_p^2} + \frac{(-1)^{m+1}}{12ak_m^2k_p^2}\left\{2\sqrt{\frac{1}{a^2}+k^2-k_n^2}-\left(k^2-k_n^2\right)\right.$$
$$\left.\times\left[-4a^2\sqrt{k^2-k_n^2}+4a^2\sqrt{\frac{1}{a^2}+k^2-k_n^2}-3a\log\left(\frac{\left(\sqrt{\frac{1}{a^2}+k^2-k_n^2}+\frac{1}{a}\right)^2}{k^2-k_n^2}\right)\right]\right\}. \tag{O.63}$$

Integral I^{mnpq}

We can now evaluate I^{mnpq} from Eq. (7.50). Using Eqs. (7.48), (O.56), (O.57) and (O.63) we obtain

$$I^{mnpq} \approx \frac{\pi b}{2k_n^2}\, I_1^{mp}(k_n : k_n < k) = I_R^{mnpq} + \mathrm{i}\, I_\chi^{mnpq}, \tag{O.64}$$

where the real part of I^{mnpq} is given by

$$I_R^{mnpq} = \frac{\pi^2 b}{2k_n^2}\left[\frac{k_p\sqrt{k_m^2-\lambda_1^2}-k_m\sqrt{k_p^2-\lambda_1^2}}{k_m^3k_p-k_mk_p^3} - \frac{\lambda_1(-1)^m \mathrm{J}_1\left(a\lambda_1\right)}{ak_m^2k_p^2}\right]\delta_{nq}$$

and the imaginary part of I^{mnpq} is given by

$$I_\chi^{mnpq} = -\frac{\pi b}{k_n^2}(A+B+C)\,\delta_{nq}$$

with

$$A = \frac{\pi\lambda_1(-1)^m \mathrm{H}_1\left(a\lambda_1\right)}{2ak_m^2k_p^2},$$

$$B = \frac{2k\sqrt{2k^2-k_n^2}+(k^2-k_n^2)\log\left(\frac{\left(\sqrt{2k^2-k_n^2}+k\right)^2}{k^2-k_n^2}\right)}{4k_m^2k_p^2} + \frac{\log\left(\frac{k^2+k_p^2}{k^2+k_m^2}\right)}{2\left(k_p^2-k_m^2\right)}$$

and

$$C = \frac{(-1)^{m+1}}{12ak_m^2k_p^2}\left\{2\sqrt{\frac{1}{a^2}+k^2-k_n^2}-\left(k^2-k_n^2\right)\right.$$
$$\left.\times\left[-4a^2\sqrt{k^2-k_n^2}+4a^2\sqrt{\frac{1}{a^2}+k^2-k_n^2}-3a\log\left(\frac{\left(\sqrt{\frac{1}{a^2}+k^2-k_n^2}+\frac{1}{a}\right)^2}{k^2-k_n^2}\right)\right]\right\}.$$

O.6 Corner - corner

In this case $k_m, k_n, k_p, k_q > k$.

O.6.1 $k_m \neq k_p$ and $k_n = k_q$

Consider Eq. (7.15):

$$I_1^{mp}(\mu : |\mu| > k) = -2\,\mathrm{i} \int\limits_{\lambda_1'}^{\infty} \frac{\left[1 - (-1)^m\ \mathrm{e}^{-ay}\right] \left|{\lambda_1'}^2 - y^2\right|^{1/2}}{\left(y^2 + k_m^2\right)\left(y^2 + k_p^2\right)}\, \mathrm{d}y,$$

where ${\lambda_1'}^2 = \mu^2 - k^2$. $I_1^{mp}(k_n : k_n > k)$ can be obtained from the above expression after substituting $\mu = k_n$. By neglecting the exponential term (which is small for large values of μ) and by changing the lower limit of integration to k we get [33, 34]

$$I_1^{mp}(k_n : k_n > k) \approx -2\,\mathrm{i} \int\limits_{k}^{\infty} \frac{\left|{\lambda_1'}^2 - y^2\right|^{1/2}}{\left(y^2 + k_m^2\right)\left(y^2 + k_p^2\right)}\, \mathrm{d}y,$$

where ${\lambda_1'}^2 = k_n^2 - k^2$. Using the approximation $\left|{\lambda_1'}^2 - y^2\right|^{1/2} \approx y$ (for $y : k \to \infty$) we get

$$I_1^{mp}(k_n : k_n > k) \approx -2\,\mathrm{i} \int\limits_{k}^{\infty} \frac{y}{\left(y^2 + k_m^2\right)\left(y^2 + k_p^2\right)}\, \mathrm{d}y.$$

Or

$$I_1^{mp}(k_n : k_n > k) \approx -\frac{\mathrm{i}\log\left(\frac{k^2+k_m^2}{k^2+k_p^2}\right)}{k_m^2 - k_p^2}. \tag{O.65}$$

O.6.2 $k_m = k_p$ and $k_n = k_q$

Consider Eq. (7.61):

$$I_1^{mp}(\mu : |\mu| > k) = -2\mathrm{i}\left[\frac{-\pi a\ \left|\lambda_1^2 - k_m^2\right|^{1/2}}{4\,k_m^2} + \int\limits_{\lambda_1'}^{\infty} \frac{\left[1 - (-1)^m\ \mathrm{e}^{-ay}\right] \left|{\lambda_1'}^2 - y^2\right|^{1/2}}{\left(y^2 + k_m^2\right)^2}\, \mathrm{d}y\right] \delta_{mp},$$

where $\lambda_1 = \mathrm{i}\lambda_1' = \mathrm{i}\,(\mu^2 - k^2)^{1/2}$. For $\mu = k_n$, the integral on the right hand side is approximated in the same fashion as before. And thus,

$$I_1^{mp}(k_n : k_n > k) \approx -2\,\mathrm{i}\left[\frac{-\pi a\,\left|\lambda_1^2 - k_m^2\right|^{1/2}}{4\,k_m^2} + \int\limits_k^\infty \frac{y}{(y^2 + k_m^2)^2}\,\mathrm{d}y\right]\,\delta_{mp}.$$

Or

$$I_1^{mp}(k_n : k_n > k) \approx \mathrm{i}\left[\frac{\pi a\,\left|k_m^2 + k_n^2 - k^2\right|^{1/2}}{2\,k_m^2} - \frac{1}{(k^2 + k_m^2)}\right]\,\delta_{mp}. \tag{O.66}$$

Appendix P

About the Kraichnan's assumption

We have the integral (from Eq. (7.4))

$$I^{mnpq} = 4 \int_0^\infty \int_0^\infty \frac{[1-(-1)^m \cos\lambda a]\,[1-(-1)^n \cos\mu b]\,\left(k^2-\lambda^2-\mu^2\right)^{1/2}}{\left(\lambda^2-k_m^2\right)\left(\lambda^2-k_p^2\right)\left(\mu^2-k_n^2\right)\left(\mu^2-k_q^2\right)}\,\mathrm{d}\lambda\,\mathrm{d}\mu. \quad \text{(P.1)}$$

Note that the limits are now from 0 to ∞. The function

$$I^{nq}(\mu) = \frac{[1-(-1)^n \cos\mu b]}{\left(\mu^2-k_n^2\right)\left(\mu^2-k_q^2\right)} \quad \text{(P.2)}$$

has a behavior as shown in Fig. P.1. It can be found that [33]

$$\int_0^\infty I^{nq}(\mu)\,\mathrm{d}\mu = \begin{cases} \frac{\pi b}{4k_n^2} & \text{if } k_n = k_q \\ 0 & \text{if } k_n \neq k_q. \end{cases} \quad \text{(P.3)}$$

Kraichnan used this behavior of the function $I^{nq}(\mu)$ to approximate it using a Dirac delta function. He used the following approximation [75]

$$\left.\frac{[1-(-1)^n \cos\mu b]}{\left(\mu^2-k_n^2\right)\left(\mu^2-k_q^2\right)}\right|_{n=q} = \frac{\pi b}{4k_n^2}\,\delta(\mu-k_n). \quad \text{(P.4)}$$

In this thesis, the above approximation is referred to as the Kraichnan's approximation. The integration (Eq. (P.1)) is lot more easier if we make this approximation in the outer integral (either over the λ domain or over the μ domain). Here, the Kraichnan's approximation is used in the integration over the μ domain. The modal interaction cases and hence the modal wavenumbers k_m, k_n, k_p and k_q are selected in such a way

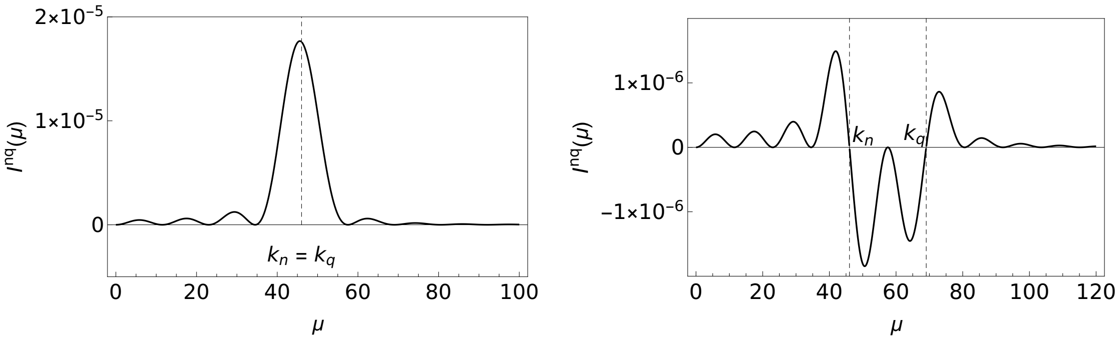

Fig. P.1 Plots of the function $I^{nq}(\mu)$ when $k_n = k_q$ and $k_n \neq k_q$ [33].

that we can make this approximation in the outer integral (μ domain), whenever the requirement arises. Before making the Kraichnan's assumption it has to be ensured that the modal wavenumbers k_n and k_q lie within the integral domain.

Using the above described behavior of $I^{nq}(\mu)$, one can assume that $I^{mnpq} \approx 0$ when $k_n \neq k_q$ for the Y edge - Y edge interaction. For the Y edge - Y edge interaction the integral I^{mnpq} is given by Eq. (7.16):

$$I^{mnpq} = 2\int_0^k \frac{[1-(-1)^n \cos \mu b]}{\left(\mu^2 - k_n^2\right)\left(\mu^2 - k_q^2\right)} I_1^{mp}(\mu : |\mu| < k)\,\mathrm{d}\mu + 2\int_k^\infty \frac{[1-(-1)^n \cos \mu b]}{\left(\mu^2 - k_n^2\right)\left(\mu^2 - k_q^2\right)} I_1^{mp}(\mu : |\mu| > k)\,\mathrm{d}\mu.$$

Here, $k_m, k_p > k$ and $k_n, k_q < k$. When $k_n = k_q$, we can use the Kraichnan's approximation to reduce the integral to

$$I^{mnpq} = \frac{\pi b}{2k_n^2} I_1^{mp}(k_n : k_n < k).$$

Here, by the Kraichnan's approximation and since $k_n < k$, only the contribution from the first integral on the right hand side of Eq. (7.16) is included. Since $k_n < k$, the value of the function $\frac{[1-(-1)^n \cos \mu b]}{(\mu^2 - k_n^2)^2}$ can be assumed to be negligible for $\mu > k$. This is true even when $k_n \neq k_q$, since $k_n, k_q < k$. It follows that when $k_n \neq k_q$ we can still approximate the integral I^{mnpq} including only the contribution from the first term on the right hand side of Eq. (7.16), i.e.,

$$I^{mnpq} = 2\int_0^k \frac{[1-(-1)^n \cos \mu b]}{\left(\mu^2 - k_n^2\right)\left(\mu^2 - k_q^2\right)} I_1^{mp}(\mu : |\mu| < k)\,\mathrm{d}\mu.$$

Since $k_n, k_q < k$ we can find that

$$\int_0^k \frac{[1-(-1)^n \cos \mu b]}{\left(\mu^2-k_n^2\right)\left(\mu^2-k_q^2\right)} \mathrm{d}\mu \approx 0$$

The integral $I_1^{mp}(\mu : |\mu| < k)$ is largely defined by the values of k_m and k_p ($k_m, k_p > k$). Hence, we can assume that I_1^{mp} does not vary much in the domain $\mu : 0 \rightarrow k$. Therefore, when $k_n \neq k_q$, we can approximate

$$I^{mnpq} \approx 0.$$

Note that to obtain the above approximation no direct substitution of the Kraichnan's assumption is made. The above approximation is obtained by making use of the cues which led to the Kraichnan's assumption.

Appendix Q

About the approximations used to obtain $I_1^{mp}(\mu)$

While deriving I^{mnpq} for different interactions, only the contributions from the dominant terms are considered. Approximations have been made in each case depending upon the range in which the panel modal wavenumbers k_m, k_n, k_p and k_p lie. In this section, some of these assumptions are discussed in detail.

Q.1 Y edge - Y edge

Approximation 1

The following approximation has been used in the Y edge - Y edge interaction case (using Eq. (O.2)):

$$\int_0^{\lambda_1} \underbrace{\frac{(-1)^{m+1}\sqrt{\lambda_1^2 - x^2}\cos ax}{\left(x^2 - k_m^2\right)\left(x^2 - k_p^2\right)}}_{t_1(x)} \mathrm{d}x \approx \int_0^{\lambda_1} \underbrace{\frac{(-1)^{m+1}\sqrt{\lambda_1^2 - x^2}\cos ax}{\left(k_m^2 - \lambda_1^2\right)\left(k_p^2 - \lambda_1^2\right)}}_{t_1^{\mathrm{approx}}(x)} \mathrm{d}x.$$

In the above equation $\lambda_1 = \sqrt{k^2 - k_n^2}$. The functions $t_1(x)$ and $t_1^{\mathrm{approx}}(x)$ for x varying from 0 to λ_1 are plotted in Fig. Q.1. For plotting, it is assumed that $a = 0.455$ m, $b = 0.546$ m, $m = 10$, $n = 3$, $p = 14$, $q = 3$ and air as the acoustic medium ($c = 343$ m/s). The functions are plotted at 1200 Hz. It can be observed that both the terms $t_1(x)$ and $t_1^{\mathrm{approx}}(x)$ have similar magnitudes in the range 0 to λ_1.

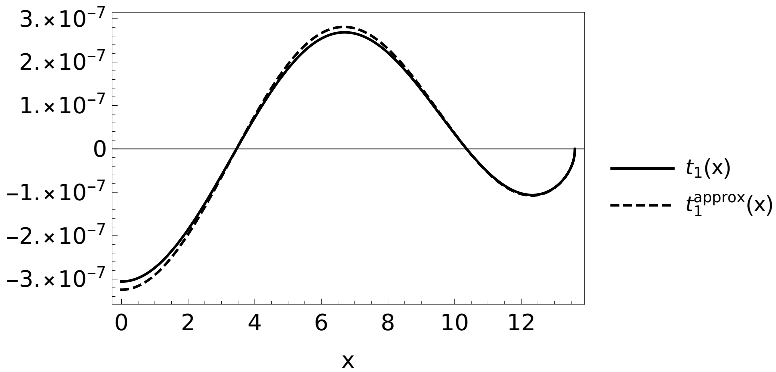

Fig. Q.1 Plots of the functions $t_1(x)$ and $t_1^{\text{approx}}(x)$ (Y edge - Y edge case).

Approximation 2

Consider the approximation

$$\int_0^k \underbrace{\frac{\sqrt{k^2 - k_n^2 + y^2}}{\left(k_m^2 + y^2\right)\left(k_p^2 + y^2\right)}}_{t_2(y)} \, \mathrm{d}y \approx \int_0^k \underbrace{\frac{\sqrt{k^2 - k_n^2 + y^2}}{k_m^2 k_p^2}}_{t_2^{\text{approx}}(y)} \, \mathrm{d}y,$$

which has been used while evaluating $T_3^1(k_n)$.

The functions $t_2(y)$ and $t_2^{\text{approx}}(y)$ for y varying from 0 to k are plotted in Fig. Q.2. The parameter values used are the same as that for the Approximation 1, above. It can be observed that the above approximation is satisfactory.

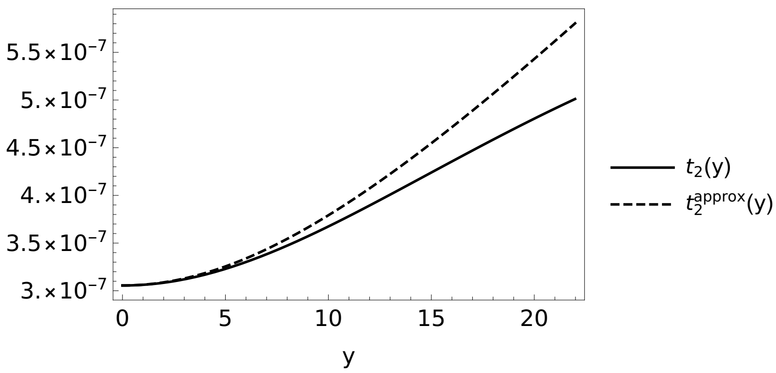

Fig. Q.2 Plots of the functions $t_2(y)$ and $t_2^{\text{approx}}(y)$ (Y edge - Y edge case).

Approximation 3

Consider the following approximation which has been used while evaluating $T_3^1(k_n)$:

$$\int_k^\infty \underbrace{\frac{\sqrt{k^2-k_n^2+y^2}}{\left(k_m^2+y^2\right)\left(k_p^2+y^2\right)}}_{t_3(y)}\,\mathrm{d}y \approx \int_k^\infty \underbrace{\frac{y}{\left(k_m^2+y^2\right)\left(k_p^2+y^2\right)}}_{t_3^{\text{approx}}(y)}\,\mathrm{d}y.$$

The functions $t_3(y)$ and $t_3^{\text{approx}}(y)$ for y varying from k to ∞ are plotted in Fig. Q.3. The parameter values used are the same as that for the Approximation 1. As seen from the figure, the above approximation holds good for the selected parameter range.

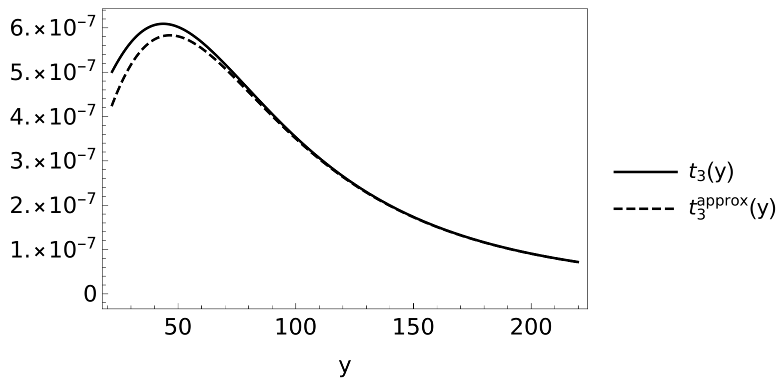

Fig. Q.3 Plots of the functions $t_3(y)$ and $t_3^{\text{approx}}(y)$ (Y edge - Y edge case).

Approximation 4

The following first order approximation (Eq. (O.9)) has been used while evaluating $T_3^2(k_n)$:

$$\mathrm{e}^{-ay} \approx \begin{cases} 1-ay & \text{when } ay<1 \\ 0 & \text{when } ay \geq 1. \end{cases}$$

This approximation has led to

$$\int_k^\infty \frac{(-1)^{m+1}\mathrm{e}^{-ay}\sqrt{k^2-k_n^2+y^2}}{\left(k_m^2+y^2\right)\left(k_p^2+y^2\right)}\,\mathrm{d}y \approx 0$$

with the assumption that $ak>\pi$. This assumption does not allow a mode with $m=1$ to be a Y edge mode (for $m=1$ to become a Y edge mode $k_m=\pi/a>k$ or $ak<\pi$). However, the frequencies at which a mode with $m=1$ would qualify to be a Y edge mode (decided by $ak<\pi$), the radiation is dominated by the corner modes. In such situations, the contribution from those Y edge modes with $m = 1$ can be neglected. This assumption ($ak > \pi$) can be used for all the interactions involving edge, two-edge and acoustically fast modes; but, not for the corner - corner modal interaction.

Q.2 AF - Y edge

Approximation 1

In the AF - Y edge interaction case, the integral $T_1(\mu : \mu = k_n)$ is given by

$$T_1(\mu : \mu = k_n) = \mathrm{P}_{k_m} \int_0^{\lambda_1} \underbrace{\frac{\left|\lambda_1^2 - x^2\right|^{1/2}}{\left(x^2 - k_m^2\right)\left(x^2 - k_p^2\right)}}_{t_1(x)} \, \mathrm{d}x$$

$$+ \mathrm{P}_{k_m} \int_0^{\lambda_1} \underbrace{\frac{-(-1)^m \cos ax \left|\lambda_1^2 - x^2\right|^{1/2}}{\left(x^2 - k_m^2\right)\left(x^2 - k_p^2\right)}}_{t_2(x)} \, \mathrm{d}x.$$

In the above equation $\lambda_1 = \sqrt{k^2 - k_n^2}$. The functions $t_1(x)$ and $t_2(x)$ for x varying from 0 to λ_1 are plotted in Fig. Q.4. For plotting, it is assumed that $a = 0.455$ m, $b = 0.546$ m, $m = 10$, $n = 2$, $p = 12$, $q = 2$ and $c = 343$ m/s. The functions are plotted at 6000 Hz. As shown in the figure, there exists a singularity at $x = k_m$ for both $t_1(x)$

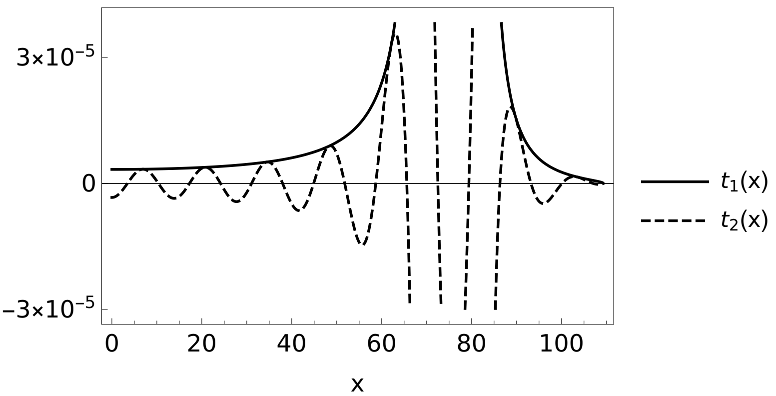

Fig. Q.4 Plots of the functions $t_1(x)$ and $t_2(x)$ (AF - Y edge case).

and $t_2(x)$. Nevertheless, the dominant contribution towards $T_1(\mu : \mu = k_n)$ is from $t_1(x)$. The term $t_1(x)$ is integrated without making any approximations. However, while integrating $t_2(x)$, the following approximation is used:

$$\mathrm{P}_{k_m} \int_0^{\lambda_1} \underbrace{\frac{-(-1)^m \cos ax \left|\lambda_1^2 - x^2\right|^{1/2}}{\left(x^2 - k_m^2\right)\left(x^2 - k_p^2\right)}}_{t_2(x)} \mathrm{d}x \approx \mathrm{P}_{k_m} \int_0^{\lambda_1} \underbrace{\frac{-(-1)^m \cos ax \left|\lambda_1^2 - x^2\right|^{1/2}}{\left(\lambda_1^2 - k_m^2\right)\left(\lambda_1^2 - k_p^2\right)}}_{t_2^{\mathrm{approx}}(x)} \mathrm{d}x.$$

The functions $t_2(x)$ and $t_2^{\mathrm{approx}}(x)$ are plotted in Fig. Q.5. It is clear from the figure

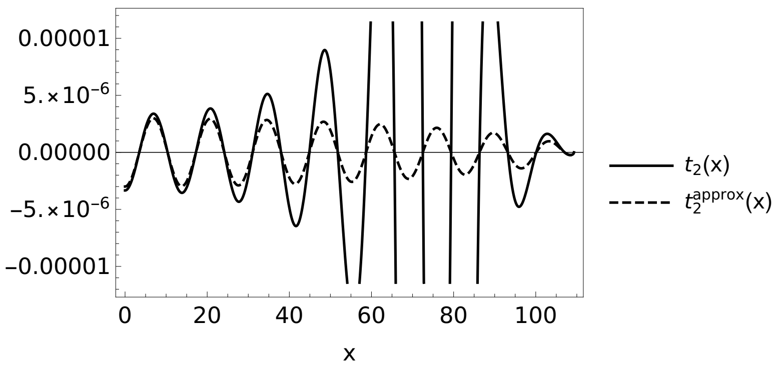

Fig. Q.5 Plots of the functions $t_2(x)$ and $t_2^{\mathrm{approx}}(x)$ (AF - Y edge case).

that $t_2^{\mathrm{approx}}(x)$ underestimates $t_2(x)$ near the singularity. However, as the contribution from the term $t_2(x)$ itself is small as compared that from $t_1(x)$, this approximation can still be used.

Approximation 2

Consider the approximation

$$\int_0^{k} \underbrace{\frac{\sqrt{k^2 - k_n^2 + y^2}}{\left(k_m^2 + y^2\right)\left(k_p^2 + y^2\right)}}_{t_3(y)} \mathrm{d}y \approx \int_0^{k} \underbrace{\frac{\sqrt{k^2 - k_n^2 + y^2}}{\left(k_m^2 + y^2\right) k_p^2}}_{t_3^{\mathrm{approx}}(y)} \mathrm{d}y,$$

which has been used while evaluating $T_3^1(k_n)$.

The functions $t_3(y)$ and $t_3^{\mathrm{approx}}(y)$ for y varying from 0 to k are plotted in Fig. Q.6. The parameter values used are the same as that for the Approximation 1, above. As shown in the figure, the above approximation is satisfactory in the range $(0, k)$.

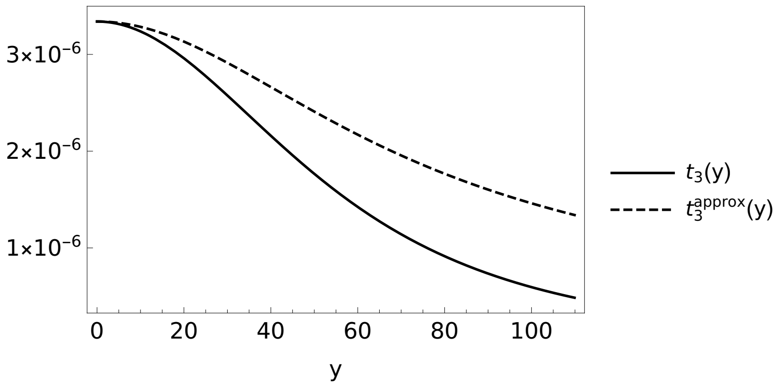

Fig. Q.6 Plots of the functions $t_3(y)$ and $t_3^{\text{approx}}(y)$ (AF - Y edge case).

Approximation 3

Consider the following approximation which has been used while evaluating $T_3^1(k_n)$:

$$\int_k^\infty \underbrace{\frac{\sqrt{k^2 - k_n^2 + y^2}}{\left(k_m^2 + y^2\right)\left(k_p^2 + y^2\right)}}_{t_4(y)} \mathrm{d}y \approx \int_k^\infty \underbrace{\frac{y}{\left(k_m^2 + y^2\right)\left(k_p^2 + y^2\right)}}_{t_4^{\text{approx}}(y)} \mathrm{d}y.$$

The functions $t_4(y)$ and $t_4^{\text{approx}}(y)$ for y varying from k to ∞ are plotted in Fig. Q.7. The parameter values chosen are the same as that for the Approximation 1. As is shown in the figure, t_4^{approx} is a good approximation for $t_4(x)$.

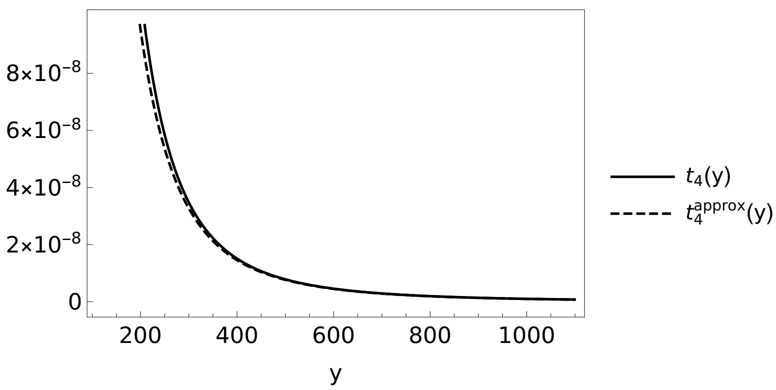

Fig. Q.7 Plots of the functions $t_4(y)$ and $t_4^{\text{approx}}(y)$ (AF - Y edge case).

Q.3 Y edge - corner

While evaluating $I_1^{mp}(\mu : |\mu| < k)$, it has been assumed that the contributions from the oscillatory $\cos ax$ and $\sin ax$ terms are negligible. The contribution from the exponential term of $I_1^{mp}(\mu : |\mu| < k)$ has also been neglected. Rewriting Eq. (7.13)

$$I_1^{mp}(\mu : |\mu| < k)$$
$$= 2\left[\int_0^{\lambda_1} \underbrace{\frac{\left|\lambda_1^2 - x^2\right|^{1/2}}{\left(x^2 - k_m^2\right)\left(x^2 - k_p^2\right)}}_{t_1(x)} \mathrm{d}x + \int_0^{\lambda_1} \underbrace{\frac{(-1)^{m+1} \cos ax \left|\lambda_1^2 - x^2\right|^{1/2}}{\left(x^2 - k_m^2\right)\left(x^2 - k_p^2\right)}}_{t_2(x)} \mathrm{d}x\right]$$
$$- 2\,\mathrm{i}\left[\int_0^{\lambda_1} \underbrace{\frac{(-1)^m \sin ax \left|\lambda_1^2 - x^2\right|^{1/2}}{\left(x^2 - k_m^2\right)\left(x^2 - k_p^2\right)}}_{t_3(x)} \mathrm{d}x + \int_0^{\infty} \underbrace{\frac{\left[1 - (-1)^m \,\mathrm{e}^{-ay}\right] \left|\lambda_1^2 + y^2\right|^{1/2}}{\left(y^2 + k_m^2\right)\left(y^2 + k_p^2\right)}}_{t_4(y)} \mathrm{d}y\right].$$

We know that for the Y edge - corner interaction, $k_m, k_p, k_q > k$ and $k_n < k$. In the above equation $\lambda_1 = \sqrt{k^2 - k_n^2}$. The behavior of each integrand for a typical Y edge - corner interaction is plotted in Fig. Q.8. For plotting, it is assumed that $a = 0.455$ m, $b = 0.546$ m, $m = 4$, $n = 2$, $p = 6$, $q = 10$ and $c = 343$ m/s. The function variations are recorded at 1450 Hz.

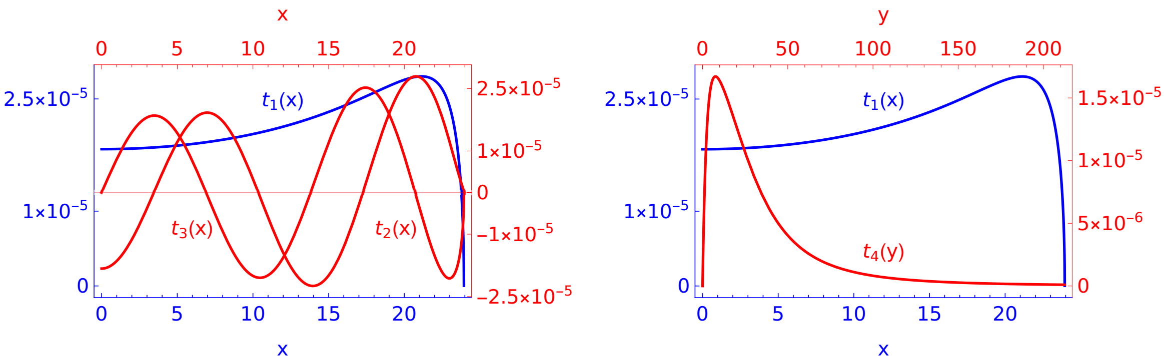

Fig. Q.8 Comparative plots of the functions $t_1(x), t_2(x), t_3(x)$ and $t_4(y)$ when $k_m, k_p, k_q > k$ and $k_n < k$.

It is observed that the terms $t_2(x)$ and $t_3(x)$ have magnitudes of the same order of $t_1(x)$. However, due to the oscillatory nature of these terms their contribution to the integral I_1^{mp} is negligible as compared to that from $t_1(x)$. It is also observed that due to the exponential function and the large values of k_m and k_p, $t_4(y)$ decays rapidly. Hence, one can neglect the contribution from $t_4(y)$ term towards $I_1^{mp}(\mu)$. Thus, the integral $I^{mp}(\mu : |\mu| < k)$ can be approximated as

$$I_1^{mp}(\mu : |\mu| < k) \approx 2 \int_0^{\lambda_1} \frac{\left|\lambda_1^2 - x^2\right|^{1/2}}{\left(x^2 - k_m^2\right)\left(x^2 - k_p^2\right)} \, \mathrm{d}x.$$

List of publications

Journal publications

1. Anoop Akkoorath Mana and Venkata R. Sonti. Sound radiation from a perforated panel set in a baffle with a different perforation ratio. *Journal of Sound and Vibration*, 372:317-341, 2016.

2. Anoop Akkoorath Mana and Venkata R. Sonti. Sound transmission through a finite perforated panel set in a rigid baffle: A fully coupled analysis. *Journal of Sound and Vibration*, 414:126-156, 2018.

3. Anoop Akkoorath Mana and Venkata R. Sonti. Sound radiation from a finite perforated panel set in a rigid baffle: A fully coupled analysis. *Wave Motion*, 85:144-164, 2019.

4. Anoop Akkoorath Mana and Venkata R. Sonti. Closed form expressions for the modal coupling coefficients of a fluid-loaded perforated panel (under preparation).

Conference publications

1. Anoop Akkoorath Mana, Venkata R. Sonti and Tulesh Kumar. A 2-D wavenumber domain formulation for the radiation efficiency of a perforated piston fixed in a baffle with an arbitrary perforation ratio. *Proceedings of The 22nd International Congress on Sound and Vibration*, Florence, Italy, 2015.

2. Anoop Akkoorath Mana and Venkata R. Sonti. Radiation efficiency of a perforated panel fixed in a baffle with an arbitrary perforation ratio. *Proceedings of the National Symposium on Acoustics*, Goa, India, 2015.